2011

A quantitative method for reproducible ionization chamber alignment to a water surface for external beam radiation therapy depth dose measurements

James Ververs
Virginia Commonwealth University

A quantitative method for reproducible ionization chamber alignment to a water surface for external beam radiation therapy depth dose measurements

A thesis dissertation submitted in partial fulfillment of the requirements for the degree of Doctor of Philosophy at Virginia Commonwealth University.

by

James Douglas Ververs
Bachelor of Science, University of Rochester, May 2006
Bachelor of Arts, University of Rochester, May 2006

Director: Jeffrey V. Siebers, Ph.D.
Professor and Director, Medical Physics Graduate Program
Department of Radiation Oncology

Virginia Commonwealth University
Richmond, Virginia
December, 2011

Acknowledgements

There are many people besides myself who have contributed to the completion of this project. First, I would like to thank my thesis advisor, Dr. Jeffrey Siebers, for his guidance and patience. No matter how much of the former I needed or how little of the latter I deserved, you were always there. It has been an honor to work for and with you. I thank my thesis committee, Dr. Geoffrey Hugo, Dr. Paul Keall, and Dr. Malcolm McEwen, for their insight and assistance with this project. I additionally thank Dr. Keall along with Dr. Sonja Dieterich and Dr. Lei Wang for arranging my visit to Stanford University and assisting with CyberKnife data collection. I also thank Dr. McEwen and Dr. Frédéric Tessier for their invaluable assistance and making me feel like a true colleague during my visit to the Ionizing Radiation Standards lab at the National Research Council of Canada in Ottawa. I thank my colleagues in the Department of Radiation Oncology at Virginia Commonwealth University for all of the help and friendly advice they have provided me. I also thank Dr. Sally Hunnicutt in the VCU Department of Chemistry for allowing me to borrow the capillary tube for the surface tension measurements. I thank Dan Schmidt and Eric DeWerd at Standard Imaging, Gerry Vantellingen at IBA Dosimetry, and Dr. Christian Pychlau and Dr. Edmund Schüle at PTW Dosimetry for loaning the ionization chambers used in this study.

My family taught me to work and motivated me to do my best without ever pushing too hard. I spent my whole life in Upstate New York until moving to Richmond for graduate school.

I know it wasn't easy to see me move away but I couldn't have done it without the strength you gave me. Erica Johnson has done more for me in the last two years than she could possibly know. Not many women would accept a finished thesis as an anniversary present.

This thesis is dedicated to the memory of Deborah Pluta. If not for the battle she lost against breast cancer, I doubt I would be trying to make my career in radiation therapy physics. I hope that this thesis does her memory proud.

Table of Contents

List of Tables

List of Figures

List of Abbreviations

AAPM	American Association of Physicists in Medicine
CSDA	Continuous slowing-down approximation
DeICERS	Depth where a cavity ionization chamber proximal edge reaches the water surface
d_{max}	Depth of maximum dose
EGSnrc	Electron Gamma Shower code package from National Research Council of Canada
EPOM	Effective point of measurement
GeV	Giga-electron volts (electron volts × 10^9)
GUI	Graphical user interface
IAEA	International Atomic Energy Agency
IC	Cavity ionization chamber
ICRU	International Commission on Radiation Units and Measurements
keV	Kilo-electron volts (electron volts × 10^3)
MC	Monte Carlo
MeV	Mega-electron volts (electron volts × 10^6)
MV	Megavolts (volts × 10^6)
NIST	National Institute of Standards and Technology
NRC	National Research Council of Canada

PDD	Percent depth-dose
PMMA	Poly-methyl methacrylate
QA	Quality assurance
r_{cav}	Cylindrical cavity ionization chamber inner radius; cavity radius
r_{max}	Maximum range in medium of charged particles originating from outside the medium
rms	Root mean squared
SSD	Source-to-surface distance
SSQD	Sum of squared differences
TG	Task Group Report
TPS	Treatment planning system
TRS	Technical Report Series
VCU	Virginia Commonwealth University

Abstract

A QUANTITATIVE METHOD FOR REPRODUCIBLE IONIZATION CHAMBER ALIGNMENT TO A WATER SURFACE FOR EXTERNAL BEAM RADIATION THERAPY DEPTH DOSE MEASUREMENTS

By James Douglas Ververs, B.S., B.A.

A dissertation submitted in partial fulfillment of the requirements for the degree of Doctor of Philosophy at Virginia Commonwealth University.

Virginia Commonwealth University, 2011.

Major Director: Jeffrey V. Siebers, Ph.D.
Professor and Director, Medical Physics Graduate Program
Department of Radiation Oncology

Ionization chambers (ICs) are the most commonly used detectors for radiation therapy dose measurements. Typical IC measurements use cylindrical ICs in a water phantom and therefore require initial IC alignment to the water surface. This alignment has long been ignored and only recently has a qualitative governing recommendation been made. This thesis describes a reproducible methodology for quantitative ionization chamber water surface alignment. Depth-ionization measurements are taken with twenty-eight IC designs under varying conditions including, but not limited to, changes in scan direction, speed, and resolution, radiation beam type, field size, energy, and electron contamination. Measurements are acquired using standard radiotherapy accelerators in the Virginia Commonwealth University Department of Radiation Oncology and at the National Research Council of Canada, where a customized scanning system capable of better than 0.15 mm IC positioning precision is used. Measurements are also

performed with standard commercial scanning equipment on the Accuray CyberKnife, a specialized radiosurgery-class accelerator. An analytical model is developed from basic principles to test the theoretical foundations of IC response near a water surface. The theoretical foundation is further validated via Monte Carlo simulation models that fully account for all details of the ICs used to take measurements. It is determined that the dose gradient as a function of depth is maximized when a given IC reaches the water surface when moving from depth in water. This effect is unchanged under all of the measurement scenarios tested. Measurements taken at 0.1 mm resolution for several seconds per point over several millimeters near the surface will yield a gradient peak that can be used for quantitative alignment. Using developed software, multiple scans at variant resolutions can be stitched into typical clinical scans so as not to significantly affect clinical measurement workflow. The recommended measurement method is developed in a format suitable for inclusion into a clinical protocol for depth-ionization measurement acquisition.

1 Introduction

External beam radiation therapy can be delivered no more accurately than the accuracy of the measurements on which treatments are based. The most ubiquitous measurements in radiation therapy calibration and quality assurance (QA) are of percent depth dose (PDD) and accelerator output. These measurements are used as the basis for treatment planning system (TPS) dose calculations, which are used to prescribe treatment dose and define the shape of the three-dimensional dose distribution. Calibration and QA measurements are performed in water, which serves as a surrogate for human tissue. The coordinate system in which measurements are performed must be established by alignment of the measurement device, typically a cavity ionization chamber (IC), to a well-defined point. Typical alignment to the water surface is done qualitatively by eye, making this alignment prone to inconsistencies between users and measurement setups, if not gross errors. This thesis improves IC alignment from a qualitative "best guess" to a quantitative evaluation, allowing deviations to be detected and corrected.

1.1 Ionization Chamber Fundamentals

ICs are the most commonly used detectors for radiation therapy dose measurements (Attix, 1986). In the following sub-sections, basic aspects of IC design and the fundamentals of IC response are described.

1.1.1 Design

The two IC types used in this work are cylindrical ICs and parallel-plate ICs. Cylindrical ICs are alternatively referred to as thimble ICs. A schematic of a generic cylindrical IC is shown

in Figure 1. A parallel-plate IC schematic is given in Figure 2. Parallel-plate ICs are sometimes referred to as plane-parallel ICs or, more colloquially, "pancake" ICs. Both types contain outer coating (wall/entrance window), a collecting electrode, and an air gap between the two. Each design also contains a guard ring and insulating material. The guard ring serves to define the electric field shape within the IC cavity and to intercept leakage currents. The insulator is used to minimize leakage currents and to support the collecting electrode, guard ring, and outer coating structurally. Detailed reviews of IC design specifics can be found in other references (Attix, 1986; DeWerd *et al.*, 2009).

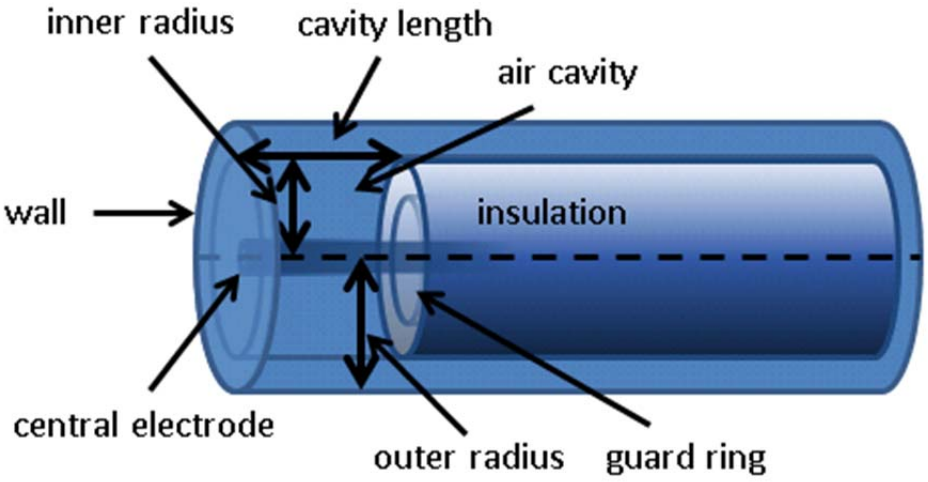

Figure 1: Schematic of a cylindrical IC. Wall parameters for the cylindrical ICs used in this work are given in Table 2. Central electrode parameters for the cylindrical ICs used in this work are found in Table 3. The central electrode is also referred to as the collecting electrode. Table 4 contains the air cavity parameters and outer diameters of the cylindrical ICs used in this work. The cylindrical IC outer radius is equal to the inner radius plus the wall thickness. In this alignment, a radiation beam would be incident from the top of the page.

Based on the volume of the given IC, cylindrical ICs are classified into three main types: micro-ICs, scanning ICs, and Farmer-type ICs. Micro-ICs are the smallest types, generally of volume ≤ 0.05 cm^3, best suited for measurements of small fields, such as those used for stereotactic applications or from non-standard accelerators such as CyberKnife (Accuray, Inc., Sunnyvale, CA) or Tomotherapy (Tomotherapy, Inc., Madison, WI). Scanning ICs are of

volume 0.1-0.3 cm^3 and are commonly used for standard water tank QA measurements (depth doses and profiles) with standard radiation therapy-class accelerators. Farmer-type ICs are named in reference to the inventor of the classic Farmer IC, which is a ~0.6 cm^3 volume cylindrical IC of pure graphite outer wall electrode and pure aluminum central electrode (Aird and Farmer, 1972).

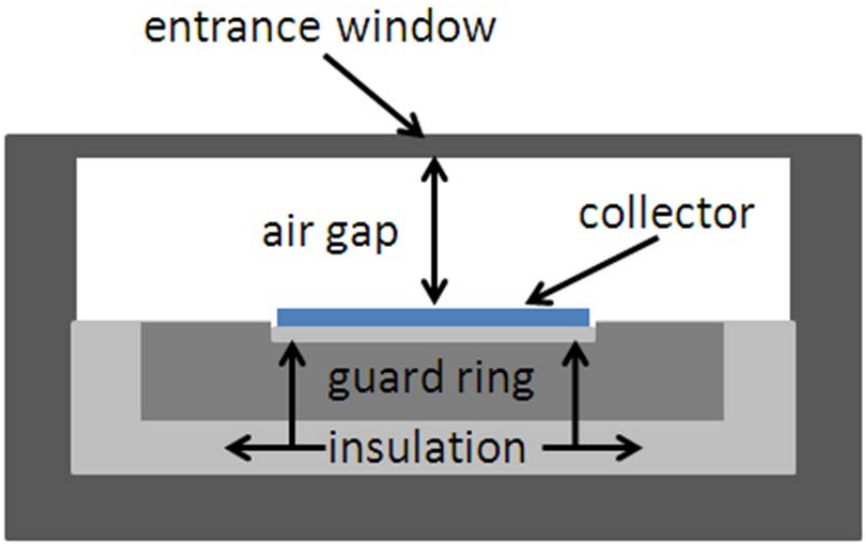

Figure 2: Schematic of a parallel-plate IC. Entrance window parameters for the parallel-plate ICs used in this work are listed in Table 5. Table 6 shows the guard ring and sensitive air volume parameters for the parallel-plate ICs used in this work. The branched arrows are used to indicate that insulation not only exists between the guard ring and wall but also between the guard ring and collector electrode. In this alignment, a radiation beam would be incident from the top of the page.

1.1.2 Response

ICs are frequently used for radiation therapy dose measurements largely because of the ease with which a given IC measurement can be converted into radiation dose to water. Absorbed dose to water is the current calibration standard recommended by reference dosimetry protocols such as American Association of Physicists in Medicine (AAPM) Task Group Report 51 (TG-51) (Almond *et al.*, 1999) and International Atomic Energy Agency (IAEA) Technical Report Series No. 398 (TRS-398) (Andreo *et al.*, 2001). Absorbed dose can be defined as energy deposited per unit mass of the material in which energy is deposited $\frac{dE}{dm}$, given

in units of $\frac{J}{kg}$, which is called the gray (Gy). The absorbed dose to a gas D_g of mass m in which charge Q is produced by radiation, is written as

$$D_g = \frac{Q}{m}\left(\overline{\frac{W}{e}}\right)_g$$

Here, $\left(\overline{\frac{W}{e}}\right)_g$ is the mean energy expended per unit charge produced within the gas. The subscript g indicates that this term is a function of the gas. For dry air, $\left(\overline{\frac{W}{e}}\right)_{air} = 33.97\ J/C$ (Boutillon and Perroche-Roux, 1987).

The charge in the gas is predominantly produced by the fluence of charged particles crossing the gas volume. Fluence is given by $\Phi = \frac{dN_e}{da}$, where N_e is the expectation value of the number of rays N that will strike the differential area element da. When the gas is contained in a cavity that is small enough to not disturb the charged particle fluence, i.e., all charged particles are able to cross the cavity, the dose to the gas cavity can be related to the dose to the surrounding medium in which charged particles are produced by the ratio of the respective average mass collision stopping powers:

$$\frac{D_w}{D_g} = \frac{{}_m\bar{S}_w}{{}_m\bar{S}_g} = \bar{S}_g^w$$

Here, D_g represents dose to the gas cavity and D_w represents dose to the medium in which charged particles are produced. The average mass collision stopping power of the gas is represented by ${}_m\bar{S}_g$ and the average mass collision stopping power of the medium is given as ${}_m\bar{S}_w$. The mass collision stopping power ratio is given in shorthand as $\bar{S}_g^w$. Stopping power is defined as the expectation value of the energy loss rate per pathlength unit x by charged particle

type Y of kinetic energy T in medium of atomic number Z, $\left(\frac{dT}{dx}\right)_{Y,T,Z}$ (Attix, 1986). Mass stopping power is obtained by dividing stopping power by the density of the stopping medium, yielding $S = \frac{dT}{\rho dx}$, most commonly given in units of $\frac{MeV}{g/cm^2}$. Mass collision stopping power is the part of the total mass stopping power due to Coulomb-force interactions with the nuclei and bound atomic electrons of the medium (Attix, 1986). These Coulomb-force interactions, or "collision" interactions, result in secondary electron production or local energy deposition. The average mass collision stopping power is obtained by averaging the mass collision stopping powers over the energy spectrum of the charged particles that cross the cavity. Stopping powers for electrons, protons, and helium ions for a range of materials have been tabulated and posted online by the Ionizing Radiation Standards group at National Institute of Standards and Technology (NIST) (Berger *et al.*, 2006). Additional information related to and values of electron stopping power are the subject of International Commission on Radiation Units and Measurements (ICRU) Report 37 (International Commission on Radiation Units and Measurements, 1984). Given the equalities above, dose to medium can be related to the charge produced in the gas cavity by

$$D_w = \frac{Q}{m}\left(\frac{\overline{W}}{e}\right)_g \bar{S}_g^w$$

Cavities for which the above relations hold true are called Bragg-Gray cavities. The ICs used in this thesis are specifically designed to behave as closely as possible to simple Bragg-Gray cavities in megavoltage radiation beams such that the above assumptions and formalism hold true. The validity of the Bragg-Gray assumptions with regard to the ICs used in this thesis can be demonstrated by considering a ^{60}Co source. Decay of ^{60}Co produces photons of energies $E_\gamma = 1.17\ MeV$ and $E_\gamma = 1.33\ MeV$ in equal probabilities. The average photon energy is then

$\bar{E}_\gamma = 1.25\ MeV$. In the therapeutic energy range, photons interact with matter predominantly through Compton scattering (Attix, 1986). In the case of 1.25 MeV photons interacting with water, 99.9% of interactions occur through Compton scattering and 0.1% occur through Rayleigh scattering. Photoelectric interactions and pair production are insignificant at the 0.1% level. Interaction coefficients have been tabulated and posted online by NIST (Berger *et al.*, 1998). The average energy of a free electron emitted via Compton scattering is given by

$$\bar{E}_{e^-} = \bar{E}_\gamma \left(\frac{\sigma_e^{tr}}{\sigma_e} \right)_{\bar{E}_\gamma}$$

In this equation, σ_e represents the total Klein-Nishina cross section, which can be thought of as the fraction of the total photon energy fluence that is lost from the primary incident photon beam via Compton scattering when passing through a given layer of material. Remembering the definition of fluence from above, energy fluence is simply the total energy summed from the rays striking some area element $\Psi = \int_0^{E_{max}} E\Phi(E)dE = E\frac{dN_e}{da}$. The Klein-Nishina energy-transfer cross section is denoted as σ_e^{tr}, which represents the energy fluence fraction that is transferred to the Compton recoil electrons when a photon beam passes through material. By these definitions, it follows that the ratio of the two, $\frac{\sigma_e^{tr}}{\sigma_e}$, represents the average fraction of incident photon energy passed to recoil electrons. Klein-Nishina cross-sections are tabulated as Appendix D.1 of *Introduction to Radiological Physics and Radiation Dosimetry* by F. H. Attix (Attix, 1986). In the case being considered, a 1.25 MeV photon yields an average of 0.588 MeV to a Compton electron.

Inherently included in the above discussion of stopping power is the idea that charged particles lose kinetic energy as they travel through matter. Charged particles interact with the majority of atoms by which they pass as they travel through any material (Attix, 1986). It is

therefore generally approximated that charged particles interact with matter continuously, and in turn lose kinetic energy continuously. This approximation is referred to as the "continuous slowing-down approximation" (CSDA). It is convenient here to define the range of a charged particle, the expectation value of the distance a charged particle of a given type and energy will travel in a given material before coming to rest. Under the CSDA, charged particle range is written mathematically as

$$R_{CSDA} \equiv \int_0^{T_0} \left(\frac{dT}{\rho dx}\right)^{-1} dT$$

where T_0 is the incident particle initial energy, and $\frac{dT}{\rho dx}$ is the mass stopping power, as described above. Charged particle ranges are also tabulated and posted online by NIST with the aforementioned stopping powers (Berger *et al.*, 2006). Following the CSDA approximation, since $\frac{dT}{\rho dx} \approx constant$, the average electron energy while slowing down can be approximated as $(\bar{E}_{e^-})_{CSDA} = \frac{\bar{E}_{e^-}}{2}$. Starting from the nominal 1.25 MV photon of the example yields an average electron energy of 0.294 MeV. The in-air range of a 0.294 MeV electron is 76.88 cm. The largest cavity in any of the ICs used in this thesis is 0.95 cm thick, which represents 1.22% of the nominal range of the electrons that will cross the cavity when irradiated. This percentage will only decrease with increased incident photon energy, thinner IC cavities, or the use of an incident electron beam. Hence, the condition that a Bragg-Gray cavity cannot disturb the charged particle fluence can be considered satisfied by the ICs used in this thesis.

The second Bragg-Gray condition requires that dose is contributed solely by the charged particles crossing the cavity, i.e., photon interactions within the cavity contribute no dose. In contrast with charged particles, photons interact very rarely when passing through matter. The

photon interaction rate is governed by exponential attenuation and the mass attenuation coefficient. This is written mathematically as

$$N = N_0 e^{-\frac{\mu}{\rho}\rho t}$$

Here, N represents the number of photons remaining from initial quantity N_0 after passing through some material of thickness t and density ρ. The quantity $\frac{\mu}{\rho}$ is the mass attenuation coefficient, a material property that describes the intensity loss in the initial narrow photon beam (Attix, 1986). Given these definitions, the quantity $\frac{N}{N_0} = e^{-\frac{\mu}{\rho}\rho t}$ represents the fraction of photons that will not interact within a thickness t of a medium of density ρ. It then follows that the quantity $1 - \frac{N}{N_0} = 1 - e^{-\frac{\mu}{\rho}\rho t}$ represents the fraction of photons that will interact. The Ionizing Radiation Standards group in the Physics Laboratory at NIST has also tabulated and posted online mass attenuation coefficients for a variety of materials (Hubbell and Seltzer, 2004).

Continuing with the example of a fluence of 1.25 MeV photons passing through a 0.95 cm thick air cavity, the probability of photon interaction within the air cavity is 6.51×10^{-5}. If this is compared with the probability of photon interaction within the thinnest wall of any IC used in this thesis, which consists of 0.0335 cm thick poly-methyl methacrylate (PMMA) and 0.009 cm thick graphite, photon interaction within the wall is over 52 times more likely. Photon interactions within the IC wall will yield electrons that will cross the cavity and deposit dose. Electrons generated in water at distances smaller than r_{max} will also cross the IC cavity and deposit dose with a probability of 1, as IC walls are machined to be thinner than the range of incident electrons. Thus, it is justifiably assumed that dose is contributed much more so by charged particles than by photons crossing the cavities of the ICs used in this thesis.

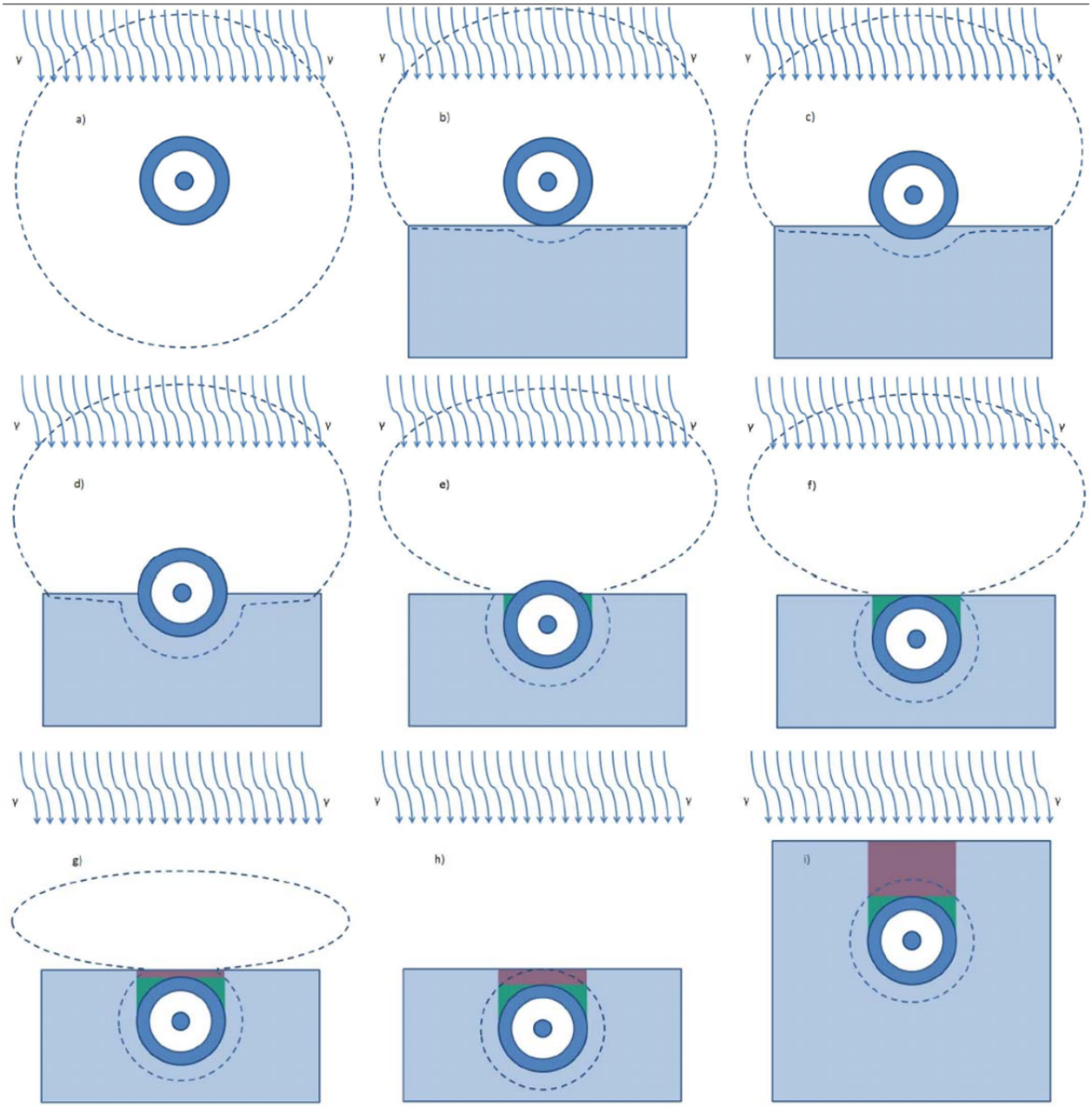

Figure 3: Dashed lines denote regions from which secondary electrons contribute to measured ionization. Panels are not intended to be to scale, except in relative comparison with one another. The wavy lines in each panel denote the direction of incident radiation but are not intended to show proximity to the water surface. Panel a) shows a cylindrical IC in air. In b), water is introduced below the IC, contributing backscattered electrons. As the IC descends into the water in panels c) and d), the water backscatter increases and the contribution from air decreases. In e), the IC is more than halfway into the water, where differential water buildup (green) increases electron fluence. In this panel, the buildup is not yet directly over the inner cavity, so the scattered contribution here will be small. In f), the IC has descended fully into the water and the differential buildup is maximized. Note that in panels e) and f), the change in the amount of water buildup as a function of depth is not constant. Panel g) shows the IC receiving additional constant water buildup (red) as it is positioned deeper in water. Panel h) shows the constant buildup and the differential buildup at greater depth, with the IC located where electrons from air no longer reach the IC cavity. In panel i), the IC is below the maximum range of the electrons produced in air, r_{max}, and is only receiving contributions from electrons produced within the IC wall and in water. The electronic disequilibrium illustrated in panels b)-h) gives rise to the buildup region in photon depth dose measurements and is largely why making accurate measurements in this region is so difficult.

Given that dose is predominantly contributed by charged particles, which have defined ranges, it is straightforward to determine a region around a given IC within which charged particles will potentially contribute to the measured dose. This is illustrated for a series of measurement scenarios in Figure 3. If an IC is used to measure dose from a megavoltage photon beam in air, as in panel a), contributing electrons will originate from the IC wall, the surrounding air, and the linear accelerator treatment head where the beam is produced. With a water tank behind the IC, as illustrated in panel b), electrons backscattered from the water will cross the IC cavity to contribute dose but the measured dose will still be dominated by electrons produced in the air, treatment head, and IC wall. If the IC is then moved into the water tank, the relative contribution by scattered electrons produced within the water will increase. This is illustrated in panels c) and d). When the IC is mostly submerged, such that the inner cavity is at or below the water surface, the differential amount of water above the cavity will increase the electron fluence incident on the cavity. In this region, illustrated in panels d), e), and f), the change in the amount of water above the cavity and the accompanying electron fluence varies as a function of depth. When the IC has descended fully beneath the water surface, the amount of water above the IC will increase constantly as a function of depth. Neglecting primary photon attenuation and the limited range of secondary electrons, this constant increase will cause the change in electron fluence to also be constant as a function of depth in this region, illustrated in panels g)-i). The water above the IC will also serve to attenuate the primary photon beam, though this effect is small. Panel h) illustrates the IC positioned at a depth equal to the maximum range in water of the electrons produced in air, r_{max}, the value of which depends on the energy of the incident electrons. Below r_{max}, as in panel i), the only electrons that can contribute to the measured dose are produced in the water around the IC and in the IC wall.

In panels a) and i) pseudo-equilibrium conditions exist in which electrons are produced within the IC wall and the uniform surrounding medium. Deviations from true equilibrium will be caused by electrons produced within the treatment head and miscellaneous scanning hardware in the radiation field within the water tank. In panels b)-g), various conditions of electronic disequilibrium are demonstrated. The disequilibrium occurs because of the change in medium surrounding the IC. Since air is ~1000 times less dense than water, the air volume surrounding the IC required to produce the same electron fluence as a surrounding water volume must be ~1000 times larger. Particularly for smaller field sizes, the irradiated air volume is not large enough to produce a fully compensatory electron fluence. The density and electron range changes between the neighboring media and the size of the air region irradiated by the incident photon beam cause the measured dose to increase rapidly as an IC descends below a water phantom surface. The shallow depths near a water phantom surface are commonly referred to as the "buildup" region, given the dose increase as a function of IC depth in water.

Electronic disequilibrium is not the only issue with taking IC measurements at the water surface and in the buildup region. There are also significant variations in measured IC response depending on the type of IC used. IC response is a function of wall material, cavity shape, and cavity volume. It is recommended that an extrapolation chamber is required to make surface dose measurements as accurately as possible (Nilsson and Montelius, 1986). Extrapolation chambers are essentially parallel-plate ICs that allow a user to systematically vary the plate separation and thus, the air cavity volume. Given multiple measurements under identical irradiation conditions for different plate separations, the measured dose can be extrapolated to zero volume, or dose to a theoretical point. Though useful, extrapolation chambers are difficult to construct and, therefore, relatively inaccessible compared with typical ICs. In a 1975 paper,

Velkley, et al. designed an empirical formalism for correcting measurements made with a typical fixed-plate parallel-plate IC to the result that would be expected to be measured with an extrapolation chamber (Velkley *et al.*, 1975). Following this development, parallel-plate ICs became most commonly used for buildup region measurements (Gerbi and Khan, 1990; Rawlinson *et al.*, 1992). When measurements with cylindrical ICs are taken in the buildup region and compared with extrapolation chambers or parallel-plate ICs, deviations can be observed (Chamberlain and Baily, 1964; Abdel-Rahman *et al.*, 2005; Parsai *et al.*, 2008). An example of deviations at depths up to the cylindrical IC outer radius between parallel-plate and cylindrical IC measurements due to the curvature and additional wall buildup of the cylindrical IC is shown in Figure 4. The differences observed here persist after the cylindrical IC scan is corrected for the effective point of measurement (EPOM). Since the parallel-plate IC proximal edge is initially aligned to the water surface, the resulting scan is corrected by shifting downstream to account for the water-equivalent thickness of the IC entrance window. The cylindrical IC scan is shifted upstream by the IC-specific EPOM shift value found by Tessier and Kawrakow (Tessier and Kawrakow, 2010). The cylindrical IC EPOM is discussed in Section 1.2.1. Beyond the cylindrical IC outer radius, the two measurements are expected to agree (McEwen *et al.*, 2008; Tessier *et al.*, 2010). Given the possible discrepancies between IC types, however, AAPM TG-105 recommends against using cylindrical ICs for accurate dose buildup measurements (Chetty *et al.*, 2007).

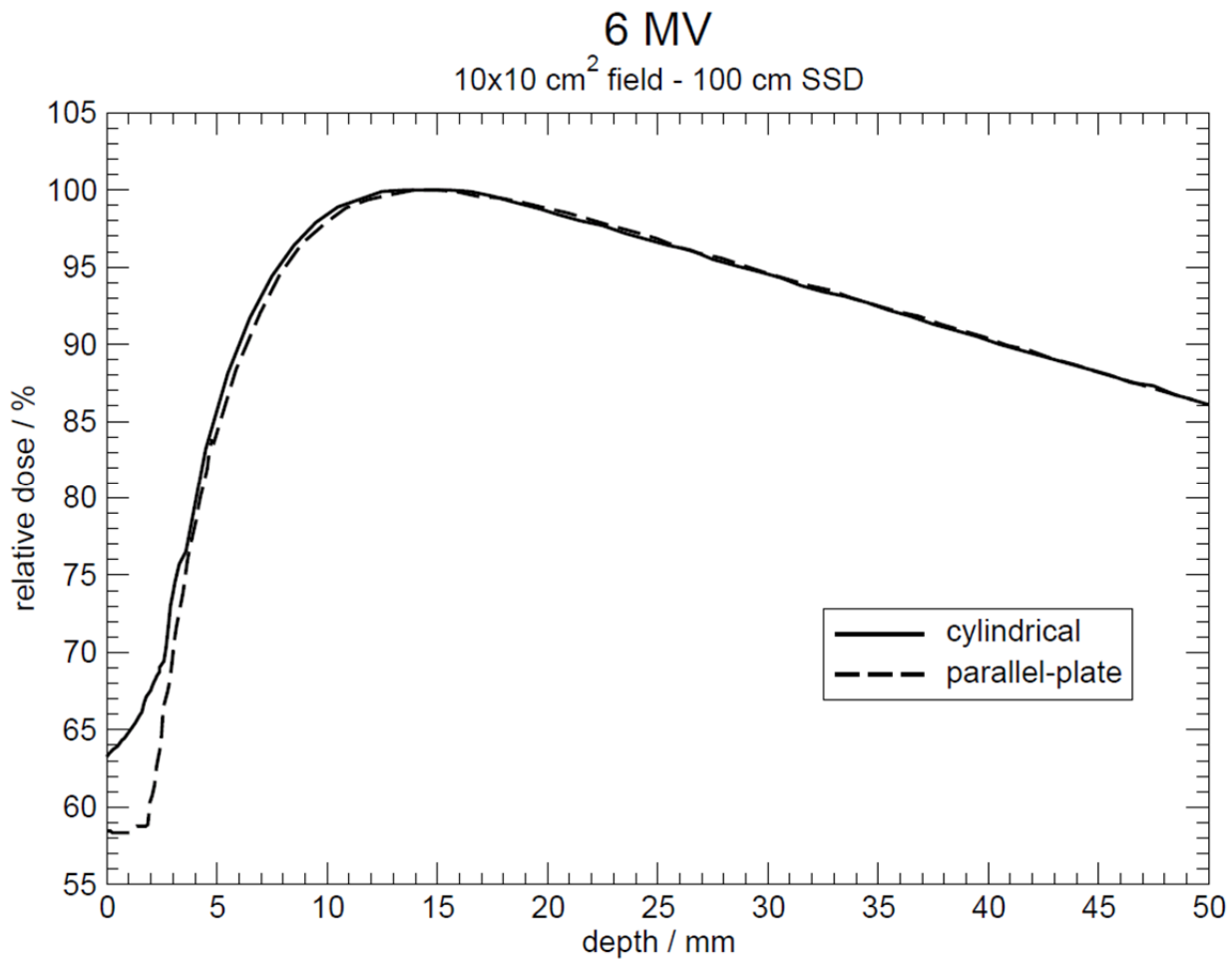

Figure 4: Illustration of volume averaging effect in buildup region with cylindrical ICs. Both measurements are taken on the same day under nominally identical irradiation conditions. The parallel-plate IC (Exradin A11) measurement is shifted downstream by its water-equivalent entrance window thickness since the top of the IC was physically aligned to the water surface. The cylindrical IC (Exradin A18) measurement is shifted upstream by the published EPOM value for this IC under the given irradiation conditions (Tessier and Kawrakow, 2010).

Given the challenges presented by electronic disequilibrium and IC volume averaging, measurements of surface and buildup dose are often regarded skeptically and infrequently used clinically. Examples of the clinically recommended de-emphasis of these regions are discussed in Section 1.2. However, the water surface provides an opportunity in clinical depth-ionization scanning to obtain information about the measurement setup at essentially zero cost.

1.2 Clinical Depth-Ionization Scanning

IC measurements as a function of depth are called depth-ionization measurements. Depth-ionization measurements are performed in initial accelerator calibration and as constancy checks to ensure that the radiation output from a given accelerator is invariant with time. The recommended code of practice for radiotherapy accelerators, AAPM TG-45, states that percent depth-ionization measurements are most easily performed using a scanning system with a water phantom (Nath *et al.*, 1994). The practical alternative to scanning in water is scanning in a solid phantom. When using a water phantom, scans can be performed continuously without the user touching the measurement setup. If a solid phantom is used for scanning, the user must shift the IC to each desired measurement position within the solid phantom by hand. This increases the time required for measurements and the potential for incorrect IC positioning. Use of a solid phantom for beam scanning also requires that a conversion be made in the measured dose from dose-to-phantom-material to dose-to-water. If scans are conducted in water, the conversion from phantom material to water is unnecessary. Depth-ionization scans are often performed with cylindrical or parallel-plate ICs. Well-guarded parallel-plate ICs are known to provide more accurate measurements in the buildup region, and are therefore explicitly recommended for depth-ionization scans (Andreo *et al.*, 2001). Since both IC types are known to be used clinically, depth-ionization measurements are made with both IC types in this thesis.

Correct depth-ionization measurements are essential, since any inaccuracies in acquired depth-ionization data have the potential to negatively impact Monte Carlo (MC) models and TPS dose calculation algorithms that these data are used to help validate and commission. Depth-ionization data are used, either directly or indirectly, in all TPS dose calculations. Accurate depth-ionization data are essential to correctly calculate the dose to be delivered to a patient.

Without properly acquired measured data against which to compare, the dose calculation algorithm used in a given clinic could be tuned to agree with incorrect results. This would introduce a systematic error into the TPS commissioning process. This error would then be propagated through each patient treatment plan generated using that software. Errors in planning can result in dose delivery errors, which can be manifested *in vivo* as a decrease in patient tumor control probability, an increase in normal tissue complication probability, or both. As acknowledged in AAPM TG-53, accurate prediction of open field depth dose is a basic, yet critical, test of any dose calculation algorithm (Fraass et al., 1998).

The water surface and buildup region have been consistently de-emphasized in protocol recommendations. In a 1963 ICRU report, it was proposed that depth-dose data should be normalized at a depth of 5 cm in water instead of at the depth of maximum dose, d_{max}, in an effort to improve the agreement with published depth dose data (International Commission on Radiation Units and Measurements, 1963). The report contained a depth dose calibration procedure which, if followed, was to produce repeatable measurements under the same radiation field conditions that showed "excellent agreement" with each other at the "*therapeutically important depths*", defined to be 5-15 cm, at the cost of considerable uncertainty in dose at the surface. The calibration procedure first called for an absorbed dose rate measurement to be taken for each field size at a depth of 5 cm in a "suitable" phantom, which was defined as either water or tissue-equivalent plastic, 30×30 cm square, and at least 15 cm thick, though 20 cm depth was deemed preferable. In the event that the radiation beam to be measured produced a $d_{max} > 5$ cm, the prescribed absorbed dose rate measurement was to be taken at a deeper point, though how much deeper was not specified. The procedure then recommended that depth dose tables, appropriate to the conditions of the dose rate measurement, should be consulted. A user was to

apply the percent depth dose (PDD) value at the point where the dose rate measurement was taken and the dose rate measurement to then compute the absorbed dose rate at d_{max}. It is acknowledged that this procedure gives *"no information"* about dose in the buildup region. Measured discrepancies of up to 10% were deemed acceptable in the buildup region, as long as the treatment target volume lay outside of it (International Commission on Radiation Units and Measurements, 1963).

A report on photon beam dosimetry by the AAPM Scientific Committee on Radiation Dosimetry in 1971 recognized that measurements at shallow depths were problematic. This report calls for IC calibration to occur at the depth of maximum dose, citing the zero gradient at this depth making this point advantageous as IC response is relatively unaffected by positioning errors (Schulz *et al.*, 1971). A 1973 ICRU report states explicitly that measurements should be made at depths within a water phantom but *not at the water surface* (International Commission on Radiation Units and Measurements, 1973). This recommendation was made while pointing out that *"the region at or close to a surface of a phantom is the most difficult in which to make accurate measurements"* (International Commission on Radiation Units and Measurements, 1973), due to the steep dose gradient and the fact that measurements are much more affected by details of the "beam defining system", or the specific geometry of a particular accelerator, than measurements at depth. Due to the known difficulty of making accurate surface measurements, AAPM TG-25 recommended electron beam relative surface dose to be defined at 0.5 mm depth, rather than at the true surface (Khan *et al.*, 1991).

In the following sub-sections, two important aspects of depth-ionization scanning are discussed. The first, the IC EPOM, must be accounted for when converting depth-ionization

readings to true depth dose. The second, IC depth alignment, is required before performing any IC measurement in water and is the focus of this thesis.

1.2.1 Ionization Chamber Effective Point of Measurement

For cylindrical ICs, the point of measurement is on the central axis of the IC (Almond *et al.*, 1999). When the IC is at a fixed depth, the measured result is recorded at the central axis point of measurement. In depth-ionization scans, the EPOM is closer to the radiation source than the IC geometric center (Almond *et al.*, 1999). The incident radiation beam predominantly enters the IC from points upstream, with additional scatter from other directions. Given the curvature of the IC face, the radiation entering the IC does so at various distances from the IC central axis. The variation in distance causes a gradient over the IC width in the resulting fluence of secondary electrons across the IC cavity. Due to this gradient, the dose to the IC cavity at a given location does not represent the dose to phantom medium at the same location. Instead, the dose to the cavity represents dose to a point in the phantom medium shifted upstream from the IC central axis by an amount proportional to the IC cavity radius, r_{cav}, to first approximation. This requires a shift of the measured depth-ionization data to match the EPOM offset from the central axis point of measurement. In AAPM TG-51 and in IAEA TRS-398, the recommended EPOM shift for all cylindrical ICs is given as -0.6 times the IC inner radius ($-0.6\times r_{cav}$) for photon beams and $-0.5\times r_{cav}$ for electron beams (Almond *et al.*, 1999; Andreo *et al.*, 2001). However, recent work by the Ionizing Radiation Standards group at the National Research Council of Canada (NRC) has shown the cylindrical IC EPOM to be considerably less general than the recommended value.

In a 2006 study (Kawrakow, 2006), Kawrakow conducted an investigation of the cylindrical IC EPOM using EGSnrc, a MC code that has previously been shown to be capable of

simulating IC cavity dose to within 0.1% systematic accuracy with respect to the IC cavity cross sections (Kawrakow, 2000a, b). The Kawrakow study was motivated by the observed discrepancies in the buildup region between measurement and MC calculation for 18 MV 40×40 cm^2 fields that were not fully accounted for in other investigations (Hartmann Siantar *et al.*, 2001; Ding, 2002a; Ding *et al.*, 2002; Ding, 2002b). In the Kawrakow work, bare air cavity simulation models were used to isolate potential EPOM dependence on cavity length and radius. Two IC simulation models were built to examine potential dependencies on the IC wall and central electrode. Potential dependencies on beam energy and field size were also investigated. Depth dose curves in water were computed using BEAMnrc (Rogers *et al.*, 2006) with the CHAMBER component module used for dose calculation. The dose calculation grid used included 300 regions at 1 mm depth spacing. The scoring region was a cylindrical volume of 1 cm radius. Dose to the IC cavity was calculated using IC models created in the EGSnrc user code CAVRZnrc (Rogers *et al.*, 2003). It was found that the proper EPOM value for a given cylindrical IC depended on all of the variables tested. When the proper EPOM shift was applied, measured depth-ionization and measured depth-dose curves were equal at all depths within ±0.5% (Kawrakow, 2006).

The results of the Kawrakow investigation provided a MC-based prediction but included no experimental verification. Thus, a follow-up study was carried out by McEwen, Kawrakow, and Ross where precise measurements were performed to test the prediction of Kawrakow (McEwen *et al.*, 2008). Citing the unsuitably large step sizes used by some commercial scanning phantoms, McEwen, Kawrakow, and Ross developed an in-house scanning system specifically designed to allow IC positioning with accuracy better than 0.15 mm (McEwen *et al.*, 2008). This system uses an optical telescope, allowing a user to align the IC at much finer resolution than by

the eye alone. The IC holder is attached to a stepper motor-driven turn screw, which causes 400 steps in IC position to be taken per mm. This scanning system has been used to take some measurements for the work described in this thesis, which will be discussed in further detail in Section 4.1.3.

In the work by McEwen, Kawrakow, and Ross (McEwen *et al.*, 2008), measurements at two photon beam energies and two field sizes were made using this customized system with a variety of commercial ICs. Three cylindrical and three parallel-plate ICs were scanned on two accelerator types. Customized ICs were built and scanned to isolate wall thickness, central electrode thickness, and central electrode material, respectively (McEwen *et al.*, 2008). Measurements for different cylindrical IC types were compared with a reference Farmer-type IC, for which the protocol-recommended EPOM shift was assumed to hold true. Cylindrical IC measurements were also compared with parallel-plate IC measurements. For parallel-plate ICs, the nominal point of measurement is taken to be the inside of the entrance window. After scaling the entrance window thickness to its equivalent thickness of water, no EPOM shift is necessary. Selected measurements are also compared with MC simulation results. In short, the conclusion that the standard cylindrical IC EPOM shift is incorrect was confirmed. Errors of 0.5-1.0 mm were typically observed if the standard shift was applied, though errors as large as 1.5 mm were seen with the Exradin A2 for the highest energy photon beam, 25 MV, and largest field size, 40×40 cm^2. The central electrode of the Exradin A2 is over four times thicker radially than the next thickest central electrode of any IC examined in the study. The Exradin A2 cavity radius is over 1.5 times larger than the cavity radius of any other IC used in the study. Other conclusions include that central electrode density does not affect the cylindrical IC EPOM and that well-guarded parallel-plate ICs should be used for depth-ionization measurements (McEwen *et al.*,

2008). Incident primary radiation enters a parallel-plate IC at the same depth at each point across the IC. Therefore, the parallel-plate IC EPOM is traditionally taken at the same depth as the nominal point of measurement, at the inside edge of the parallel-plate IC entrance window (Schulz *et al.*, 1983; Almond *et al.*, 1999). Parallel-plate IC depth-ionization measurements require an EPOM shift that scales the entrance window thickness to its equivalent thickness of water, as shown by McEwen, Kawrakow, and Ross (McEwen *et al.*, 2008).

Using detailed MC models of 12 cylindrical IC types, Tessier and Kawrakow categorized the EPOM on an IC-specific basis at two photon beam energies and two field sizes (Tessier and Kawrakow, 2010). The proper EPOM shift was found to be up to 25% smaller than the previously recommended $-0.6 \times r_{cav}$ value for Farmer-type ICs and up to 80% smaller for the smallest IC tested (Exradin A14SL). Results indicated EPOM shift dependence on incident beam parameters, IC cavity length, IC central electrode radius, and IC wall thickness. The systematic dependence was such that the authors claimed that a proper EPOM shift parameterization in terms of design parameters was conceivable (Tessier and Kawrakow, 2010). Tessier, Hooten, and McEwen have reported that it is possible to design a cylindrical IC with a wall thickness chosen such that no EPOM offset is required (Tessier *et al.*, 2010). The required wall thickness is IC-dependent, proportional to the IC cavity radius (Tessier *et al.*, 2010).

Though the IC EPOM offset is a necessary correction for depth-ionization scans to be used clinically, it is not applied to measurements taken in this thesis, unless specifically noted otherwise. The main reason for this is that the goal of this work is to establish the positional origin from which an EPOM offset should be applied. The IC-specific EPOM offsets found in the work by Tessier and Kawrakow (Tessier and Kawrakow, 2010) can be applied to measurements described in this thesis as an additional test of setup alignment. Furthermore, if

measurements are taken with an independently established origin, the scanning method developed here can be used to determine the proper EPOM shifts for ICs currently lacking IC-specific recommended values. This can be achieved by shifting a depth-ionization curve measured with an IC for which the IC-specific EPOM offset value is unknown to a depth-ionization curve measured with a different IC that has been shifted by the established EPOM shift for that IC.

1.2.2 Ionization Chamber Depth Alignment

This thesis focuses on IC depth alignment, a more fundamental issue than the proper EPOM offset. The EPOM shift is a correction that must be made before depth-ionization measurements can be converted to true depth dose. Proper IC depth alignment must be established for any IC measurement performed in water, including calibration measurements performed at a single depth. The IAEA considers it clinically impractical to attempt to position an IC for measurements at reference depth with <1 mm accuracy (Andreo *et al.*, 2001). TRS-398 recommends a procedure where an IC is positioned at an independently precisely known depth within ~1 mm of reference depth before a measurement is taken. The IC position is then corrected by shifting the IC within the original ±1 mm of reference depth until a measured result is obtained that matches using previously measured depth dose data (Andreo *et al.*, 2001).

The most recent AAPM report on accelerator QA, AAPM TG-142, requires that PDD_{10}, the relative dose value at a depth of 10 cm read from the PDD curve, stay within ±1% of the baseline value previously established in beam commissioning for a given accelerator (Klein *et al.*, 2009). Table 1 shows the positioning errors that would create a 1% change in measured PDD, for reference depths of 5 (PDD_5) and 10 cm (PDD_{10}), for the four photon beam energies studied in this thesis along with representative 1.25 MV ^{60}Co machine data listed in *The Physics of*

Radiology (Johns and Cunningham, 1983). Table 1 shows that IC positioning errors of ~2-3 mm are required to change PDD_5 and PDD_{10} by ±1%. It is implicitly assumed when calculating the IC positioning errors listed in Table 1 that IC positioning uncertainty is the sole cause of measurement uncertainty. However, uncertainty in measured PDD values comes from additional sources such as the actual year-to-year variation in accelerator output. Given the additional sources of overall measurement uncertainty, it is reasonable to assume that an actual IC depth positioning tolerance of ~1.0-1.5 mm is required to maintain agreement with the 1% tolerance in measured PDD_{10} recommended by AAPM TG-142 (Klein *et al.*, 2009). This tolerance represents the IC positioning necessary to compare PDDs after d_{max}. If it is desired, as it is in this thesis, to compare PDDs in the buildup region, where the dose gradient is much greater than after d_{max}, the required IC positioning accuracy is <1 mm.

Table 1: IC positioning errors that would be required to change PDD_5 and PDD_{10} by ±1% from their nominal values for the four photon beam energies examined in this thesis. PDD_5 and PDD_{10} are the relative dose values read from a PDD curve at 5 and 10 cm, respectively. Data at 1.25 MV are taken from PDD tables for 10×10 cm^2 fields at 100 cm SSD presented in *The Physics of Radiology* (Johns and Cunningham, 1983). All other data are all taken from measurements of 10×10 cm^2 fields at 100 cm SSD made with an IBA CC13. Where error in the positioning uncertainty is given, it is caused by the asymmetry in measured PDD values around the data point in question. Where no error in the positioning uncertainty is given, the neighboring tabulated data points are symmetric around the PDD value in question to 3 significant figures. The 6 and 18 MV beams are measured at VCU on a Varian 2300 with an IBA Blue Phantom. The 10 and 25 MV beams are measured at the NRC on an Elekta Precise with a customized high-precision scanning system.

	From PDD location:	5 cm	10 cm
Energy (MV)	PDD σ (%)	Position σ (mm)	
1.25	1	2.2	2.6 ± 0.1
6	1	2.3 ± 0.4	2.8 ± 0.4
10	1	2.6	2.9 ± 0.3
18	1	3.3 ± 0.3	3.0 ± 0.3
25	1	3.7 ± 0.1	3.2 ± 0.1

An early step in performing any set of depth-ionization measurements is to position the IC at the water tank surface. AAPM TG-106 recommends a method of water surface identification for cylindrical ICs by examining the IC reflection from beneath the water surface and setting zero depth at the point at which the IC forms a perfect circle with its reflection (Das

et al., 2008). The figure from AAPM TG-106 (Das *et al.*, 2008) demonstrating proper IC water surface alignment is reprinted here as Figure 5. An example of the effect of IC misalignment on resulting acquired data is shown in Figure 6. This figure shows measurements taken on the same accelerator, under nominally identical radiation field conditions. The origin of the first measurement taken in 2005 is 2.1 mm deeper than the second scan, which much more closely agrees with measurements taken in subsequent years. However, agreement with other measurements does not guarantee that the latter 2005 scan is correct. As long as the alignment used is consistent, however incorrect it may be, coinciding data sets will be produced. Without reference data that is known to have been acquired with a properly aligned IC, no IC depth-ionization measurement can be known to be absolutely correct.

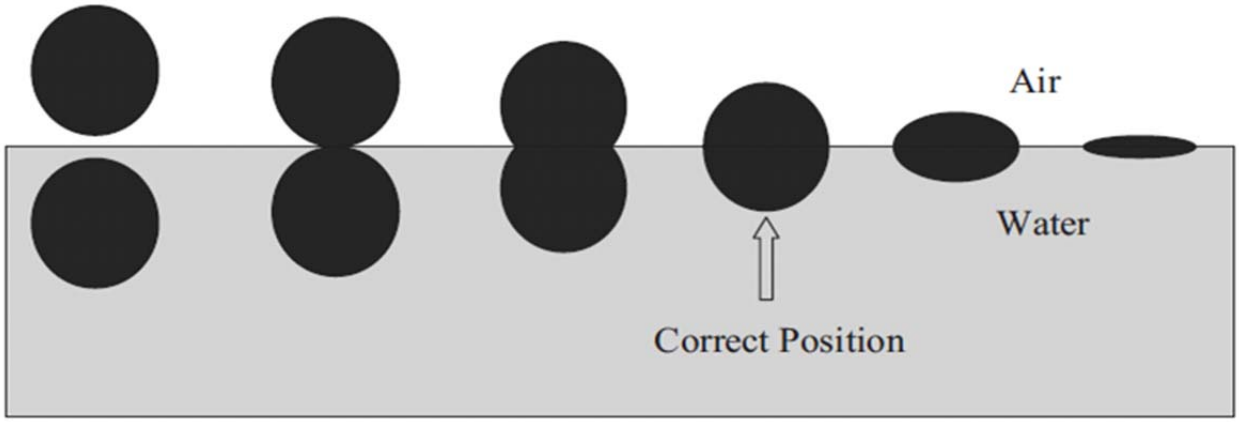

Figure 5: Illustration of the AAPM recommendation for qualitative cylindrical IC alignment to a water surface. When looking at the end of the IC from below the water surface, two distinct circles will be seen when the IC is at depth in water. As the IC is moved toward the surface, the circles will join together. When the center of the IC is located at the water surface, labeled here as the "Correct Position", one complete circle is observed. If the IC is moved beyond the water surface into air, the circle flattens out. (Reprinted from Das, et al., (2008) with permission from American Association of Physicists in Medicine.)

In an attempt to provide precise direct measurement of IC depth, a 1995 technical note by Tailor and Tello details a device they call a "water phantom depth gauge" (Tailor and Tello, 1995). The gauge starts with a ruler, graduated in 1 mm increments, that is placed vertically on top of the radiation detector. The end of the ruler is cut off such that the removed zero position would coincide with the detector point of measurement. The ruler is held in place vertically atop

the detector by a pair of plastic strips balanced by counterweights. A second assembly consisting of two pointers and two metal clips is attached to the ruler such that the water surface depth is to be read at the bottom edge of the clips. Given the cut of the ruler, the ruler reading at the bottom clip edge represents the distance from the water surface to the detector point of measurement (Tailor and Tello, 1995).

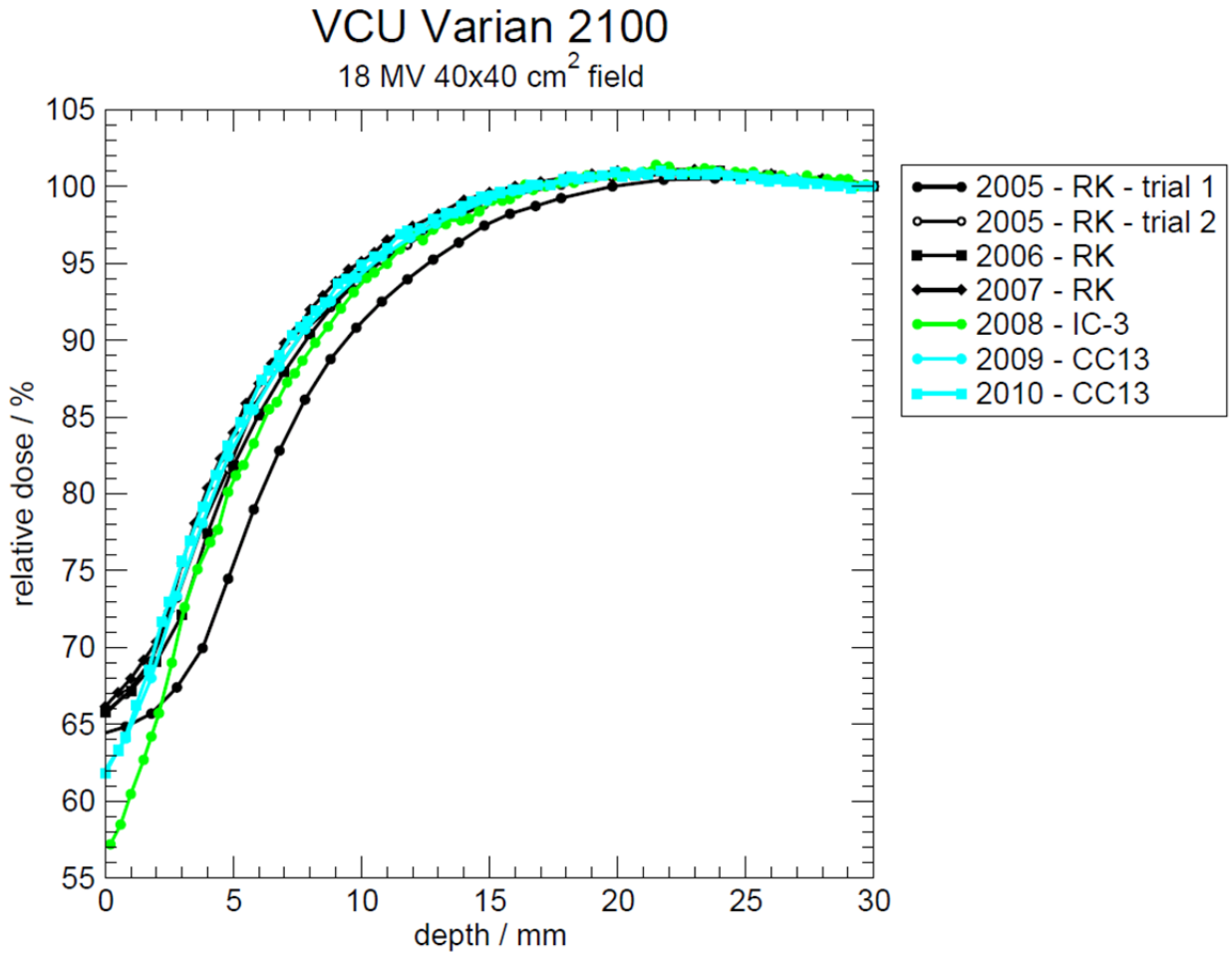

Figure 6: VCU annual QA PDD data from the same machine operating at 18 MV for a 40×40 cm^2 field showing the effect of clinical IC misalignment. The two measurements from 2005 show origins differing by 2.1 mm in the z-direction. All scans have had the AAPM TG-51 recommended EPOM shifts of $0.6 \times r_{cav}$ applied, where r_{cav} is the IC inner radius. All scans are normalized to 100% at d_{max}. Dependence on chamber dimensions is evident from 0-5 mm. The Wellhöfer IC-3, a micro-IC, gives surface dose that is ~9% lower than is measured with the CC13. The CC13 surface dose measurements are ~6% lower than recorded with the RK.

To set the detector to a desired depth, the pointer assembly is first slid over the ruler to where the bottom clip edge is at the desired depth. The detector is then moved vertically until a

gap of 1-2 mm thickness is observed between the water surface and pointer tips. From here, the quoted procedure essentially amounts to the alignment procedure from AAPM TG-106 (Das *et al.*, 2008) shown in Figure 5, with the difference being that the pair of pointers is being considered instead of an IC. The device is then removed from the detector and placed in the water tank outside of the radiation field to minimize water displacement errors (Tailor and Tello, 1995) Each gauge is custom-built for a given detector. The device is claimed to be capable of 0.1 mm measurement precision (Tailor and Tello, 1995). The publication states that the device is commercially available but the company that was offering the device at the time of publication has since been bought out and the device is no longer for sale.

Recent work by Bouchard, Seuntjens, and Kawrakow has examined the impact of random positioning errors on measurements in non-standard beams, i.e., beams produced by accelerators that are not capable of producing stationary 10×10 cm^2 fields incident upon a water tank at 90° at 100 cm SSD, such as CyberKnife or Tomotherapy (Bouchard *et al.*, 2011). However, the errors considered in the work by Bouchard, Seuntjens, and Kawrakow are treated as random occurrences, as they are handled by isotropically sampling from a probability distribution. The work described in this thesis deals with positioning errors that occur based in a common root cause: the ambiguity in IC alignment at a water surface. Furthermore, the implementation of the method by Bouchard, Seuntjens, and Kawrakow is specifically noted to be of limited accuracy near phantom surfaces or other interfaces (Bouchard *et al.*, 2011). An inherent hypothesis of the work in this thesis is that many positioning errors stem from incorrect IC alignment to the water surface, thus the focus in this thesis is at or near the water phantom surface.

1.3 Thesis Objectives

The first objective of this thesis is to establish a method for conducting depth-ionization measurements that ensures depth positional accuracy to within 0.15 mm. The gradient peak in depth-ionization data caused by electron buildup at the change in surrounding medium as an IC moves from water into air is used to provide users a way to detect, and subsequently correct, any IC positioning errors. The dependencies of this method on radiation field parameters and IC design are quantified. Measurements are conducted with twenty-eight cylindrical and parallel-plate IC types, in photon and electron beams, from standard radiotherapy-class linear accelerators and a radiosurgery-class Accuray CyberKnife.

The second objective of this thesis is to use a depth-ionization simulation model to characterize the gradient peak. A simple analytic model of IC response is used to examine the theoretical basis for the appearance of the depth gradient peak in measurements. MC simulation is also used, as it has been shown to be capable of providing the necessary accuracy to serve as a gold standard against which measurements can be compared (Kawrakow, 2000b). It is used to test idealized IC geometries to determine quantitatively the functional dependencies of IC response on inner and outer IC radii, as well as IC wall thickness.

The third objective of this thesis is to create a template institutional protocol for acquiring depth-ionization data. Given the measurement procedure and computational model, a protocol is devised to guide a user through the steps required to obtain high-accuracy depth-ionization data. This procedure will lead to measured data to serve as institutional gold standards for future scans. To implement the protocol into clinical practice more efficiently, a program taking output from existing scanning control software has been created that allows a user to acquire a scan and determine and correct any existing offset in IC alignment so as to acquire more accurate,

properly aligned scans for the remainder of the measurement acquisition session. The protocol outlined here covers proper IC scanning and positioning procedures and should allow improper setups to be detected and corrected, when necessary.

1.4 Thesis Outline

In Chapter 2, earlier investigations both in-house and with collaborators are described that provide the initial rationale for believing that a PDD scan feature could be used to independently establish IC alignment. Several methods of determining IC depth alignment are examined and the choice of the IC gradient peak as the IC alignment metric is justified.

In Chapter 3, the theoretical relationship between the scan gradient and IC alignment is established through the use of a simple analytical model and MC simulation studies including a detailed IC model. This relationship is established to verify further the empirical findings of the studies described in Chapter 2.

Chapter 4 describes the equipment and experimental methods used to validate the existence of a scan gradient peak as an IC reaches the water surface when scanning from water into air. A wide range of possible dependencies of the gradient peak location on scan procedure variation, radiation field parameters, and IC type is examined to establish the generality of the findings.

In Chapter 5, a prototype scanning protocol is outlined that can be implemented by a general clinical user to establish his or her own IC surface alignment quantitatively. Upon determining any existing IC alignment offset, IC position can be corrected such that all subsequent scan data is acquired with a properly aligned IC. This will help to improve intra-setup scan reproducibility for a given scanning session and inter-setup scan reproducibility

across multiple measurement instances. Following an established scanning procedure will help to improve inter-user scan reproducibility.

The overall conclusions of this thesis are described in Chapter 6.

2 Feasibility Studies

In this chapter, previous studies by the author with collaborators are discussed. These studies have indicated the possibility of defining a single PDD scan feature that is robust against changes in incident radiation field parameters that provides IC alignment information. The results of the studies described here motivated the expansion of the investigation into the experiments described in the remainder of this thesis. Initial studies indicate that the PDD second derivative is a useful metric for determining IC alignment, though perhaps less useful for noisy data or scan resolution finer than 0.5 mm. PDD scan first derivatives and curve fitting of the original PDD scan data are considered as alternatives to the second derivative for obtaining alignment information and the final choice of a primary alignment metric is explained.

2.1 Single Cylindrical Ionization Chamber Study

As previously shown in Figure 6, nominally identical data acquisitions can result in observed deviations. Motivated to find a quantitative metric to evaluate IC water surface alignment, an in-house single-cylindrical IC study was performed (Ververs *et al.*, 2009b). The full report is included as Appendix I of this thesis, beginning on page 287. It was hypothesized that a reasonable water surface alignment metric should be independent of radiation field parameters, as the true water surface position will not be affected by changes in the incident radiation field. Therefore, depth-ionization measurements were taken for variations in incident photon energy, radiation field size, and electron contamination conditions. Measurements with a

single RK type cylindrical IC (see Table 2, Table 3, and Table 4 for cylindrical IC parameters) were taken for five square photon fields (5×5, 10×10, 20×20, 30×30, and 40×40 cm^2) at 6 and 18 MV with and without a 1 mm thick lead foil placed in the beam. All measurements were taken from water through the water surface into air. Scans were taken at 1 mm resolution, except from d_{max} to 20 mm into air above the water surface, where scan resolution was 0.5 mm. Measurements were compared with one another as functions of field size, beam energy, and electron contamination by curve matching near the surface to demonstrate that the shapes of the curves agreed. Having noted that PDD scan curvature changes when extended into air, second derivatives were computed. Peaks in the computed scan second derivatives were observed within measurement resolution (0.5 mm) of one another for all changes in beam configuration. While the curve matching and derivatives were used to show relative alignment, absolute alignment was tested by comparing with MC simulations, performed with and without a simulated model of the RK IC included. In the MC simulations containing a simulated IC model, perfect IC alignment can be assumed, since the water surface and IC locations are defined exactly by the user. Simulations were performed for 6 MV 10×10 cm^2, 6 MV 40×40 cm^2, and 18 MV 40×40 cm^2 open fields. Offsets between measured and simulated curves for each radiation field was quantified by minimizing the sum of squared differences between the two following the formula,

$$SSQD = \sum_x w_x \left[PDD_{ref}(x) - SF \times PDD_{test}(x + \delta) \right]^2$$

Here, x represents a given depth, ref and $test$ refer to reference (MC) and test (measured) conditions, w_x represents a weighting factor taken as the inverse of the root mean squared combined variance in the ref and $test$ data values at x, SF is a scaling factor that accounts for any arbitrary difference in normalization, and δ represents any possible shift in IC

alignment between ref and $test$ conditions. Given the observed noise in the simulated second derivatives, MC depth-dose data was smoothed with a Savitzky-Golay filter, as implemented by Kawrakow (Kawrakow, 2002) and second derivatives were recomputed. The peaks in the second derivatives of the smoothed MC data occurred within ~0.1 mm of the depth at which a perfectly aligned IC should reach the water surface. A -0.6 mm shift in absolute positioning of the measurements as compared with simulations was found when minimizing the SSQD between computed and measured depth-ionization curves. With this measurement offset properly accounted for, the measured second derivative peaks also occurred within ~0.1 mm of the point at which a perfectly aligned IC should reach the water surface. The relative insensitivity (within 0.5 mm measurement resolution) of the measured second derivative peaks to changes in beam energy, field size, and electron contamination were considered promising enough to merit expansion of the work to consider other cylindrical IC designs.

2.2 Expanded Multiple Cylindrical Ionization Chamber Study

During the initial single-IC study, a collaboration was formed between the group at Virginia Commonwealth University (VCU) and the Ionizing Radiation Standards group at the NRC. For the next phase of the project, a collaborator (M. McEwen) used a customized high-precision scanning system, described in part in other publications (McEwen *et al.*, 2008) and within this thesis in Section 4.1.3, to take depth-ionization measurements with eleven cylindrical ICs. The ICs used are a subset of the ICs listed in Table 2, Table 3, and Table 4. The ICs used specifically in this experiment are listed in the legends of Figure 10 and Figure 11.

Table 2: Wall parameters for the cylindrical ICs used in this thesis. The Wellhöfer IC-10 has been nominally replaced by the IBA CC13. The PTW 233642 has been nominally replaced by the PTW 31010. Numbers given in parentheses represent the contribution of individual components in walls comprised of multiple materials. For the IBA RK, the first number represents the PMMA component and the second represents the contribution from the graphite/epoxy mixture. C552 is a Shonka air-equivalent plastic. Poly-methyl methacrylate (PMMA) is more commonly referred to by one of its trade names: Lucite®, Perspex®, or Plexiglas®. The v1 and v2 designations of the Exradin A2 indicate different customized constructions by Standard Imaging of the same IC. The Exradin A2 v1 has the same wall thickness as the commercially available version while the Exradin A2 v2 has a doubly thick wall.

IC Type	Material	Density (g/cm^3)	Thickness (cm)	Mass Thickness (g/cm^2)
Exradin A12	C552	1.76	0.05	0.088
Exradin A12S	C552	1.76	0.05	0.088
Exradin A14SL	C552	1.76	0.11	0.1936
Exradin A16	C552	1.76	0.05	0.088
Exradin A18	C552	1.76	0.1	0.176
Exradin A19	C552	1.76	0.05	0.088
Exradin A1SL	C552	1.76	0.11	0.1936
Exradin A2	C552	1.76	0.1	0.176
Exradin A2 v1	C552	1.76	0.1	0.176
Exradin A2 v2	C552	1.76	0.2	0.352
IBA CC01	C552	1.76	0.05	0.088
IBA CC04	C552	1.76	0.04	0.07
IBA CC08	C552	1.76	0.04	0.07
IBA CC13	C552	1.76	0.04	0.07
IBA CC25	C552	1.76	0.04	0.07
IBA FC65-G	Graphite	1.82	0.04	0.073
Wellhöfer IC-10	C552	1.76	0.04	0.0704
Wellhöfer IC-3	Graphite		0.04	
IBA CCRK	PMMA/graphite-epoxy mix	1.267 (1.2/1.4)	0.15 (0.1/0.05)	0.19
PTW 233642	PMMA/graphite	1.11 (1.19/0.82)	0.07 (0.055/0.015)	0.078
PTW 30013	PMMA/graphite	1.33 (1.19/1.85)	0.0425 (0.0335/0.009)	0.0565
PTW 31010	PMMA/graphite	1.11 (1.19/0.82)	0.07 (0.055/0.015)	0.078
PTW 31014	PMMA/graphite	1.288 (1.19/1.85)	0.066 (0.057/0.009)	0.085
PTW 31016	PMMA/graphite	1.288 (1.19/1.85)	0.066 (0.057/0.009)	0.085

This study expanded on the initial investigation, which is summarized in Section 2.1. In the work discussed in Section 2.1, MC simulation is used to provide the gold standard against which test measurements are compared. In this work, an optical telescope is used to independently verify IC alignment before scans are performed. The procedure through which the telescope, and subsequently the IC, is aligned to the water surface is given in Section 4.1.3. IC alignment relative to the telescope is varied, though the IC longitudinal axis is always kept

parallel to the water surface. Most scans were conducted with the ICs oriented at a 45° angle relative to the optical telescope. Other scans were performed with ICs in an end-on (0°) or side-on (90°) orientation relative to the telescope. The optical telescope remained in a constant position throughout all measurements. IC orientation relative to the telescope was examined to ensure bias did not exist in the optical alignment method. Examining IC orientation in this fashion also tests for any bias caused by possible small asymmetries in the incident radiation field or directional dependencies in IC response.

Table 3: Central electrode parameters for the cylindrical ICs used in this thesis. ICs for which not all information is provided are older models for which data sheets cannot be found. The Wellhöfer IC-10 has been nominally replaced by the IBA CC13. The PTW 233642 has been nominally replaced by the PTW 31010. Density of the graphite/epoxy mixture used for the IBA RK is specified for the bulk material by the manufacturer, not by individual components. C552 is a Shonka air-equivalent plastic. Poly-methyl methacrylate (PMMA) is more commonly referred to by one of its trade names: Lucite®, Perspex®, or Plexiglas®. The v1 and v2 designations of the Exradin A2 indicate different customized constructions by Standard Imaging of the same IC. Both customized versions contain a thinner central electrode than the commercially available A2.

IC Type	Material	Density (g/cm^3)	Length (cm)	Diameter (cm)	Mass Thickness (g/cm^2)
Exradin A12	C552	1.76	2.16	0.1	0.176
Exradin A12S	C552	1.76	0.75	0.1	0.176
Exradin A14SL	C552	1.76	0.150	0.03	0.0528
Exradin A16	C552	1.76	0.127	0.03	0.0528
Exradin A18	C552	1.76	0.64	0.1	0.176
Exradin A19	C552	1.76	2.16	0.1	0.176
Exradin A1SL	C552	1.76	0.44	0.1	0.176
Exradin A2	C552	1.76	0.84	0.46	0.8096
Exradin A2 v1	C552	1.76	0.84	0.1	0.176
Exradin A2 v2	C552	1.76	0.84	0.1	0.176
IBA CC01	Steel	8.5	0.28	0.035	0.2975
IBA CC04	C552	1.76	0.21	0.1	0.176
IBA CC08	C552	1.76	0.15	0.1	0.176
IBA CC13	C552	1.76	0.33	0.1	0.176
IBA CC25	C552	1.76	0.75	0.1	0.176
IBA FC65-G	Aluminum	2.7	2.0	0.1	0.27
Wellhöfer IC-10	C552	1.76			
Wellhöfer IC-3	Graphite		0.38	0.1	
IBA CCRK	Graphite-epoxy mix	1.4	0.90	0.1	0.14
PTW 233642	Aluminum	2.7	0.50	0.1	0.27
PTW 30013	Aluminum	2.7	2.12	0.11	0.297
PTW 31010	Aluminum	2.7	0.50	0.11	0.297
PTW 31014	Aluminum	2.7	0.415	0.03	0.081
PTW 31016	Aluminum	2.7	0.16	0.03	0.081

Table 4: Air cavity parameters and outer diameters for the cylindrical ICs used in this thesis. ICs for which not all information is provided are older models for which complete data sheets cannot be found. The Wellhöfer IC-10 has been nominally replaced by the IBA CC13. The PTW 233642 has been nominally replaced by the PTW 31010. The Exradin A2 is commercially available, while the Exradin A2 v1 and Exradin A2 v2 are customized constructions by Standard Imaging. The smaller air cavity diameter for the A2 v2 is a consequence of the doubly thick wall in this design.

	Air Cavity			IC
IC Type	**Volume (cm^3)**	**Length (cm)**	**Diameter (cm)**	**Diameter (cm)**
Exradin A12	0.65	2.48*	0.61	0.71
Exradin A12S	0.25	1.06*	0.61	0.71
Exradin A14SL	0.016	1.0*	0.4	0.635
Exradin A16	0.007	0.24*	0.24	0.34
Exradin A18	0.125	0.86*	0.49	0.69
Exradin A19	0.62	2.5*	0.61	0.71
Exradin A1SL	0.057	0.6*	0.4	0.635
Exradin A2	0.54	1.2*	0.95	1.14
Exradin A2 v1	0.53	1.2*	0.95	1.14
Exradin A2 v2	0.53	1.0*	0.85	1.14
IBA CC01	0.01	0.36	0.2	0.3
IBA CC04	0.04	0.16	0.4	0.48
IBA CC08	0.08	0.4	0.6	0.68
IBA CC13	0.13	0.58	0.6	0.68
IBA CC25	0.25	1.0	0.6	0.68
IBA FC65-G	0.65	2.31	0.62	0.7
Wellhöfer IC-10	0.14		0.6	0.68
Wellhöfer IC-3	0.028	0.33	0.3	0.38
IBA CCRK	0.12	1.0	0.4	0.7
PTW 233642	0.125	0.65	0.55	0.69
PTW 30013	0.6	2.3	0.61	0.69
PTW 31010	0.125	0.65	0.55	0.68
PTW 31014	0.015	0.5	0.2	0.332
PTW 31016	0.016	0.29	0.29	0.422
* - Calculated from directly reported values				

Most scans were performed with a signal acquisition time of 2 seconds per measurement point. For the smallest IC tested (0.01 cm^3 active cavity volume), acquisition time was increased to 10 s/pt., due to the small collecting volume. Two other ICs were scanned under nominally identical radiation field conditions for different acquisition times, to investigate the sensitivity of the measured results to the acquisition time. Two customized versions of the Exradin A2 IC, built to be identical in every way except IC wall thickness for initial use in the EPOM experimental work by McEwen, Kawrakow, and Ross (McEwen *et al.*, 2008) described in

Section 1.2.1, were used in this study to isolate the effect of wall thickness on the measured results. The measurements for this study were performed in 6, 10, and 25 MV photon beams, produced by an Elekta Precise (Elekta, Inc., Crawley, United Kingdom) accelerator. Some measurements were performed with a lead foil present in the beam path, to study the effect of electron contamination. The work summarized in Section 2.1 used 6 and 18 MV photon beams from a Varian 2100 accelerator. Accelerator types are discussed in Section 4.1.1 of this thesis. All scans were conducted from water to air at 0.5 mm measurement resolution.

The second derivatives of all measurements were computed and plotted. The work described in Section 2.1 indicated that, for the IBA CCRK, a peak in the second derivative should exist at the point where the IC reaches the water surface. Given the results of the study described in Section 2.1, it was expected that this peak location should not depend on radiation field parameters. It was hypothesized that second derivative peak location would be dependent of the IC outer radius and wall thickness as these parameters dictate when the IC and the inner cavity reach the water surface.

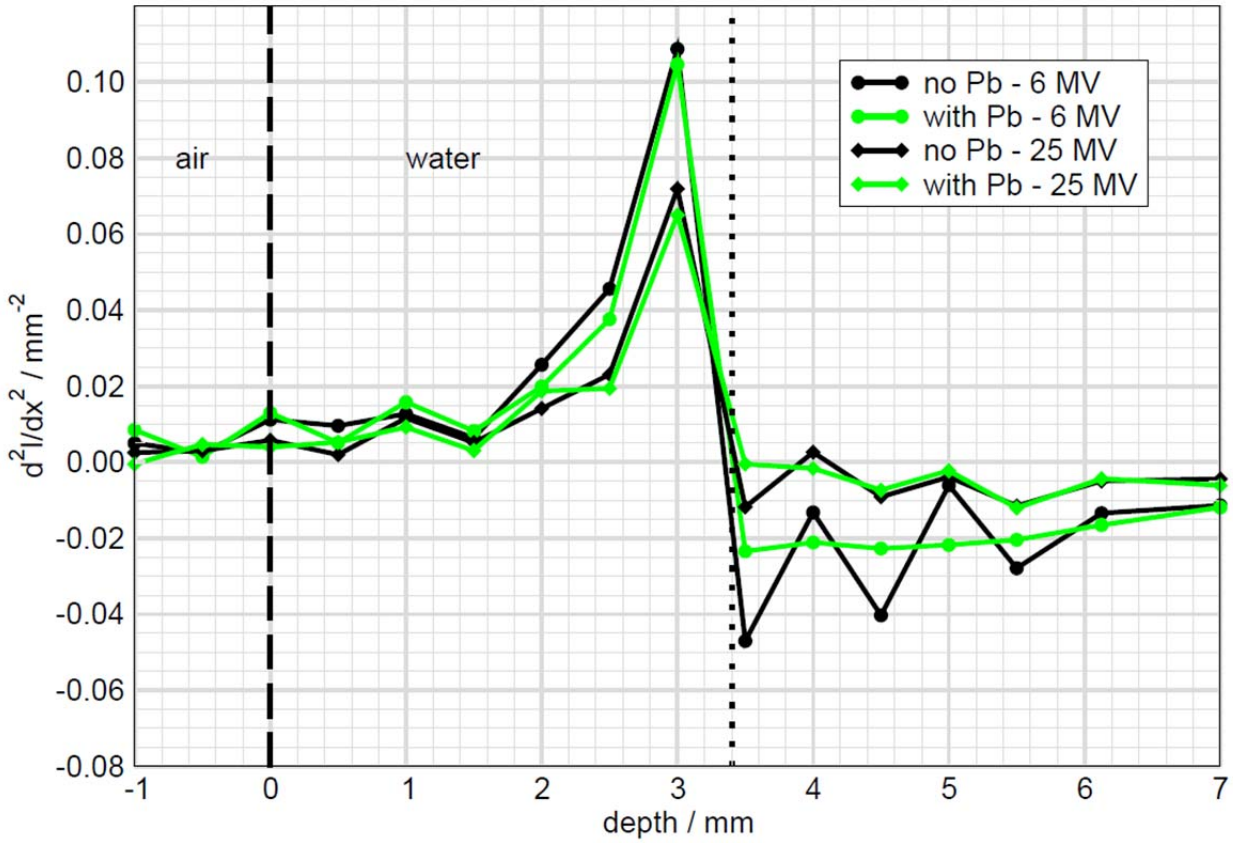

Figure 7: Second derivative peaks from scans with an IBA CC13 cylindrical IC for a 10×10 cm^2 field. Scans are performed from water to air at 0.5 mm resolution. No change in second derivative peak location occurs with a change in incident photon beam energy or electron contamination. The second derivative peak is 0.4 mm shallower than the DeICERS. The dashed line represents the nominal water surface position. The dotted line represents the DeICERS.

As expected, beam energy and electron contamination did not affect second derivative peak location. This is shown for the IBA CC13 cylindrical IC in Figure 7. IC orientation relative to the optical telescope also does not affect second derivative peak location as shown, again for the IBA CC13, in Figure 8. The location of the second derivative peaks shown in Figure 7 and in Figure 8 does not appear to depend on radiation field parameters; however, the peak is located 0.4 mm shallower than the depth where the IC edge reaches the surface (DeICERS). Though 0.4 mm is within the 0.5 mm measurement resolution, the optical telescope alignment procedure should ensure proper IC alignment to within 0.15 mm (McEwen *et al.*, 2008). This discrepancy indicates that measurements at finer resolution may be required with this IC. Signal acquisition time, within a range of 1-10 s, was found to have no effect on second

derivative peak location, within the 0.5 mm measurement resolution. An example of the independence of second derivative peak location from signal acquisition time for the PTW 31010 cylindrical IC is shown in Figure 9. With this IC, the second derivative peak occurs within 0.05 mm of the DeICERS. The effect of signal acquisition time is revisited in this thesis in Section 4.2.2.2.

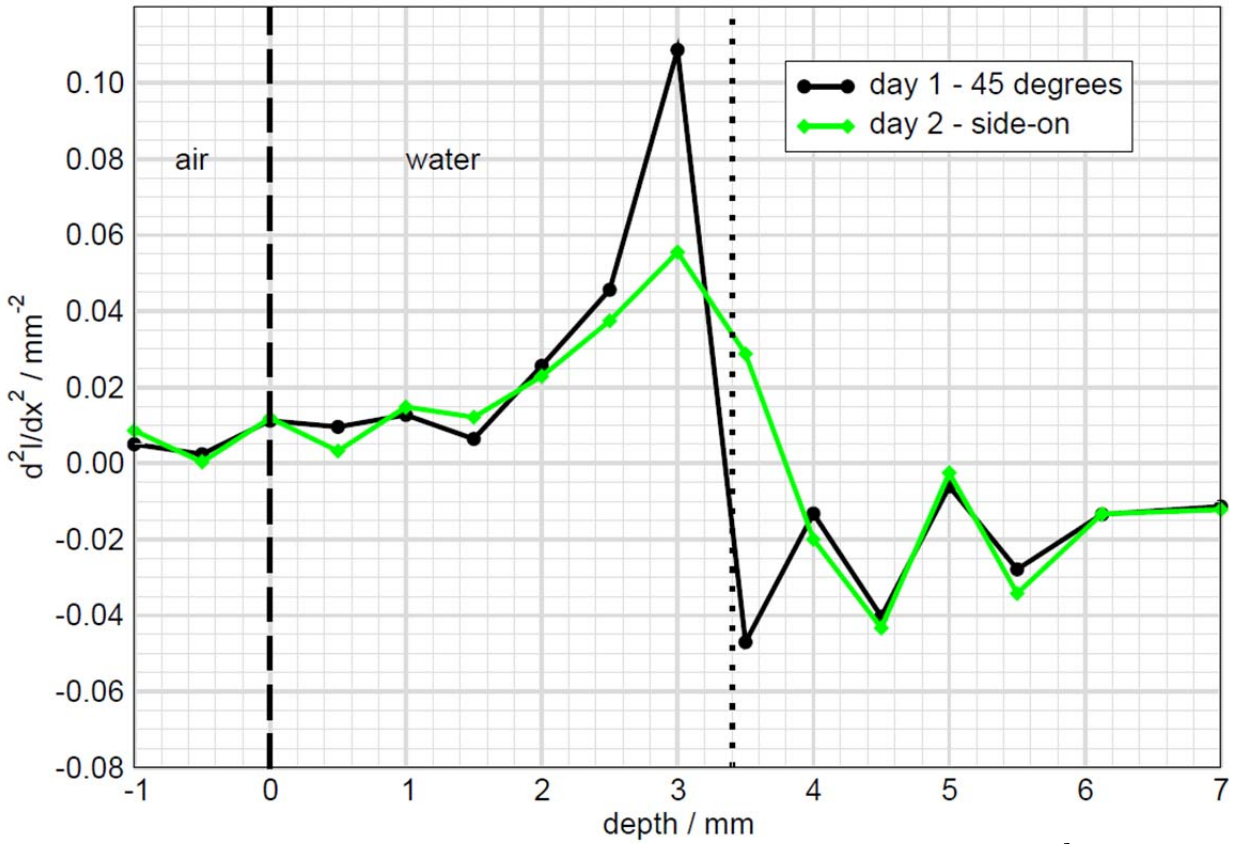

Figure 8: Second derivative peaks from scans with an IBA CC13 cylindrical IC for a 10×10 cm^2 field. Scans are performed from water to air at 0.5 mm resolution. No change in second derivative peak location occurs with a change in IC alignment relative to the optical telescope used for alignment. The difference in peak heights indicates that peaks will not always be observed at the same height when performing multiple trials of the same measurement. There is no physical reason for the change in IC alignment tested here to affect second derivative peak height. The second derivative peak is 0.4 mm shallower than the DeICERS. The dashed line represents the nominal water surface position. The dotted line represents the DeICERS.

Figure 10 shows that for the same incident beam energy and field size, the eight similarly-sized ICs (6.35-7.0 mm outer radius) exhibit second derivative peaks within the 0.5 mm measurement resolution of one another, with the smallest IC, the IBA CC01, and the two largest types, Exradin A2 v1 and v2 showing anticipated dependencies on IC outer radius and

wall thickness. When each IC outer radius was subtracted from the second derivative peak location, as shown in Figure 11, each individual peak occurred within measurement resolution of the nominal water surface, though the maximum deviation between inflection peaks was >0.8 mm. The total spread in second derivative peaks measured in this work called into question the effect of scan resolution on second derivative peak resolution and location. It was concluded that measurements at <0.5 mm resolution would be required to properly evaluate the scan second derivative as a metric for quantitative IC water surface alignment. The influence of scan resolution is examined in Section 4.2.3. Portions of this work were presented as part of the 2009 AAPM Young Investigators Symposium (Ververs *et al.*, 2009a) and at the International Union for Physical and Engineering Sciences in Medicine World Congress 2009 on Medical Physics and Biomedical Engineering (Siebers *et al.*, 2009).

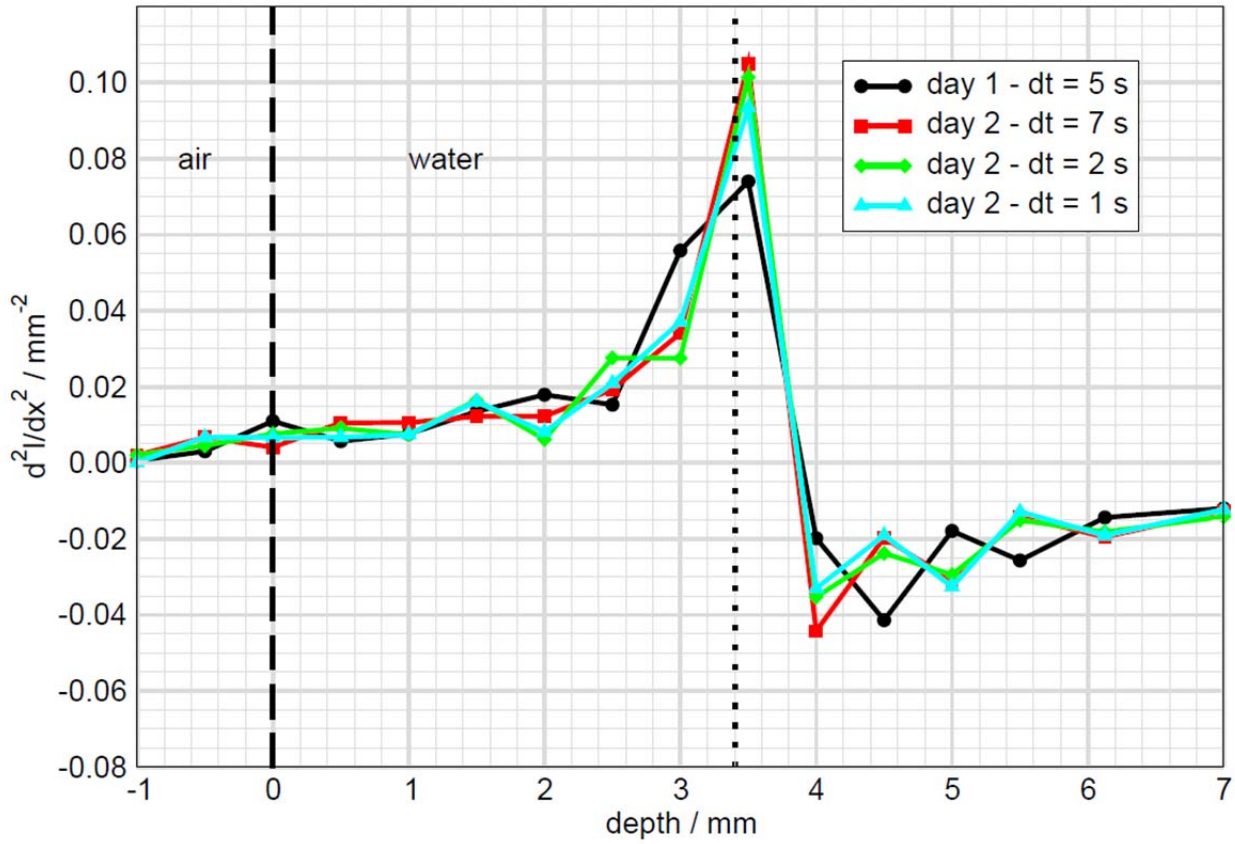

Figure 9: Second derivative peaks from scans with a PTW 31010 cylindrical IC for a 10×10 cm^2 field. Scans are performed from water to air at 0.5 mm resolution. No change in second derivative peak location occurs with a change in signal acquisition time. The second derivative peak is 0.05 mm deeper than the DeICERS. The dashed line represents the nominal water surface position. The dotted line represents the location of the DeICERS.

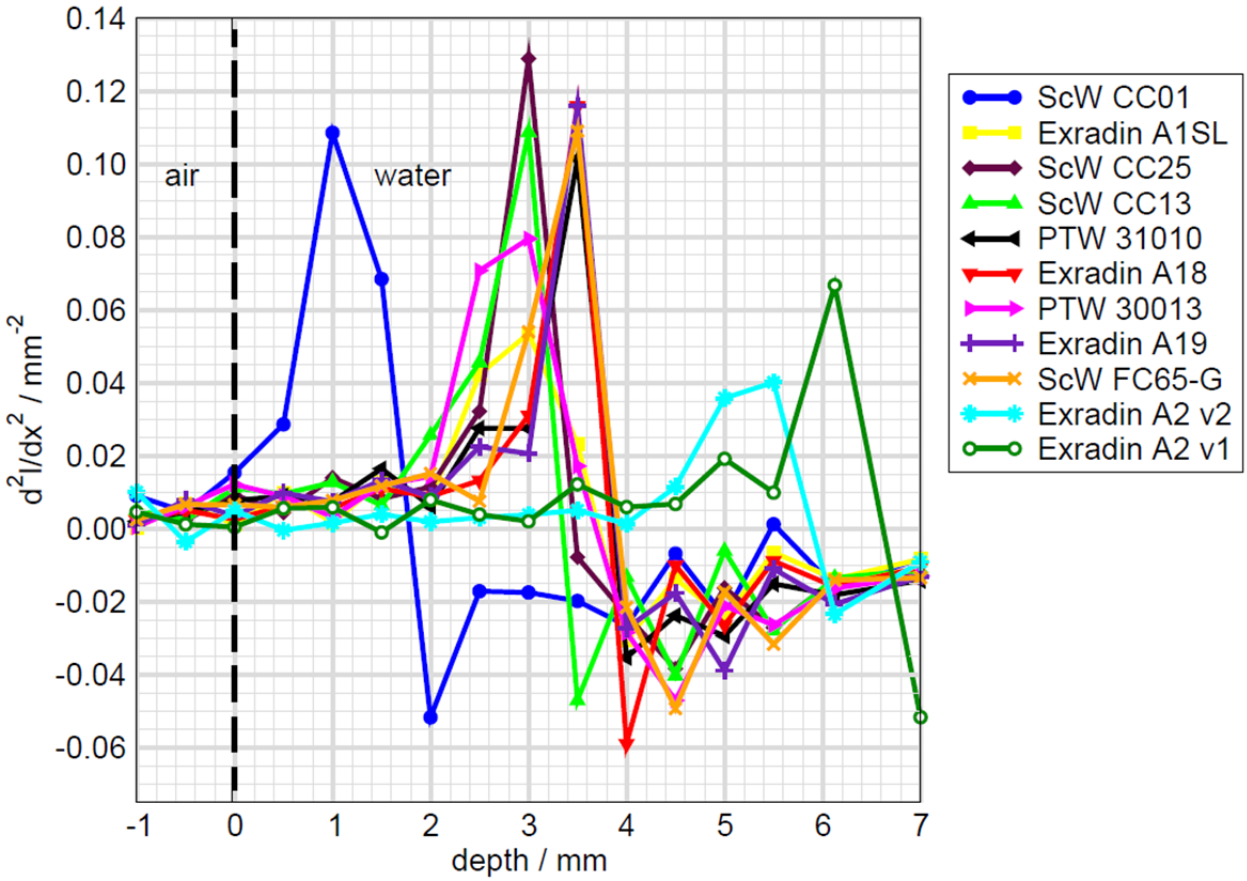

Figure 10: Comparison of second derivative peak locations for all eleven IC types scanned in the study described in Section 2.2. All data are computed from scans taken for 6 MV 10×10 cm^2 fields. The legend is sorted by IC outer radius from smallest to largest. The dashed line represents the nominal water surface position.

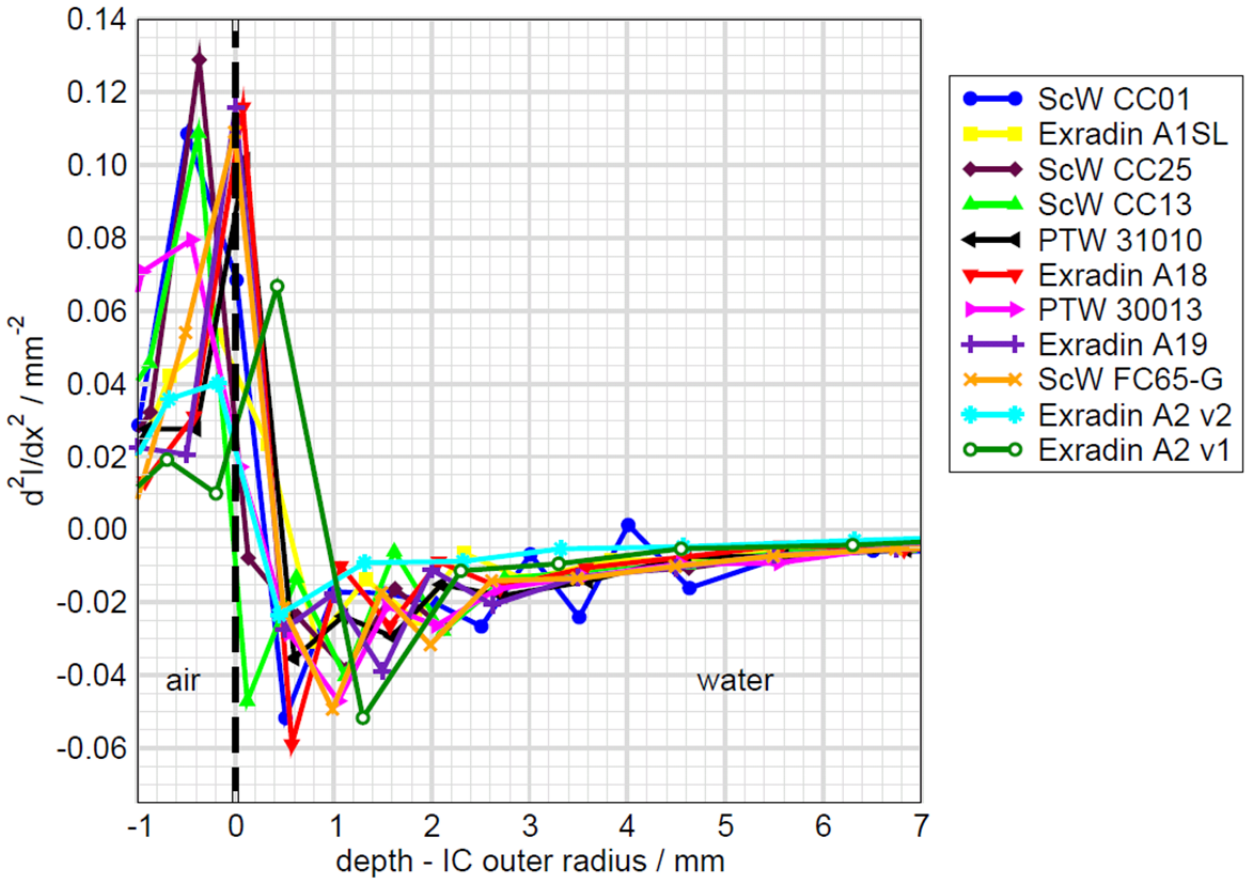

Figure 11: Comparison of second derivative peak locations after each corresponding IC outer radius is subtracted for all eleven IC types scanned in the study described in Section 2.2. All data are computed from scans taken for 6 MV 10×10 cm^2 fields. The legend is sorted by IC outer radius from smallest to largest. The dashed line represents the nominal water surface position.

2.3 Ionization Chamber Alignment Methods

Though the second derivative is the only metric used for quantitatively determining IC alignment in the works described in Section 2.1 and Section 2.2, there are other possible methods to be considered. Given that the work described above demonstrated that the second derivative shows promise as an IC alignment metric, the first derivative is a natural choice to examine. If quantitative IC alignment information could simply be obtained from the original scan data, this would be useful as no additional derivative computations would be required after data are obtained. Options for IC alignment methods and metrics are discussed in Section 2.3.1 and 2.3.2.

2.3.1 Derivatives

The second derivative was used successfully for scans taken at 0.5 mm resolution in the studies described in Section 2.1 and Section 2.2. However, as mentioned in Section 2.1, the second derivatives of the MC-simulated data required smoothing due to the high relative noise level. This served notice as an early indication that the second derivative might not be a suitable metric for dealing with measurement noise or the stochastic noise inherent in MC simulations. The conclusion of the expanded multiple cylindrical IC study that measurements at finer than 0.5 mm resolution were required provided an additional source of concern as relative positioning uncertainty, $\frac{\sigma_x}{x}$, is generally increased with finer resolution for fixed scan time. Since full functional forms for the measured data do not exist, derivatives are computed via simple finite gradient, $y' = \frac{y_2 - y_1}{x_2 - x_1} = \frac{\Delta y}{\Delta x}$. Using this method, the relative noise in the computed derivative is increased by decreasing the denominator, as happens for scans taken at fine resolution.

The interplay between the first two derivatives, scan resolution, and data noise can be derived using a set of any three data points $(x_1, y_1), (x_2, y_2), (x_3, y_3)$. Assume each y_i is of some inherent uncertainty, or noise, Δy_i. Also, assume that there exists in each location x_i some positioning uncertainty Δx_i. First derivatives are evaluated at the points $(x'_{1.5}, y'_{1.5}), (x'_{2.5}, y'_{2.5})$ while the second derivative is evaluated at point (x''_2, y''_2). The points at which first derivatives are evaluated are defined as $x'_{1.5} = \frac{x_1 + x_2}{2}$ and $x'_{2.5} = \frac{x_2 + x_3}{2}$, respectively. Uncertainties in first derivative evaluation points are then $\Delta x'_{1.5} = \frac{\sqrt{\Delta x_1^2 + \Delta x_2^2}}{2}$ and $\Delta x'_{2.5} = \frac{\sqrt{\Delta x_2^2 + \Delta x_3^2}}{2}$. The first derivatives are written as $y'_{1.5} = \frac{y_2 - y_1}{x_2 - x_1}$ and $y'_{2.5} = \frac{y_3 - y_2}{x_3 - x_2}$. The propagated uncertainties in the first derivative points are then

$\Delta y'_{1.5} = \frac{\sqrt{(x_2-x_1)^2(\Delta y_1^2+\Delta y_2^2)+(y_2-y_1)^2(\Delta x_1^2+\Delta x_2^2)}}{(x_2-x_1)^2}$ and $\Delta y'_{2.5} = \frac{\sqrt{(x_3-x_2)^2(\Delta y_2^2+\Delta y_3^2)+(y_3-y_2)^2(\Delta x_2^2+\Delta x_3^2)}}{(x_3-x_2)^2}$.

These expressions show that as data is acquired at finer resolution, the noise in the first derivatives will be increased. The second derivative is written as

$$y''_2 = \frac{(y'_{2.5} - y'_{1.5})}{(x'_{2.5} - x'_{1.5})} = \frac{2[(y_3 - y_2)(x_2 - x_1) - (y_2 - y_1)(x_3 - x_2)]}{(x_3 - x_1)(x_3 - x_2)(x_2 - x_1)}$$

The uncertainty in the second derivative is given by

$$\Delta y''_2 = \frac{\sqrt{(x'_{2.5} - x'_{1.5})^2[(\Delta y'_{1.5})^2 + (\Delta y'_{2.5})^2] + (y'_{2.5} - y'_{1.5})^2[(\Delta x'_{1.5})^2 + (\Delta x'_{2.5})^2]}}{(x'_{2.5} - x'_{1.5})^2}$$

If it is assumed that the data is acquired at constant resolution, it can be written that $(x_2 - x_1) = (x_3 - x_2) = x_{res}$. To further simplify the final expression, it is also assumed that the uncertainty in each x_i is the same Δx and the uncertainty in each y_i is the same Δy at each point (x_i, y_i). This allows the expression for the second derivative error to be written as

$$\Delta y''_2 = \frac{\sqrt{4x_{res}^2\Delta y^2 + \Delta x^2[(y_3 - y_2) - (y_2 - y_1) + 2(y_3 - y_2)^2 + 2(y_2 - y_1)^2]}}{x_{res}^3}$$

This shows that regardless of the chosen data resolution, noise in the second derivative will be amplified as compared with the first derivative. This amplification will only become greater for finer resolution. It can be drawn from the expression that the worst noise amplification will occur in regions of large differences in y for a given resolution, such as the buildup region of the depth-ionization curve. Given the issue of noise propagation, particularly for fine resolution, the first derivative is deemed a better metric than the second. The utility of the first derivative for quantifying IC alignment at a water surface is shown using analytical and computational models in Chapter 3.

2.3.2 Curve Matching

There are several methods by which a test PDD curve could be matched to a reference curve. As demonstrated in the study discussed in Section 2.1, minimizing the SSQD between test and reference scans is a viable option, provided suitable reference data is available against which comparisons can be performed. Reference data can be obtained through MC simulations where the water surface position is known exactly, using a model of the IC in question, or by taking measurements where the IC alignment can be independently established, such as with the optical telescope used in the NRC scanning system. Alternatively, if derivatives prove to be a robust metric for evaluating IC alignment, reference data can be obtained for a given IC by carefully scanning following a standardized procedure and evaluating the scan derivatives. This reference data can then be used for comparison with future scans. This will be discussed further in Chapter 5. The work in this thesis in part examines the degree to which measurements with standard clinical equipment can be taken similarly to reference measurements. Reference MC calculations for all of the required scenarios would require substantial computation time and resources. The in-house simulations described in Section 3.2 required thousands of CPU hours. Therefore, dependencies of the clinical scan process are examined in hopes of reducing the number of reference measurements necessary to establish a known water surface alignment.

One alternative to comparisons with reference measurements or simulations is to compare test measurements with a set functional form to find the surface location. Here, the difficulty is in determining a functional form that is sufficiently general as to handle multiple variables in the test scans, such as radiation field conditions and IC types. The freeware graphics program *extrema* (version 4.4.5, © Joseph L. Chuma) is used to develop a scriptable method of fitting a given measured, or simulated, curve to a functional form. The functional form is split

into two pieces, one for the portion of the buildup curve that occurs totally in water, along with data after d_{max}, and the other to account for the portion of the scan that occurs as the IC is emerging through the water surface into air, for a scan taken from water into air. To illustrate the two pieces within the context of Figure 3, the first fit occurs over the portion of the curve representing panels f)-i) and the second fit occurs over the portion of the curve representing panels a)-e).

The idea of splitting a functional form into two pieces stems from a paper by Das, McNeeley, and Cheng (Das *et al.*, 1998). In this work, electron depth-ionization measurements were conducted with a cylindrical IC up to 35 mm above the water surface. By fitting a linear function representing IC response in air to another linear function representing in-water response, the optimal EPOM shift from the surface and surface dose were determined. The surface doses calculated from the fits were then compared with surface doses measured with a parallel-plate IC and found to be within 3% error for five electron beam energies (Das *et al.*, 1998). Figure 12 illustrates the fitting technique for one 6 MeV and one 6 MV measurement, both made at VCU for the same field size and SSD with an IBA CC13. Fitting was done by eye to produce Figure 12; the dashed lines are simply for illustrative purposes. In principle, the fitting approach demonstrated here could have been applied to parallel-plate IC measurements. The purposes of the work by Das, McNeeley, and Cheng (Das *et al.*, 1998), however, were to find electron beam EPOM shifts and surface doses. Surface dose and the EPOM are generally both considered to be well-understood for parallel-plate ICs. Linear fitting in water is not used in this work as photon beams yield a much less linear buildup response in water than do electron beams.

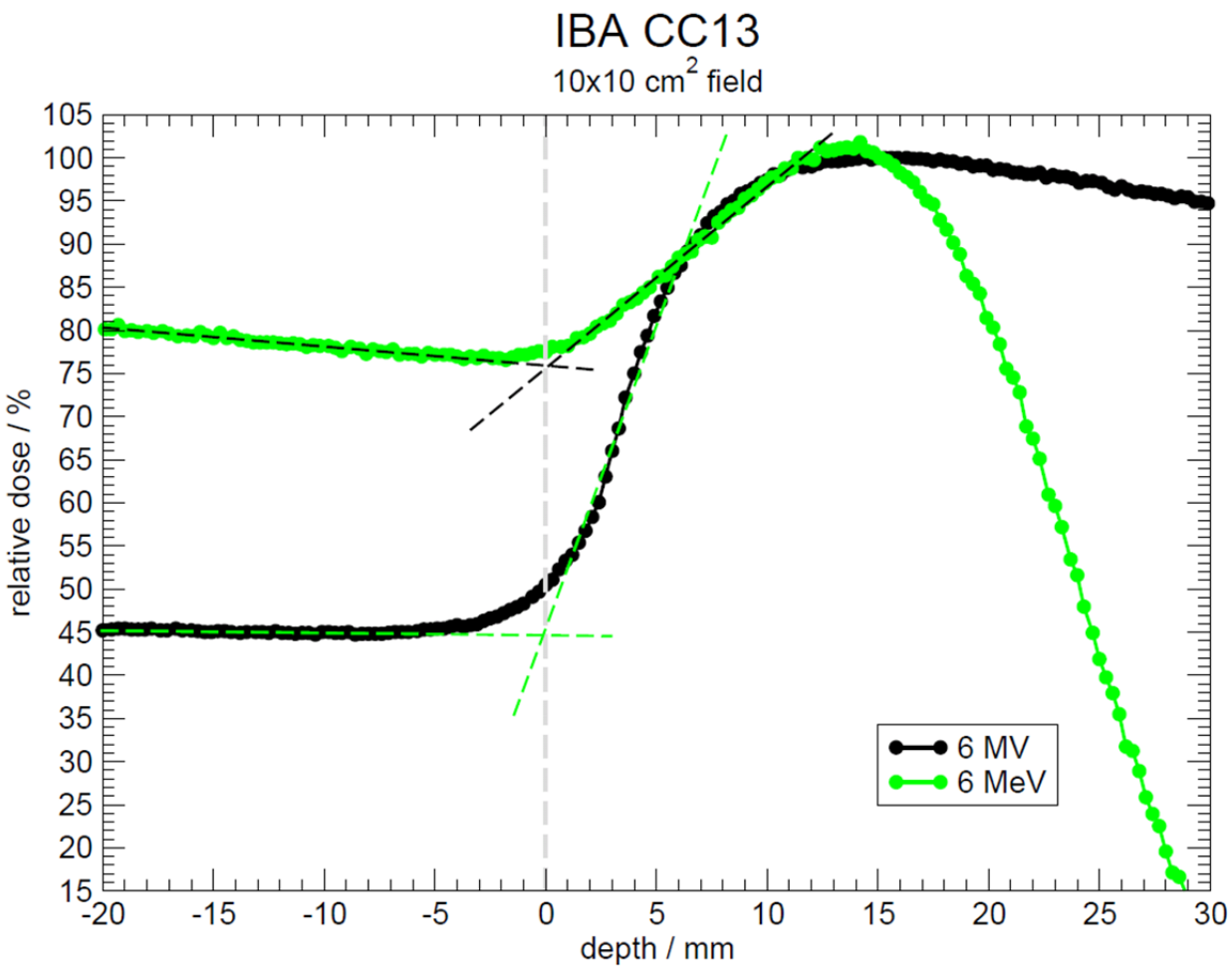

Figure 12: Comparison of a 6 MV photon scan with a 6 MeV electron scan to demonstrate the relative linearity of electron buildup response as compared with photon response in the same region. Both scans are taken with an IBA CC13 in a 10×10 cm^2 field. Scans are taken from water to air in continuous mode at 0.3 mm nominal resolution at low speed (1.75 mm/s). The dashed grey line represents the nominal water surface location. Contrasting dashed lines are drawn to demonstrate the fitting method of Das, McNeeley, and Cheng (Das *et al.*, 1998) who used the method to estimate the EPOM shift and surface dose for electron beam measurements with a cylindrical IC.

In the fitting routine used for this thesis, an initial estimate of the location of the occurrence of the functional form split is taken as the IC outer radius. This is presumed to be true for a perfectly aligned measurement. A window of a user-defined width is set around the initial guess and possible fit junction locations are then iterated over, at a user-defined interval, within that window. The optimal fitting junction is determined by computing the χ^2 goodness of fit parameter for the in-air and in-water fits, summing the total χ^2 for each iteration of fit junction location, and finding the minimum total χ^2. The χ^2-minimization approach is used to find

optimal EPOM values in the works by Kawrakow (Kawrakow, 2006) and Tessier and Kawrakow (Tessier and Kawrakow, 2010). The expression for χ^2, as computed in *extrema*, is

$$\chi^2 = 2\sum_k \left[f(x_k, p_{min}) - y_k + y_k \ln \frac{y_k}{f(x_k, p_{min})} \right]$$

Here, f represents the expression to be fitted, x_k is the abscissa of the measured data set at index k, y_k is the ordinate of the measured data set at index k, and p_{min} are the set of fitting parameters that provide the best fit. There is an assumption made by the χ^2 formulation that each y_k can be described by Poisson statistics, which in turn forces the assumption that the error in each y_k is independently random.

After tests of various functional forms and qualitative comparison with measurements, the in-water functional form is taken empirically to be $y = ae^{bx} + cx + d$. The in-air functional form varies depending on which class of IC is being tested. If the tested IC is a cylindrical design, the in-air functional form is $y = ae^{bx} + c$, while if the tested IC is a parallel-plate design, the in-air functional form used is $y = ax + b$. To assess the ability of these functional forms to provide meaningful IC depth alignment information, functional fits to data taken at the NRC with the customized scanning system described in publication (McEwen *et al.*, 2008) and in Section 4.1.3 are described here. The NRC measurements are chosen for this test because of the high resolution at which measurements are conducted (0.1 mm near the water surface) and because the depth alignment of each IC used for these measurements is independently known to be of high precision. Therefore, any observed deviations when applying the functional fits described here are attributed to issues with the fits rather than the measurements themselves. The location of the junction of the applied fits is iterated at 0.05 mm intervals over a 1 mm window around the IC outer radius.

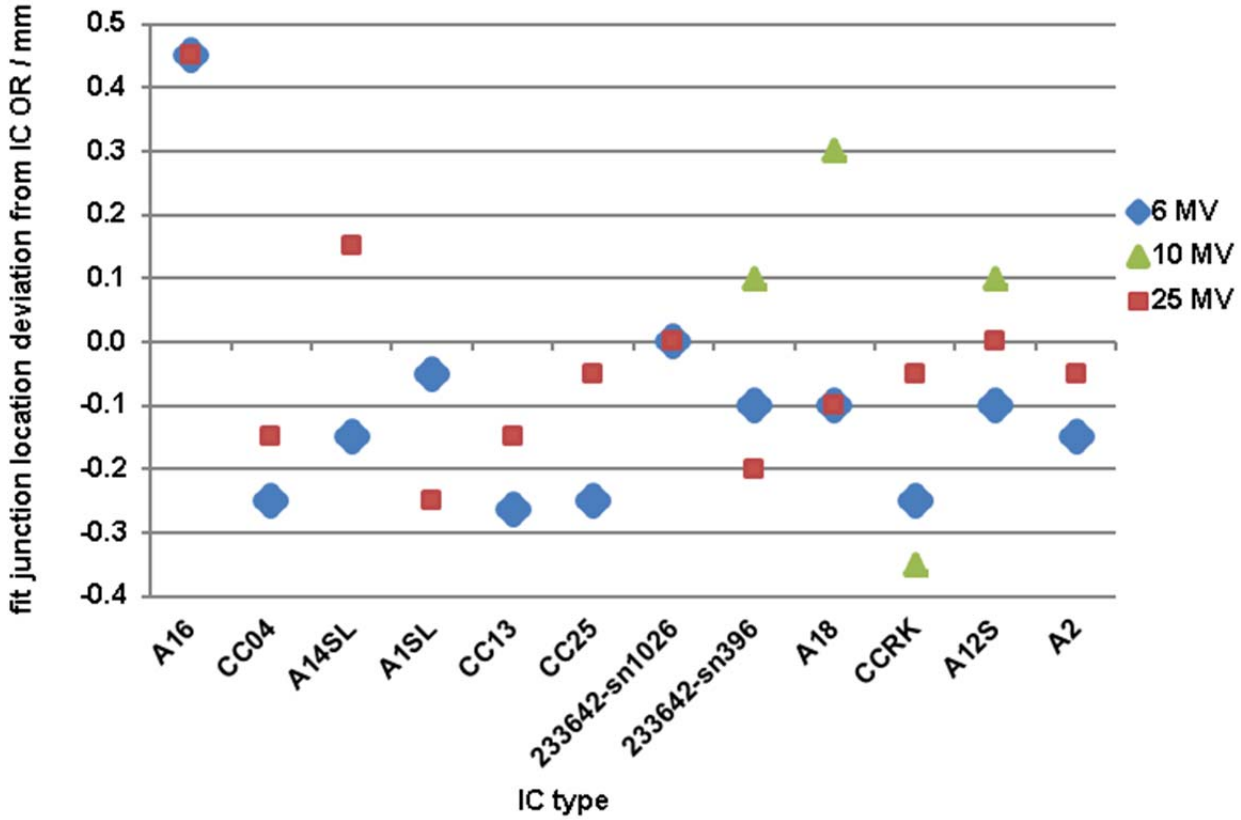

Figure 13: Results of functional fits applied to measurements taken with 12 cylindrical IC models at NRC using the customized high-precision scanning system. The y-axis is the deviation of the optimal location for the junction of the two functional fits, as determined by total χ^2 minimization, from the IC outer radius (OR). The x-axis is sorted by IC OR from smallest to largest. The IC OR is the expected location of the optimal fit junction. Only 4 IC models are scanned in 10 MV beams. All ICs are scanned at 6 and 25 MV. All scans are conducted at 0.1 mm resolution in the region of interest near the surface from water to air in 10×10 cm^2 fields at 100 cm SSD.

The results of the fits are shown in Figure 13. Though all deviations of optimal fit junction location from IC outer radius are <0.5 mm, there are several undesirable results. If the fits are to be believed, there is a notable IC alignment dependence on incident beam energy, which is not supported by previous work with scan second derivatives or by intuition. Figure 13 also indicates a lack of alignment consistency in IC models of the same nominal type. Two PTW 233642 models are scanned, serial number (SN#) 1026 and SN# 396. SN# 396 exhibits a 0.3 mm spread in optimal fit junction location while SN# 1026 indicates perfect alignment. A 0.3 mm deviation in IC alignment for outwardly identical ICs of the same type by the same user is unlikely when using the scanning system used for the NRC measurements. While the curve

fitting approach described here may be suitable for detecting gross alignment errors, given that all discrepancies observed here still occur within ±0.5 mm, it does not appear capable of reliably evaluating alignment at the desired precision of 0.15 mm.

2.4 Conclusions

Scan second derivatives, though used in early studies to evaluate IC water surface alignment, are not suitable for use with noisy data. Additionally, second derivatives provide ambiguous alignment information in some instances with 0.5 mm scan resolution. Scan first derivatives, or gradients, are more robust against scan noise than are second derivatives. Fitting original scan data acquired at high resolution (0.1 mm) with functional forms indicates IC scan alignment dependencies on radiation beam energy that are not observed when using scan second derivatives. Additionally, functional form-based curve fitting indicates a variation in alignment of models of the same IC type that is twice the initial alignment uncertainty. Therefore, scan gradients are deemed the most reliable metrics of the considered methods. Chapter 3 begins by considering the theory behind the relationship of the IC signal gradient to the air/water interface.

3 Theory

As presented thus far, the identification of a PDD scan feature that provides information about IC alignment has been solely empirical. At the conclusion of Chapter 2, the scan first derivative is identified as the metric to be used to evaluate IC depth scan alignment. In this chapter, the influence of the air/water interface at the water surface on IC signal is evaluated theoretically. The evaluation begins with a simple analytical model of IC response and continues by considering MC simulation models used to isolate individual design parameters of cylindrical ICs.

3.1 Analytical Model

Before describing the analytical model in detail, the limiting assumptions of the model are made explicit at the outset. The analytical model contains a number of assumptions that limit the direct applicability of the model to real measurement conditions. First, it is assumed that electrons have infinite range with no energy loss. Secondary electrons, in reality, have short ranges (~1.8 mm in water for 0.5 MeV electrons), that are determined using the CSDA approximation that assumes electrons lose energy continuously as they pass through matter. Electrons are assumed to be produced in only the forward direction and to follow the same straight paths as the photons of the incident beam. In reality, electrons travel in generally jagged paths, where the changes in direction are caused by frequent interactions with the nuclei and atomic electrons of the medium. Given the above assumptions, IC response is assumed to be

directly proportional to electron pathlength through the IC, while absorbed dose in a cavity depends on the charged particle fluence, mass collisional stopping power of the cavity material, and the mass thickness crossed by charged particles. It is assumed that the incident photon beam is unattenuated with increasing water thickness. In practice, as photon beams pass through material, lower energy photons are preferentially attenuated, which increases the mean energy of the primary beam with depth of material. This beam "hardening" effect is compensated for in practice by low-energy scattered photons, for which this model also does not account. The IC model used is a simple cylindrical central axis cross-section, not including a central electrode, a hemispherical end cap, or any treatment of three-dimensional IC volume. The incident photon beam is assumed to be parallel and infinite. Real therapy beams diverge from an apparent source position to a defined field size at a defined SSD.

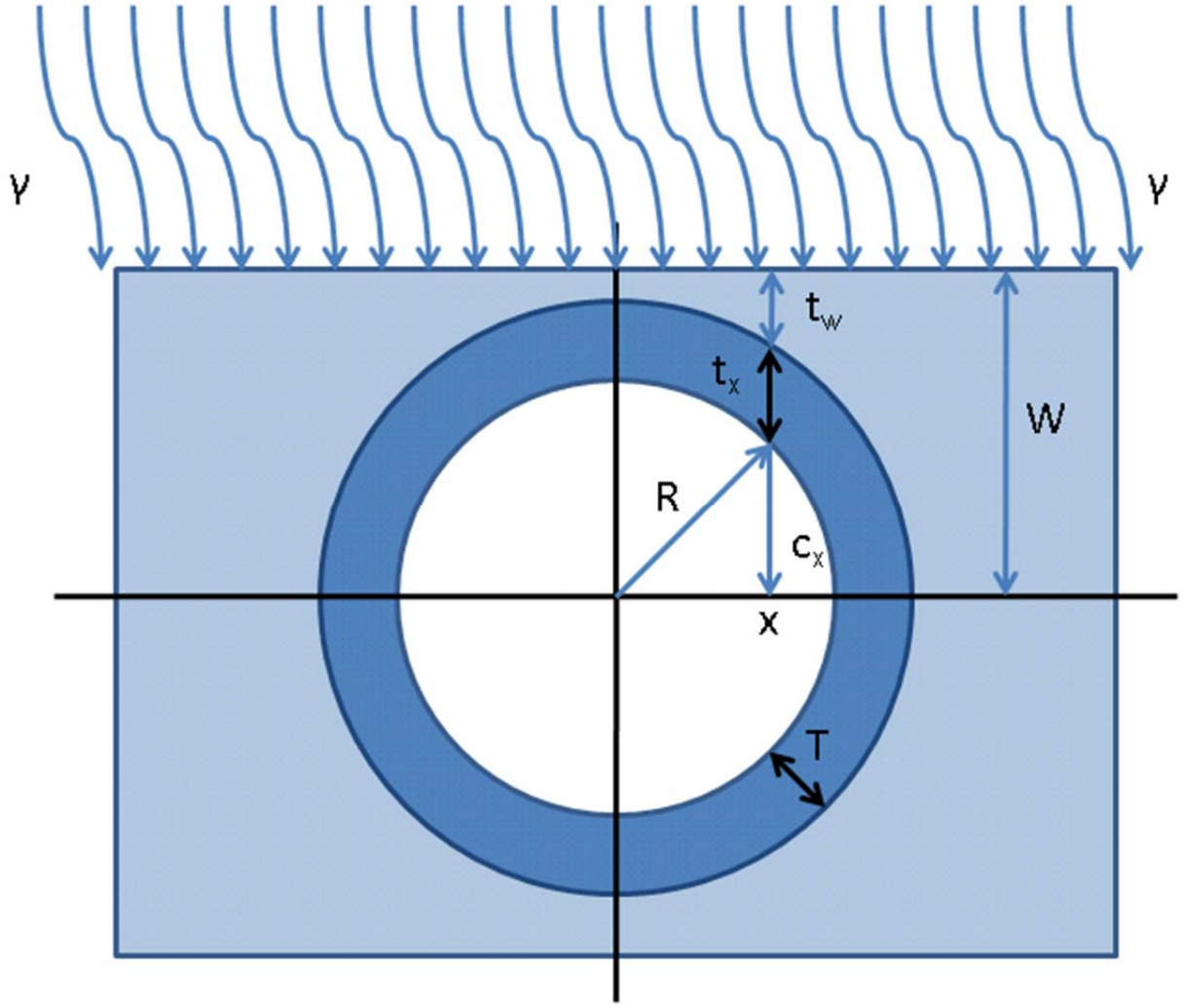

Figure 14: Geometry of the analytical model used to test idealized cylindrical IC response dependence on the IC cavity radius, R, IC wall thickness, T, and water height relative to the IC central axis, W, given an incident parallel photon beam. The position along the IC axis at which a single photon ray passes through the IC is denoted as x. The photon pathlength through the IC is denoted c_x and the pathlength through the wall is given as t_x. Photon pathlength through the water between the IC and the water surface is denoted t_w.

An analytical model is developed to provide a simple geometry-based evaluation of theoretical IC response. The analytical model geometry is shown in Figure 14. The model represents a cross-sectional slice of a simplified cylindrical IC of inner cavity radius R and wall thickness T without a central electrode. The IC is placed in water and is subjected to a parallel photon beam. At any given IC depth, the water surface is a given distance W away from the IC central axis. The total distance that must be traveled by each photon ray to reach the IC central axis is given by $c_x + t_x + t_w$, where c_x is the pathlength through the air cavity, t_x is the wall

pathlength, and t_w is the pathlength through water. It is assumed that the total signal in the air cavity is a linear combination of signals provided by the wall and by the water, respectively. The wall-dependent signal is essentially constant for a wall of constant thickness, so that the total signal is in turn proportional to the water-dependent signal. The water-dependent signal is assumed to be directly proportional to the electron pathlength through water t_w for all rays. Therefore, $s_w \propto \int_{x_w}^{R} t_w(x)dx$, where s_w is the total water-dependent signal, x is the distance from the IC origin at which a given ray crosses the IC central axis, and x_w is the x-coordinate at which water begins to contribute to the collected signal. Water contributes to the signal when the water level has reached the point where $W = R + T$, thus $x_w = \sqrt{(R+T)^2 - W^2}$, $R + T \geq W$. When the IC is below the water surface, x_w equals 0 for $R + T < W$. Expressing t_w as a function of x gives $t_w = W - (c_x + t_x)$, where $c_x + t_x = \sqrt{(R+T)^2 - x^2}$ for any $x \in [0, R]$. This provides everything necessary to fully state the integral,

$$s_w \propto \int_{\sqrt{(R+T)^2 - W^2}}^{R} W - \sqrt{(R+T)^2 - x^2}\,dx$$

The final evaluated expression is given as

$$s_w \propto \frac{1}{2}\left[2WR - R\sqrt{2W - T^2 + 2RT} - (R+T)^2 \tan^{-1}\frac{R}{\sqrt{T^2 + 2RT}} - W\sqrt{(R+T)^2 - W^2} + (R+T)^2 \tan^{-1}\frac{\sqrt{(R+T)^2 - W^2}}{W}\right]$$

Mathematica (version 5.0.1.0, Wolfram Research, Inc., Champaign, IL) is used to compute the integral. The resulting expression is used in a Matlab (version 7.10.0.499, The MathWorks, Inc., Natick, MA) script that plots total response as a function of water above the IC central axis, along with the first and second derivatives of response, for a given choice of IC

inner radius and wall thickness. Running the script for an inner IC radius of 3.0 mm and 0.4 mm wall thickness gives the results shown in Figure 15. Both the response gradient (1st derivative) and curvature (2nd derivative) change noticeably at the IC outer radius. Though not shown here, this result has been reproduced for a wide range of inner radii and wall thicknesses. It bears pointing out again that this is representative of the response through a single cross-sectional slice of a simple IC. The response from real cylindrical ICs is proportional to the total IC volume, V_{tot}, which includes the cylindrical volume, V_{cyl}, and the volume of the hemispherical end cap, V_{hemi}, such that $V_{tot} = V_{cyl} + V_{hemi}$. For most cylindrical ICs, the cylindrical volume, where the IC outer radius is constant, will dominate the end cap volume, where the IC outer radius changes. For micro-ICs, however, the hemispherical end cap region can be >50% of the total IC volume. This can affect the IC response gradient by blurring the observed change, as different cross-sectional slices of the hemispherical IC cap will meet the water surface at different depths.

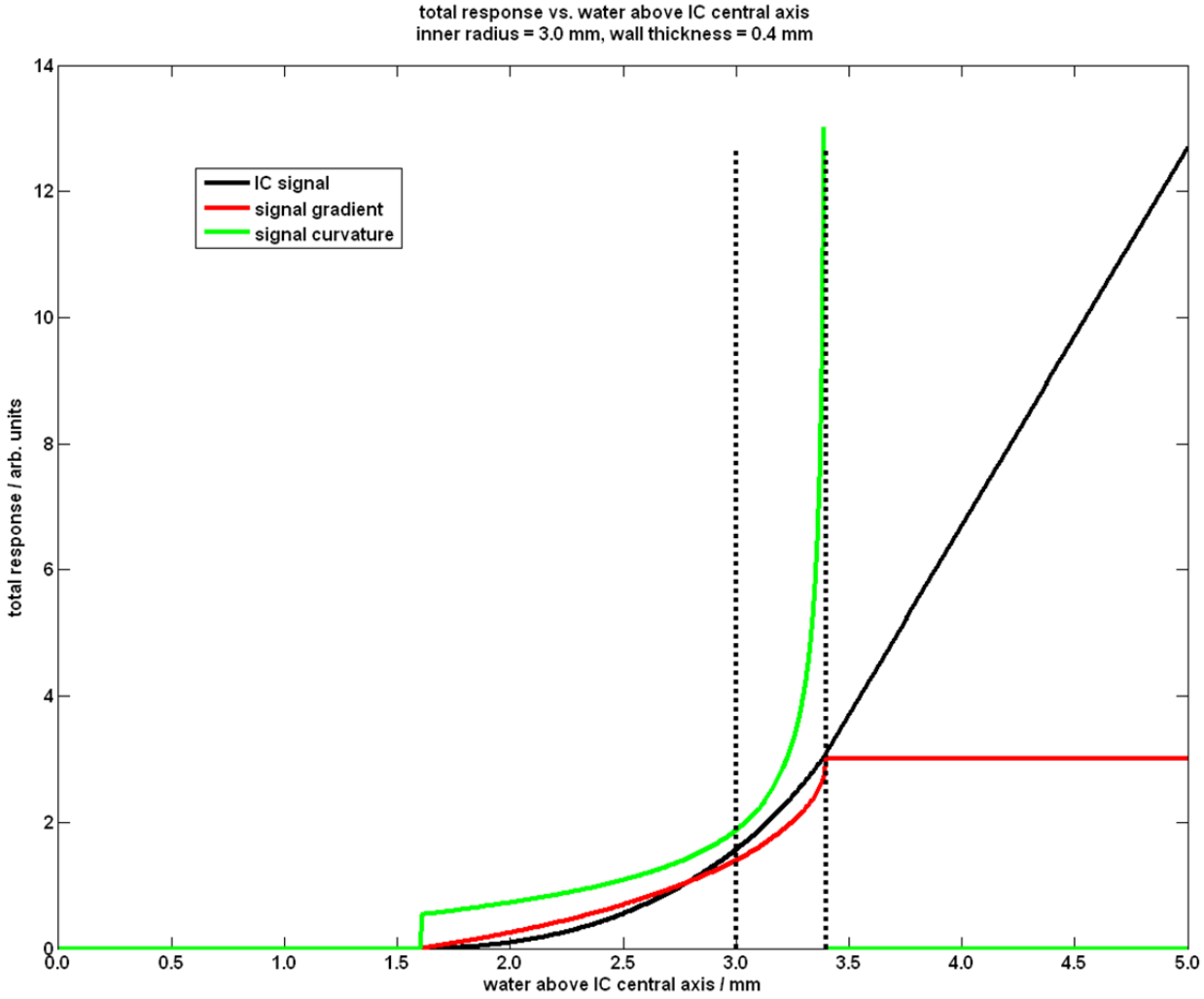

Figure 15: IC response as a function of the water height above the IC central axis with corresponding first and second derivatives as determined by the analytic model. The shapes of the response gradient and response curvature both change noticeably at the IC outer radius. Inner and outer IC radii are denoted by dotted lines. Inner radius and wall thickness dimensions are chosen to match the IBA CC13.

3.2 Monte Carlo Simulations

The physics models in MC code packages are far superior to the physics contained in the analytical model. Thus, rather than continue with the analytical model, an examination of scan gradient dependence on IC design features is conducted using the EGSnrc code system (Kawrakow, 2000a, b; Kawrakow and Rogers, 2003). BEAMnrc (Rogers *et al.*, 2006), a user code designed specifically for medical linear accelerator treatment head particle transport simulations, is used to model the Varian accelerator treatment head. A detailed discussion of the

use of MC to model medical linear accelerator photon beams is given in a review article by Verhaegen and Seuntjens (Verhaegen and Seuntjens, 2003). Separate simulations, also using BEAMnrc, including a model of the Elekta Precise accelerator installed at the NRC are conducted by Dr. Frédéric Tessier of the NRC. The xz- and yz- schematic views of the VCU Varian geometry are shown in Figure 16 and Figure 17, respectively. The monitor chamber and mirror do not completely appear in these screenshots. Several aspects of the institutional beam model have been updated in this version from what has been previously published upon (Libby *et al.*, 1999; Siebers *et al.*, 1999; Keall *et al.*, 2003). Updates are made to match electron contributions from various shielding components, as indicated by other authors (Kase *et al.*, 1996; Bednarz, 2008; Chibani and Ma, 2007; Chibani *et al.*, 2011).

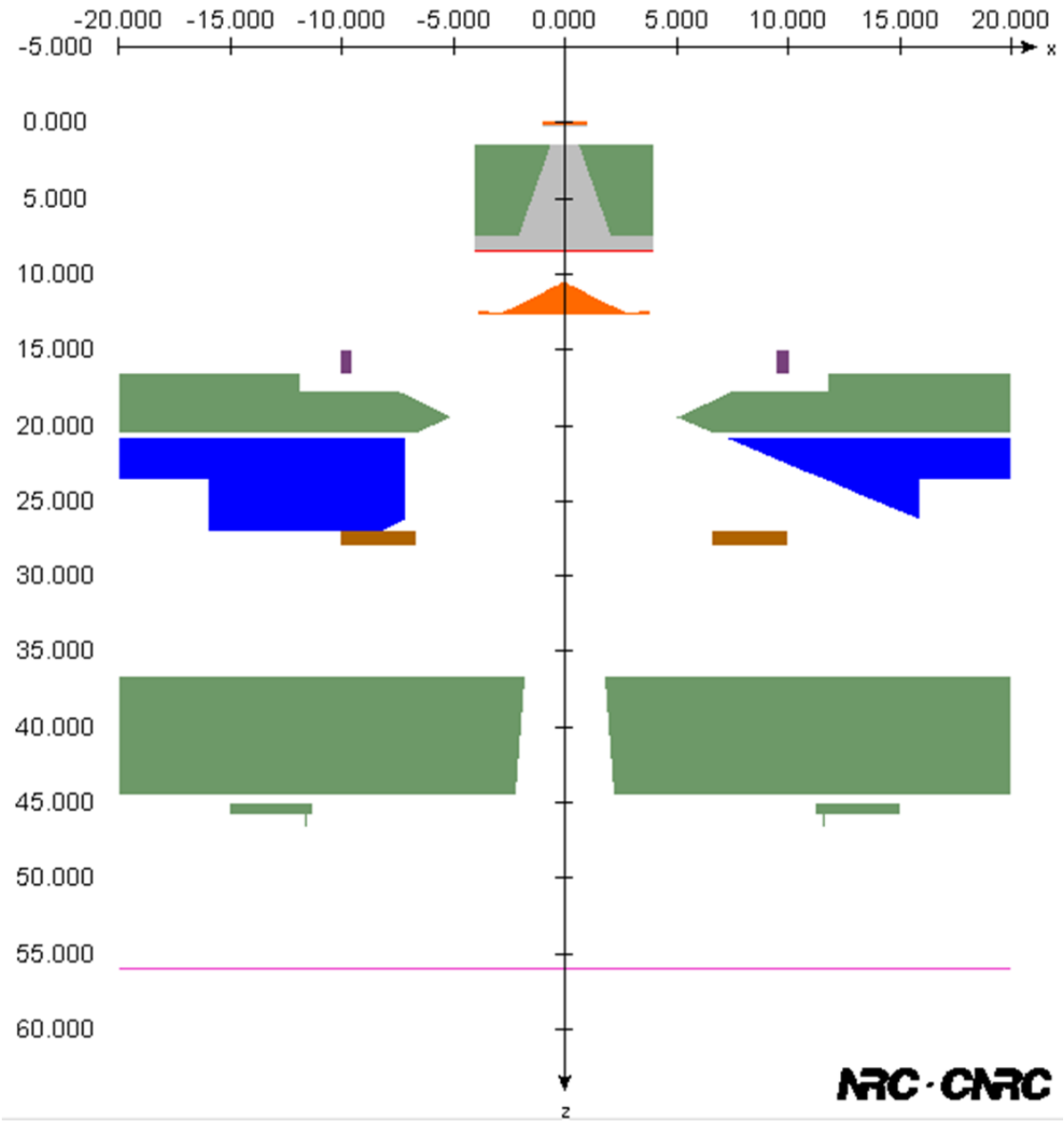

Figure 16: Screen capture from the BEAMnrc GUI showing a schematic of the xz-plane of the 6 MV treatment head geometry for the Varian 2100/2300 series. The jaws here are set to give a 10×10 cm^2 field. Air is represented in white. The target, primary collimator and exit window, flattening filter, monitor chamber, mirror, jaws, and polyester film sheet at the end of the treatment head are shown here, along with multiple shielding components. Vacuum is depicted in grey, beryllium is red, copper is orange, polyimide film is purple, polyester film is pink, and steel is brown. Polyimide film and polyester film are more commonly referred to by the trade names Kapton® and Mylar®, respectively. Shielding is shown in green (tungsten) and blue (lead).

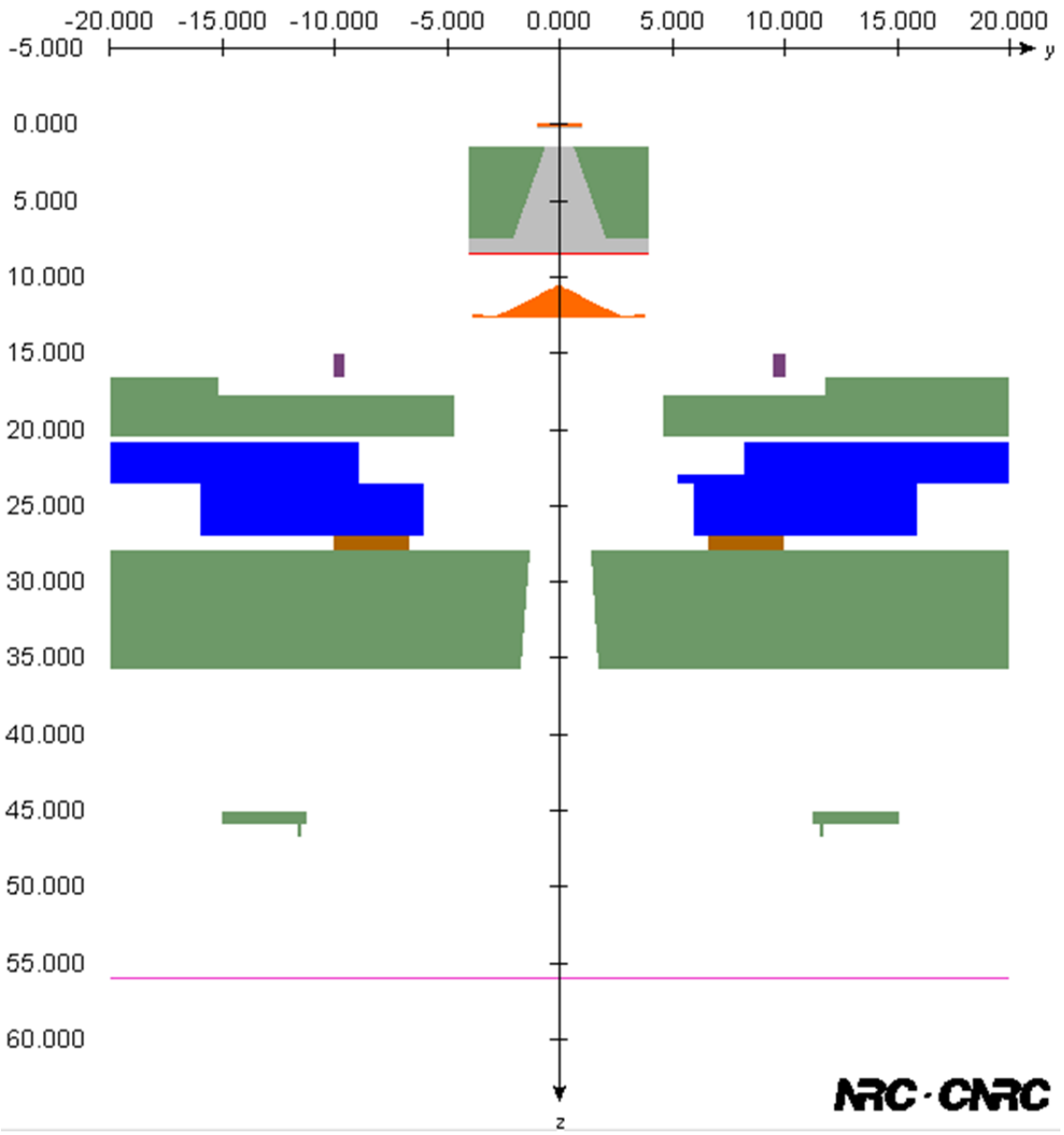

Figure 17: Screen capture from the BEAMnrc GUI showing a schematic of the yz-plane of the 6 MV treatment head geometry for the Varian 2100/2300 series. The jaws here are set to give a 10×10 cm^2 field. Air is represented in white. The target, primary collimator and exit window, flattening filter, monitor chamber, mirror, jaws, and polyester film sheet at the end of the treatment head are shown here, along with multiple shielding components. Vacuum is depicted in grey, beryllium is red, copper is orange, polyimide film is purple, polyester film is pink, and steel is brown. Polyimide film and polyester film are more commonly referred to by the trade names Kapton® and Mylar®, respectively. Shielding is shown in green (tungsten) and blue (lead).

The egs_chamber user code (Wulff *et al.*, 2008), based on the egspp C++ library (Kawrakow, 2005) is designed to model the radiation dose accumulated within the cavity of an IC. Inclusion of an IC model in MC dose calculations is a technique that has been used by a

number of authors to improve the agreement between measurements and simulations (Abdel-Rahman *et al.*, 2005; Tonkopi *et al.*, 2005; Kawrakow, 2006; Chibani and Ma, 2007; McEwen *et al.*, 2008). In the work described here, a model of the Exradin A18 geometry designed, and graciously shared, by Dr. Tessier is used for all egs_chamber calculations. The full IC and simplified IC models are shown in Figure 18. The full model contains detail outside the active cavity region such as the insulation, guard ring, and washer that is used to clamp the electrode, guard ring, and insulation to the IC stem. This model is used in all NRC simulations and denoted as the "full IC" in figure captions showing results of simulations conducted at VCU. A simplified IC model is also shown, where the region outside the active IC cavity is made a layer of conductive plastic seated into the aluminum IC stem. Simulations using this IC model were only performed at VCU and are denoted as "simple IC" in relevant figure captions.

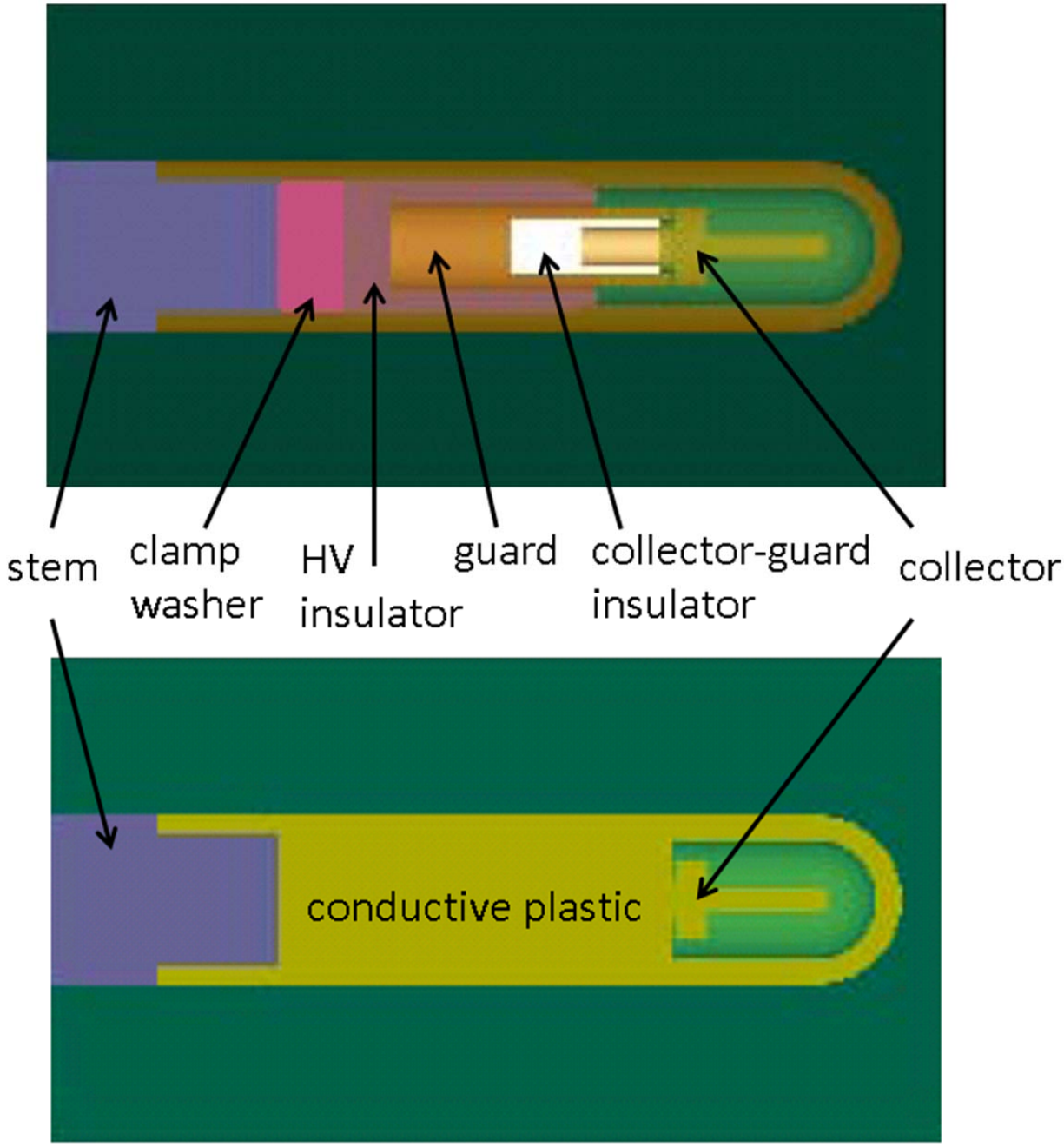

Figure 18: Full and simplified models of the Exradin A18 cylindrical IC used for VCU MC simulations. The detail of the full model outside the active cavity region is replaced in the simple model by a layer of conductive plastic.

3.2.1 Computational Model Comparisons

Comparisons are made of in-house Exradin A18 measurements with simulations using the updated VCU Varian head model, linked as a shared library particle source as described by Tonkopi, et al., (Tonkopi *et al.*, 2005). Examples are shown for a 6 MV 10×10 cm^2 field in Figure 19 and for an 18 MV 4×4 cm^2 field in Figure 20. These comparisons show that in-air dose is not yet modeled perfectly but the objective of the simulations here is to examine the impact of changes in IC design parameters on the depth dose gradient. Dr. Tessier also performed simulations using the same nominal Exradin A18 IC geometry placed in an independent virtual phantom with incident particles from an independent model of the NRC Elekta Precise accelerator. The NRC Elekta Precise head model has been validated and documented in previous publications (Tonkopi *et al.*, 2005; Kawrakow, 2006; McEwen *et al.*, 2008; Tessier and Kawrakow, 2010).

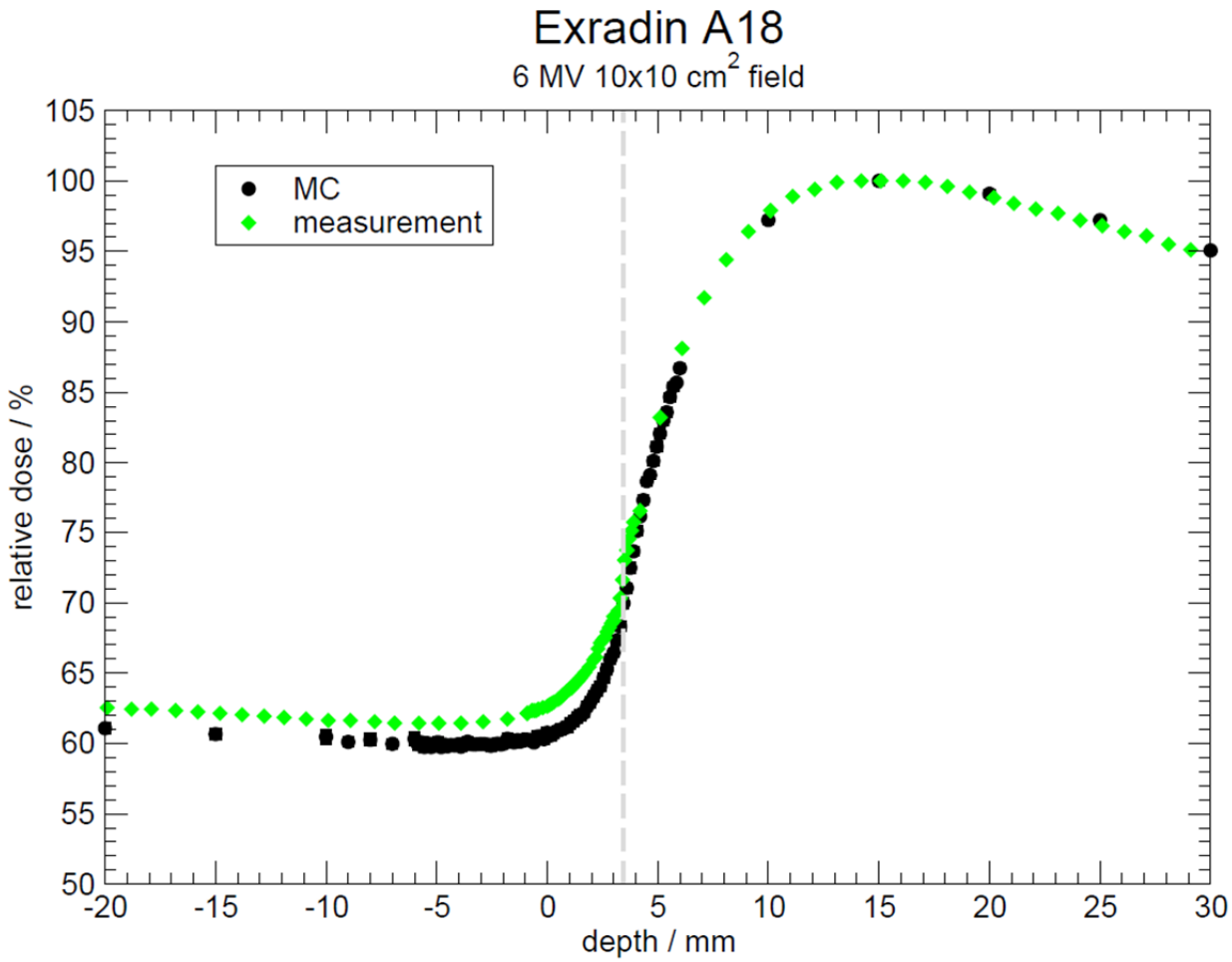

Figure 19: Comparison of VCU 2100 6 MV 10×10 cm^2 field Exradin A18 measurement with simulation of the same conditions using an updated treatment head model and a model of the IC. The measured and simulated curves appear to diverge from one another slightly beyond the IC outer radius, denoted by the dashed grey line. Measured dose is ~2.5% higher than simulated in air. This in-air dose difference corresponds with a ~3% difference in the actual IC wall mass thickness from what is used in the simulation.

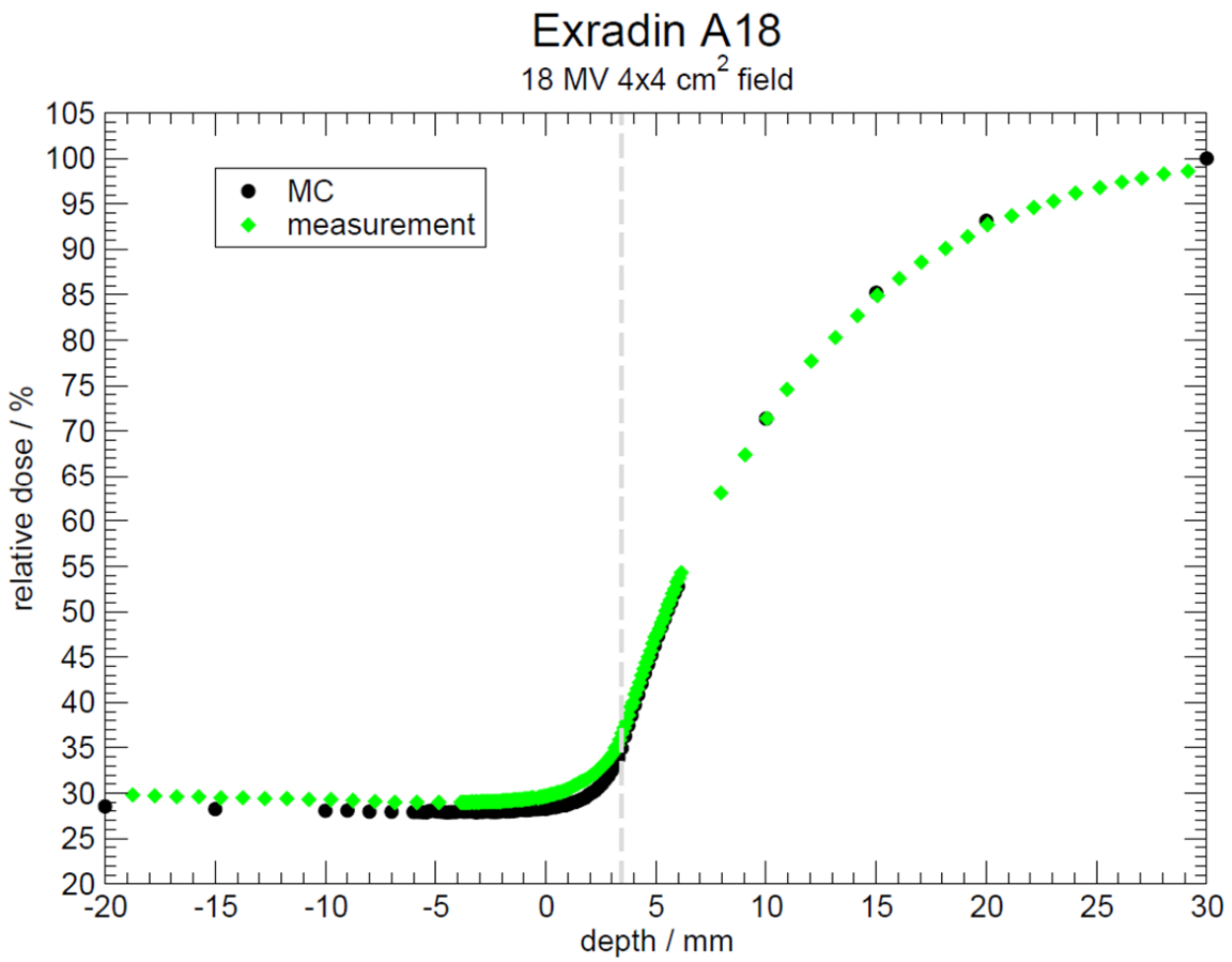

Figure 20: Comparison of VCU 2100 18 MV 4×4 cm^2 field Exradin A18 measurement with simulation of the same conditions using an updated treatment head model and a model of the IC. The measured and simulated curves appear to diverge from one another slightly beyond the IC outer radius, denoted by the dashed grey line. Measured dose is ~3% higher than simulated in air.

Simulated curves from the Elekta Precise at 6 and 25 MV are shown compared with analogous measurements in Figure 21. The accompanying simulated depth dose gradients are shown in Figure 22. Dr. Tessier used a penalized spline algorithm to smooth the gradients, the results of which are shown as the solid lines in Figure 22. The calculated dose gradients exhibit peaks at the DeICERS for both energies. Both the Varian and Elekta accelerators deliver 6 MV beams, so the computational models are directly compared at this energy. The simulated dose from both models is shown in Figure 23 and the accompanying dose gradients are shown in Figure 24. From these figures, it is established that it is reasonable to expect similar dose

gradients from the two accelerator types when using the same IC type. This also further establishes the validity of using the NRC beam model as an independent check on the in-house MC results.

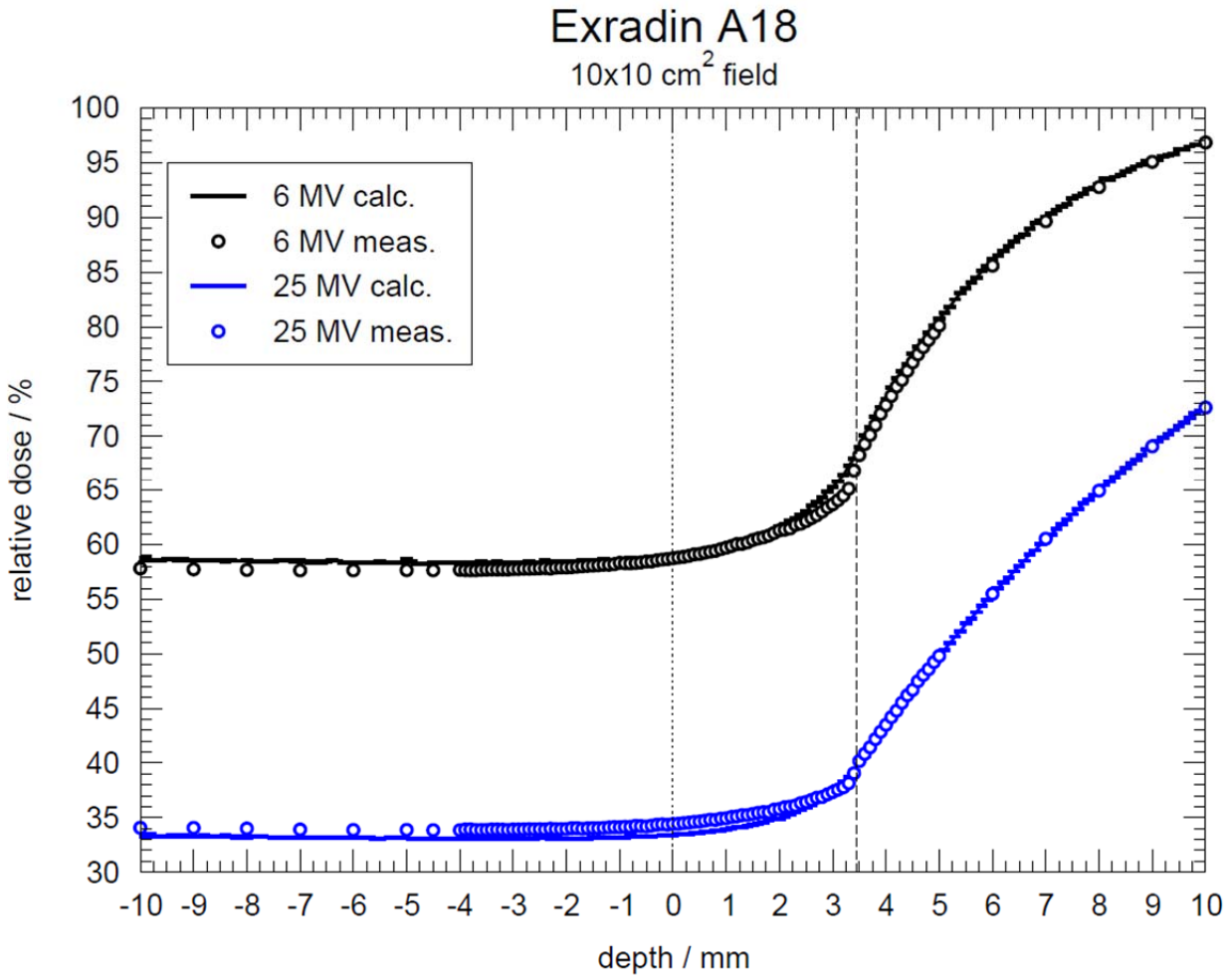

Figure 21: Exradin A18 response to 6 and 25 MV beams from the NRC Elekta Precise. Simulations using the NRC beam model are shown as straight lines. Measurements are displayed as open circles. The dotted line represents the water surface. The dashed line represents the IC outer radius when the IC is centered at the dotted line. The simulations are performed by Dr. Frédéric Tessier.

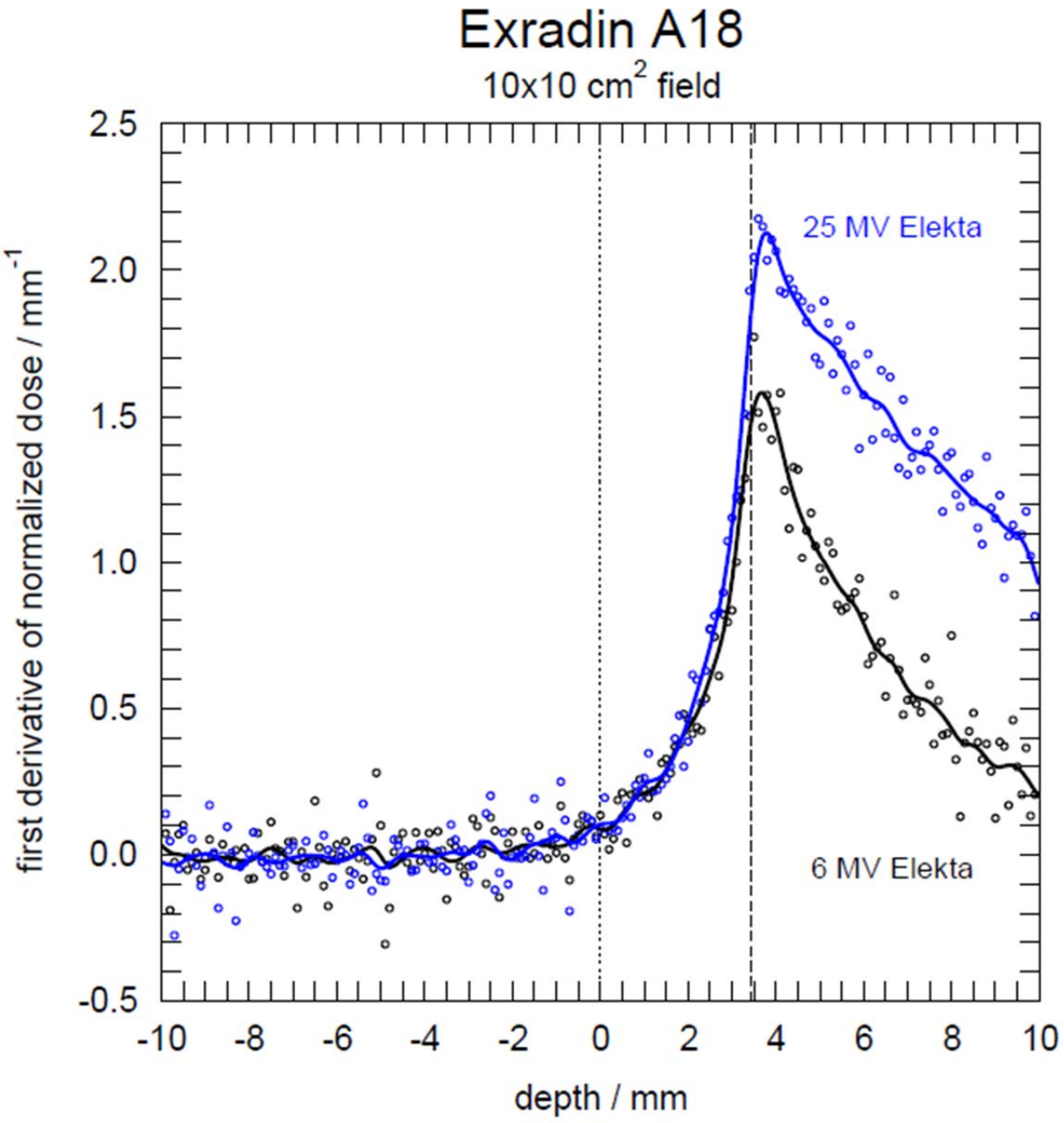

Figure 22: Simulated gradient in Exradin A18 response to 6 and 25 MV beams from the NRC Elekta Precise beam model. The dotted line represents the water surface. The dashed line represents the IC proximal edge location when the IC is centered at the dotted line. The smooth lines running through each data set represent data smoothing performed with a penalized spline algorithm. These simulations are performed by Dr. Frédéric Tessier.

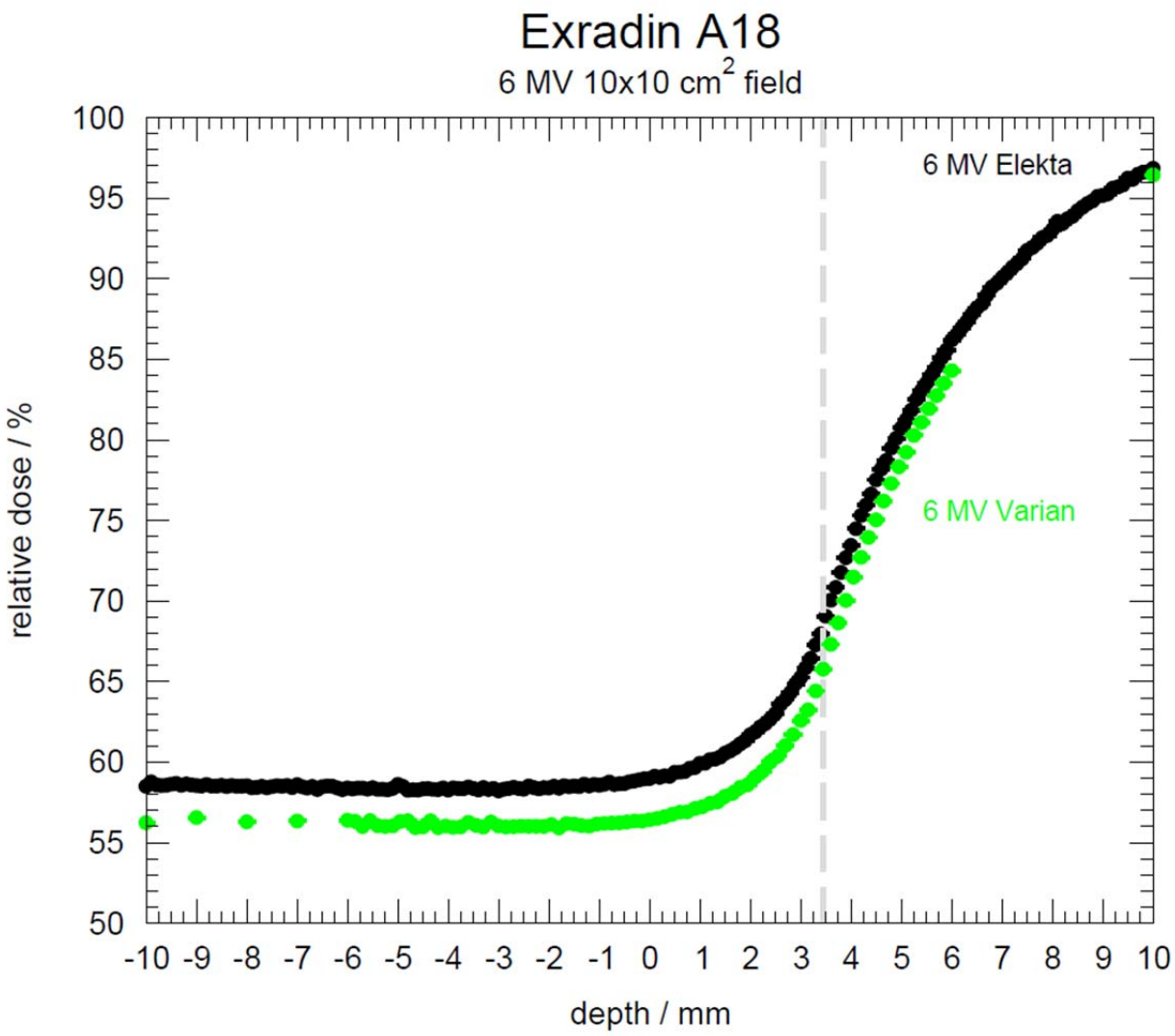

Figure 23: Comparison of the VCU Varian beam model with the NRC Elekta beam model. The dashed line represents the IC central axis location when the IC proximal edge reaches 0.0 mm. The Elekta simulation is performed by Dr. Frédéric Tessier.

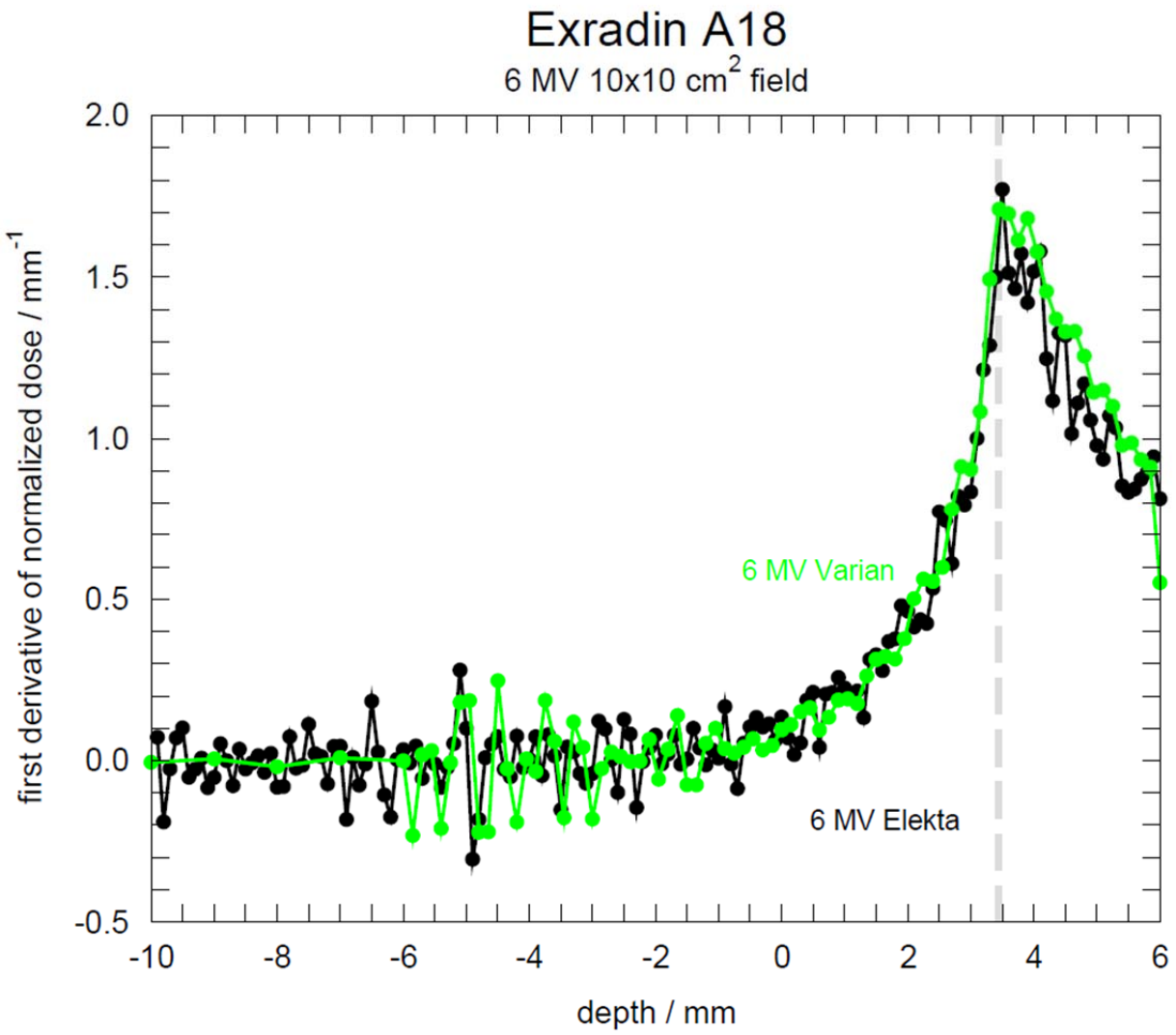

Figure 24: Comparison of Exradin A18 response gradients as calculated using the VCU Varian and NRC Elekta beam models. Both simulations exhibit a peak in the gradient at the grey dotted line, which represents the IC central axis location when the proximal edge reaches the water surface at 0 mm. The Elekta simulation is performed by Dr. Frédéric Tessier.

3.2.2 Ionization Chamber Design Parameter Dependencies

Three cylindrical IC design parameters are varied to investigate the dependence of dose gradient peak location on these parameters. The parameters investigated are central electrode thickness, wall thickness, and air cavity thickness. It is expected that changes in these three parameters will affect the height or location of the dose gradient peak, or both. Initial simulations are performed at VCU with both the full and simplified Exradin A18 computational

models discussed in Section 3.2. All VCU simulations use a BEAMnrc model of the 6 MV 4×4 cm^2 Varian photon beam as the source of incident particles. The derivative of each simulated PDD is computed and plotted. After verifying that the results of simulations with the full and simplified models agree, the simplified computational model is modified in a series of simulations to isolate the three design parameters individually. The limits of the range over which each parameter is modified are determined by the dimensions of the realistic IC model. A real Exradin A18 cylindrical IC contains a 0.5 mm thick central electrode in the active cavity region, with a 1.0 mm thick wall, and a 1.95 mm thick air cavity between the two. Outside the active cavity region, the central electrode is 1.6 mm thick, which decreases the air cavity thickness to 0.85 mm in this region. These parameters serve as the starting point for all simulations.

Three simulations are performed at VCU to test the influence of central electrode thickness on the dose gradient peak. In these simulations, the wall thickness and IC outer radius are held constant at 1.0 mm and 3.45 mm, respectively. One simulation uses an IC model with no central electrode, containing only a 2.45 mm radially thick air cavity. Another uses a 1.6 mm thick central electrode, representing the thickest portion of the real electrode. A third contains a 2.35 mm thick central electrode, which is the thickest the central electrode can be made without disturbing the 1.0 mm thick wall and a minimal air gap of 0.1 mm between the electrode and wall.

Two simulations are performed at VCU to test the influence of changes in wall thickness on the dose gradient peak. The realistic central electrode model is used in these simulations, which is 0.5 mm thick in the active cavity region and is up to 1.6 mm thick outside the active cavity region. The IC outer radius is held constant at 3.45 mm. One simulation uses an IC

model with a 0.1 mm thick wall, which is assumed to be representative of minimal realistic IC wall thickness. Reproducibly machining an IC wall at 0.1 mm thickness would be a considerable undertaking. Here, the air cavity thickness is 2.75 mm in the active cavity region and 1.65 mm outside the active cavity. The other simulation uses a 1.75 mm thick wall, which is the thickest wall that can be defined while maintaining at least a 0.1 mm air gap between the wall and central electrode without interfering with the maximal central electrode thickness of 1.6 mm.

Another pair of simulations is performed at VCU to test the dependence of gradient peak location on changes in outer radius. In these simulations, the realistic central electrode model is used and the wall thickness is held constant at 1.0 mm. The air cavity thickness is changed to change the IC outer radius. In one simulation, the air cavity is modified to be 3.0 mm thick in the active cavity region and 1.9 mm thick outside the cavity. This modification is representative of a 1.05 mm increase in air cavity thickness and in IC outer radius, making the outer radius 4.50 mm. The amount of increase in IC outer radius was chosen because it is not unreasonably large compared with the range of outer radii of the cylindrical ICs used in this thesis (1.055 to 5.7 mm) yet still large enough that a change in gradient peak location should be observable if one occurs. It is also convenient to the 0.15 mm scoring geometry resolution used in all simulations. The other simulation uses an air cavity that is 1.35 mm thick in the cavity region and 0.25 mm thick outside the active region. This represents a reduction in the air cavity thickness and IC outer radius of 0.6 mm, giving an outer radius of 2.85 mm. The air cavity thickness could not be reduced by 1.05 mm because doing so would cause the wall and central electrode to collide outside the active cavity.

At the request of the author, independent simulations are performed by Dr. Tessier at the NRC, using the full Exradin A18 IC model with a BEAMnrc model of the 25 MV 10×10 cm^2

Elekta Precise beam as the source of incident particles. These simulations are performed as an independent check on the VCU implementation of the Exradin A18 IC model. In one set of simulations, the wall thickness and air cavity thickness are held constant while the central electrode thickness is varied. Four simulations are run with central electrode thicknesses of 1.0, 1.5, 2.0, and 2.35 mm, respectively. In another set of simulations, the central electrode thickness and air cavity thickness are unchanged, while the wall thickness is changed such that the IC outer radius changes consequently. Five simulations are run with wall thicknesses of 0.5, 1.0, 2.0, 3.0, and 4.0 mm, respectively. The Exradin A18 models with these wall thicknesses result in IC outer radii of 2.95, 3.45, 4.45, 5.45, and 6.45 mm. Dr. Tessier smoothed each computed dose gradient with a penalized spline algorithm for display purposes. The penalized spline is not expected to model the gradient peak exactly. As shown by the analytical model in Figure 15, in a noiseless idealized scenario, the change in the first and second derivatives is discontinuous at the IC outer radius. Smooth functions like splines cannot accurately reproduce discontinuities. In total, nine simulations were performed at VCU and an additional nine were performed by Dr. Tessier at the NRC. The NRC computer infrastructure is larger than at VCU, enabling greater precision in the NRC results.

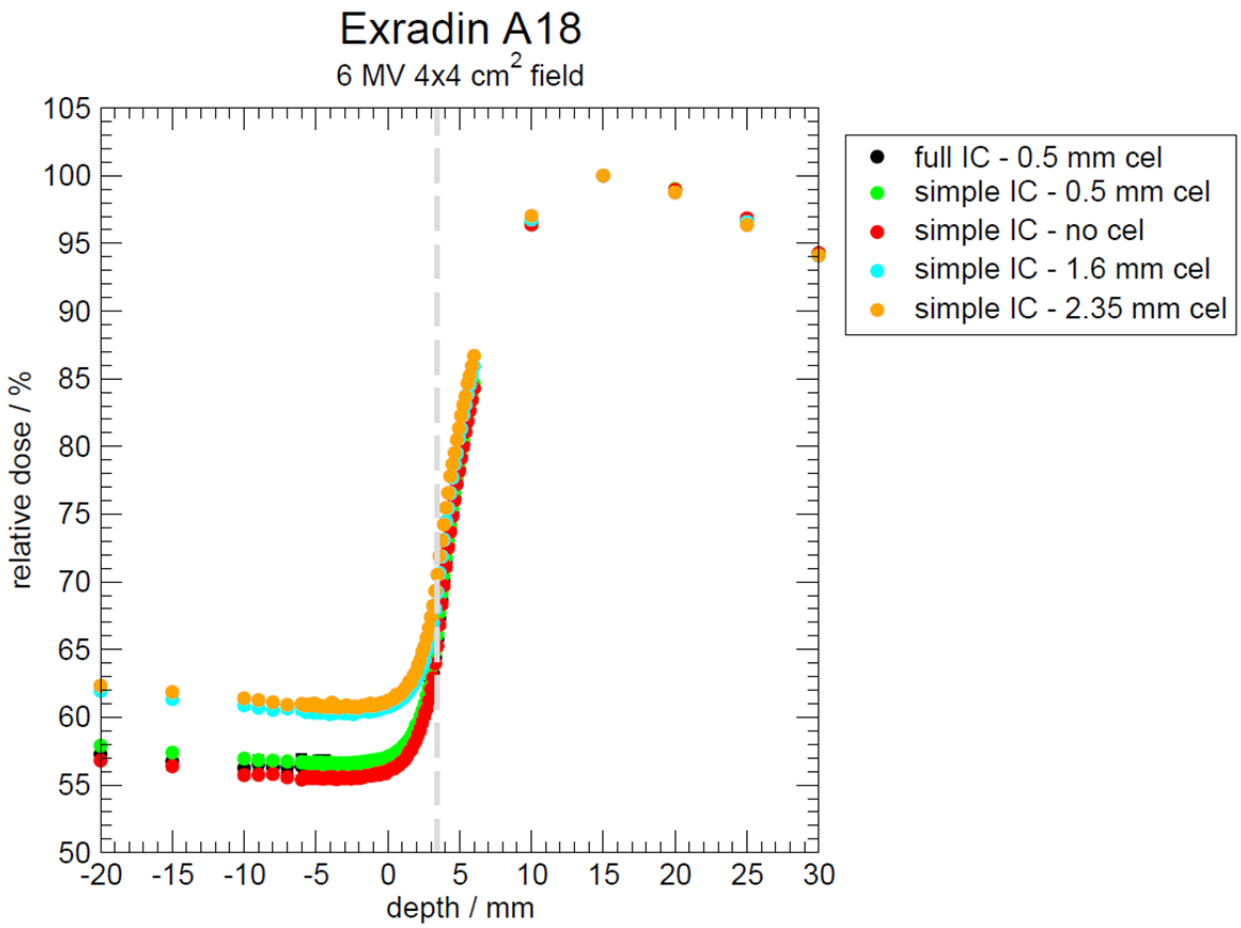

Figure 25: Exradin A18 simulated PDDs for a range of central electrode radial thicknesses. The distinction between "full IC" and "simple IC" represents the amount of detail contained in the IC model beyond the active cavity region. 2.35 mm is the largest radius able to be specified without causing a collision of the central electrode with the IC wall. There is an observable dependence of in-air dose on central electrode thickness.

Central electrode variations are discussed first, beginning with the PDDs shown in Figure 25. As the central electrode thickness increases, so too does the simulated in-air dose. This is expected, as more bound atomic electrons will be freed via Compton scattering events within a thicker electrode than a thin electrode. This means that these free electrons will then traverse the IC cavity, depositing dose as they travel. The simulation for the thickest electrode shows little change in the in-air dose from the simulation with the next thickest electrode because the remaining air cavity is almost totally in the hemispherical end cap volume for the thickest electrode simulation and side scatter from the electrode makes a small contribution in this region. Figure 26 shows the gradients for the central electrode test. Though the results are noisy, all

gradient peaks occur at the DeICERS, as denoted by the dashed grey line. The central electrode thickness test simulations that yielded the results shown in Figure 25 and Figure 26 were conducted for an average of 1328 CPU-hours per simulation. The highest uncertainty in the dose computed in any voxel in any of the VCU simulations is 0.77% of the calculated dose. The highest uncertainty voxel was scored in the full IC simulation, which is displayed in each figure of VCU simulation results. The calculated dose uncertainty in the central electrode thickness tests is 0.08%.

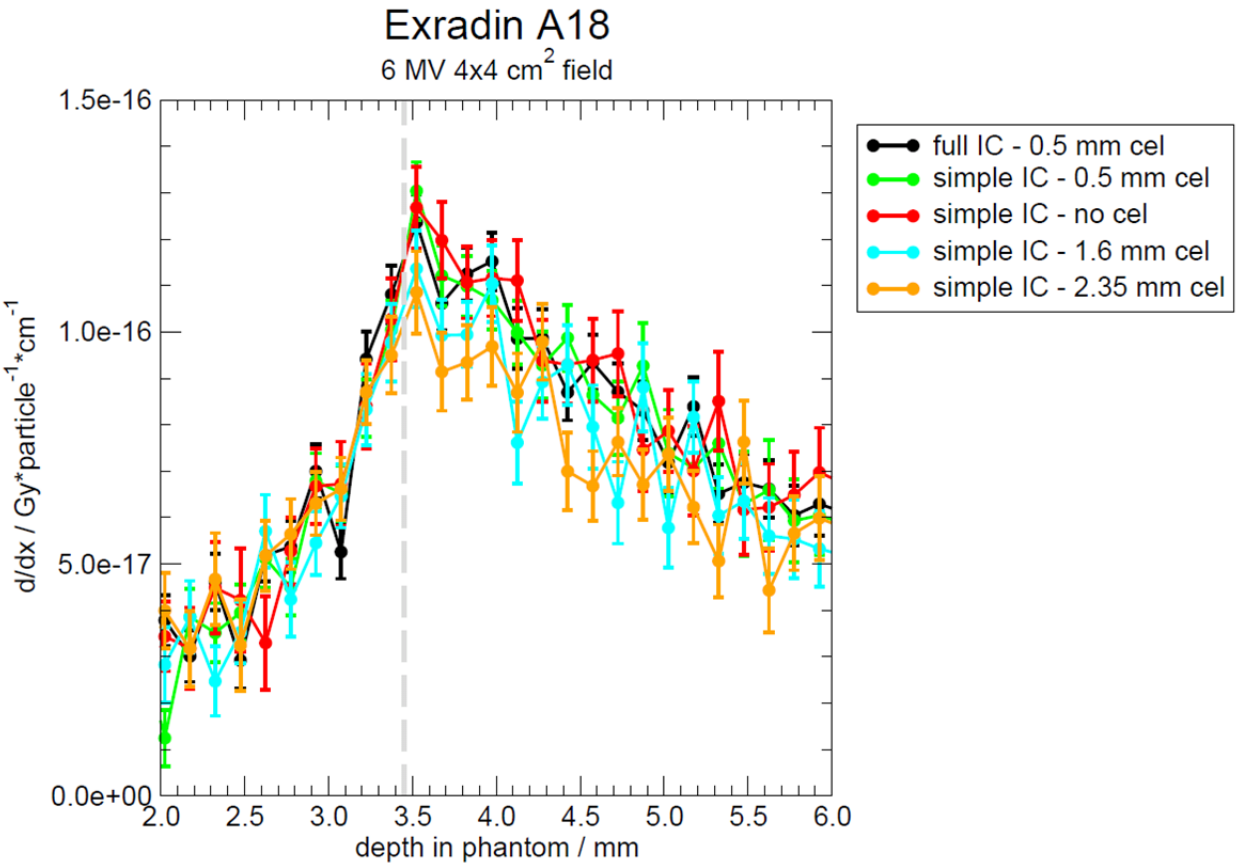

Figure 26: Evaluation of Exradin A18 simulated response gradient dependence on central electrode radial thickness using the VCU beam model. The distinction between "full IC" and "simple IC" represents the amount of detail contained in the IC model beyond the active cavity region. All differences are well within simulation uncertainty and all gradient peaks occur at the DeICERS, denoted by the dashed line.

The results of the independent test conducted by Dr. Tessier are shown in Figure 27. Here, for different choices of central electrode radial thickness, gradient peaks are still exhibited

at the DeICERS. The penalized spline fits of each data set, performed by Dr. Tessier, help to demonstrate that gradient peak height depends inversely on central electrode thickness. However, no dependence on gradient peak location is observed. This means that a gradient peak should be more easily detected from a real IC with a thin central electrode. This finding is an important indicator for the measurements with different ICs described in Section 4.5. This makes sense, as the dose gradient peak is caused by a buildup of electrons originating outside of the IC cavity that subsequently deposit dose within the cavity. As the IC central electrode is thickened, a larger fraction of dose is deposited by free electrons generated in the central electrode within the cavity. This serves to blur the gradient peak. Only two IC types of the models used in this thesis contain thicker electrodes than the Exradin A18, but the difference (10%) is not expected to be large enough for any IC central electrode to cause any issues in detecting a gradient peak.

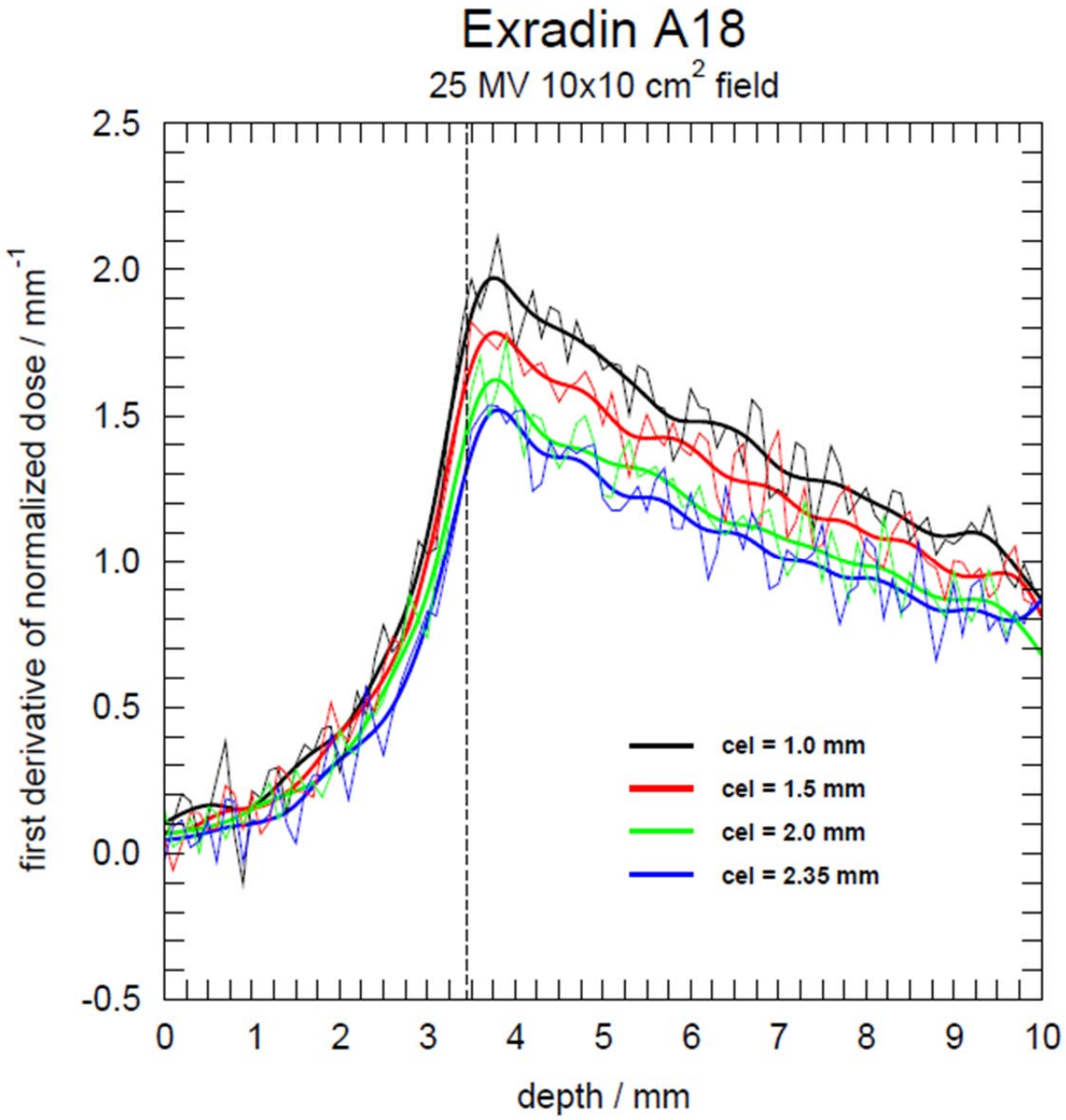

Figure 27: Evaluation of Exradin A18 simulated response gradient dependence on central electrode radial thickness using the NRC beam model. All gradient peaks occur at the DeICERS, denoted by the dashed line. The smooth lines running through each data set represent data smoothing performed with a penalized spline algorithm. These simulations are performed by Dr. Frédéric Tessier.

The central electrode thickness test simulations performed by Dr. Tessier were performed for an average of 3183 CPU-hours per simulation. The NRC simulations required more time than the VCU simulations because of the differences in the incident beam used in each set of simulations. The NRC-simulated 25 MV 10×10 cm^2 field provides more, higher energy, particles

than does the 6 MV 4×4 cm^2 field used in the VCU simulations. Higher energy particles in a larger field will undergo more interactions than lower energy particles in a smaller field, which will require more time to track. The highest uncertainty in the dose scored in any voxel in the NRC central electrode thickness test simulations is 0.89% of local dose while the nominal dose uncertainty in most voxels is 0.09%.

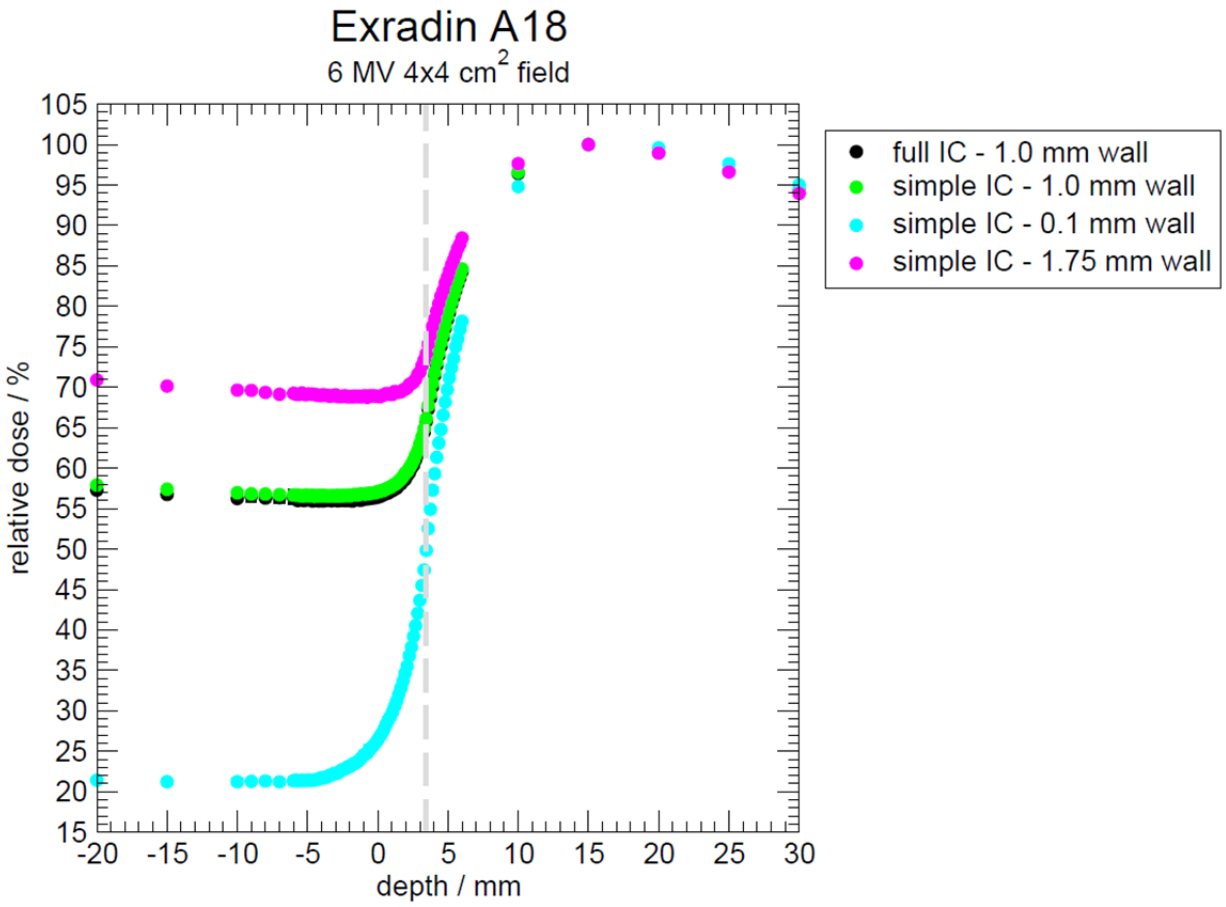

Figure 28: Exradin A18 simulated PDDs for a range of wall thicknesses. The distinction between "full IC" and "simple IC" represents the amount of detail contained in the IC model beyond the active cavity region. In this test, the IC outer radius is held constant and the wall is moved in toward the IC central axis, changing the IC inner radius. The 1.75 mm thick wall is the thickest wall possible for the same IC outer radius.

Next, the dependence of gradient peak location and height on IC wall thickness is examined. PDDs for the cases simulated with the VCU beam model are shown in Figure 28. In-air dose differences of ~350% are observed between simulations conducted with the 0.1 mm thick- and 1.75 mm thick-walled ICs. This difference is caused by the increase in free electrons

produced via photon interactions within the thicker IC wall. Figure 29 shows the IC response gradients for the PDDs shown in Figure 28. All tests exhibit gradient peaks at the DeICERS, where the IC proximal edge reaches the water surface. It is clear here that the thinly-walled IC exhibits a more easily detected gradient peak. This result is confirmed in simulations by Dr. Tessier in which gradient peak location shifts deeper with increased wall thickness, as shown in Figure 30. The observed gradient peaks occur at each respective DeICERS, with a strong inverse dependence of gradient peak height on wall thickness. This is expected, referring back to Figure 3, as an IC with more inherent buildup will measure less of a gradient effect. The VCU wall thickness test simulations were performed for an average of 1130 CPU-hours, resulting in a nominal dose uncertainty of 0.11%. The wall thickness test simulations performed by Dr. Tessier averaged 3225 CPU-hours with a nominal dose uncertainty of 0.09%.

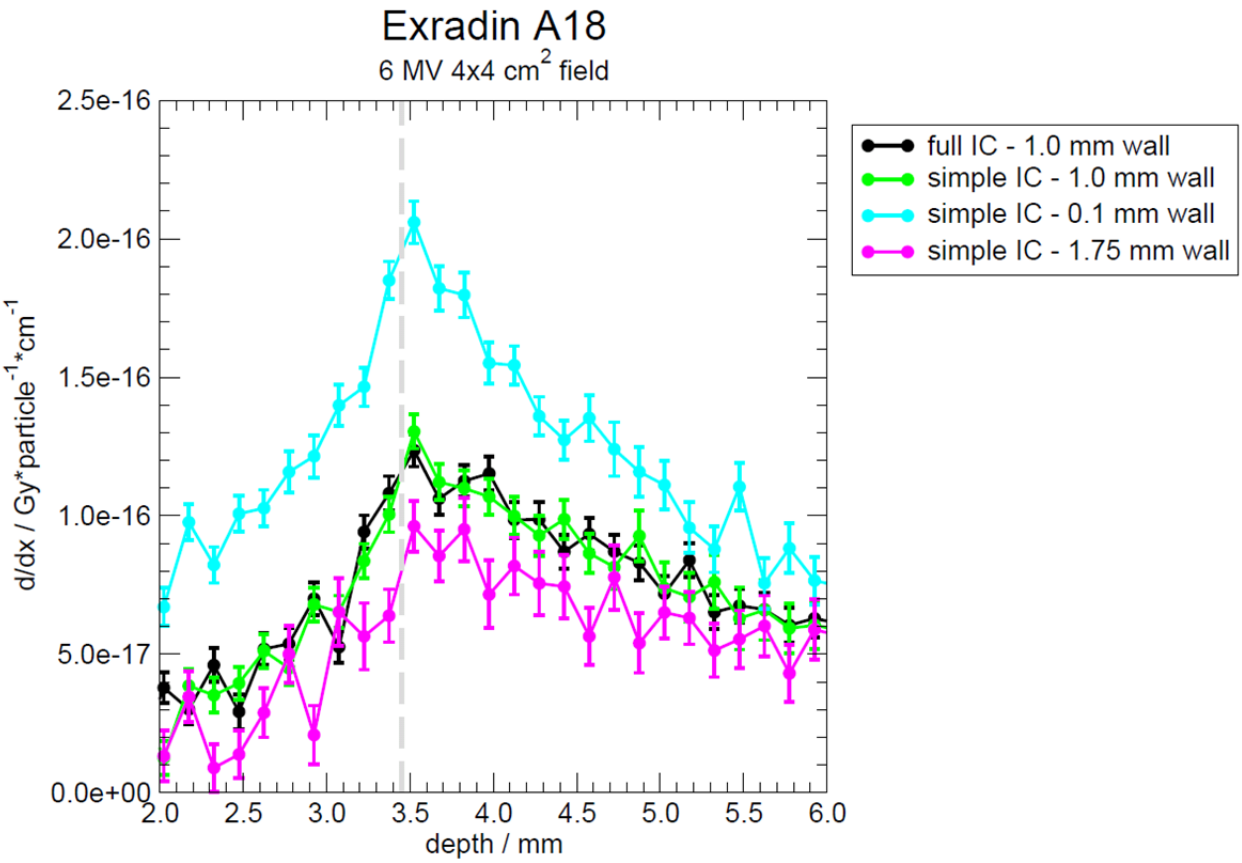

Figure 29: Evaluation of Exradin A18 simulated response gradient dependence on wall thickness using the VCU beam model. In this test, the IC outer radius is held constant and the wall is moved in toward the IC central axis, changing the IC inner radius. The distinction between "full IC" and "simple IC" represents the amount of detail contained in the IC model beyond the active cavity region. All gradient peaks occur at the DeICERS, denoted by the dashed line. The most thinly walled IC exhibits a gradient peak that is notably easier to resolve than those from tests with other wall thicknesses.

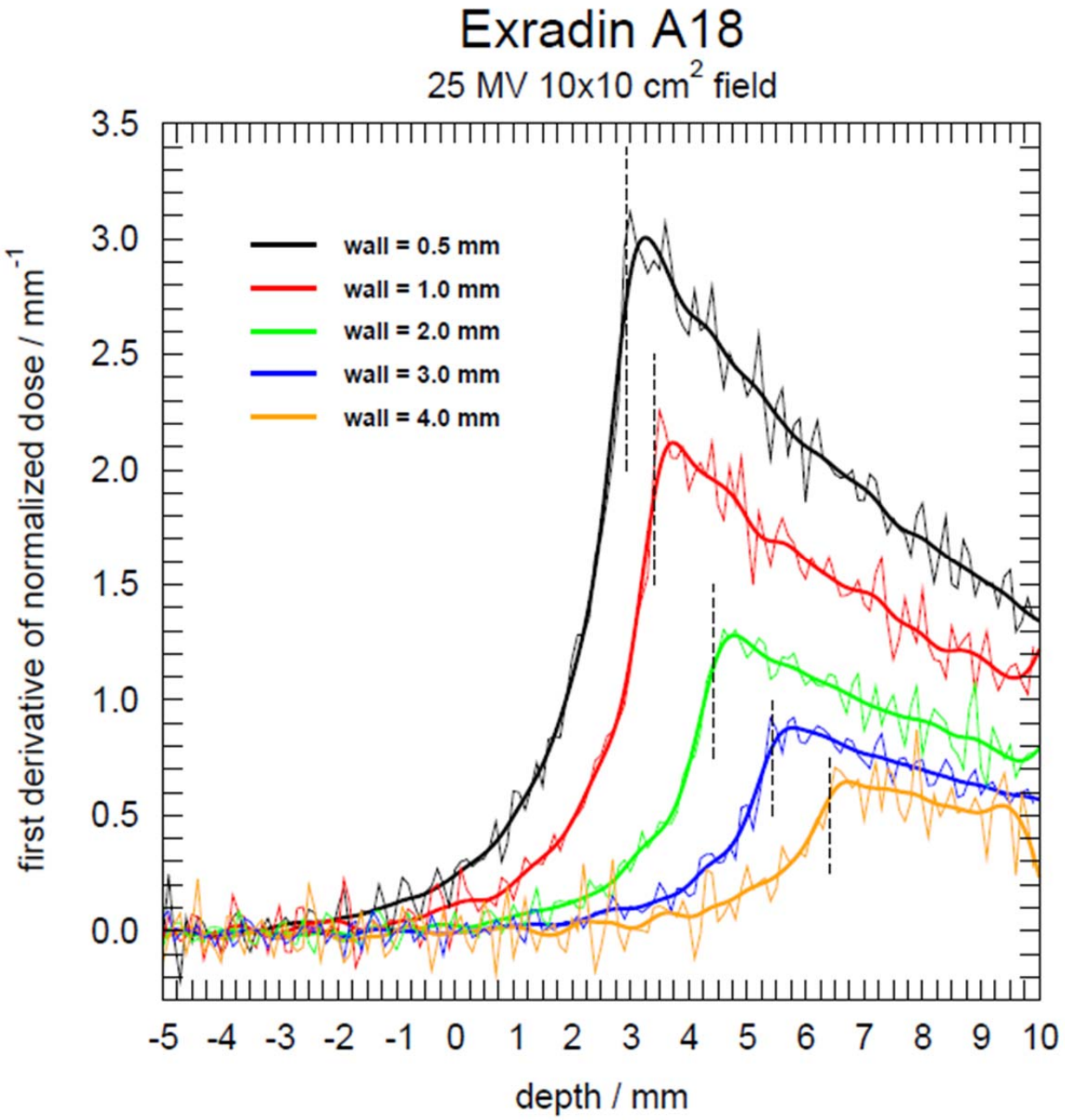

Figure 30: Evaluation of Exradin A18 simulated response gradient dependence on wall thickness using the NRC beam model. Here, the IC inner radius was held constant and the wall thickness was expanded radially, changing the outer radius. Each individual dashed line represents the DeICERS for that test. All gradient peaks occur at the DeICERS. The smooth lines running through each data set represent data smoothing performed with a penalized spline algorithm. These simulations are performed by Dr. Frédéric Tessier.

The last simulation results to discuss are those where IC outer radius is changed by holding wall thickness constant and increasing the inner air cavity radius. Figure 31 shows that the resulting PDDs are very similar. The accompanying gradients, shown in Figure 32, show

changes in gradient peak location that correspond with each DeICERS. The air cavity radius modification simulations took, on average, 1240 CPU-hours with a nominal dose uncertainty of 0.10%.

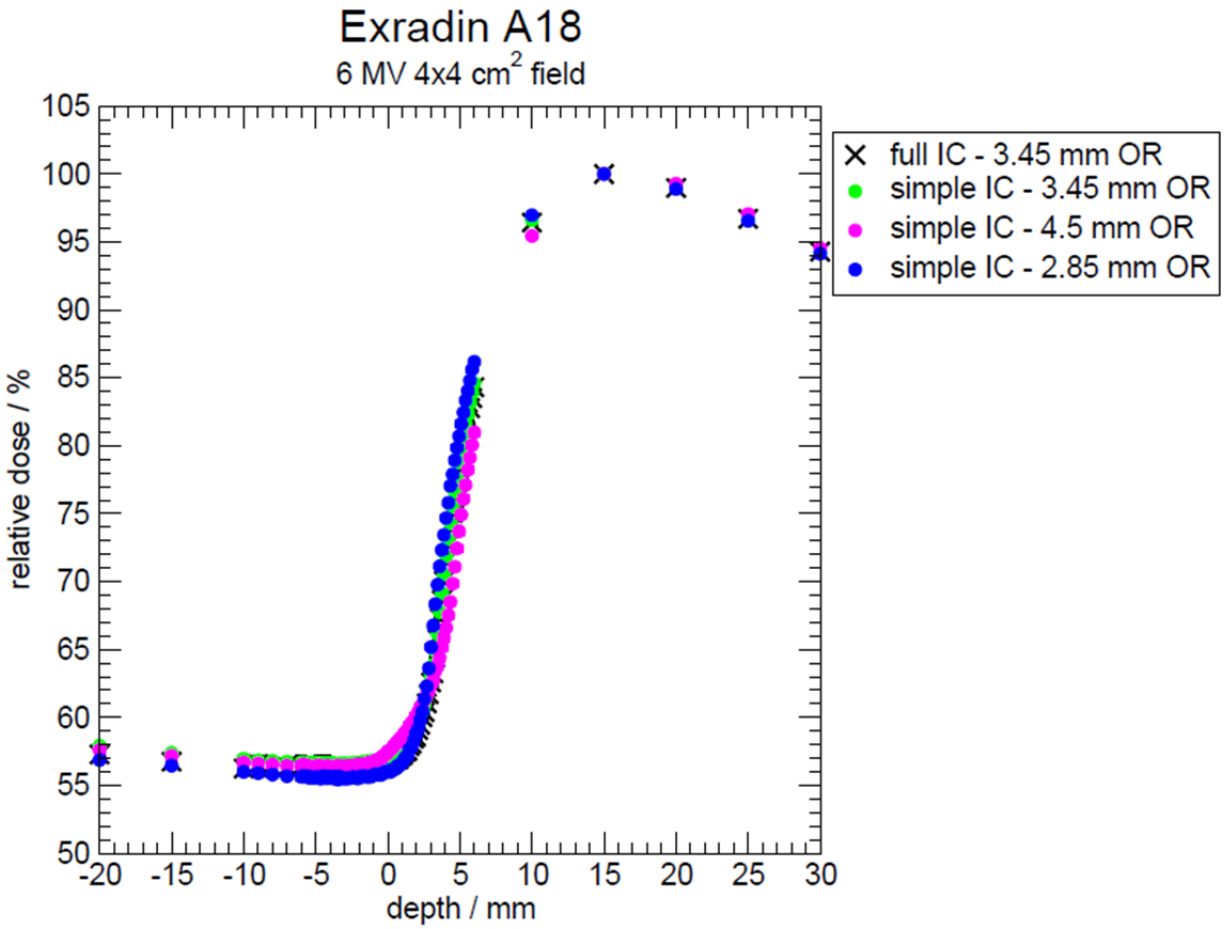

Figure 31: Exradin A18 simulated PDDs for constant central electrode and wall thickness but varying the inner radius, such that outer radius (outer radius = inner radius + wall thickness) shifts. The curvature of each trial near the water surface is proportional to the IC outer radius. The distinction between "full IC" and "simple IC" represents the amount of detail contained in the IC model beyond the active cavity region.

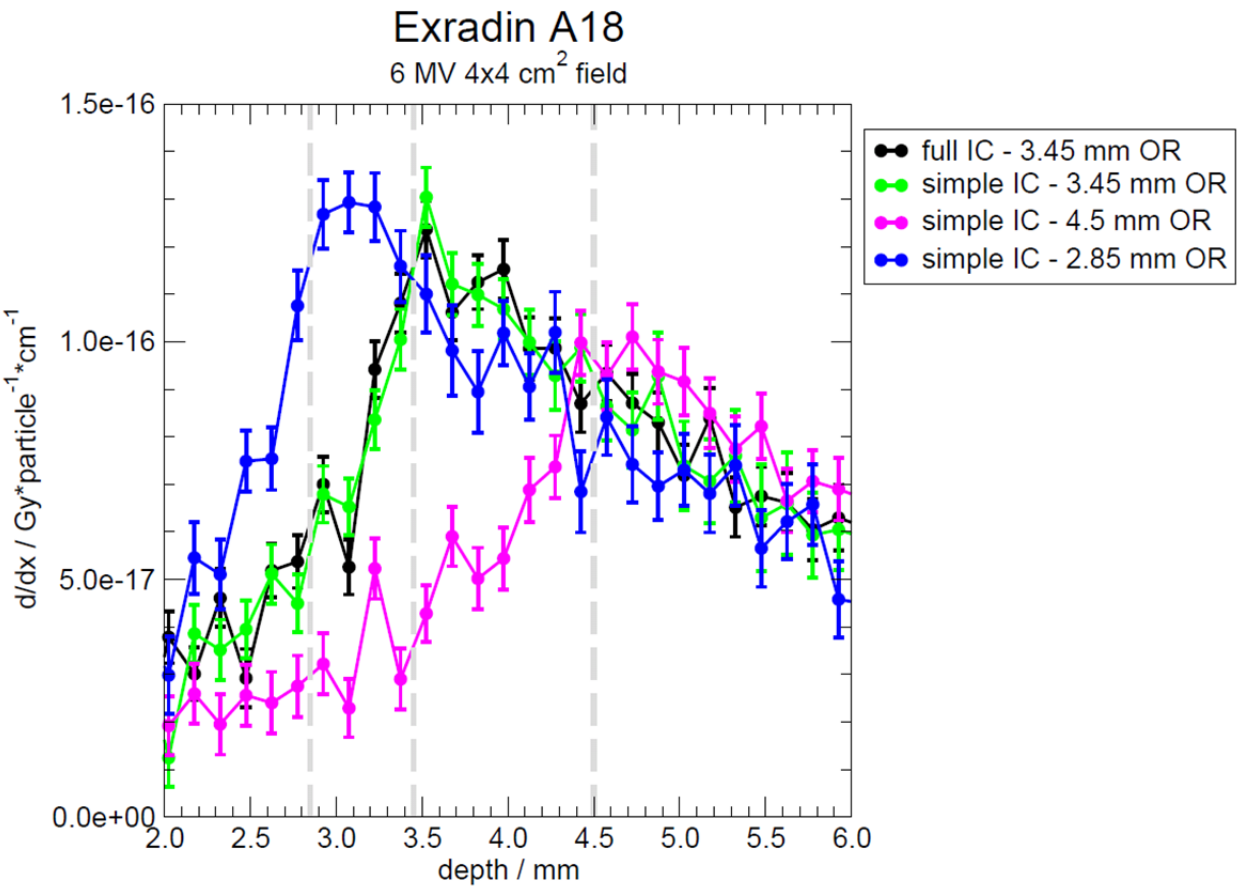

Figure 32: Evaluation of simulated Exradin A18 response gradient dependence on outer radius changes. The distinction between "full IC" and "simple IC" represents the amount of detail contained in the IC model beyond the active cavity region. The gradient peak of each simulated curve occurs at its own DeICERS.

3.3 Conclusions

Despite a number of assumptions that differ from reality, the analytical model shows that a change in the dose gradient, and second derivative, occurs exactly at the point at which a cylindrical IC reaches the water surface. The series of MC simulations performed in-house and by Dr. Tessier at the NRC shows that the gradient peak is most easily observed from measurements made with ICs having thin walls and thin central electrodes. Variations in IC central electrode, air cavity, or wall thickness that do not affect the overall IC outer radius do not affect the dose gradient peak location. For simulations of overall uncertainty that is small compared with typical measurement uncertainty, the dose gradient peak is observable and its

location depends only on IC outer radius. The dose gradient, therefore, shows a clear advantage over simply using original PDD data to identify the water surface as the PDD is dependent on differential electron contamination with field size. The next chapter demonstrates the ability to determine the dose gradient peak under real measurement conditions.

4 Experimental Validation

This thesis combines an extensive series of measurements with proof-of-principle analytical model- and MC simulation-based investigations to establish the ability of depth-dose data to be used to align an IC to the water surface, as well as its theoretical foundation. In this chapter, the accelerators, ICs, and other equipment used to perform the measurements will be discussed, as well as the specifics of the measurements themselves and the measured results. Measurements are performed here to examine the ability to resolve the dose gradient peak under a variety of conditions. Variations in scanning procedure and IC setup are tested. The extent to which confounding factors such as water evaporation and surface tension might affect the dose gradient peak is examined. Dependencies on radiation field parameters and IC type are evaluated. It is the aim of this chapter to show that the dose gradient peak is a robust metric of IC water surface alignment and can be found, for a well-aligned measurement, at the point at which an IC reaches the water surface when scanning from water to air.

4.1 Equipment

This section describes the accelerators, ICs, scanning systems and other equipment used to take PDD measurements. Measurements are taken in-house at VCU, at Stanford University, and at the National Research Council of Canada.

4.1.1 Accelerators

Three accelerator types are used to generate radiation output that is measured in this work. The most frequently used for this project is of the 2100/2300 series from Varian Medical Systems, Inc. (Palo Alto, CA). The Varian accelerators used supply two photon beam energies (6 and 18 MV) and five electron beam energies (6, 9, 12, 16, and 20 MeV) and are capable of producing radiation fields as large as 40×40 cm^2 at 100 cm SSD. Figure 16 shows a schematic of an xz-view of the 6 MV clinical treatment head geometry, generated using the BEAMnrc graphical user interface (GUI) (Treurniet *et al.*, 2010). This GUI allows visualizations of accelerator geometries specified using BEAMnrc (Rogers *et al.*, 2006), which is a user code of the EGSnrc code package (Kawrakow, 2000a; Kawrakow and Rogers, 2003) that is used for all of the simulations discussed in Section 3.2. The yz-view is shown in Figure 17. The major components are, in descending order from the incident electron source, the target, primary collimator and exit window, flattening filter, monitor chamber, mirror, and jaws. A more detailed description of the treatment head model used for MC calculations is given in Section 3.2.1. Predominantly, measurements are taken from a 2300 series machine, though some are from an older 2100 series machine. The two machines used here are "matched", meaning that the output of these machines is nominally identical. Output between the two machines should be expected to be very similar, as they are both of the same schematic design. Even so, where measurements made on the 2100 machine are being discussed in this thesis, the distinction will be made clear. All in-house experiments are conducted using Varian accelerators.

The work performed at Stanford University is conducted on an Accuray CyberKnife. CyberKnife is a specialized accelerator that generates only 6 MV photons and produces circular radiation fields, up to 6 cm in diameter. The accelerator is mounted on a robotic arm, which

allows six degrees of freedom in finding the optimal beam configuration for a given patient treatment. Measurements here are performed at an SSD of 78.5 cm. This distance can be modified but cannot extend to 100 cm, which is considered standard for conventional accelerators (e.g., Varian 2300).

An Elekta Precise is used at the NRC. Though installed at a standards laboratory, it is a typical commercial-grade accelerator. This machine produces beams at three photon energies (6, 10, and 25 MV) and five electron energies (4, 8, 12, 18, and 22 MeV). The Precise features a multiple flattening filter design, with filters located above and below the primary collimator, where an additional steel filter is placed in the beam line for high energy beams (Klein *et al.*, 2003). The maximum achievable dose rate with the Precise is 500 monitor units per minute (500 MU/min), while the 2300 can produce up to 600 MU/min for photons and up to 1000 MU/min for electrons.

4.1.2 Ionization Chambers Tested

Three manufacturers provided ICs to be used in this work: IBA Dosimetry Inc. (Schwarzenbruck, Germany), Standard Imaging, Inc. (Fitchburg, WI), and PTW Dosimetry, Inc. (Freiburg, Germany). Generic IC schematics generously shared by Standard Imaging for the Exradin ICs used in this project are shown in Figure 33. IC design parameters are specified in a series of tables, beginning with the outer wall specifications for cylindrical ICs, given in Table 2. Next are the central electrode parameters, shown in Table 3. Table 4 lists the air cavity properties of each cylindrical IC along with its outer diameter. Table 5 lists entrance window properties for the parallel-plate ICs used in this thesis. Guard ring and sensitive volume dimensions for the parallel-plate ICs are listed in Table 6. In all tables, values are either taken directly from documentation provided by the respective IC manufacturers or calculated based on

manufacturer-provided information (IBA Dosimetry, 2007; PTW Dosimetry, 2007; Standard Imaging, 2008).

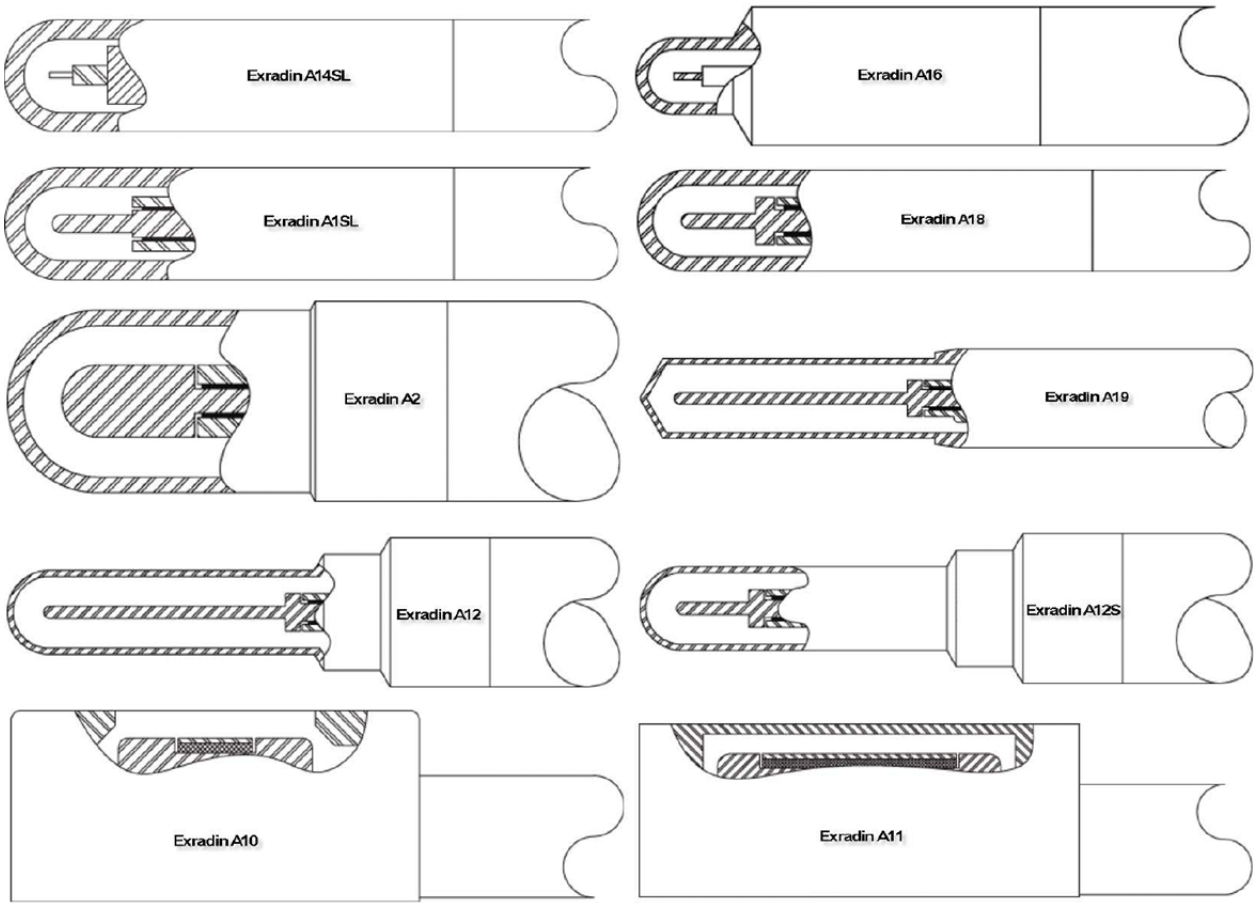

Figure 33: Generic schematic designs for the Exradin ICs used in this thesis printed with permission of Standard Imaging, Inc. The A14SL and A16 are micro-ICs. The A1SL, A18, and A2 are scanning ICs. The Farmer-type ICs shown are the A19, A12, and A12S. The A10 and A11 are parallel-plate designs.

The IBA CC13 and PTW 23343 (Markus) ICs are used for most of the experiments in this thesis. They are chosen as representative cylindrical and parallel-plate types, respectively. The CC13 is chosen as a representative cylindrical IC because it is the default IBA scanning IC that is intended for use with the IBA scanning system. As discussed in Section 4.1.3, the IBA scanning system is used for all in-house measurements and the Accuray CyberKnife measurements conducted at Stanford University. Another IBA CC13 model is used as the reference field IC for all measurements performed at VCU for this thesis.

Table 5: Entrance window parameters for the parallel-plate ICs used in this thesis. Numbers given in parentheses represent the contribution of individual components in windows comprised of multiple materials. Polyimide film is an insulating film with good X-ray transmittance properties, also used for linear accelerator transmission monitor chambers, as seen in Figure 16 and Figure 17. Polyimide film is commonly referred to by the trade name Kapton®. C552 is a Shonka air-equivalent plastic. Poly-methyl methacrylate (PMMA) is more commonly referred to by one of its trade names: Lucite®, Perspex®, or Plexiglas®. The PMMA listed in the 23343 and 34045 ICs represents the waterproof cap of each IC. $(C_2H_4)_n$ is the chemical formula for polyethylene.

IC Type	Material	Density (g/cm^3)	Thickness (cm)	Mass Thickness (g/cm^2)
Exradin A10	Polyimide film	0.772	0.005	0.00386
Exradin A11	C552	1.76	0.01	0.0176
PTW 23343	PMMA/$(C_2H_4)_n$/air	0.82 (1.19/0.92/1.205E-3)	0.13 (0.087/0.003/0.04)	0.106
PTW 34001	PMMA/graphite/varnish	1.18 (1.19/0.82/1.19)	0.112 (0.1/0.002/0.01)	0.132
PTW 34045	PMMA/$(C_2H_4)_n$/air	0.82 (1.19/0.92/1.205E-3)	0.13 (0.087/0.003/0.04)	0.106

Table 6: Guard ring and sensitive volume dimensions for the parallel-plate ICs used in this thesis.

	Guard Ring	Sensitive Volume		
IC Type	Width (cm)	Air Gap (cm)	Diameter (cm)	Volume (cm^3)
Exradin A10	0.43	0.2	0.54	0.051
Exradin A11	0.44	0.2	2.00	0.62
PTW 23343	< 0.02	0.2	0.53	0.055
PTW 34001	0.4	0.2	1.5	0.35
PTW 34045	0.2	0.1	0.5	0.02

The PTW 23343 is chosen as a representative parallel-plate IC as something of a worst case scenario. McEwen, Williams, and DuSautoy have noted specifically that this IC type is not suitable for reference dosimetry due to response issues related to the IC design (McEwen *et al.*, 2001). One PTW 23343 design issue is that the IC is not itself waterproof, thus usage in water requires a PMMA waterproof cap. Given that the waterproof cap thickness is not known precisely, all PTW 23343 measurements are made with the face of the IC cap aligned to the water surface rather than attempting to align precisely to the inside of the entrance window, which is the nominal point of measurement for parallel-plate IC measurements (Almond *et al.*, 1999).

Another major design issue with the PTW 23343 is its very small guard ring as compared with other parallel-plate ICs. As shown in Table 6, the PTW 23343 guard ring width is at least an order of magnitude smaller than that of any other parallel-plate IC used in this thesis. As noted by Pearce, Thomas, and DuSautoy, the small guard ring allows many more electrons to enter the IC cavity through the side walls than do other better-guarded parallel-plate IC designs (Pearce *et al.*, 2006). This can cause a significant perturbation of the incident electron fluence across the IC cavity. As shown in IAEA TEC-1173, the unsuitable guard ring and extra in-scattering through the IC walls cause the Markus IC EPOM to be shifted 0.5 mm downstream from its proper location at the inner surface of the entrance window (International Organization for Standardization, 1993). Pearce, Thomas, and DuSautoy additionally note that the Markus IC high voltage plate is "top-hat" shaped, which causes electric field distortions at the periphery of the collecting volume (Pearce *et al.*, 2006). A recommended code of practice for the use of parallel-plate ICs in high energy photon and electron beams, IAEA TRS-381, tabulates desirable properties for a parallel-plate IC (Almond *et al.*, 1997). In this table, a ratio of guard ring width to cavity height of ≥ 1.5 is listed as desired. As shown in Table 6, this ratio for the PTW 23343 is <0.1. Therefore, it is assumed that if the relative dose gradient as measured with the PTW 23343 can be used to determine the water surface location under certain conditions, this should remain true for well-guarded parallel-plate IC types as well.

4.1.3 Scanning Systems

Measurements conducted at VCU and Stanford use an IBA Blue Phantom® with the OmniPro-Accept software. The total tank volume is 216.2 L, though the standard for measurements made in this thesis is to fill the tank with ~113 L water. The system uses an integrated dual-channel electrometer with a measurement range from 5×10^{-11} A to 5×10^{-7} A,

maximum current resolution of 2×10^{-14} A, leakage current $<10^{-15}$ A, and a time constant of 0.02 s. The quoted positioning reproducibility of the scanning system is 0.1 mm. The quoted overall positioning accuracy of the system is ±0.5 mm. The smallest achievable scan resolution using the IBA system is 0.1 mm. If 0.1 mm resolution is to be achieved over any region of a given scan with the IBA system, the entire scan must be performed at that resolution.

Table 7: Water surface displacement for each of the eighteen ICs used for in-house measurements. The displacement of the water surface caused by the Blue Phantom drive motors, shown in the middle column, is compensated for within the scanning software. The water surface displacement caused by the IC holder is not compensated for but is within the range of other measurement uncertainties.

IC Type	Water surf. disp. by drive motors (mm)	Water surf. disp. by IC holder (mm)
Exradin A10	0.4	0.07
Exradin A11	0.4	0.07
Exradin A12	0.3	0.07
Exradin A12S	0.3	0.07
Exradin A16	0.3	0.07
Exradin A18	0.3	0.07
Exradin A19	0.3	0.07
Exradin A1SL	0.3	0.07
IBA CC01	0.4	0.07
IBA CC04	0.4	0.07
IBA CC08	0.4	0.07
IBA CC13	0.4	0.07
IBA CC25	0.4	0.07
PTW 23343	0.4	0.07
PTW 31010	0.3	0.07
PTW 31016	0.3	0.07
PTW 34001	0.4	0.07
PTW 34045	0.4	0.07

A feature of the OmniPro-Accept software that is very useful for this particular project is what is described as a “water surface correction”. This is used to account for the portions of the scanning arm and drive motors that emerge from the water ahead of the IC by correcting for the amount by which the water level should fall by removing the volume of these components from below the surface. If not measured for each new IC installed, the software will assume a nominal value that will likely be inappropriate for that IC. The measurement is made by first

centering the IC at the water surface then measuring the distance from the water surface to the top of one of the drive motors, to the nearest 1 mm. The IC holder causes water displacement that is not compensated for within the scanning software. A table of the water surface displacement values for each of the 18 IC models used for in-house measurements is given in Table 7.

The inflexibility of the IBA scanning system, in terms of spatial and sampling resolution, is overcome by splitting scans into small pieces then re-combining them with in-house software. The OmniPro-Accept software allows scan data to be saved in .rfb, .asc, and .dat formats. The .rfb format is strictly proprietary and is inaccessible except through the OmniPro-Accept software. The .asc format creates an ASCII text file of the relevant scan information, which is read by in-house software. Each piece of the scan is read out into a separate .txt file with its accompanying incident beam energy, particle type, and field size information. In additional .txt files, the scan data are sorted and the computed first and second derivatives are tabulated. A second in-house routine stitches the scan pieces back together and, in the case of the original scan data, re-normalizes the scan such that 100% relative dose is ensured at d_{max}, so as to overcome any discrepancies in normalization when scans were acquired. This is done since although IC gain settings are set to attempt to achieve 100% relative dose at d_{max}, actual measured relative dose at d_{max} will vary from scan to scan.

The scanning system used for the Elekta Precise measurements at the NRC is a customized construction and has been briefly described in an earlier publication (McEwen *et al.*, 2008). The customized system offers multiple advantages over the IBA system in scan and equipment flexibility. It also provides absolute accuracy of 0.15 mm and <0.1 mm relative precision (Tessier *et al.*, 2010). The aspect of the custom system that is the most immediately

notable improvement over conventional scanning systems is the use of an attached optical telescope to independently track water surface location and IC alignment.

IC alignment to the water surface is achieved by following the procedure outlined here. Starting with a focused telescope, the crosshairs within the telescope are first aligned to the magnified water surface. The telescope is aligned to the water surface by resolving a disturbance in the water surface caused by the presence of the IC. The telescope alignment can be confirmed by moving the IC below the water surface and identifying the water surface as the point halfway between the IC and its reflection. Next, the telescope is lowered by an amount equal to the IC outer radius, which is previously measured with a set of digital calipers. The IC is then moved within the tank such that its lower edge meets the crosshairs of the telescope. Additional confirmation is then provided by optically measuring the apparent IC diameter (½ IC in water, ½ IC reflection in air) and comparing with the measured value obtained with the digital calipers. This ensures that the IC is centered, within uncertainty of the eye of the telescope user, generally 10-40 micron (McEwen, 2011). Since the water surface location is independently tracked with the telescope for these measurements, inter-scan evaporation can be monitored and corrected.

4.1.4 Ancillary Equipment

While the most notable equipment is itemized and discussed in the following sub-sections, other equipment, which is generally not used in standard QA measurements, is used for in-house measurements and is therefore mentioned here. A tape measure is aligned to the cross-hairs on the water tank and taped in place to allow quantification of changes in the water level, in 1 mm increments. This has also proved useful in providing a quick quantitative check of water level consistency across multiple setups. Additionally, a sling psychrometer is used to measure the relative humidity in the air in the treatment room. The psychrometer contains two

thermometers, one of which is covered by a cloth wick that must be dampened before use. After spinning the psychrometer, the wet and dry thermometers are read. The difference in the two readings is a function of the rate at which water evaporates from the wick while being spun. This temperature difference is converted into a relative humidity reading from a slide-rule type scale on the psychrometer face.

4.2 Scan Parameter Dependencies

Depth dose scans have numerous variables. Scan direction, speed, and resolution are parameters that a user is able to alter on a scan-by-scan basis. The height of the water level within the tank can also vary between measurement sessions. It is also important to establish the setup reproducibility possible using a given scanning system. Examinations of the parameters listed here are described in the following sub-sections.

4.2.1 Scan Direction

PDD scans can be acquired in two directions. The IC can either start from a location deep in water and move toward the water surface or start at, or near, the water surface and move down into the water tank. An example of the way in which scan direction change manifests itself in acquired depth dose data is shown in Figure 34. All data here have been shifted to account for the EPOM of each detector, as recommended by AAPM TG-51 (Almond *et al.*, 1999). The curve that visibly deviates from the rest in the range from 0-6 mm depth is scanned by starting at the water surface and continuing into water. All other scans are started at depth in water and finish at the water surface. The behavior seen in the deviant curve is caused by water surface tension.

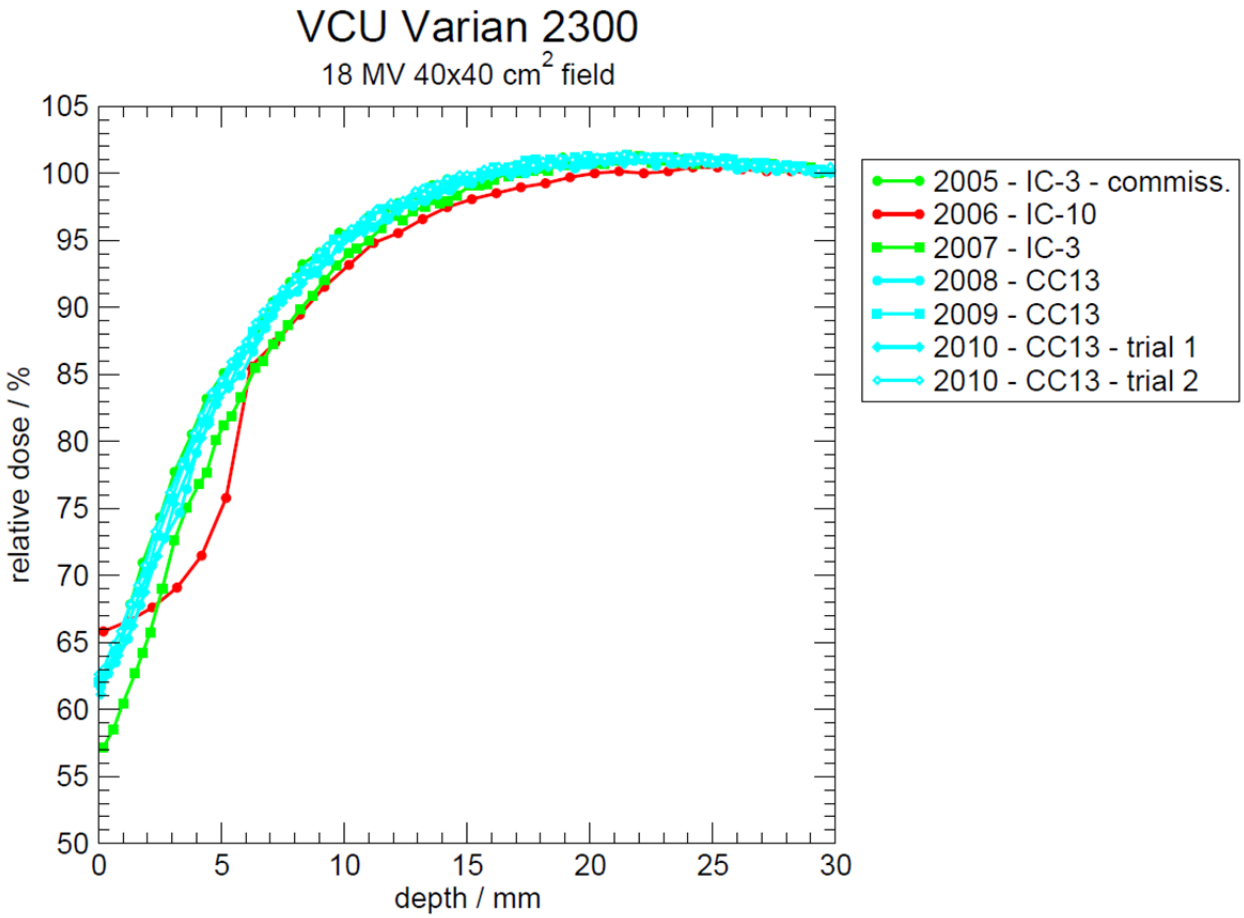

Figure 34: PDD data from the same machine operating at 18 MV for a 40×40 cm^2 field showing the effect of scan direction on resulting scan data. The 2005 data is from initial accelerator commissioning. All other scans are performed as part of annual QA. All scans have had the AAPM TG-51 recommended EPOM shifts of 0.6×r_{cav} applied, where r_{cav} is the IC inner radius. All scans are normalized to 100% at d_{max}. From 0 to 6 mm, the measurement performed with the IC-10 has a different shape than all other measurements. The IC-10 measurement is started at 0 mm, the nominal water surface, and scanned into water. All other measurements began with the IC fully submerged in water and brought to the surface. The different shape of the IC-10 scan is caused by air being dragged by the IC below the water surface.

A scan from water to air is shown in the left column of Figure 35 in panels a)-c). Panel a) shows the IC at the DeICERS. In panel b), the IC has passed through the water surface into air, with water adhering to the IC. The water on the IC will cause a small backscatter increase. In panel c), the water has fallen away from the IC, placing the IC fully in air. The right column of Figure 35 shows a scan from air to water in panels d)-f). Panel d) shows the IC at the air-to-water DeICERS. In panel e), the IC causes a downward forming meniscus, which results in the water surface being displaced below its original location. When the water surface is displaced deeper by the IC, air is present at depths where water would remain undisturbed in a scan

conducted from water to air. When the IC moves deep enough to overcome the water surface tension, the IC leading edge breaks through the surface and water splashes over the IC, as shown in panel f). The downward displacement of a water surface by an IC moving from air to water has been visually confirmed on several occasions by the author. It is expected that when scanning from water to air, the gradient peak will occur at the DeICERS. If water were perfectly static, the IC in an air-to-water scan would first be fully submerged at the DeICERS of a water-to-air scan. However, water surface tension will affect the depth at which IC submersion occurs, as discussed above. Water surface tension is investigated in Section 4.3.2.

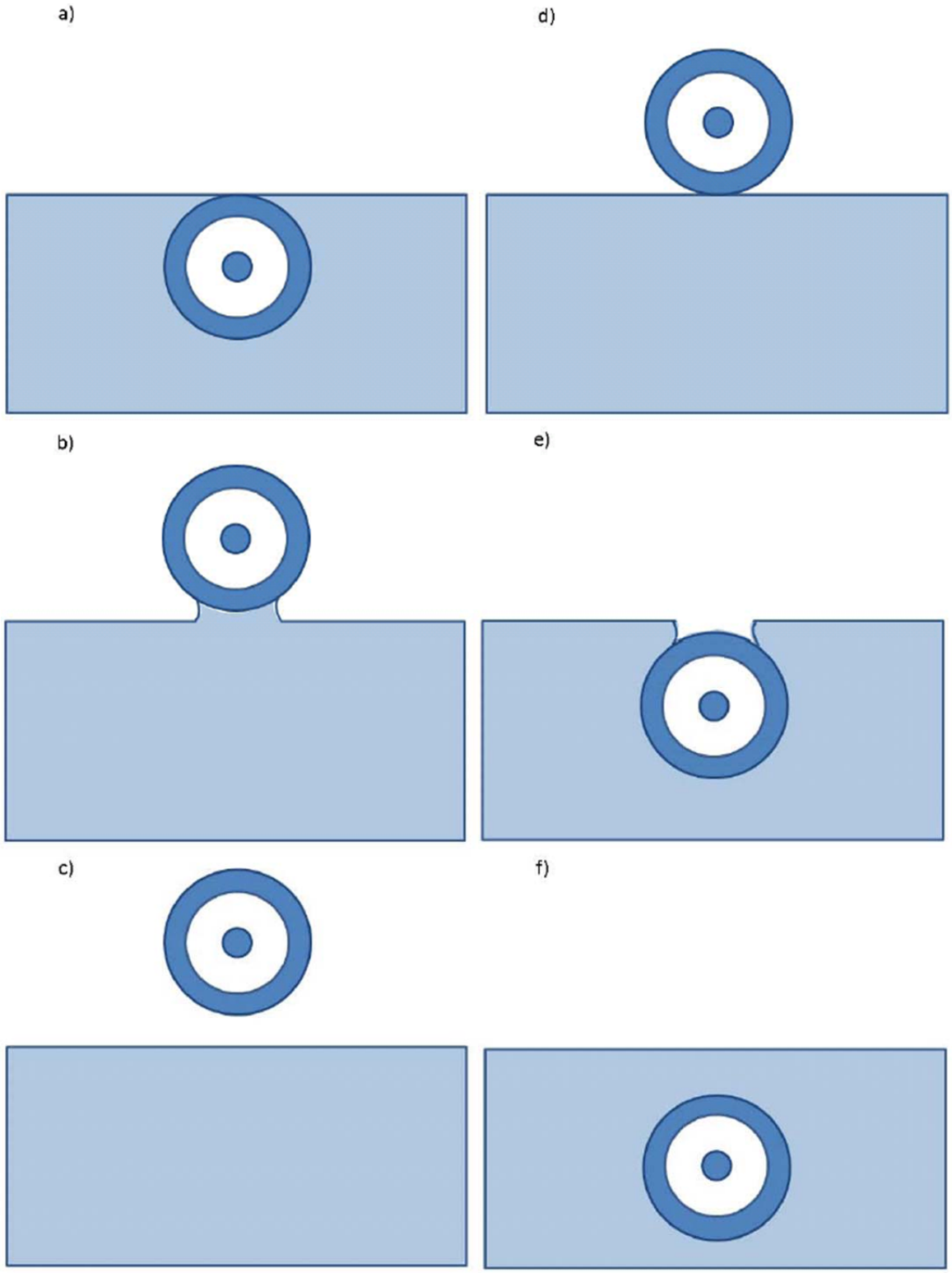

Figure 35: Illustration of the role played by scan direction in the interplay between an IC and a realistic water surface. The left column represents a scan from water to air while the right column shows an air-to-water scan. The meniscus demonstrated in panel b) provides a minimal signal increase from water backscatter. Panel e) shows the meniscus that affects the buildup between the IC and the radiation source in a scan from air to water. The reduction of effective buildup in panel e) is a major effect compared with the increased backscatter shown in panel b).

To test the influence of scan direction on gradient peak location, measurements in both directions are taken with five IBA cylindrical ICs: CC01, CC04, CC08, CC13, and CC25. Scans are performed at 0.1 mm resolution with each IC in 6 and 18 MV beams for 10×10 and 40×40 cm^2 fields from the Varian 2300 accelerator. Scans are taken with a single IC from water to air then from air to water at both energies for each field size before changing the IC. All scans are conducted in step-by-step mode, where the IC is held in place for 1 s at each measurement depth, over which time 50 individual readings are taken and averaged. Between measurement depths, each IC is moved at the low scan speed, 1.75 mm/s. These ICs are chosen for this experiment because all ICs fit coaxially into the same holder. The holder is designed such that each chamber fits into the holder centered at the same physical location within the water tank. This is important because this experiment is not controlled for water evaporation. Since all scans are centered at the same physical location, a correction has been applied to account for the water evaporation rate where necessary. The first scans taken are the 18 MV 40×40 cm^2 scans conducted with the CC01, thus there is no evaporation correction applied here. The last scans taken for this experiment are the 18 MV 40×40 cm^2 scans conducted with the CC25, by which time just over 24 hours had transpired, corresponding to an evaporation correction of 1.8 mm. A discussion of how the evaporation rate applied as a correction in this work is determined is found in Section 4.3.1.1.

The 6 MV scan data measured with the CC01 are shown in Figure 36. In-air dose is increased by ~45% for the 40×40 cm^2 field compared with the 10×10 cm^2 field. An increase in in-air dose is expected for larger fields as the larger opening of the collimating jaws allows more electrons scattered from components within the accelerator treatment head to reach the IC cavity. Some electrons produced within the jaws defining the large field will also scatter into the IC

volume and contribute dose. Scan direction-dependent relative dose differences occur over a depth range from -1 to 4 mm. The direction-dependent dose differences are caused by the replacement of displaced water with air in air-to-water scans and by the displacement of water into air in water-to-air scans.

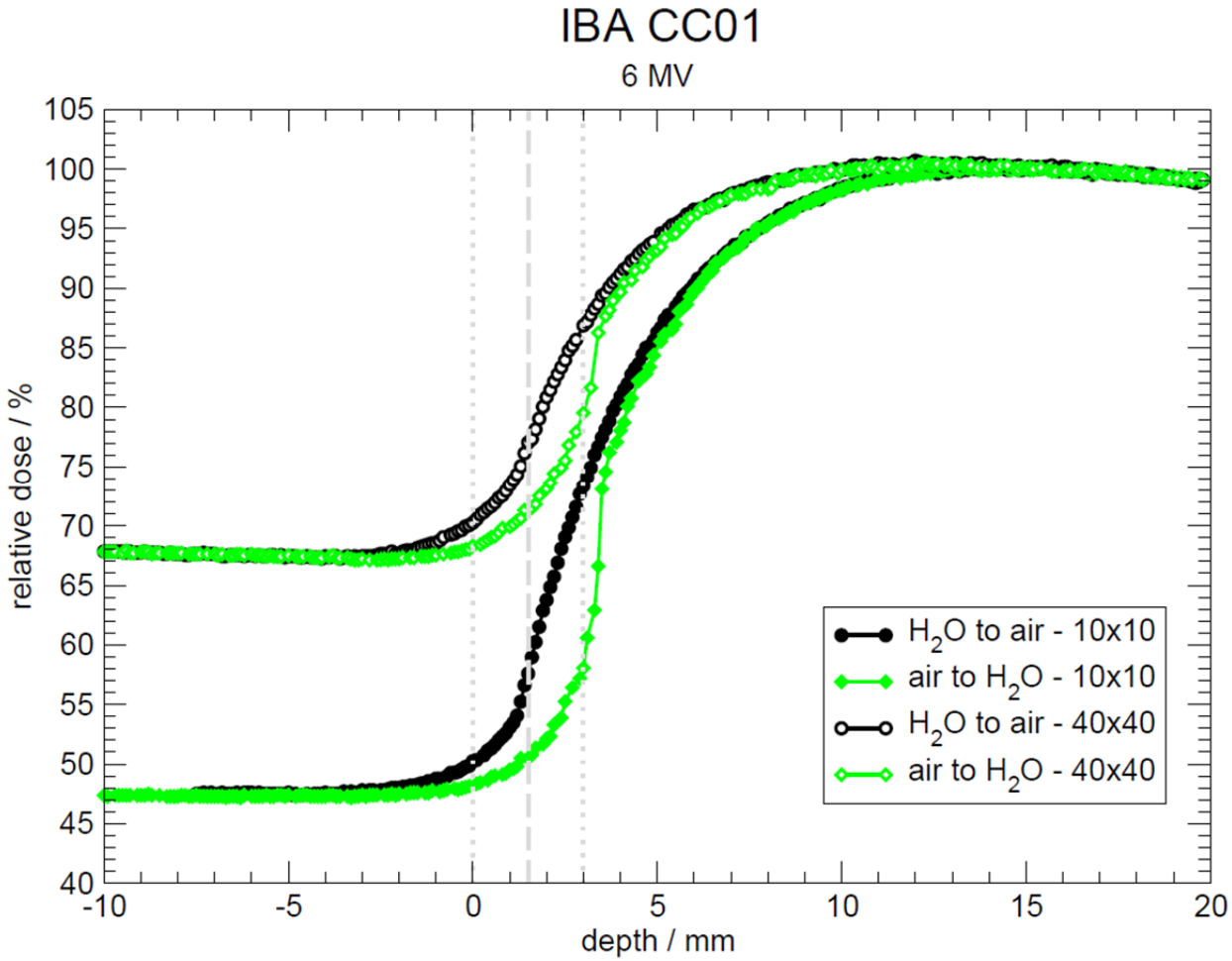

Figure 36: PDDs measured with the IBA CC01 for the Varian 2300 6 MV beam at 10×10 and 40×40 cm^2 fields. For both fields, scans are conducted at 0.1 mm resolution through the air/water interface in both directions. At each depth, 50 readings are made over a 1 s period and the resulting average is displayed. The grey dashed line marks the DeICERS when scanning from water to air and the depth at which the IC should first be fully submerged when scanning from air to water. The dotted grey lines represent the diameter of the IC when the IC is centered at the dashed grey line.

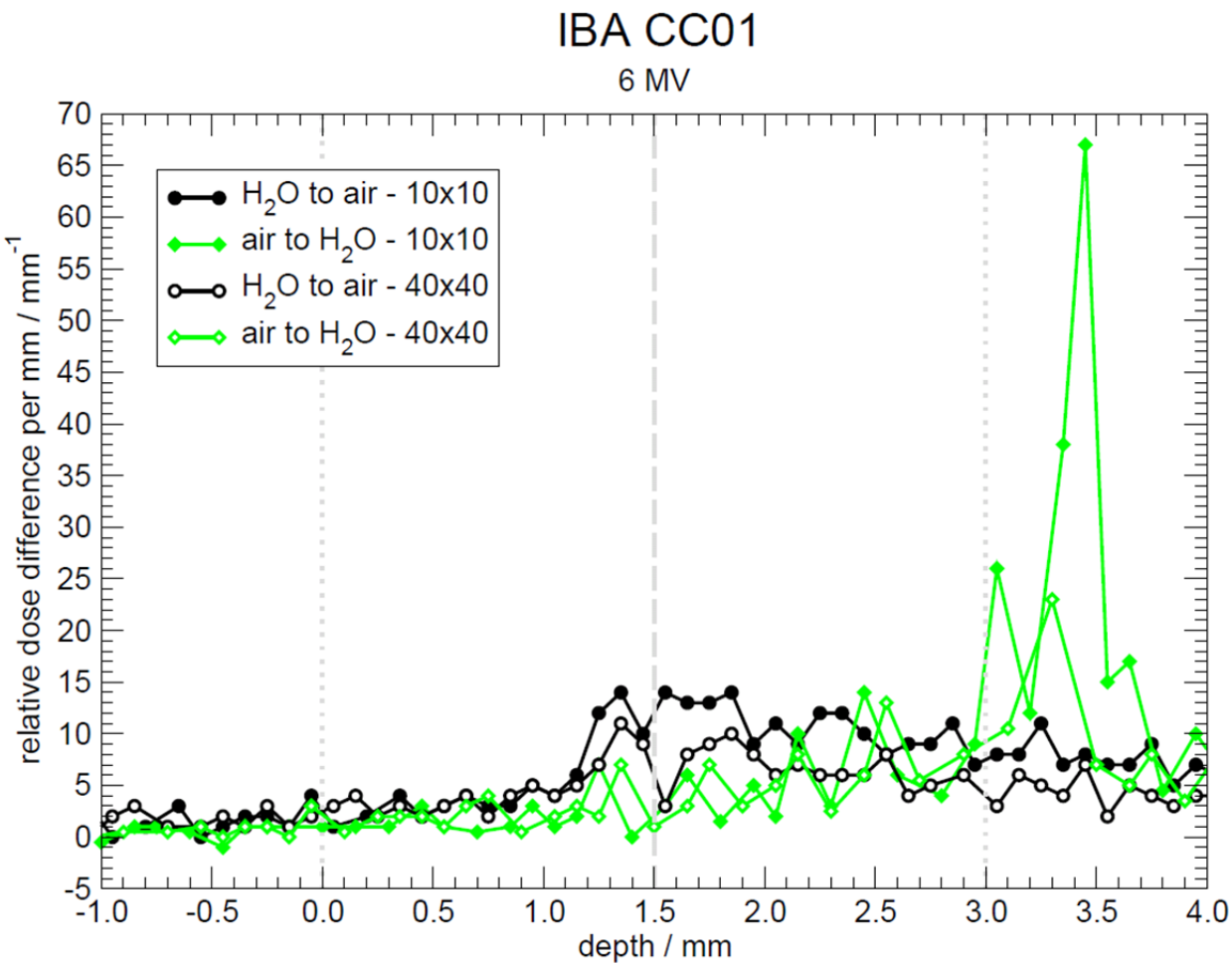

Figure 37: First derivatives of the scans shown in Figure 36. The air-to-water 10×10 cm^2 field gradient peak is over 3 times greater than the analogous 40×40 cm^2 field gradient peak. The relative lack of a definitive gradient peak in the water-to-air scans is due, at least in part, to the 1 s/pt. sampling resolution used for these scans. When scanning from air to water, the gradient peak occurs deeper in the water than when scanning from water to air due to the water surface being displaced below its nominal location by the IC. The grey dashed line represents the DeICERS for water-to-air scans. The dotted grey lines represent the diameter of the IC when the IC is centered at the dashed grey line.

The CC01 6 MV first derivatives are shown in Figure 37. The DeICERS of the water-to-air gradient peaks is at 1.5 mm. The air-to-water 40×40 cm^2 field peak is located at 3.3 mm depth while the air-to-water 10×10 cm^2 field peak occurs at 3.45 mm. The height of the air-to-water gradient peaks indicates that once the air-to-water meniscus is broken, water splashes back in over the IC quickly. The difference in observed gradient peak locations indicates that the IBA CC01 displaces water ~2 mm below the nominal surface location when scanning from air to water.

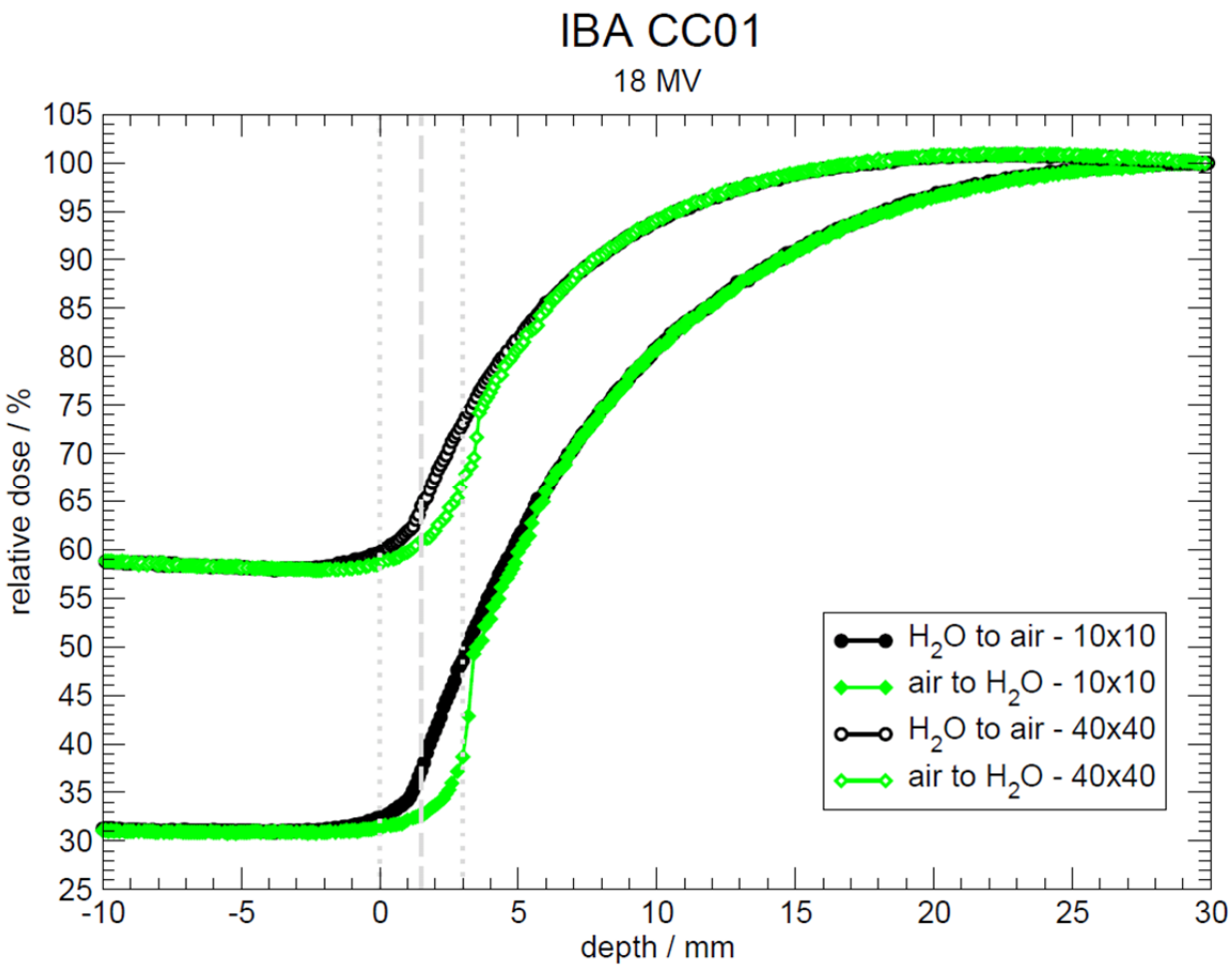

Figure 38: PDDs measured with the IBA CC01 for the Varian 2300 18 MV beam at 10×10 and 40×40 cm^2 fields. For both fields, scans are conducted at 0.1 mm resolution through the air/water interface in both directions. At each depth, 50 readings are made over a 1 s period and the resulting average is displayed. The grey dashed line marks the DeICERS when scanning from water to air and the depth at which the IC should first be fully submerged when scanning from air to water. The dotted grey lines represent the diameter of the IC when the IC is centered at the dashed grey line.

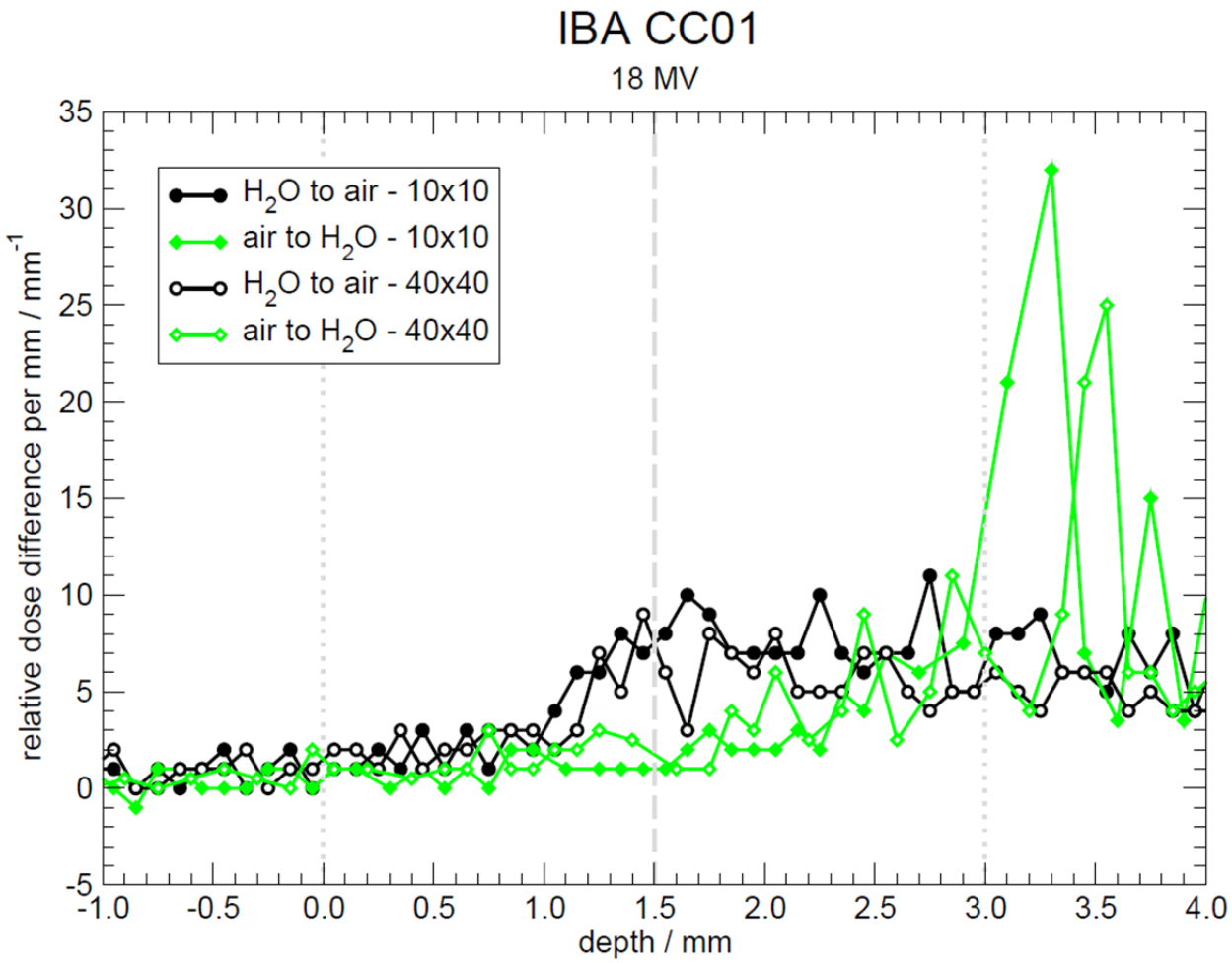

Figure 39: First derivatives of the scans shown in Figure 38. The relative lack of a definitive gradient peak in the water-to-air scans is due, at least in part, to the 1 s/pt. sampling resolution used for these scans. When scanning from air to water, the gradient peak occurs deeper in the water than when scanning from water to air due to the water surface being displaced below its nominal location by the IC. The grey dashed line represents the DeICERS for water-to-air scans. The dotted grey lines represent the diameter of the IC when the IC is centered at the dashed grey line.

The CC01 18 MV scans are found in Figure 38. Here, the in-air dose is increased by ~90% for the larger field size. As in Figure 36, the direction-dependent relative dose differences occur over a depth range from -1 to 4 mm. The CC01 18 MV calculated gradients are shown in Figure 39. For the 10×10 cm^2 field, the water-to-air gradient peak occurs at 1.65 mm depth and the air-to-water gradient peak occurs at 3.2 mm depth. This is taken to mean that the 10×10 cm^2 field air-to-water scan displaced water 1.55 mm below the nominal water surface. The 40×40 cm^2 field gradient peaks occur at 1.45 mm depth and 3.55 mm depth when scanning from water-to-air and from air-to-water, respectively. This means nominally that in the 18 MV 40×40 cm^2 field

air-to-water scan, the IBA CC01 displaced water 2.1 mm below the surface. As there is no logical reason for the water meniscus to be a function of incident beam energy or field size, these scans indicate that the amount of water displaced below the surface is not always the same for each air-to-water measurement with the same IC. The average water-to-air gradient peak location over the four CC01 measurements is 1.45±0.12 mm, which is within the computed standard deviation of the DeICERS at 1.5 mm. However, the total spread in the gradient peak locations of 0.3 mm is still larger than desired. Alignment of the CC01 is revisited in Section 4.5.1. As compared with the scans shown in Section 4.5.1, the scans in this section represent alignments of an inexperienced user without any tool (e.g., optical telescope) allowing independent water surface alignment verification. The scans shown here were performed primarily to investigate the scan direction dependence of measured results.

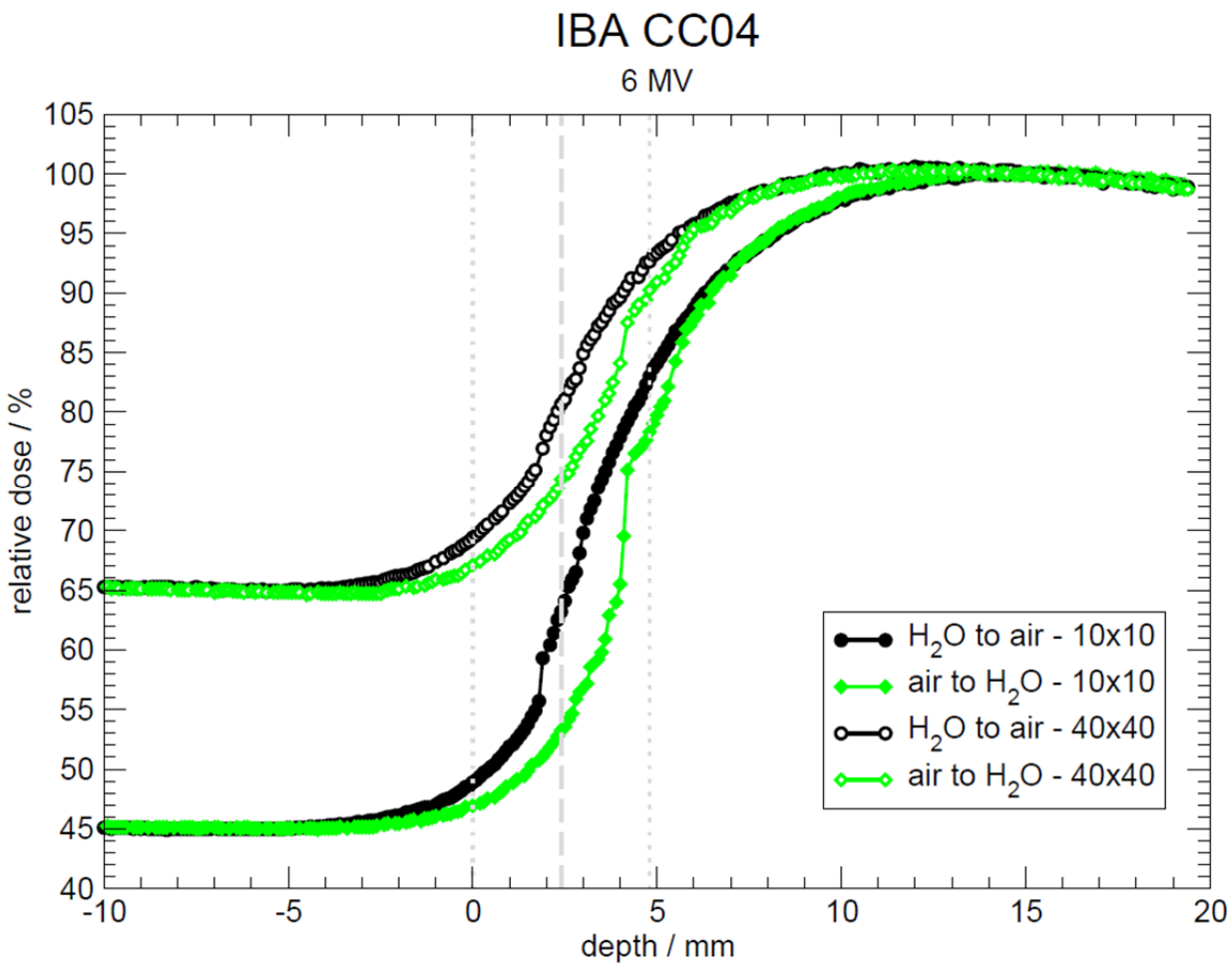

Figure 40: PDDs measured with the IBA CC04 for the Varian 2300 6 MV beam at 10×10 and 40×40 cm^2 fields. For both fields, scans are conducted at 0.1 mm resolution through the air/water interface in both directions. At each depth, 50 readings are made over a 1 s period and the resulting average is displayed. The grey dashed line marks the DeICERS when scanning from water to air and the depth at which the IC should first be fully submerged when scanning from air to water. The dotted grey lines represent the diameter of the IC when the IC is centered at the dashed grey line.

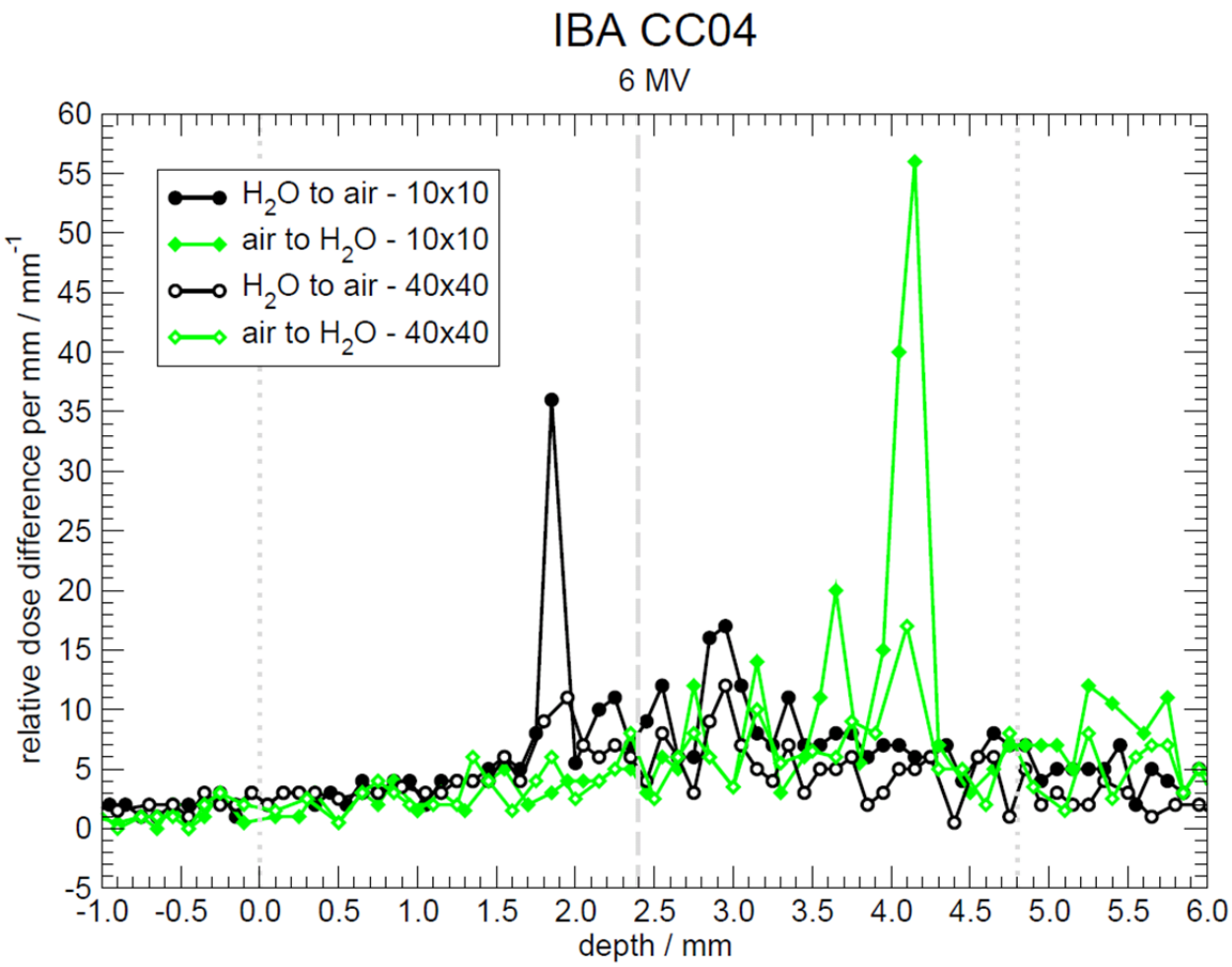

Figure 41: First derivatives of the scans shown in Figure 40. When scanning from air to water, the gradient peak occurs deeper in the water than when scanning from water to air due to the water surface being displaced below its nominal location by the IC. All scans are corrected for evaporation. The grey dashed line represents the DeICERS for water-to-air scans. The dotted grey lines represent the diameter of the IC when the IC is centered at the dashed grey line.

The 6 MV PDDs for the CC04 are shown in Figure 40. The depth range over which scan direction-dependent relative dose differences occur is expanded from what was observed with the CC01 to -2 to 6 mm with this IC. This expansion is not unexpected as the CC04 outer diameter is 4.8 mm and the CC01 outer diameter is 3.0 mm. Dose in air is increased by ~44% for the large field over the small field, which is consistent with measurements at 6 MV with the CC01. This is also consistent with 6 MV results measured with the CC01. Figure 41 shows the 6 MV CC04 relative dose gradients. For the 10×10 cm^2 field, the water-to-air gradient peak occurs at 1.85 mm, while the air-to-water scan pushes 2.3 mm of water below the nominal

surface position. For the 40×40 cm^2 field, the water-to-air gradient peak occurs at 1.95 mm, while the air-to-water scan pushes 2.15 mm of water below the nominal surface position. The water-to-air DeICERS for the CC04 is 2.4 mm.

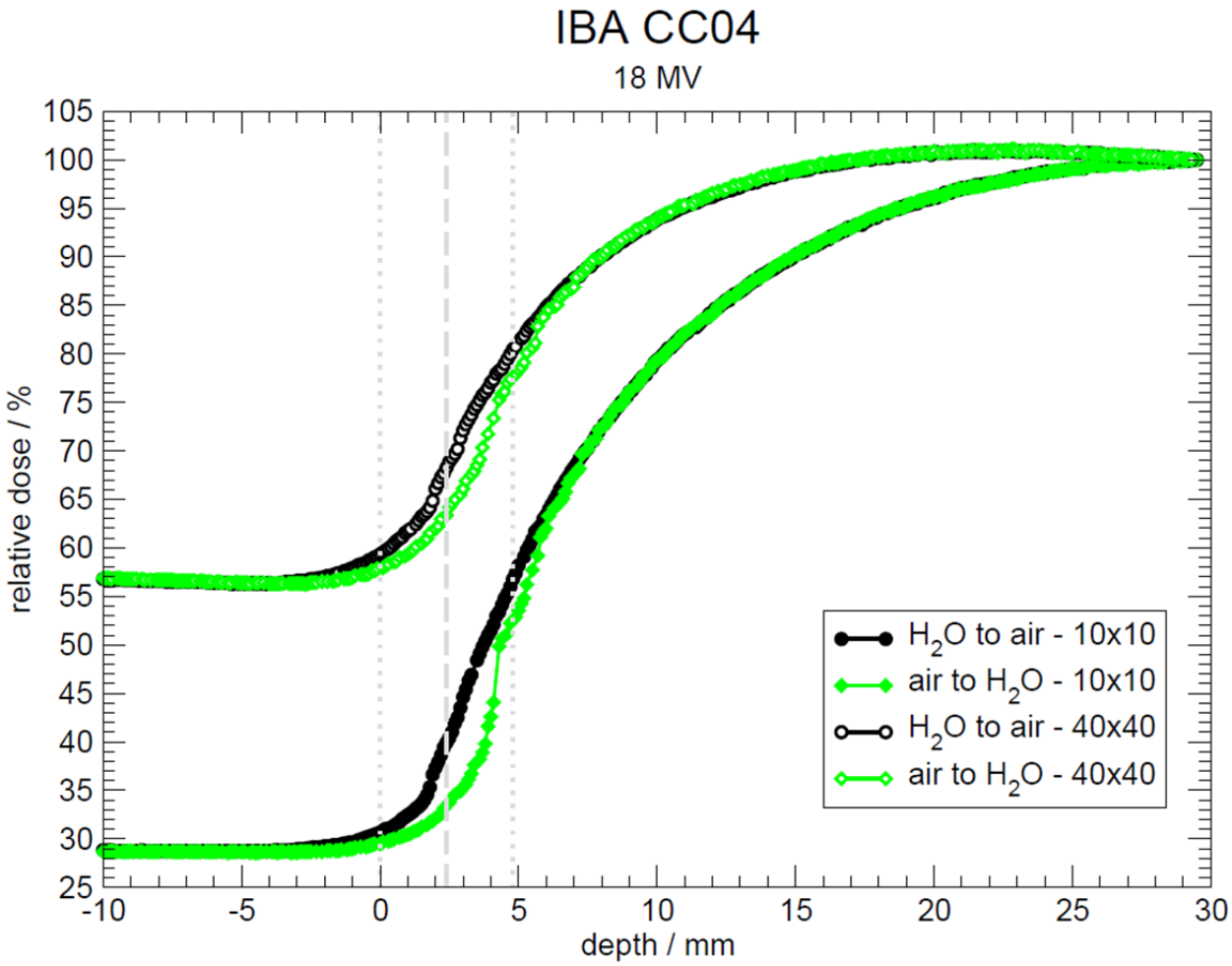

Figure 42: PDDs measured with the IBA CC04 for the Varian 2300 18 MV beam at 10×10 and 40×40 cm^2 fields. For both fields, scans are conducted at 0.1 mm resolution through the air/water interface in both directions. At each depth, 50 readings are made over a 1 s period and the resulting average is displayed. The grey dashed line marks the DeICERS when scanning from water to air and the depth at which the IC should first be fully submerged when scanning from air to water. The dotted grey lines represent the diameter of the IC when the IC is centered at the dashed grey line.

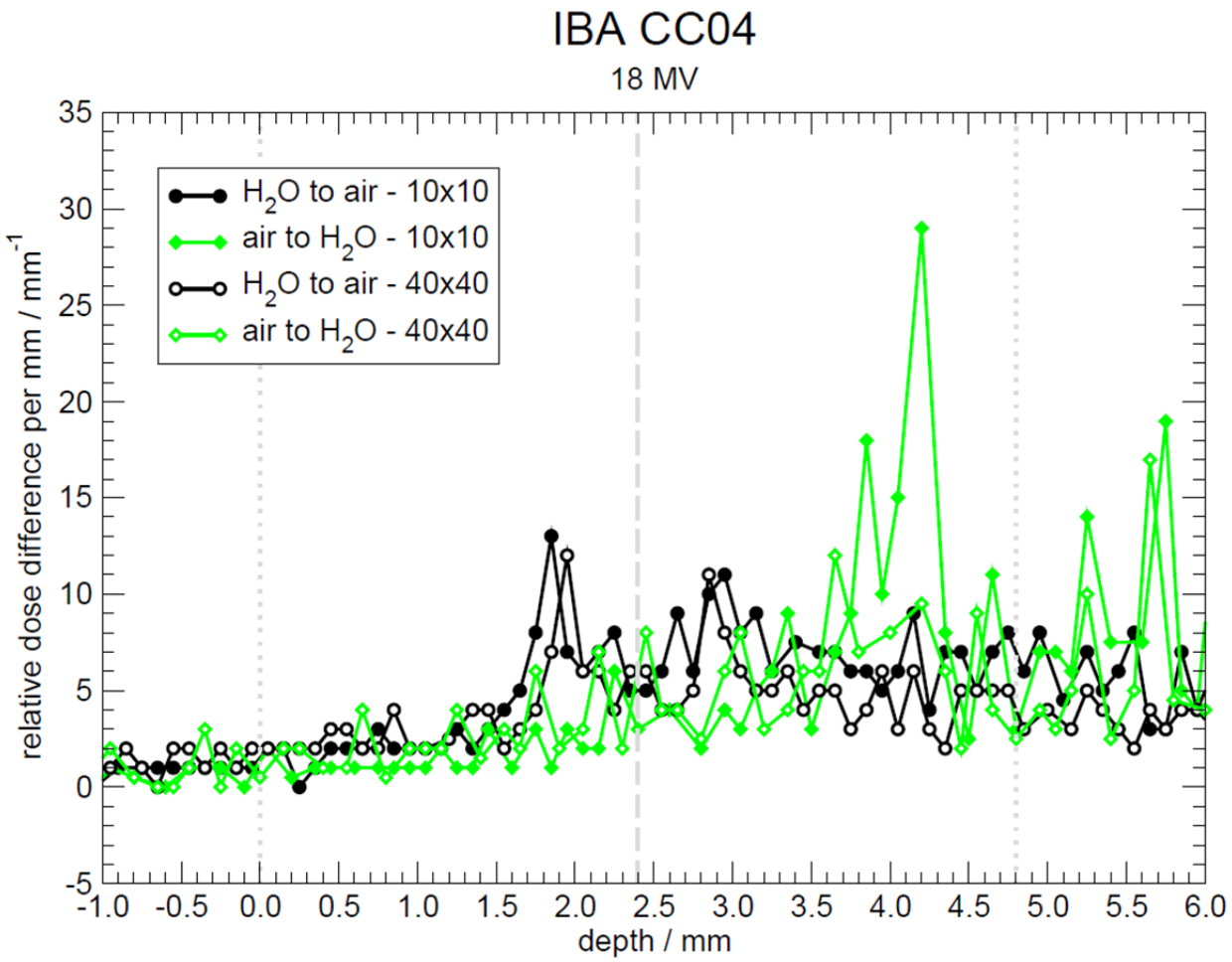

Figure 43: First derivatives of the scans shown in Figure 42. When scanning from air to water, the gradient peak occurs deeper in the water than when scanning from water to air due to the water surface being displaced below its nominal location by the IC. The grey dashed line represents the DeICERS for water-to-air scans. The dotted grey lines represent the diameter of the IC when the IC is centered at the dashed grey line.

The CC04 18 MV PDDs are displayed in Figure 42. Here, direction-dependent relative dose differences are observed from -1 to 6 mm. In-air dose is increased by ~93% for the large field as compared with the small field. This is also consistent with CC01 18 MV measurements. The CC04 18 MV relative dose gradients are shown in Figure 43. The water-to-air gradient peaks occur at 1.85 mm and 1.95 mm for the small field and large field cases, respectively. The small field air-to-water scan displaces the water surface 2.35 mm below its nominal location. For the large field, no definitive air-to-water gradient peak is observed. The four water-to-air gradient peaks for the CC04 give an average gradient peak location of 1.90±0.05 mm. In

contrast to the CC01 measurements, the spread of these trials is acceptable (0.1 mm) but the IC is consistently aligned ~0.5 mm below the water surface. The DeICERS for a well-aligned CC04 scan is 2.4 mm. Given the apparent positioning error, alignment of the CC04 is revisited in Section 4.5.1, where alignment is performed more carefully. With alignment performed by an experienced user, the apparent positioning error shown here is resolved in later measurements.

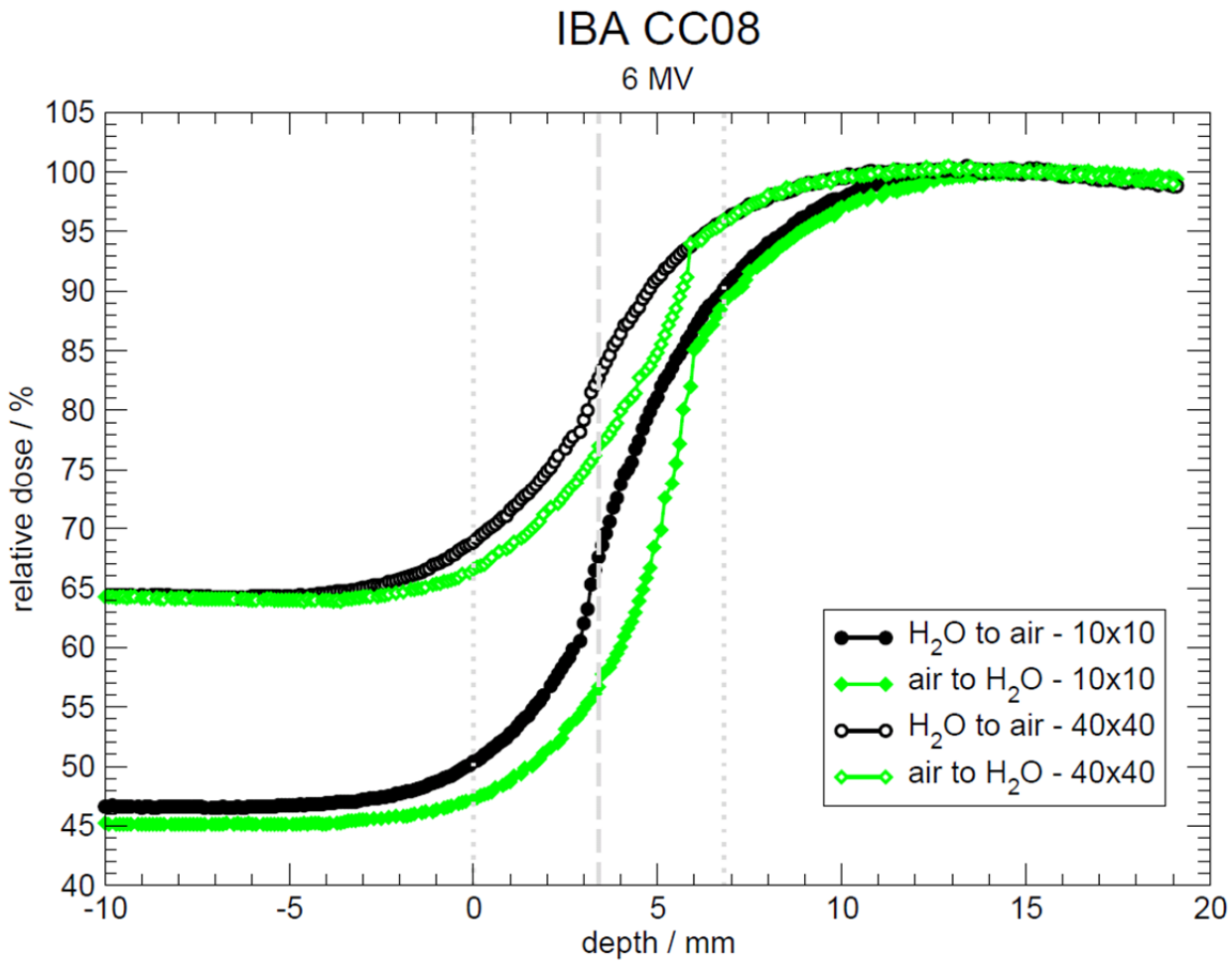

Figure 44: PDDs measured with the IBA CC08 for the Varian 2300 6 MV beam at 10×10 and 40×40 cm^2 fields. For both fields, scans are conducted at 0.1 mm resolution through the air/water interface in both directions. At each depth, 50 readings are made over a 1 s period and the resulting average is displayed. The grey dashed line marks the DeICERS when scanning from water to air and the depth at which the IC should first be fully submerged when scanning from air to water. The dotted grey lines represent the diameter of the IC when the IC is centered at the dashed grey line.

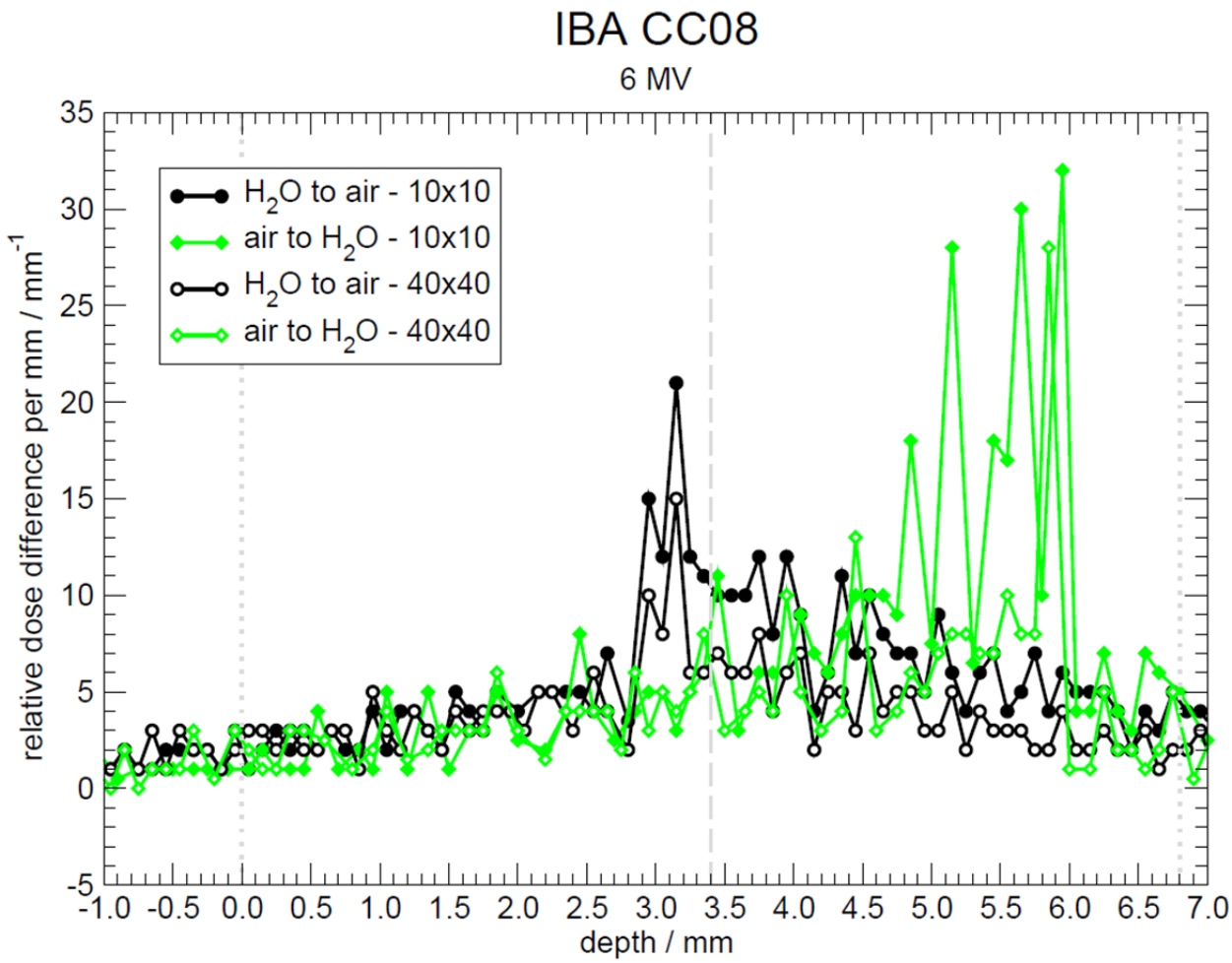

Figure 45: First derivatives of the scans shown in Figure 44. The relative noise in these gradients is influenced by the relatively low 1 s/pt. sampling resolution used for the original scans. The relationship between sampling resolution and gradient noise is discussed in Section 4.2.2. When scanning from air to water, the gradient peak occurs deeper in the water than when scanning from water to air due to the water surface being displaced below its nominal location by the IC. The grey dashed line represents the DeICERS for water-to-air scans. The dotted grey lines represent the diameter of the IC when the IC is centered at the dashed grey line.

The 6 MV CC08 PDDs are shown in Figure 44. The depth range over which scan direction-dependent relative dose differences occur is from -3 to 6 mm. This is an expansion from the range for the CC04 IC, again because the CC08 outer diameter is 6.8 mm, whereas the CC04 outer diameter is 4.8 mm. The dose in air is ~41% higher for the 40×40 cm^2 field than the 10×10 cm^2 field, which agrees with the 6 MV measurements with the CC01 and CC04. Figure 45 shows the 6 MV CC08 relative dose gradients. The water-to-air gradient peaks occur at 3.15 mm for both field sizes. The DeICERS for CC08 water-to-air gradient peaks is at 3.4 mm.

The difference in the measured peak location from the DeICERS is attributable to the alignment of an inexperienced user. The 10×10 cm^2 field air-to-water scan displaces 2.7 mm of water below the nominal water surface location before the IC becomes fully submerged. In the 40×40 cm^2 field case, the air-to-water scan pushes 2.8 mm of water below the nominal surface location.

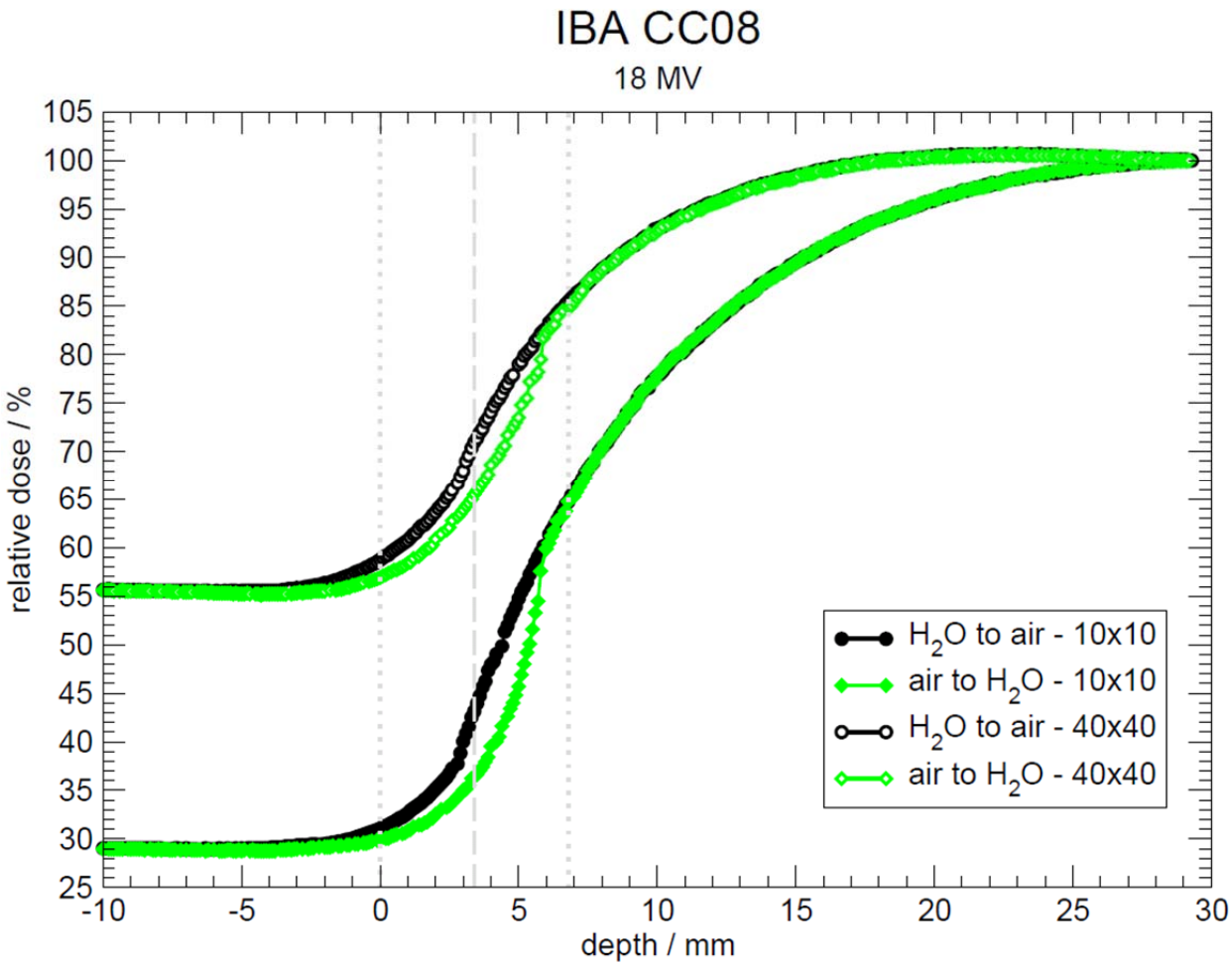

Figure 46: PDDs measured with the IBA CC08 for the Varian 2300 18 MV beam at 10×10 and 40×40 cm^2 fields. For both fields, scans are conducted at 0.1 mm resolution through the air/water interface in both directions. At each depth, 50 readings are made over a 1 s period and the resulting average is displayed. The grey dashed line marks the DeICERS when scanning from water to air and the depth at which the IC should first be fully submerged when scanning from air to water. The dotted grey lines represent the diameter of the IC when the IC is centered at the dashed grey line.

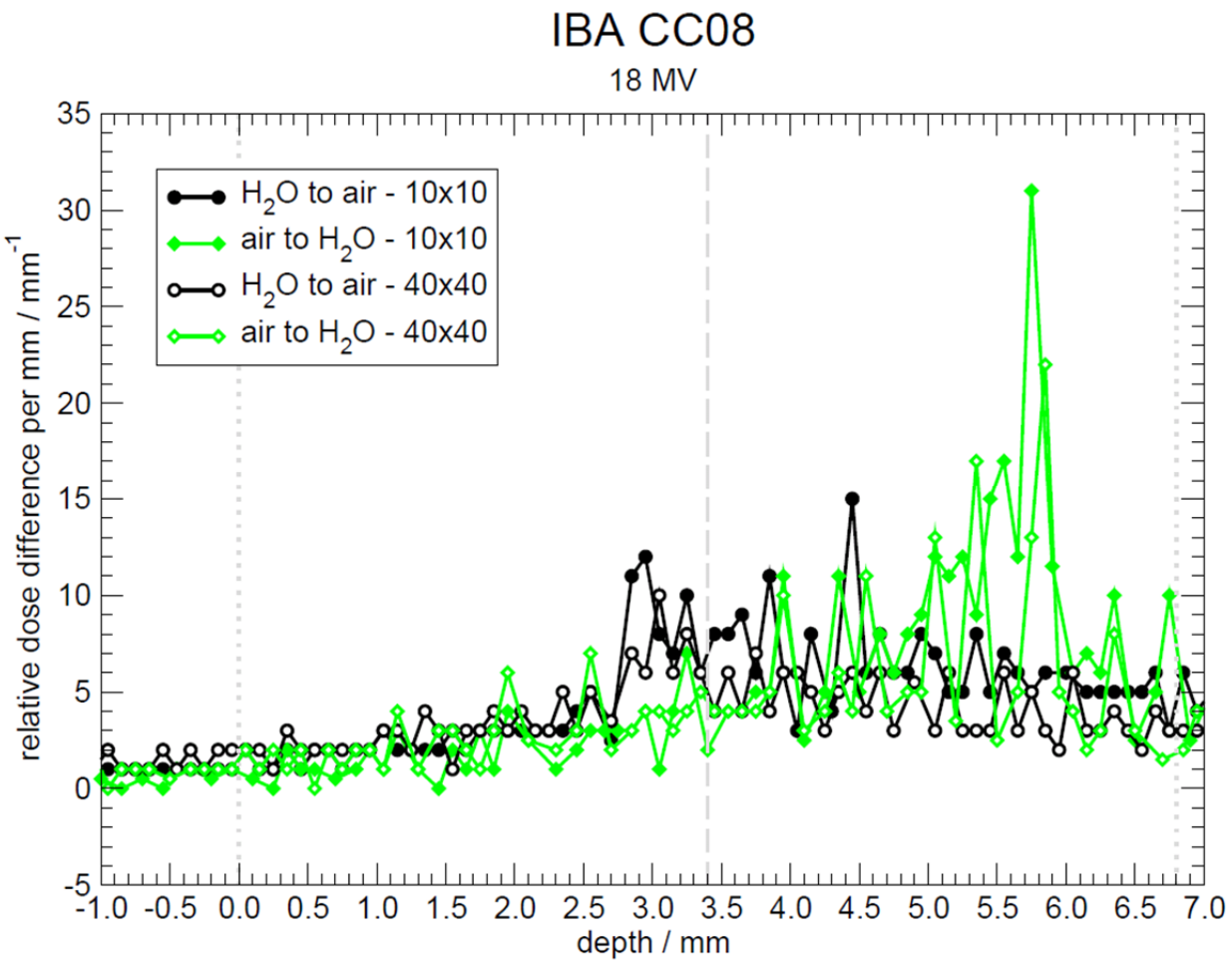

Figure 47: First derivatives of the scans shown in Figure 46. The relative noise in these gradients is influenced by the relatively low 1 s/pt. sampling resolution used for the original scans. The relationship between sampling resolution and gradient noise is discussed in Section 4.2.2. When scanning from air to water, the gradient peak occurs deeper in the water than when scanning from water to air due to the water surface being displaced below its nominal location by the IC. The grey dashed line represents the DeICERS for water-to-air scans. The dotted grey lines represent the diameter of the IC when the IC is centered at the dashed grey line.

Figure 46 depicts the CC08 18 MV PDDs. The difference in in-air dose for the 40×40 cm^2 field compared with the 10×10 cm^2 field agrees with 18 MV measurements with other ICs. The range over which scan direction-dependent relative dose differences occur is -1 to 6 mm. Figure 47 shows the 18 MV CC08 gradients. The water-to-air gradient peaks occur at 2.95 and 3.05 for the small field and large field, respectively. The DeICERS for the CC08 is 3.4 mm. Differences are attributable to a lack of experience in IC alignment. Scans at both field sizes indicate that in the air-to-water scans, the IC pushed 2.8 mm of water below the nominal

water surface location before finally being submerged. The four measured water-to-air gradient peaks for the CC08 yield an average gradient peak location of 3.08±0.08 mm. The four gradient peaks exhibited a 0.2 mm total spread in location. This shows that the CC08 was consistently aligned ~0.3 mm below the water surface. Alignment of the CC08 is revisited in Section 4.5.1.

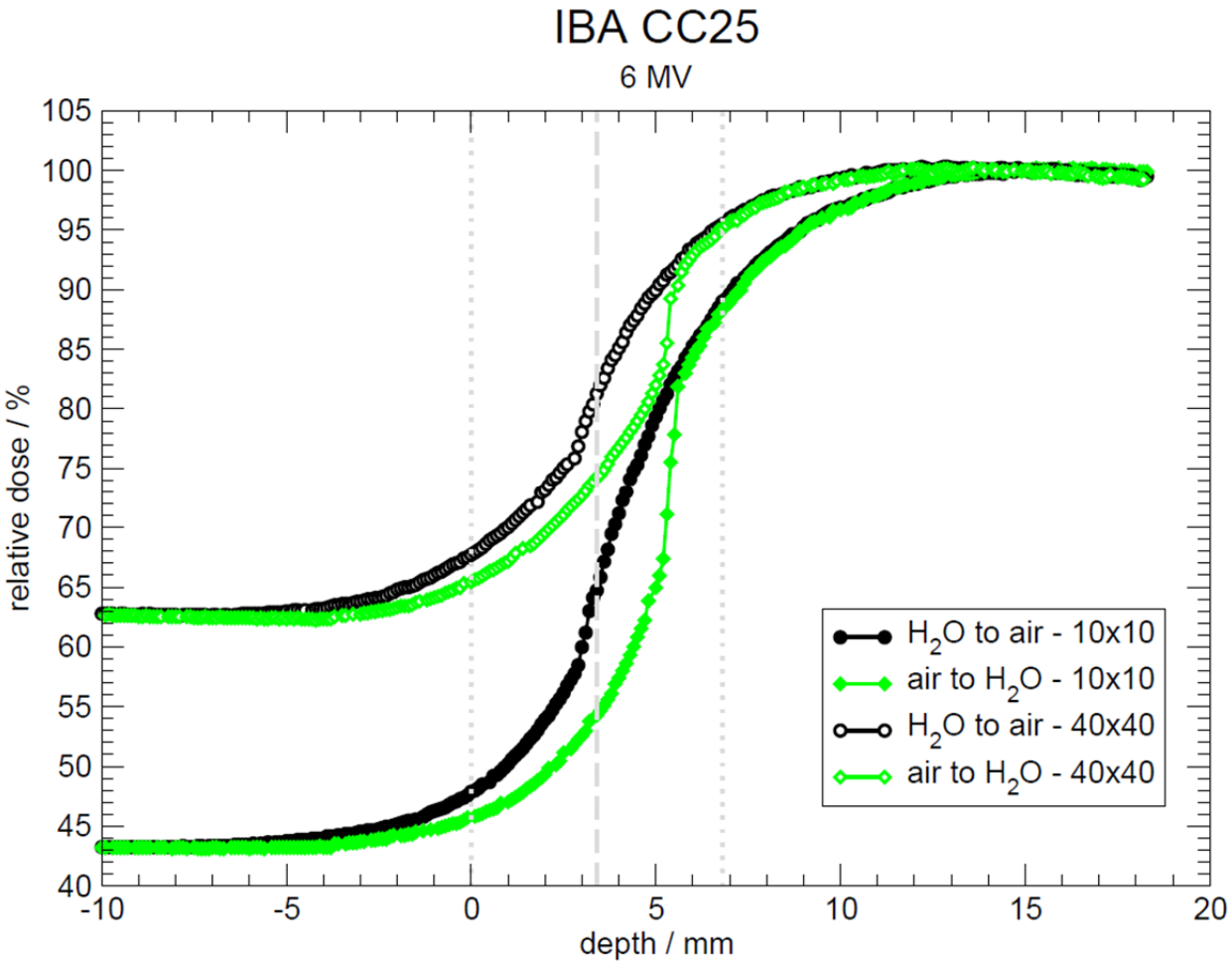

Figure 48: PDDs measured with the IBA CC25 for the Varian 2300 6 MV beam at 10×10 and 40×40 cm^2 fields. For both fields, scans are conducted at 0.1 mm resolution through the air/water interface in both directions. At each depth, 50 readings are made over a 1 s period and the resulting average is displayed. The grey dashed line marks the DeICERS when scanning from water to air and the depth at which the IC should first be fully submerged when scanning from air to water. The dotted grey lines represent the diameter of the IC when the IC is centered at the dashed grey line.

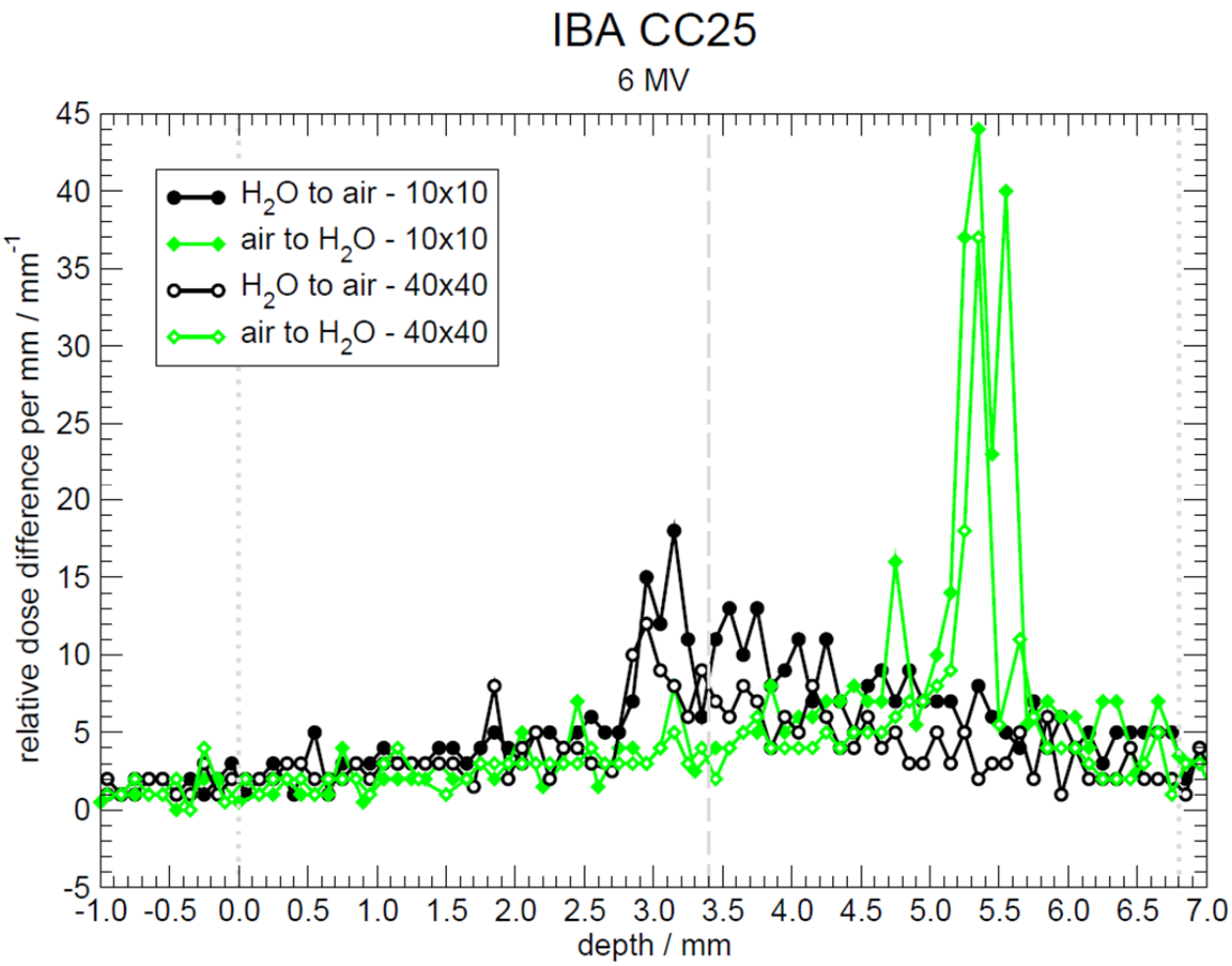

Figure 49: First derivatives of the scans shown in Figure 48. The air-to-water gradient peaks are over twice as high as the analogous water-to-air gradient peaks. When scanning from air to water, the gradient peak occurs deeper in the water than when scanning from water to air due to the water surface being displaced below its nominal location by the IC. The grey dashed line represents the DeICERS for water-to-air scans. The dotted grey lines represent the diameter of the IC when the IC is centered at the dashed grey line.

Data for the CC25 6 MV scans are found in Figure 48. The CC25 is the largest volume IC of any used in this experiment but its outer diameter is the same as the CC08 and CC13, 6.8 mm. Therefore, the depth range over which scan direction-dependent relative dose differences occur does not increase for this IC compared with the range for the CC08. The range here is from -2 to 6 mm. A ~47% increase in dose in air occurs when the field size is changed from 10×10 cm^2 to 40×40 cm^2. This is consistent with the 6 MV measurements with the other three ICs described in this section. The CC25 6 MV gradients are given in Figure 49. Water-to-

air gradient peaks occur at 2.95 and 3.15 mm for the small and large fields, respectively. The DeICERS for the CC25 water-to-air gradient peak is 3.4 mm. These differences are resolved with more careful alignment. Air-to-water scans displace 2.2 mm of water below the nominal surface location in measurements for the small field. When measuring the large field, air-to-water scans push 2.4 mm of water below the nominal surface location.

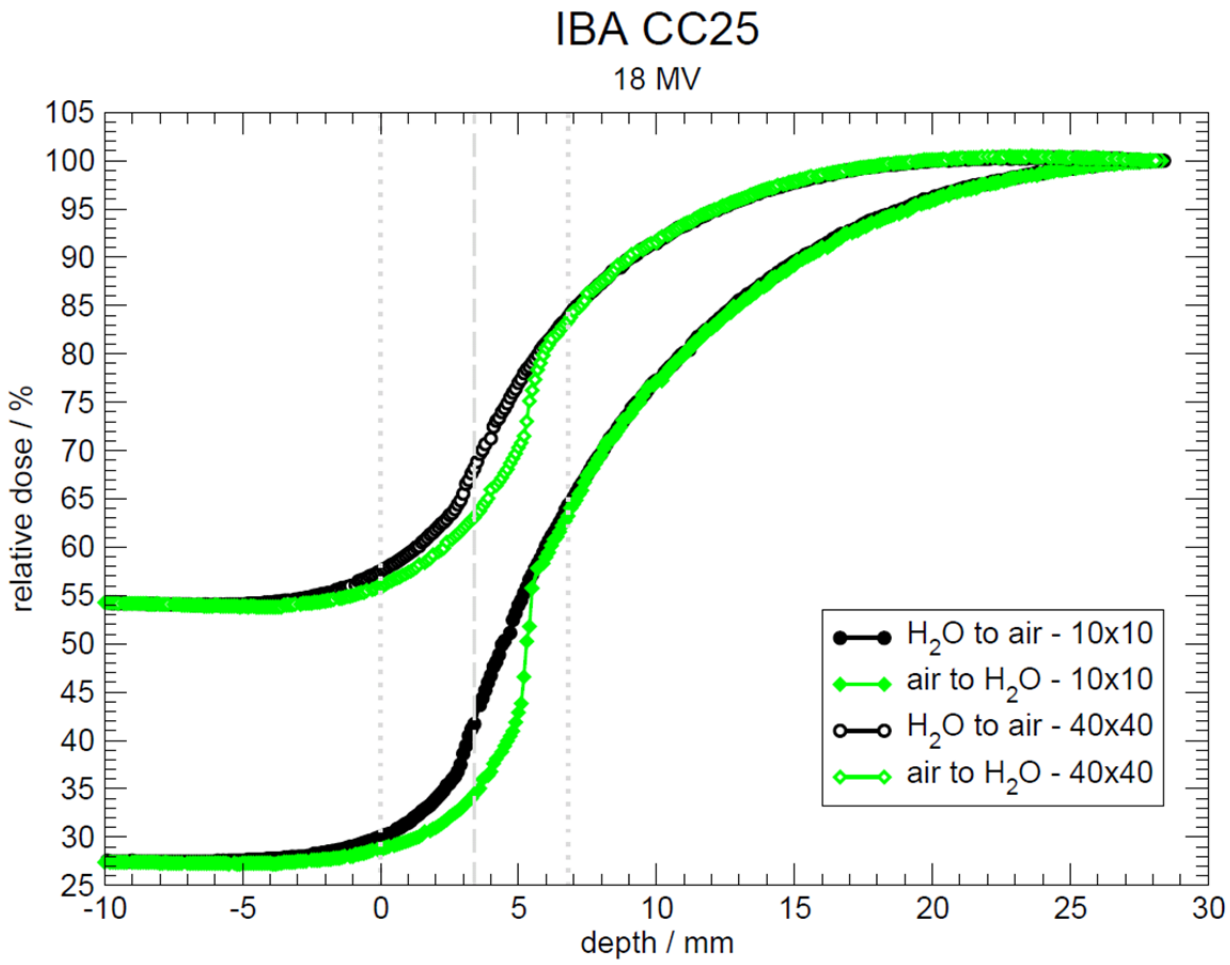

Figure 50: PDDs measured with the IBA CC25 for the Varian 2300 18 MV beam at 10×10 and 40×40 cm^2 fields. For both fields, scans are conducted at 0.1 mm resolution through the air/water interface in both directions. At each depth, 50 readings are made over a 1 s period and the resulting average is displayed. The grey dashed line marks the DeICERS when scanning from water to air and the depth at which the IC should first be fully submerged when scanning from air to water. The dotted grey lines represent the diameter of the IC when the IC is centered at the dashed grey line.

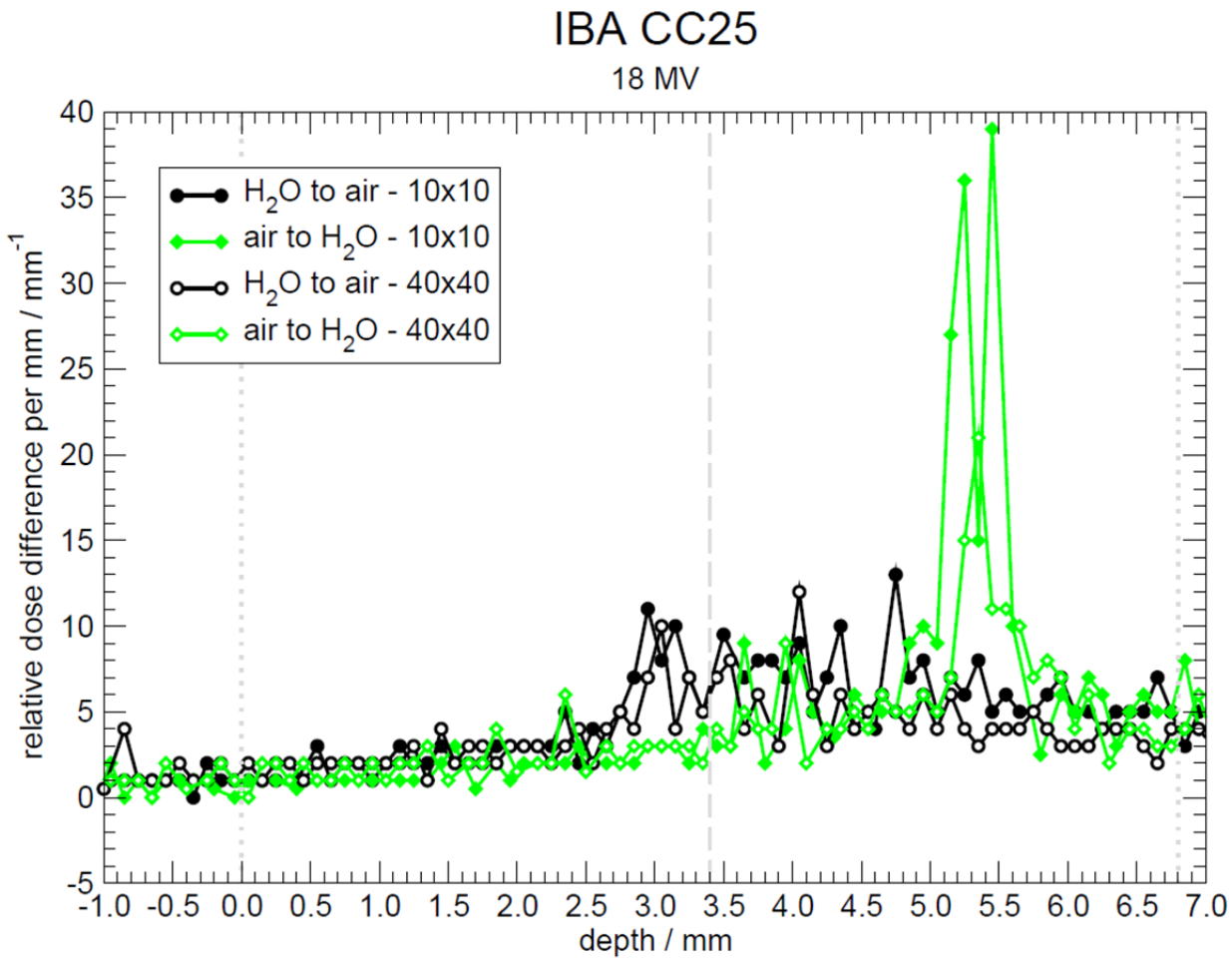

Figure 51: First derivatives of the scans shown in Figure 50. The air-to-water gradient peaks are over twice as high as the analogous water-to-air gradient peaks. When scanning from air to water, the gradient peak occurs deeper in the water than when scanning from water to air due to the water surface being displaced below its nominal location by the IC. The grey dashed line represents the DeICERS for water-to-air scans. The dotted grey lines represent the diameter of the IC when the IC is centered at the dashed grey line.

Figure 50 contains the 18 MV CC25 PDD data. Dose in air is 103% higher for the large field than for the small field. This is generally consistent with the 18 MV measurements with other ICs used in this experiment. The range over which scan direction-dependent relative dose differences occur is from -1 to 6 mm. The 18 MV CC25 gradients are shown in Figure 51. Water-to-air gradient peaks occur at 2.95 and 3.05 mm for the small and large fields, respectively. The water-to-air DeICERS is 3.4 mm. The difference between measured gradient peak locations and the DeICERS indicates a misalignment caused primarily by a lack of user experience. Scans

for the 10×10 cm^2 field indicate that 2.3 mm of water is pushed below the nominal surface position. Scans for the 40×40 cm^2 field indicate that 2.5 mm of water is displaced below the nominal surface position. The four water-to-air CC25 gradient peaks show an average location of 3.03±0.08 mm with a total spread of 0.2 mm. This indicates that the CC25 was aligned ~0.3 mm below the nominal surface position. The fact that the CC25 and CC08 appear to have been misaligned by roughly the same amount indicates that the misalignment was consistent for these two ICs of the same outer radius. The similar misalignment amounts seen for similarly-sized ICs indicate consistent user technique. Alignment of the CC25 is revisited in Section 4.5.1, where user experience and technique are improved.

The CC13 is the last IC scanned for this experiment before adding soap to the water for the surface tension experiment described in Section 4.3.2.2, thus results for the CC13 are discussed in Section 4.3.2.2. Among all scans with all ICs for both fields and incident beam energies, the scan direction-dependent differences in gradient peak location range from 1.55 to 2.80 mm, with a dependence on IC outer radius. The reproducibility of VCU air-to-water scan data has not been quantified; therefore, the observed direction-dependent differences might not be consistent with repeated measurements. The increased relative noise in the scans with smaller ICs contributes to ambiguity in the location of some gradient peaks, which in turn contributes to the range in direction-dependent differences. The ICs used in this experiment are apparently consistently aligned too deeply in the water, as seen by the water-to-air gradient peaks consistently appearing to the left of the grey dashed lines on the gradient plots. Alignment of the CC01, CC04, CC08, and CC25 with increased experience and improved technique is described in Section 4.5.1. The general conclusion of the in-house scan direction measurements is that scanning from air to water creates a gradient peak that is unsuitable for use as an alignment

metric, due to the chaotic way in which water splashes over an IC when the surface tension is broken. Inter-scan IC positioning inconsistencies in this experiment are overcome in later measurements, acquired after the positioning inconsistencies were detected, where measurements were performed until signal was acquired at all depths at the desired resolution, without skipping points.

Scan direction is also examined at other sites with additional equipment. CyberKnife measurements are taken with three ICs: the PTW 31014, Exradin A16, and IBA IC-10. Results shown here are from measurements taken using a collimator that produces a field of 60 mm diameter. This is the largest CyberKnife field measured and is the most directly comparable with the 10×10 cm^2 fields produced by other accelerators. At the SSD used in CyberKnife measurements, a standard 10×10 cm^2 field projects to a 7.85×7.85 cm^2 field. The PTW 31014 scans are shown in Figure 52 with the accompanying gradients in Figure 53. Scans with the Exradin A16 are shown in Figure 54. The gradients of the Exradin A16 scans are displayed in Figure 55. Figure 56 shows PDDs measured with the Wellhöfer IC-10, with the respective gradients being shown in Figure 57. The noise in the CyberKnife scans appears reduced compared with the VCU scan direction measurements due to the coarser resolution of the CyberKnife scans. Small inconsistencies in IC positioning between trials (e.g., moving the IC to 1.1 mm depth instead of the user-specified 1.0 mm) produce noise in scans at 0.1 mm resolution but are obscured when scanning at 1.0 mm resolution. The general conclusions from VCU measurements that gradient peak height is increased but the location is substantially displaced from the DeICERS for air-to-water scans hold here.

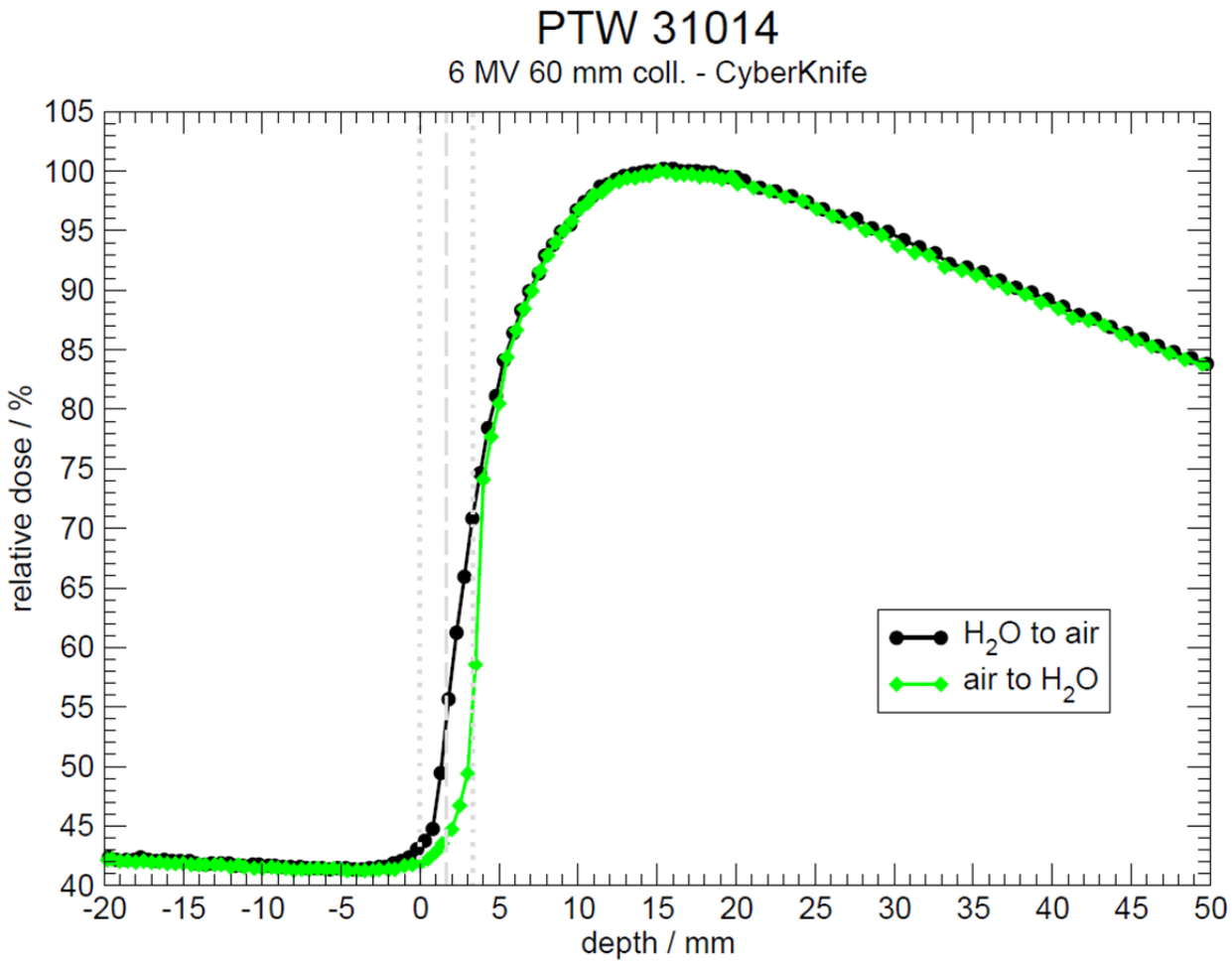

Figure 52: PDDs measured with the PTW 31014 on the Accuray CyberKnife. The collimator is circular producing a field of 6 cm diameter at an SSD of 78.5 cm. Scans are conducted at 0.5 mm resolution within ±20 mm of the surface and at 1 mm resolution for the remaining depths. The IC is stationed at each depth for 0.3 seconds, in which time 15 readings are taken and the resulting averages are displayed. The grey dashed line marks the DeICERS when scanning from water to air and the depth at which the IC should first be fully submerged when scanning from air to water. The dotted grey lines represent the diameter of the IC when the IC is centered at the dashed grey line.

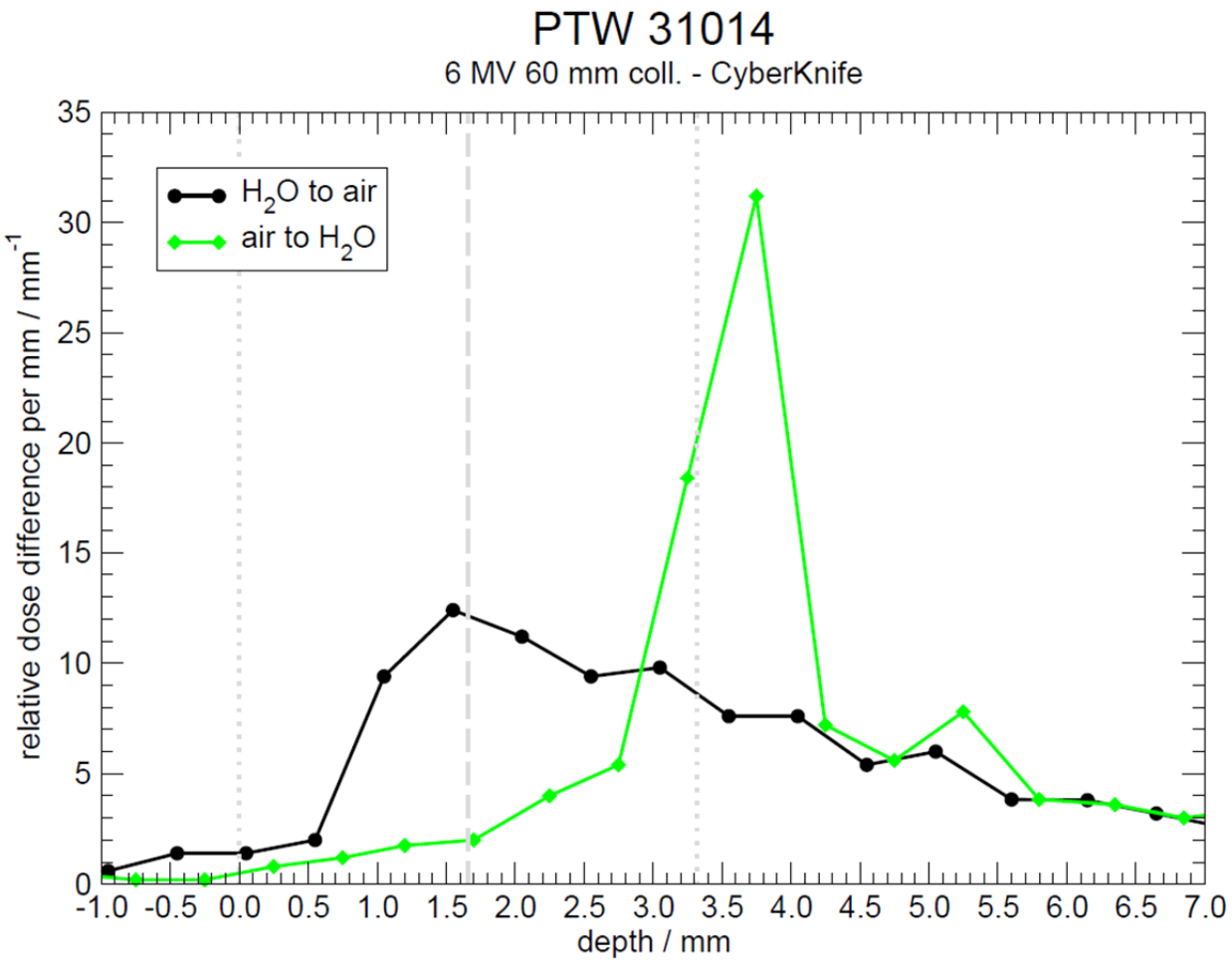

Figure 53: First derivatives of the scans shown in Figure 52. When scanning from air to water, the gradient peak occurs deeper in the water than when scanning from water to air due to the water surface being displaced below its nominal location by the IC. The grey dashed line represents the DeICERS for water-to-air scans. The dotted grey lines represent the diameter of the IC when the IC is centered at the dashed grey line.

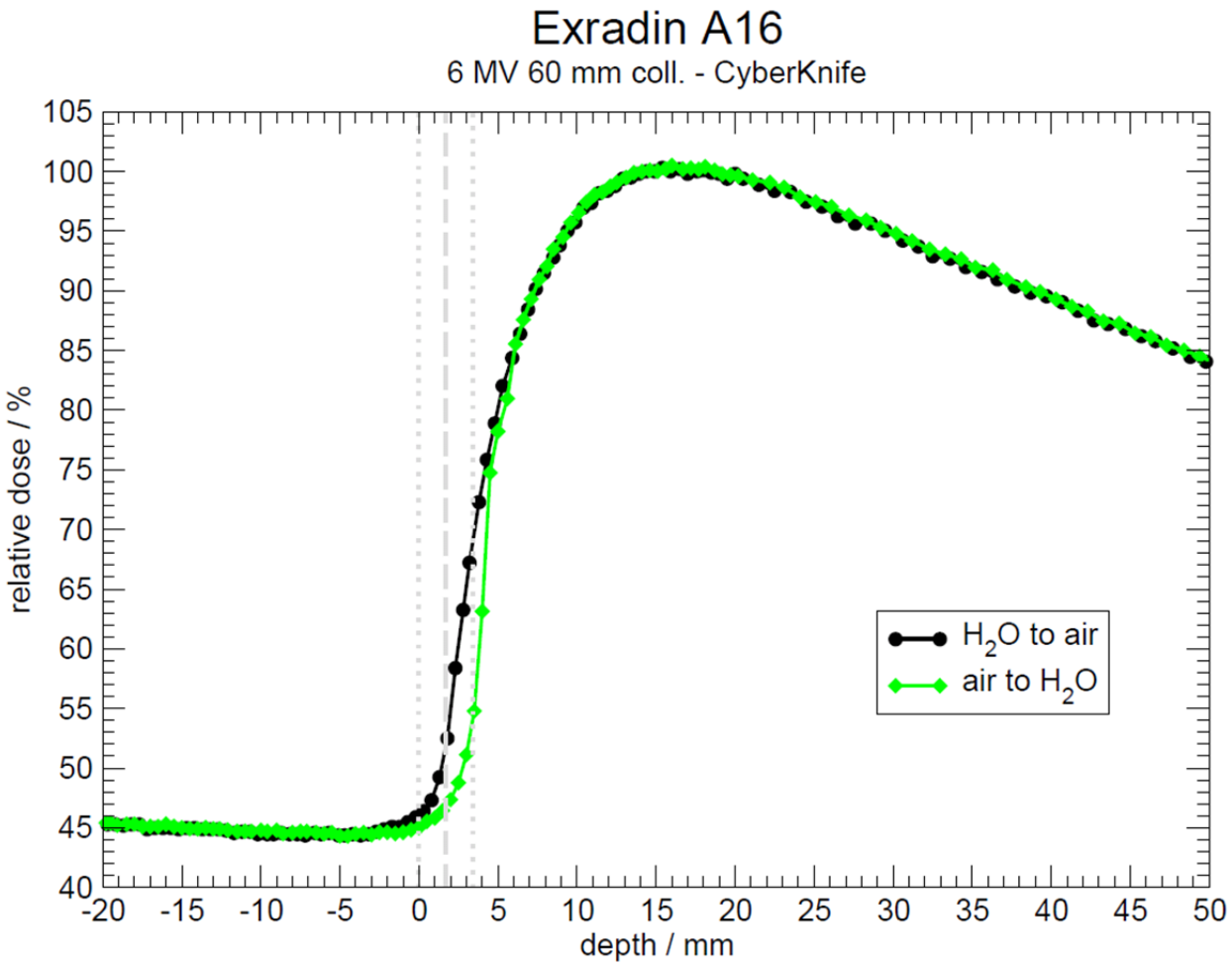

Figure 54: PDDs measured with the Exradin A16 on the Accuray CyberKnife. The collimator is circular producing a field of 6 cm diameter at an SSD of 78.5 cm. Scans are conducted at 0.5 mm resolution within ±20 mm of the surface and at 1 mm resolution for the remaining depths. The IC is stationed at each depth for 0.3 seconds, in which time 15 readings are taken and the resulting averages are displayed. The grey dashed line marks the DeICERS when scanning from water to air and the depth at which the IC should be fully submerged when scanning from air to water. The dotted grey lines represent the diameter of the IC when the IC is centered at the dashed grey line.

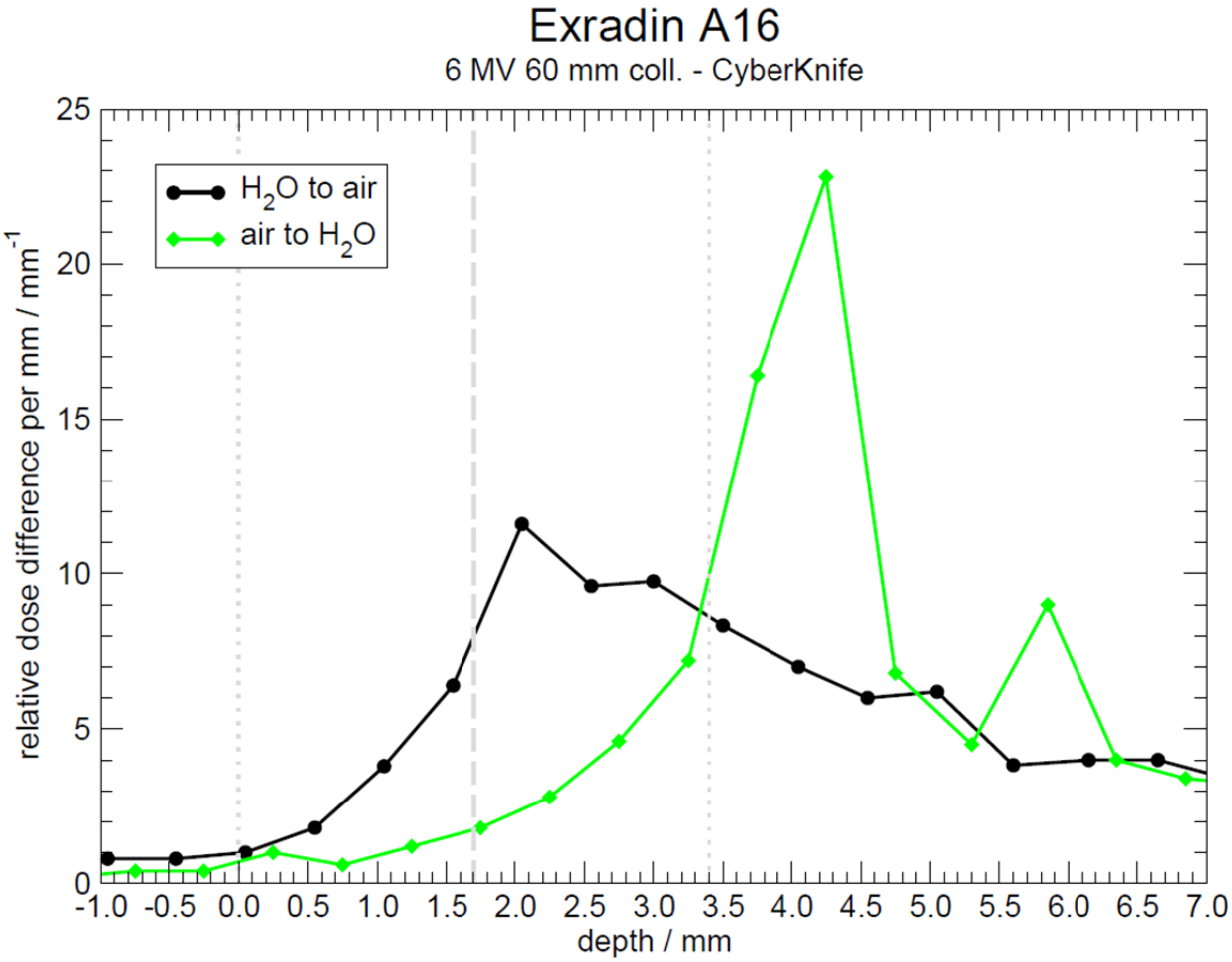

Figure 55: First derivatives of the scans shown in Figure 54. When scanning from air to water, the gradient peak occurs deeper in the water than when scanning from water to air due to the water surface being displaced below its nominal location by the IC. The grey dashed line represents the DeICERS for water-to-air scans. The dotted grey lines represent the diameter of the IC when the IC is centered at the dashed grey line.

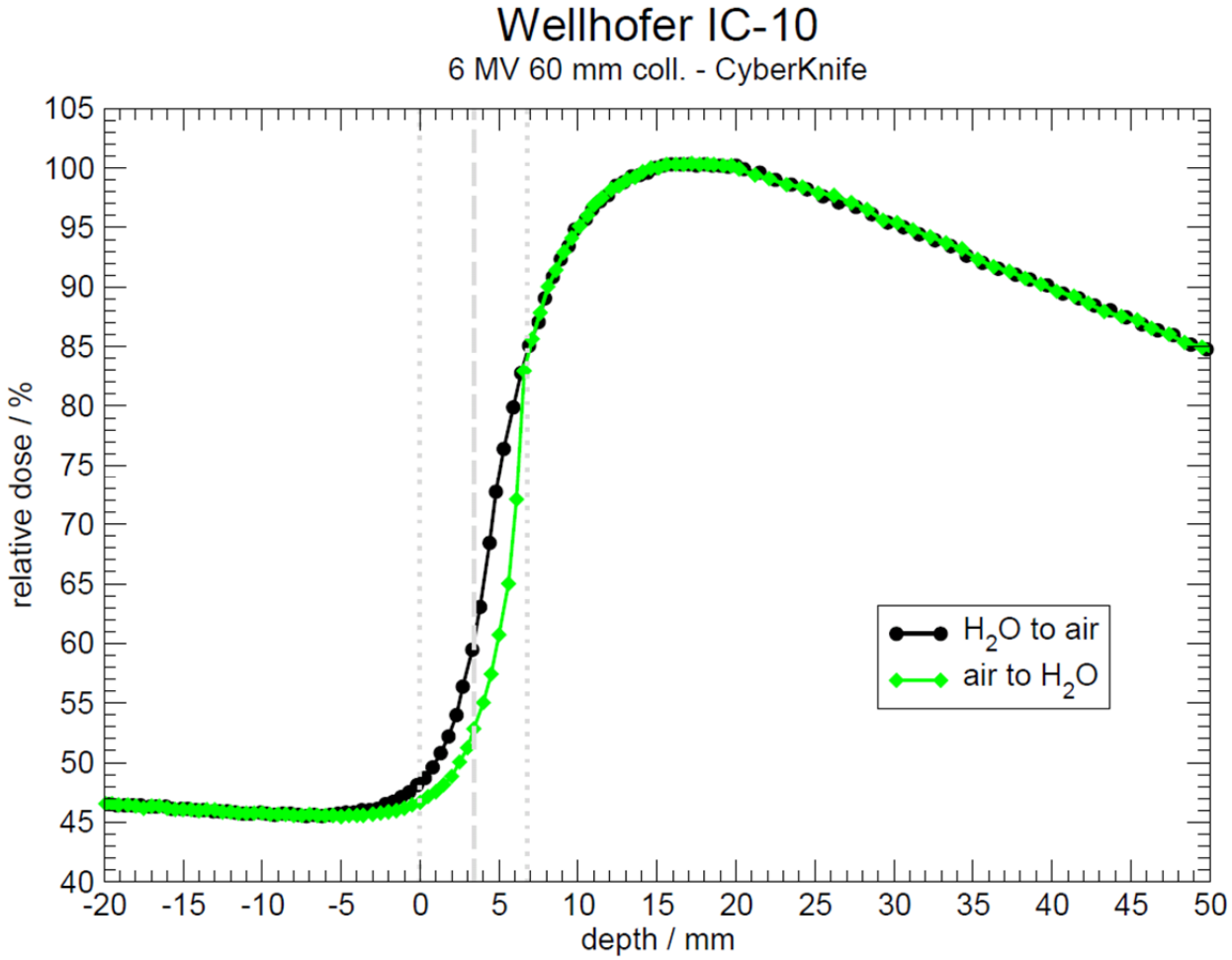

Figure 56: PDDs measured with the Wellhöfer IC-10 on the Accuray CyberKnife. The collimator is circular producing a field of 6 cm diameter at an SSD of 78.5 cm. Scans are conducted at 0.5 mm resolution within ±20 mm of the surface and at 1 mm resolution for the remaining depths. The IC is stationed at each depth for 0.3 seconds, in which time 15 readings are taken and the resulting averages are displayed. The grey dashed line marks the DeICERS when scanning from water to air and the depth at which the IC should be fully submerged when scanning from air to water. The dotted grey lines represent the diameter of the IC when the IC is centered at the dashed grey line.

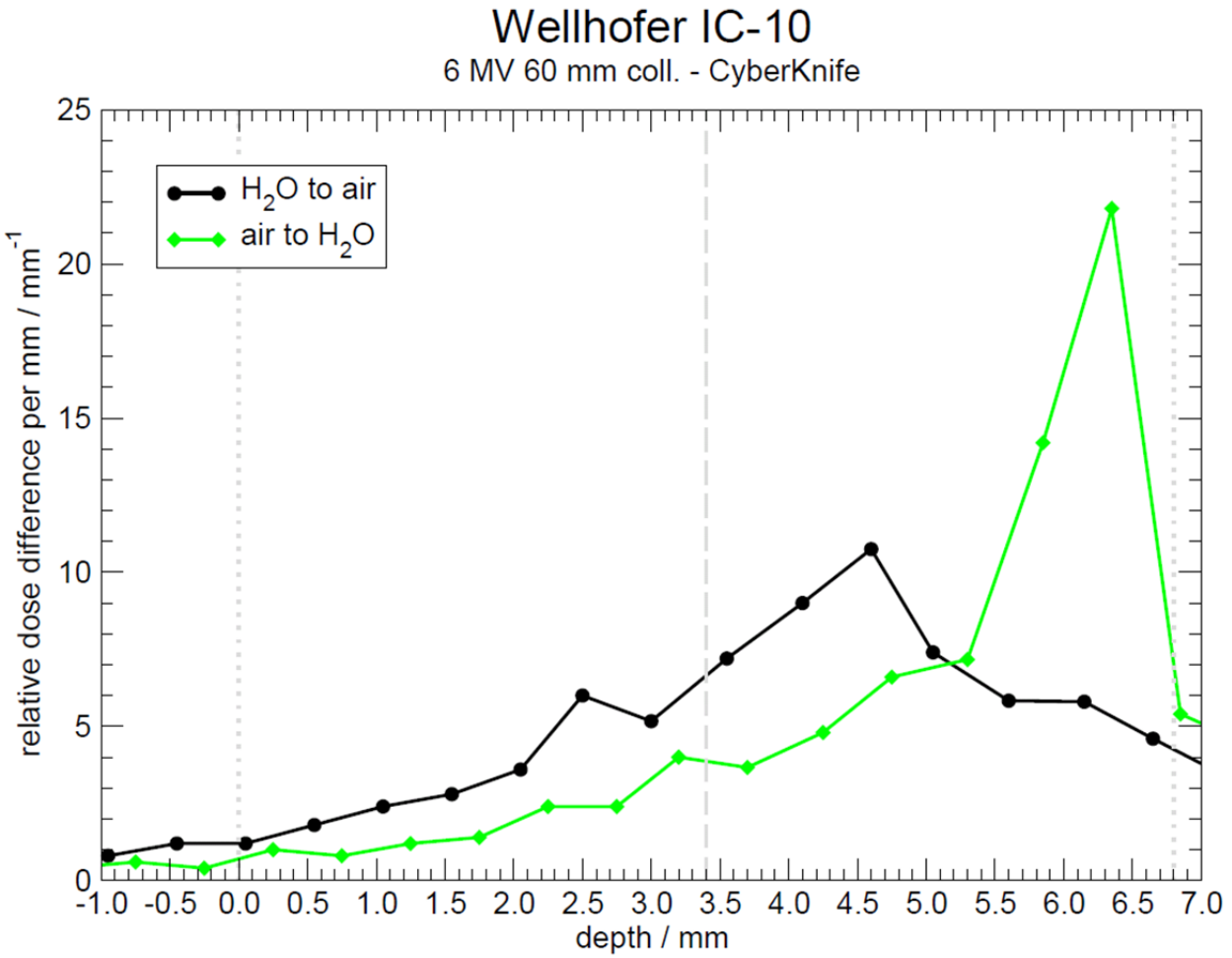

Figure 57: First derivatives of the scans shown in Figure 56. When scanning from air to water, the gradient peak occurs deeper in the water than when scanning from water to air due to the water surface being displaced below its nominal location by the IC. The grey dashed line represents the DeICERS for water-to-air scans. The dotted grey lines represent the diameter of the IC when the IC is centered at the dashed grey line.

Further consideration is afforded to scan direction in the measurements acquired at the NRC with the high-precision customized scanning system. Two ICs are scanned in both directions through the air/water interface: the IBA CC13 and the Exradin A18. The IBA CC13 is featured in in-house measurements and the Exradin A18 is the basis of the computational IC model used in the MC calculations described in Section 3.2. Measurements are performed for 6 MV 10×10 cm^2 fields. The IBA CC13 scans are shown in Figure 58 with the accompanying gradients shown in Figure 59. Figure 60 and Figure 61 show the analogous data for the Exradin A18. Again, in-air scans display increased gradient peak height but also substantial

displacement of the observed gradient peak from the DeICERS. Observation of the same trend in all measurement sets from all locations gives additional confidence that the observed directional differences are caused by the physical interaction of a given IC with the water surface, rather than any property of a given radiation field or measurement setup.

In summary of the scan direction experiments, scans from water to air can reproduce gradient peak locations. Scanning from air to water gives gradient peak locations dependent on water surface tension. Water surface tension is investigated in Section 4.3.2. The discrepancies between observed water-to-air gradient peak and DeICERS locations for a given IC are expected to be representative of typical misalignments by inexperienced users. With improved scanning technique and increased user experience, VCU water-to-air measurements shown in Section 4.5.1 show improved agreement between gradient peak and DeICERS locations for the ICs tested here. Measurements with precise alignment facilitated by the unique NRC equipment also show coincidence of water-to-air gradient peak and DeICERS locations.

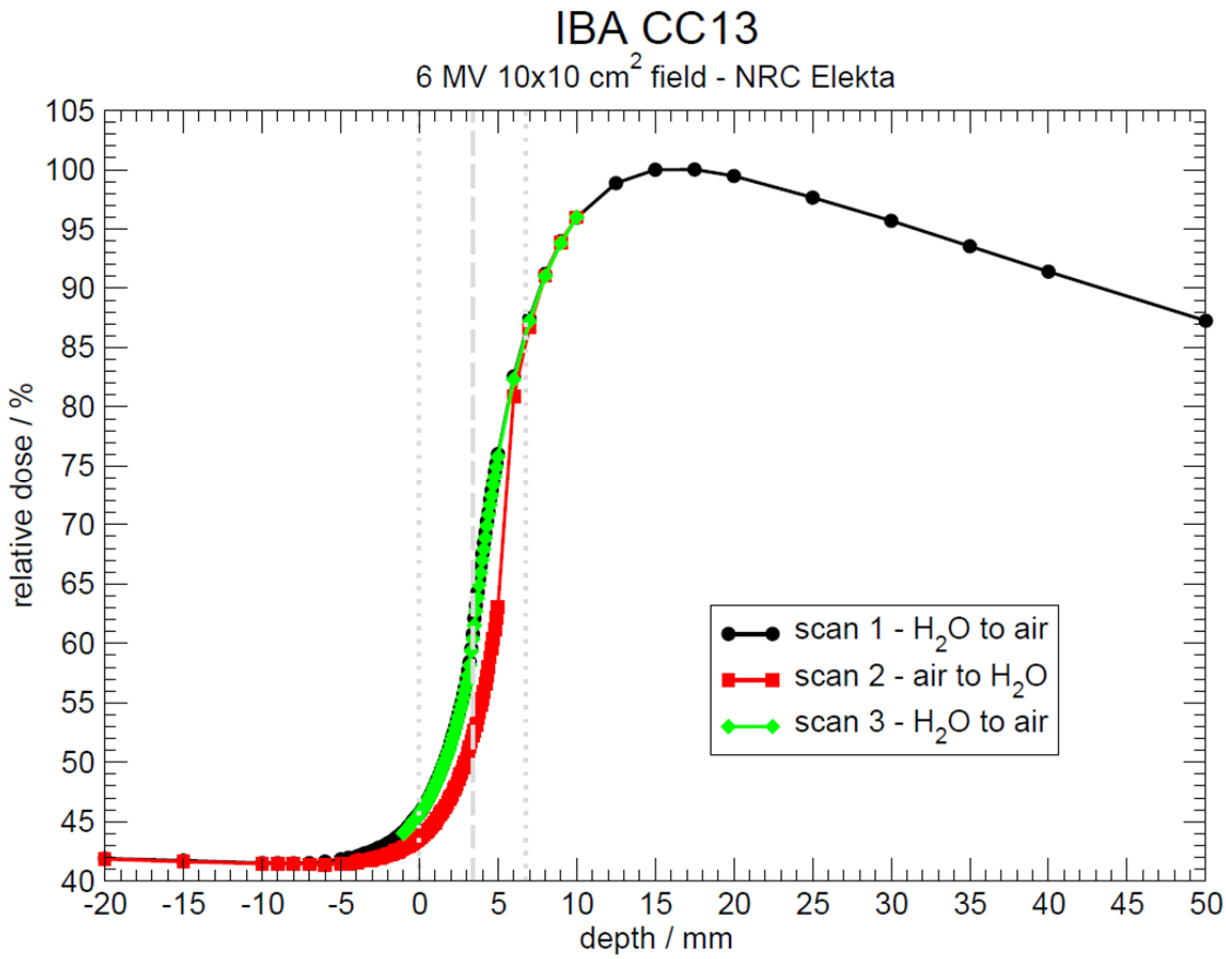

Figure 58: PDDs measured with the IBA CC13 on the Elekta Precise at the NRC for the 6 MV beam at a 10×10 cm^2 field. Scans are acquired at with a sampling rate of 4 seconds per point at 0.1 mm resolution in the region of most interest around the IC outer radius. The grey dashed line marks the DeICERS when scanning from water to air and the depth at which the IC should first be fully submerged when scanning from air to water. The dotted grey lines represent the diameter of the IC when the IC is centered at the dashed grey line.

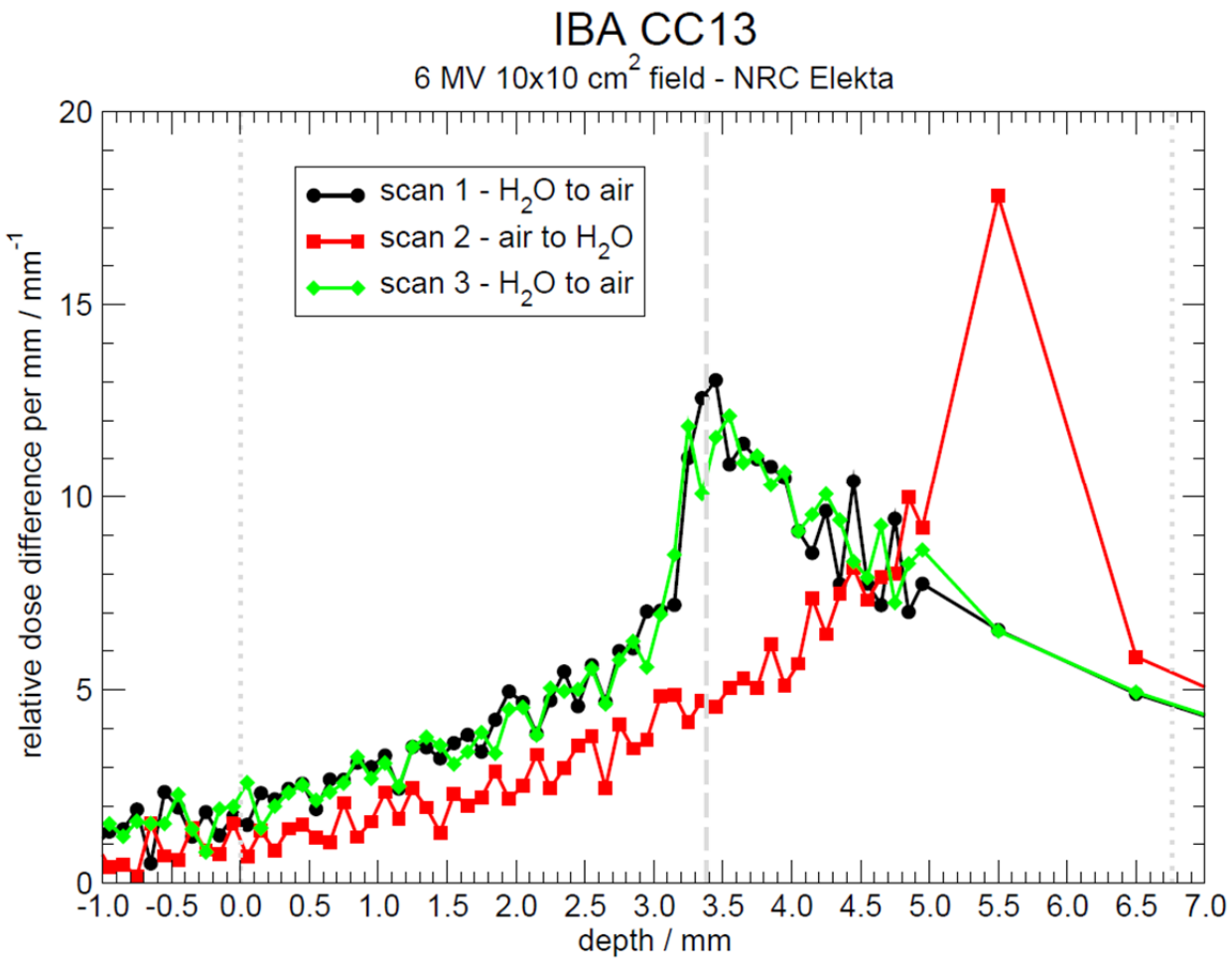

Figure 59: First derivatives of the scans shown in Figure 58. When scanning from air to water, the gradient peak occurs deeper in the water than when scanning from water to air due to the water surface being displaced below its nominal location by the IC. The grey dashed line represents the DeICERS for water-to-air scans. The dotted grey lines represent the diameter of the IC when the IC is centered at the dashed grey line.

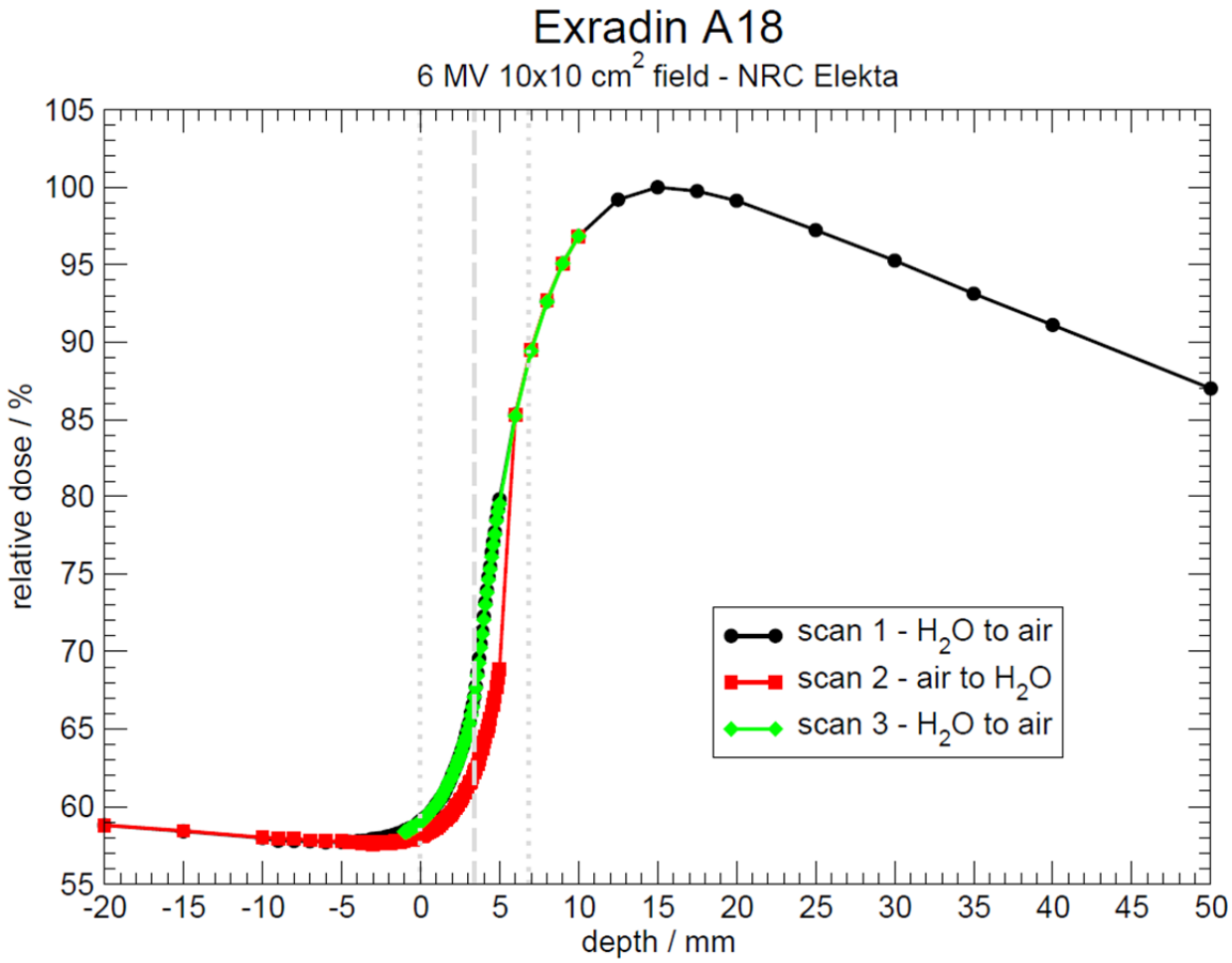

Figure 60: PDDs measured with the Exradin A18 on the Elekta Precise at the NRC for the 6 MV beam at a 10×10 cm^2 field. Scans are acquired at with a sampling rate of 4 seconds per point at 0.1 mm resolution in the region of most interest around the IC outer radius. The grey dashed line marks the DeICERS when scanning from water to air and the depth at which the IC should first be fully submerged when scanning from air to water. The dotted grey lines represent the diameter of the IC when the IC is centered at the dashed grey line.

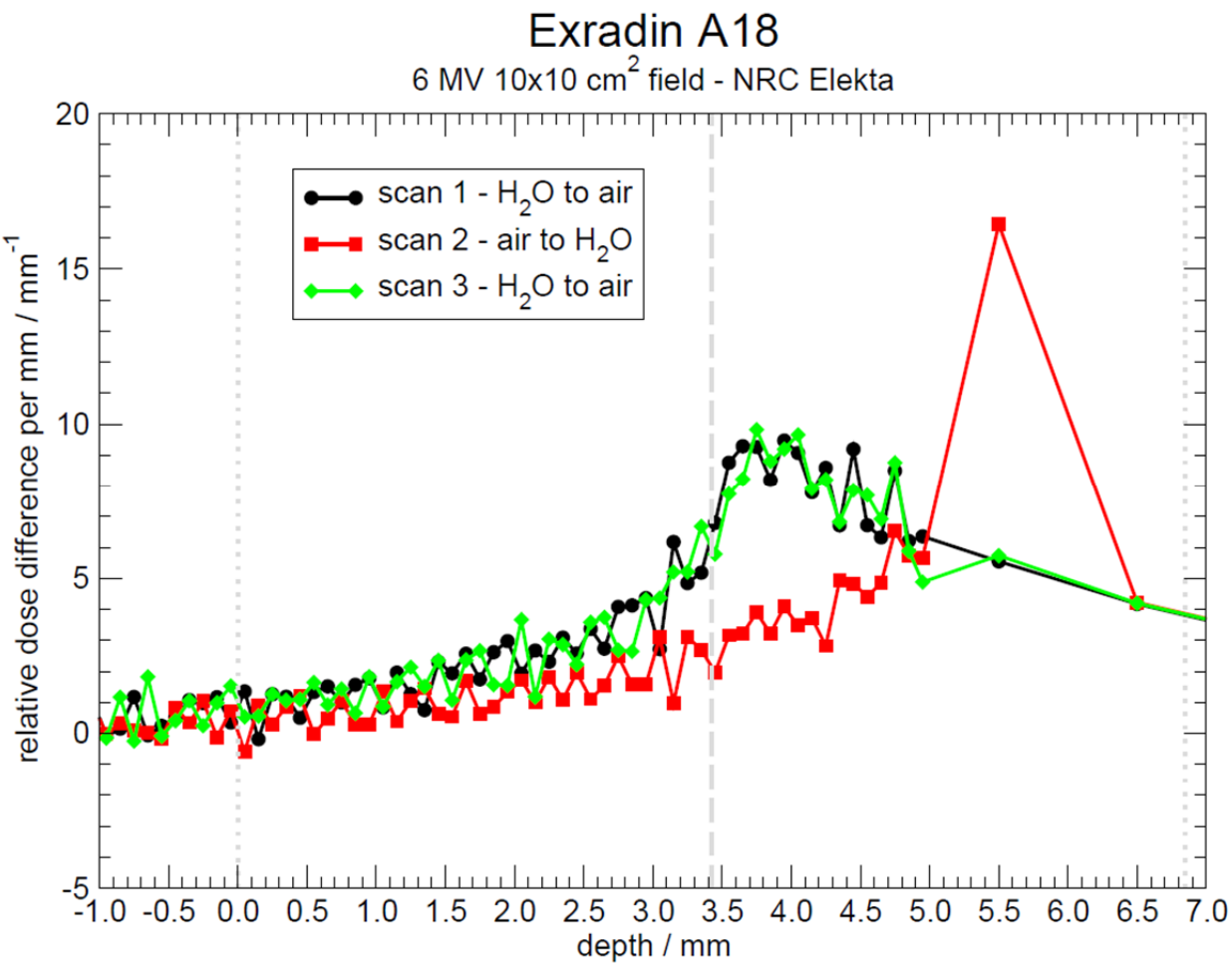

Figure 61: First derivatives of the scans shown in Figure 60. When scanning from air to water, the gradient peak occurs deeper in the water than when scanning from water to air due to the water surface being displaced below its nominal location by the IC. The grey dashed line represents the DeICERS for water-to-air scans. The dotted grey lines represent the diameter of the IC when the IC is centered at the dashed grey line.

4.2.2 Scan Speed

There are two modes in which scans can be acquired: continuous and step-by-step. In continuous mode with the IBA system, scans can be performed continuously at one of three speeds: 15 mm/s, 5.13 mm/s, or 1.75 mm/s. At 15 mm/s, data are recorded at 0.7 mm intervals along the scan. At 5.13 mm/s, data spacing is changed to 0.4 mm. Scans taken at 1.75 mm/s are acquired on 0.3 mm intervals. In step-by-step mode, the speed settings still represent the pace at which the IC will be moved between measurement points. However, there is an additional sampling parameter that determines how long the IC will remain in place to take each individual reading. For long sampling times and fine data resolution, the chosen scan speed becomes relatively meaningless. If the user selects step-by-step mode, the IC must remain in place at each measurement location for at least 0.1 s, in which time five individual readings are taken and averaged for the resulting measurement. The number of samples to be averaged per measurement point can be increased up to 500, in increments of 5, for a maximum dwell time of 10 s at each measurement location. This sampling parameter is not modifiable mid-scan. When using the NRC system, scans are conducted in a stepwise fashion, by default. The user sets the sampling time freely with no system restrictions.

4.2.2.1 Continuous Mode

In-house measurements are taken in continuous mode at all three speeds in a single setup. Measurements are performed with the IBA CC13 on the Varian 2100 series accelerator. All measurements are acquired for 10×10 cm^2 fields. Incident photon beams of 6 and 18 MV nominal beam energy are tested. Electron beams of 6 and 20 MeV nominal energy are also examined. All displayed scans are performed from water into air. The 6 MV scan gradients are displayed in Figure 62. There appears to be an increase in the relative noise of the gradient of

the slowest scan, compared with the faster scans, but this may be a consequence of the finer resolution of the slower scan. Recall, the IBA software changes scan resolution with the choice in scan speed when working in continuous mode. The analogous 18 MV data are shown in Figure 63.

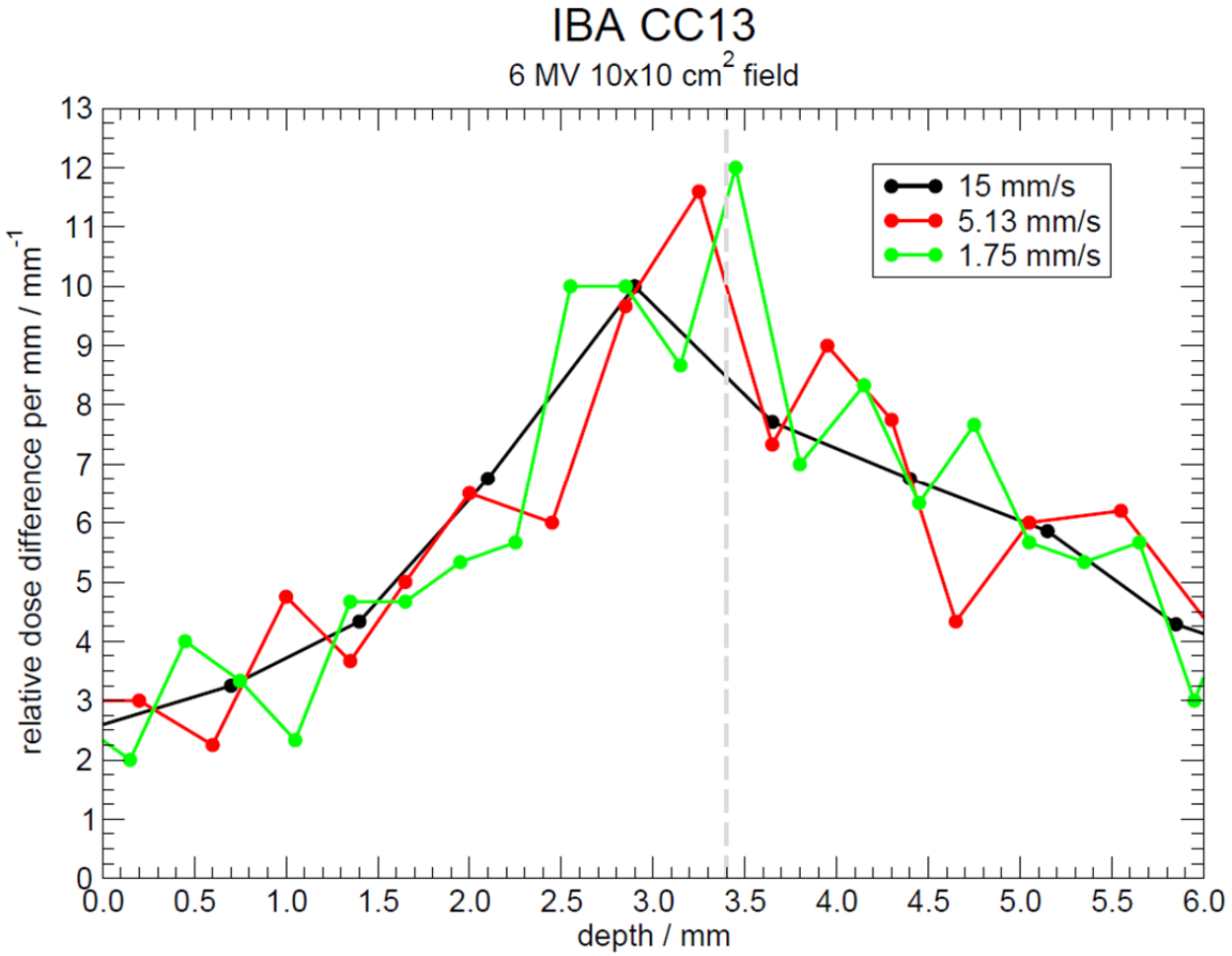

Figure 62: First derivatives of PDDs measured with the IBA CC13 for a 6 MV 10×10 cm^2 field. Measurements are taken on the 2100 series accelerator. Each scan is conducted from water to air with the IC moving continuously throughout the scan. The scan at 15 mm/s is acquired at 0.7 mm resolution. The scan at 5.13 mm/s is acquired at 0.4 mm resolution. 0.3 mm resolution is achieved for the scan at 1.75 mm/s. The grey dashed line represents the DeICERS. All gradient peaks occur within the respective scan resolutions of the DeICERS. The IBA software does not allow for scan speed and resolution to be tested independently of one another while working in continuous mode.

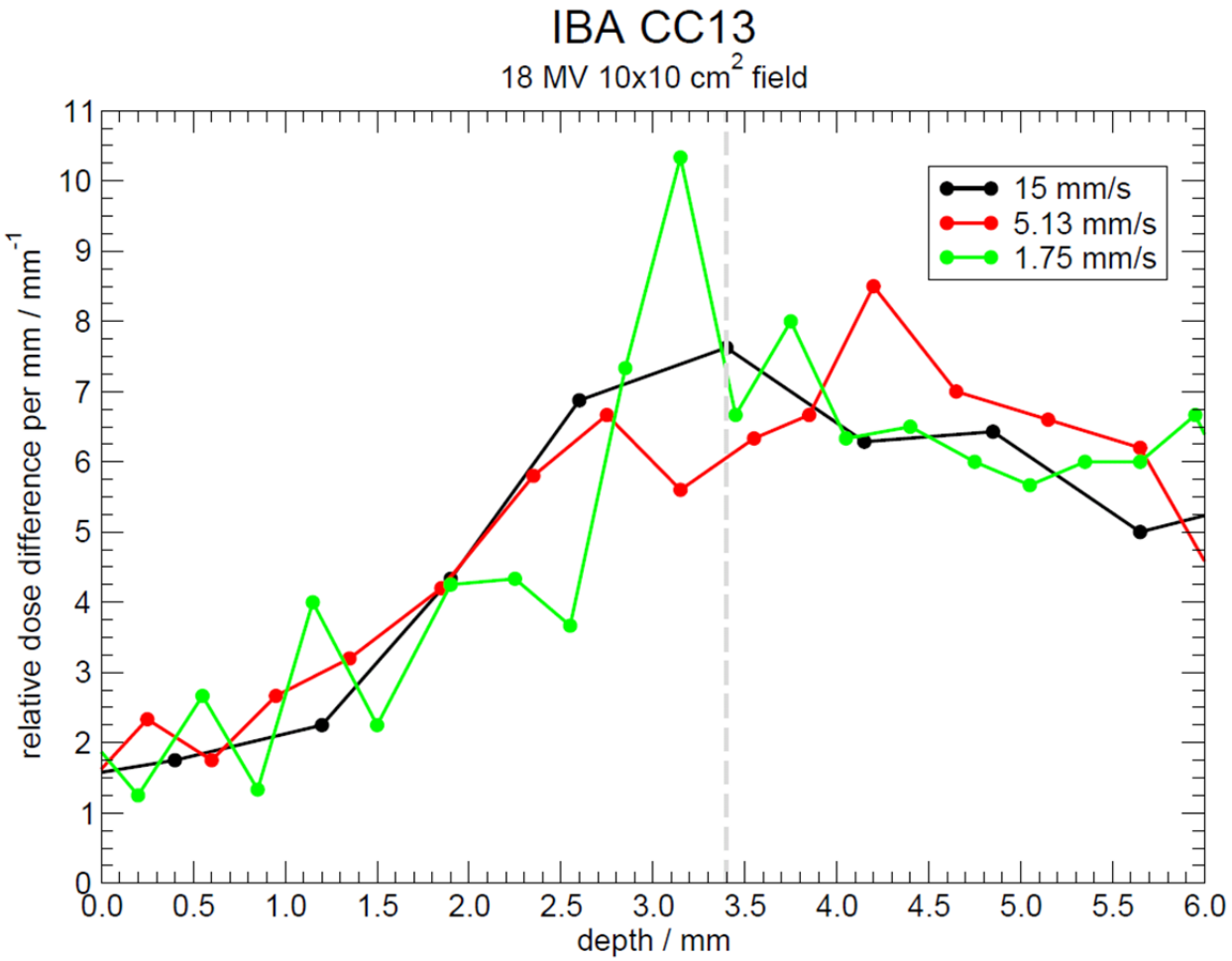

Figure 63: First derivatives of PDDs measured with the IBA CC13 for an 18 MV 10×10 cm^2 field. Measurements are taken on the 2100 series accelerator. Each scan is conducted from water to air with the IC moving continuously throughout the scan. The scan at 15 mm/s is acquired at 0.7 mm resolution. The scan at 5.13 mm/s is acquired at 0.4 mm resolution. 0.3 mm resolution is achieved for the scan at 1.75 mm/s. The grey dashed line represents the DeICERS. The gradient peaks of the high- and low-speed scans occur within scan resolution of the DeICERS but the medium-speed gradient peak is 0.8 mm deeper than the DeICERS. The IBA software does not allow for scan speed and resolution to be tested independently of one another while working in continuous mode.

The 6 MeV electron scan gradients are displayed in Figure 64. It is apparent from the overall noise level that the usage of 6 MeV continuous scan gradients for water surface alignment is inappropriate. The 20 MeV data in Figure 65 indicate that continuous scan gradients are too noisy for precise alignment for the full range of electron energies. Given the increased gradient noise in electron scans, electron measurements are de-emphasized while other aspects of the measurement procedure are evaluated throughout the remainder of Section 4.2. Further electron measurements are only discussed in Section 4.2.5 and Section 4.4.1.

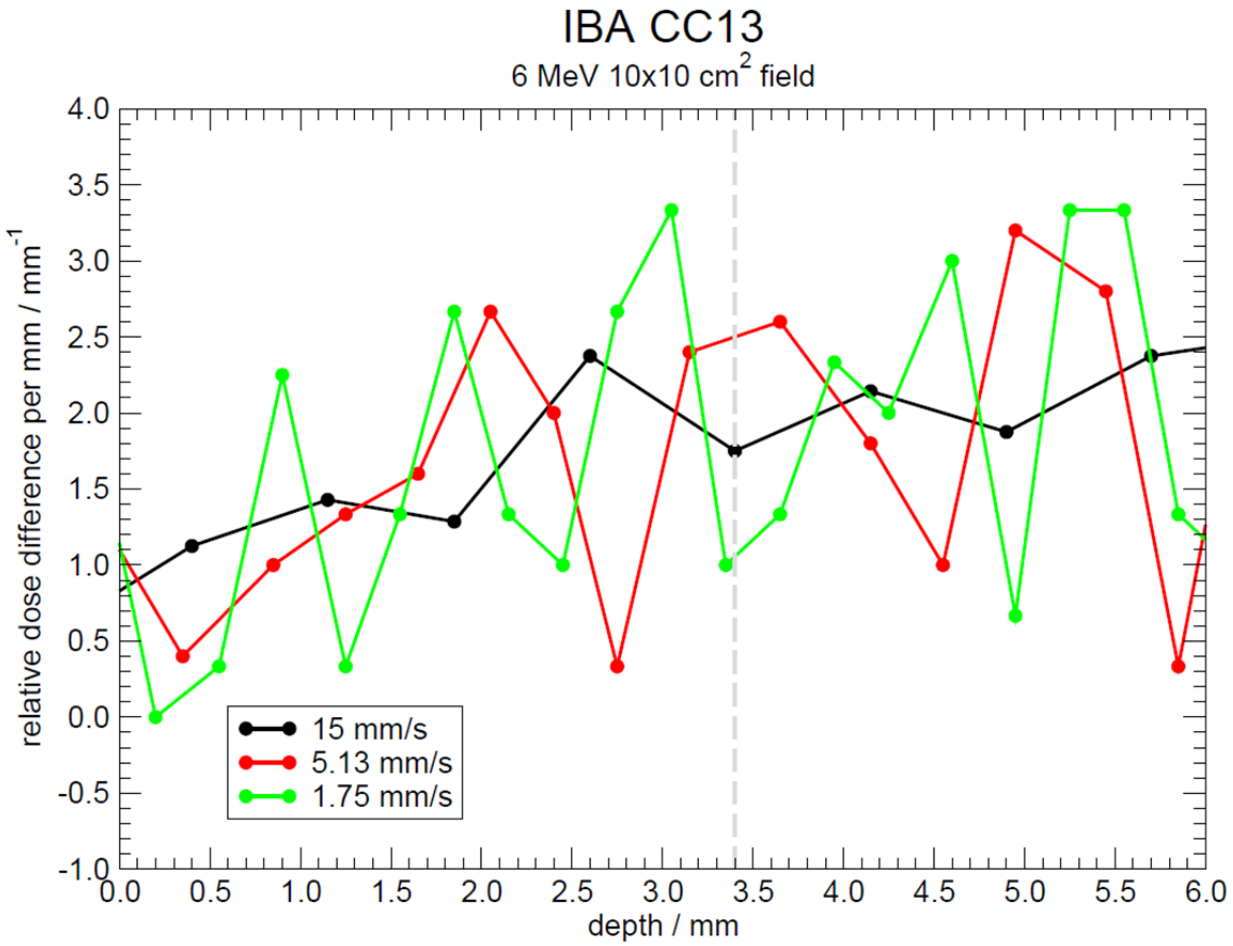

Figure 64: First derivatives of PDDs measured with the IBA CC13 for a 6 MeV 10×10 cm^2 field. Measurements are taken on the 2100 series accelerator. Each scan is conducted from water to air with the IC moving continuously throughout the scan. The grey dashed line represents the DeICERS. Gradient peaks are not definitively established here due to an increase in the relative noise of the electron scan gradients. The IBA software does not allow for scan speed and resolution to be tested independently of one another while working in continuous mode.

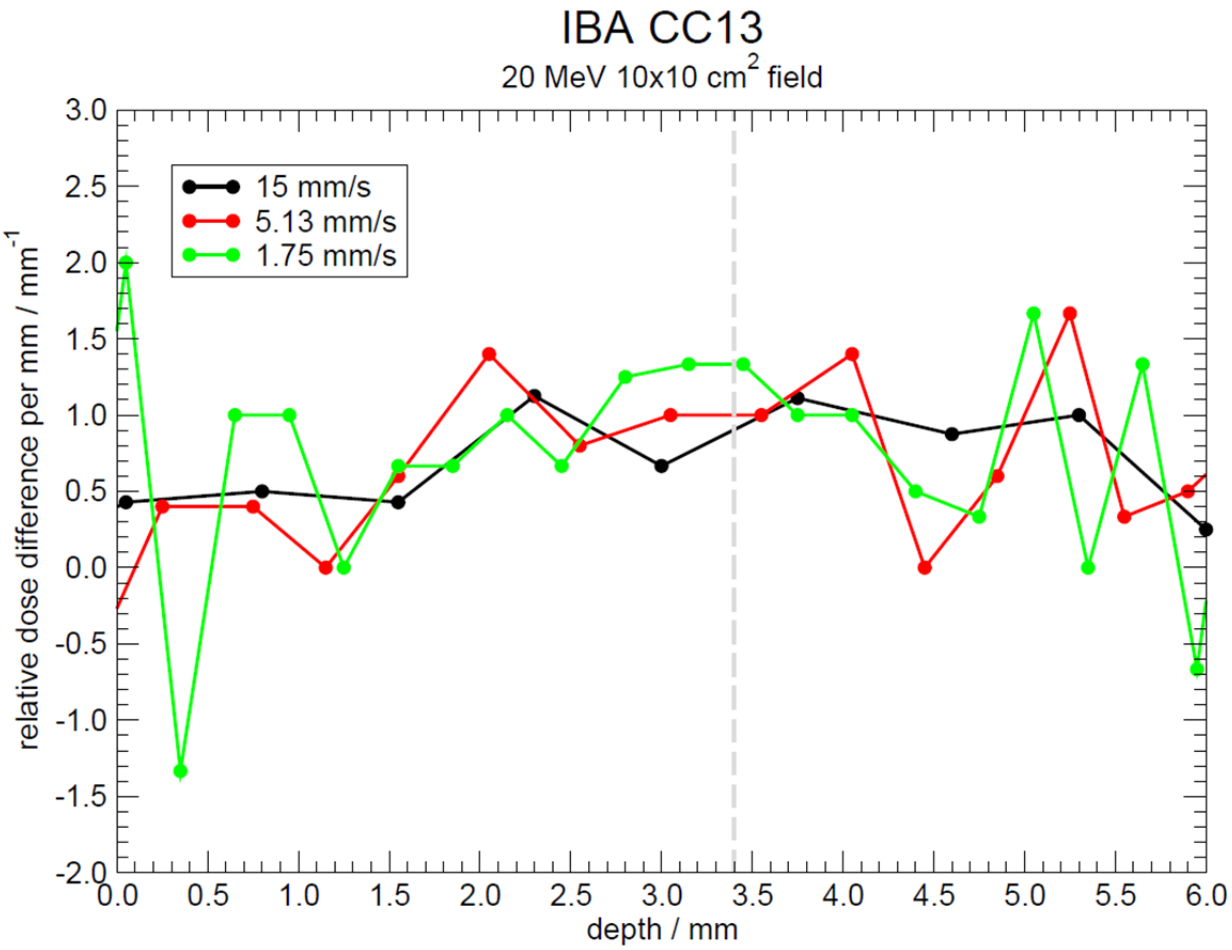

Figure 65: First derivatives of PDDs measured with the IBA CC13 for a 20 MeV 10×10 cm^2 field. Measurements are taken on the 2100 series accelerator. Each scan is conducted from water to air with the IC moving continuously throughout the scan. The grey dashed line represents the DeICERS. Gradient peaks are not definitively established here due to an increase in the relative noise of the electron scan gradients. The IBA software does not allow for scan speed and resolution to be tested independently of one another while working in continuous mode.

4.2.2.2 Step-by-Step Mode

As part of the same measurement session in which the continuous mode scans shown in Section 4.2.2.1 are taken, 6 MV scans are also taken in step-by-step mode. The step-by-step scans are taken at 1 mm resolution for the quickest sampling rates (0.1, 0.2, and 0.3 s/pt.) allowed by the IBA software. The measured gradients are shown in Figure 66. The gradient peaks occur within 0.1 mm of one another for the three sampling rates tested due to IC positioning variations in the original scans and the observed peaks are 0.25-0.3 mm shallower in

water than the DeICERS, a difference that is within setup uncertainty and measurement resolution for this experiment.

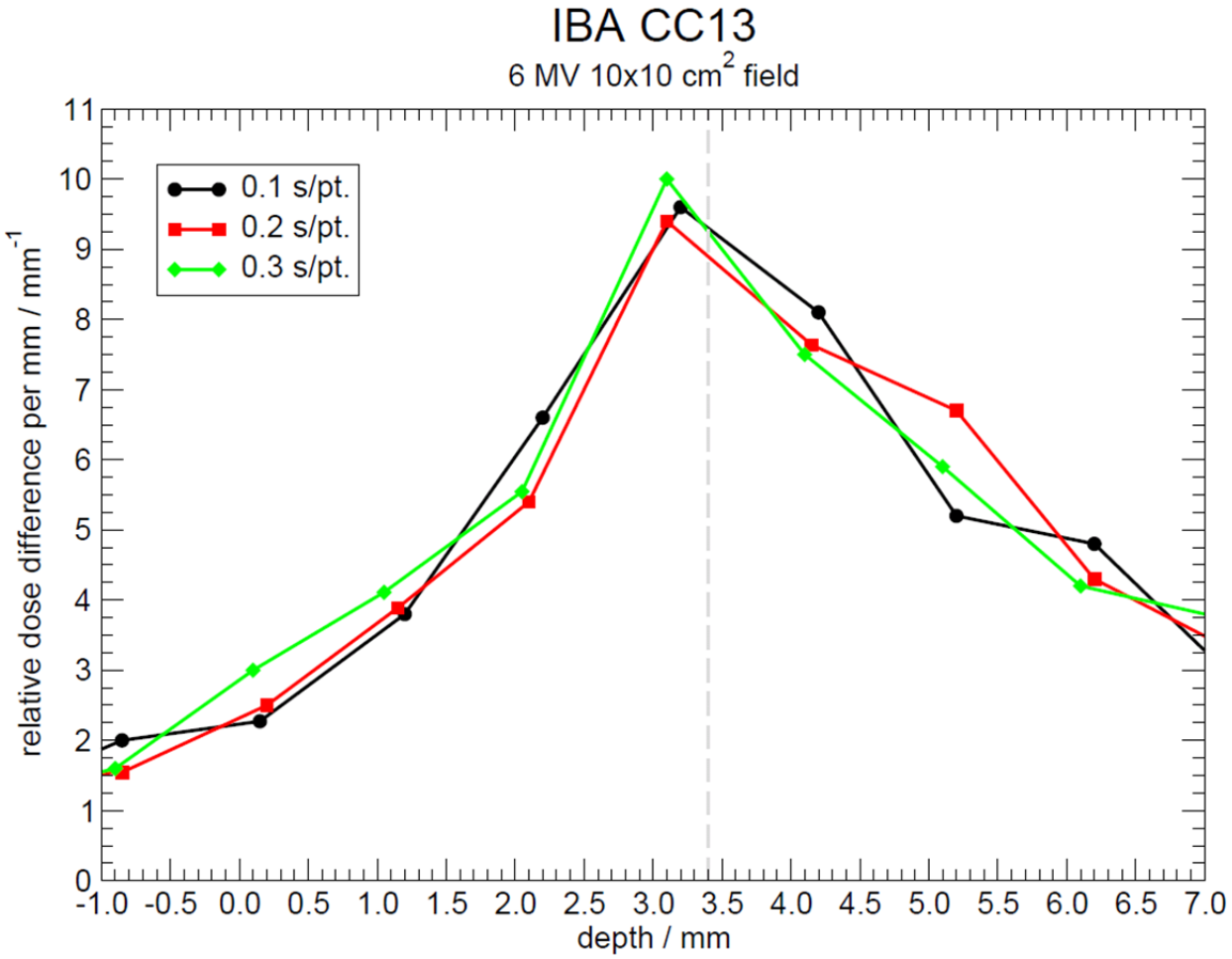

Figure 66: First derivatives of PDDs measured with the IBA CC13 for a 6 MV 10×10 cm^2 field from the Varian 2100. Scans are conducted at 1 mm resolution in step-by-step mode where the IC remains in place at each measurement depth for a user-defined time. Multiple readings are taken over this time and averaged for display. The times selected here represent 5, 10, and 15 samples per point, respectively. The observed gradient peaks are consistent with one another to within 0.1 mm due to IC positioning variations between trials and 0.25-0.3 mm shallower than the DeICERS, which is within uncertainty. The DeICERS is denoted by the grey dashed line.

In a separate experiment, the effect of longer scan signal acquisition times on the resulting data is investigated. Measurements are taken at 0.1 mm resolution with the IBA CC13 in a 6 MV 10×10 cm^2 field from a Varian 2300 accelerator. Scans are performed at 1 s/pt., 2.5 s/pt., 5 s/pt., and 10 s/pt. These sampling times represent the acquisition of 50, 125, 250, and 500 individual IC readings at each measurement location. Since longer sampling times allow for

more IC readings to be taken, it is hypothesized that longer sampling times should improve the signal-to-noise ratio of the measured PDDs and, more importantly, the relative dose gradients.

The relative dose gradients from this experiment are shown in Figure 67. For well-aligned measurements, the DeICERS is 3.4 mm. For the scan acquired at 1 s/pt., a relative peak occurs at 3.45 mm. The amplitude of this peak, however, is similar to the amplitude of the measurement noise. It is difficult to observe that a gradient peak occurred at that location for the 1 s/pt. scan. The scan at 2.5 s/pt. shows two relative peaks in the gradient at 2.75 and 3.75 mm. The scan at 5 s/pt., however, shows a peak at 3.45 mm. The scan at 10 s/pt. shows a peak at 3.25 mm. The noise in these scans is largely contributed by positioning inconsistencies, much like the measurements in the scan direction experiment discussed in Section 4.2.1. The discrepancy in peak locations indicates that sampling times of ≥5 s/pt. near the DeICERS may be required.

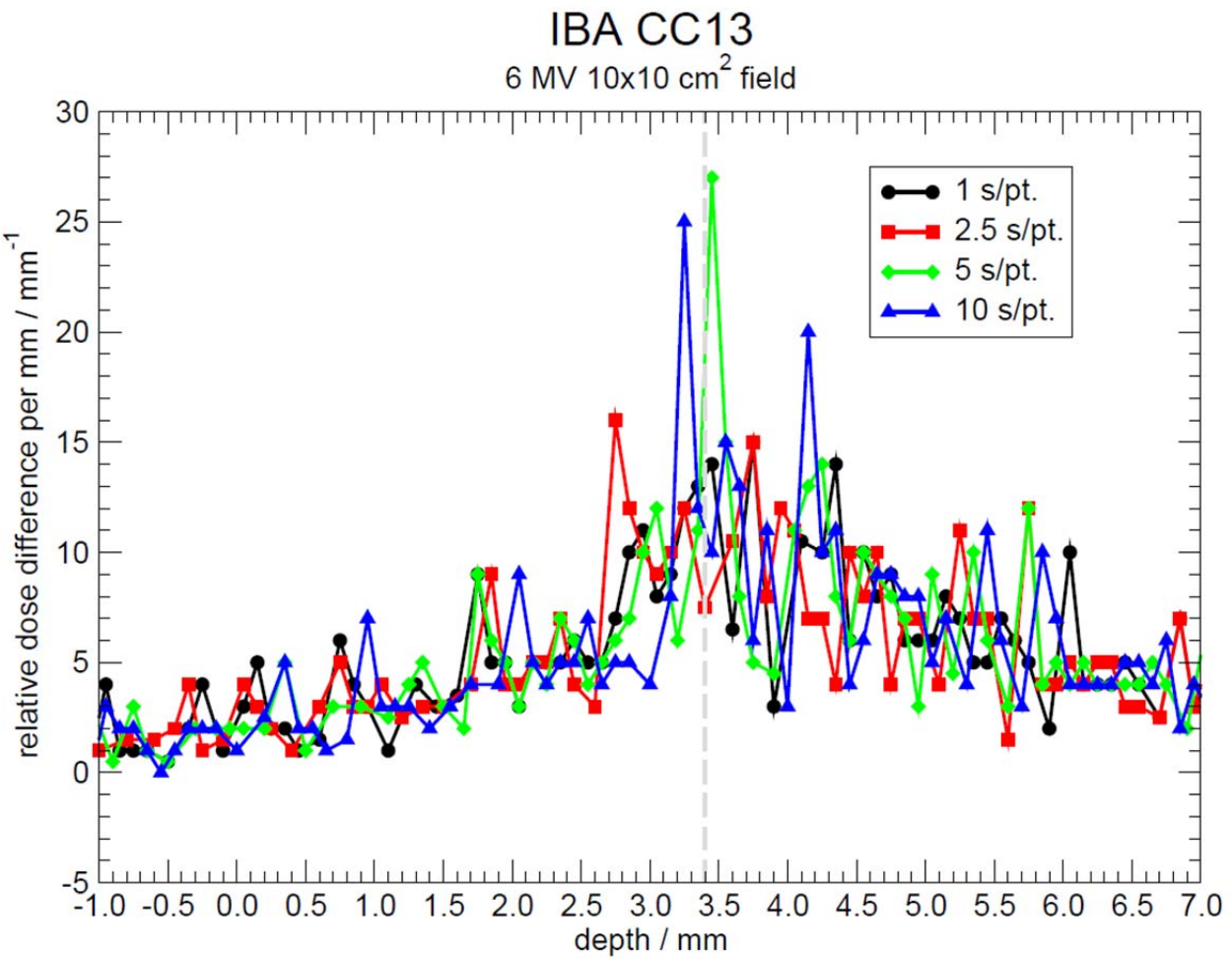

Figure 67: First derivatives of PDDs measured with the IBA CC13 on the Varian 2300 for a 6 MV 10×10 cm^2 field. Scans are conducted in step-by-step mode at 0.1 mm resolution and corrected offline for evaporation. Gradient peaks become more distinguishable relative to the noise level in each scan for longer sampling times. The grey dashed line represents the DeICERS.

Sampling resolution for the IBA CC13 in step-by-step mode is also investigated using the high-precision scanning system at the NRC. PDDs are scanned from 50 mm in water to 20 mm above the water surface in air. The finest resolution used is 0.1 mm from 5 to -5 mm. Scans are performed in the Elekta Precise 6 MV 10×10 cm^2 beam at 2 s/pt., 4 s/pt., and 10 s/pt. The relative dose gradients are shown in Figure 68. The gradient peaks of the two quickest scans occur at 3.25 mm. The scan at 10 s/pt. exhibits the highest gradient peak and occurs at 3.35 mm, which is within 0.05 mm of the DeICERS for a well-aligned measurement, 3.4 mm. The 0.05 mm difference is negligible as the scans are performed with 0.1 mm resolution. The

displayed portions of the calculated first derivatives that are not at the peak, such as the region from -4 to 3 mm, show an expected reduction in the relative noise of each scan with increased sampling time.

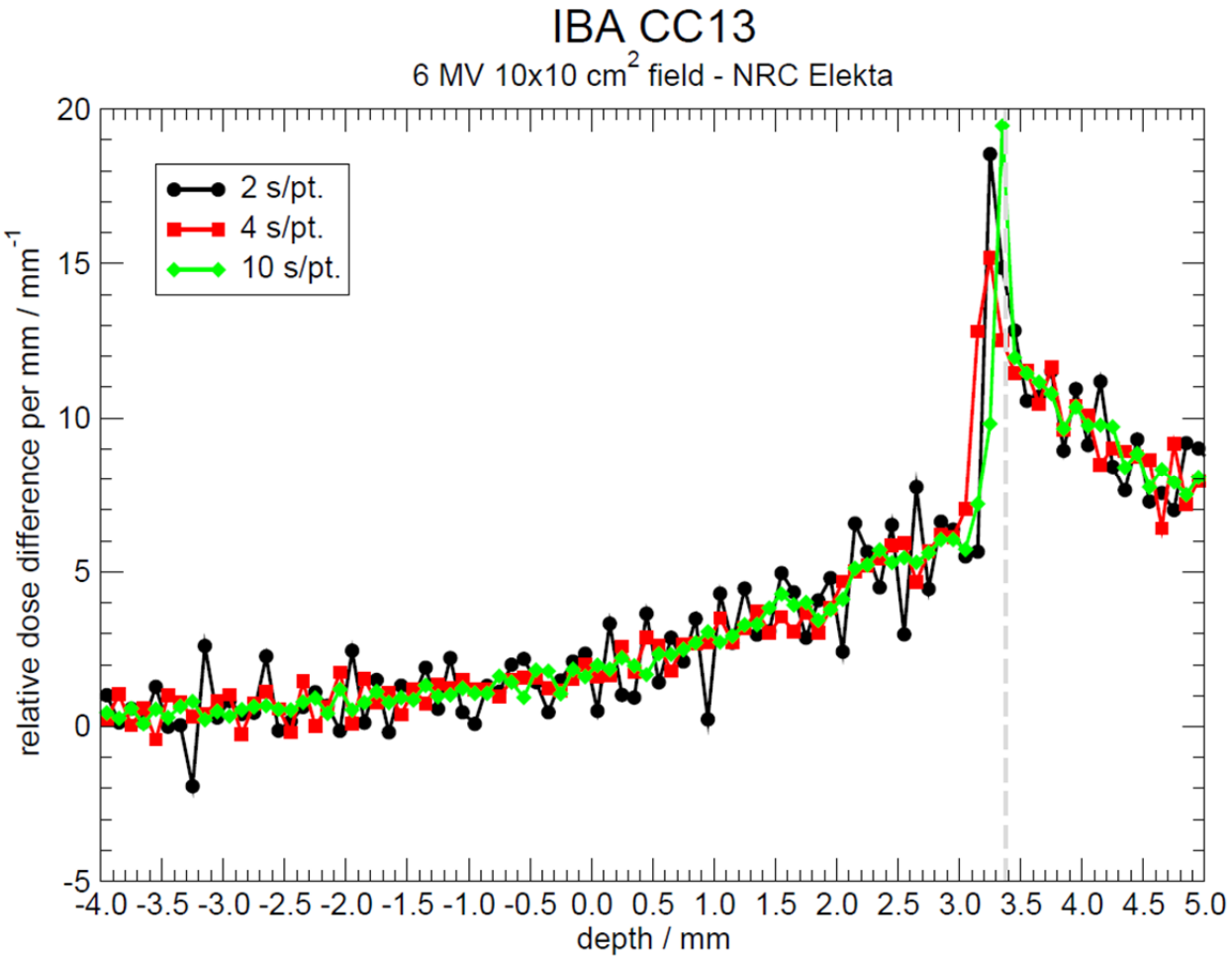

Figure 68: First derivatives of PDDs measured with the IBA CC13 for a 6 MV 10×10 cm^2 field from the NRC Elekta Precise. These scans are aligned using the NRC customized high-precision scanning system. The relative noise level in each scan decreases with increasing sampling time. Gradient peaks occur within 0.1 mm of one another and within 0.15 mm of the DeICERS, denoted by the grey dashed line.

Sampling resolution is also examined in-house for the PTW 23343, commonly referred to as the Markus IC. Measurements are made from water to air in the 6 MV 10×10 cm^2 beam from the Varian 2300 accelerator. The first scan is from 50 mm below the water surface to 20 mm above the surface in air in continuous mode at low speed. The IC travels at 1.75 mm/s at 0.3 mm resolution. Driving the IC through the water surface in continuous mode causes water to

remain atop the IC as it emerges through the water surface into air. After this scan, the face of the IC is dried with a paper towel and a second scan is performed from 20 mm above the water surface back to the nominal water surface location of 0 mm. This scan is also performed in continuous mode at 1.75 mm/s speed and 0.3 mm resolution. The IC is then lowered into the tank to 15 mm depth and a third scan is performed in step-by-step mode with 10 s/pt. sampling resolution from 2.5 mm deep in water to 1.5 mm above the water surface in air. The resulting PDDs are shown in Figure 69. The figure inset is a photograph of the water droplet present on the IC face after the first scan. The water-to-air continuous scan shows ~0.5 mm effective water buildup on the IC as relative dose increases in air from ~61% at the surface to ~66% by 3 mm into air. At 20 mm above the surface, the water buildup causes a ~23% difference in measured dose compared with the dose measured with a dry IC. The agreement between the continuous air-to-water scan with the dry IC and the water-to-air step-by-step scan in the region from the surface to 1.5 mm into air indicates that scanning slowly near the surface affords enough time for water to drip from the IC face at each measurement location. Scanning slowly through the water surface prevents water buildup from forming on the IC face and gives a more accurate relative dose measurement in air.

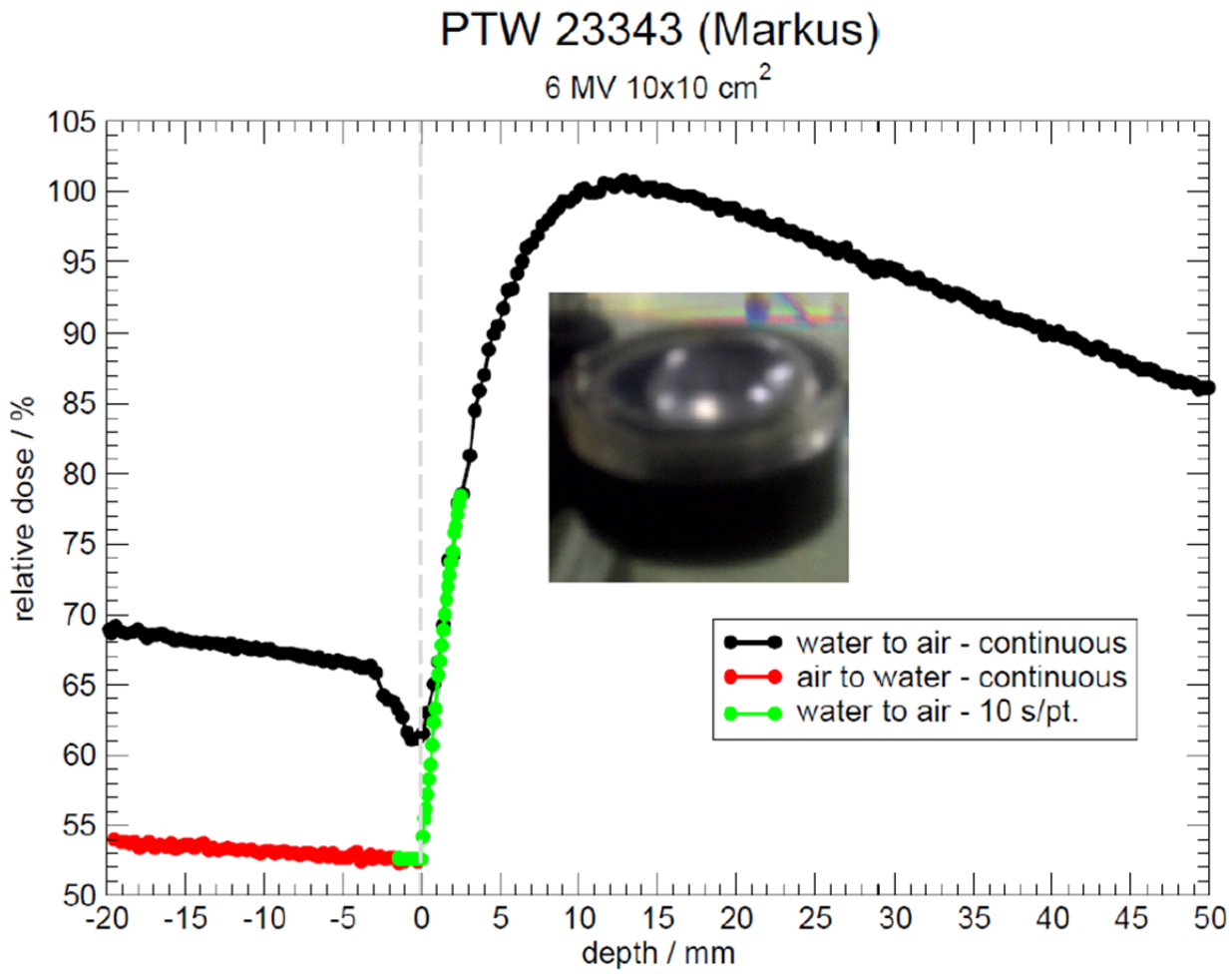

Figure 69: PDDs measured with PTW Markus parallel-plate IC with 30 cm H_2O in the tank at 100 cm SSD. The full water-to-air curve is measured in continuous mode, which moves the IC continuously throughout the scan at 0.3 mm nominal resolution. The inset shows a photograph of the water droplet on the IC face at the completion of this scan. The chamber face is then dried and a scan is performed from -20 mm to 0 mm, again in continuous mode. The IC is then driven to 15 mm depth before a final scan is done from 2.5 to -1.5 mm in step-by-step mode, where the IC is held in position for 10 s at each depth before an average reading is made and the IC is moved to the next location. The observed rise in relative dose after breaking the water surface in the water-to-air scan is attributed to the water droplet forming on the IC face, contributing effective water buildup of ~0.5 mm. Performing scans at the slowest speed allows enough time for water to drip off of the IC face as it emerges through the surface.

The alignment of these scans is evaluated by examining the relative dose gradients, displayed in Figure 70. The continuous water-to-air scan exhibits a gradient peak at ~1.6 mm but this peak is proven to be a false indicator of the water surface location when compared with the scan acquired in step-by-step mode. The step-by-step gradient peak occurs at 0.05 mm. At shallower depths, the relative dose gradient falls directly to zero. This additional condition is necessary for determining proper parallel-plate IC alignment.

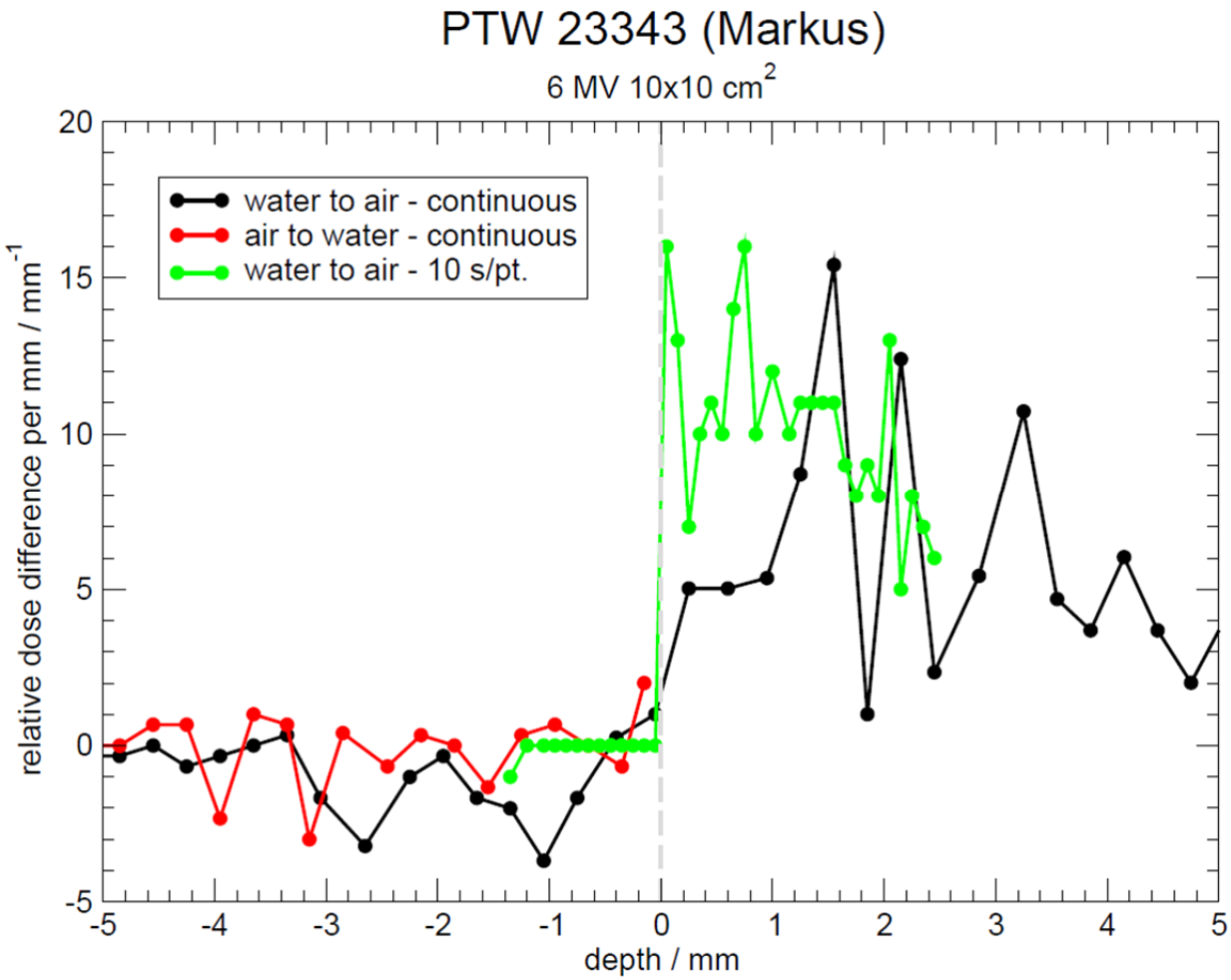

Figure 70: First derivatives of the scans shown in Figure 69. The water-to-air scan performed in continuous mode appears to exhibit a gradient peak at ~1.6 mm but the gradient is too noisy to determine the depth at which the gradient goes to zero. The scan performed at 10 s/pt. sampling resolution exhibits a peak at 0.05 mm after which the gradient drops to zero, indicating that the measurements performed here are all well-aligned.

Cylindrical ICs cause a small gradient in the incident buildup due to the variation in distance from the IC central axis at which a given electron enters the IC cavity. In contrast, parallel-plate ICs present a uniform face to the incident radiation beam, maintaining a nominally constant buildup thickness. Since this buildup is nominally constant, the fluence gradient is nominally zero. Therefore, it is expected for parallel-plate IC measurements that the gradient peak that signals the presence of the water surface is the local maximum beyond which the gradient goes to zero. In practice, the scan gradient is slightly negative due to the inverse square falloff of the incident beam. To summarize the results of the experiments described in this

section, scans in a step-by-step fashion are preferred over scans performed continuously. Additionally, sampling times of 5-10 s/pt. are preferred for gradient peak location identification.

4.2.3 Scan Resolution

It is shown in Chapter 3 that the scan gradient changes at the point at which an IC reaches the water surface. In Chapter 2, some discrepancies, within scan resolution, are shown between observed gradient peak and DeICERS locations for scans acquired at 0.5 mm resolution. The objective of the experiment described in this section is to determine the scan resolution necessary to reliably determine the relative dose gradient peak. The experiment begins with scans acquired at 0.1 mm resolution from 5 to -5 mm using the NRC high-precision scanning system. PDD scans are performed with ICs placed in 6 MV 10×10 cm^2 fields from the Elekta Precise accelerator. Relative dose data acquired with three ICs are used for this experiment: Exradin A18, IBA CCRK, and Exradin A16. The Exradin A18 is chosen because it is the basis of the computational model used for all MC simulations described in Chapter 3. The A18 is also the default Exradin scanning IC. The IBA CCRK is chosen because its geometry differs from that of most cylindrical ICs. The CCRK does not have a hemispherical cap on its end, making the IC collection geometry the difference of two cylinders, the central electrode subtracted from the inner wall dimension. The CCRK was also used for all measurements in the initial study described in Section 2.1. The Exradin A16 is chosen because it is the IC with the smallest active volume tested in this thesis.

Each original scan at 0.1 mm resolution is downsampled to replicate 0.2, 0.3, 0.4, 0.5, and 1.0 mm data spacing. In this way, the experiment is controlled for any possible variation in relative output and signal-to-noise ratio between measurements, as the underlying data is

identical for each IC tested at different resolutions. Multiple data sets are created at downsampled resolution from the original data. For each IC, two data sets are created at 0.2 mm resolution while ten sets are created at 1.0 mm resolution. The relative dose gradients are computed for each original scan and all downsampled data sets and gradient peak locations are evaluated. The gradient peak location is computed for each set of computed gradients at a given resolution for a given IC.

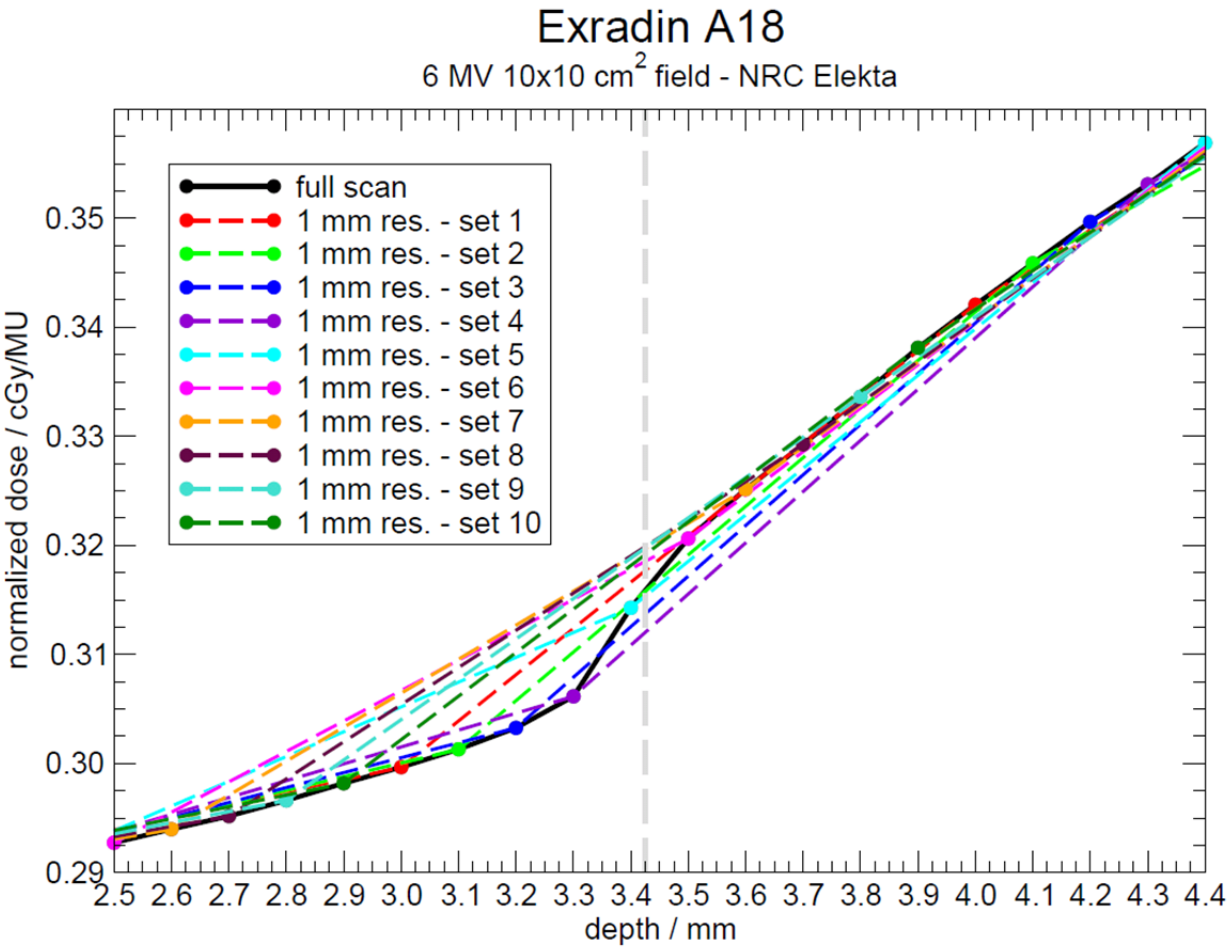

Figure 71: Resolution test starting with an Exradin A18 scan acquired with the NRC high-precision scanning system at 0.1 mm resolution. The data set is downsampled for increasingly coarser resolutions. The coarsest resolution examined is shown here for comparison. The figure is scaled such that one data point of each downsampled data set is shown on either side of the DeICERS, denoted by the grey dashed line. The colored dashed lines show the range of possible slopes through the DeICERS for scans at 1 mm resolution. The Exradin A18 IC is chosen for resolution testing because it is used in this work for measurements and as a simulation model.

PDDs for the Exradin A18 are shown in Figure 71. To avoid cluttering the figure, only the original scan data and the most coarsely downsampled sets are plotted. The grey dashed line represents the Exradin A18 DeICERS, 3.45 mm. Observable differences in the PDD slope of different sets sampled at 1 mm resolution through the grey dashed line occur, indicating change in the relative dose gradient. Relative dose gradients are shown in Figure 72. Here, the gradients of all sets up to 0.4 mm resolution are shown for completeness. Only the first and last data sets of 0.5 and 1.0 mm resolution are shown. The gradient of the original scan at 0.1 mm resolution displays a peak 0.1 mm from the DeICERS. Downsampling to 0.2 mm resolution yields two data sets showing gradient peak locations that differ by 0.1 mm. For coarser resolution, the gradient peak location is shifted deeper into the water. The gradient peak shifts deeper into the water because the rate at which the PDD slope increases below the DeICERS is greater than the rate at which it decreases above the DeICERS. The gradient peak signifies an inflection point, the point at which the curvature of the original data changes sign.

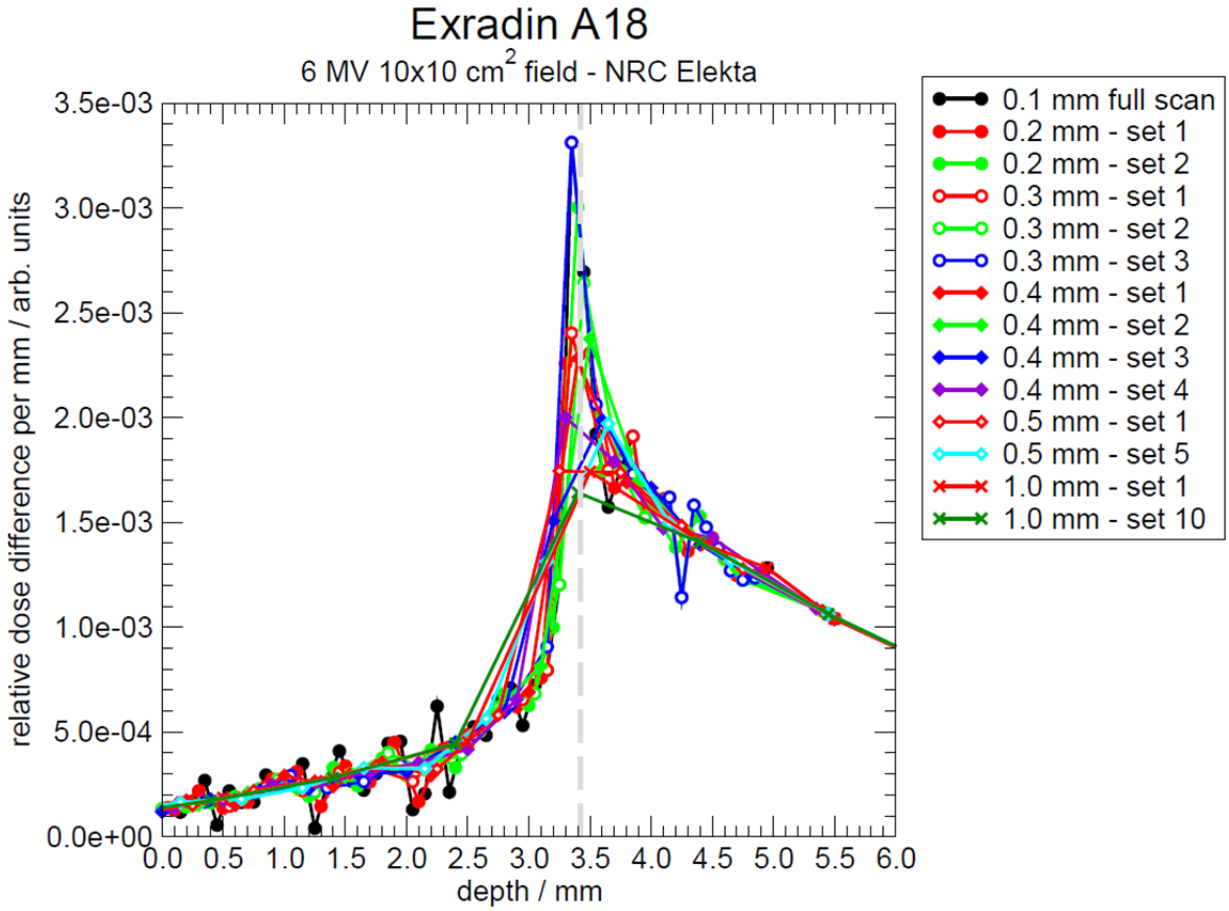

Figure 72: First derivatives of the data sets downsampled from the original set shown in Figure 71. The original data set, at 0.1 mm resolution, yields a gradient peak 0.1 mm from the DeICERS, denoted by the grey dashed line. The discrepancy is within measurement uncertainty. As resolution increases, the peak location occurs deeper in the water.

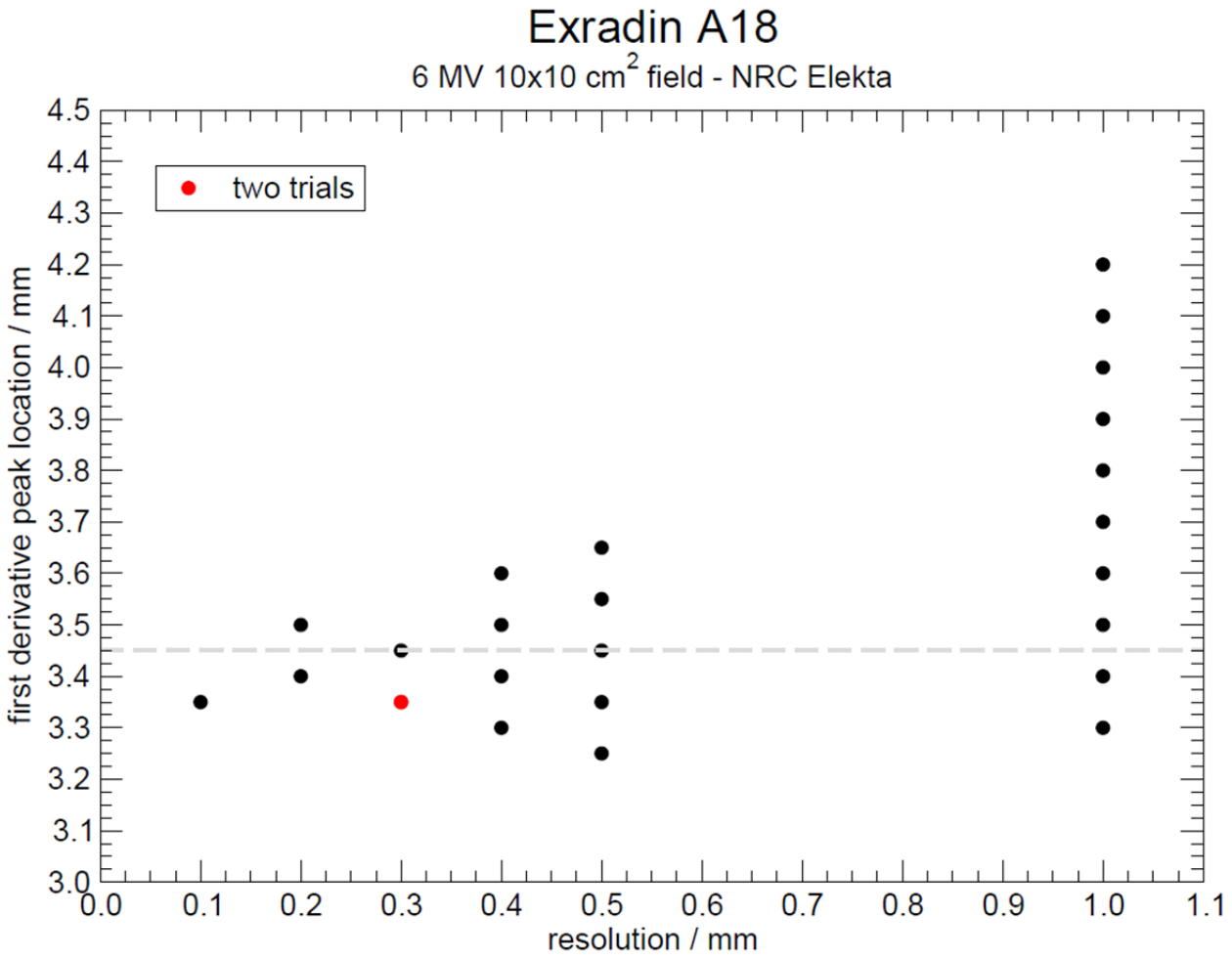

Figure 73: Gradient peak location as a function of scan resolution for the Exradin A18. The maximum spread of observed gradient peak locations increases with degraded resolution. The mean peak location changes by 0.4 mm when resolution changes from 0.1 mm to 1.0 mm. The grey dashed line represents the DeICERS.

The shift in gradient peak location as a function of data resolution for the Exradin A18 is shown quantitatively in Figure 73. At 0.5 mm resolution, all observed gradient peaks occur within 0.2 mm of the DeICERS. A 0.2 mm difference from the DeICERS should contribute negligibly to overall measurement uncertainty. At 1 mm resolution, the average gradient peak is 0.4 mm deeper in water than is measured at 0.1 mm resolution. The 0.3 mm difference between the apparent gradient peak location from scans conducted at 1.0 mm resolution and the DeICERS indicates that 1.0 mm resolution is unsuitable for this work. For clinical depth-dose scans taken

at 1 mm resolution, an IC alignment uncertainty of 0.3 mm is possible if using gradient peak location for IC alignment.

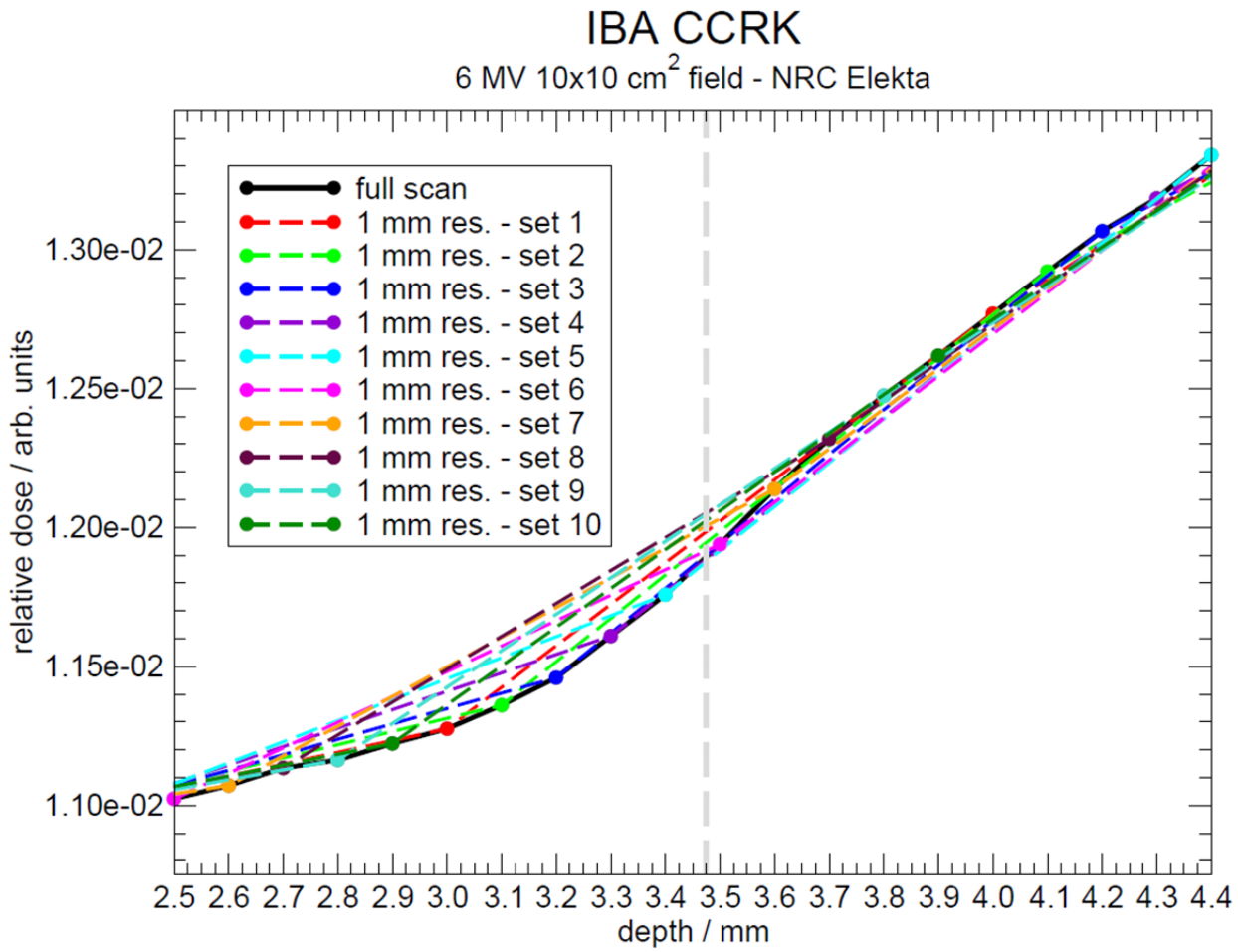

Figure 74: Resolution test starting with an IBA CCRK scan acquired with the NRC high-precision scanning system at 0.1 mm resolution. The data set is downsampled for increasingly coarser resolutions. The coarsest resolution examined is shown here for comparison. The figure is scaled such that each one data point of each downsampled data set is shown on either side of the DeICERS, denoted by the grey dashed line. The colored dashed lines show the range of possible slopes through the DeICERS for scans at 1 mm resolution. The CCRK is chosen for resolution testing due to its lack of a hemispherical cap, making the IC geometry purely cylindrical.

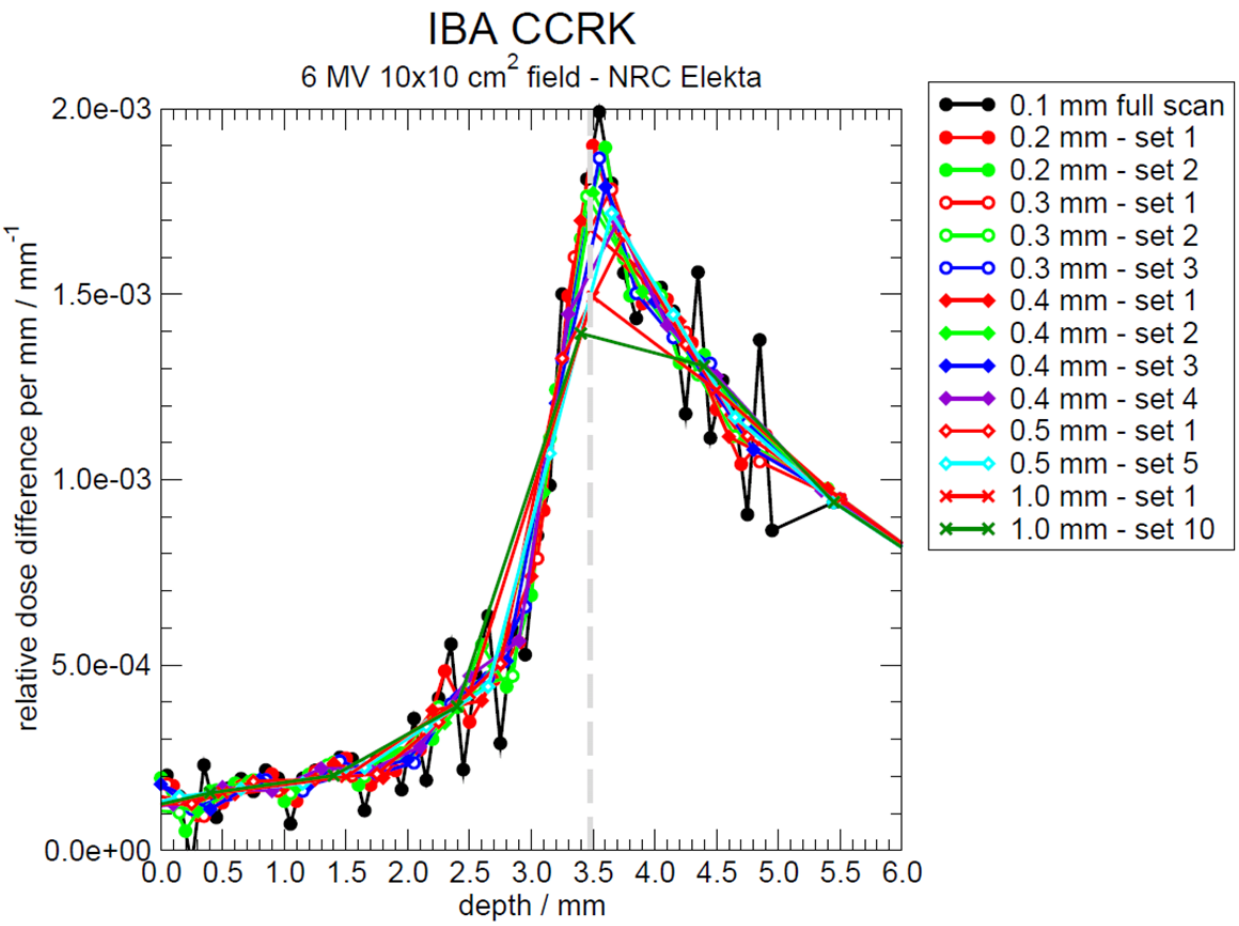

Figure 75: First derivatives of the data sets downsampled from the original set shown in Figure 74. The original data set, at 0.1 mm resolution, yields a gradient peak 0.05 mm from the DeICERS, denoted by the grey dashed line. The difference between the gradient peak location and the DeICERS is within measurement uncertainty. As resolution increases, the peak location is pulled deeper into the water.

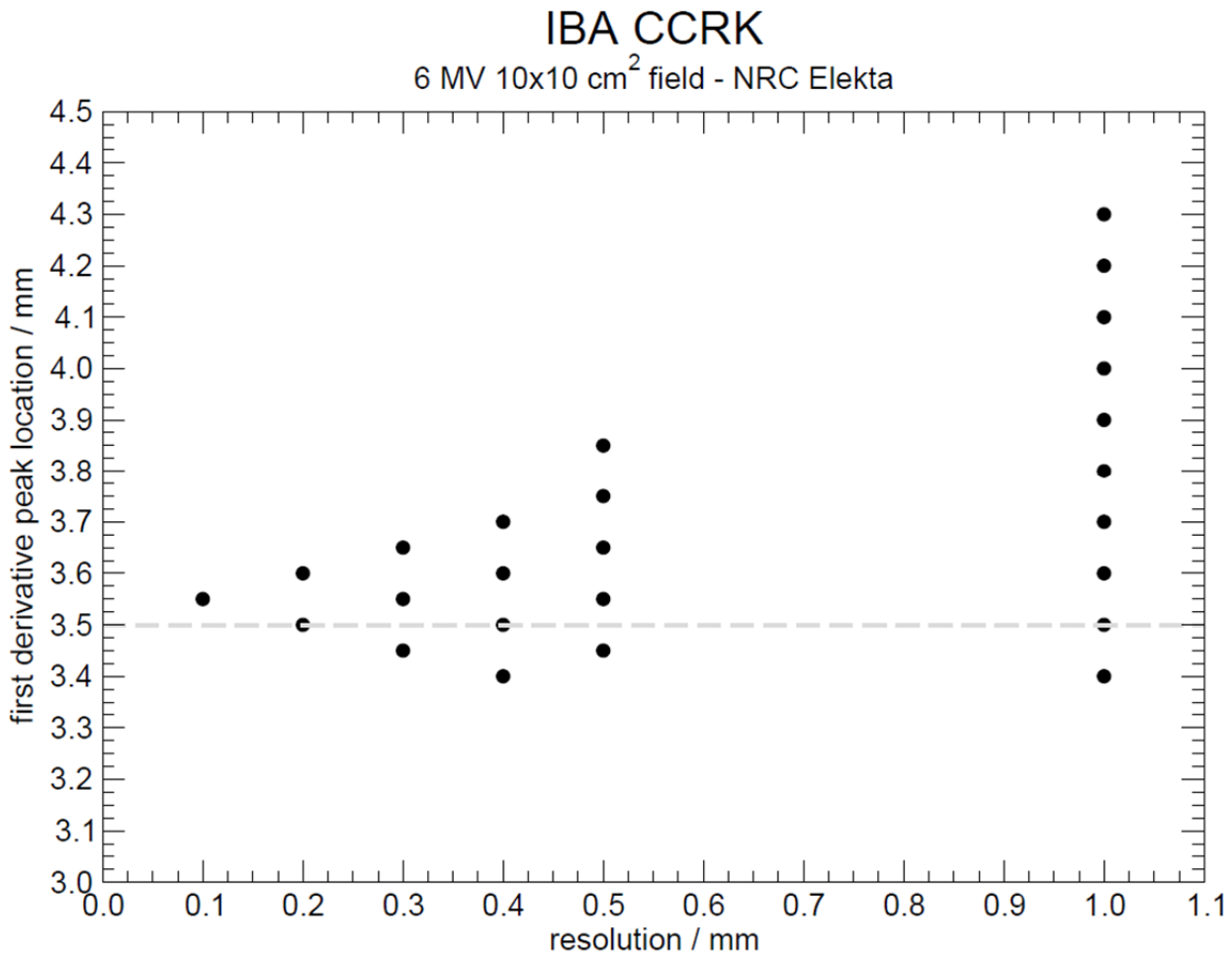

Figure 76: Gradient peak location as a function of scan resolution for the IBA CCRK. The maximum spread of observed gradient peak locations increases with degraded resolution. The mean peak location changes by 0.3 mm when resolution changes from 0.1 mm to 1.0 mm. The grey dashed line represents the DeICERS.

PDDs for the IBA CCRK acquired from 10 to -10 mm are shown in Figure 74. The grey dashed line at 3.5 mm represents the DeICERS. As with the Exradin A18, slope changes near the grey line are observed between scans downsampled to 1 mm resolution. PDD gradients are shown in Figure 75. The gradient peak location is shifted increasingly deeper in the water with coarser scan resolution as discussed above. The gradient peak location shift as a function of scan resolution is quantified in Figure 76. For the CCRK, the observed gradient peak from the scan at 0.1 mm resolution occurs 0.05 mm from the DeICERS of 3.5 mm. The mean gradient peak location computed from multiple data sets created at 1 mm resolution occurs 0.3 mm deeper than

the DeICERS. Sampling at 0.4 mm resolution yields all gradient peaks within 0.2 mm of the DeICERS, indicating that 0.4 mm resolution could be suitable for use with this IC. Scanning at relatively coarse resolution such as 1.0 mm is not suitable for this work.

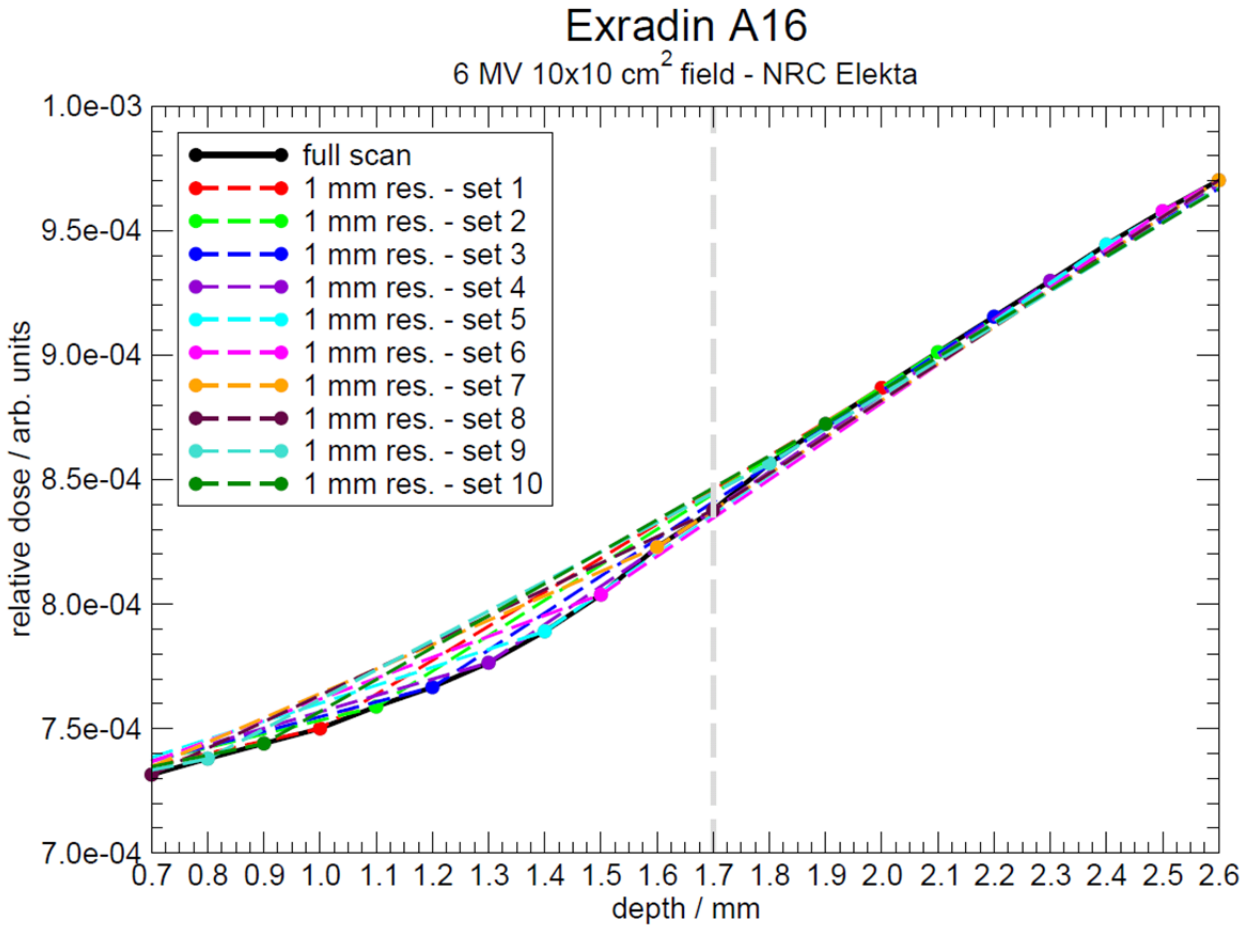

Figure 77: Resolution test starting with an Exradin A16 scan acquired with the NRC high-precision scanning system at 0.1 mm resolution. The data set is downsampled for increasingly coarser resolutions. The coarsest resolution examined is shown here for comparison. The figure is scaled such that each one data point of each downsampled data set is shown on either side of the DeICERS, denoted by the grey dashed line. The colored dashed lines show the range of possible slopes through the DeICERS for scans at 1 mm resolution. The Exradin A16 is chosen for resolution testing because it has the smallest active cavity volume of any IC used in this thesis.

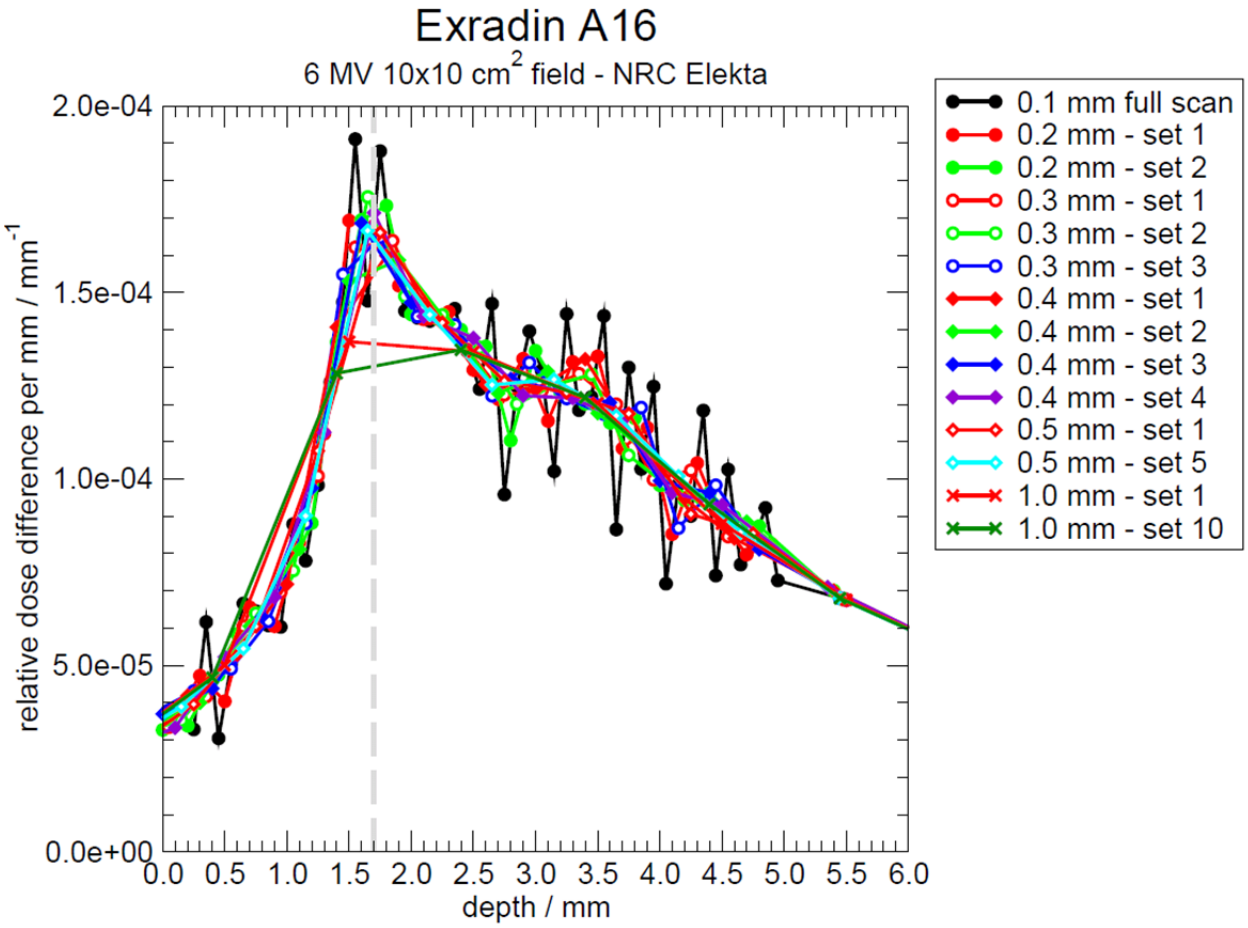

Figure 78: First derivatives of the data sets downsampled from the original data set shown in Figure 77. The original data set, at 0.1 mm resolution, yields a gradient peak 0.15 mm from the DeICERS, denoted by the grey dashed line. The discrepancy in peak location from the DeICERS is within uncertainty. As resolution increases, the peak location is pulled deeper into the water.

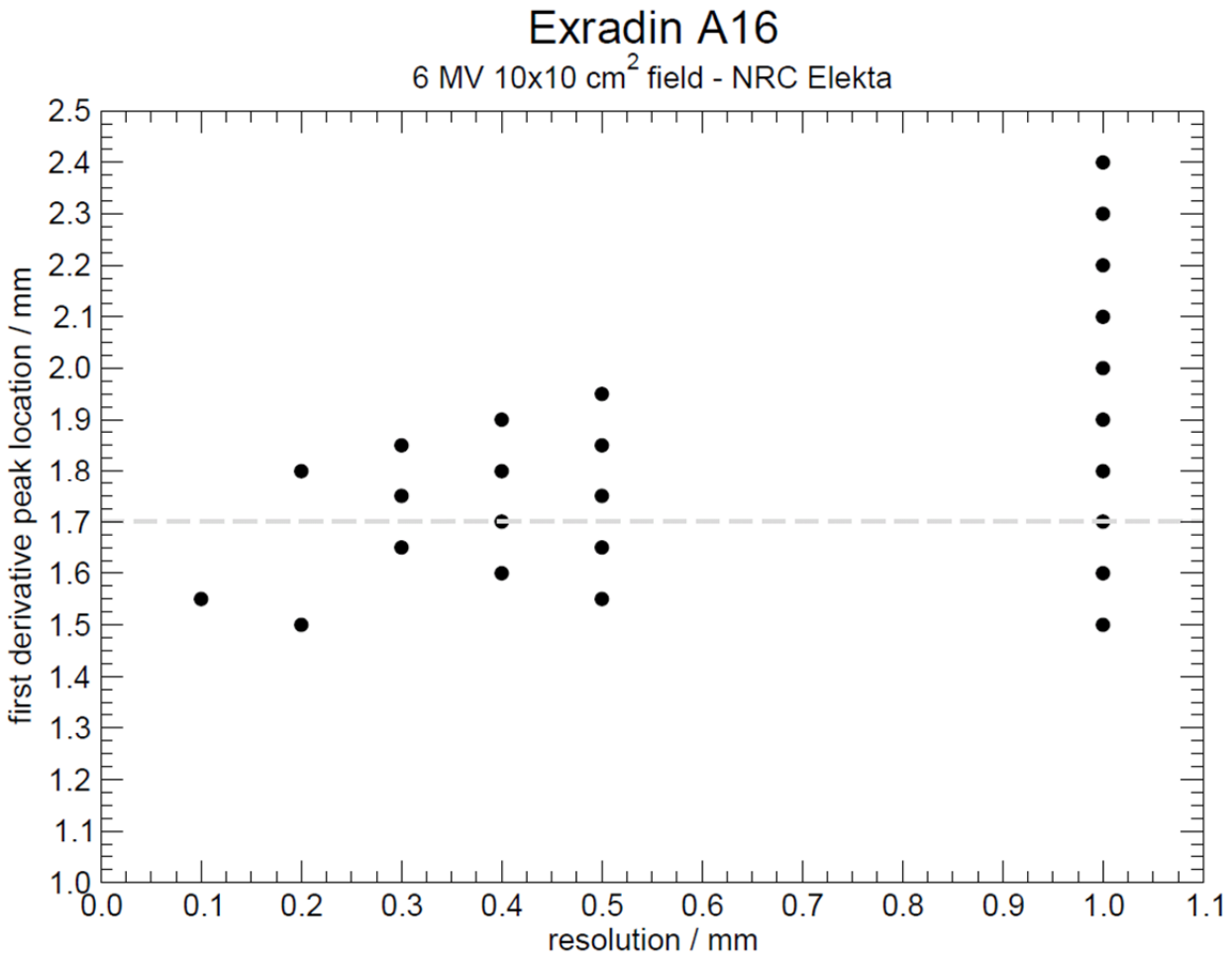

Figure 79: Gradient peak location as a function of scan resolution for the Exradin A16. The maximum spread of observed gradient peak locations increases with degraded resolution. The mean peak location changes by 0.4 mm when resolution changes from 0.1 mm to 1.0 mm. The grey dashed line represents the DeICERS.

The Exradin A16 cylindrical IC demonstrates little not already observed with the first two considered ICs. The PDDs shown in Figure 77 exhibit slope differences for coarse resolution near the DeICERS, represented by the grey dashed line. The PDD gradients shown in Figure 78 demonstrate a gradient peak location 0.15 mm shallower than the DeICERS. The Exradin A16 is a micro-IC for which the gradient peak may appear upstream of the DeICERS due to the IC collecting volume being more hemispherical than cylindrical. The mean gradient peak shifts deeper into the water with resolution changing from 0.1 to 1.0 mm. Figure 79 shows that apparent gradient peak location is shifted 0.4 mm into the water by changing resolution from 0.1 to 1.0 mm. With this IC, sampling at 0.4 mm resolution yields all gradient peaks within

0.2 mm of the DeICERS, indicating the suitability of this resolution for general work. Generally, micro-ICs are only used to measure clinical PDDs for small-field applications such as radiosurgery, where precision is of increased importance compared with standard radiation therapy.

In summary, the ability to resolve the gradient peak accurately is strongly resolution-dependent. For the IBA scanning system, the finest scan resolution achievable is 0.1 mm, which is recommended for use near the water surface. Away from the water surface, resolution may be set more coarsely. When changing scan resolution from 0.1 to 1.0 mm for the three ICs tested here, apparent gradient peak location changed from 0.3 to 0.4 mm.

4.2.4 Scan Reproducibility

Depth-ionization measurements are not perfectly reproducible. As has been discussed throughout this thesis, deviations in IC alignment to the nominal water surface can, and do, occur. Angular deviations in IC alignment with respect to the water surface can also occur. Even for identically specified scans, the scanning tank hardware can move the IC to slightly different measurement positions, e.g., 5.1 mm depth instead of a specified 5.0 mm, and typically does so at least once per scan. Investigations of the factors influencing overall scan reproducibility are discussed in the following sub-sections.

4.2.4.1 Ionization Chamber Alignment Reproducibility

This section describes quantification of the reproducibility achievable when aligning an IC to the water surface by eye. For the cylindrical IC used in this study, the IBA CC13, the alignment procedure is the AAPM TG-106 (Das *et al.*, 2008) recommended method illustrated in Figure 5. For the parallel-plate IC used in this study, the PTW 23343 (Markus), the front face of

the IC is nominally aligned to the water surface. When using the IBA Blue Phantom, the water surface position is defined relative to IC position. Therefore, each time an IC is placed into its holder in the tank, the water surface position must be re-defined. In this experiment, 26 cylindrical IC alignments to the water surface and 25 parallel-plate IC alignments to the water surface are performed. In each trial, after the IC is aligned and the water position is re-established, the IC position relative to the water tank is recorded. After each alignment, a scan is performed from 10 to 9 mm at 0.1 mm resolution. The scan origin is set for each alignment but the IC is not sent to the water surface so no DeICERS is established. The positional standard deviation for each IC type is computed. Since acquiring all trials requires multiple tank setups, the true water surface position can vary between the trials. To account for this, the trials are further broken down into sub-groups, wherein water evaporation is expected to be the dominant source of any change in water surface position. Water evaporation corrections are made where necessary.

Table 8: Standard deviation of the positions of the depth origin for twenty-six alignments of the IBA CC13 cylindrical IC type and twenty-five alignments of the PTW Markus parallel-plate IC type. Since several alignments took place between disturbances of the water level, evaporation was a potential confounding factor. The standard deviations shown here envelop the combined uncertainty in IC positioning at the water surface and in filling the water tank to the same level in each instance.

	std. dev. of scan origin (mm)	
IC type	uncorrected	evaporation corrected
IBA CC13	0.22	0.21
PTW 23343	0.27	0.25

Table 8 shows the uncorrected and evaporation-corrected standard deviations in IC positioning for each IC type. Uncorrected positioning error is found to be 0.22 mm for the cylindrical IC and 0.27 mm for the parallel-plate IC. After applying an evaporation correction, these errors are reduced to 0.21 and 0.25 mm, respectively. These errors include the uncertainty in IC alignment to the water surface and uncertainty in the total amount of water with which the

tank is filled. Figure 80 shows the data broken down in subgroups where the water volume is nominally constant. This figure more accurately represents true alignment uncertainty than does Table 8. Here, all alignment uncertainties are <0.25 mm. Excepting the first group of PTW 23343 alignments, all uncertainties are <0.15 mm. The general uncertainty reduction over the five sub-groups is representative of an increase in user familiarity with the alignment procedure. The data presented here are representative of a nominal best-case scenario for alignment reproducibility. Relative to the objectives of typical clinical PDD scanning, this investigator is unusually concerned with the precision of IC localization at the water surface. These uncertainties are representative of a user who has performed hundreds of IC alignments by eye for this thesis. It is expected that the uncertainty levels shown here are smaller than those that would be obtained by a less experienced user. The tangible benefit of user experience is demonstrated by the reduction of discrepancies between gradient peak and DeICERS locations for ICs originally tested in the scan direction experiment shown in Section 4.2.1 that are re-tested and shown in Section 4.5.1.

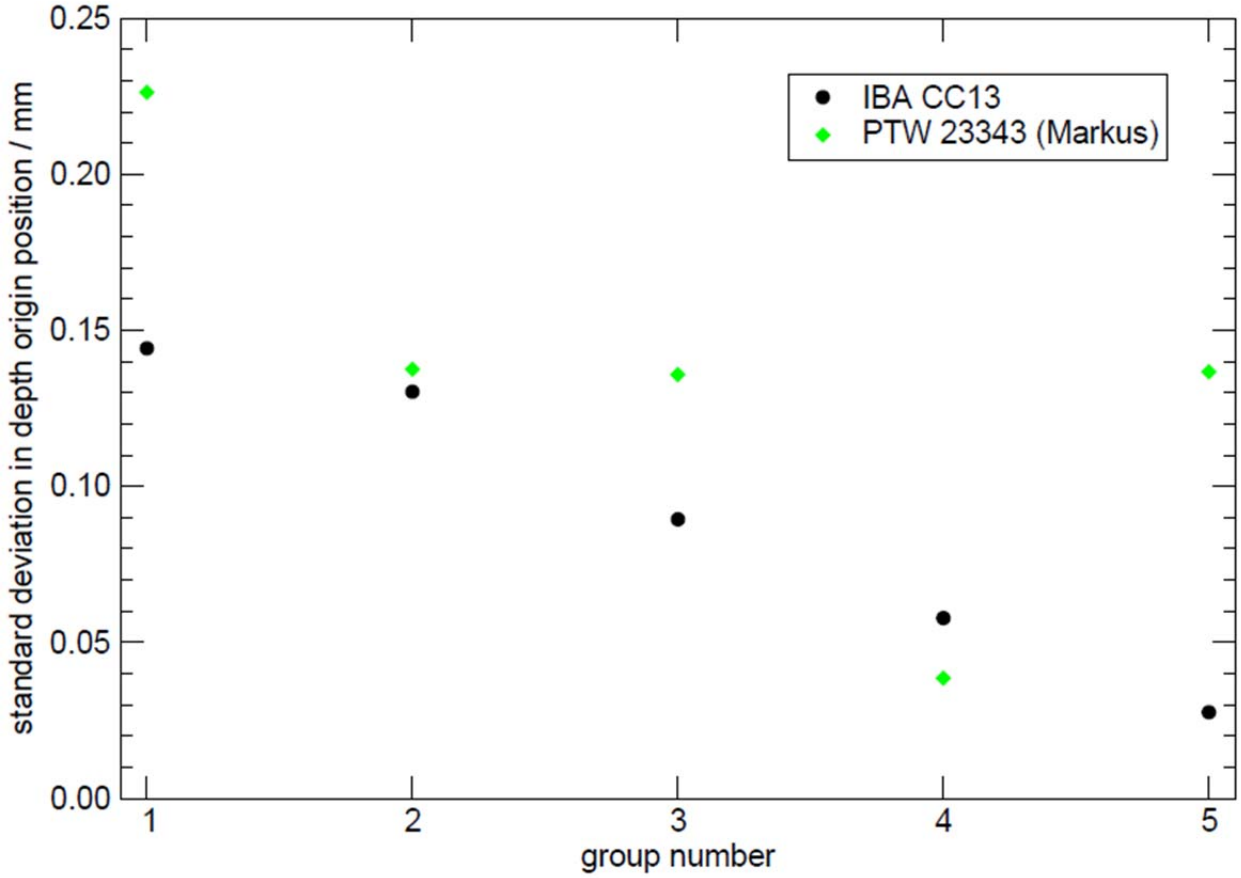

Figure 80: Setup reproducibility broken down into subgroups within which any change in the water surface location is expected to be dominated by evaporation. The y-values here are better estimates of true alignment uncertainty than the overall uncertainty estimates presented in Table 8. Alignment becomes more consistent over the course of the experiment.

4.2.4.2 Ionization Chamber Angular Offset

For an IC to be properly aligned to the water surface, it must also be properly leveled. A properly leveled cylindrical IC has its longitudinal axis parallel to the water surface. A level parallel-plate IC is positioned with the IC entrance window parallel to the water surface. Deviations in IC positioning away from perfect leveling offset the geometry of the IC collecting volume with respect to the radiation source and change the amount of water buildup over the IC active volume. Therefore, it is hypothesized that IC angular offset affects IC response and the resulting response gradient. To test this hypothesis, measurements are taken with a cylindrical IC, the IBA CC13, and a parallel-plate IC, the PTW 23343 (Markus). In both cases, scans are

acquired with the ICs offset over a range from level (0°) to 5° tilted into the water, in 1° increments. These IC angular offsets are illustrated in Figure 81. The cylindrical IC origin is the circular IC end away from the gantry. The parallel-plate IC origin is the top surface edge away from the gantry. The cylindrical IC is also scanned when tilted away from the water surface, at an angle of -1°. All angular positioning is measured using a protractor. Angular offsets are induced by altering the orientation of the IC holder with respect to the scanning arm on which it is mounted.

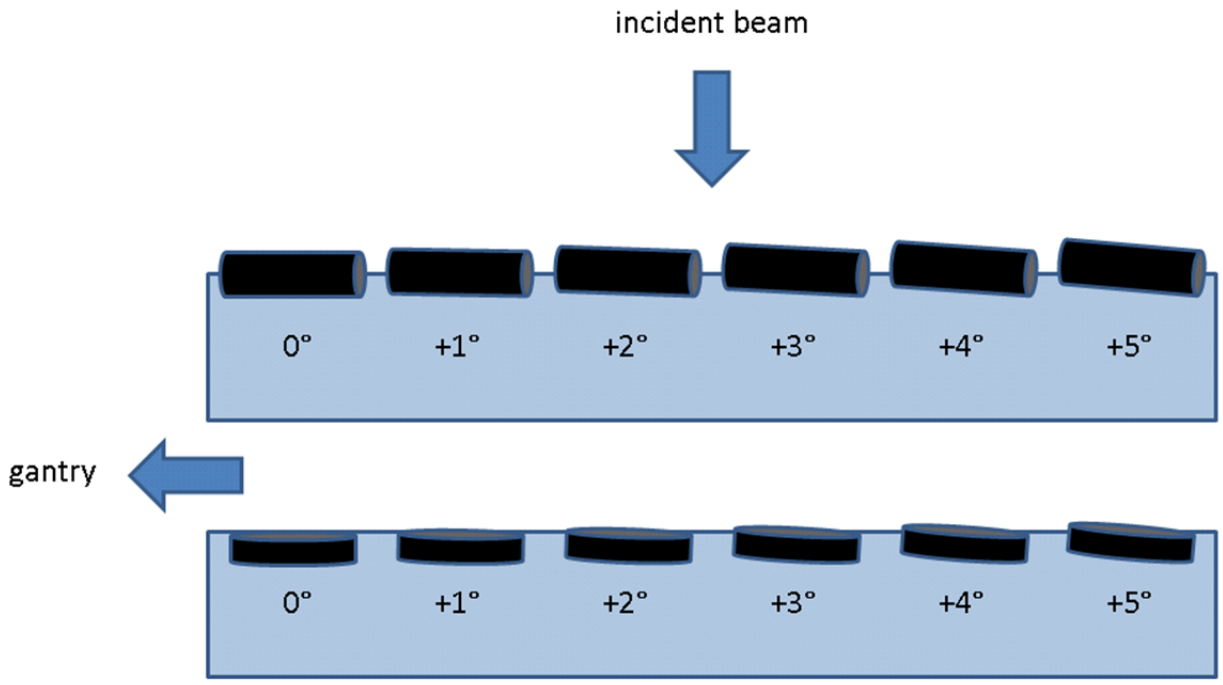

Figure 81: Illustration of the IC angular offsets induced in the experiment described in Section 4.2.4.2. The top panel shows a cylindrical IC and the bottom panel shows a parallel-plate IC. The radiation beam would be incident from the top of the page. The gantry would be to the left of the page. The view shown here is analogous to looking through the side of the water tank.

PDDs measured with the IBA CC13 cylindrical IC are shown in Figure 82. At 20 mm above the water surface in air, the dose measured with the IC tilted 5° into the water is ~4% higher than the dose measured with the IC tilted 1° out of the water. This maximal difference in relative dose values is reduced at depths in air closer to the water surface and below the water surface. After d_{max}, it would be expected that small angular variations should average out and

indeed there are no apparent differences between scans. The relative dose gradients for the PDDs measured with the IBA CC13 are shown in Figure 83. The gradient peak from the scan with the IC aligned parallel to the water surface (0°) occurs at a position 0.05 mm shallower than the DeICERS, denoted by the grey dashed line. The difference in gradient peak and DeICERS locations is within measurement uncertainty. The maximal change in gradient peak location due to angular offset of the cylindrical IC in this experiment is 0.35 mm.

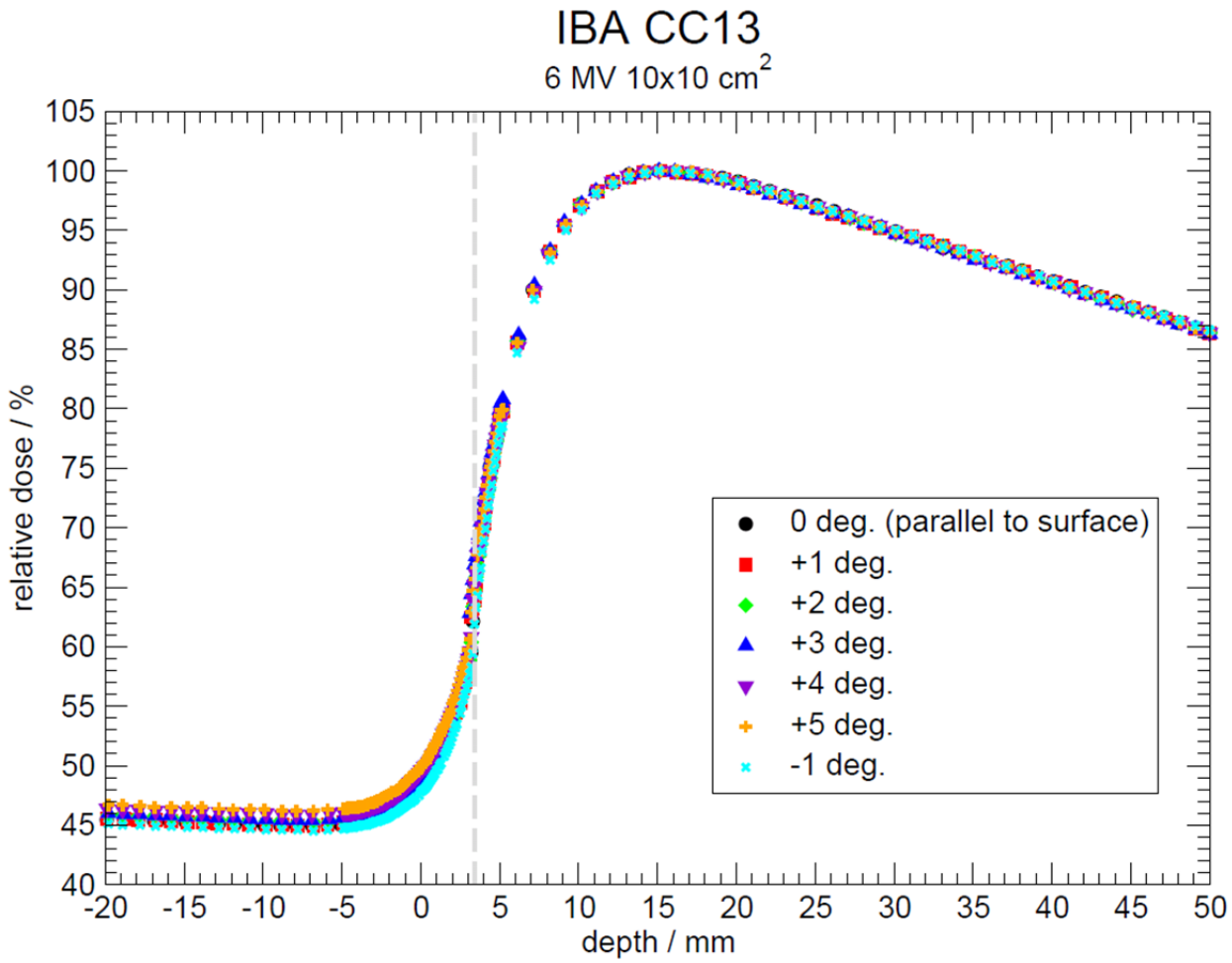

Figure 82: PDDs measured with the IBA CC13 cylindrical IC for a 6 MV 10×10 cm^2 field with the IC misaligned with respect to the water surface by varying amounts. Here, 0° corresponds with the IC axis of symmetry laying parallel to the water surface. Trials labeled +1-5° correspond with the IC being tilted such that the IC cavity is displaced below the water surface by an increasing amount. The trial labeled +5° represents the greatest amount of angular displacement that could be introduced to the IC holder while still successfully fastening the holder to the scanning arm assembly within the water tank. The trial labeled -1° corresponds with the IC cavity being tilted out of the water when the IC is nominally aligned to the surface and is as much angular offset as could be administered in this direction.

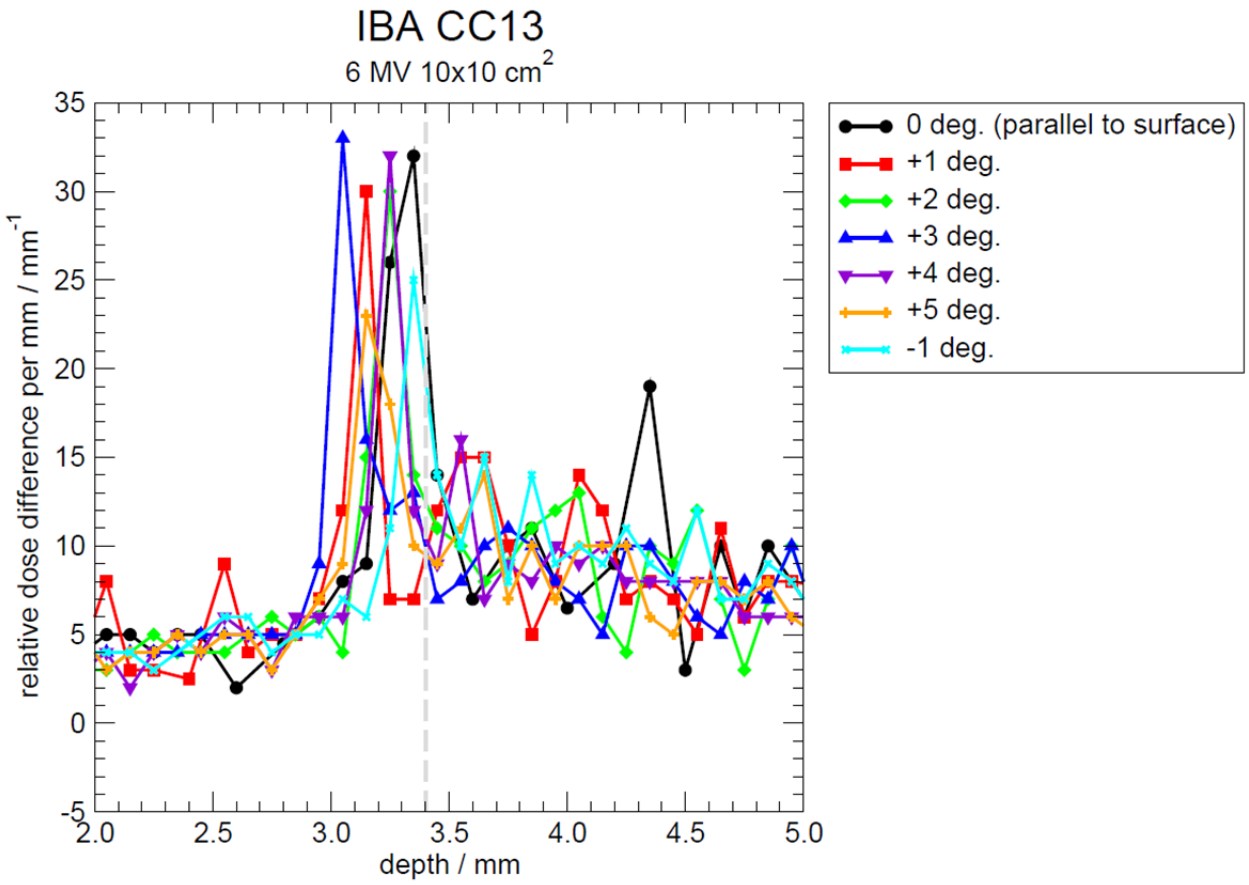

Figure 83: First derivatives of the scans shown in Figure 82. The cylindrical IC geometry is relatively robust against angular offsets, as the greatest deviation from the nominal CC13 outer radius is 0.35 mm. The gradient peak from the scan taken with the IC axis of symmetry parallel to the water surface is located at the first point beyond the DeICERS (3.4 mm).

Figure 84 shows PDDs measured with the PTW 23343 parallel-plate IC. Dose deviations of ~19% between the IC aligned at 0° and the IC aligned 5° tilted into the water are observed at a depth of 3 mm. At 2 mm, the deviation between the same two scans is ~38%. These deviations indicate that the parallel-plate IC geometry is much less robust against IC angular offsets than the cylindrical IC geometry. This indication is borne out by the relative dose gradients, shown in Figure 85. With the parallel-plate IC well-aligned, the observed gradient peak occurs 0.05 mm deeper in the water than the DeICERS, a difference that is within measurement uncertainty. Offsetting the IC by 1° into the water moves the gradient peak 0.9 mm deeper into the water. Changing the angular offset from 1° to 2° shifts the gradient peak deeper by another 0.6 mm.

Increasing the angular offset from 2° to 3° again shifts the gradient peak 0.6 mm deeper. The amount of change in gradient peak location with angular offset decreases as increasing the angular offset from 3° to 4° shifts the gradient peak deeper by 0.2 mm. A 5° angular offset induces no shift in the gradient peak location compared with the gradient peak obtained with the IC offset by 4°. Overall, a 2.3 mm shift in gradient peak location is induced by changing the angle of the IC relative to the water surface by 4-5°. It would be expected that the gradient peak location would change by a constant amount per degree of angular offset. The variability in the amount of gradient peak shift per degree indicates a possible inconsistency in the angular alignment of the holder. Further measurements for each angular offset would be required to verify the gradient peak locations for non-zero IC angular offset. The data shown here indicate that if PDDs are to be measured with a parallel-plate IC, care must be taken to ensure that the IC face is parallel to the water surface.

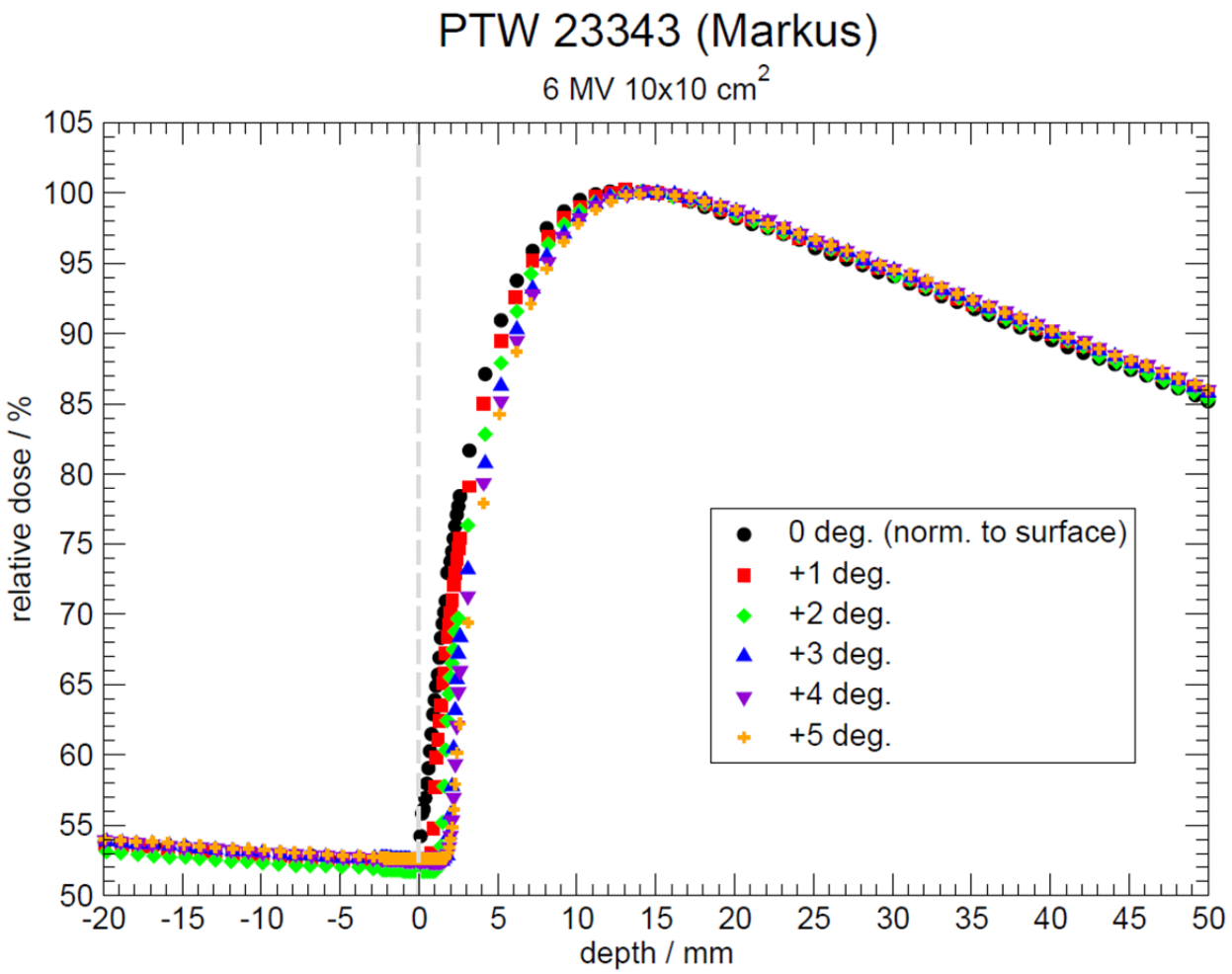

Figure 84: PDDs measured with the PTW Markus parallel-plate IC for a 6 MV 10×10 cm^2 field with the IC intentionally misaligned with respect to the water surface by varying amounts. Here, 0° corresponds with the IC axis of symmetry laying perpendicular to the water surface. Trials labeled +1-5° correspond with the IC being tilted such that the IC edge away from the accelerator gantry is displaced below the water surface by an increasing amount. The trial labeled +5° represents the greatest amount of angular displacement that could be introduced to the IC holder while still successfully fastening the holder to the scanning arm assembly within the water tank. The parallel-plate IC holder could not be tilted in the opposite direction by any substantial amount.

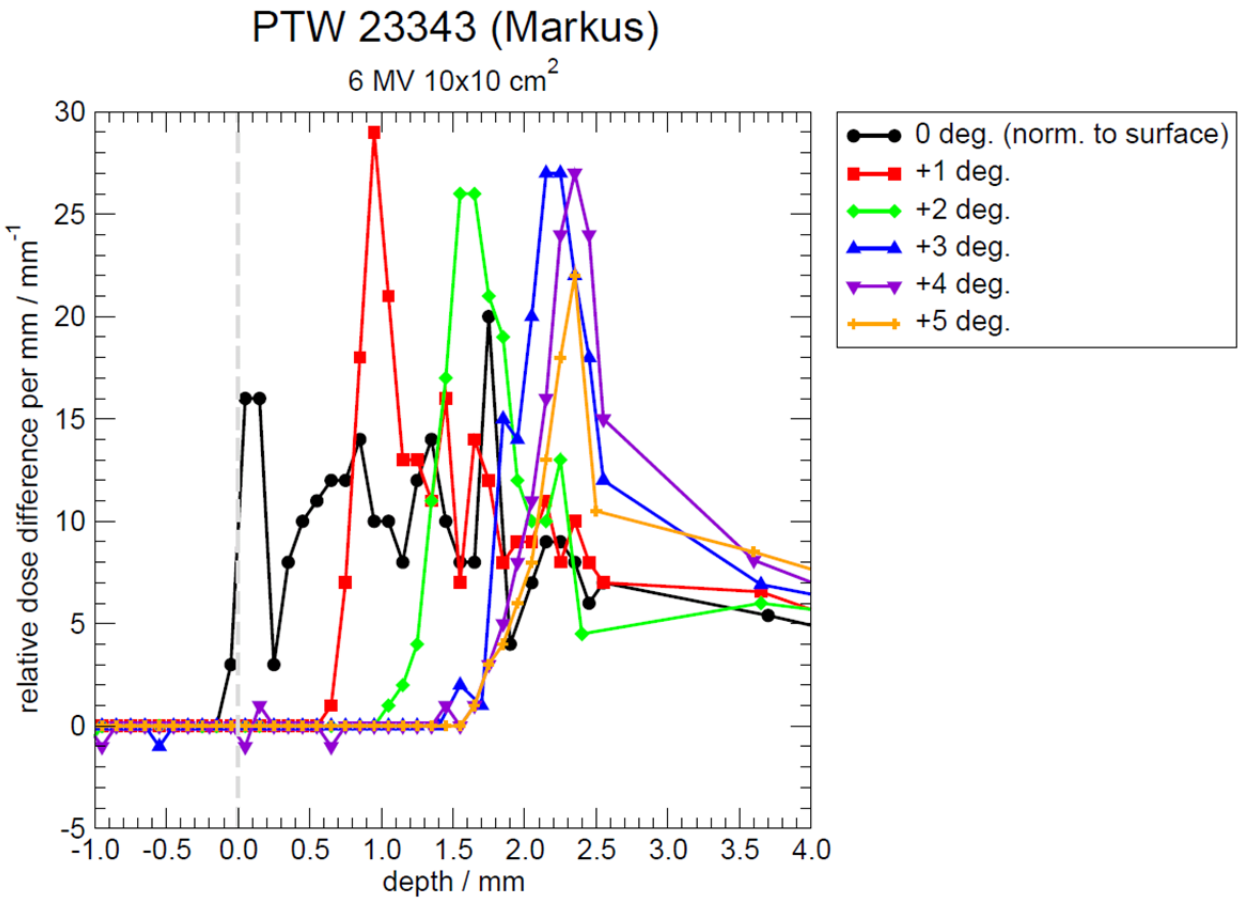

Figure 85: First derivatives of the scans shown in Figure 84. The parallel-plate IC geometry is not robust against angular offsets, as a 1° change shifts the gradient peak by 0.9 mm. The amount of gradient peak displacement plateaus, as both a 4° and 5° angular offset induce a 2.3 mm gradient peak shift. The gradient peak from the scan taken with the IC axis of symmetry perpendicular to the water surface occurs within 0.05 mm of the nominal water surface.

4.2.4.3 Water Tank Equipment Positioning Reproducibility

The majority of the measurements taken for this thesis project are taken using an IBA Blue Phantom filled with water such that the water surface is aligned to the crosshairs etched on the tank sides, 30 cm above the platform on which the tank sits. Hundreds of PDDs are acquired, wherein the stepper motors and drive belts that move the IC do so over the same limited range each time. It is possible that over time, the drive belts could become worn-in, such that data measured in this region of the tank might no longer accurately represent data measured in other parts of the tank. To test this possibility, scans are acquired under the same nominal radiation

field conditions, 6 and 18 MV 10×10 cm^2 fields, with three different amounts of water in the tank. After filling the tank to a given amount, the tank platform height is adjusted such that the water surface remains at a fixed 100 cm SSD. Performing the same scans with different amounts of water in the tank forces the tank hardware to operate at different heights within the tank. The tank is filled with 20.5, 30, and 45 cm of water. As noted above, 30 cm is the height to which the water level is usually raised. A water level height of 20.5 cm represents the minimum amount of water with which the tank could be filled that allows the tank to be raised to 100 cm SSD without colliding with the accelerator head. A water level height of 45 cm represents the approximate maximum amount of water held in the accompanying reservoir from which the tank is filled.

PDDs are measured with a representative cylindrical IC, the IBA CC13, and a representative parallel-plate IC, the PTW 23343 (Markus). All measurements are taken from 50 mm below the water surface to 20 mm above the water surface in air. From 4 to -1 mm for the CC13 and from 2.5 to -2.5 mm for the PTW 23343, scans are acquired at 0.1 mm resolution. Outside of these regions, 1 mm resolution is used for both IC types. The nominal sampling resolution at most measurement points is 1 s/pt. For the PTW 23343 measurements, a sampling resolution of 10 s/pt. is used over the range from 2.5 to -2.5 mm. From 4 to 3 mm, for the CC13, the sampling rate used is 4 s/pt. In cases where inter-scan evaluation determines the sampling rate is insufficient, the sampling rate is increased to 10 s/pt. Relative dose gradients are computed for each measurement. The CC13 relative dose gradients are shown in Figure 86. All gradient peaks occur at the same location, 0.05 mm shallower than the DeICERS marked by the grey dashed line. The discrepancy between the gradient peak and DeICERS locations is within the measurement step size and overall uncertainty.

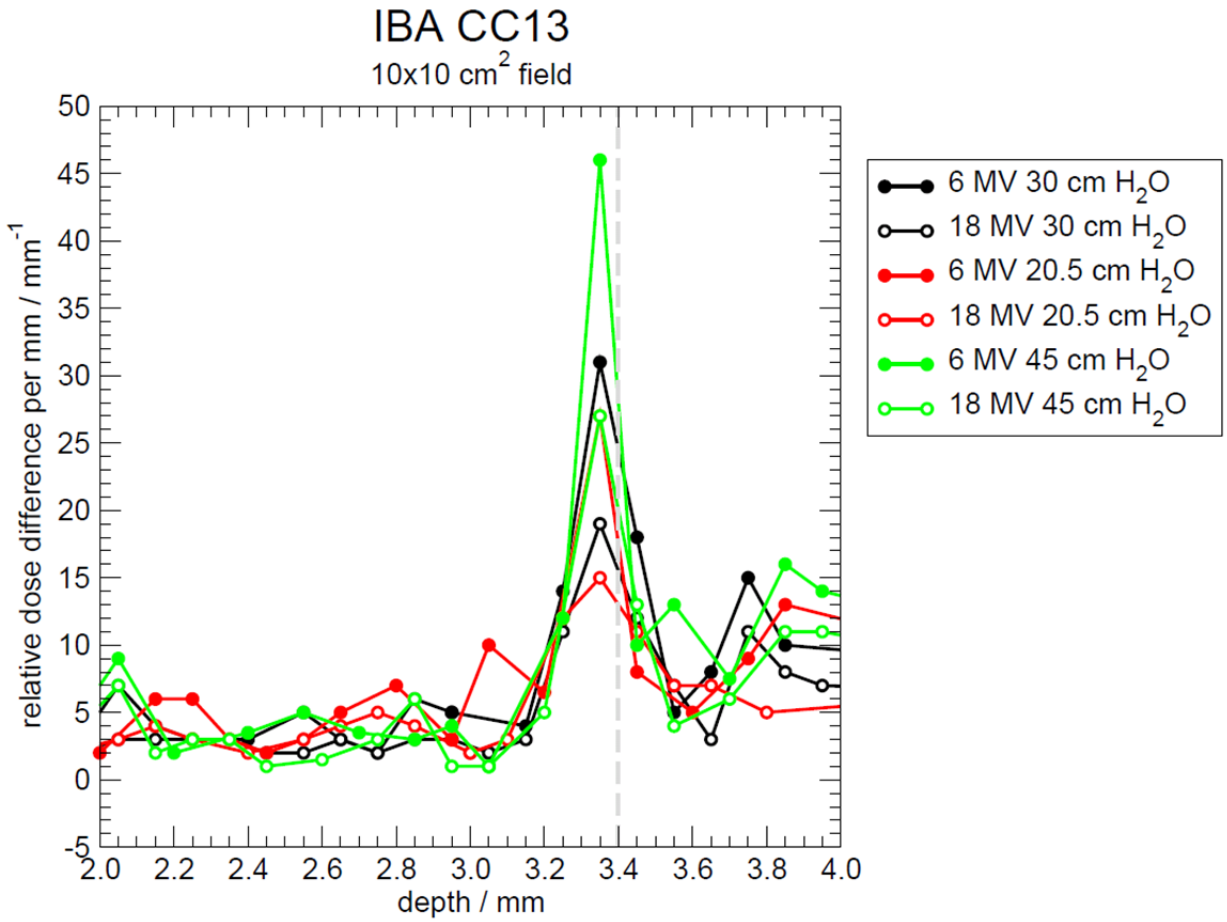

Figure 86: First derivatives of PDDs measured with the IBA CC13 cylindrical IC at a 10×10 cm^2 field for 6 and 18 MV at three water levels. The tank is shifted vertically so that all three water levels correspond to 100 cm SSD. 30 cm H_2O represents the height of the crosshairs on the tank, the default tank alignment position. 20.5 cm H_2O represents the minimum amount of water able to be brought to 100 cm SSD without colliding the tank and the accelerator. 45 cm H_2O represents the approximate maximum water amount held in the reservoir able to be pumped into the tank. For all changes in energy and water level, the gradient peak is observed at the first gradient point beyond the IC outer radius. Increasing the sampling time in the narrow region of interest around the IC outer radius reduces noise. Ensuring 0.1 mm resolution is achieved in each scan by rescanning until no positional slips occur helps to amplify the observed peaks. The grey dashed line marks the DeICERS at 3.4 mm.

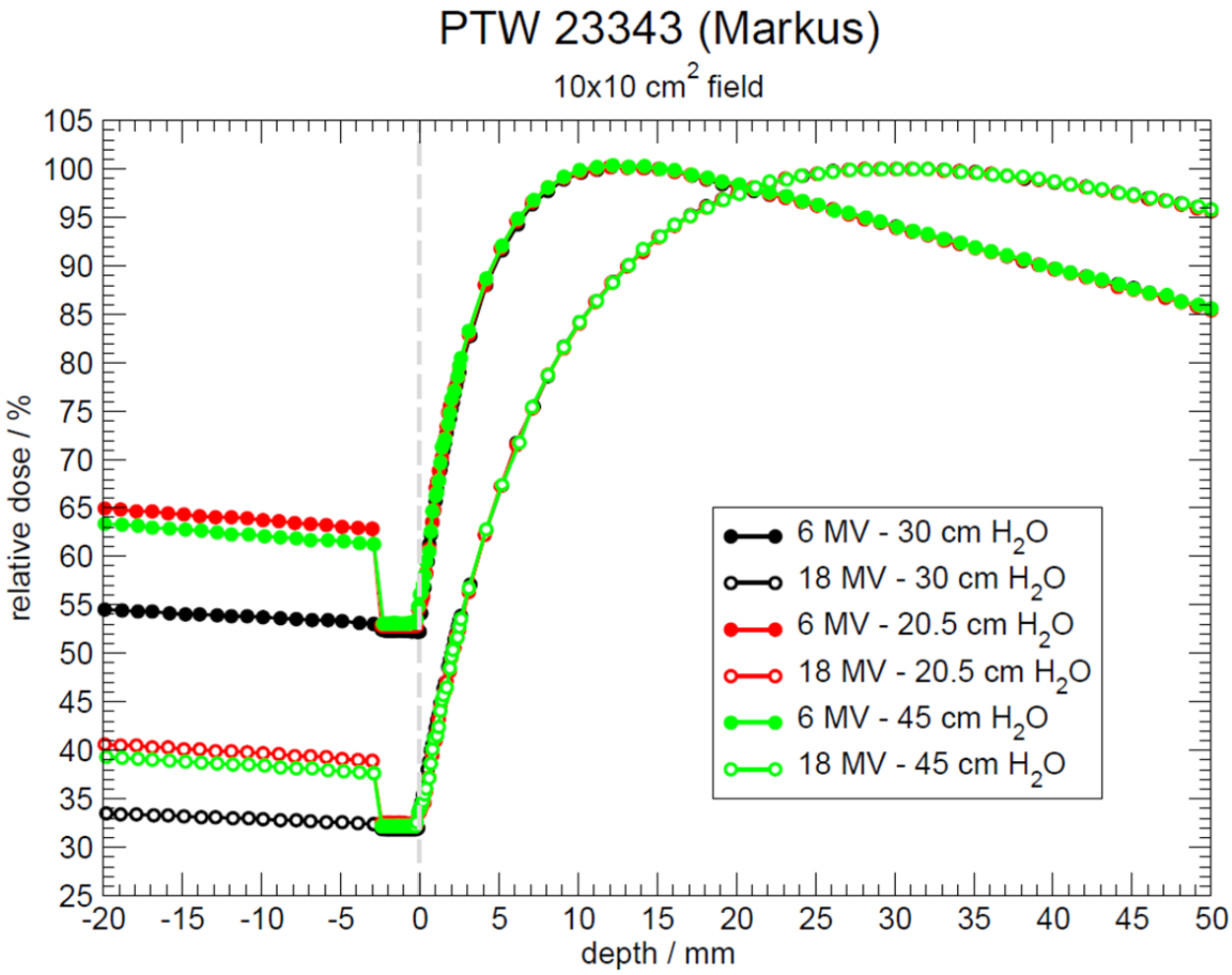

Figure 87: PDDs measured with the PTW Markus parallel-plate IC at a 10×10 cm^2 field for 6 and 18 MV at three water levels. The tank is shifted vertically so that all three water levels correspond to 100 cm SSD. 30 cm H_2O represents the height of the crosshairs on the tank, the default tank alignment position. 20.5 cm H_2O represents the minimum amount of water able to be brought to 100 cm SSD without colliding the tank and the accelerator. 45 cm H_2O represents the approximate maximum water amount held in the reservoir able to be pumped into the tank. All scans are performed from depth in water through the surface into air. Scans are performed at 1 mm resolution from 50 to 3 mm and from -3 to -20 mm. From 2.5 to -2.5 mm, data is acquired at 0.1 mm resolution. Each data point represents an average of, at minimum, 50 sample readings, taking place over 1 second intervals. From 2.5 to -2.5 mm, the sampling rate is 10 seconds per point (500 samples). The jumps in the in-air signal at the non-standard water depths are artifacts caused by water pooling on the IC surface differently for scans at different sampling times that are stitched together. Figure 69 shows the physical explanation for the sampling time dependence and a solution. The grey dashed line marks the DeICERS.

The PDDs measured with the PTW 23343 are shown in Figure 87. Recalling Figure 69, it appears that water is pooled on the IC face above the water surface for the measurements at alternative water levels. A ~2.5% difference in dose in air exists between measurements taken with the two non-standard water amounts. Measurements in 30 cm of water have little water pooling on the IC surface in this case. Figure 88 shows the relative dose gradients for scans with

the PTW 23343. Measurements with 20.5 and 45 cm of water in the tank exhibit gradient peaks 0.15 mm above the water surface, which is the DeICERS in this case. The gradient peaks from the scans with 30 cm of water in the tank are ±0.05 mm from the DeICERS. Though the parallel-plate IC scans showed a 0.15 mm deviation in gradient peak position from the DeICERS with non-standard water levels, this difference is within measurement uncertainty and is not a large enough effect to cause a meaningful discrepancy in PDD scans taken at typical resolution. The larger issue concerning the use of parallel-plate ICs is to ensure that the IC face is dry in air if measurements are to be taken through the water surface. As should be the case for a well-constructed scanning system, the stepper motors and drive belts perform equally well at different heights in the tank. Gradient peak location is unaffected by water level, as expected.

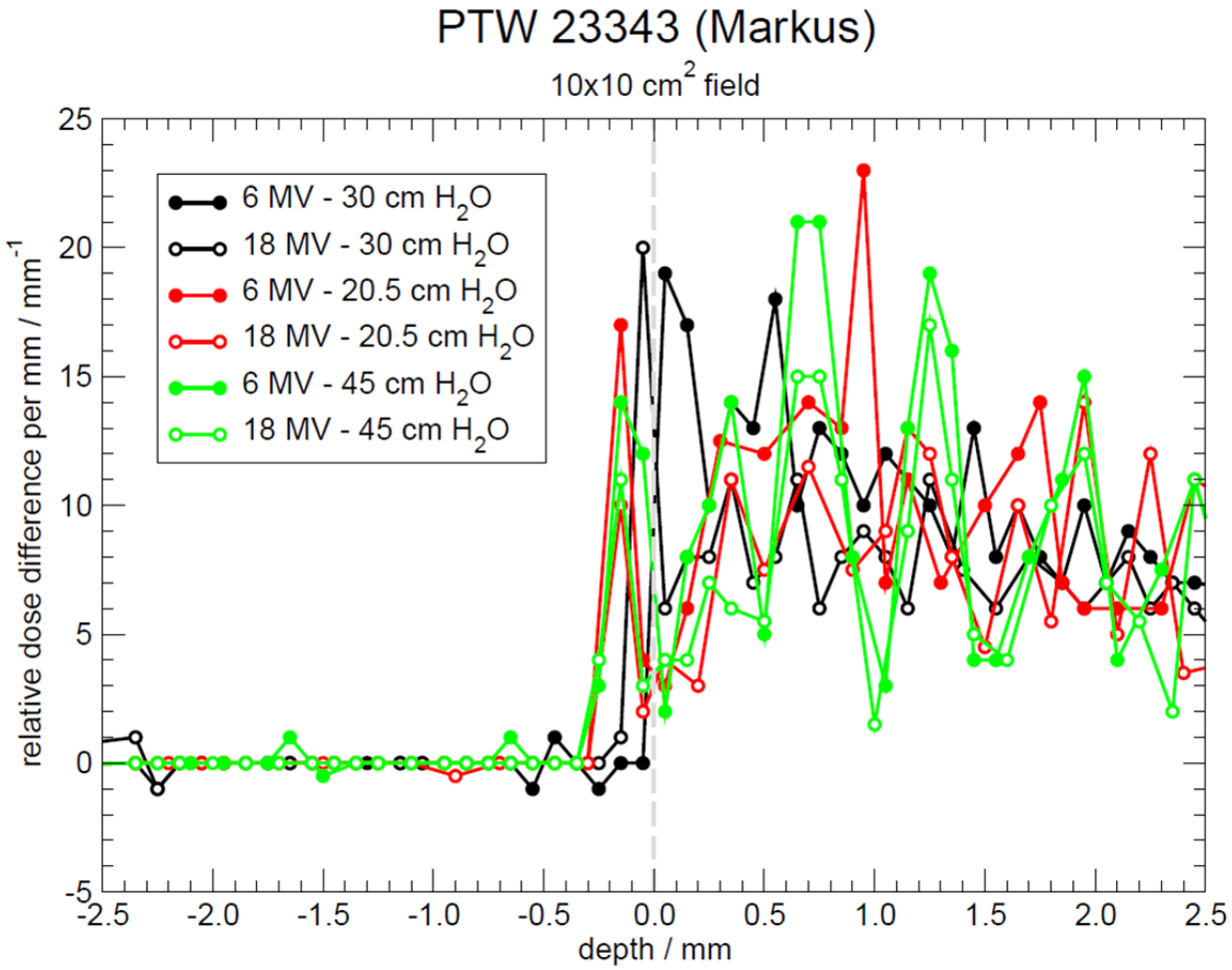

Figure 88: First derivatives of the scans shown in Figure 87. The salient feature is not necessarily overall peak height but the relative maximum beyond which the gradient goes to zero. All gradient peaks occur within 0.15 mm of the water surface.

4.2.5 Bias Voltage Polarity

A change in the absolute value of IC response that occurs when the polarity of the applied bias voltage is reversed is known as the polarity effect. The polarity effect is caused by direct radiation interactions with IC components (Abdel-Rahman *et al.*, 2006). For parallel-plate ICs, electrons stopping in or being knocked out of the parallel-plate IC collecting electrode cause the difference in measured response with bias voltage polarity. This effect is shown by Johns, Aspin, and Baker for photon beams (Johns *et al.*, 1958) and by Van Dyk and MacDonald for electron beams (Van Dyk and Macdonald, 1972). The polarity effect is also influenced by the

shapes of the IC collecting volume and the electric field lines within the volume. Though the polarity effect is generally smaller for cylindrical ICs than for parallel-plate ICs, it has been documented for cylindrical ICs by multiple groups (Aget and Rosenwald, 1991; Nisbet and Thwaites, 1998). Aget and Rosenwald have shown that the polarity effect for cylindrical ICs is caused, in large part, by radiation interactions with the IC stem and cable (Aget and Rosenwald, 1991). McEwen has shown that the necessary polarity effect correction for cylindrical ICs is generally larger for ICs of smaller volume (McEwen, 2010). An examination of the polarity effect for parallel-plate ICs in photon beams showed that the polarity effect is largest in the buildup region portion of the depth-dose curve (Gerbi and Khan, 1987).

The possible dependence of gradient peak location on bias voltage polarity is investigated in this work. At VCU, measurements are acquired with the IBA CC13 and the PTW 23343 (Markus). The Markus IC design has been noted by several authors as having a particularly problematic polarity effect compared with other ICs. Nisbet and Thwaites noted that for the electron beam energy range from 5-20 MeV, the Markus IC design demonstrated the largest energy-dependent spread in polarity correction factors of the four IC designs studied (Nisbet and Thwaites, 1998). The other IC designs studied in the work by Nisbet and Thwaites are Roos (parallel-plate), NACP-02 (parallel-plate), and Farmer (cylindrical) (Nisbet and Thwaites, 1998). McEwen, Williams, and DuSautoy studied 46 ICs of the same four basic types as studied in the work by Nisbet and Thwaites and singled out the Markus IC design as the only design that exhibited intra-model polarity correction variability (McEwen *et al.*, 2001). As discussed in Section 4.1.2, the Markus IC serves in this thesis as a worst-case demonstration.

For both ICs used at VCU for this experiment, scans are performed for two photon beam energies, 6 and 18 MV, and two electron beam energies, 6 and 20 MeV, supplied by the Varian

2300. Measurements are repeated with an applied bias voltage of +300 and -300 V for each IC and beam energy. All measurements are done in 10×10 cm^2 fields. Since the polarity effect is worsened for small cylindrical ICs (McEwen, 2010), polarity measurements are taken at the NRC with two small ICs, the Exradin A1SL (0.057 cm^3 active volume) and IBA CC04 (0.04 cm^3 active volume). The NRC measurements are taken in 6 MV 10×10 cm^2 fields from the Elekta Precise. Again, measurements are repeated with applied bias voltage of +300 and -300 V for each IC.

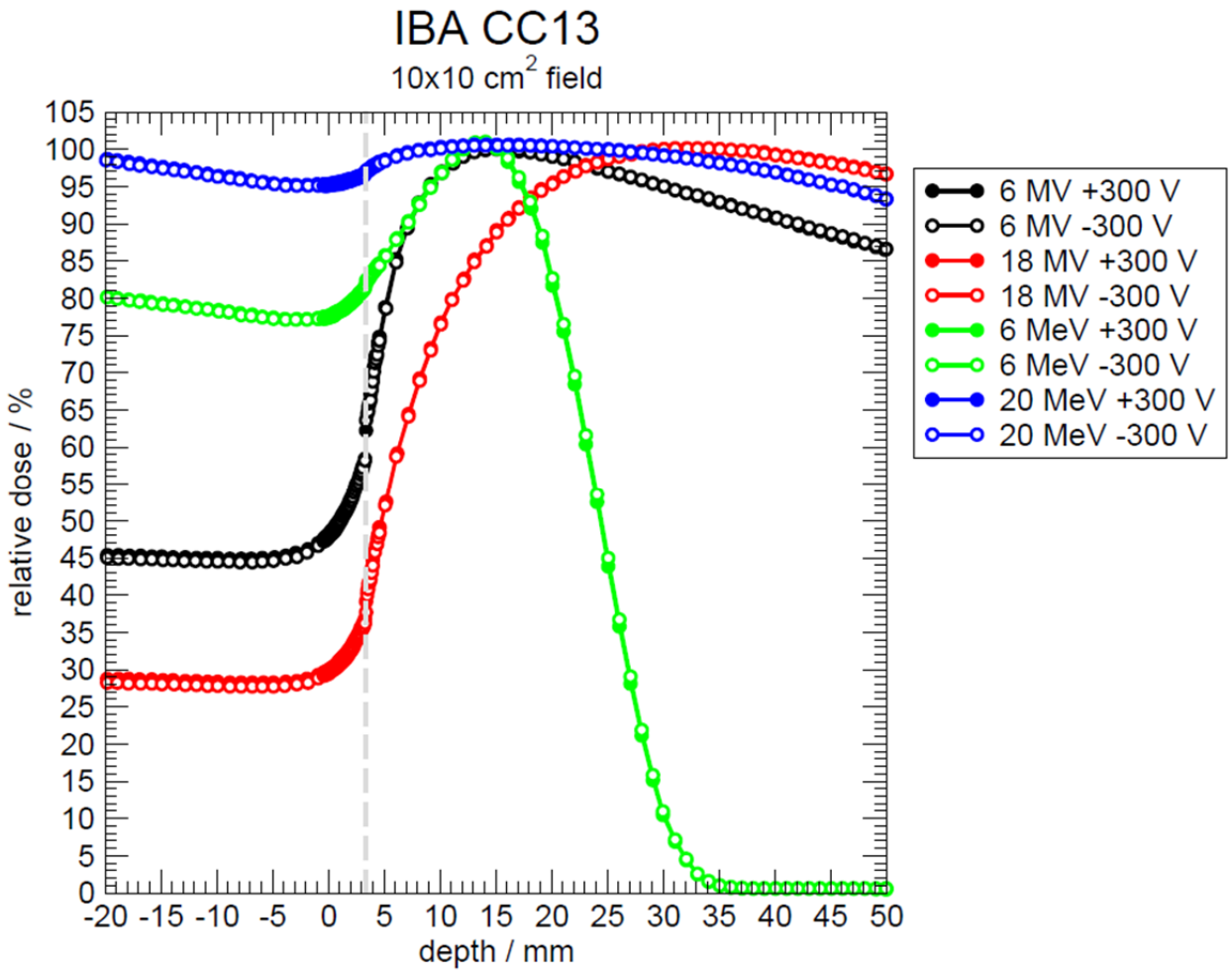

Figure 89: PDDs measured by the IBA CC13 cylindrical IC at 100 cm SSD for a 10×10 cm^2 field for photon beam energies of 6 and 18 MV and electron beam energies of 6 and 20 MeV, each while ±300 V bias voltage is applied to the IC. The two photon beam energies are the only two energies produced by the Varian 2300 while the two electron beam energies are the lowest and highest energies possible, respectively. All scans are performed from depth in water through the surface into air. Scans are performed at 1 mm resolution from 50 to 4 mm and from -1 to -20 mm. From 4 to -1 mm, data is acquired at 0.1 mm resolution. Each data point represents an average of, at minimum, 50 sample readings, taking place over 1 second intervals. From 4 to 3 mm, the sampling rate is 4 seconds per point (200 samples), or, in some cases, 10 seconds per point (500 samples). The grey dashed line marks the DeICERS.

Figure 89 shows the PDDs measured at VCU for the IBA CC13 cylindrical IC. Scan resolution is 1 mm from 50 to 4 mm depth in water and from 1 mm to 20 mm above the water surface in air. From 4 mm deep in water to 1 mm above the water surface, 0.1 mm scan resolution is used. From 4 to 3 mm, the IC is held in place for 4 s/pt., or if necessary, 10 s/pt. Outside of this range, the IC acquires signal for 1 s/pt. Figure 90 shows the CC13 scan

gradients. All gradient peaks occur 0.05 mm shallower than the DeICERS, denoted by the grey dashed line. This difference is within measurement uncertainty.

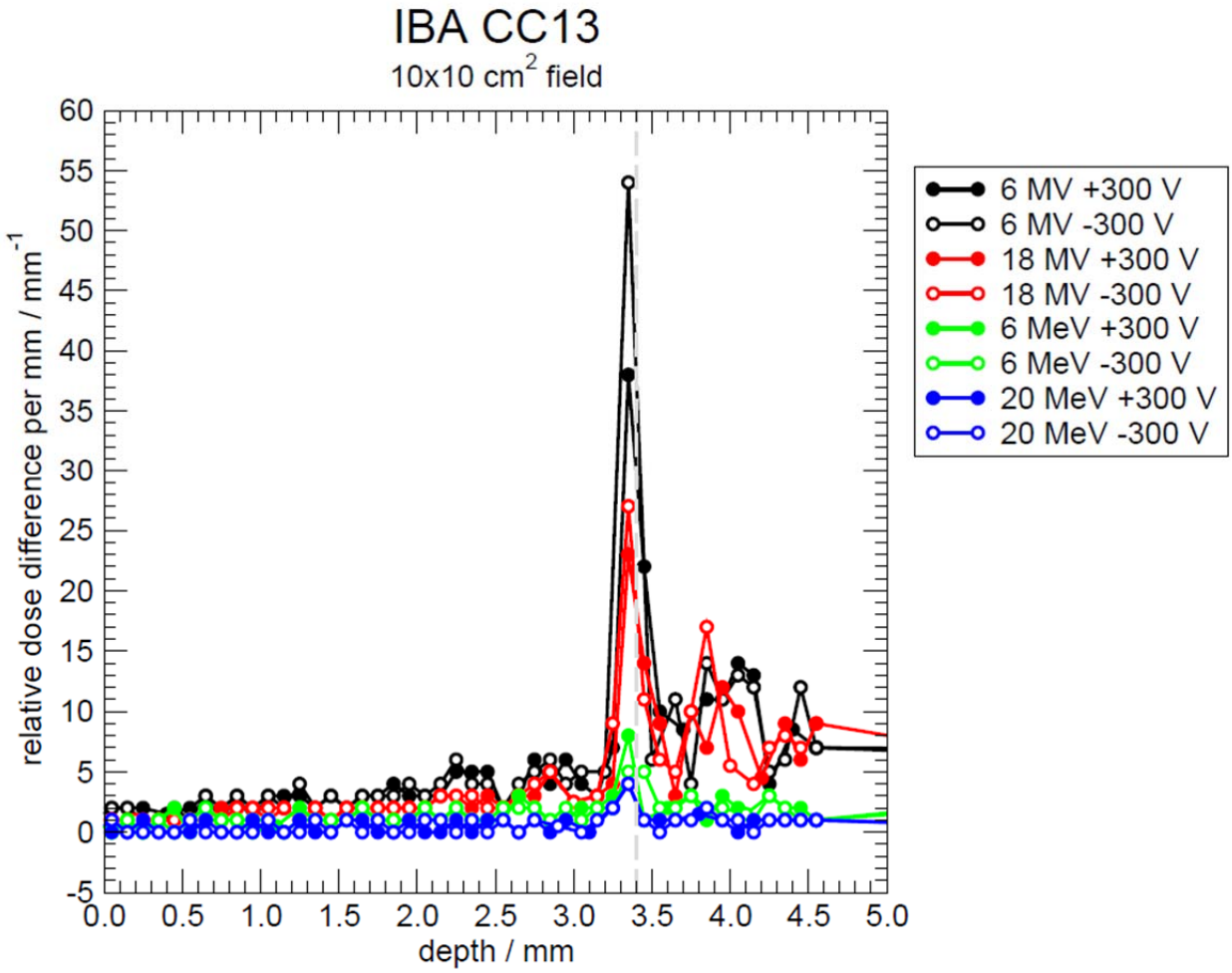

Figure 90: First derivatives of the scans shown in Figure 89. For all changes in energy, particle type, and bias voltage polarity, the gradient peak occurs at the first point beyond where the CC13 outer radius reaches the water surface (3.4 mm).

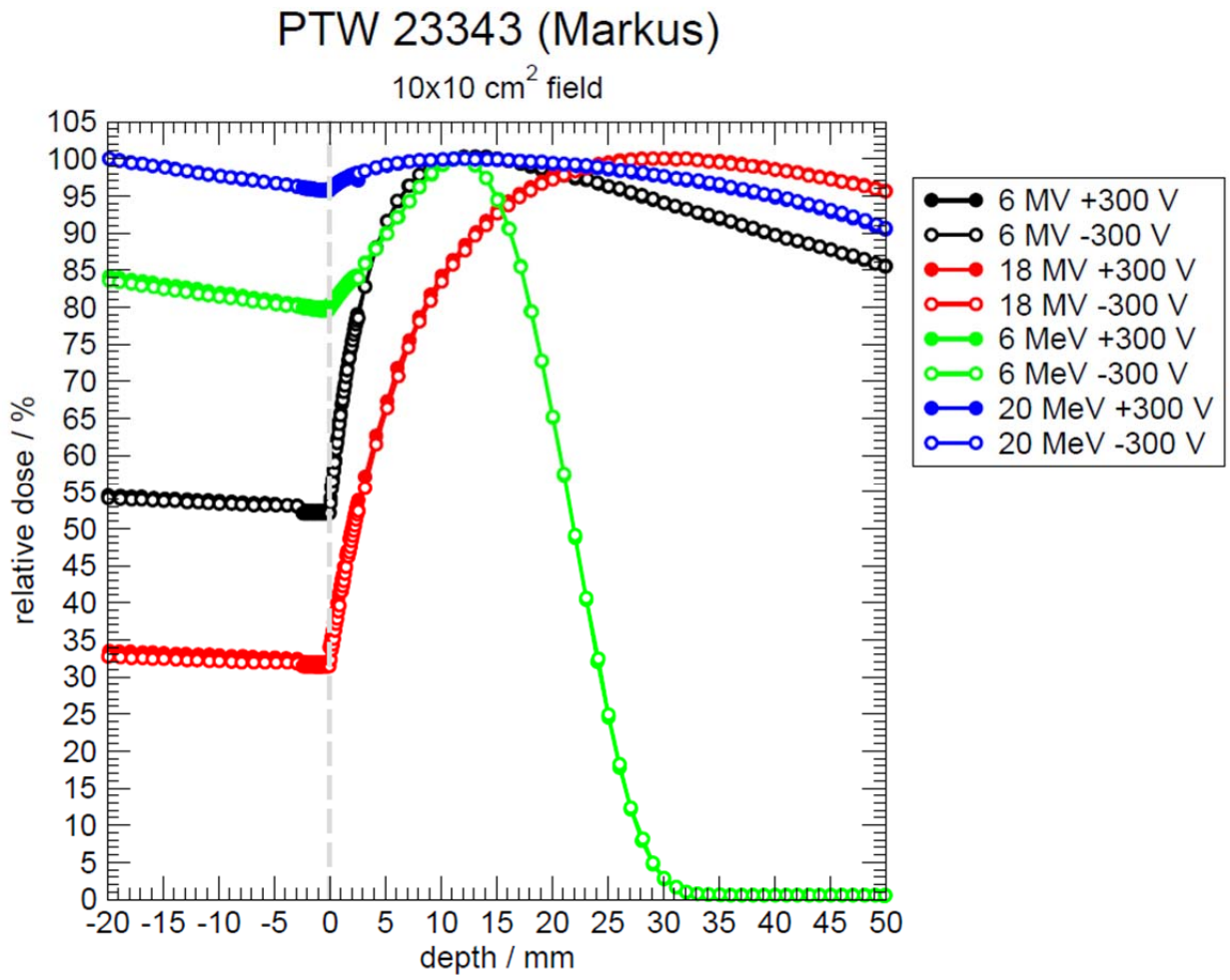

Figure 91: PDDs measured by the PTW Markus parallel-plate IC at 100 cm SSD for a 10×10 cm^2 field for photon beam energies of 6 and 18 MV and electron beam energies of 6 and 20 MeV, each while ±300 V bias voltage is applied to the IC. The two photon beam energies are the only two energies produced by the Varian 2300 while the two electron beam energies are the lowest and highest energies possible, respectively. All scans are performed from depth in water through the surface into air. Scans are performed at 1 mm resolution from 50 to 3 mm and from -3 to -20 mm. From 2.5 to -2.5 mm, data is acquired at 0.1 mm resolution. Each data point represents an average of, at minimum, 50 sample readings, taking place over 1 second intervals. From 2.5 to -2.5 mm, the sampling rate is 10 seconds per point (500 samples). The small increases in the in-air signal at the two photon beam energies are artifacts caused by the way scans at different sampling times are stitched together. Figure 69 shows the physical explanation for the sampling time dependence and a solution. The grey dashed line marks the nominal water surface location.

The PTW 23343 PDDs measured at VCU are shown in Figure 91. From 50 to 3 mm depth in water and from 3 to 20 mm above the water surface in air, scans are acquired at 1 mm spatial resolution and with 1 s/pt. sampling resolution. From 2.5 mm in water to 2.5 mm above the surface in air, spatial resolution is 0.1 mm and sampling resolution is 10 s/pt. Figure 92 shows the gradients of the PTW 23343 scans. Electron scan gradient peaks occur within 0.05 mm of the DeICERS for both polarities. For the standard polarity for measurements taken

in this thesis (+300 V), both photon scan gradient peaks also occur within 0.05 mm of the DeICERS. With the polarity reversed, however, both photon scan gradient peaks occur 0.15 mm deeper than the DeICERS. This difference is within setup uncertainty and not expected to affect typical clinical PDD scanning.

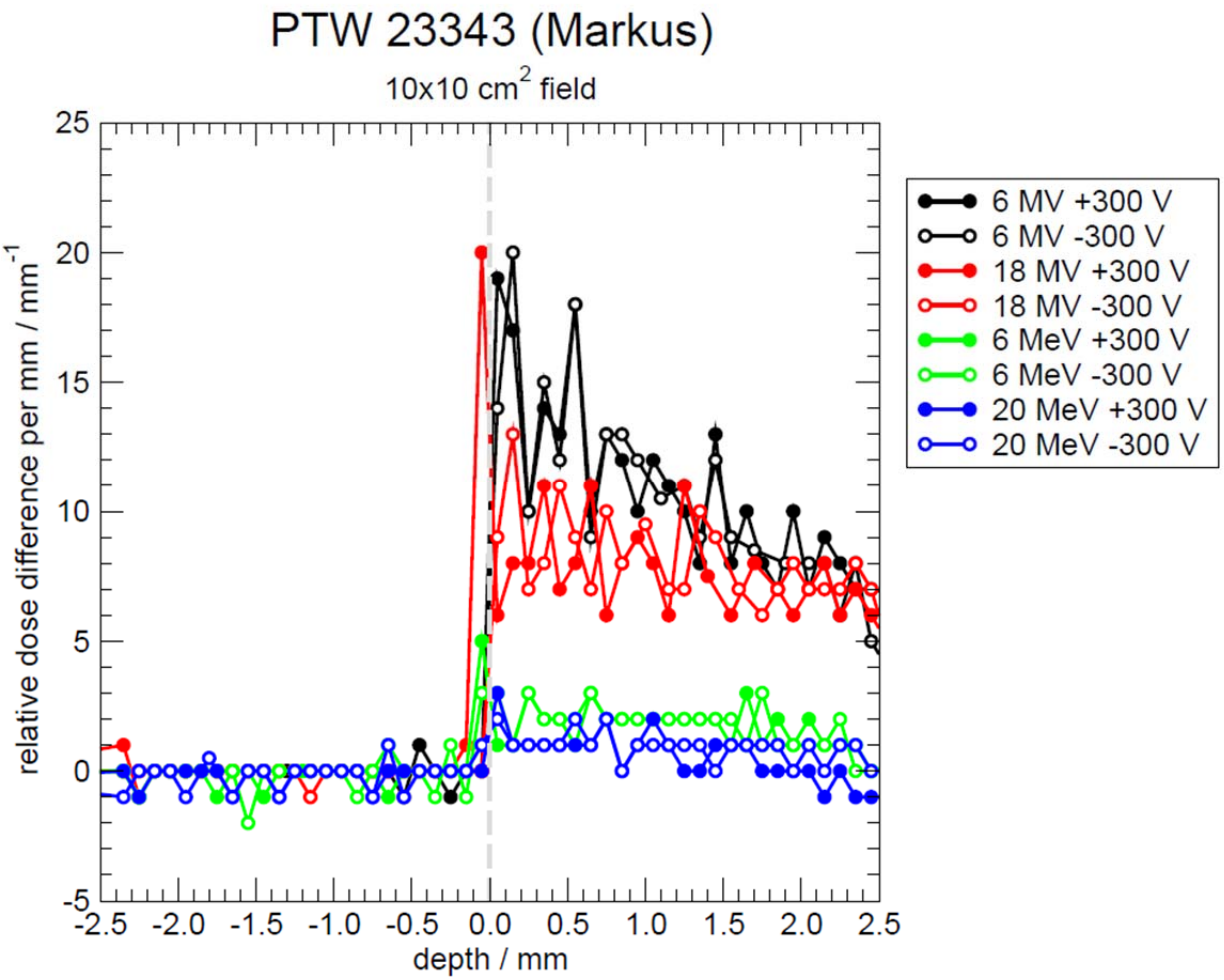

Figure 92: First derivatives of the scans shown in Figure 91. All gradient peaks occur within 0.15 mm of the water surface. The salient feature is not necessarily overall peak height but the relative maximum beyond which the gradient goes to zero.

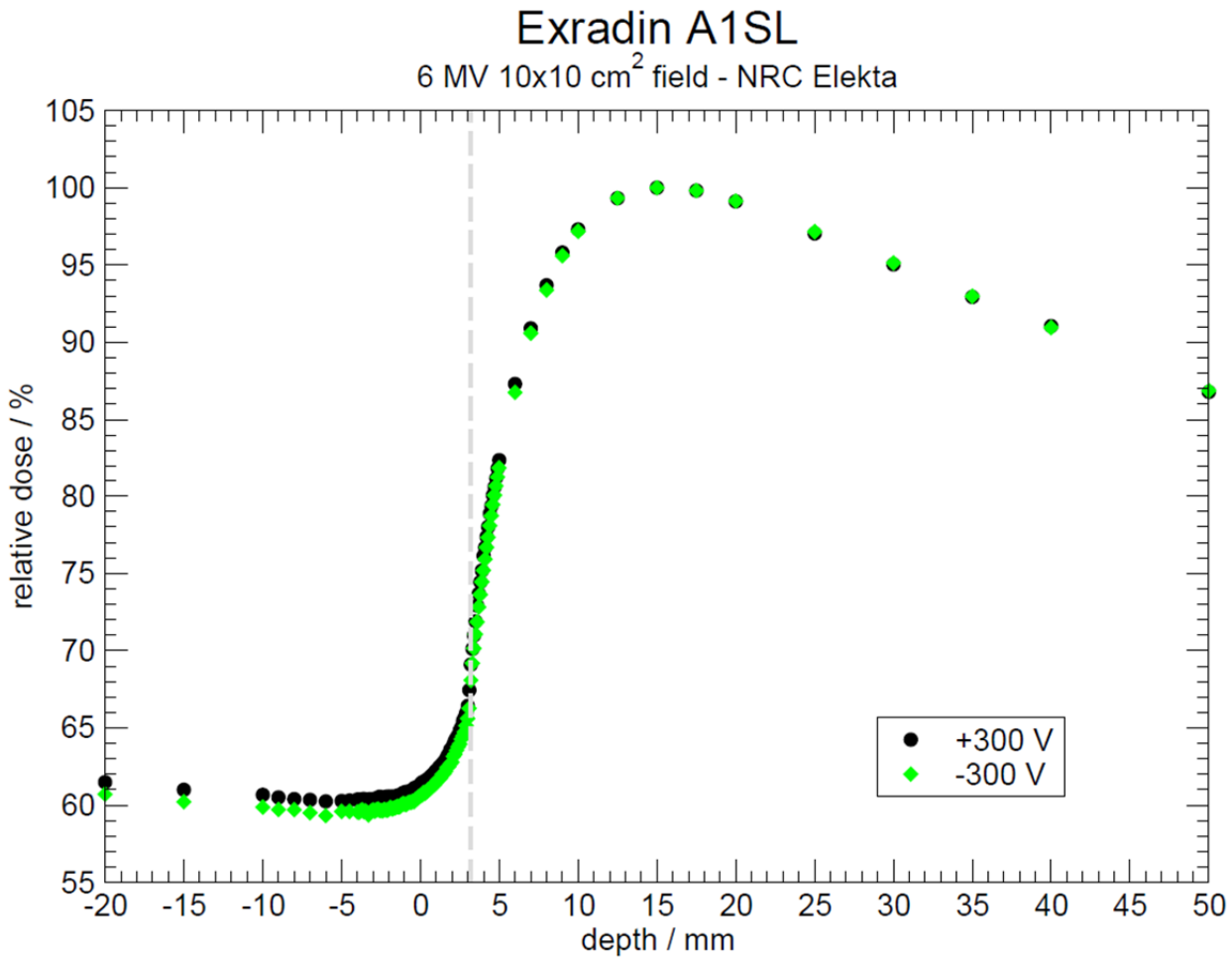

Figure 93: PDDs measured with the Exradin A1SL in a 6 MV 10×10 cm^2 field using the NRC scanning system. Bias voltage polarity is switched between these scans causing a decrease in measured relative dose in the buildup region and in air.

PDDs measured at the NRC with the Exradin A1SL are shown in Figure 93. Dose in air is ~1.5% lower with reversed polarity. Measurements are taken with 4 s/pt. sampling resolution and at variable spatial resolution. From 5 mm in water to 4 mm above the surface in air, scan spatial resolution is 0.1 mm. The Exradin A1SL scan gradients are shown in Figure 94. Both gradient peaks occur at the same location, 0.025 mm shallower than the DeICERS. The difference between gradient peak and DeICERS location is within the measurement step size.

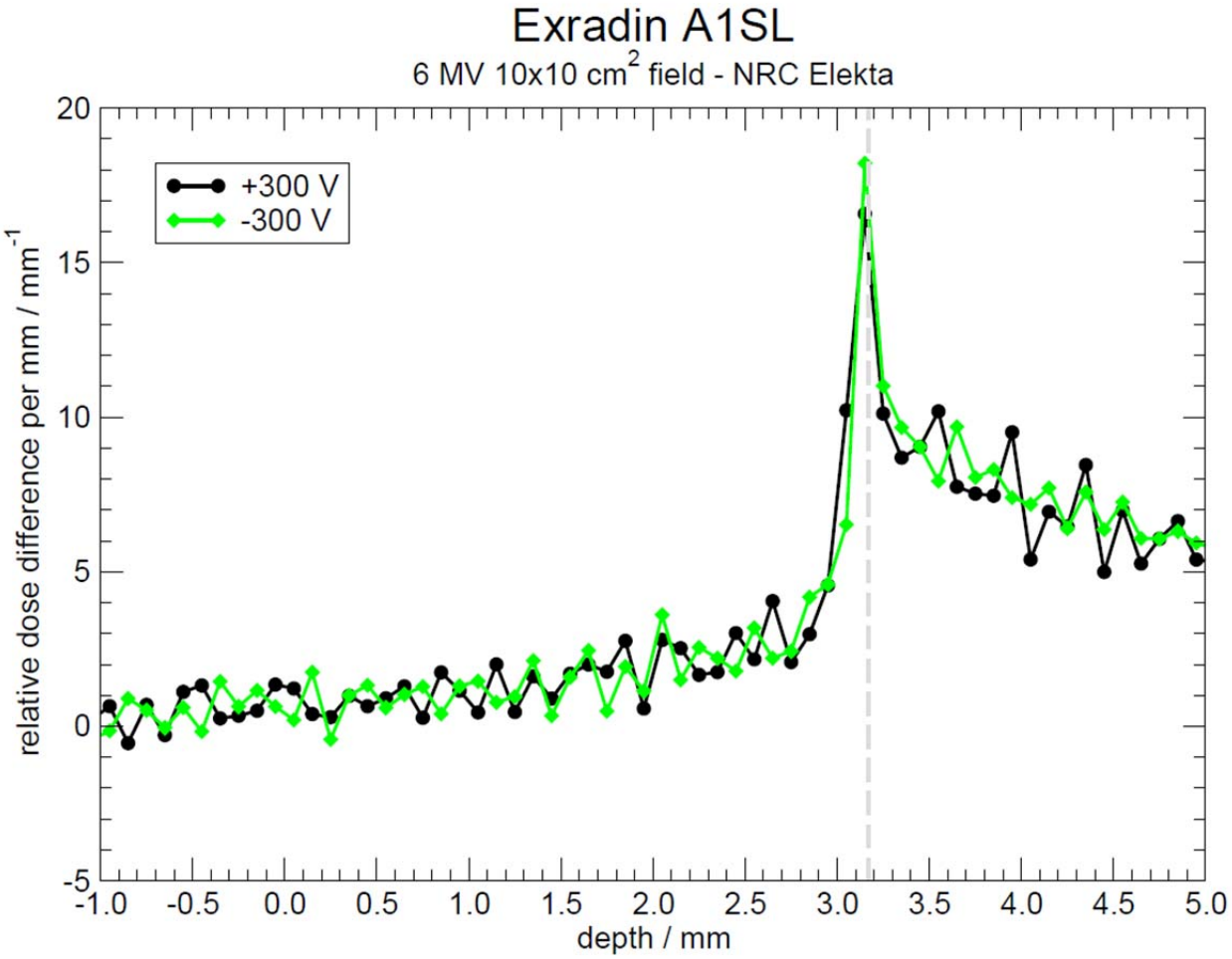

Figure 94: First derivatives of the scans shown in Figure 93. A bias voltage polarity switch has no effect on the location of the gradient peak.

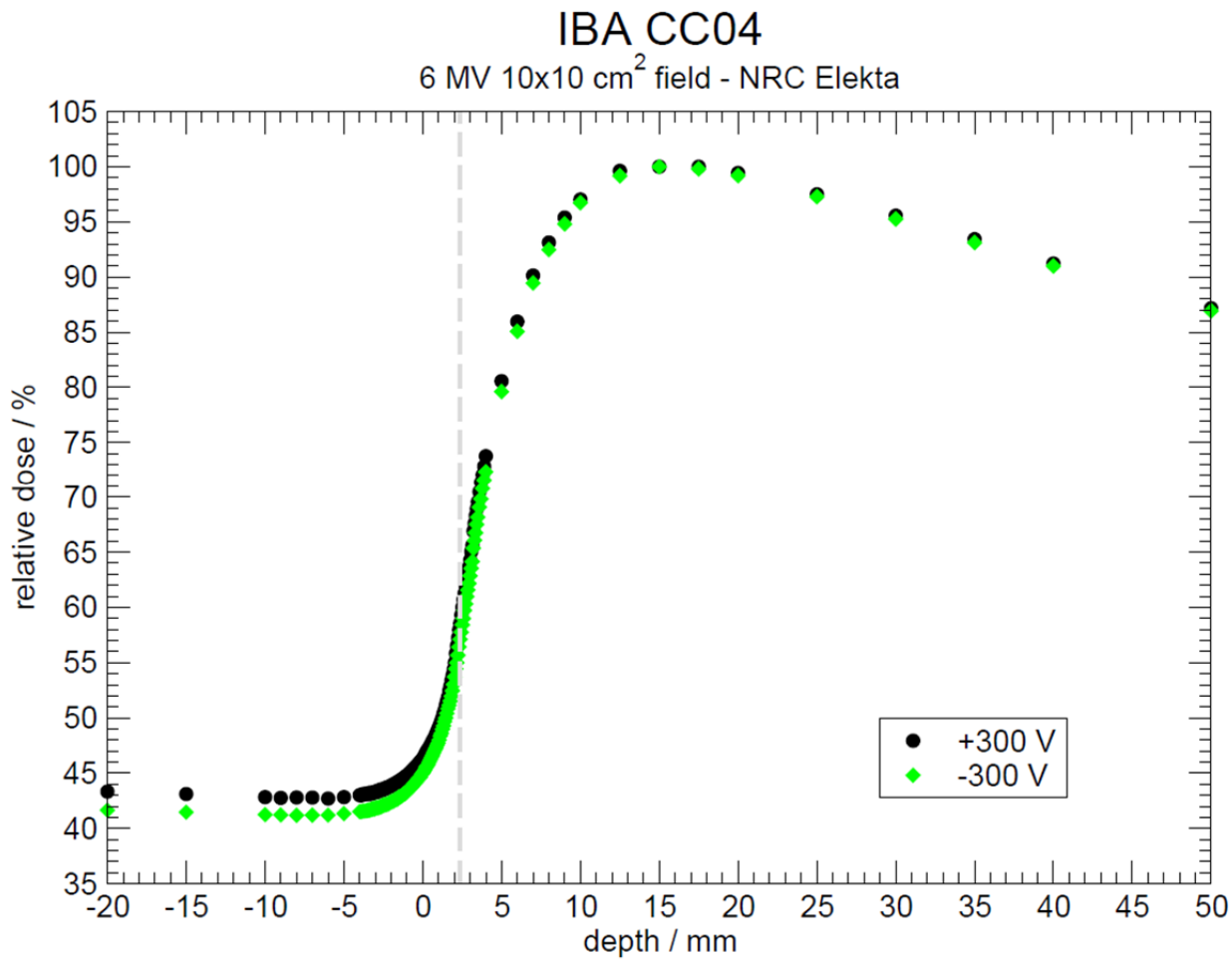

Figure 95: PDDs measured with the IBA CC04 in a 6 MV 10×10 cm^2 field using the NRC scanning system. Bias voltage polarity is switched between these scans causing a decrease in measured relative dose in the buildup region and in air.

Figure 95 shows the PDDs measured at the NRC with the IBA CC04. A larger polarity effect is observed for this IC than for the Exradin A1SL, as in-air dose differences reach ~5% at 20 mm above the water surface. Again, differences are negligible beyond d_{max}. Measurements are taken with 4 s/pt. sampling resolution. Scan spatial resolution varies but is 0.1 mm from 5 mm in water to 4 mm above the water surface. CC04 scan gradients are shown in Figure 96. Since the original scans failed to show convincing gradient peaks, an additional trial not shown in Figure 95 is shown here for illustrative purposes. The next-day scan is shifted 0.05 mm deeper than the original scans. The secondary gradient peak at 3.2 mm is caused by the

concentric insulation design of the CC04. The observed ~0.3 mm discrepancy between the observed gradient peaks and the DeICERS is caused by the shape of the collecting volume. The small CC04 active volume is more hemispherical than cylindrical. For truly cylindrical IC designs, the edge of the IC active volume meets the water surface all at once. In a hemisphere, each portion of the IC volume meets the water surface at a slightly different depth. This is discussed in Section 3.1. Other CC04 measurements are shown in Section 4.5. The results of the experiments shown here demonstrate that bias voltage polarity does not affect gradient peak location.

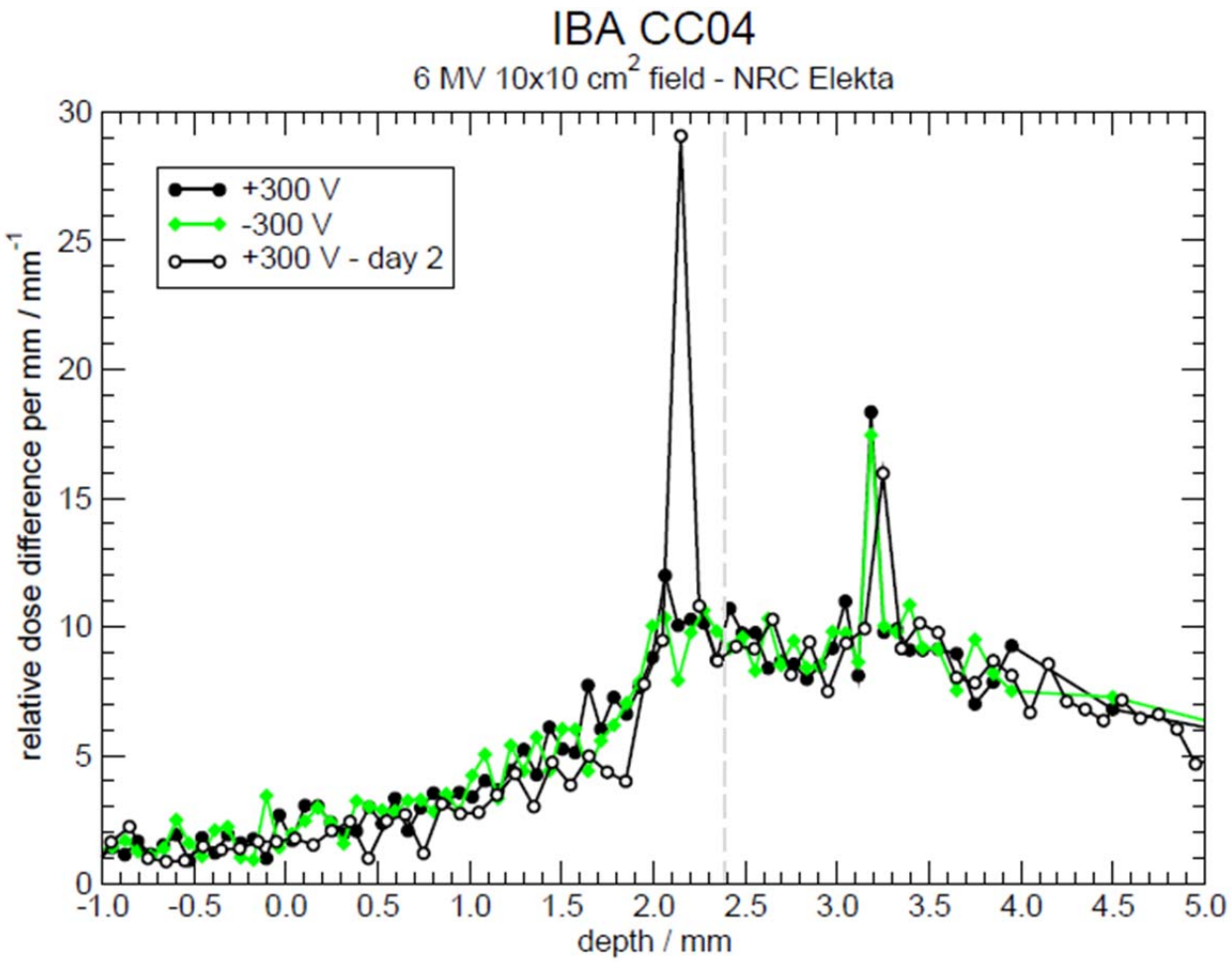

Figure 96: First derivatives of the scans shown in Figure 95. The switch in bias voltage polarity has no effect on gradient peak location. The secondary peak at 3.2 mm is an artifact of the concentric insulation design of the IBA CC04 consistent with other CC04 measurements. An extra trial at the original polarity is used to show the true gradient peak location as the early trials exhibited small peaks. The trial on day 2 is shifted 0.05 mm deeper than the trials on day 1.

4.3 Confounding Factors

In the following sub-sections, the evaporation and surface tension of the water in which all measurements are taken are discussed. If these measurement system properties are not properly accounted for, discrepancies in scan results can arise that would otherwise be unable to be properly accounted for.

4.3.1 Water Evaporation

Water evaporation is not of immediate concern in typical clinical PDD measurements, as individual measurements are usually done in a minute or less. However, for day-long (≥8 hr.) measurement sessions, or in cases where the water tank is set up at night and scanning is not performed until the next day, water level evaporation can affect measured PDDs. AAPM TG-106 recommends checking the water level at least once every ~6 hours (Das *et al.*, 2008). In this work, where individual scans taken at 0.1 mm resolution near the surface can require 15-20 minutes each, water evaporation is of particular concern.

4.3.1.1 Retrospective Correction Determination

A nominal water evaporation rate of 0.075 mm/hr. has been determined by filling the water tank to a known height (30 cm) then tracking the water level over a period of roughly 2 ½ weeks (>430 hours). The tank was left undisturbed during this time, so that evaporation was the only mechanism through which water could leave the tank. This is not the case in measurement scenarios, where water is removed from the tank in additional ways such as being wiped from an IC and/or IC holder being switched out of the tank or by being absorbed by a paper towel used to check SSD. Practical evaporation corrections are made in 0.1 mm increments because this is the finest resolution at which the IC can be moved using the IBA Blue Phantom. Though the sling

psychrometer described in Section 4.1.4 was not available for use during every measurement session, there are 47 relative humidity measurements accumulated representing 38 individual measurement sessions. The highest recorded relative humidity measurement is 55%, recorded for an April measurement session, while the lowest recorded measurement is 22%, for a March session. No seasonal trend in humidity is observed as the VCU treatment room atmosphere is maintained at the same generally ambient levels year-round. All relative humidity measurements are displayed in Figure 97. Where possible, the sling psychrometer measurements are compared with a digital display of relative humidity found on the wall of the treatment room.

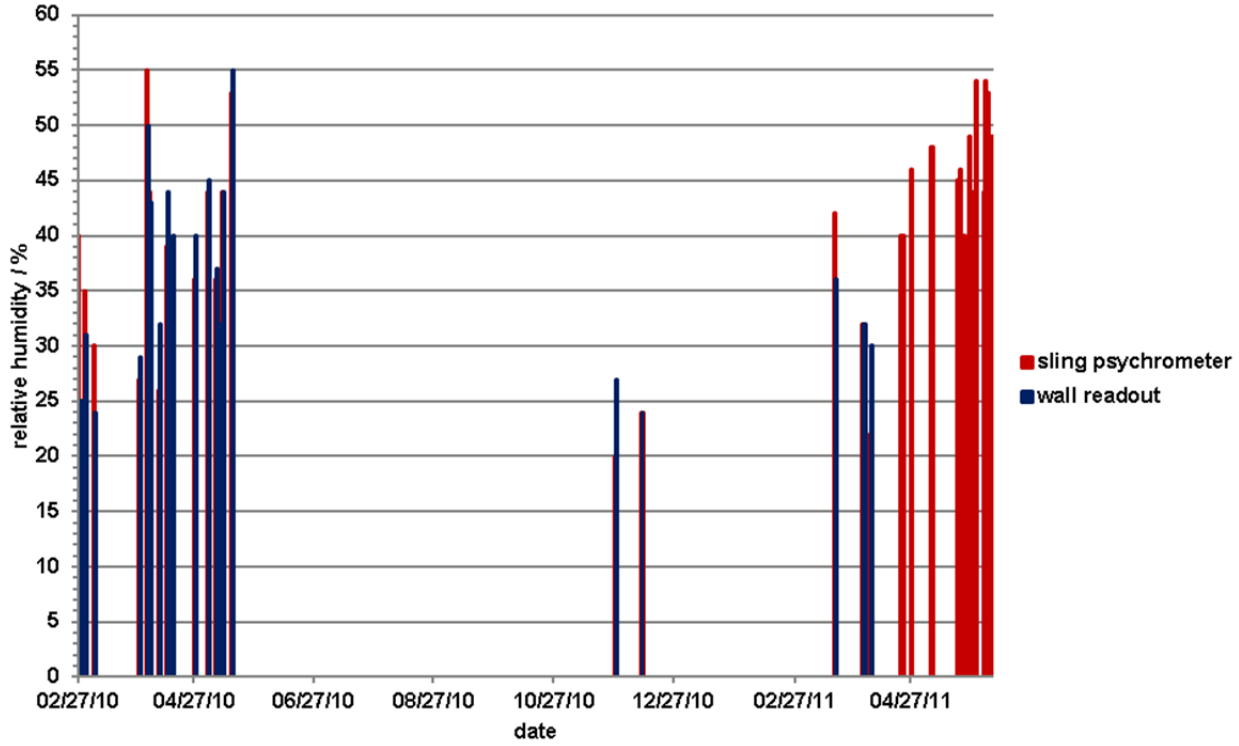

Figure 97: All 47 relative humidity measurements from 38 individual scanning sessions plotted over time. All readings are taken in-house inside a treatment room. The wall readout data comes from a digital display inside the treatment room. This display no longer shows relative humidity as of mid-April 2011.

The suitability of a retrospective evaporation correction is tested in the following way. First, the amount of theoretically predicted evaporation over the course of a given session must be calculated. This is done by multiplying the calculated nominal evaporation rate of

0.075 mm/hr. by the amount of time over which measurements are taken. The amount of time over which measurements are taken can be determined by independently recording the start and end time of each measurement session and computing the difference of the two. The OmniPro-Accept software records the timestamp of each measurement. The difference between the first and last scans of the session is then computed, with and without the evaporation correction applied. The scans are performed with the same IC without any setup changes having been performed between scans. Since scans may yield information at slightly different x-values for nominally identical scans, cubic splines of all three scans are computed. The splines for all three data sets are computed at the x-values of the first scan of the session. The first scan is subtracted from the spline of the last scan of the session and from the spline of the evaporation-corrected last scan of the session.

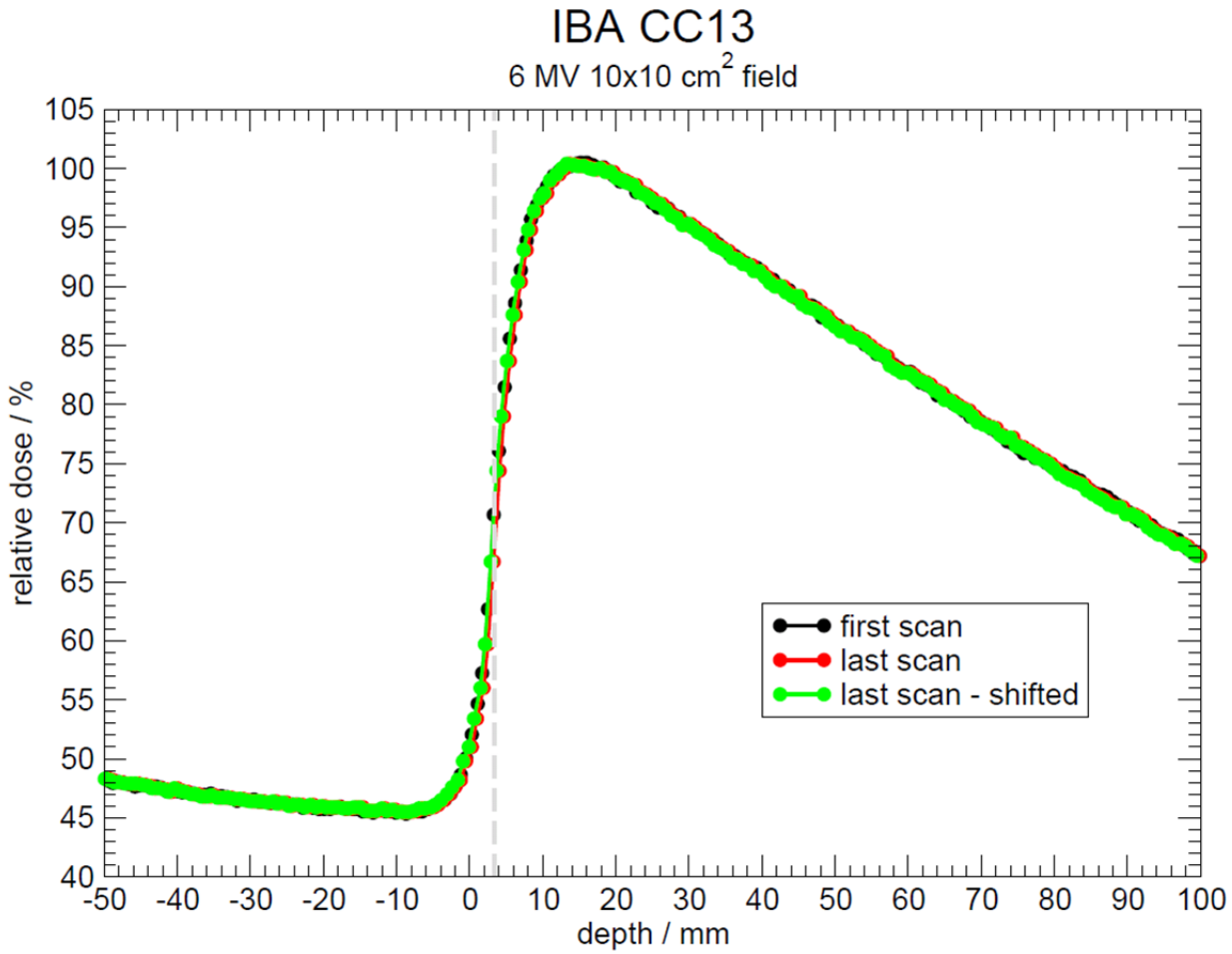

Figure 98: Test of the suitability of the evaporation corrections made for the measurements shown in Figure 62 through Figure 66. The first and last scans of this session are acquired in continuous mode at 15 mm/s with the IBA CC13 for a 6 MV 10×10 cm^2 field from the Varian 2100. The calculated evaporation correction amount, by which the last scan is shifted, is 0.4 mm. The evaporation shift represents an elapsed time between the first and last scans of 5.6 hours.

This process is demonstrated by example here. Figure 98 shows PDDs from the beginning and end of the session in which measurements testing scan speed are performed. The measurement session for which the intra-session evaporation is being tested here is described in Section 4.2.2.1. The calculated evaporation correction for the last measurement of this session is 0.4 mm. For this computational exercise, however, the full amount is tested. Over the depth range in Figure 98, evaporation-caused differences in the measured PDDs are barely observable as a 0.4 mm correction is difficult to notice over a range of 150 mm. Figure 99 shows the difference plots for the PDDs shown in Figure 98. The difference of the cubic spline of the last

scan from the first scan indicates differences within ±0.5% at most depths. Evaporation corrections are often not made for typical PDD scans, because the scanning is done in the course of a few hours and because 0.5% PDD differences are not typically deemed clinically relevant. At a depth of ~5 mm, however, a ~4.0% relative dose difference is observed over the course of the session for a 6 MV beam. With the evaporation correction applied, the relative dose at ~5 mm is not ~4% low but ~1% high. Application of the evaporation correction makes the observed inter-scan relative dose differences within ±1% at all depths.

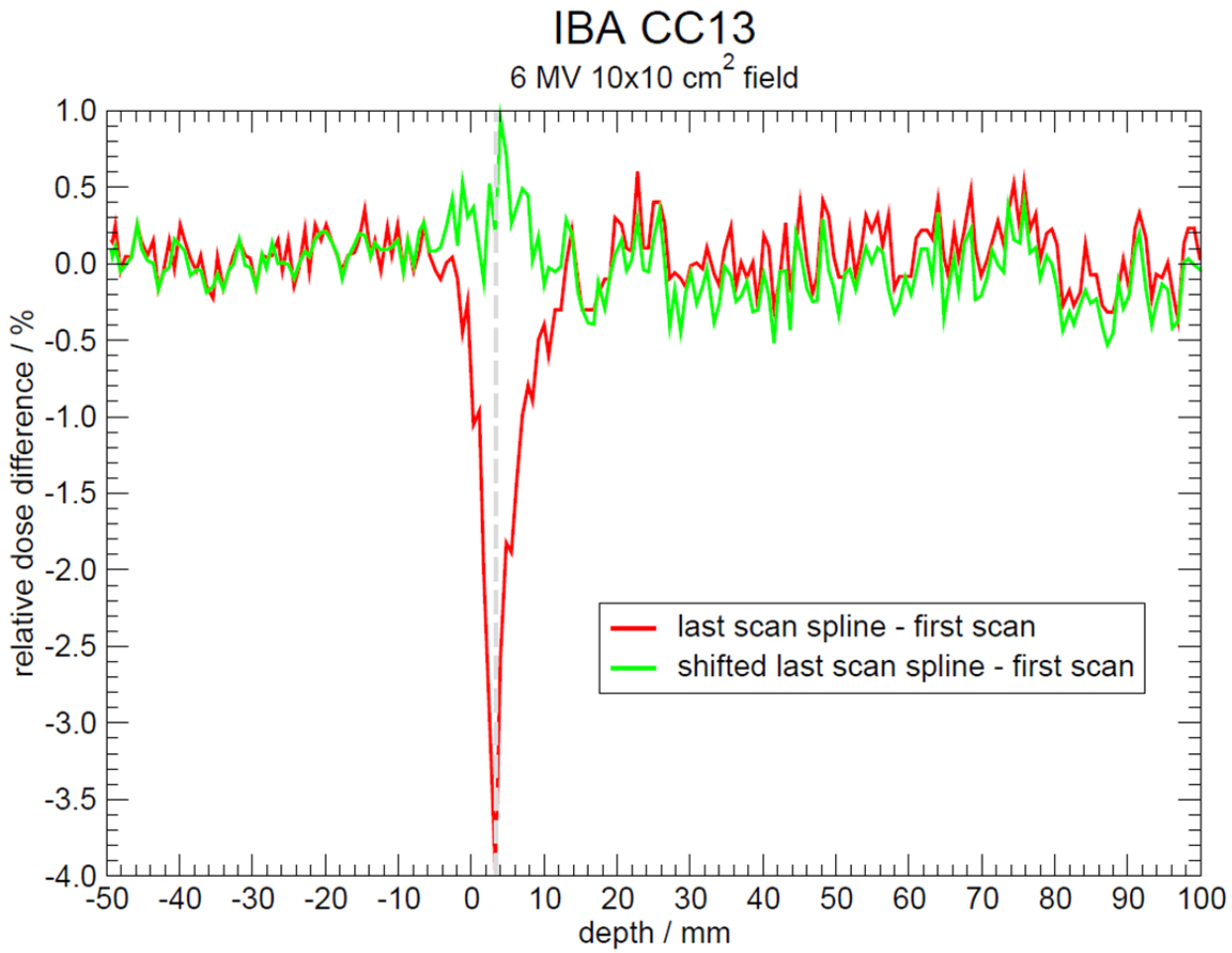

Figure 99: Cubic splines of the three PDDs shown in Figure 98 are computed at the measurement depths of the first scan. The original first scan is then subtracted from each spline function and the differences are plotted. The red line indicates that at most depths, the differences in measured relative dose caused by evaporation are within ±0.5%. Around the point at which the IC reaches the water surface, indicated by the grey dashed line, evaporation causes up to a 4% change in measured relative dose. When the calculated evaporation rate correction is made, inter-scan differences are within ±1% at all depths.

4.3.1.2 Inter-Scan Water Surface Location Correction

This method is used to track the water surface as water leaves the tank. Water can leave the tank by evaporating into the atmosphere or by being dried from equipment, soaked into a paper towel used to check SSD, or carried by the skin of a hand placed in the tank to make an adjustment. At the NRC, the water surface was tracked simply using the optical telescope and the alignment procedure described in Section 4.1.3. In-house measurements are corrected in cases where discrepancies are observed from scan-to-scan. In this case, the IC is moved to at least 15 cm depth, so that its presence near the surface does not bias observation. The IC is then re-aligned to the water surface, following the procedure recommended by TG-106 (Das *et al.*, 2008) shown in Figure 5. The IBA software records IC position relative to the user-defined isocenter. If the positional readout is observed to differ from the previously defined water surface, the new IC position is set as the new water surface location. Following this process, the water surface is consistently tracked at 0.1-0.2 mm intervals.

4.3.2 Water Surface Tension

In 1991, AAPM TG-25, a report on clinical electron beam dosimetry, acknowledged that water surface tension contributes to the difficulty in making measurements near a water surface (Khan *et al.*, 1991). Water surface tension is very closely related to scan direction due to the different ways in which water adheres to the IC as the IC passes through the water surface in either direction. Figure 100 displays both scenarios. In the left panel, an air pocket is formed below the nominal water surface when the IC is scanned from air into water. When the IC is scanned from water to air, water is pulled above the surface as shown in the right panel. Given that the radiation beam is incident from above the IC in all measurements, air replacing water between the IC and the radiation source is expected to have a significant effect on gradient peak

location. It is hypothesized that by reducing water surface tension, it should be possible to reduce the effect of scanning direction on the gradient peak location.

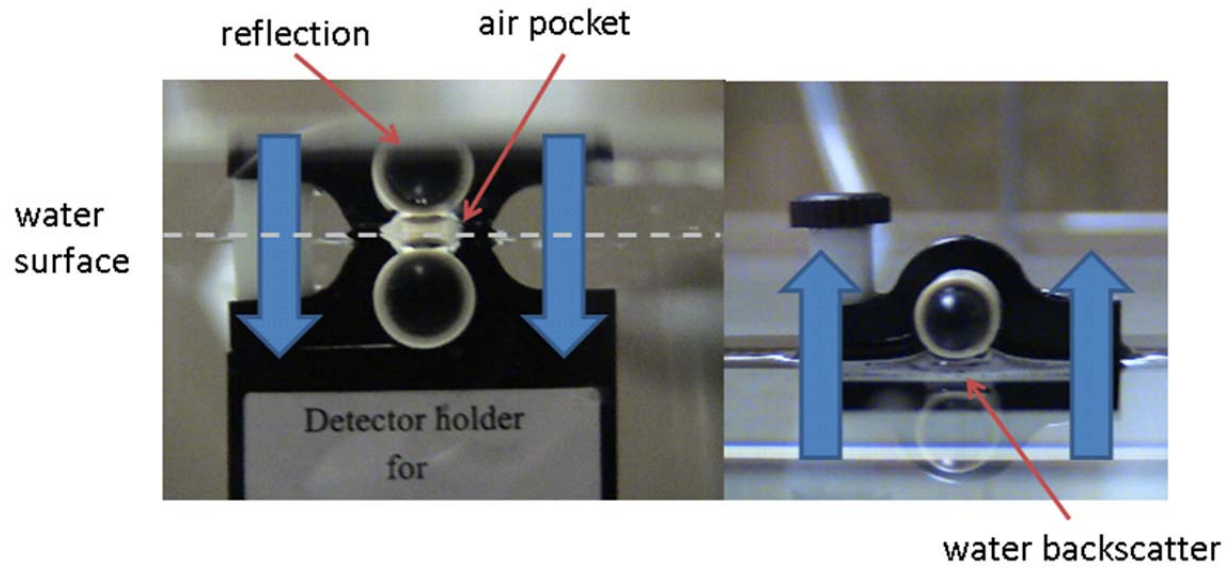

Figure 100: Photographs of the IBA CC13 cylindrical IC near the surface showing the two scenarios in which water surface tension has the potential to affect measured relative dose. In the left panel, the IC has been scanned from air into water, creating a small air pocket above the IC where water should be present. In the right panel, the IC has been scanned from water into air, pulling a small amount of water through the surface where air should be behind the IC. Given that the radiation beam is incident from above the IC in all measurements, the scenario depicted in the left panel is expected to have a larger effect on gradient peak location than the increased backscatter caused in the right panel.

There has been work published indicating a possibility of decreasing water surface tension through irradiation (Weon *et al.*, 2008) but the dose rate required to cause water surface tension reduction by this mechanism is much greater than is possible with the accelerators used in this work. In the work by Weon, *et al.*, a 2.5 GeV beam line is used where dose rates on the order of ~1000 Gy/s are produced. The baseline dose rate used is 3 Gy/s, or 1800 cGy/min, where no change in water surface tension is observed (Weon *et al.*, 2008). The highest dose rate achievable with a Varian 2300 accelerator is ~1000 cGy/min, assuming proper accelerator output calibration. It is known that water surface tension can be reduced by adding detergent to the water. The amount of surface tension reduction able to be achieved by the addition of detergent is tested first on a small scale, with a capillary tube in a glass cylinder, then on a larger scale in

the water tank. The surface tension of a given liquid can be calculated from the difference in heights of the liquid level in a capillary tube and a larger glass cylinder using the following relation (Batchelor, 1967).

$$\gamma = \frac{\rho g r d}{2 \cos \theta}$$

Here, γ is the surface tension term, measured in N/m, ρ is the material density measured in kg/m^3 (water = 1000; liquid soap ≈ 900), r is the capillary tube radius, (2.5 ± 0.5) ×10^{-4} m, d is the distance between the meniscus formed in the capillary tube and the liquid level in the cylinder, measured in m, and θ is the contact angle between the meniscus and glass side of the capillary tube. The water-glass contact angle has been found to be 0° at room temperature (Richards and Carver, 1921). A 0° contact angle indicates that the glass is strongly hydrophilic and the water is completely spread out on the glass surface. Liquid soap density is taken to be 0.9 g/cm^3 because it represents an effective average of the densities of two of the main ingredients of the soap used in this experiment, water and ethanol. Water has a known density of 1.0 g/cm^3 and the density of ethanol has been established as 0.79 g/cm^3 (Richards and Coombs, 1915). Soap is a type of surfactant, a material that reduces surface tension through adsorption at the liquid-gas interface. Surfactants are amphiphilic, meaning that one part of the surfactant molecule is hydrophilic and the other part is hydrophobic. The hydrophilic portion of the surfactant molecule will bond with water while the hydrophobic portion bonds with air (Hills, 1999). Through this bonding, or adsorption, the interfacial energy is reduced, which results in a reduction of surface tension (Hills, 1999).

4.3.2.1 Capillary Tube Measurements

The capillary tube used to take the initial surface tension measurements is a 25 cm long piece of glass of 0.5 cm outer diameter with an inner bore of 0.05 ± 0.01 cm diameter. This 20% uncertainty in the capillary tube bore dimension is the largest contributor to the uncertainty of the capillary tube surface tension measurements. The capillary tube is inserted into the inner bore of a rubber stopper, which is used to seal the top of a 3.5 cm inner diameter tabulated glass cylinder. Before sealing the cylinder, the cylinder must be filled with water. The water should be allowed to reach room temperature, as water surface tension is known to decrease with increasing temperature (Vargaftik *et al.*, 1983). Over the range of 15-30°C, the variation in accepted water surface tension values is ~3.2%. To force water into the capillary tube, a rubber bulb is affixed to the cylinder tabulation and squeezed until the water/detergent mixture has passed through the entirety of the capillary tube. Once the bulb has been squeezed fully enough, the liquid level within the capillary tube drops below the liquid level in the larger cylinder, then rises by capillary action to its final height at equilibrium caused by the surface tension of the solution. Liquid dishwashing detergent is added to the water via a syringe of 10 ml total volume, marked in 0.2 ml increments. The rubber stopper is dried and removed from the glass cylinder and detergent is plunged from the syringe into the cylinder. The detergent should be mixed with the water by gently swirling the cylinder. The rubber stopper is then re-fixed to the glass cylinder mouth and measurements are resumed. As the objective of the experiment is to establish how much reduction in water surface tension is possible, soap is added incrementally until it is apparent that no further surface tension reduction is being achieved. Other methods for measuring surface tension were considered but the capillary action method was chosen because

the author was allowed to borrow equipment from the VCU Department of Chemistry by Dr. Sally Hunnicutt.

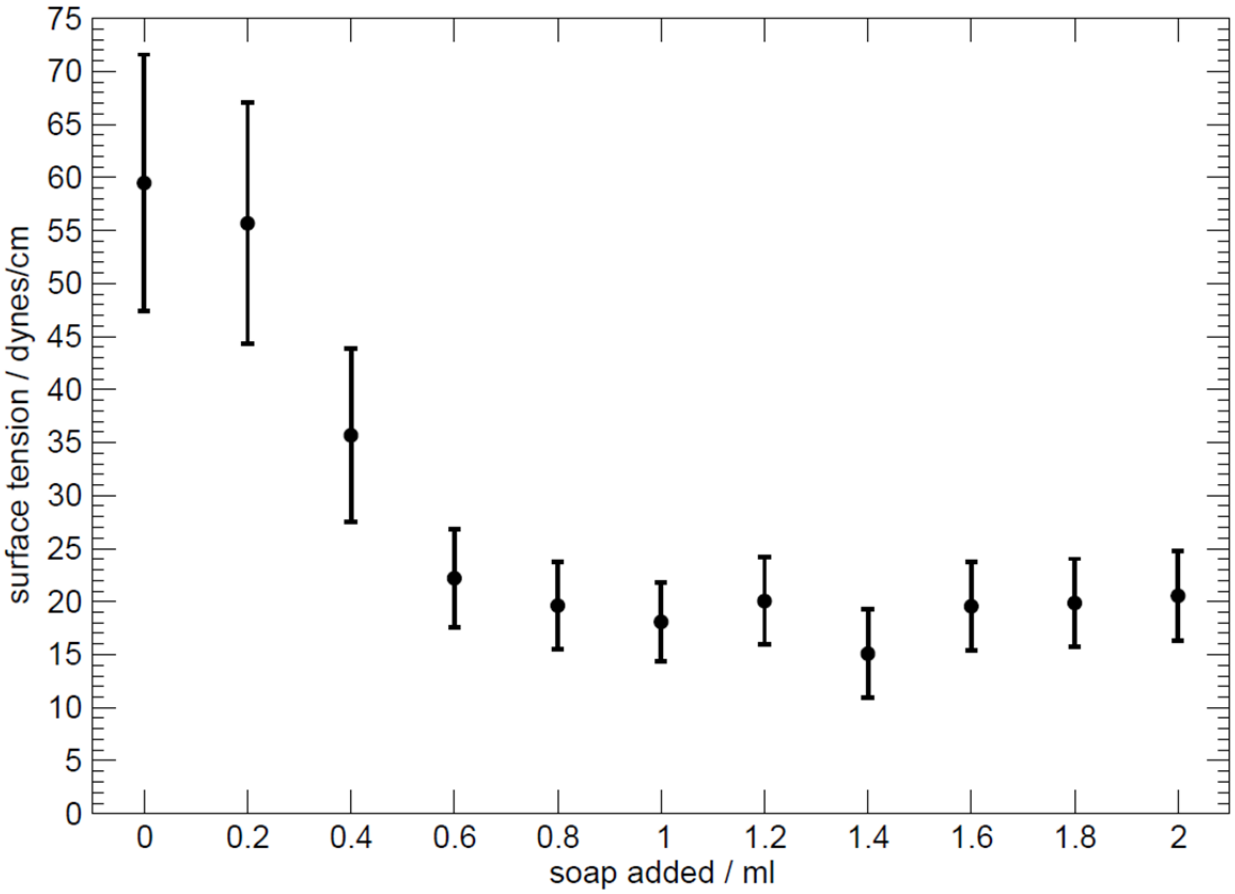

Figure 101: Capillary tube measurements of the reduction in water surface tension achievable by adding different amounts of liquid dishwashing detergent to the water. The most soap added here represents a 2.3% addition by volume to the water being tested. Error bars represent the total uncertainty budget, which is dominated by the 20% uncertainty in the capillary tube bore radius. All data points with soap added represent the average of ten measurements. Only nine trials are recorded for the measurement of water with no soap added. Surface tension is reduced to ~1/3 of its original value by adding 1 ml of soap to 86.6 ml of water but no additional reduction is achieved by doubling the soap volume.

Results of the capillary tube measurements are shown in Figure 101. Surface tension is reduced from 59.5 mN/m for water to 18.1 mN/m with 1 ml soap added to 88.6 ml of water but no further reduction is seen by doubling the amount of liquid detergent added. The surface tension calculation assumes the solution density is held at 1.0 g/cm^3 throughout all trials. Adding 2 ml soap to the water represents a 2.3% increase in the total volume of the solution, which corresponds with a <0.5% adjustment in the solution density. All data points with soap

added represent the average of ten trials. Without soap, nine trials are recorded. The size of the error bars represents the overall uncertainty in the experiment, assuming 0.5% uncertainty in solution density, accounting for the standard deviation of individual measurements (Type A uncertainty) as well as the 0.1 cm increment on the capillary tube scale (Type B), and the 20% manufacturer-quoted uncertainty in the capillary tube bore.

4.3.2.2 Ionization Chamber Scans

It is found from the capillary tube measurements described in Section 4.3.2.1 that 1 ml of soap is required to achieve maximal surface tension reduction for the tested water volume of 86.6 ml. To maintain this soap/water proportion in the water tank, which is filled with ~113 L of water, 1.3 L of soap is added to the water tank. Dispersion of the soap throughout the water is visually confirmed by noting the color change of the tank contents. Scans are taken at 0.1 mm nominal resolution for 10×10 cm^2 and 40×40 cm^2 fields, each at 6 and 18 MV incident photon beam energy, between 20 and -10 mm for 6 MV scans and between 30 and -10 cm for 18 MV scans, with and without soap added to the water.

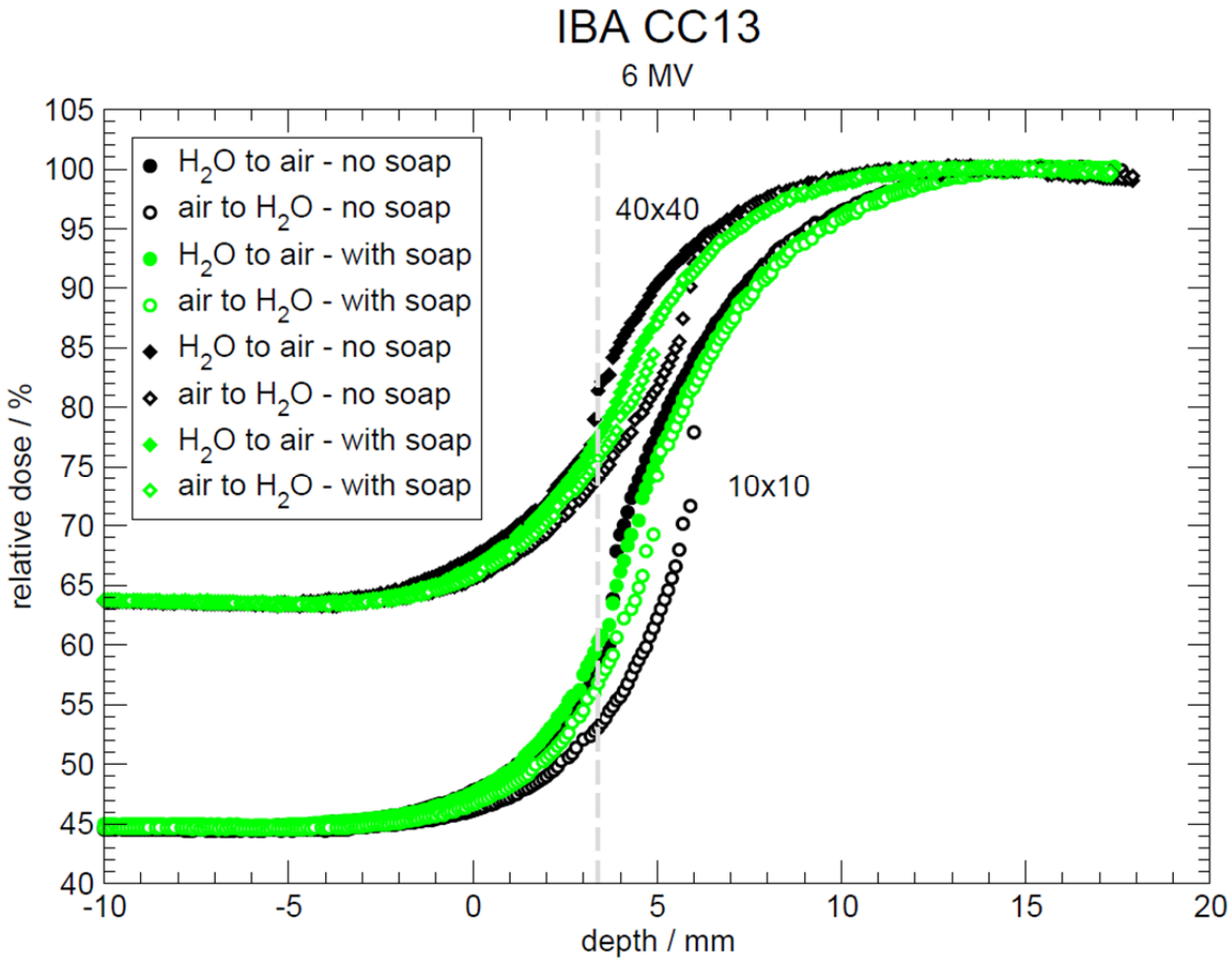

Figure 102: PDDs measured with the IBA CC13 for the Varian 2300 6 MV beam at 10×10 and 40×40 cm^2 fields. For both fields, scans are conducted at 0.1 mm resolution through the air/water interface in both directions with and without dishwashing detergent added to the water. At each depth, 50 readings are made over a 1 s period and the resulting average is displayed. Adding dish soap to the water reduces, but does not eliminate, differences in the measured relative dose depending on the direction in which the IC is passing through the water surface. A possible misalignment of the IC when acquiring the 10×10 cm^2 field scan without soap is also indicated. The grey dashed line marks the DeICERS when scanning from water to air and the depth at which the IC should first be fully submerged when scanning from air to water.

The 6 MV scan data is shown in Figure 102. As with the capillary tube measurements, adding soap reduces water surface tension such that differences between water-to-air and air-to-water scans are reduced, but these differences are not eliminated. The grey dashed line represents the DeICERS when scanning from water to air and the point at which the IC should be fully submerged when scanning from air to water. Direction-dependent scan differences to the right of this line indicate that in practice, the IC is not fully submerged at this location when

scanning from air to water. The first derivatives of the 6 MV scans are shown in Figure 103. The distance of the gradient peak for the water-to-air 10×10 cm^2 scan without soap from the dashed grey line, the DeICERS, indicates a possible misalignment in this scenario. The objective of this particular experiment was not exact alignment but an evaluation of the effect of water surface tension on scanning. The largest gradient peak observed is for the air-to-water 10×10 cm^2 scan without soap, at 5.95 mm, indicating that without soap present, the IC travels over 2 mm below the water surface before the air pocket developing behind the IC breaks, restoring the water surface to its previous location. An investigation of the impact of scan direction on measured results is discussed in Section 4.2.1. The water-to-air scans with soap added indicate no definitive gradient peaks but both air-to-water scans exhibit gradient peaks at 4.95 mm, meaning that scan direction-dependent differences are overcome 1 mm shallower in the water with soap present in the tank than without.

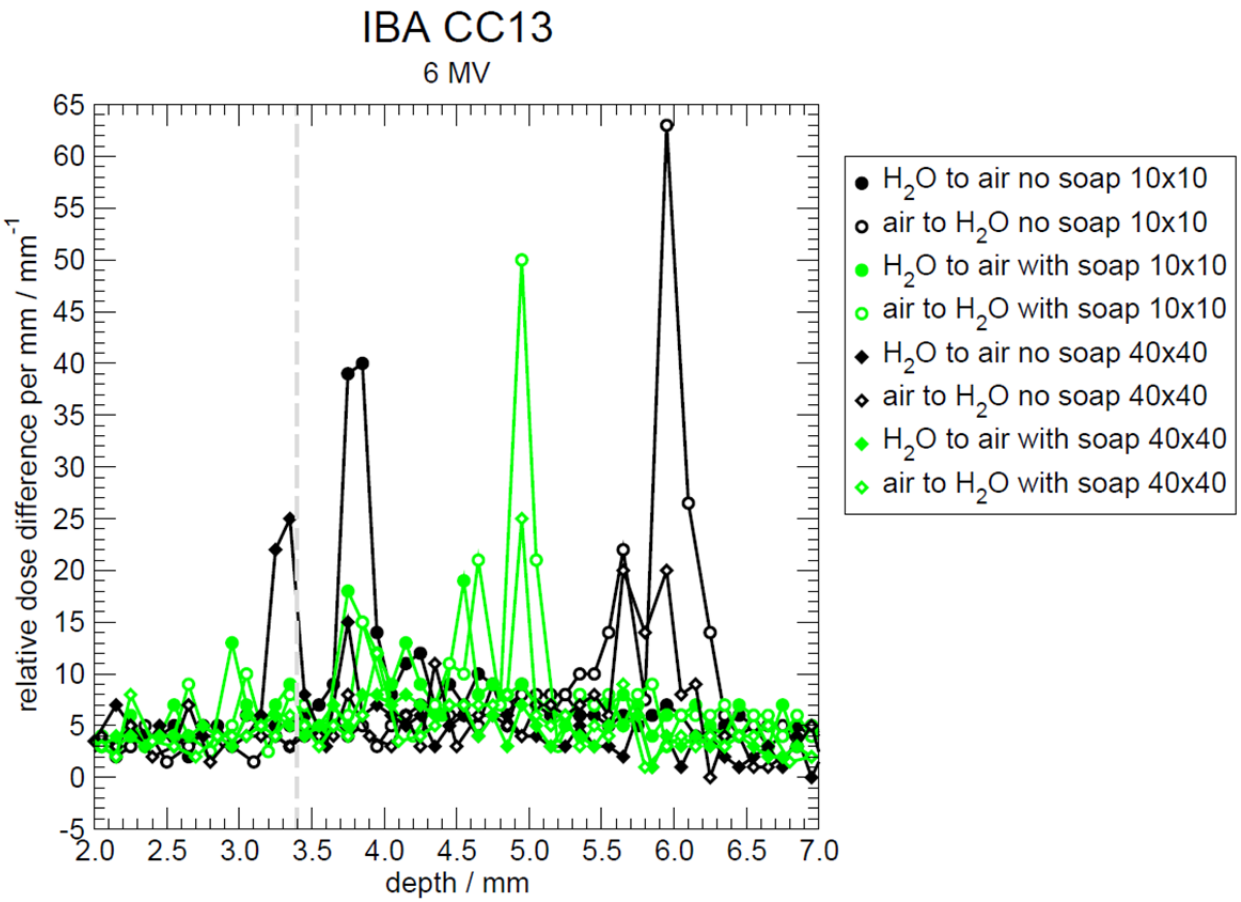

Figure 103: First derivatives of the scans shown in Figure 102. The distance from the solid black data points to the dashed grey line indicates that the 10×10 cm^2 field scan without soap may have been misaligned, though the observed discrepancy is still within 0.5 mm. When scanning from air to water, the gradient peak occurs deeper in the water than when scanning from water to air due to the water surface being displaced below its nominal location by the IC. The grey dashed line represents the DeICERS for water-to-air scans. Adding dishwashing detergent to the water shifts the air-to-water gradient peak closer to the water surface. When scanning from water to air with soap added, no definitive gradient peak is observed.

The 18 MV scans are shown in Figure 104. These scans all indicate good alignment as evidenced by the with-soap scan differences being visibly bounded by the without-soap scan differences. Alignment is further examined by looking at the scan derivatives, shown in Figure 105. The water-to-air 10×10 cm^2 scan without soap here is better aligned than its 6 MV counterpart, as indicated by the gradient peak lying closer to the dashed grey line. As in Figure 103, both air-to-water scans with soap added exhibit gradient peaks at 4.95 mm, indicating consistency of the effect of adding soap with incident beam energy and field size. The gradients of three trials from soapy water to air under each set of radiation field conditions previously

described in this section are averaged and displayed in Figure 106. The measurement noise within these three trials does not allow a definitive conclusion about the existence, or lack thereof, of a gradient peak for these scans. These measurements suffered from the positioning inconsistencies discussed in Section 4.2.1. The averaged scans shown in Figure 106 are downsampled to 0.5 mm resolution and re-plotted in Figure 107. Here, a gradient peak is indicated 0.9 mm deeper than the DeICERS. The discrepancy between gradient peak and DeICERS location is partially caused by the relatively coarse scan resolution, as shown in Section 4.2.3. More trials at finer sampling resolution are required to establish the gradient peak definitively for scans with soapy water. It may be that the soap increases slippage of the stepper motors and drive belts within the tank.

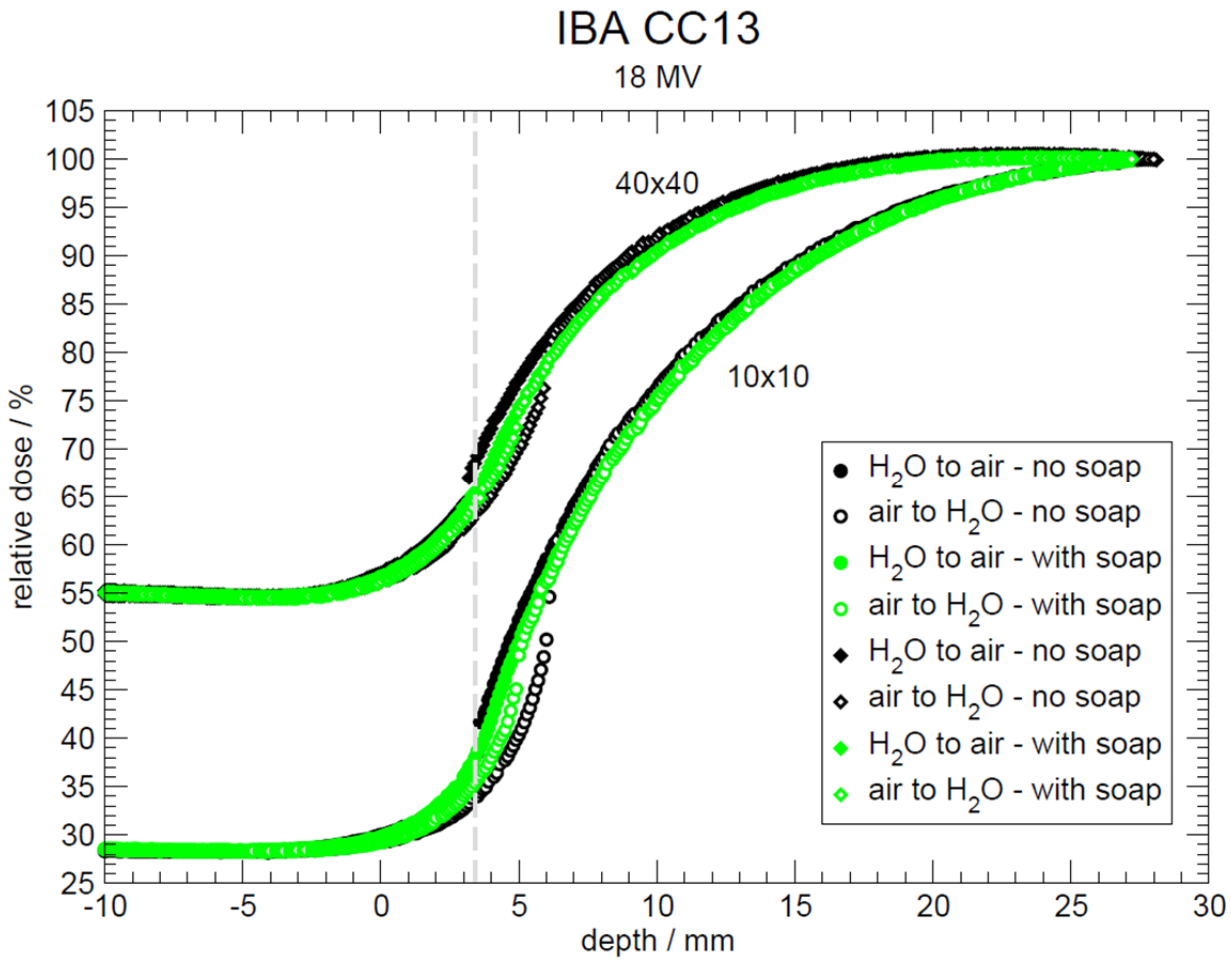

Figure 104: PDDs measured with the IBA CC13 for the Varian 2300 18 MV beam at 10×10 and 40×40 cm^2 fields. For both fields, scans are conducted at 0.1 mm resolution through the air/water interface in both directions with and without dishwashing detergent added to the water. At each depth, 50 readings are made over a 1 s period and the resulting average is displayed. Adding dish soap to the water reduces, but does not eliminate, differences in the measured relative dose depending on the direction in which the IC is passing through the water surface. The grey dashed line marks the DeICERS when scanning from water to air and the depth at which the IC should first be fully submerged when scanning from air to water.

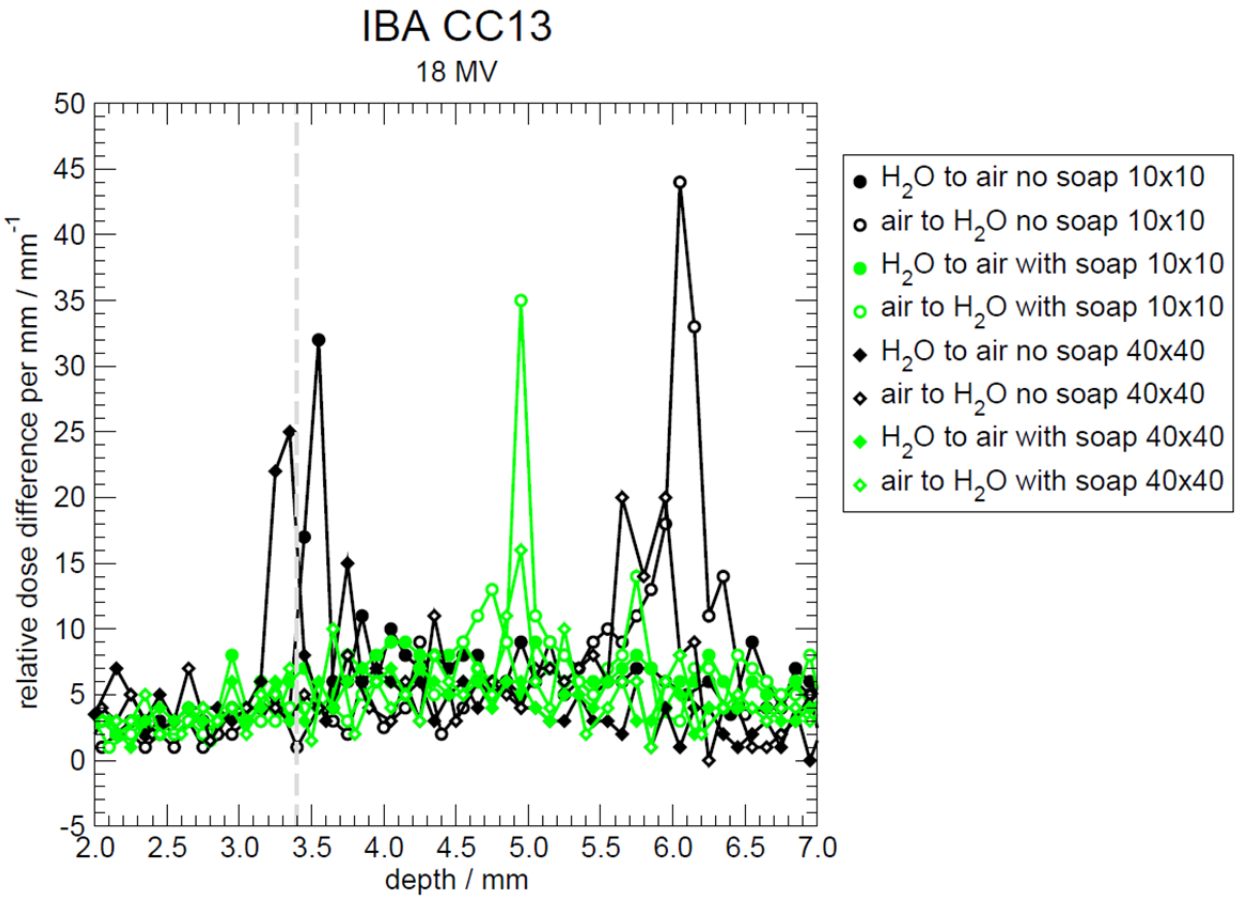

Figure 105: First derivatives of the scans shown in Figure 104. When scanning from air to water, the gradient peak occurs deeper in the water than when scanning from water to air due to the water surface being displaced below its nominal location by the IC. The grey dashed line represents the DeICERS for water-to-air scans. Adding dishwashing detergent to the water shifts the air-to-water gradient peak closer to the water surface. When scanning from water to air with soap added, no definitive gradient peak is observed.

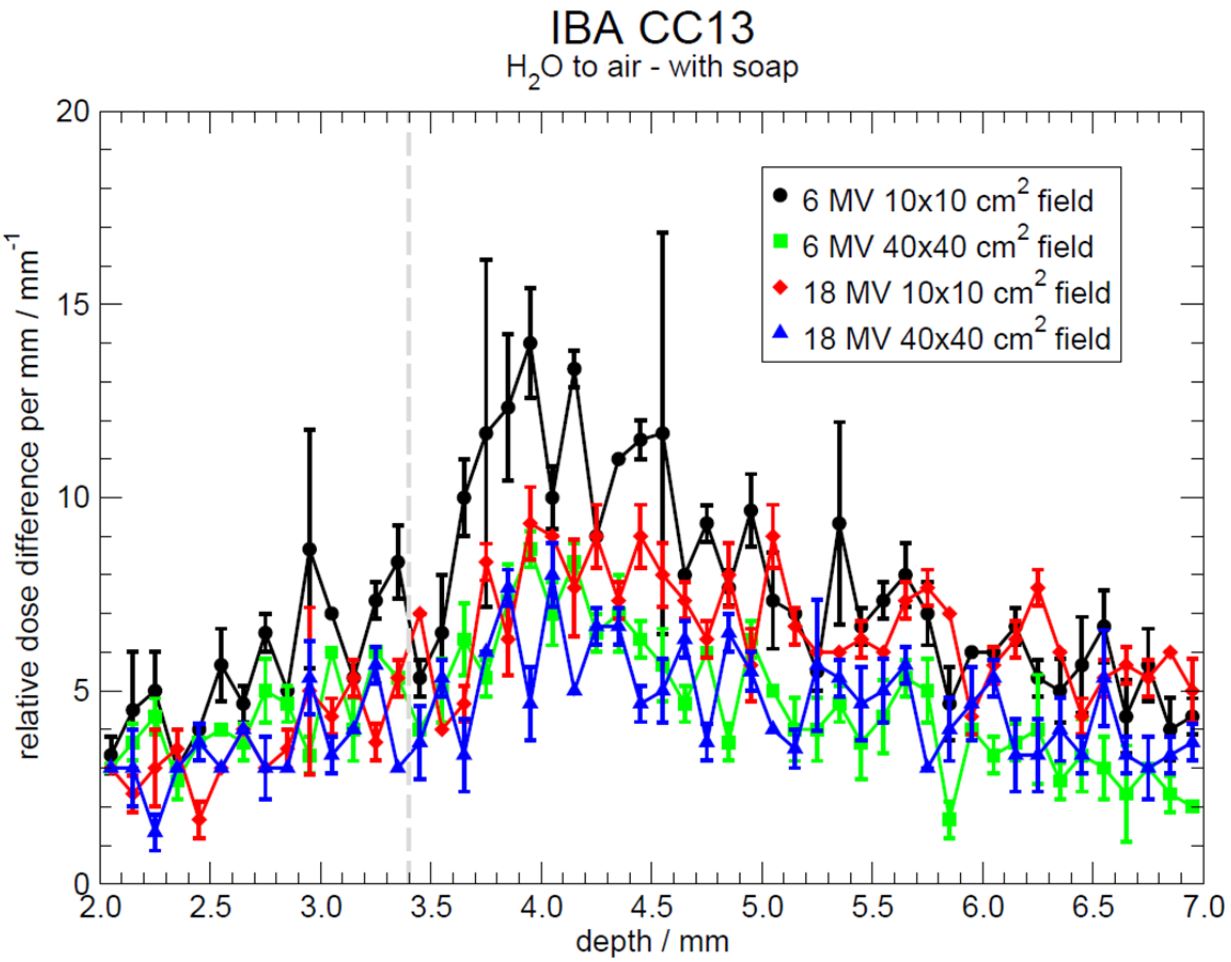

Figure 106: First derivatives of three repeated trials from water to air with soap added to the water tank under various radiation field conditions. The data shown here include the water-to-air scans with soap shown in Figure 103 and Figure 105. Measurement noise is too great to establish a gradient peak, or the lack thereof, definitively.

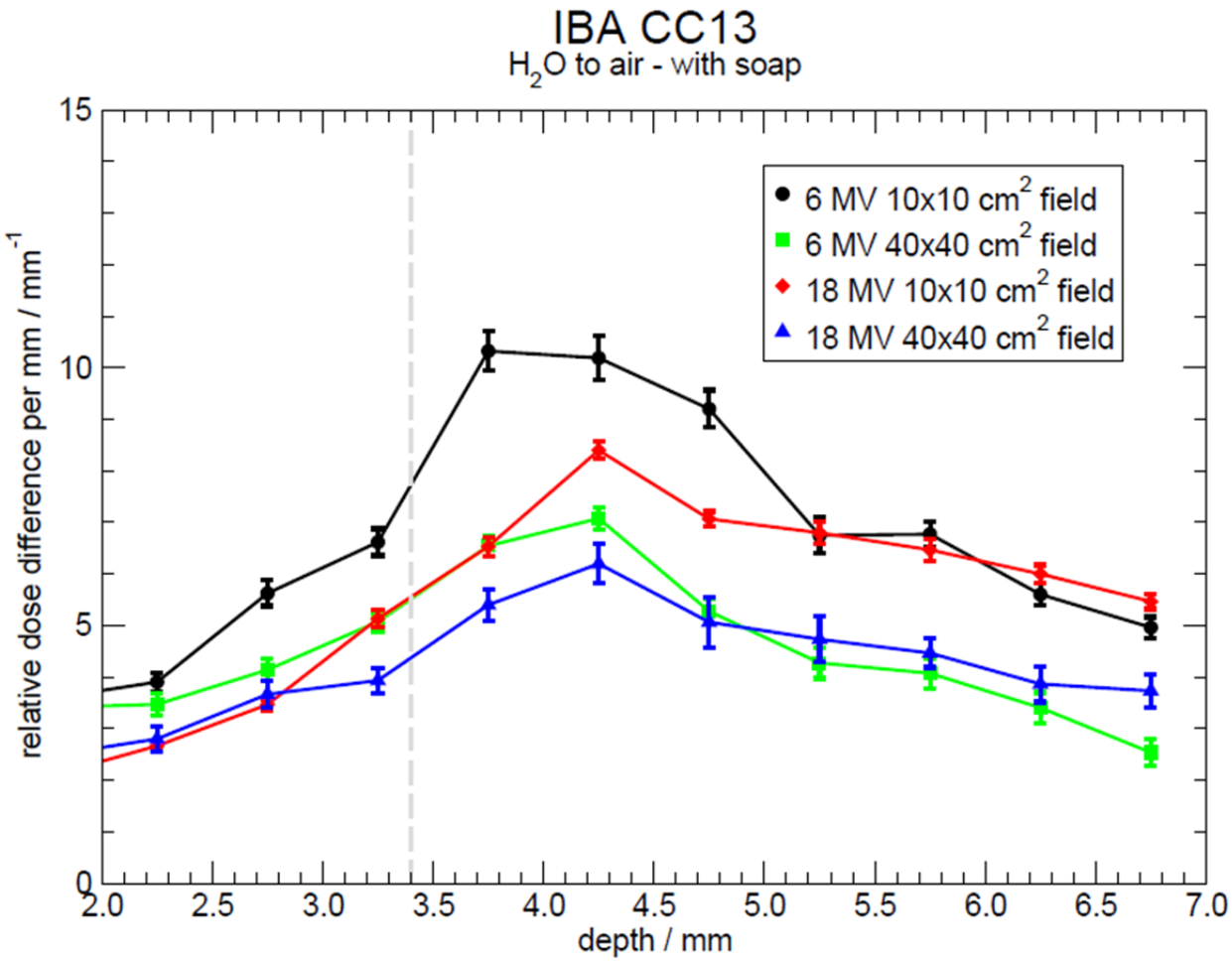

Figure 107: Data from Figure 106 downsampled to 0.5 mm resolution. A gradient peak is indicated 0.9 mm deeper in water than the DeICERS. The discrepancy between gradient peak and DeICERS location is partially caused by the scan resolution as shown in Section 4.2.3.

4.3.2.3 Conclusions

Liquid dishwashing detergent is useful to reduce water surface tension; however, surface tension cannot be completely eliminated. Adding soap appears to eliminate the gradient peak when scanning from water to air. When scanning from air to water, soap shifts the gradient peak ~1 mm closer to the water surface. Given that the gradient peaks observed in scanning from air-to-water even after adding soap are still ~1.5 mm deeper than the DeICERS when scanning from water to air, it is recommended that scans be performed only from water to air. This finding is in agreement with AAPM TG-70, which recommends scans in water to be directed toward the

surface to "reduce the effect of meniscus formation" (Gerbi *et al.*, 2009). Since the reduction in water surface tension caused by adding soap to the water greatly reduces the gradient peak when scanning from water to air, it is additionally observed that adding soap to water provides no actual benefit for this method. Therefore, the use of soapy water in depth dose measurements is expressly not recommended.

4.4 Radiation Field Dependencies

Previous work (Ververs *et al.*, 2009b) indicated no dependence at the 0.5 mm level on photon beam energy, field size, or electron contamination for measurements performed with a single IC on a single accelerator. In this section, the examination of radiation field dependencies is expanded to include multiple accelerator types, particle types, field sizes, SSDs, and contaminant electron amounts.

4.4.1 Beam Type and Energy

In this section, three comparisons are made. All measurements described in this section are made with the IBA CC13 cylindrical IC. First, measurements made under the same nominal radiation field conditions, 6 MV 10×10 cm^2 field 100 cm SSD, from two accelerator types are compared. VCU measurements from the Varian 2300 with the IBA Blue Phantom are compared with NRC measurements from the Elekta Precise taken with the customized high-precision scanning system. The second test compares Varian 2300 measurements for the minimum and maximum electron beam energies, 6 and 20 MeV. The electron measurements are also taken for a 10×10 cm^2 field at 100 cm SSD. Finally, measurements of incident beams of different particle types are directly compared. Measurements on the Varian 2300 are taken for a 6 MV photon beam and a 6 MeV electron beam. Both measurements are taken for a 10×10 cm^2 field at

100 cm SSD. All VCU measurements are taken at 0.1 mm resolution from 5 mm depth in water to 1 mm above the water surface. The NRC measurement is taken at 0.1 mm resolution from 5 mm depth in water to 5 mm above the water surface.

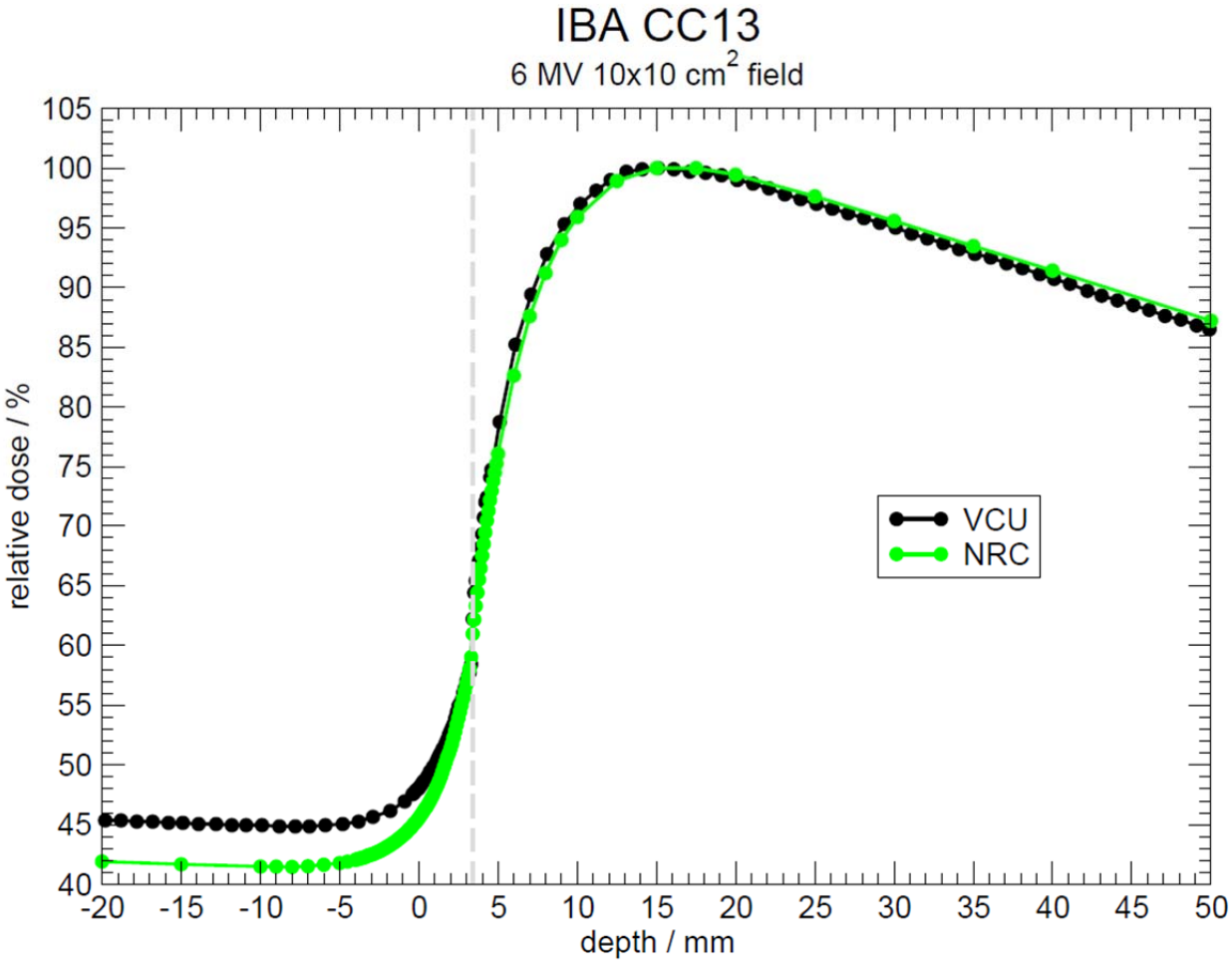

Figure 108: Comparison of the VCU Varian 2300 6 MV beam with the NRC Elekta Precise 6 MV beam. The Elekta accelerator produces fewer electrons in air, which results in a ~7% difference in measured dose in air. The difference could also be at least partially caused by a small difference in the wall thicknesses of the IBA CC13 models used to take measurements at VCU and the NRC, respectively.

Figure 108 shows the PDDs for the inter-accelerator comparison. The ~7% dose decrease for the NRC measurement compared with the VCU measurement from 10 to 20 mm above the water surface in air shows either that the Elekta accelerator produces fewer electrons in air than the Varian accelerator or a difference in treatment head components between the two accelerator types. Measurements were taken at each location with different CC13 models, so the

difference could also be partially caused by small variations in IC wall mass density. The accompanying gradients are shown in Figure 109. Both gradient peaks occur at the same location, 0.05 mm shallower than the DeICERS. The difference in gradient peak and DeICERS locations is within measurement uncertainty. The customized scanning system reduces the measurement noise compared with the VCU measurement noise.

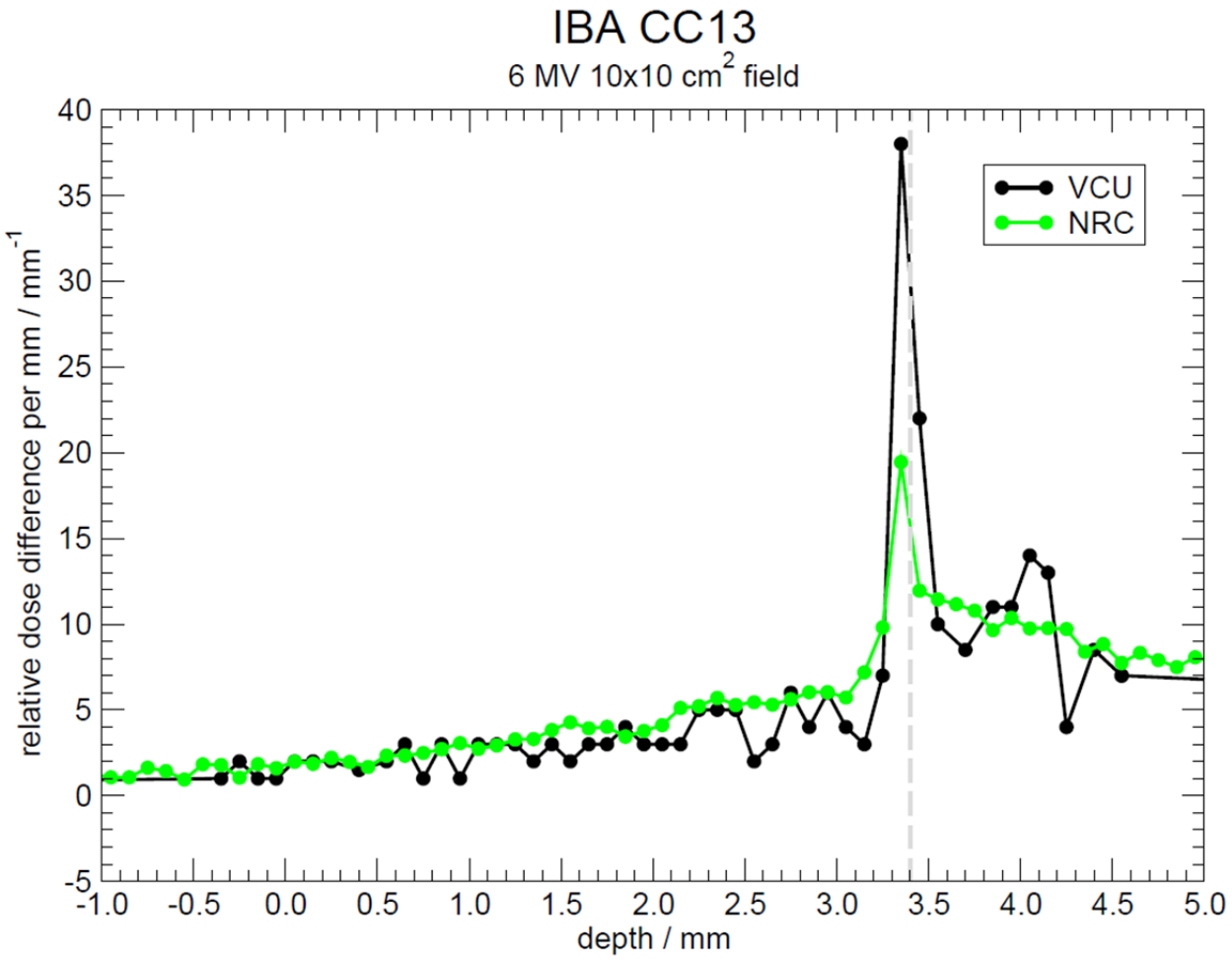

Figure 109: First derivatives of the scans shown in Figure 108. Both gradient peaks occur at the DeICERS, as denoted by the grey dashed line.

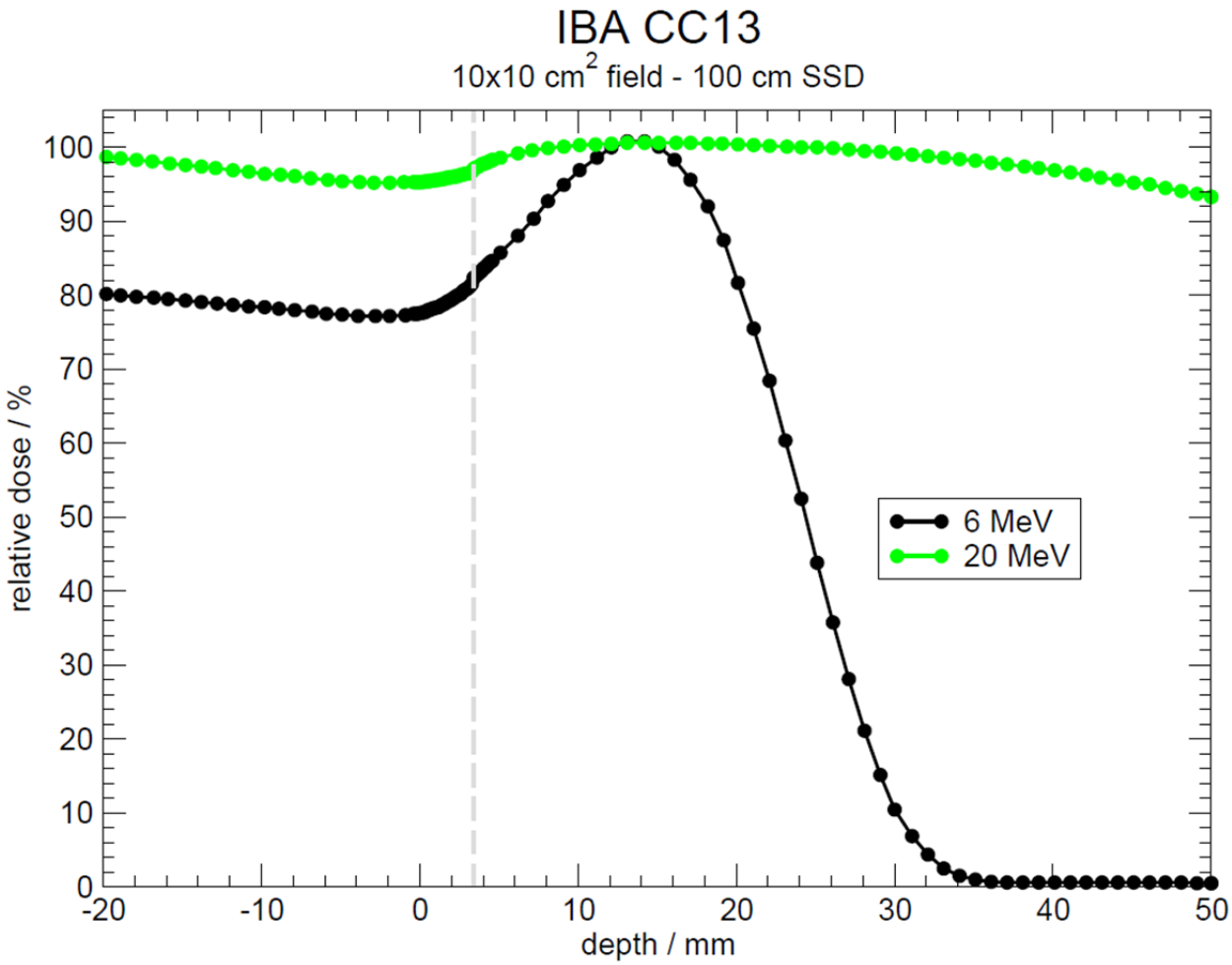

Figure 110: PDD comparison for a change in incident electron beam energy under otherwise identical measurement conditions. Measurements are acquired from the Varian 2300 with the IBA Blue Phantom.

Figure 110 shows PDDs for the electron beam energy comparison. Again, the grey dashed line indicates the IC central axis location at which the IC proximal edge should reach the water surface for a well-aligned measurement. It is clear that the PDD gradient is steeper near the grey dashed line for the 6 MeV scan than the 20 MeV scan. This is borne out in Figure 111. Both gradient peaks occur 0.05 mm shallower than the DeICERS, which is within measurement uncertainty.

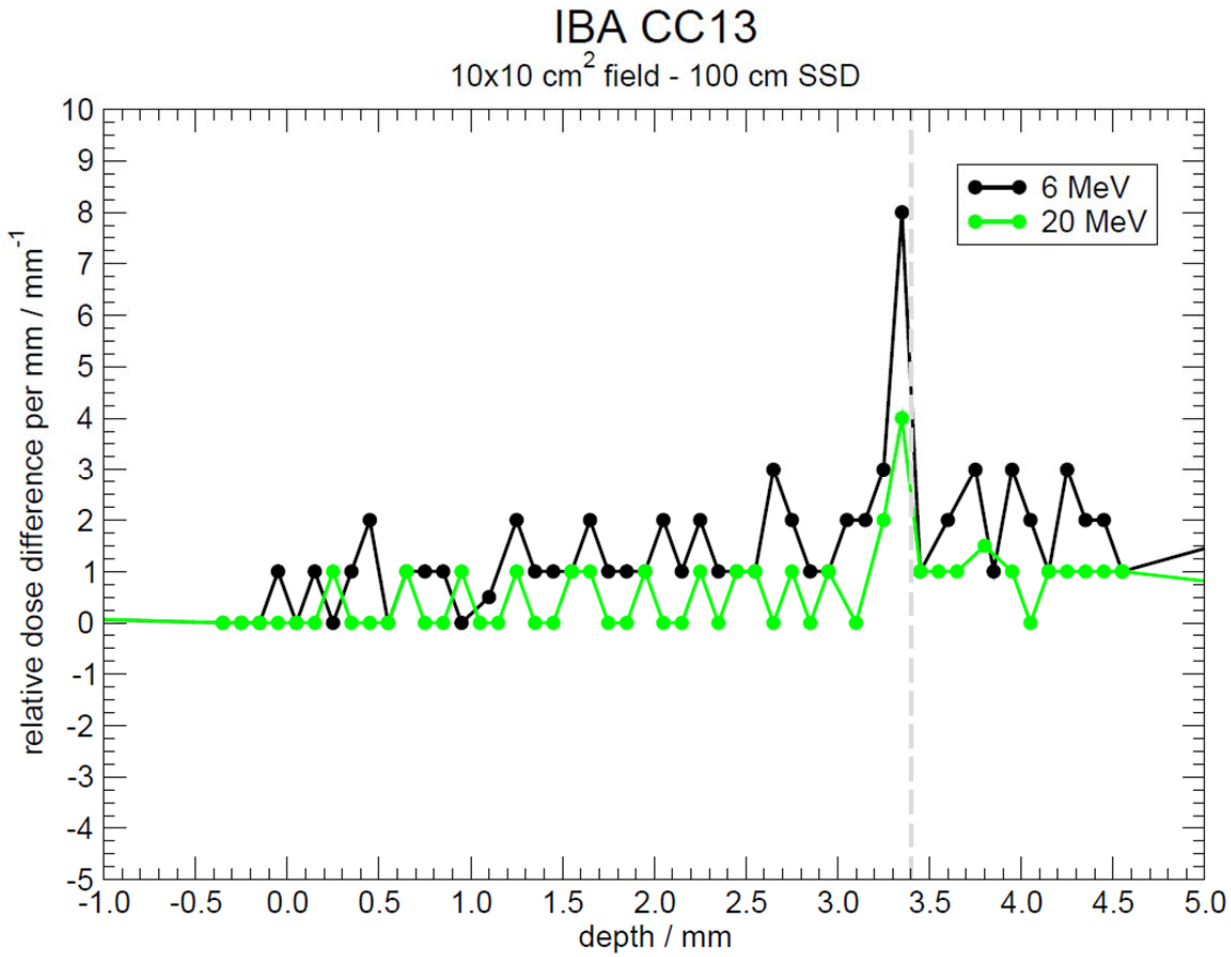

Figure 111: First derivatives of the scans shown in Figure 110. Gradient peak location is invariant with incident electron beam energy.

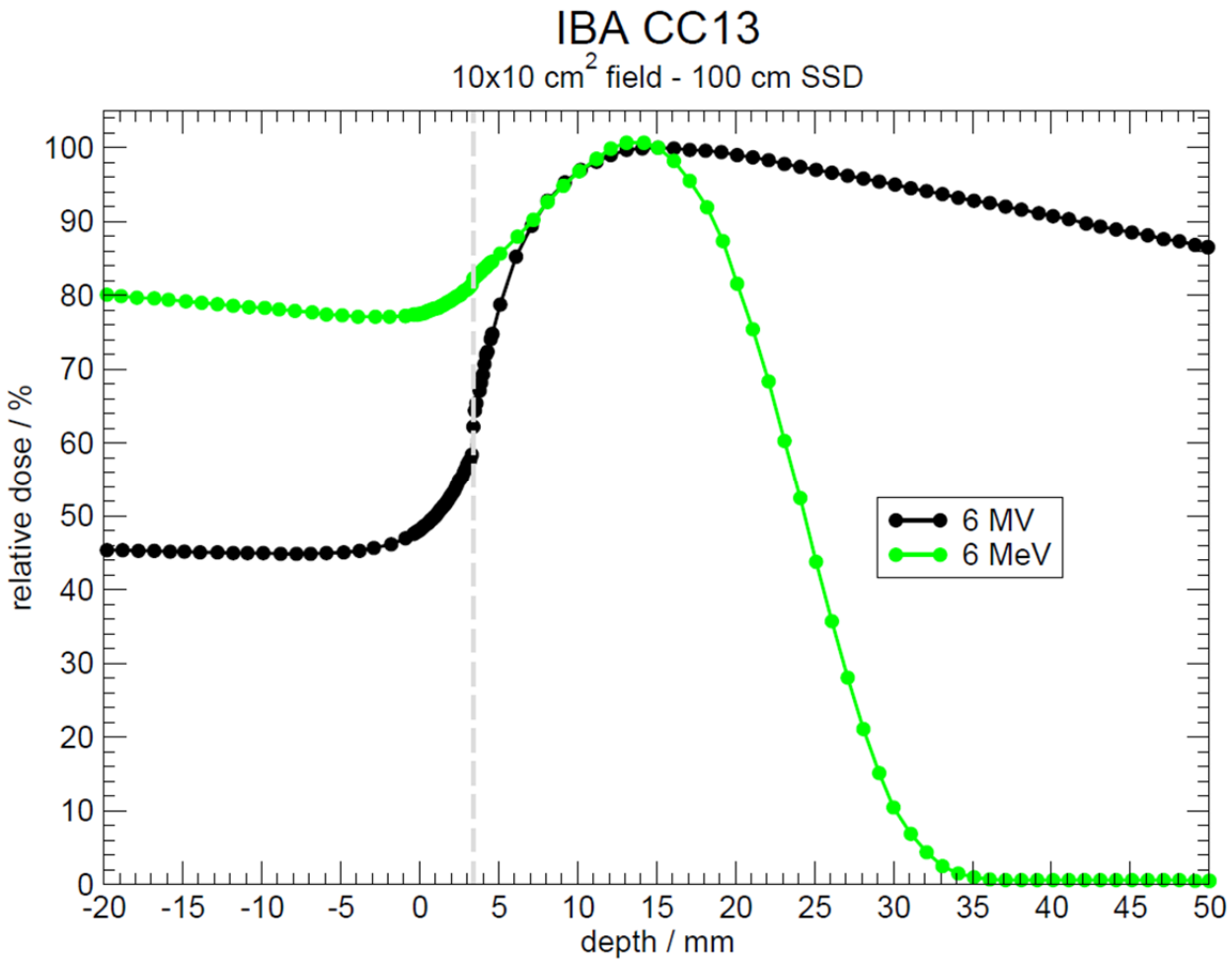

Figure 112: PDD comparison for a change in incident particle type under otherwise identical measurement conditions.

PDDs for the particle type comparison are shown in Figure 112. Similar scans acquired in continuous mode are used to illustrate the relative linearity of electron measurements compared with photon measurements in Figure 12. The measurements shown in Figure 112 are taken in step-by-step mode. The grey dashed line again represents the IC central axis location at which the IC proximal edge should reach the water surface for a well-aligned measurement. The 6 MV PDD gradient is clearly steeper than the 6 MeV PDD gradient near the grey dashed line. The relative steepness of the 6 MV PDD compared with the 6 MeV PDD near the grey dashed line is confirmed in Figure 113, where the 6 MV peak is 4.75 times higher than the 6 MeV peak. Both peaks occur at the same location, 0.05 mm shallower than the DeICERS. The 0.05 mm

difference in peak location from the DeICERS is within measurement uncertainty. The results of this section show that CC13 gradient peak location is unaffected at the 0.1 mm scan resolution level by changes in accelerator type, particle type, and incident beam energy.

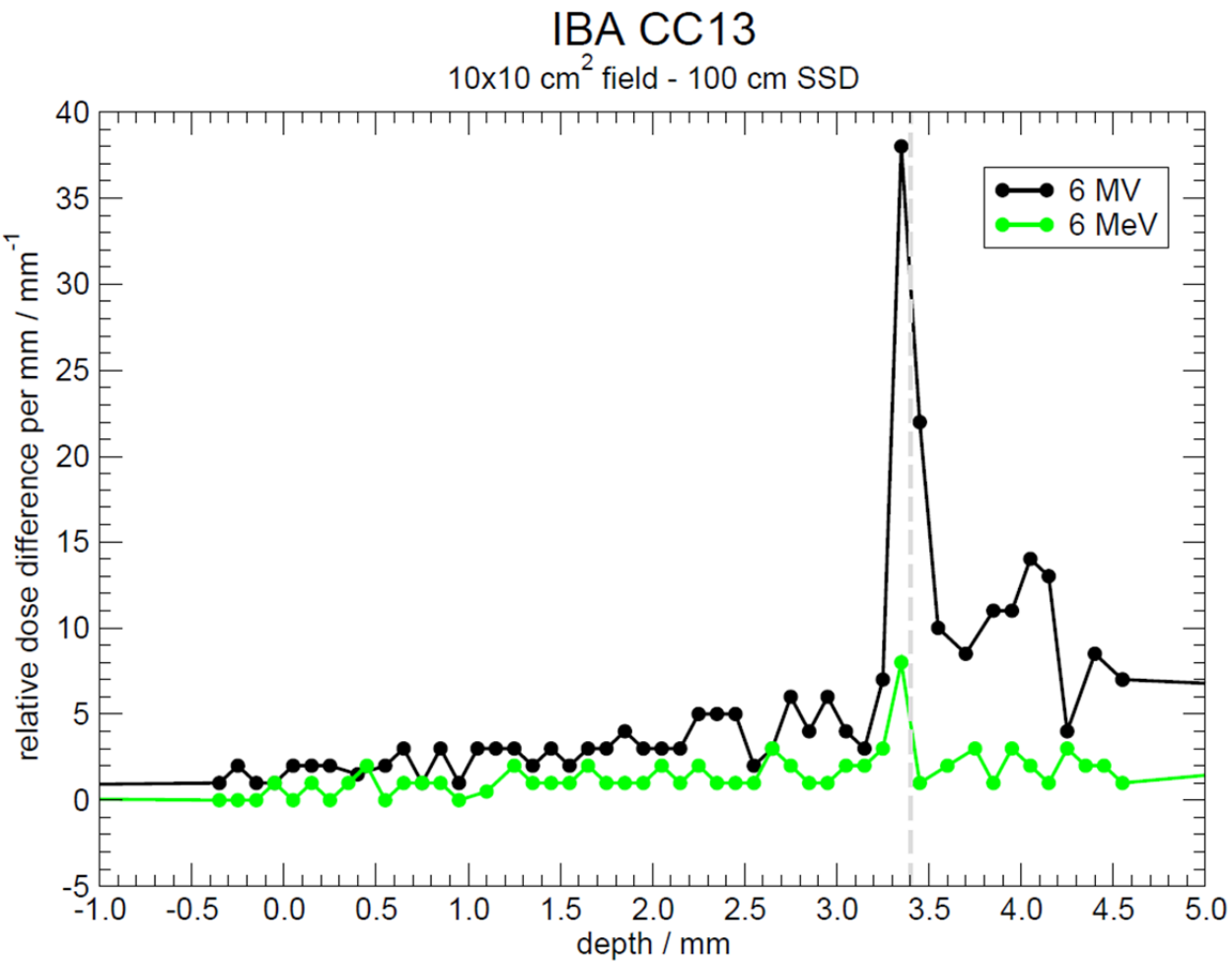

Figure 113: First derivatives of the scans shown in Figure 112. Photon irradiation yields a gradient peak almost four times higher than obtained via electron irradiation. The difference in gradient peak height is expected as electron buildup response is more linear than photon buildup response. However, gradient peak location is unchanged.

4.4.2 Field Size

Field size directly impacts the treatment head scatter component of the incident radiation beam. Given an incident primary photon beam, electrons originating from various treatment head components will scatter into the beam path via Compton interactions. For small fields, these contaminant electrons will likely be absorbed by the collimating jaws before leaving the

treatment head. For larger fields, the jaws are less likely to intercept head-scattered electrons, making it more likely that these electrons will reach the IC to be measured. A larger primary beam also will irradiate more of the water in the tank, creating more phantom-scattered electrons that might also be measured by the IC. Since it is possible that an increase in scattered electrons with larger field size could shift or obscure the gradient peak, the gradient peak dependence on field size is evaluated in this section.

Measurements at VCU are taken with three IC types: the IBA CC13 cylindrical IC, the PTW 23343 (Markus) parallel-plate IC, and the PTW 31010 cylindrical IC. All VCU measurements are taken at 100 cm SSD for incident photon beam energies of 6 and 18 MV. Measurements with the CC13 and the 23343 are taken at four field sizes: 5×5, 10×10, 20×20, and 40×40 cm^2. Measurements with the 31010 are taken for the fields listed above and a 30×30 cm^2 field. For all VCU scans, 0.1 mm resolution is used near the DeICERS. For the CC13 scans, 0.1 mm resolution is used from 4 mm in water to 1 mm above the water surface in air. The 23343 scans are taken at 0.1 mm resolution from 2.5 mm in water to 2.5 mm above the surface in air. The 31010 scans use 0.1 mm resolution from 5 mm below the surface in water to 5 mm above the surface in air.

Sampling resolution for the CC13 and 23343 measurements is at least 1 s/pt. at all depths. For the CC13 scans, from 4 to 3 mm in water, the sampling resolution is 4 s/pt., except the 6 MV 10×10 cm^2 field scan, which used 10 s/pt. sampling resolution. The 23343 scans are taken at 10 s/pt. sampling resolution from 2.5 mm in water to 2.5 mm above the surface in air. The 31010 6 MV measurements are taken at 2 s/pt. sampling resolution at all depths. The 31010 18 MV measurements are taken at 4 s/pt. sampling resolution at all depths. Later, the 31010 measurements are re-done in three cases using variable sampling resolution. The 6 MV 5×5 cm^2,

6 MV 10×10 cm^2, and 18 MV 5×5 cm^2 scans are done using 10 s/pt. sampling resolution from 4 mm to 3 mm in water and 1 s/pt. sampling resolution at all other depths. For all scans, the slowest sampling resolution used is displayed in the results.

The field size dependence of measured results is also tested using three ICs in the 6 MV beam of the Accuray CyberKnife. For this accelerator, field size is defined via cylindrical collimators producing circular fields. Standard accelerators, such as the Varian 2300, use orthogonally-opposed pairs of rectangular jaws to define rectangular fields. Measurements are taken with three cylindrical ICs: the PTW 31014, Exradin A16, and IBA IC-10. Each IC is scanned in circular fields of 10, 20, 30, and 60 mm diameter. CyberKnife measurements are acquired at 0.5 mm resolution from 20 mm in water to 20 mm above the surface in air with 0.3 s/pt. sampling resolution. Recall that degraded resolution will shift the observed gradient peak location, as shown in Section 4.2.3.

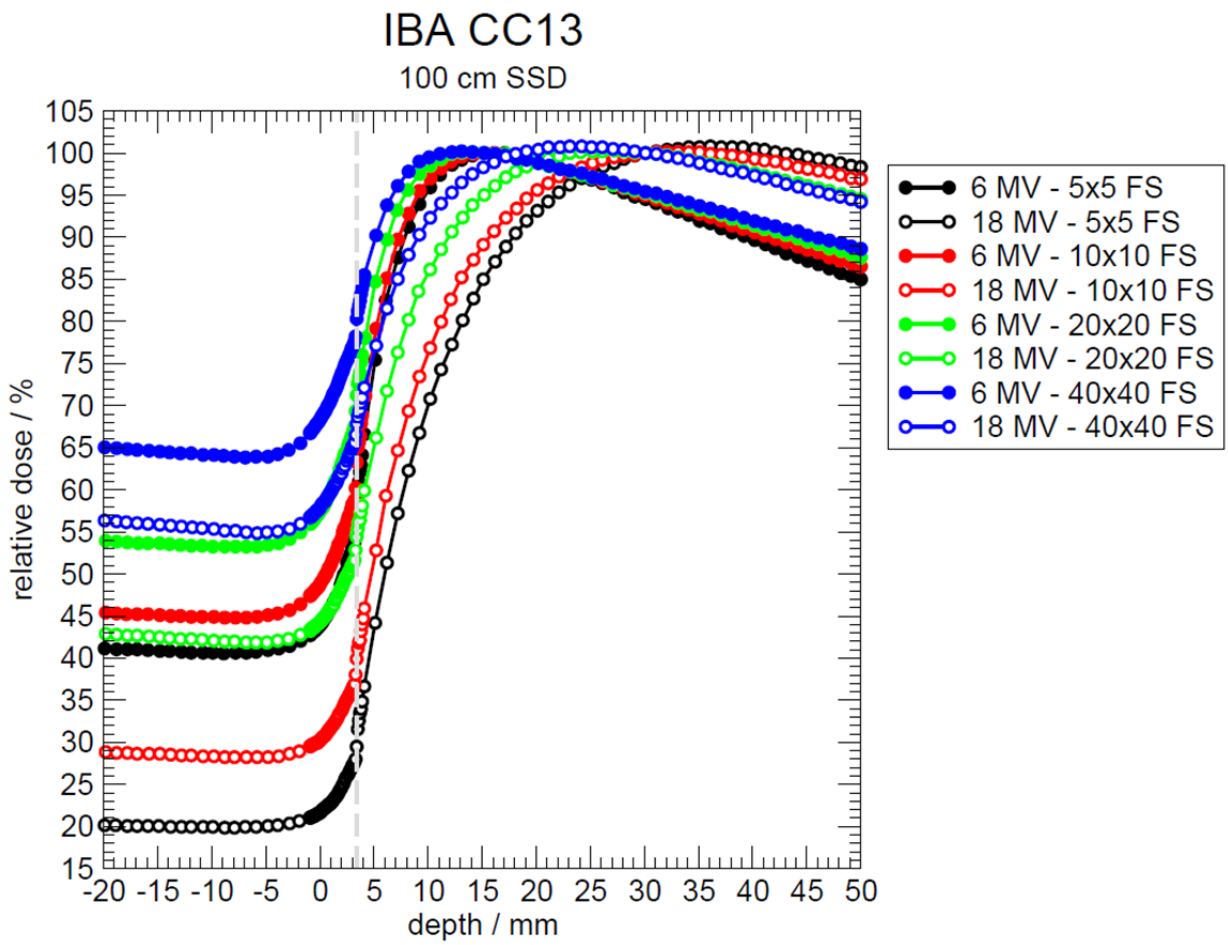

Figure 114: PDDs measured with the IBA CC13 cylindrical IC for two photon beam energies and four field sizes at 100 cm SSD. Scans are performed from 50 mm in water to 20 mm above the water surface in air at 1 s/pt. From 4 mm to -1 mm, scan resolution is 0.1 mm. Outside of this region, scans are acquired at 1 mm resolution. From 4 mm to 3 mm, scan sampling resolution is 4 s/pt., or in some cases, 10 s/pt.

Figure 114 shows the PDDs measured with the IBA CC13. The in-air relative dose increases with field size for both energies. Beyond d_{max}, relative dose in water increases with increasing field size for the 6 MV beam and decreases with increasing field size for the 18 MV beam. Deeper in water, the increased phantom scatter will yield larger doses for larger fields at both energies. The CC13-measured relative dose gradients are shown in Figure 115. All scans exhibit gradient peaks within ±0.05 mm of the DeICERS, marked by the grey dashed line. The difference in location is within measurement uncertainty. Scans at the smallest field sizes exhibit taller gradient peaks than scans at the larger field sizes due to reduced in-air dose for smaller

fields. The 6 MV 10×10 cm^2 field scan, acquired with 10 s/pt. sampling resolution from 4 to 3 mm, shows the clearest peak.

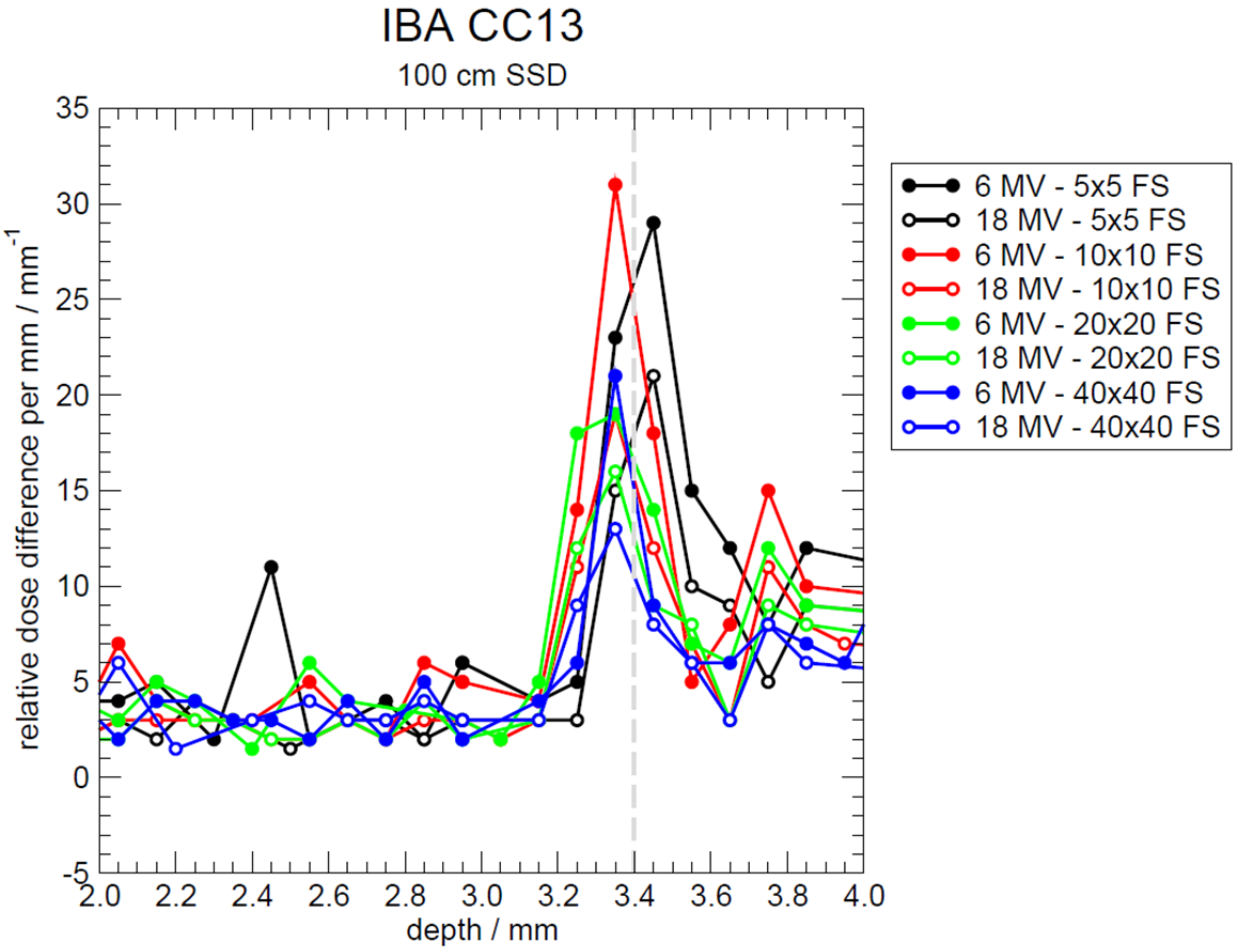

Figure 115: First derivatives of the scans shown in Figure 114. For all changes in beam energy and field size, all gradient peaks are located within 0.05 mm of the DeICERS, denoted by the grey dashed line. The grey dashed line represents the DeICERS when perfectly aligned.

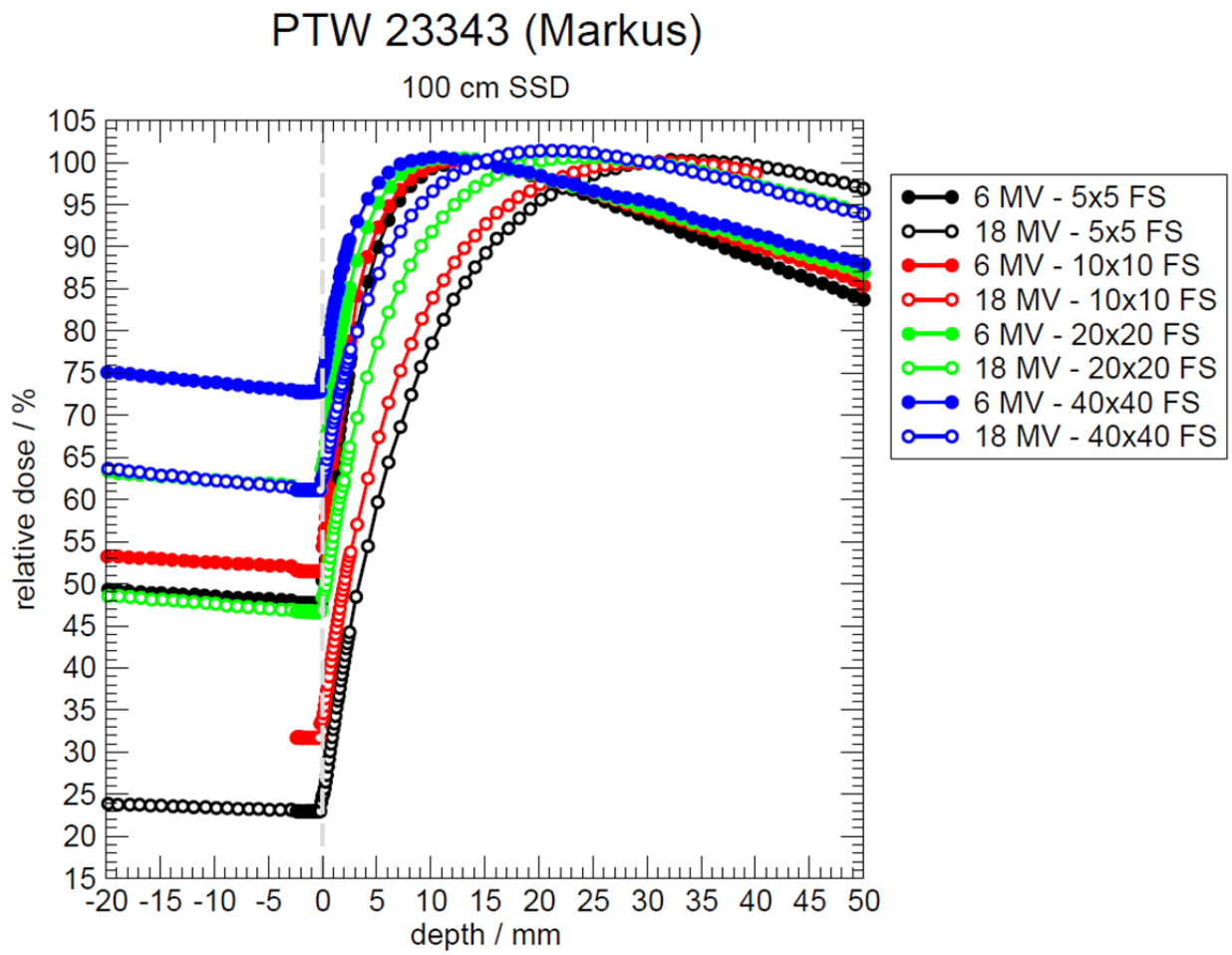

Figure 116: PDDs measured with the PTW 23343 parallel-plate IC for two photon beam energies and four field sizes at 100 cm SSD. Scans are performed from 50 mm in water to 20 mm above the water surface in air at 1 s/pt., except for the 18 MV 10×10 cm^2 field scan, which stops at -2.5 mm. From 2.5 mm to -2.5 mm, scan resolution is 0.1 mm. Outside of this region, scans are acquired at 1 mm resolution. From 2.5 mm to -2.5 mm, scan sampling resolution is 10 s/pt.

PDDs measured with the PTW 23343 are shown in Figure 116. As with the CC13, relative dose in air increases with field size. The 6 MV measurements show an increase in relative dose in water with increased field size while the 18 MV measurements show a decrease in relative dose in water with increased field size. By a depth of 50 mm in water, the 6 MV beam dose is being contributed largely by electrons produced in the water phantom, more of which will be produced for larger fields. The same trend in dose with field size is not established until deeper in the water phantom for the 18 MV beam, as it is more penetrating. The in-air relative dose increase with field size is larger than observed for the CC13. The discrepancy is

caused primarily by the change in effective buildup provided by the different IC walls and secondarily by the increased scatter through the IC wall for the 23343, due to the unsuitably small guard ring.

Figure 117 shows the PTW 23343 scan gradients. All gradient peaks occur within 0.25 mm of the DeICERS. Excepting the 18 MV 10×10 cm^2 field scan, all peaks are within 0.15 mm of the DeICERS. The 18 MV 10×10 cm^2 field scan is considered anomalous, as the 6 MV 10×10 cm^2 field scan exhibits a gradient peak 0.05 mm shallower than the DeICERS and no real gradient peak location dependence on energy is known to exist. The discrepancy may be partially contributed by water pooling on the IC surface, evaporation, or a small IC angular offset relative to the water surface.

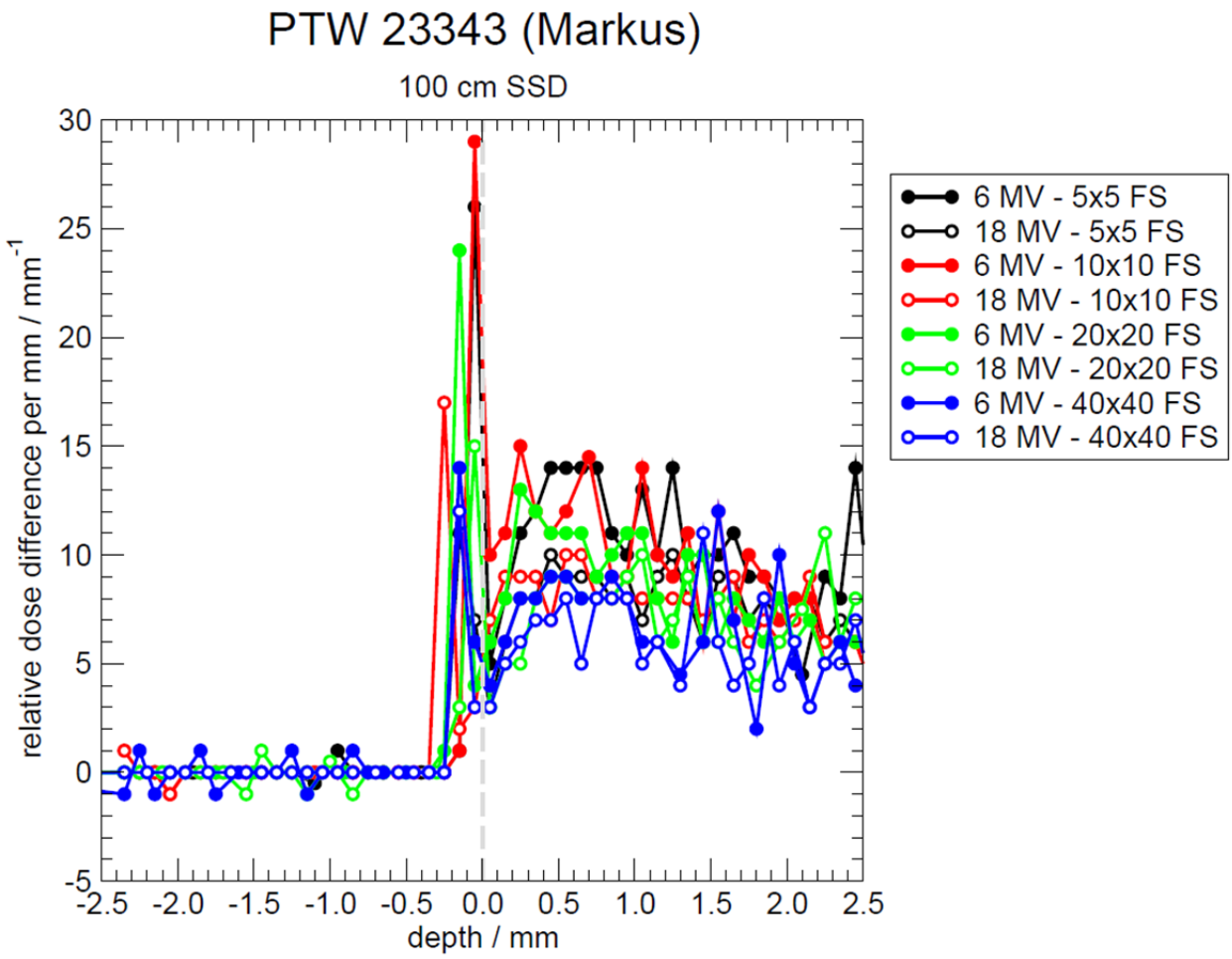

Figure 117: First derivatives of the scans shown in Figure 116. All gradient peaks occur within 0.25 mm of the DeICERS, denoted by the grey dashed line. Excepting the 18 MV 10×10 cm^2 field scan, all gradient peaks occur within 0.15 mm of the DeICERS.

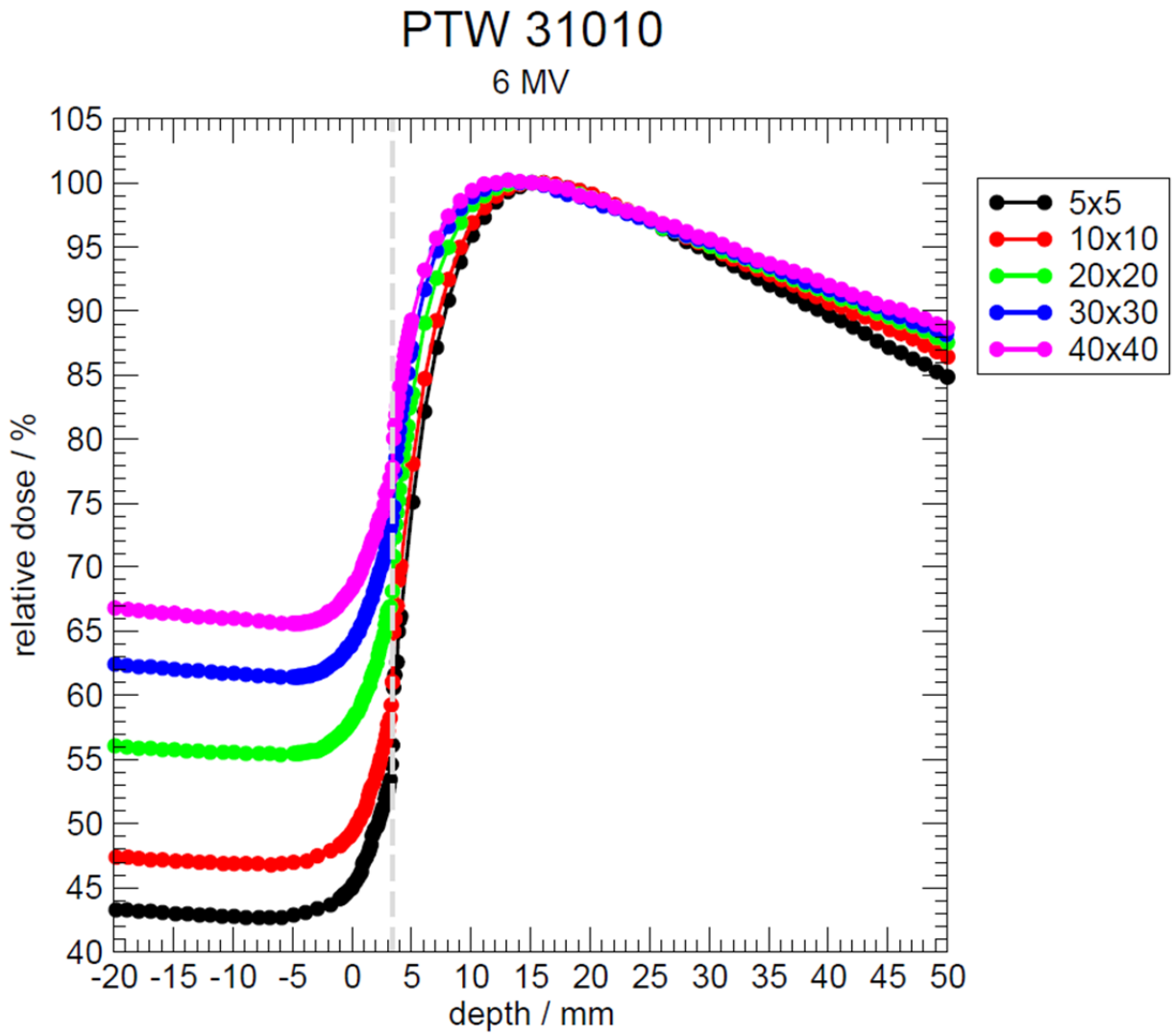

Figure 118: PDDs measured with the PTW 31010 cylindrical IC for the Varian 2300 6 MV beam at 100 cm SSD. All scans are performed from water to air. Measurement resolution from 5 mm to -5 mm is 0.1 mm for all scans.

Figure 118 shows the 6 MV PDDs measured with the PTW 31010. Relative dose in air and in water beyond d_{max} increases with increasing field size, as expected. The relative dose gradients are shown in Figure 119. The gradient peaks measured for four of the five field sizes occur precisely at the DeICERS, with the 30×30 cm^2 field scan exhibiting a gradient peak 0.1 mm deeper in the water. This difference is considered within measurement uncertainty.

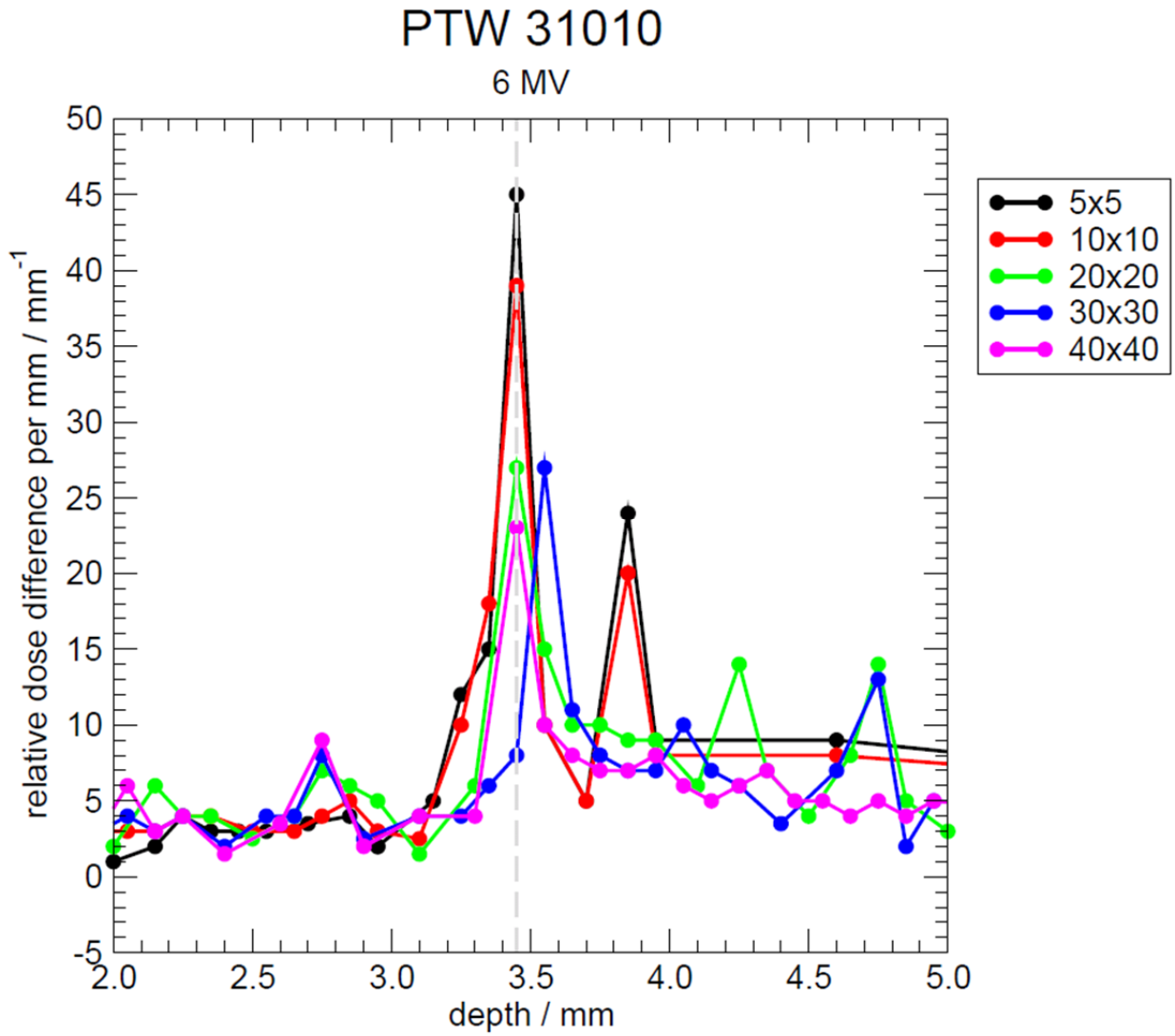

Figure 119: First derivatives of the scans shown in Figure 118. All gradient peaks occur within 0.1 mm of the DeICERS, denoted by the grey dashed line. The grey dashed line represents the DeICERS if perfectly aligned.

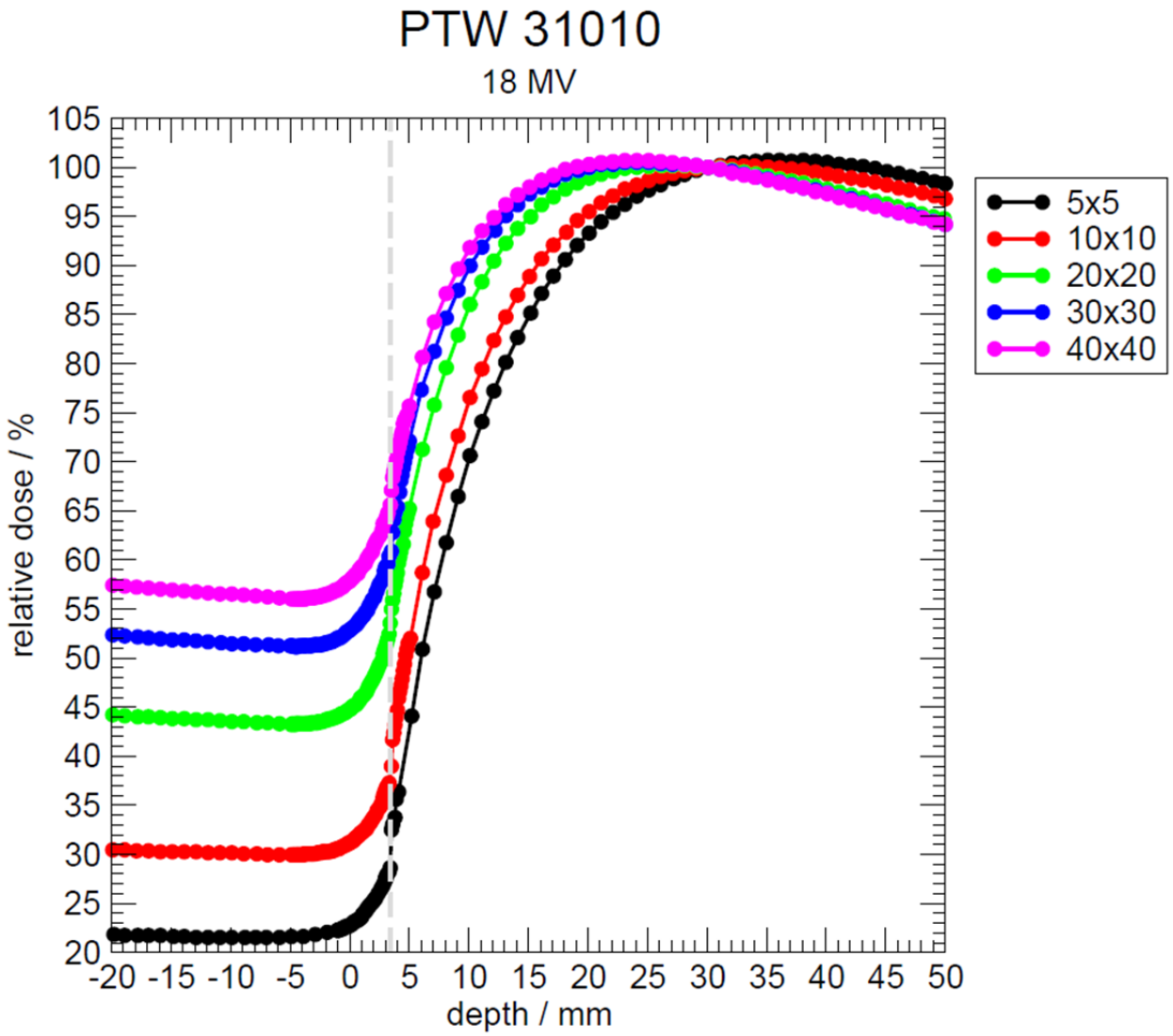

Figure 120: PDDs measured with the PTW 31010 cylindrical IC for the Varian 2300 18 MV beam at 100 cm SSD. All scans are performed from water to air. Measurement resolution from 5 mm to -5 mm is 0.1 mm for all scans.

PDDs measured for the 18 MV beam are shown in Figure 120. For 18 MV measurements, relative dose in air increases with increasing field size but decreases with increasing field size in water beyond d_{max}. This relationship is also expected. Figure 121 shows the relative dose gradients for the 18 MV measurements. All gradient peaks occur within 0.1 mm of the DeICERS. The 5×5 cm^2 field scan, which was performed with the slowest possible sampling resolution from 4 to 3 mm, exhibits the highest peak.

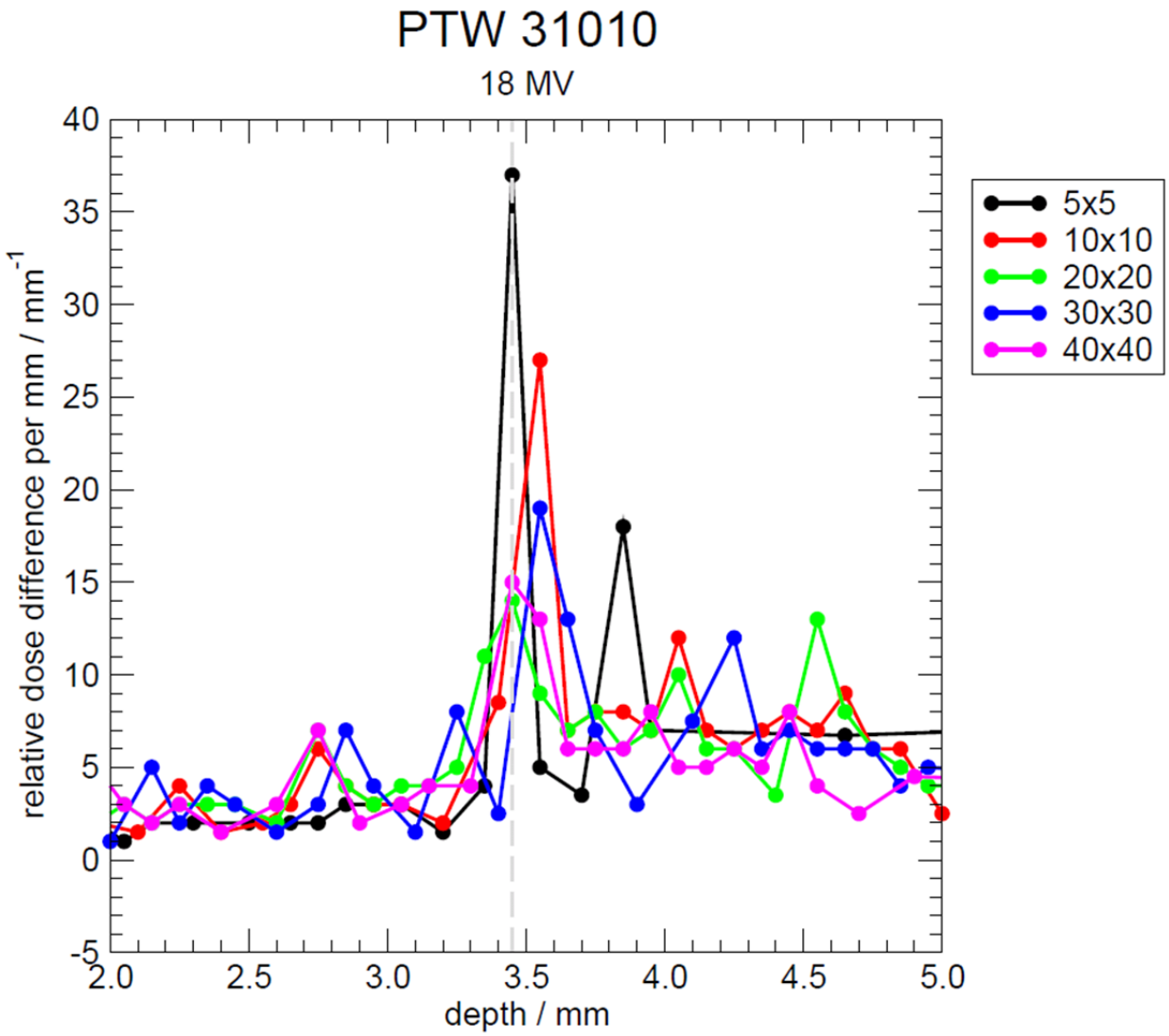

Figure 121: First derivatives of the scans shown in Figure 120. All gradient peaks occur within 0.1 mm of the DeICERS, denoted by the grey dashed line. The grey dashed line represents the DeICERS if perfectly aligned.

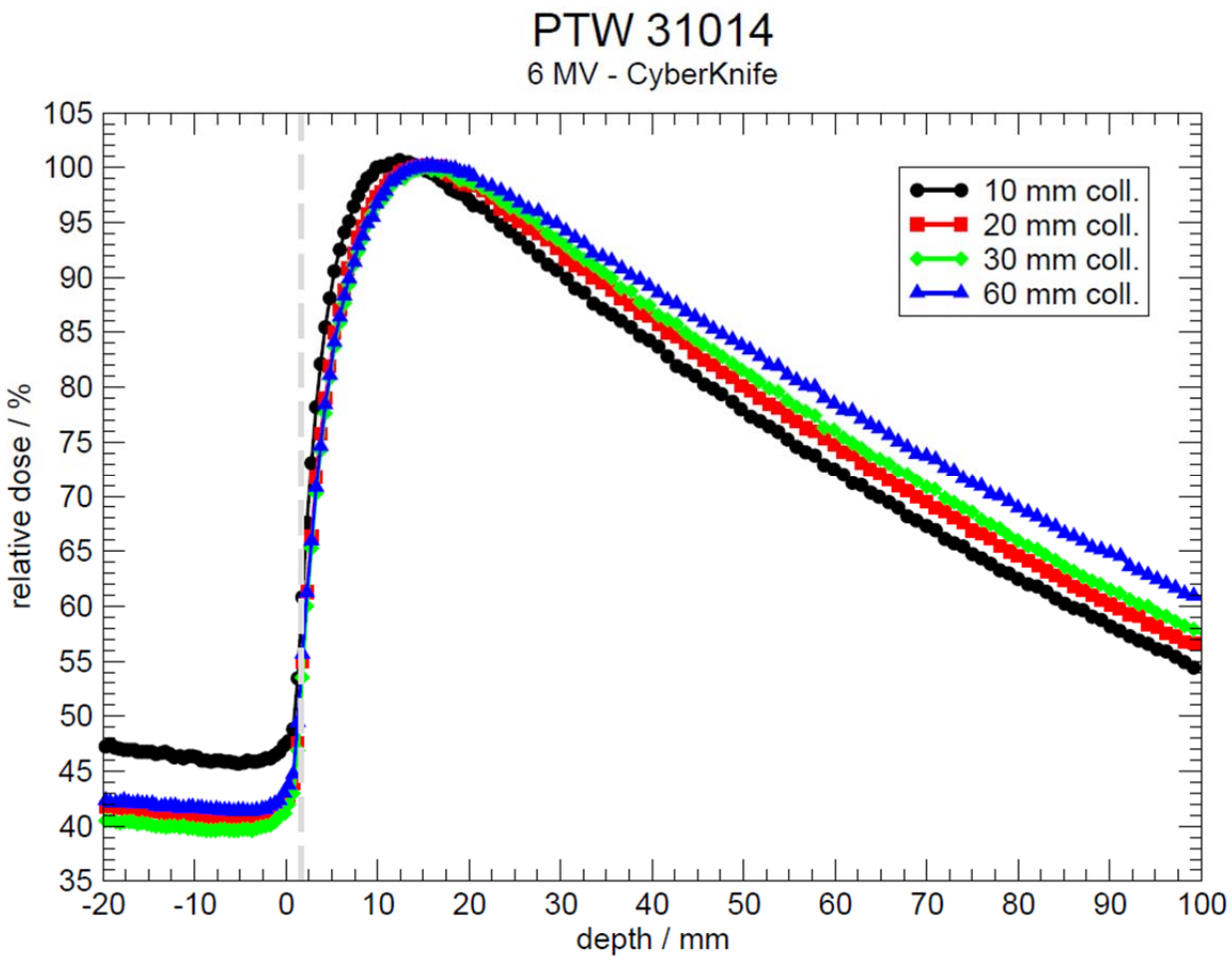

Figure 122: PDDs measured with the PTW 31014 cylindrical IC in the Accuray CyberKnife 6 MV beam at 78.5 cm SSD. All measurements are performed from water to air. From 100 mm to 20 mm, scans are performed at 1 mm resolution. Measurement resolution is 0.5 mm from 20 mm to -20 mm. Each data point represents the average of 15 readings, taken over 0.3 s intervals.

PDDs measured from the Accuray CyberKnife with the PTW 31014 cylindrical IC are shown in Figure 122. Dose in air is similar for the three largest fields but increased by ~13% for the smallest field. The smallest field is not large enough to maintain uniformity over the IC volume, causing the dose increase. In water beyond d_{max}, relative dose increases with increasing field size as expected. The relative dose gradients are shown in Figure 123. All gradient peaks occur at the same location, within 0.16 mm of the DeICERS. The discrepancy between gradient peak and DeICERS location is within measurement step size.

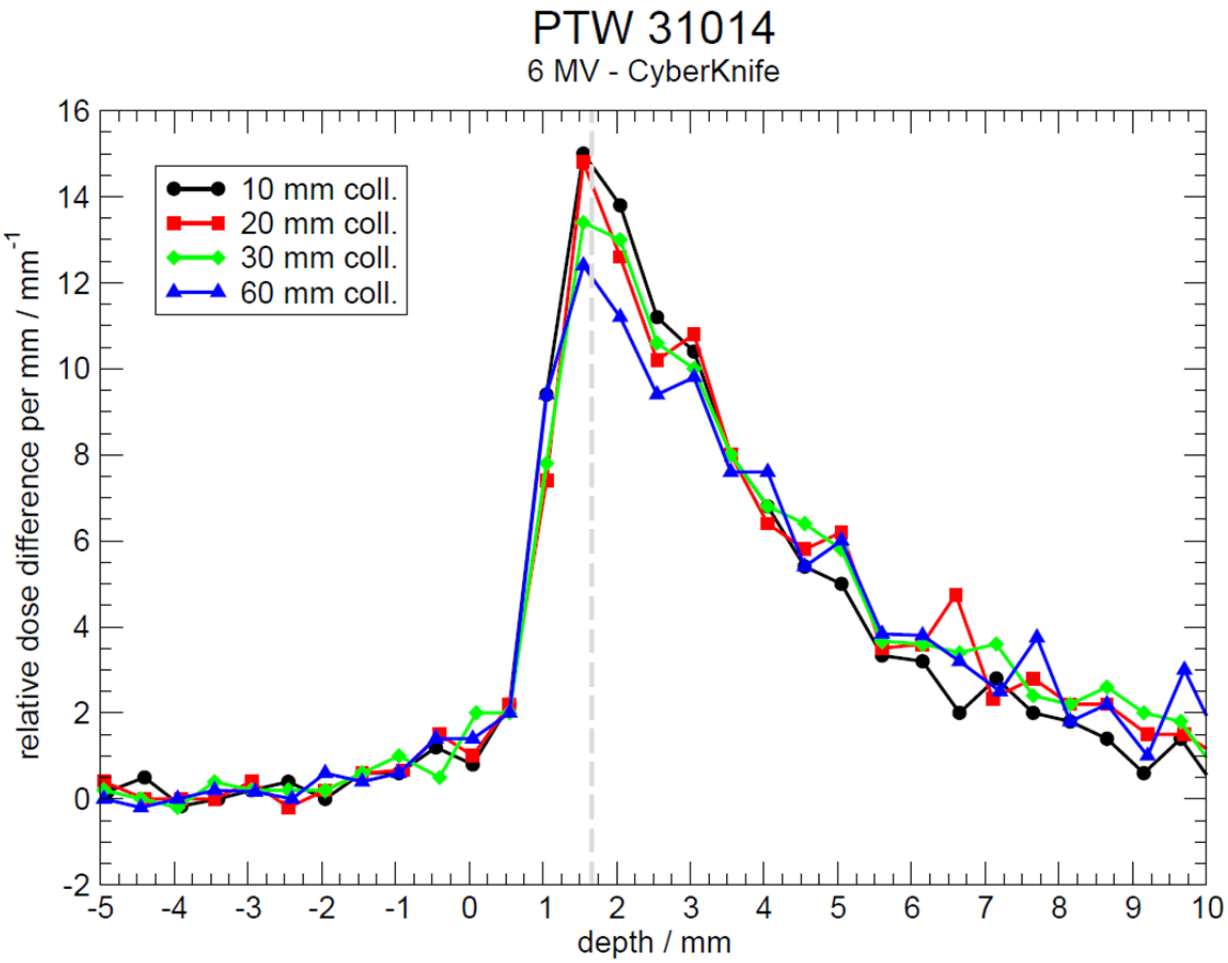

Figure 123: First derivatives of the scans shown in Figure 122. There is no change in gradient peak location for the four field sizes compared.

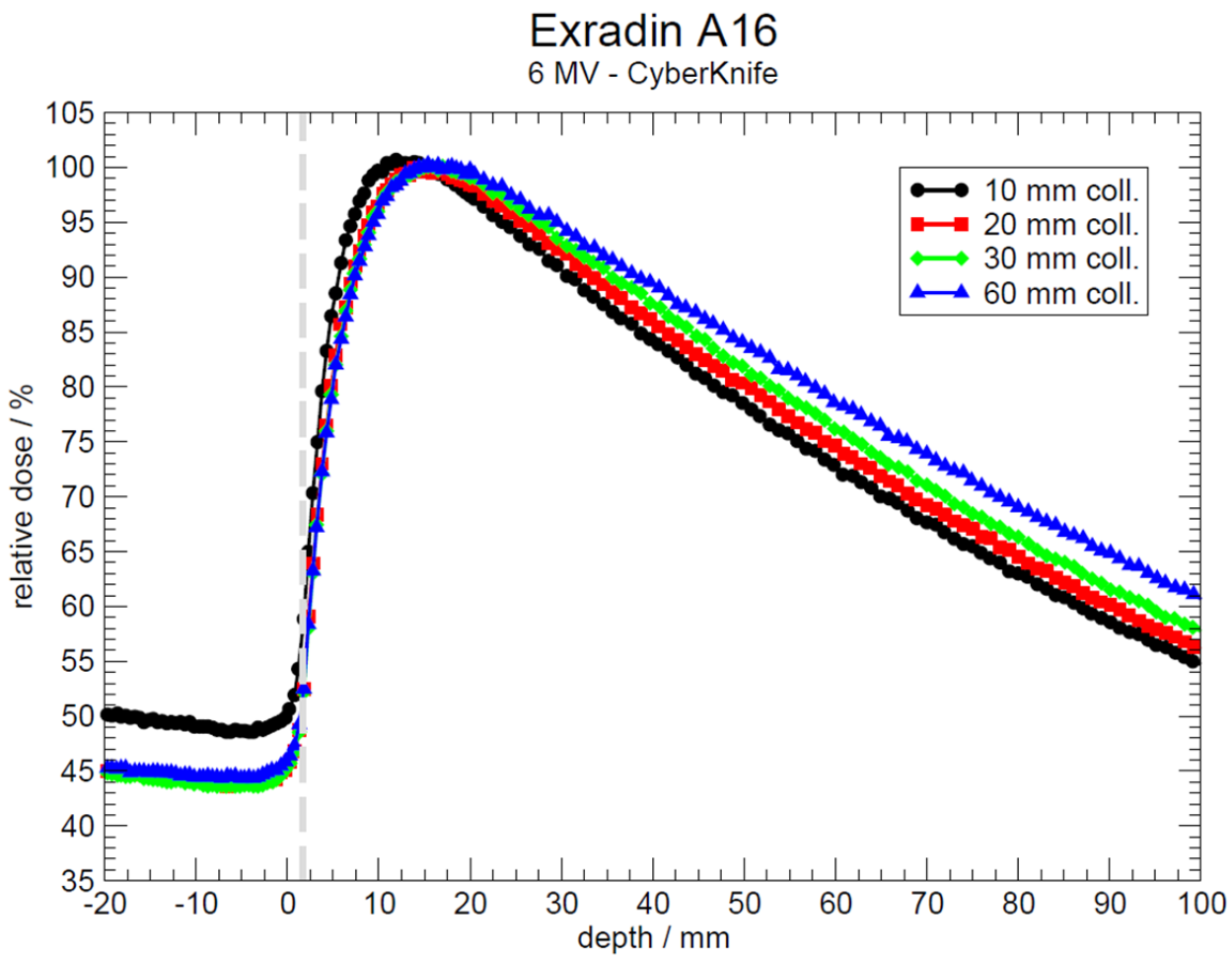

Figure 124: PDDs measured with the Exradin A16 cylindrical IC in the Accuray CyberKnife 6 MV beam at 78.5 cm SSD. All measurements are performed from water to air. From 100 mm to 20 mm, scans are performed at 1 mm resolution. Measurement resolution is 0.5 mm from 20 mm to -20 mm. Each data point represents the average of 15 readings, taken over 0.3 s intervals.

Figure 124 shows the PDDs measured with the Exradin A16 on the Accuray CyberKnife. As with the PTW 31014, the in-air relative doses for the three largest fields are similar. The measurement for the smallest field shows a ~11% increase in dose in air. At depths in water beyond d_{max}, relative dose increases with increasing field size. The relative dose gradients are shown in Figure 125. All gradient peaks occur at the same depth, within 0.3 mm of the DeICERS. For the 0.5 mm resolution used in these measurements, this discrepancy is within measurement uncertainty.

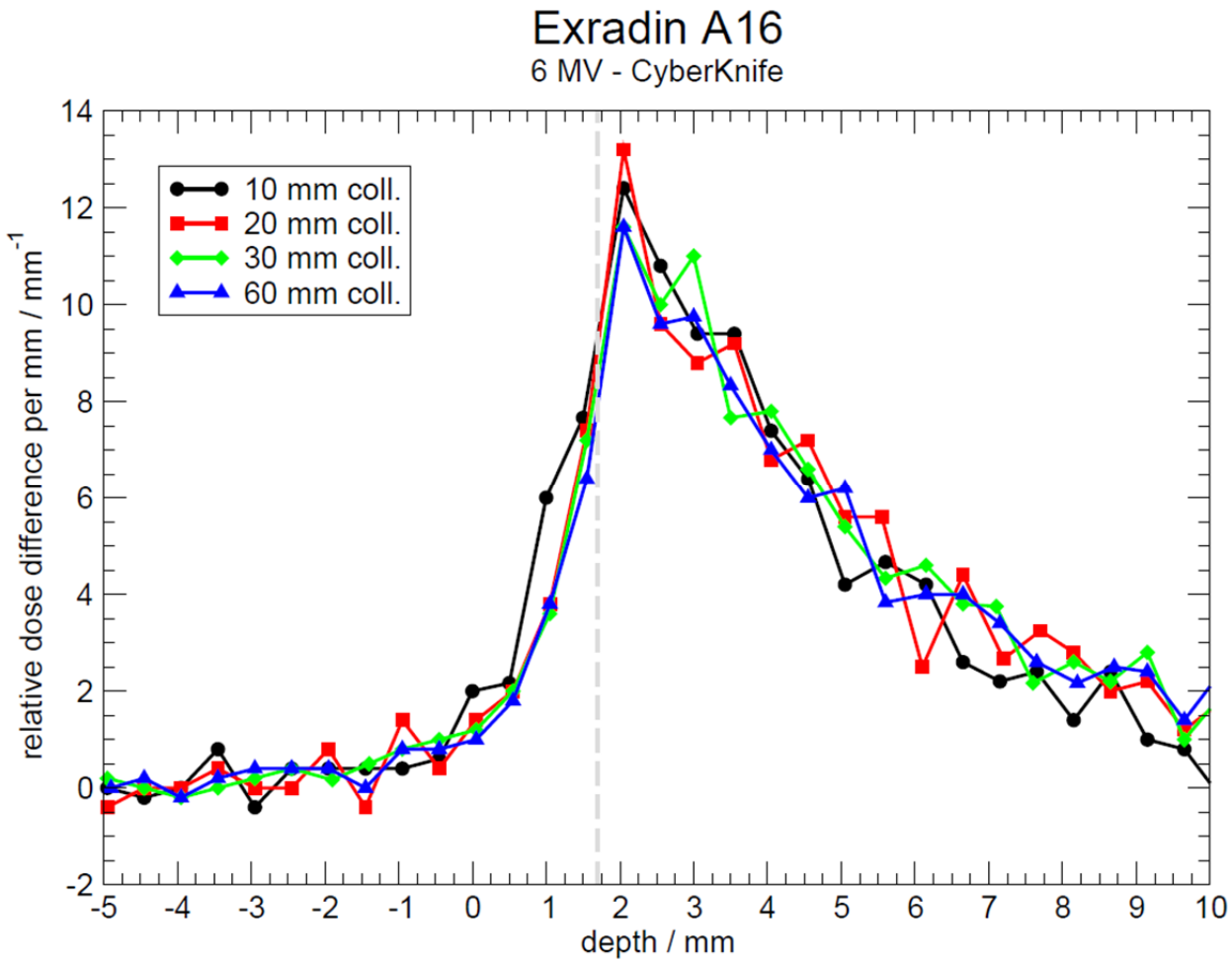

Figure 125: First derivatives of the scans shown in Figure 124. There is no difference in gradient peak location for the four field sizes compared. This is consistent with other accelerators and ICs.

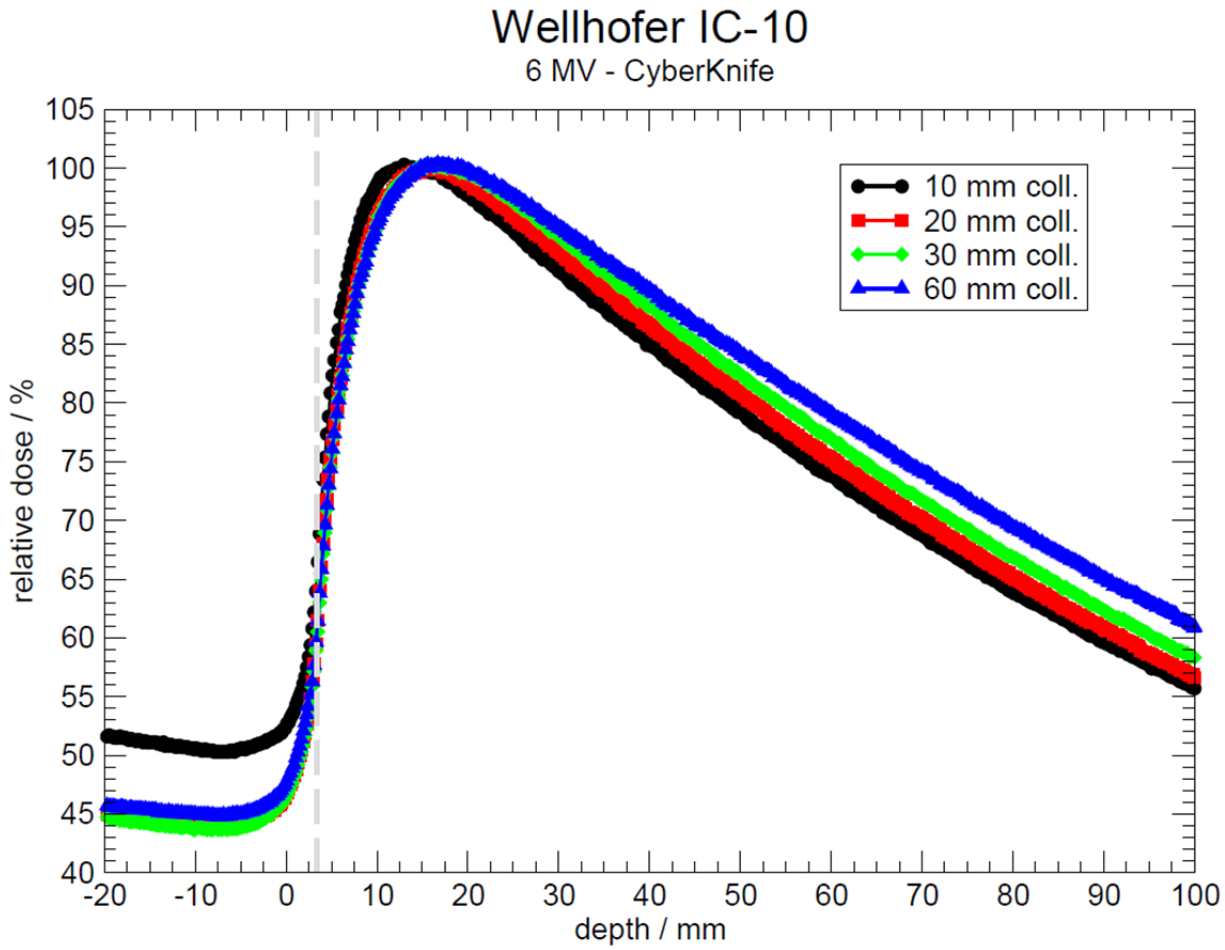

Figure 126: PDDs measured with the Wellhöfer IC-10 cylindrical IC in the Accuray CyberKnife 6 MV beam at 78.5 cm SSD. All measurements are performed from water to air. From 100 mm to 20 mm, scans are performed at 1 mm resolution. Measurement resolution is 0.2 mm from 20 mm to -20 mm. Each data point represents the average of 15 readings, taken over 0.3 s intervals.

PDDs measured with the Wellhöfer IC-10 are shown in Figure 126. Relative doses in air are similar for the three largest fields. The smallest field measurement shows a ~14% increase in dose in air compared with the three other fields. The relative dose gradients for the IC-10 are shown in Figure 127. The measurements at the three largest field sizes exhibit gradient peaks at the same location, within 0.25 mm of the DeICERS. The peak at 4.55 mm for the measurement with the 20 mm diameter field is expected to have been caused by measurement noise as a consequence of acquiring relatively few samples per point (15) in these measurements. If the origin of this peak were physical, it would be expected to appear in scans at larger field sizes.

All CyberKnife scans show gradient peak locations that are within overall measurement uncertainty of the respective DeICERS for each IC and field size tested.

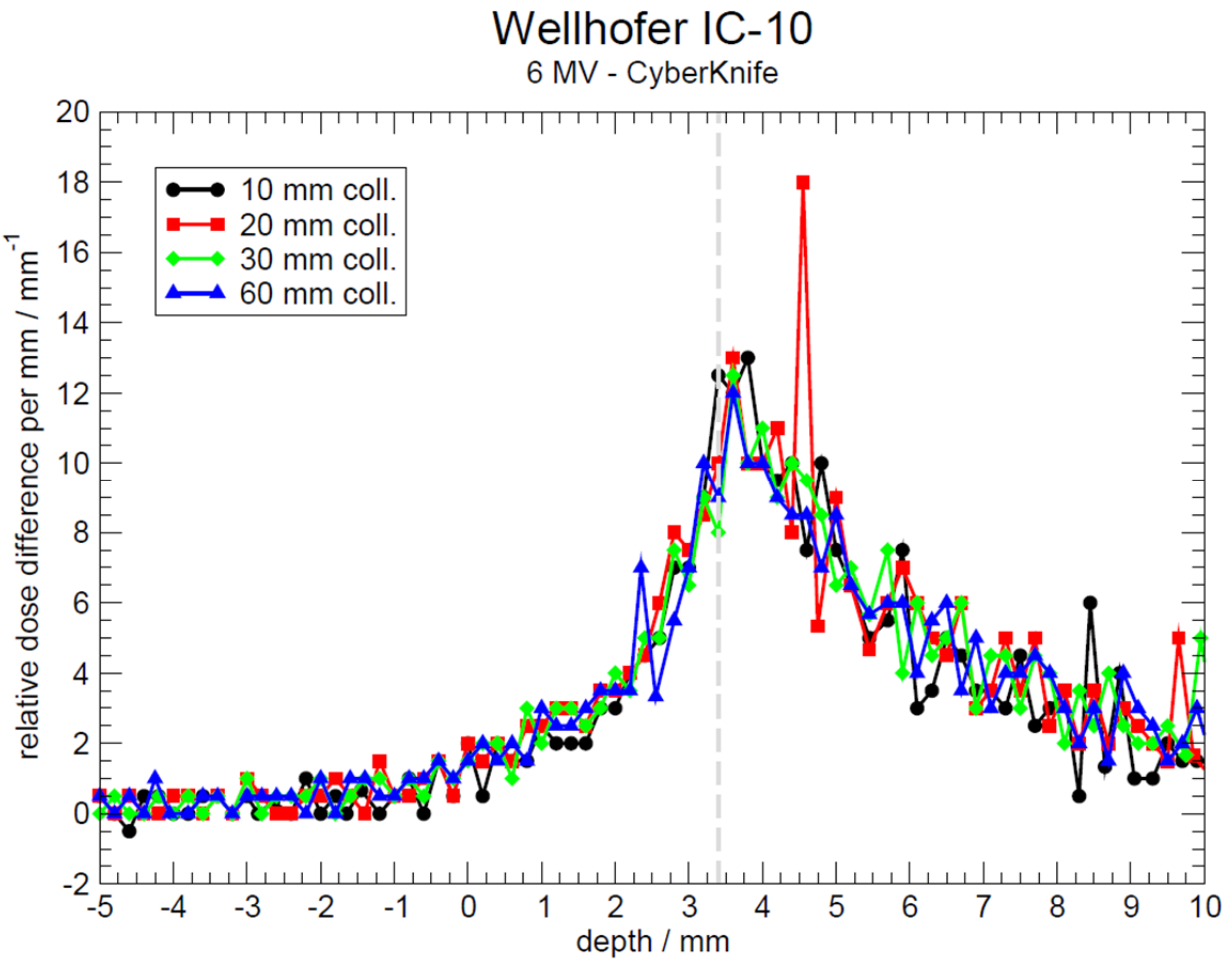

Figure 127: First derivatives of the scans shown in Figure 126. For the three largest field sizes, there is no change in gradient peak location. The gradient peak location for the smallest field size appears to be shared between neighboring points as a consequence of the discrete gradient calculation.

4.4.3 Source-to-Surface Distance

The possible influence of SSD on gradient peak location is tied to field size. Larger fields provide more electron scatter and effective electron source locations. The in-air relative dose is therefore expected to be higher for measurements taken closer to the accelerator treatment head. To test the dependence of gradient peak location on SSD, measurements are taken with the IBA CC13 cylindrical IC and PTW 23343 (Markus) parallel-plate IC in 6 and

18 MV photon beams from the Varian 2300. Scans are taken at both energies with each IC for four field sizes: 5×5, 10×10, 20×20, and 40×40 cm^2. For all combinations of field size and incident beam energy, measurements with both ICs are repeated for two SSDs: 90.5 and 127.5 cm. A change is SSD is achieved by maintaining the water level and raising and lowering the platform on which the water tank sits. An SSD of 90.5 cm represents the closest the water surface could be brought to the end of the treatment head without colliding the water tank and accelerator. An SSD of 127.5 cm represents the lowest position to which the tank platform can be lowered.

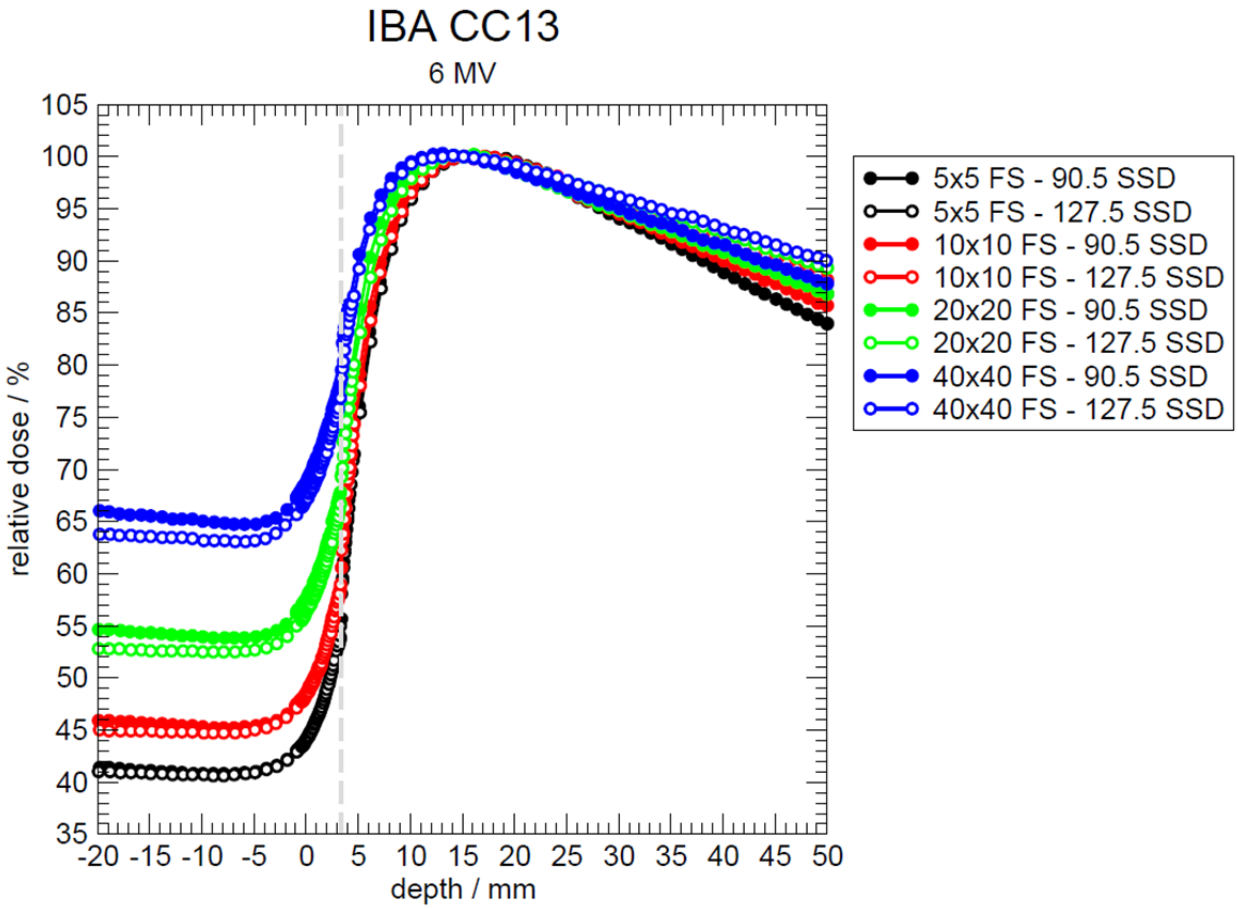

Figure 128: PDDs measured with the IBA CC13 cylindrical IC for extended and shortened SSD at 6 MV for four field sizes each. 90.5 cm SSD is the shortest SSD that can be achieved without colliding the tank and accelerator. 127.5 cm SSD is the farthest distance from the accelerator to which the tank can be lowered. All scans are performed from depth in water through the surface into air. Scans are performed at 1 mm resolution from 50 to 4 mm and from -1 to -20 mm. From 4 to -1 mm, data is acquired at 0.1 mm resolution. Each data point represents an average of, at minimum, 50 sample readings, taking place over 1 second intervals. From 4 to 3 mm, the sampling rate is 4 seconds per point (200 samples), or, in some cases, 10 seconds per point (500 samples). The grey dashed line marks the DeICERS at 3.4 mm.

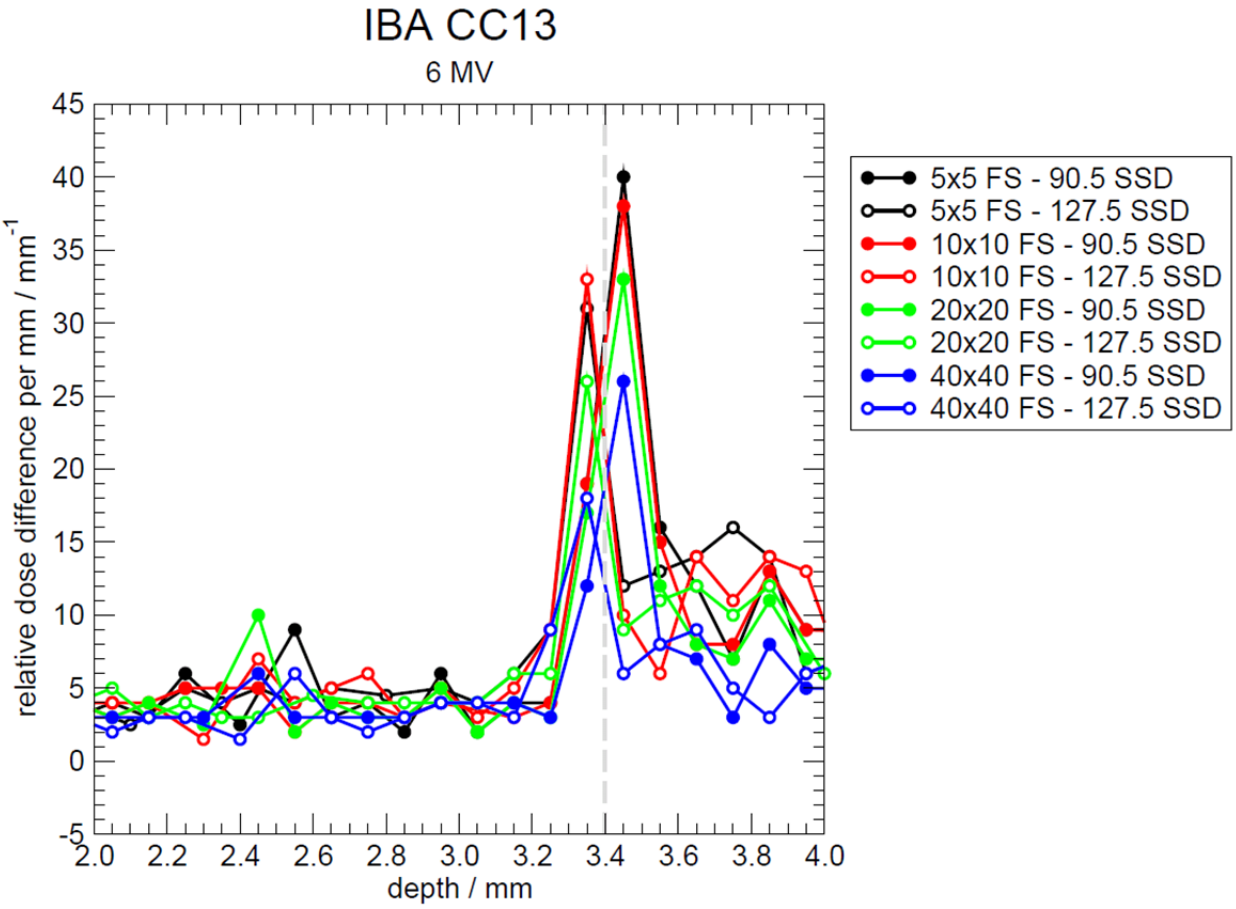

Figure 129: First derivatives of the scans shown in Figure 128. All gradient peaks are observed within 0.05 mm of the known IC outer radius.

Figure 128 shows the 6 MV PDDs measured with the IBA CC13. As expected, in-air relative doses are higher for the smaller SSD. The SSD-dependent difference in relative dose in air increases for larger field size as more scattered electrons from within the treatment head reach the IC. The 6 MV gradient peaks shown in Figure 129 all occur within 0.05 mm of the DeICERS, which is within measurement uncertainty. The CC13 18 MV PDDs are shown in Figure 130. As seen for scans at 6 MV, relative doses in air are greater for smaller SSD. The SSD-dependent relative dose difference increases with larger field size. The 18 MV relative dose gradients are shown in Figure 131. All gradient peaks occur within 0.05 mm of the

DeICERS, marked by the grey dashed line. The difference between the location of the gradient peaks and the DeICERS is within measurement uncertainty.

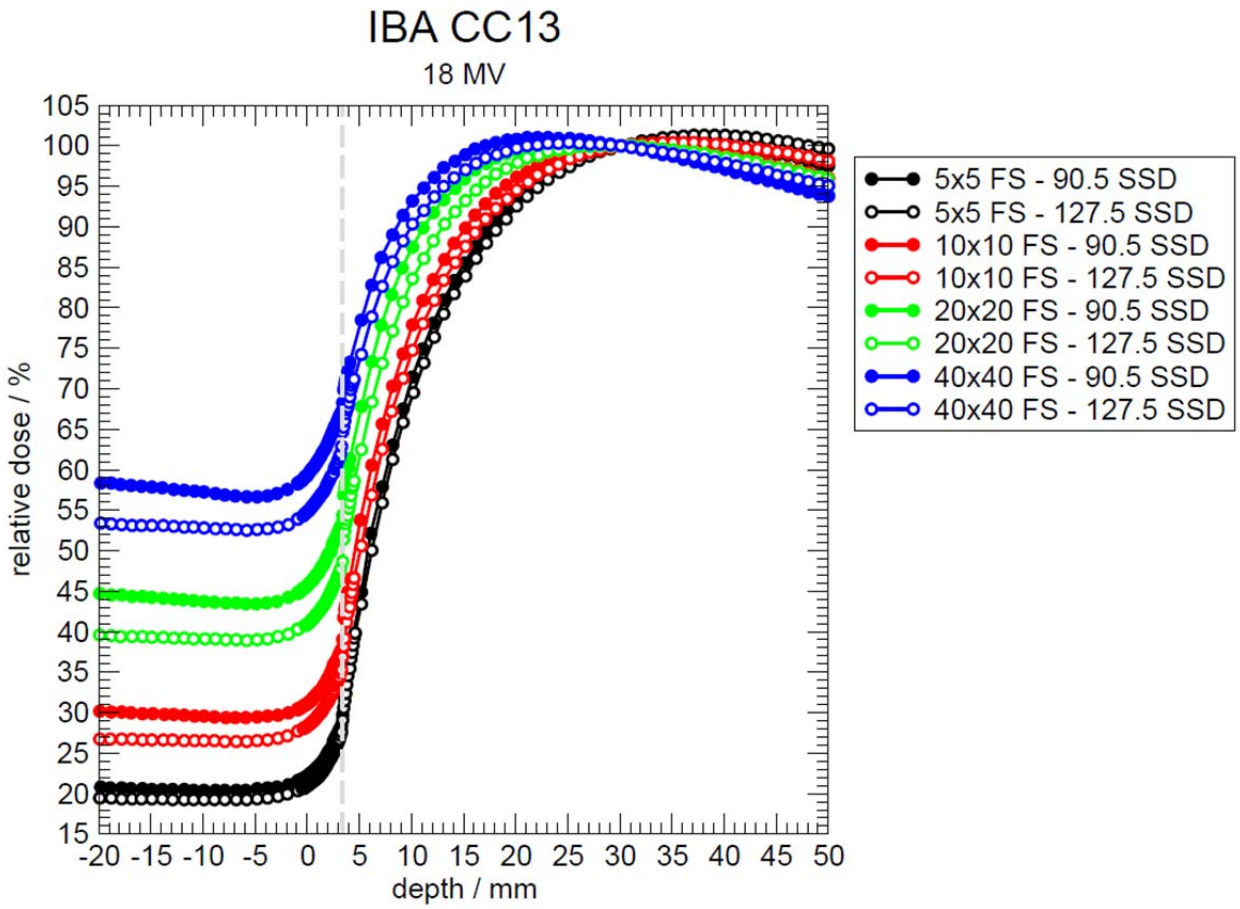

Figure 130: PDDs measured with the IBA CC13 cylindrical IC for extended and shortened SSD at 18 MV for four field sizes each. 90.5 cm SSD is the shortest SSD that can be achieved without colliding the tank and accelerator. 127.5 cm SSD is the farthest distance from the accelerator to which the tank can be lowered. All scans are performed from depth in water through the surface into air. Scans are performed at 1 mm resolution from 50 to 4 mm and from -1 to -20 mm. From 4 to -1 mm, data is acquired at 0.1 mm resolution. Each data point represents an average of, at minimum, 50 sample readings, taking place over 1 second intervals. From 4 to 3 mm, the sampling rate is 4 seconds per point (200 samples), or, in some cases, 10 seconds per point (500 samples). The grey dashed line marks the DeICERS at 3.4 mm.

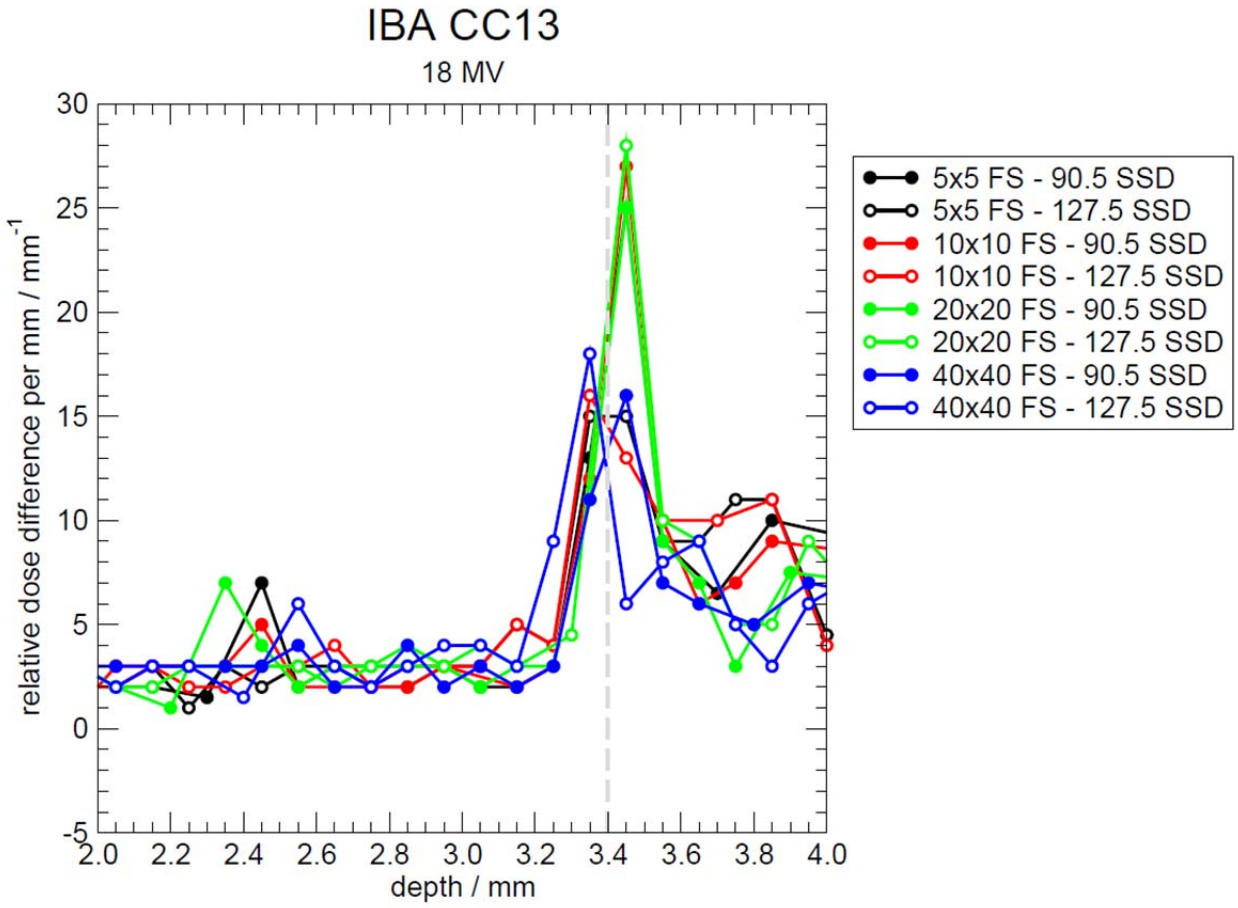

Figure 131: First derivatives of the scans shown in Figure 130. All gradient peaks occur within 0.05 mm of the DeICERS, a discrepancy that is within the 0.1 mm measurement step size.

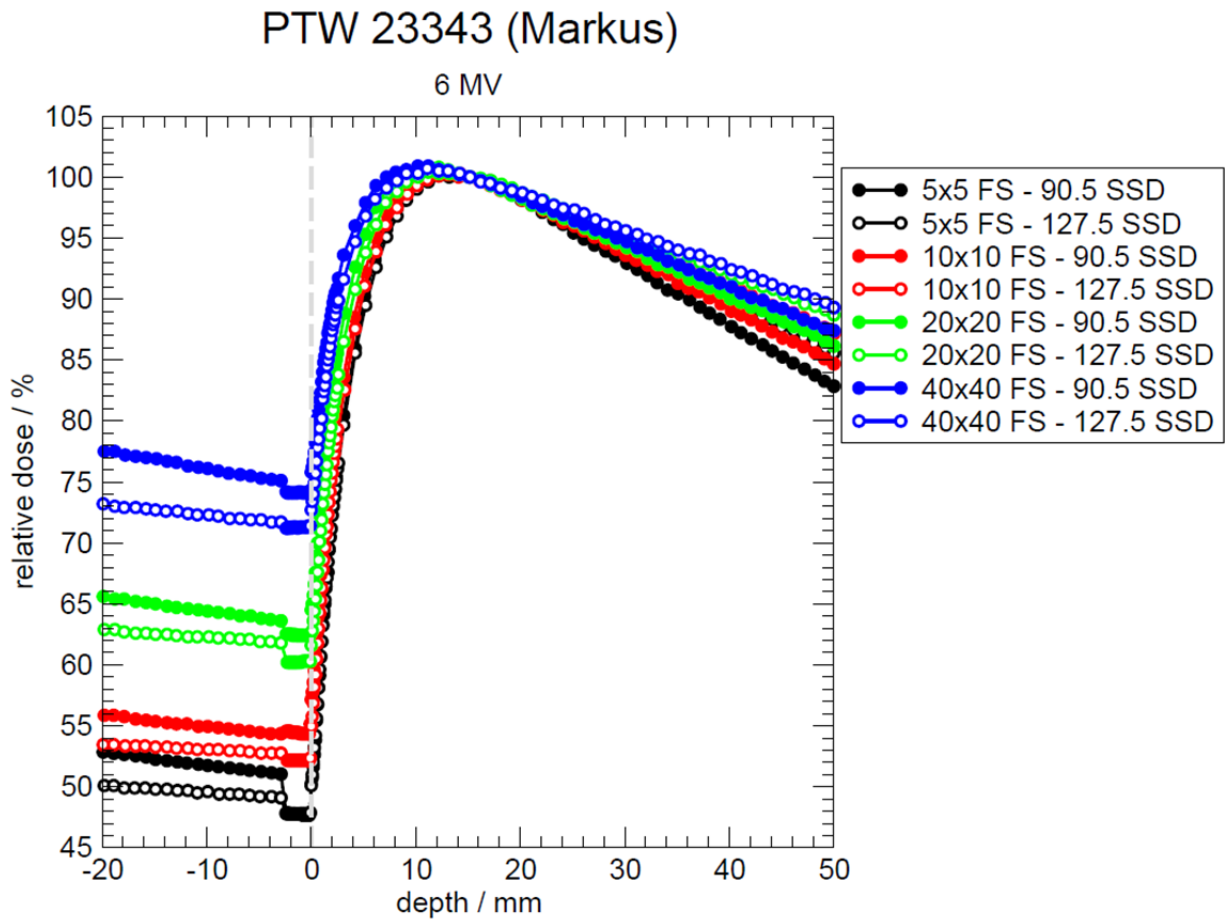

Figure 132: PDDs measured with the PTW Markus parallel-plate IC for extended and shortened SSD at 6 MV for four field sizes each. 90.5 cm SSD is the shortest SSD that can be achieved without colliding the tank and accelerator. 127.5 cm SSD is the farthest distance from the accelerator to which the tank can be lowered. All scans are performed from depth in water through the surface into air. Scans are performed at 1 mm resolution from 50 to 3 mm and from -3 to -20 mm. From 2.5 to -2.5 mm, data is acquired at 0.1 mm resolution. Each data point represents an average of, at minimum, 50 sample readings, taking place over 1 second intervals. From 2.5 to -2.5 mm, the sampling rate is 10 seconds per point (500 samples). The strange jumps in the in-air signal are artifacts caused by the way scans at different sampling times are stitched together. Figure 69 shows the physical explanation for the sampling time dependence and a solution. The grey dashed line marks the nominal water surface.

PDDs measured for the 6 MV beam with the PTW 23343 are shown in Figure 132. The change in relative dose in air for the same scan between 2.5 and 3 mm above the water surface in air is a consequence of the change in scan sampling resolution. The IC acquires signal at most points of the scan for 1 s/pt. From 2.5 mm in water to 2.5 mm above the water surface in air, the sampling resolution is 10 s/pt. As shown in Figure 69, scans acquired at 1 s/pt. can collect water on the IC front face, which increases measured relative dose. Scans sampled at 10 s/pt. move the IC slowly enough through the water surface for the water to drip away from the IC front face,

yielding a more accurate relative dose reading. The same dependencies of in-air relative dose on SSD are observed for the parallel-plate IC as for the cylindrical IC. Figure 133 shows the 6 MV relative dose gradients measured with the 23343. All gradient peaks occur 0.05 mm from the water surface, which is within measurement uncertainty.

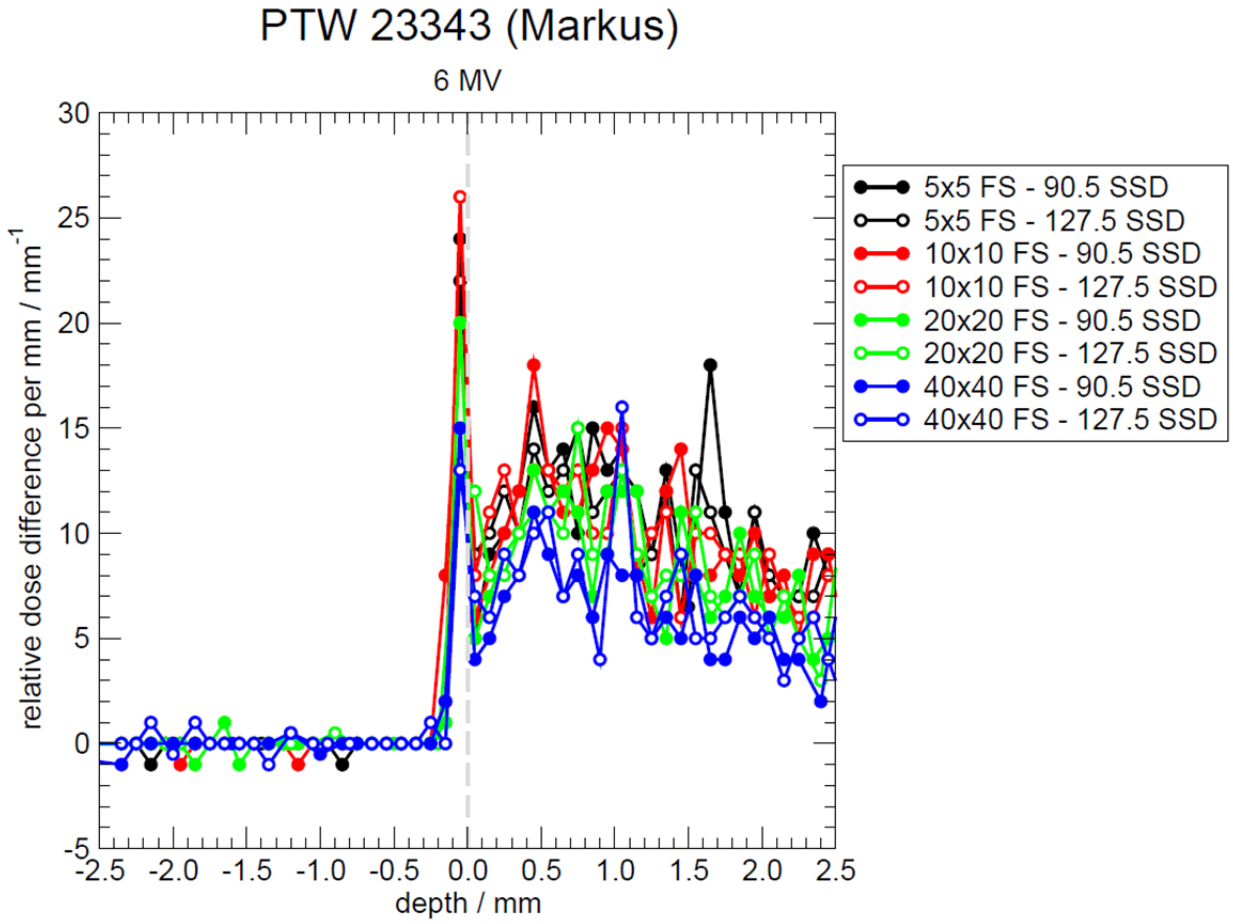

Figure 133: First derivatives of the scans shown in Figure 132. All gradient peaks occur as the PTW Markus parallel-plate IC emerges from water into air. The salient feature is not necessarily overall peak height but the relative maximum beyond which the gradient goes to zero.

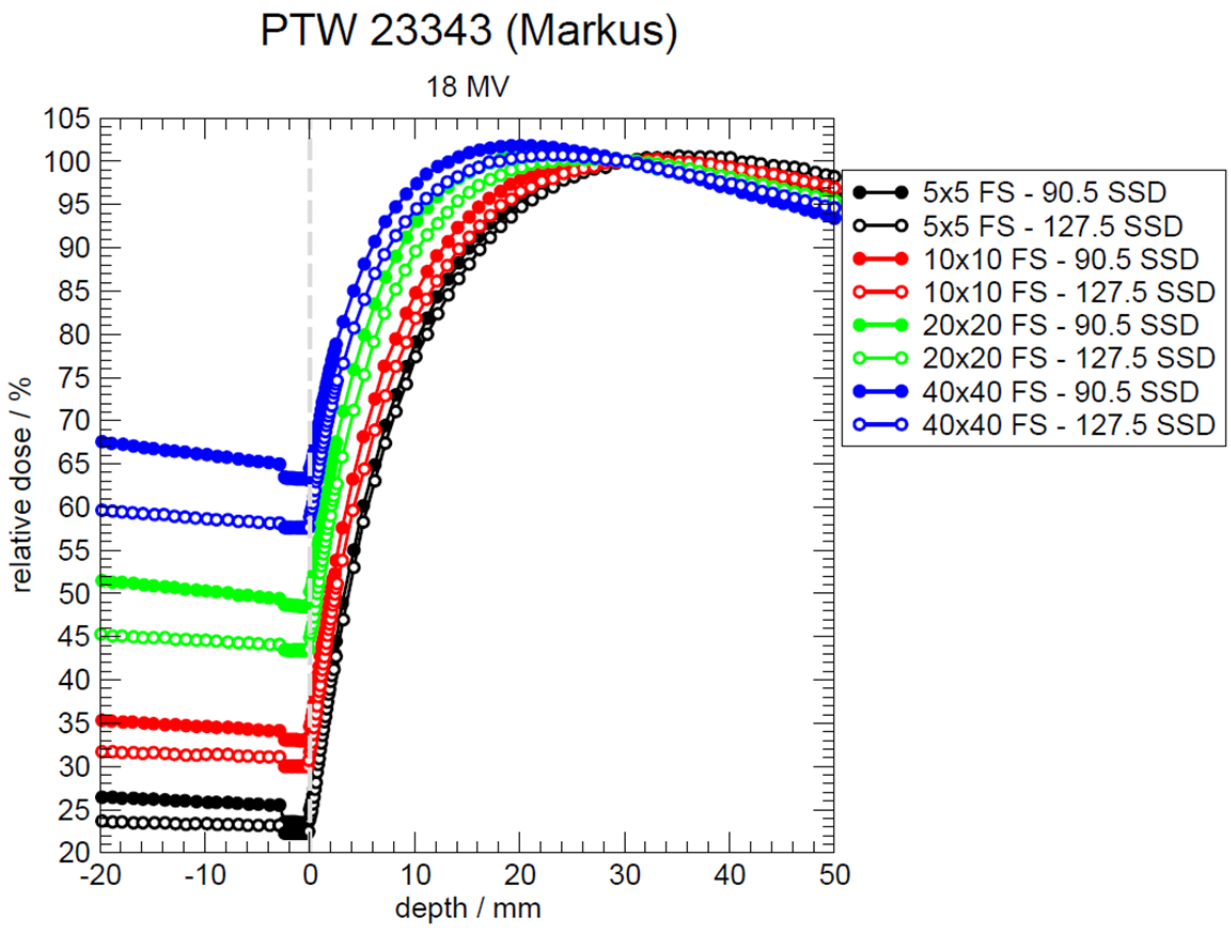

Figure 134: PDDs measured with the PTW Markus parallel-plate IC for extended and shortened SSD at 18 MV for four field sizes each. 90.5 cm SSD is the shortest SSD that can be achieved without colliding the tank and accelerator. 127.5 cm SSD is the farthest distance from the accelerator to which the tank can be lowered. All scans are performed from depth in water through the surface into air. Scans are performed at 1 mm resolution from 50 to 3 mm and from -3 to -20 mm. From 2.5 to -2.5 mm, data is acquired at 0.1 mm resolution. Each data point represents an average of, at minimum, 50 sample readings, taking place over 1 second intervals. From 2.5 to -2.5 mm, the sampling rate is 10 seconds per point (500 samples). The strange jumps in the in-air signal are artifacts caused by the way scans at different sampling times are stitched together. Figure 69 shows the physical explanation for the sampling time dependence and a solution. The grey dashed line marks the nominal water surface.

The 18 MV PDDs are shown in Figure 134. The same changes in relative dose between 2.5 and 3 mm above the water surface in air are seen here as are seen in the 6 MV PDDs measured with this surface. Again, the presence of water on the IC front face for more quickly acquired scans causes this difference. In-air relative dose increases with decreased SSD. The SSD-dependent difference in relative dose increases with increased field size as more contaminant electrons from within the treatment head cross the IC. As seen in Figure 135, all 18 MV gradient peaks occur 0.05 mm from the water surface location in air, which is a

negligible difference. The measurements discussed in this section indicate that gradient peak location does not depend on SSD.

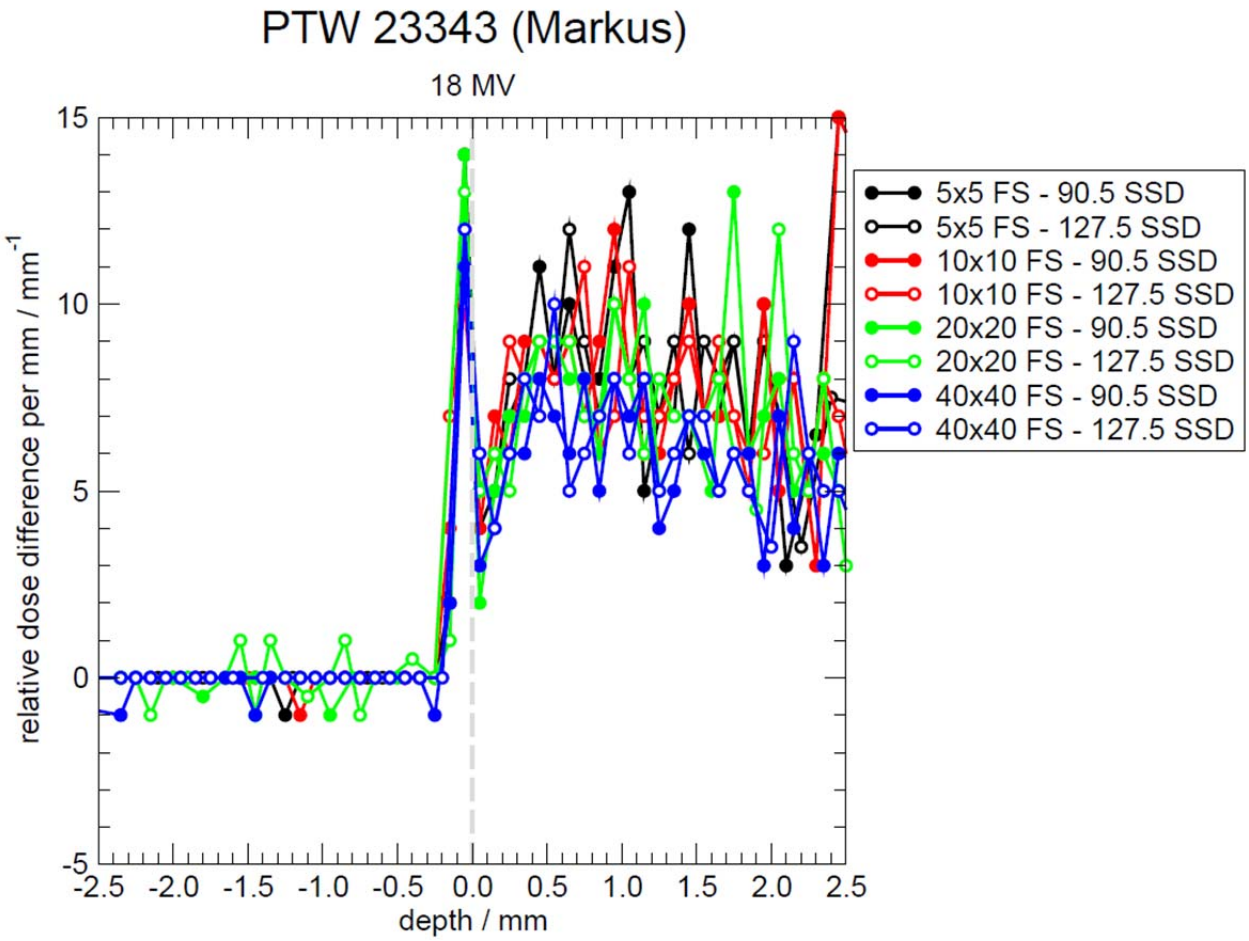

Figure 135: First derivatives of the scans shown in Figure 134. All gradient peaks occur as the PTW Markus parallel-plate IC emerges from water into air. The salient feature is not necessarily overall peak height, but the relative maximum beyond which the gradient goes to zero.

4.4.4 Electron Contamination

The contaminant electrons discussed in the previous two sections can be problematic for reference dosimetry. As the electrons are produced by radiation interactions with accelerator components, it follows that the amount of electron contamination in a given photon beam is accelerator-dependent. AAPM TG-51 recommends removal of the contaminant electrons originating from the accelerator treatment head via placement of a 1 mm thick lead foil in the beam path for reference dosimetry measurements of photon beams with incident energy ≥10 MV

(Almond *et al.*, 1999). The lead foil will absorb electrons from the treatment head and provide a constant source of electrons that can be consistently corrected for than the treatment head-dependent scattered electrons.

In this section, the effect of placing a lead foil in the beam path on the gradient peak location is tested. Measurements are taken with the IBA CC13 cylindrical IC and the PTW 23343 (Markus) parallel-plate IC in 6 and 18 MV photon beams from the Varian 2300 accelerator. Scans are performed for 10×10 cm^2 fields with and without a lead foil placed in the beam path, taped to the bottom of the accelerator treatment head. With the lead foil in the beam path, scans with each IC are taken at both energies for three additional field sizes: 5×5 cm^2, 20×20 cm^2, and 40×40 cm^2. Scans with the CC13 are performed at 0.1 mm resolution from 4 mm in water to 1 mm above the surface in air. Scans with the 23343 are performed at 0.1 mm resolution from 2.5 mm in water to 2.5 mm above the water surface in air.

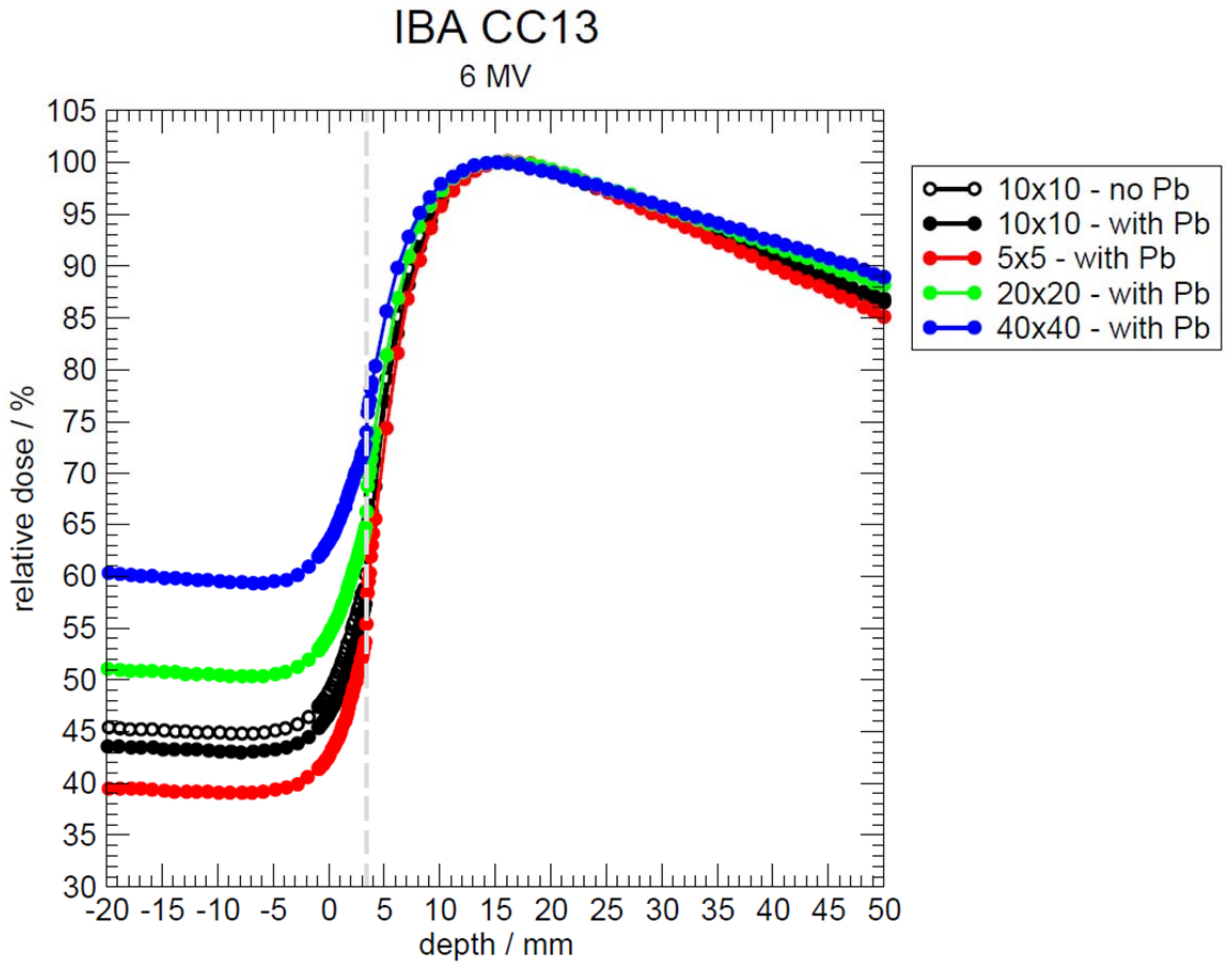

Figure 136: PDDs measured with the IBA CC13 cylindrical IC at 6 MV at 100 cm SSD for four field sizes with a 1 mm thick lead foil placed in the beam. A 10×10 cm^2 field scan without the lead foil is included as a reference. All scans are performed from depth in water through the surface into air. Scans are performed at 1 mm resolution from 50 to 4 mm and from -1 to -20 mm. From 4 to -1 mm, data is acquired at 0.1 mm resolution. Each data point represents an average of, at minimum, 50 sample readings, taking place over 1 second intervals. From 4 to 3 mm, the sampling rate is 4 seconds per point (200 samples), or, in the case of the scan without the lead foil, 10 seconds per point (500 samples). The grey dashed line marks the DeICERS at 3.4 mm.

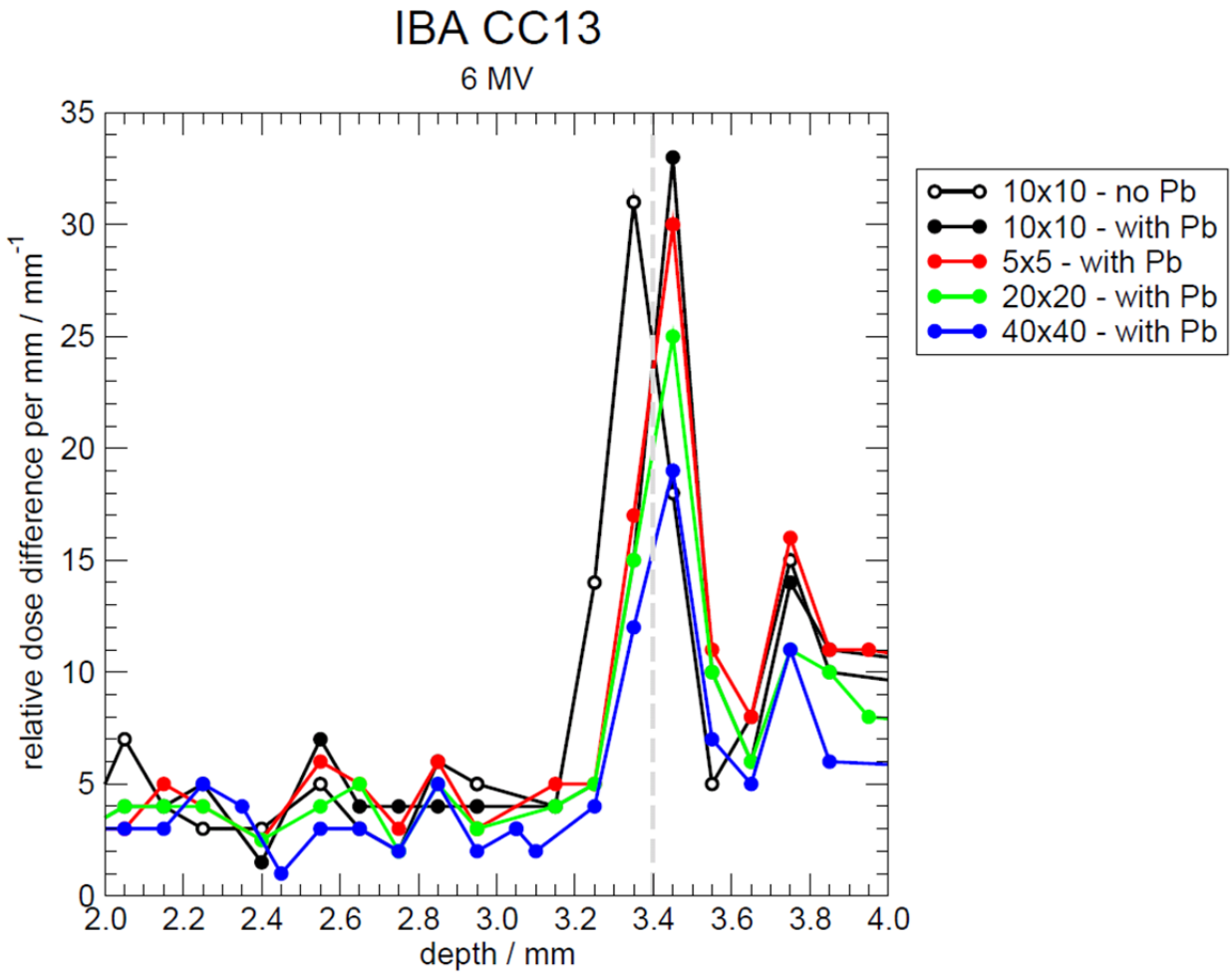

Figure 137: First derivatives of the scans shown in Figure 136. All gradient peaks occur within 0.05 mm of the DeICERS, a discrepancy that is within the 0.1 mm measurement step size.

Figure 136 shows the 6 MV PDDs measured with the IBA CC13. The measurement without the lead foil in place shows a ~5% greater in-air dose than the measurement for the same field with the lead foil in the beam path. The relative dose gradients shown in Figure 137 all exhibit peaks within 0.05 mm of the DeICERS, marked by the grey dashed line. The difference between the location of the gradient peaks and the DeICERS is within measurement uncertainty.

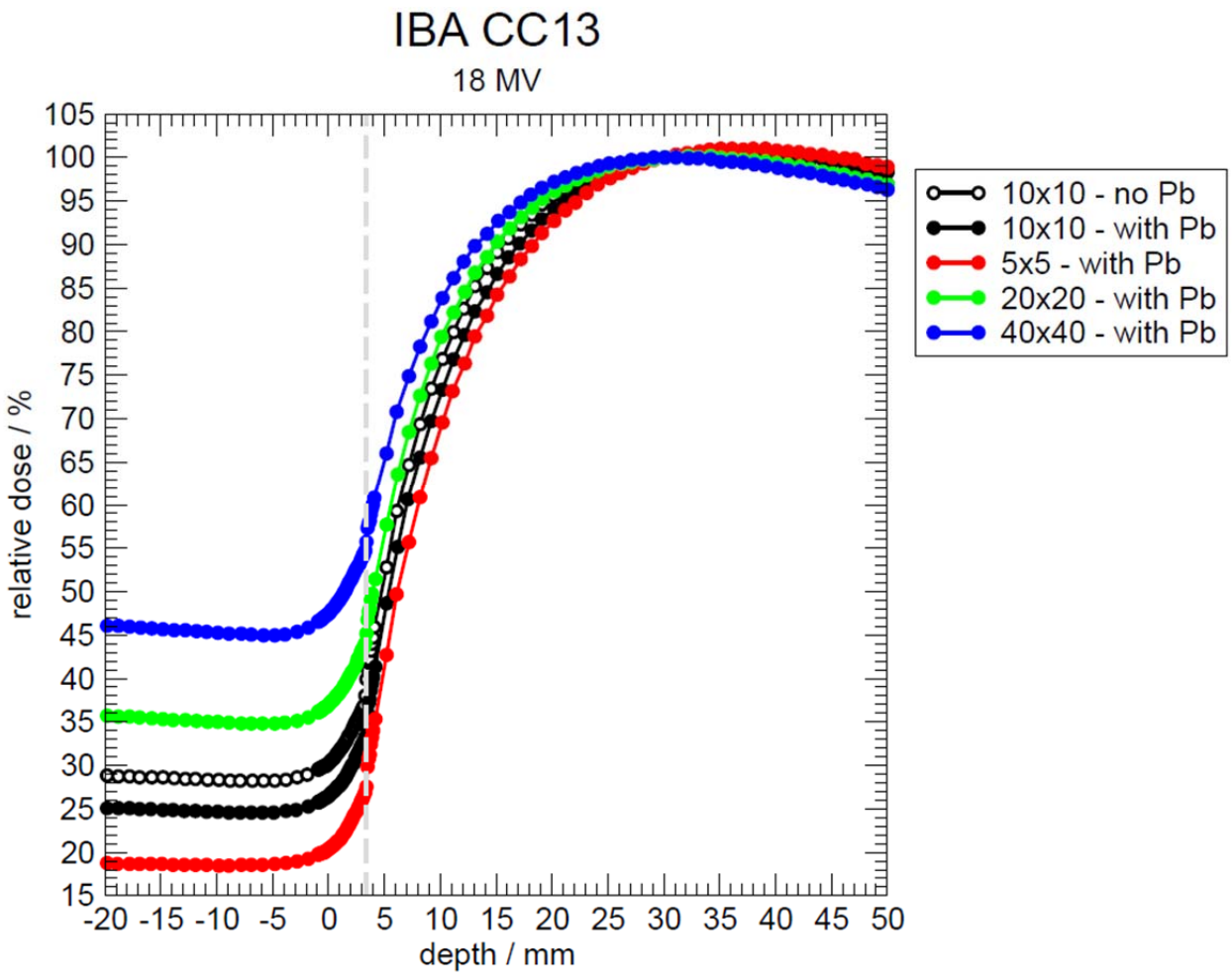

Figure 138: PDDs measured with the IBA CC13 cylindrical IC at 18 MV at 100 cm SSD for four field sizes with a 1 mm thick lead foil placed in the beam. A 10×10 cm^2 field scan without the lead foil is included as a reference. All scans are performed from depth in water through the surface into air. Scans are performed at 1 mm resolution from 50 to 4 mm and from -1 to -20 mm. From 4 to -1 mm, data is acquired at 0.1 mm resolution. Each data point represents an average of, at minimum, 50 sample readings, taking place over 1 second intervals. From 4 to 3 mm, the sampling rate is 4 seconds per point (200 samples). The grey dashed line marks the DeICERS at 3.4 mm.

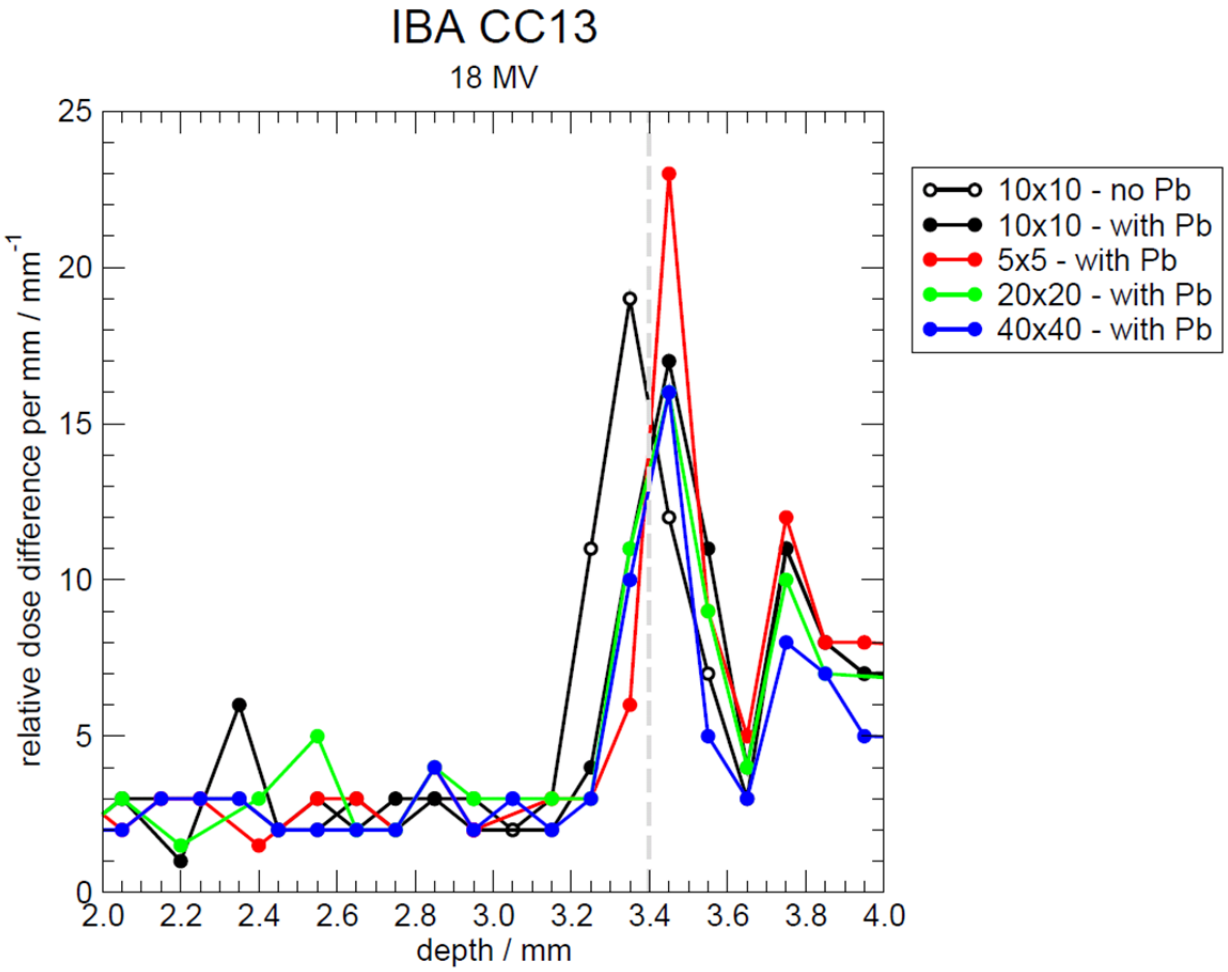

Figure 139: First derivatives of the scans shown in Figure 138. All gradient peaks occur within 0.05 mm of the known CC13 outer radius (3.4 mm).

The 18 MV PDDs measured with the IBA CC13 are shown in Figure 138. The lead foil-dependent dose difference is ~16% in this case. The relative dose gradients are shown in Figure 139. All gradients exhibit peaks occurring within 0.05 mm of the DeICERS, a difference within measurement uncertainty.

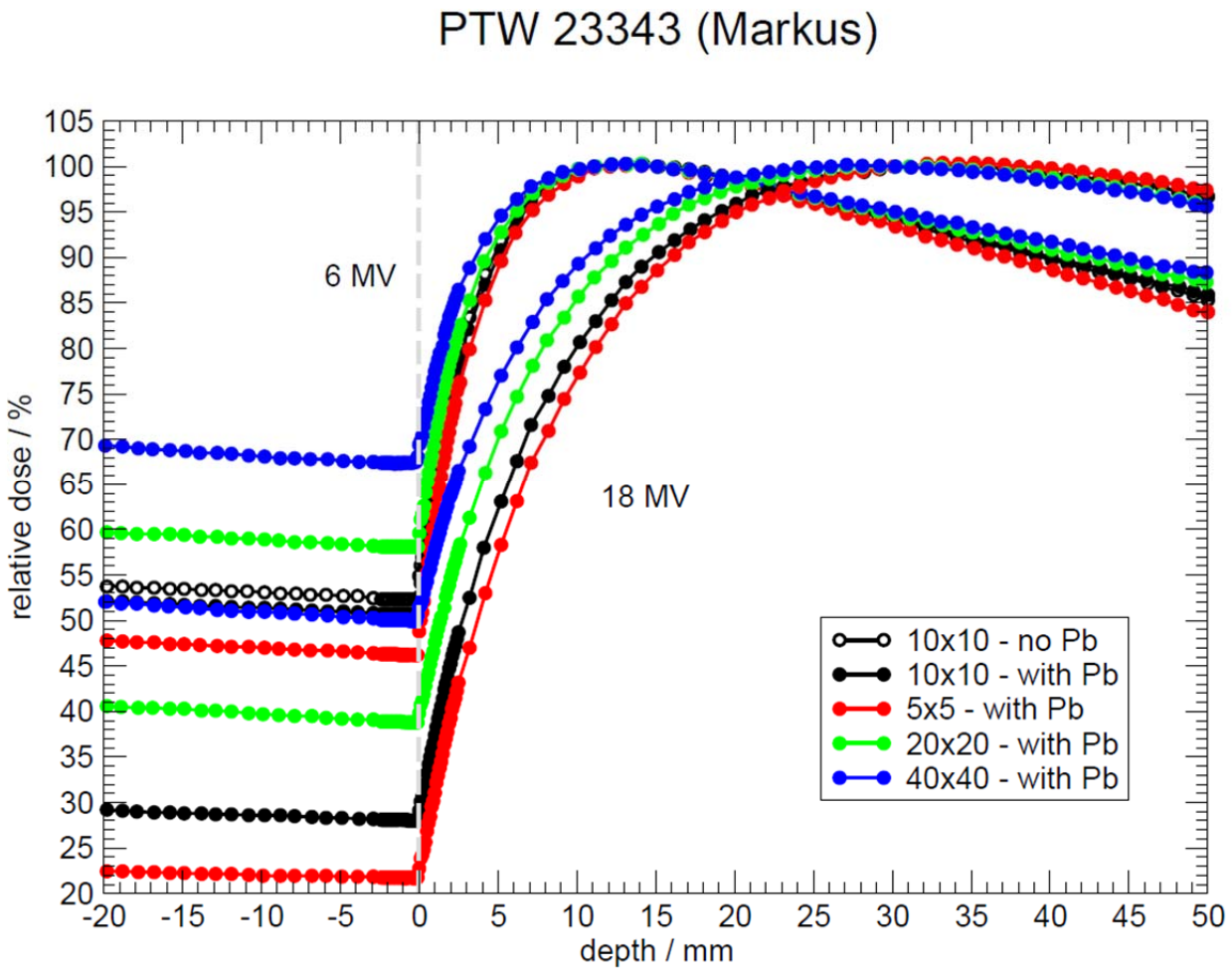

Figure 140: PDDs measured with the PTW Markus parallel-plate IC at 6 and 18 MV at 100 cm SSD each for four field sizes with a 1 mm thick lead foil placed in the beam. A scan of a 6 MV 10×10 cm^2 field without the lead foil is included as a reference. All scans are performed from depth in water through the surface into air. Scans are performed at 1 mm resolution from 50 to 3 mm and from -3 to -20 mm. From 2.5 to -2.5 mm, data is acquired at 0.1 mm resolution. Each data point represents an average of, at minimum 50 sample readings, taking place over a 1 second interval. From 2.5 to -2.5 mm, the sampling rate is 10 seconds per point (500 samples). The grey dashed line marks the DeICERS.

All PDDs measured with the PTW 23343 for this experiment are shown in Figure 140. A ~4% increase in dose in air is observed without the lead foil in the beam path for the 10×10 cm^2 field scan, which is not inconsistent with the increase observed for the IBA CC13. The 6 MV relative dose gradients are shown in Figure 141. All gradient peaks occur at the same location, 0.05 mm shallower than the DeICERS. Figure 142 shows the relative dose gradients for the 18 MV scans. In this case, all gradient peaks occur within ±0.05 mm of the DeICERS. Both differences are within measurement uncertainty. It is concluded from the results of this

experiment that placement of a lead foil in the beam path to reduce the contaminant electrons reaching the IC has no effect on the ability of the gradient peak location to identify the water surface.

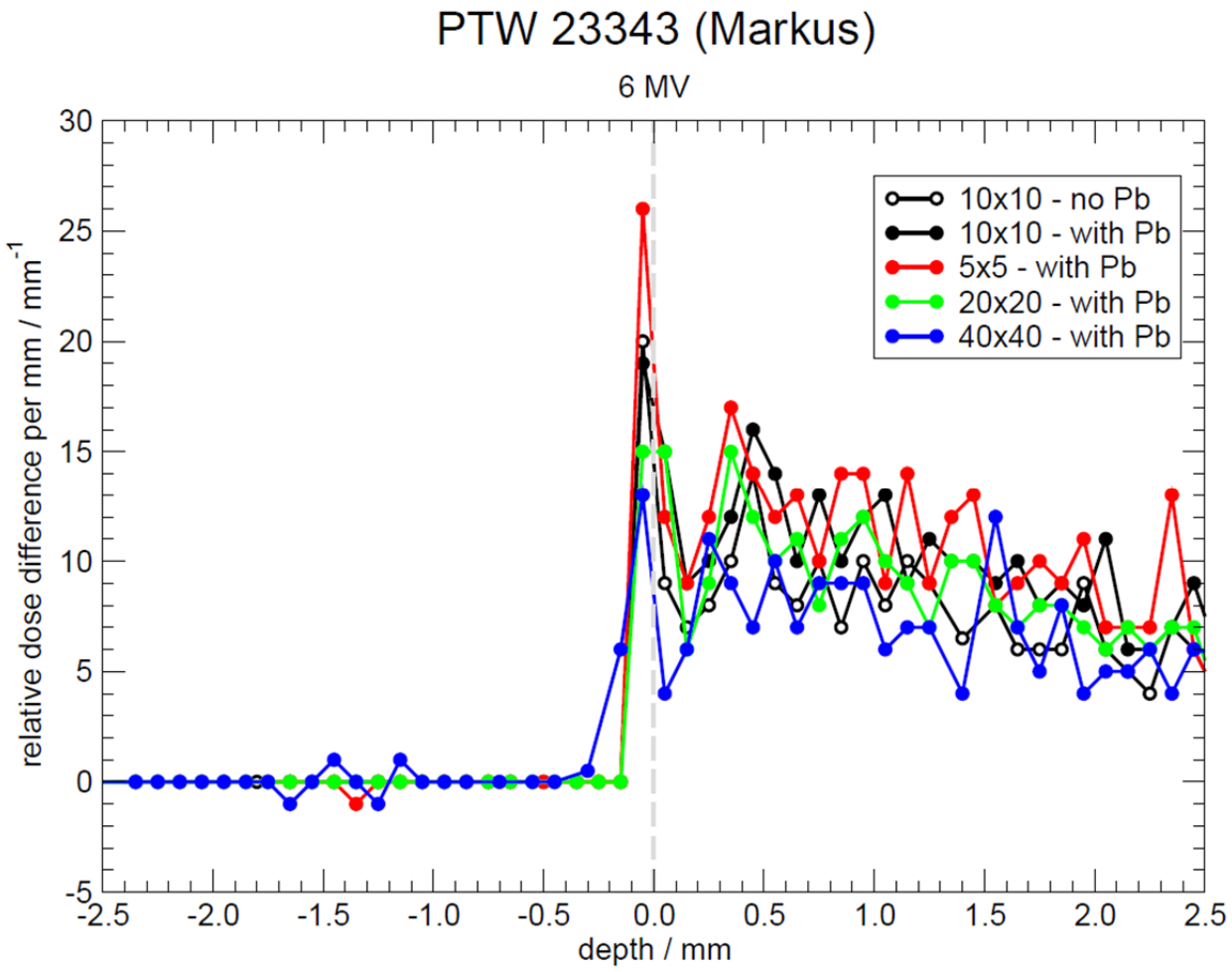

Figure 141: First derivatives of the 6 MV scans shown in Figure 140. All gradient peaks occur immediately as the PTW Markus parallel-plate IC emerges from water into air. Though the gradient peaks are relatively clean here, the salient feature is not necessarily overall peak height, but the relative maximum beyond which the gradient goes to zero.

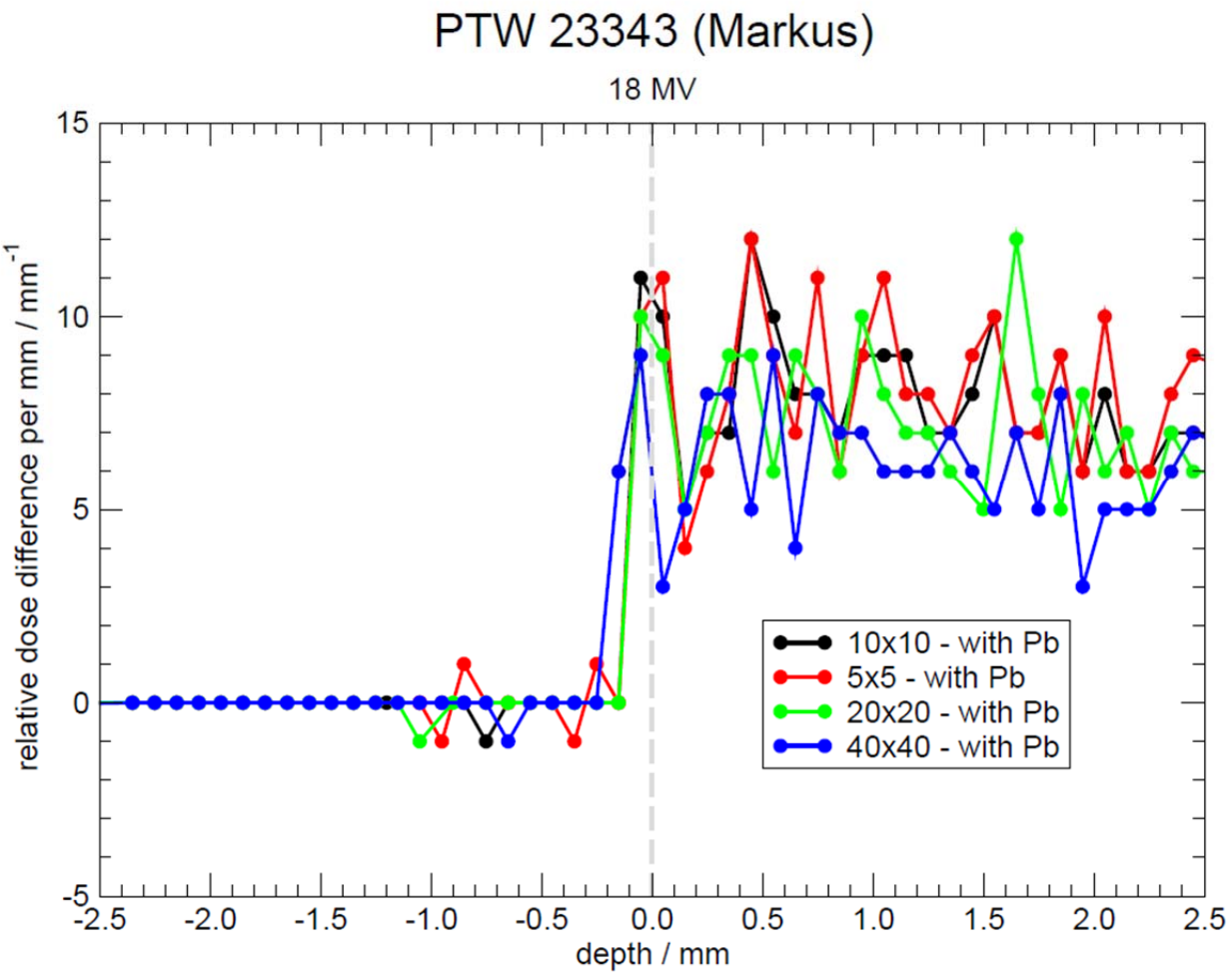

Figure 142: First derivatives of the 18 MV scans shown in Figure 140. All gradient peaks occur within 0.05 mm of the point at which the PTW Markus parallel-plate IC emerges from water into air. The noise in the in-water Markus signal increases with beam energy. The salient feature is not necessarily overall peak height, but the relative maximum beyond which the gradient goes to zero.

4.5 Ionization Chamber Type

It is shown throughout this work that the relative dose gradient peak occurs at the point at which an IC first reaches the water surface for measurements with several ICs and for several calculation scenarios. In the following sub-sections, IC measurements not already discussed with different IC designs are shown. The measurements are sorted by the site at which they are taken. First, measurements taken at VCU with the IBA Blue Phantom are discussed, grouped as cylindrical IC measurements and parallel-plate IC measurements. The next section describes measurements taken at the NRC with the custom-built high-precision scanning system.

4.5.1 Virginia Commonwealth University

In-house measurements at VCU are taken with 14 cylindrical IC types and 5 parallel-plate IC types. Measurements with the IBA CC13 and PTW 31010 cylindrical ICs have already been covered in this thesis and will not be repeated here. The PTW 23343 (Markus) parallel-plate IC has also been discussed thoroughly and will not be covered in this section. All measurements shown here are taken on the Varian 2300 accelerator in 6 and 18 MV photon beams set to 10×10 cm^2 fields at 100 cm SSD. The ICs used for in-house measurements are all initially aligned following the method recommended by AAPM TG-106 (Das *et al.*, 2008). Measurements with the remaining 12 cylindrical IC types are shown in Section 4.5.1.1. The remaining 4 parallel-plate IC types are covered in Section 4.5.1.2.

4.5.1.1 Cylindrical Ionization Chamber Designs

All cylindrical IC measurements are performed from 50 mm below the water surface to 20 mm above the water surface in air. Scan spatial resolution is always 0.1 mm around the DeICERS. In all gradient plots, this depth is designated by a grey dashed line. The order in which IC measurements are presented is the same order in which the ICs appear in Table 2, Table 3, and Table 4. PDDs measured on the VCU Varian 2300 in 6 and 18 MV photon beams with the cylindrical ICs borrowed for this thesis not already discussed are shown in Figure 143. The Exradin A1SL and A18 models have walls doubly thick of the rest of the ICs scanned here, yielding an increased in-air dose relative to other ICs. The schematic designs of all of the Exradin ICs are shown in Figure 33.

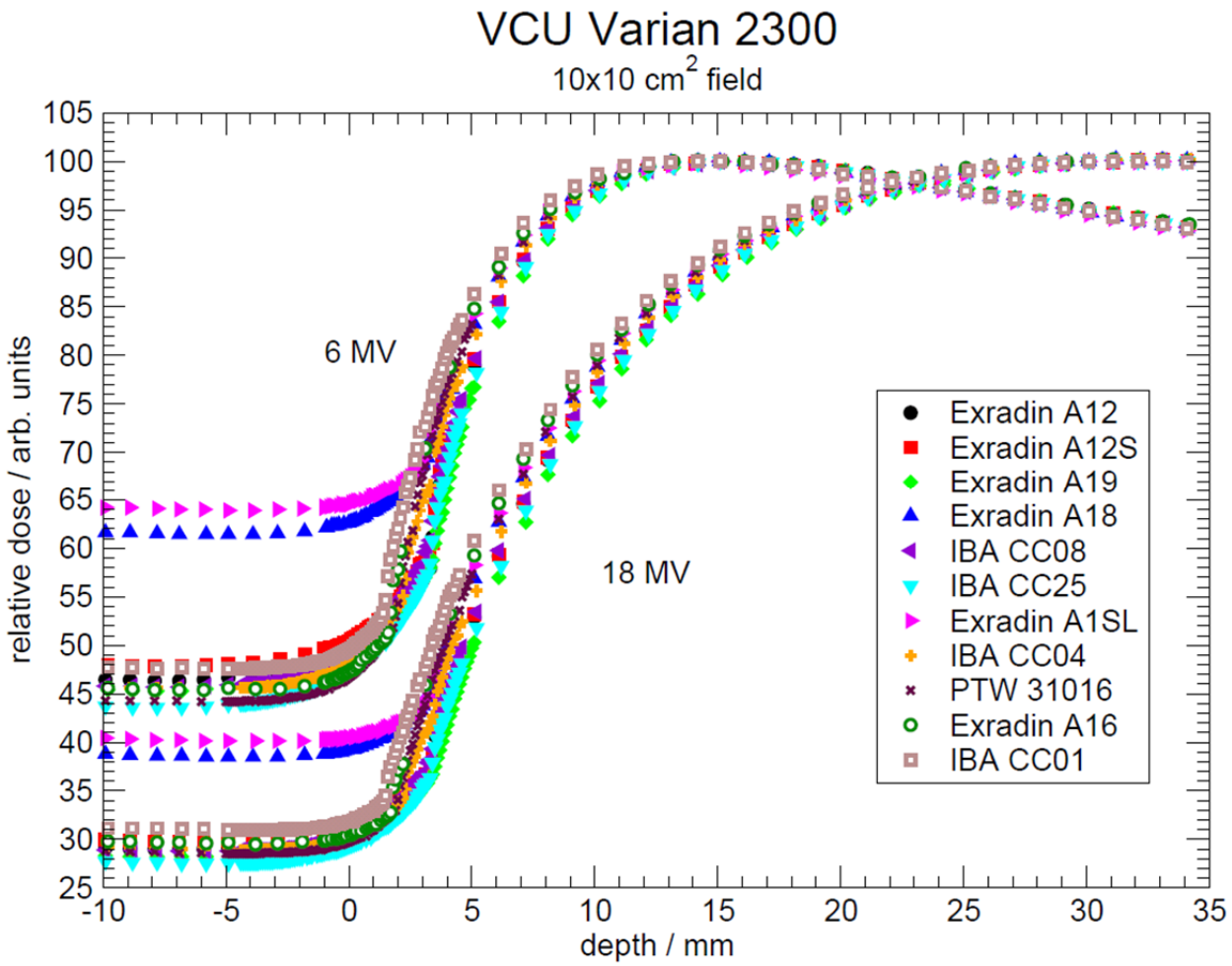

Figure 143: PDDs measured at VCU on the Varian 2300 in 6 and 18 MV beams with the cylindrical ICs used for this thesis. All 6 MV scans are normalized to 100% relative dose at 15 mm depth. All 18 MV scans are normalized to 100% relative dose at 30 mm depth. The legend is sorted by IC outer radius.

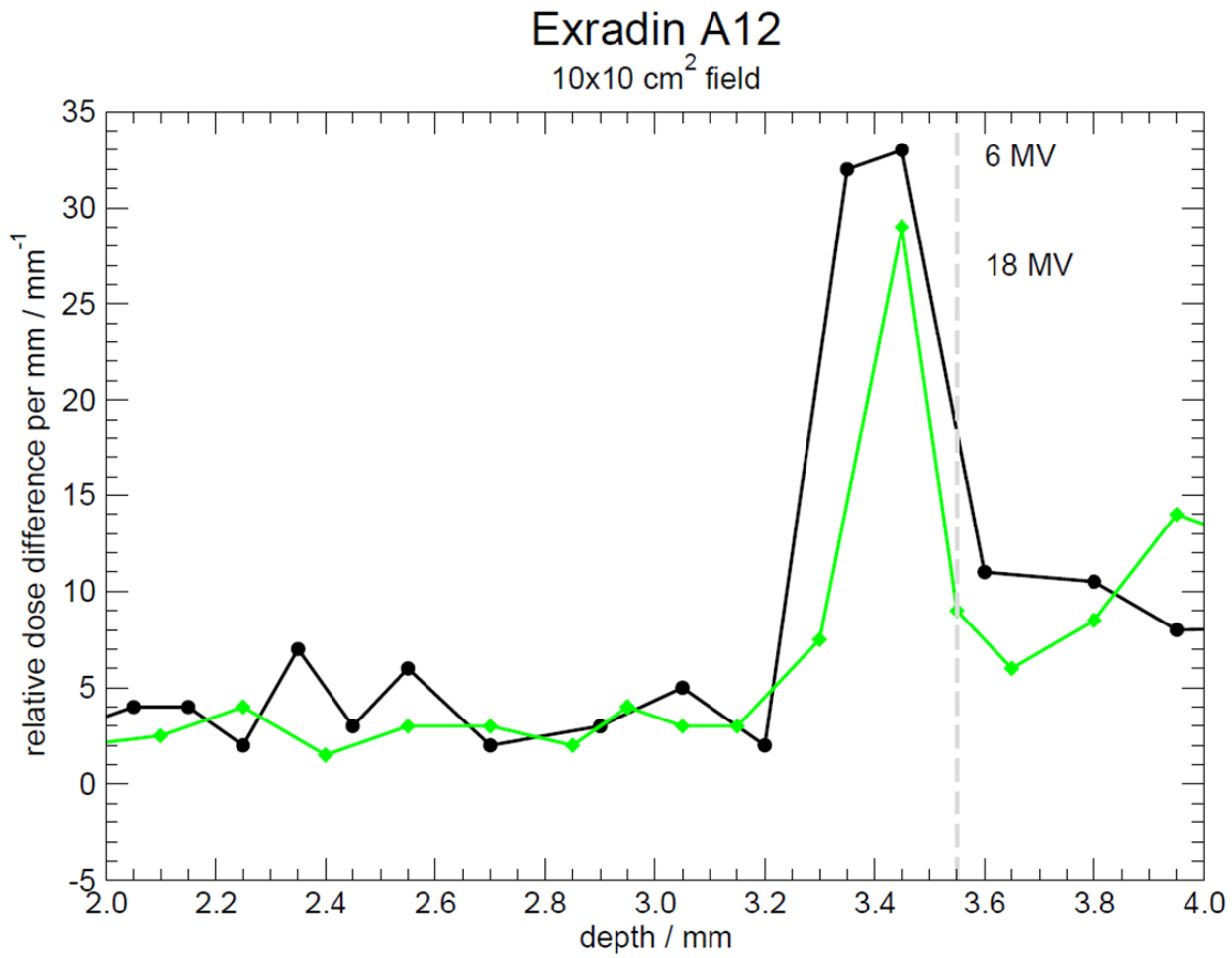

Figure 144: First derivatives of PDDs measured with the Exradin A12 cylindrical IC for the Varian 2300 6 and 18 MV beams at a 10×10 cm^2 field. The grey dashed line marks the DeICERS.

The Exradin A12 relative dose gradients are shown in Figure 144. The gradients of scans at both photon energies exhibit peaks at the same location, 0.1 mm shallower than the DeICERS, 3.55 mm. This is within the uncertainty of the VCU measurements. The Exradin A12S relative dose gradients are shown in Figure 145. The gradient peaks from scans at both energies occur 0.1 mm shallower than the DeICERS, 3.55 mm, which is within measurement uncertainty and consistent with the Exradin A12 measurements. Figure 146 shows the Exradin A16 relative dose gradients. Scans at both energies exhibit gradient peaks at the same location, 0.05 mm deeper in water from the DeICERS of 1.7 mm. This difference is within measurement uncertainty.

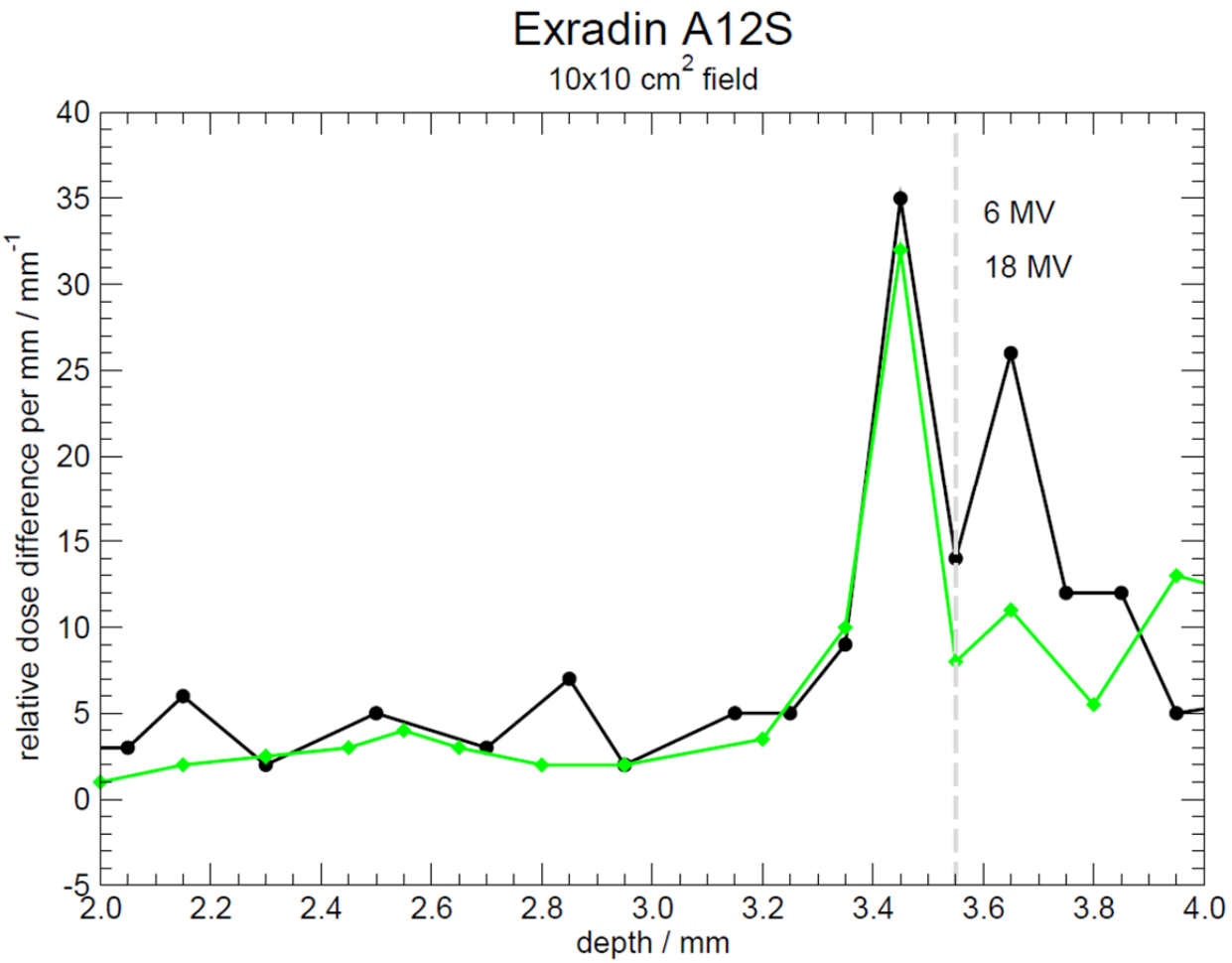

Figure 145: First derivatives of PDDs measured with the Exradin A12S cylindrical IC for the Varian 2300 6 and 18 MV beams at a 10×10 cm^2 field. The grey dashed line marks the DeICERS.

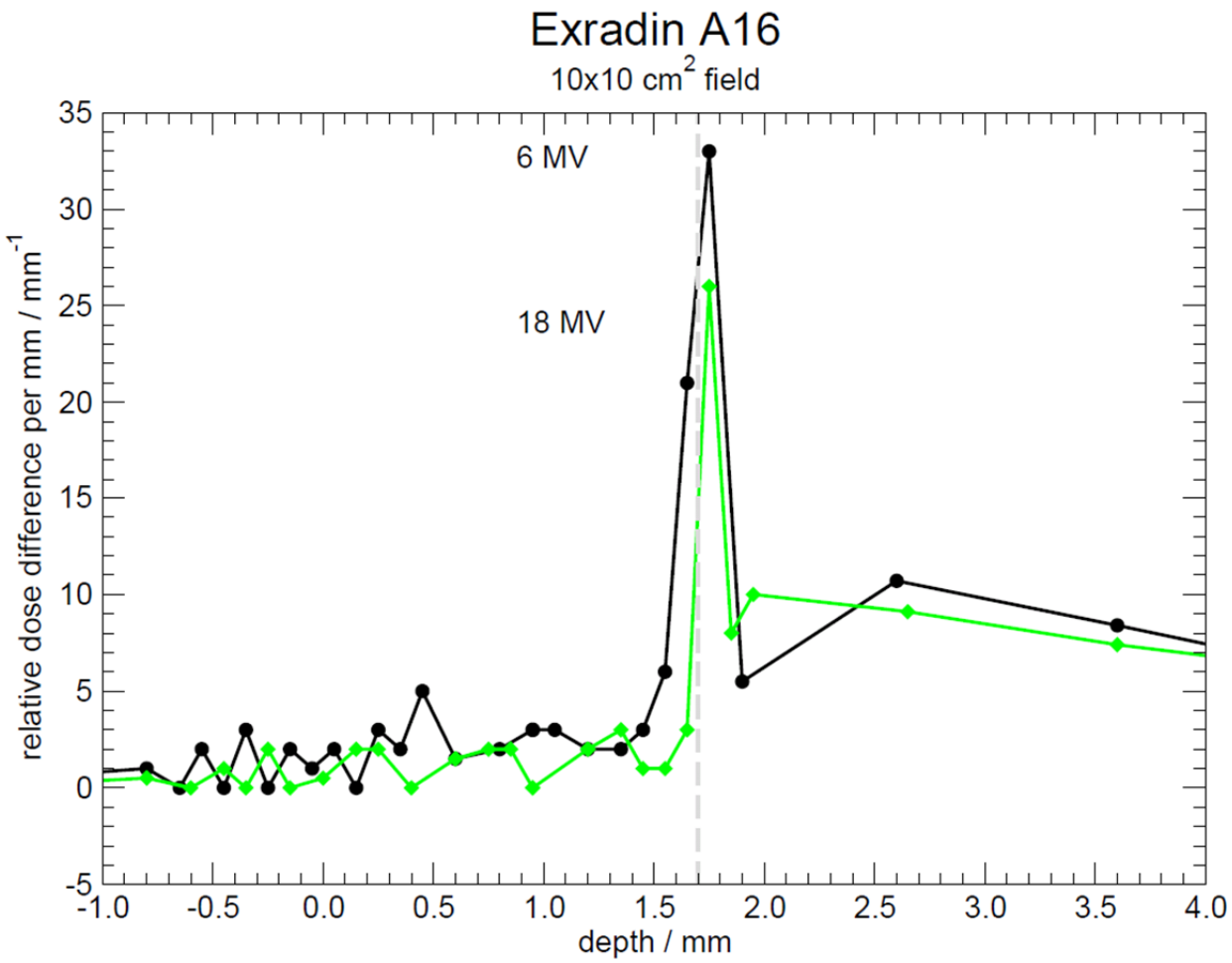

Figure 146: First derivatives of PDDs measured with the Exradin A16 cylindrical IC for the Varian 2300 6 and 18 MV beams at a 10×10 cm^2 field. The grey dashed line marks the DeICERS.

The gradients in relative dose measured with the Exradin A18 are shown in Figure 147. The gradients of scans at both energies exhibit peaks at the same location, which corresponds with the DeICERS of 3.45 mm. The Exradin A19 relative dose gradients are shown in Figure 148. The gradient peaks for scans at both energies occur at the DeICERS, 3.55 mm. The Exradin A1SL relative dose gradients are shown in Figure 149. There is a 0.1 mm discrepancy between the two gradient peaks but the DeICERS of 3.175 mm lies between the two measured gradient peaks and the 0.1 mm discrepancy is within measurement uncertainty.

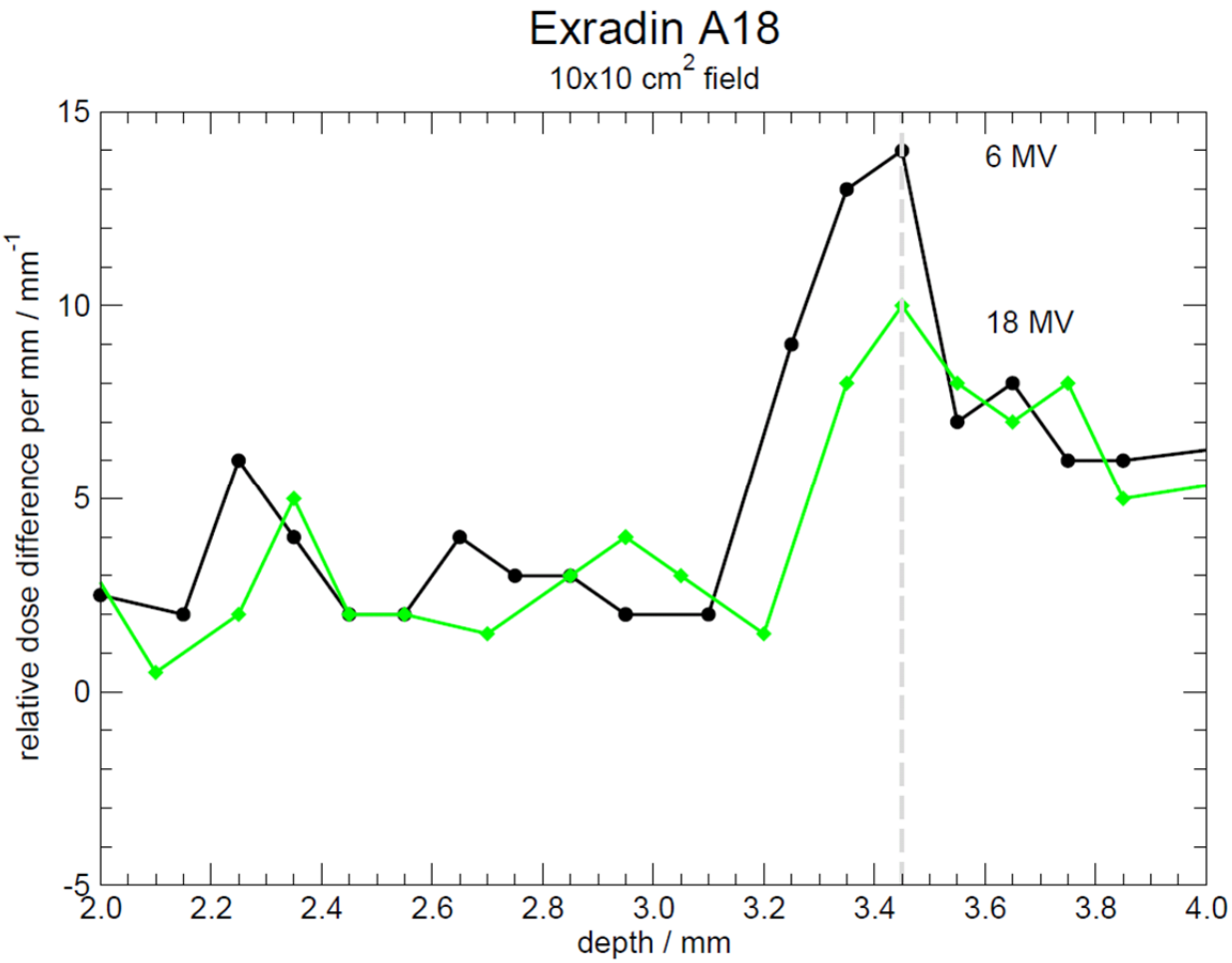

Figure 147: First derivatives of PDDs measured with the Exradin A18 cylindrical IC for the Varian 2300 6 and 18 MV beams at a 10×10 cm^2 field. The grey dashed line marks the DeICERS.

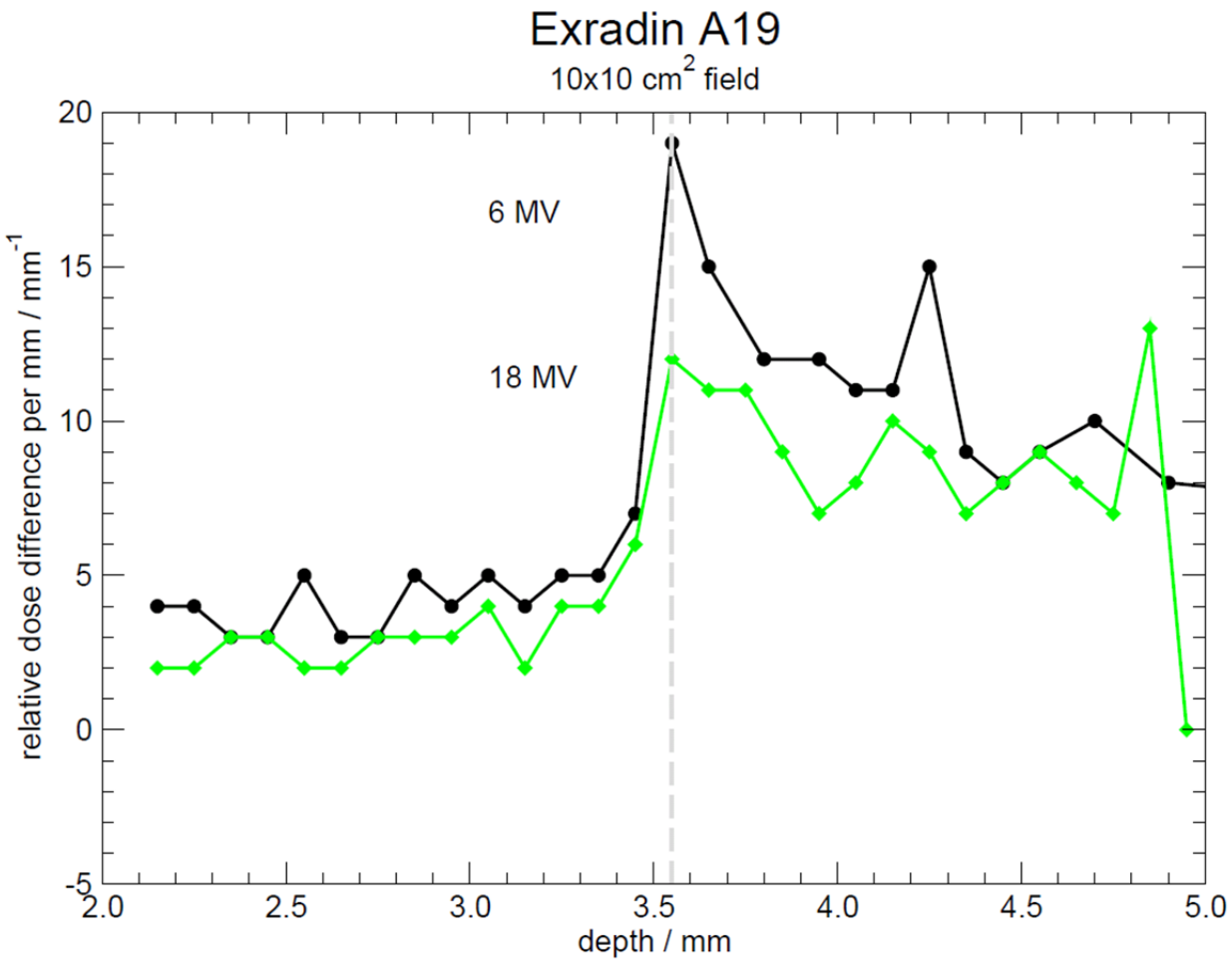

Figure 148: First derivatives of PDDs measured with the Exradin A19 cylindrical IC for the Varian 2300 6 and 18 MV beams at a 10×10 cm^2 field. The grey dashed line marks the DeICERS.

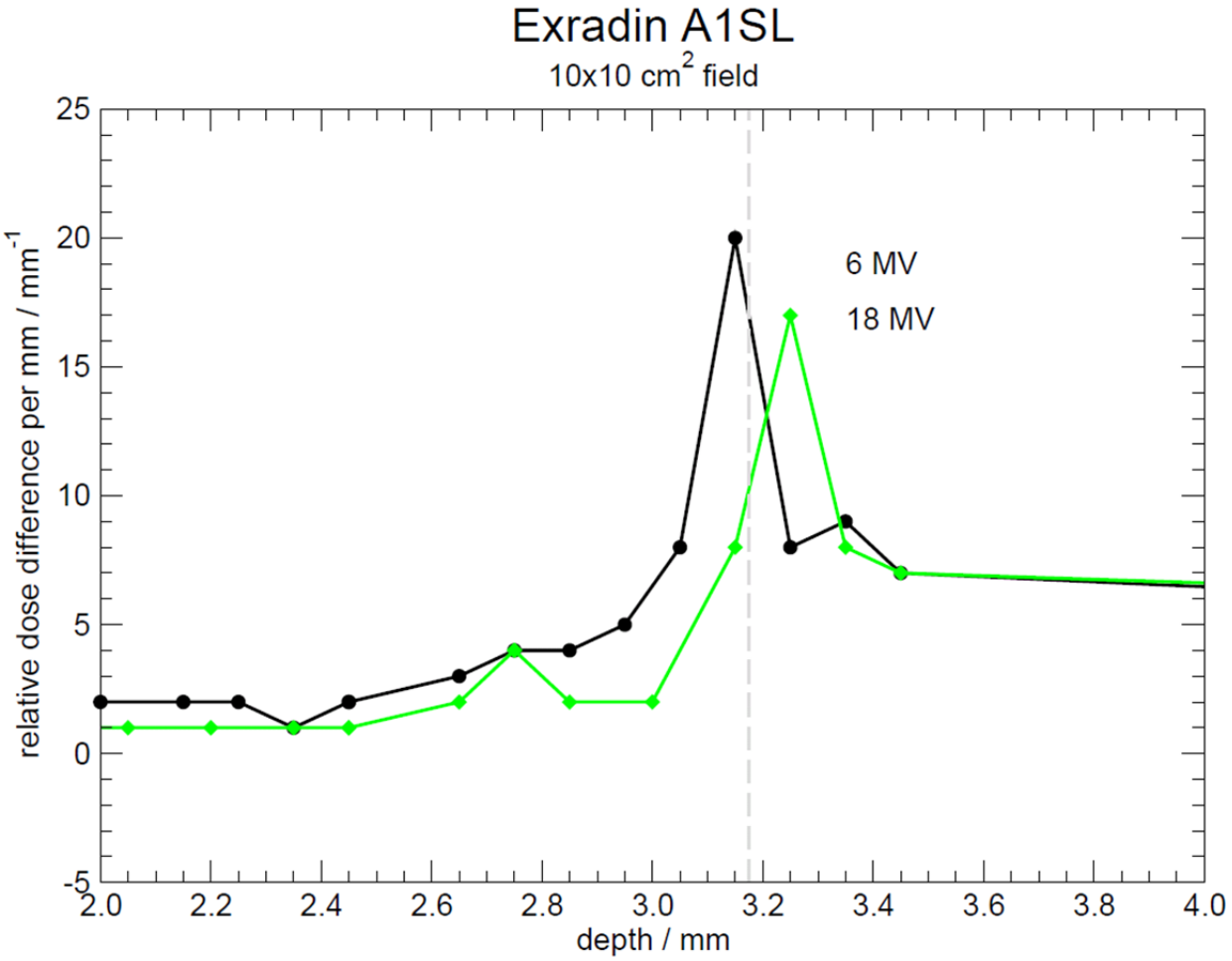

Figure 149: First derivatives of PDDs measured with the Exradin A1SL cylindrical IC for the Varian 2300 6 and 18 MV beams at a 10×10 cm^2 field. The grey dashed line marks the DeICERS.

The IBA CC01 relative dose gradients are shown in Figure 150. The CC01 is most like the Exradin A16, of the designs shown in Figure 33, except that it has a longer central electrode of different material than the A16. Both gradient peaks occur at the same location, 0.05 mm deeper in water than the DeICERS of 1.5 mm. The discrepancy between the location of the gradient peaks and the DeICERS is within measurement uncertainty. The IBA CC04 relative dose gradients are shown in Figure 151. The CC04 is a slightly larger version of the CC01, though with a central electrode similar to those used in most Exradin ICs. Gradients of scans at both energies exhibit peaks at the same location, 0.05 mm shallower than the DeICERS of

2.4 mm. The 0.05 mm discrepancy is within the uncertainty of the measurement setup. Given the large hemispherical component of the CC04 cavity volume, where IC radius is variable with respect to the water surface, this result may in fact indicate a small misalignment of the IBA CC04.

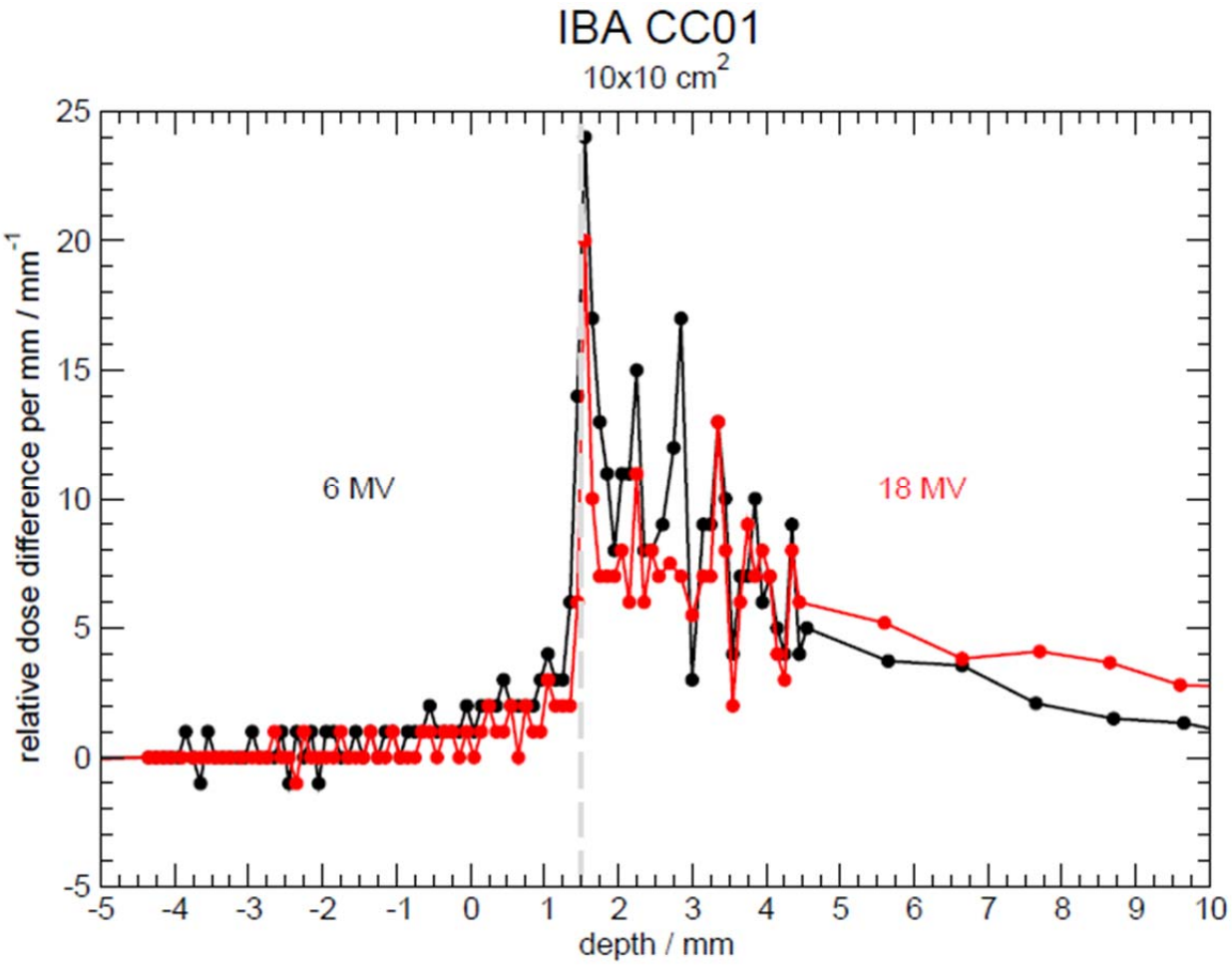

Figure 150: First derivatives of PDDs measured with the IBA CC01 cylindrical IC for the Varian 2300 6 and 18 MV beams at a 10×10 cm^2 field. The grey dashed line marks the DeICERS.

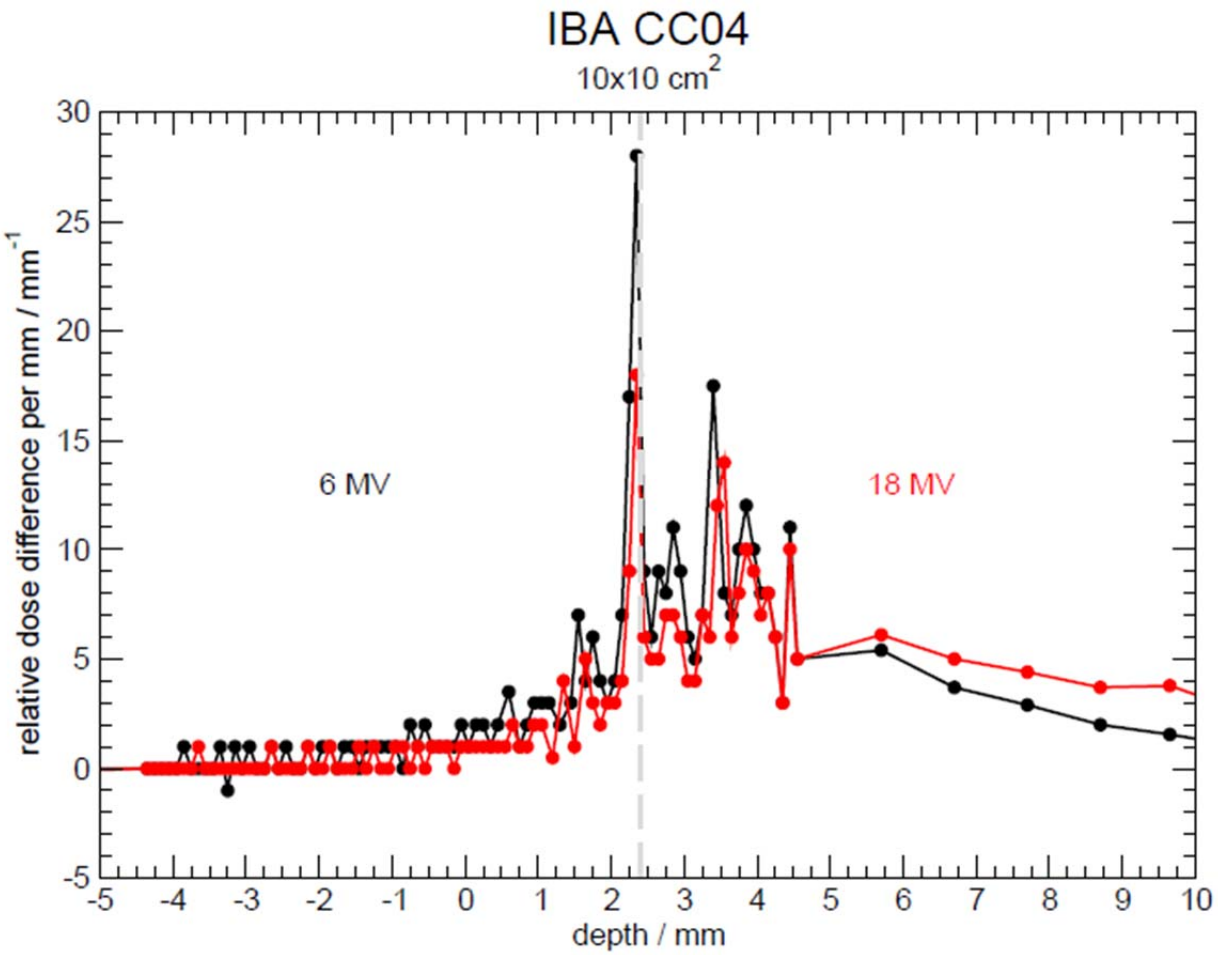

Figure 151: First derivatives of PDDs measured with the IBA CC04 cylindrical IC for the Varian 2300 6 and 18 MV beams at a 10×10 cm^2 field. The grey dashed line marks the DeICERS.

Figure 152 shows the IBA CC08 relative dose gradients. The CC08 is a larger version of the CC04 with a shorter central electrode. As with the CC04, the CC08 active volume is largely hemispherical. The gradient peaks from scans at both energies occur at the same location, 0.05 mm deeper in water than the DeICERS of 3.4 mm. The 0.05 mm discrepancy is within measurement uncertainty. Relative dose gradients for the IBA CC25 are shown in Figure 153. The CC25 has a longer air cavity and central electrode than the CC08 but the two are otherwise identical. The 6 MV scan shows a gradient peak 0.05 mm shallower than the DeICERS of 3.4 mm. The 18 MV scan shows two adjacent gradient points at the same maximal height that are ±0.05 mm from the DeICERS. These differences are within measurement uncertainty.

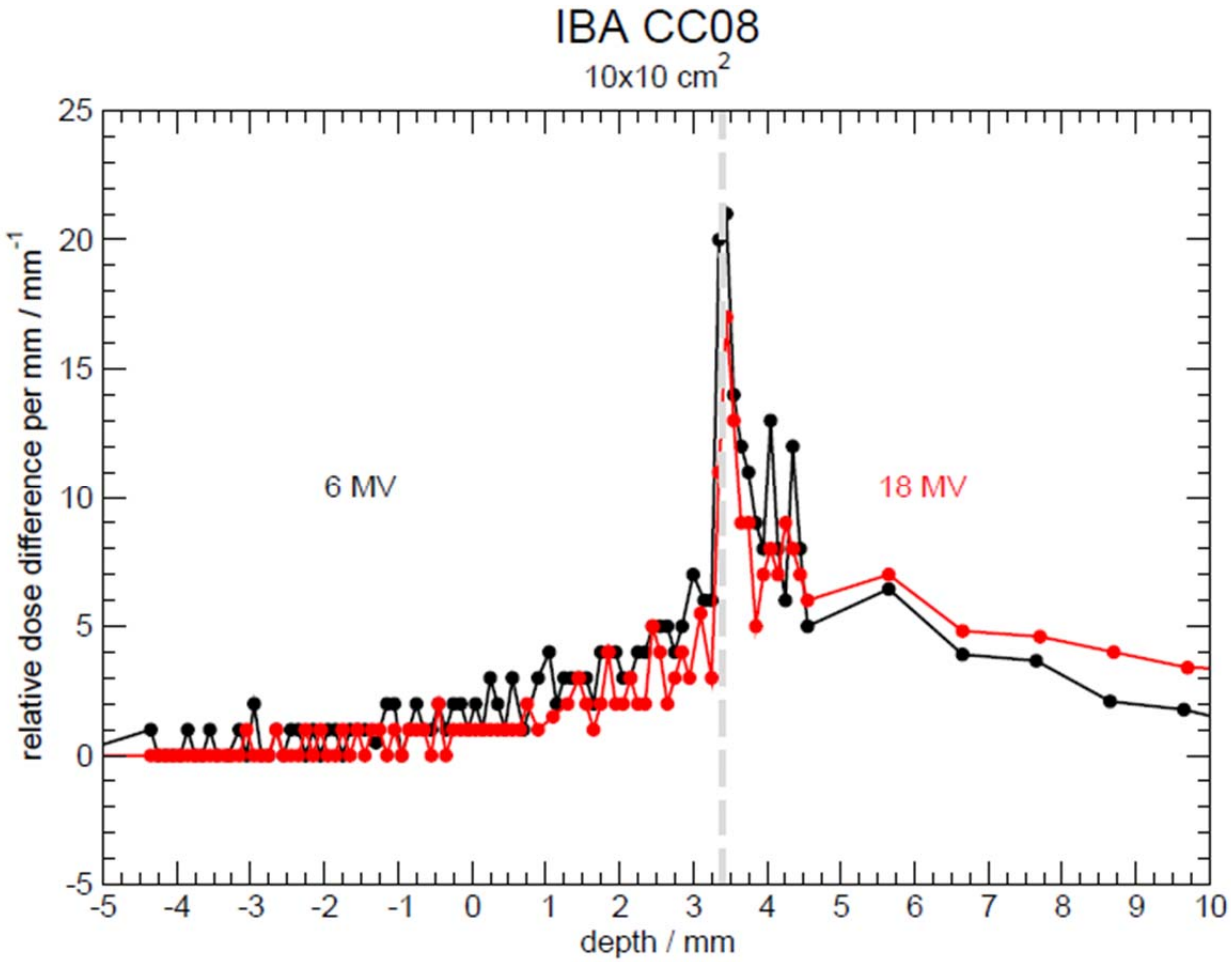

Figure 152: First derivatives of PDDs measured with the IBA CC08 cylindrical IC for the Varian 2300 6 and 18 MV beams at a 10×10 cm^2 field. The grey dashed line marks the DeICERS.

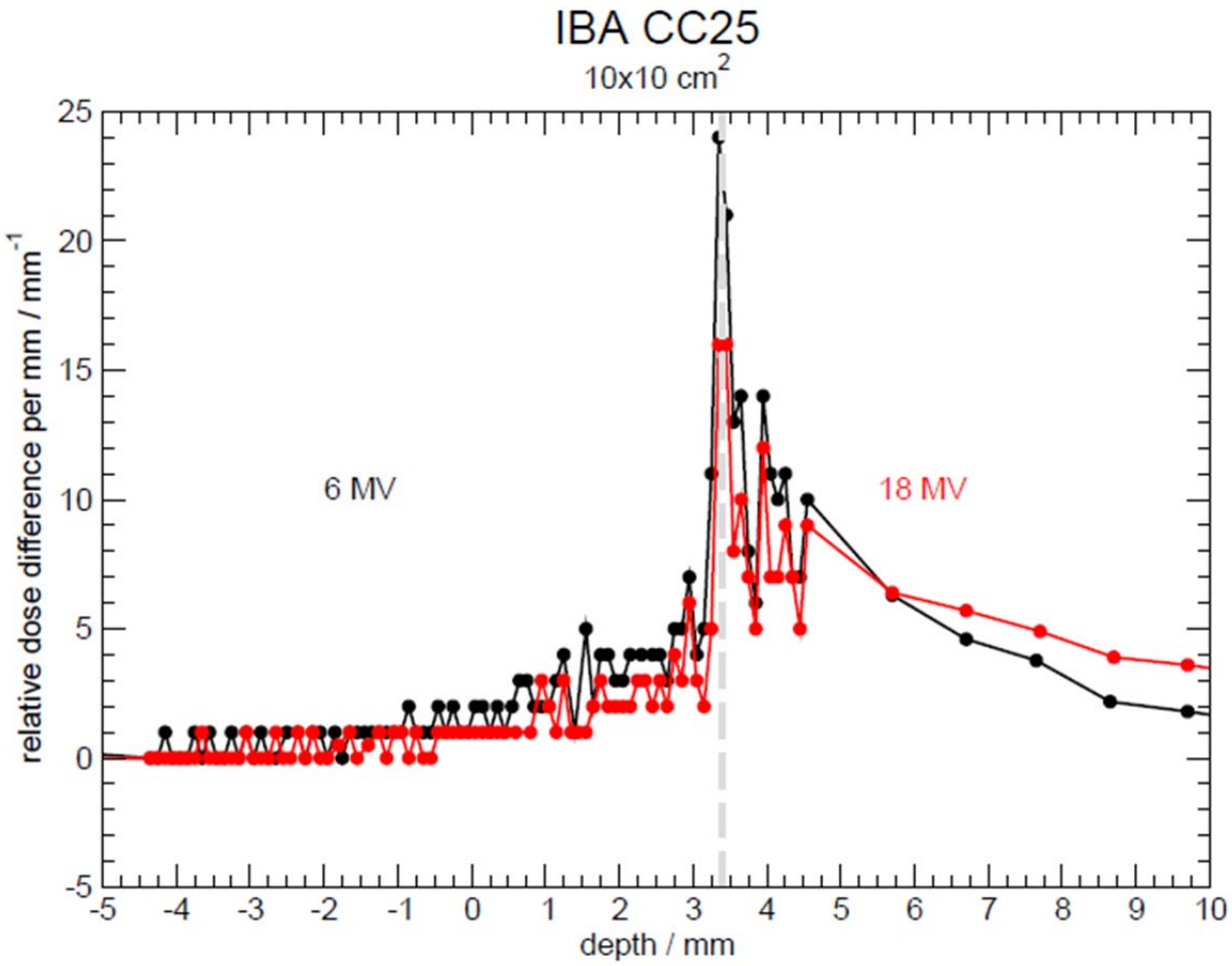

Figure 153: First derivatives of PDDs measured with the IBA CC25 cylindrical IC for the Varian 2300 6 and 18 MV beams at a 10×10 cm^2 field. The grey dashed line marks the DeICERS.

The relative dose gradients for the PTW 31016 are shown in Figure 154. The PTW 31016 is a micro-IC with the same nominal cavity volume as the Exradin A16, though the designs are different. Scans at both energies exhibit gradient peaks at the same location, 0.06 mm shallower than the DeICERS of 2.11 mm. The peak at 2.7 mm in the 6 MV scan is presumed to be caused by noise as there is no similar feature present in the 18 MV scan. All in-house cylindrical IC measurements show gradient peaks that are within measurement uncertainty of the DeICERS.

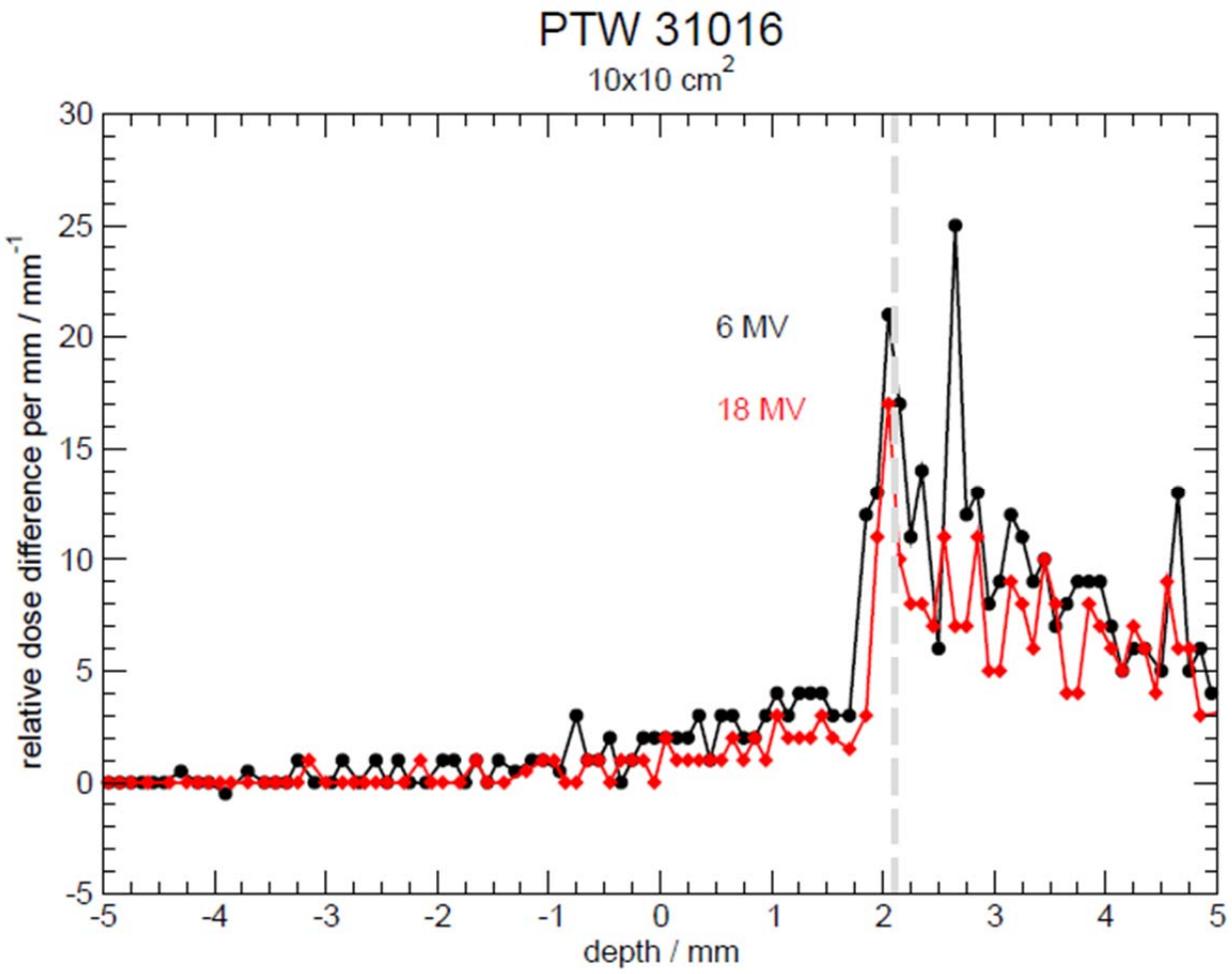

Figure 154: First derivatives of PDDs measured with the PTW 31016 cylindrical IC for the Varian 2300 6 and 18 MV beams at a 10×10 cm^2 field. The grey dashed line marks the DeICERS.

4.5.1.2 Parallel-Plate Ionization Chamber Designs

Most parallel-plate IC measurements are performed from 50 mm below the water surface to 20 mm above the water surface in air. Additional air-to-water measurements are performed for one parallel-plate IC after the IC face is dried. Scan spatial resolution is always 0.1 mm around the DeICERS. In all gradient plots, this depth is designated by a grey dashed line. The order in which parallel-plate IC measurements are presented here is the same order in which parallel-plate ICs are listed in Table 5 and Table 6. For all parallel-plate IC designs, the DeICERS is the water surface. PDDs measured on the VCU Varian 2300 in 6 and 18 MV photon beams with the parallel-plate ICs used for this thesis that have not yet been discussed are

shown in . Relative dose gradients for the Exradin A10 are shown in Figure 156. For both incident photon energies, the gradient peaks occur at the same location, 0.05 mm deep in water.

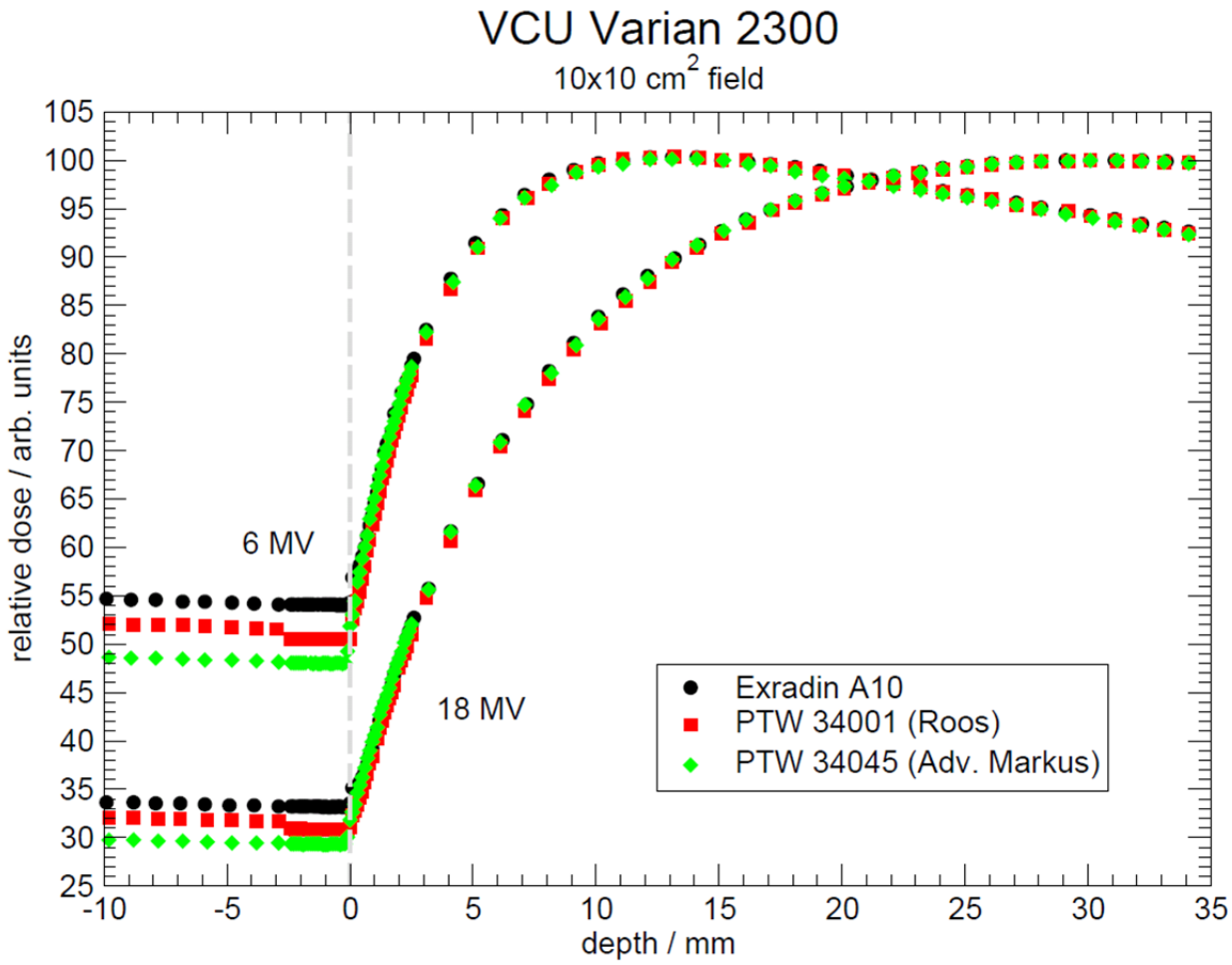

Figure 155: PDDs measured at VCU on the Varian 2300 in 6 and 18 MV beams with three of the parallel-plate ICs borrowed for this thesis not already discussed. The Exradin A11 is shown separately.

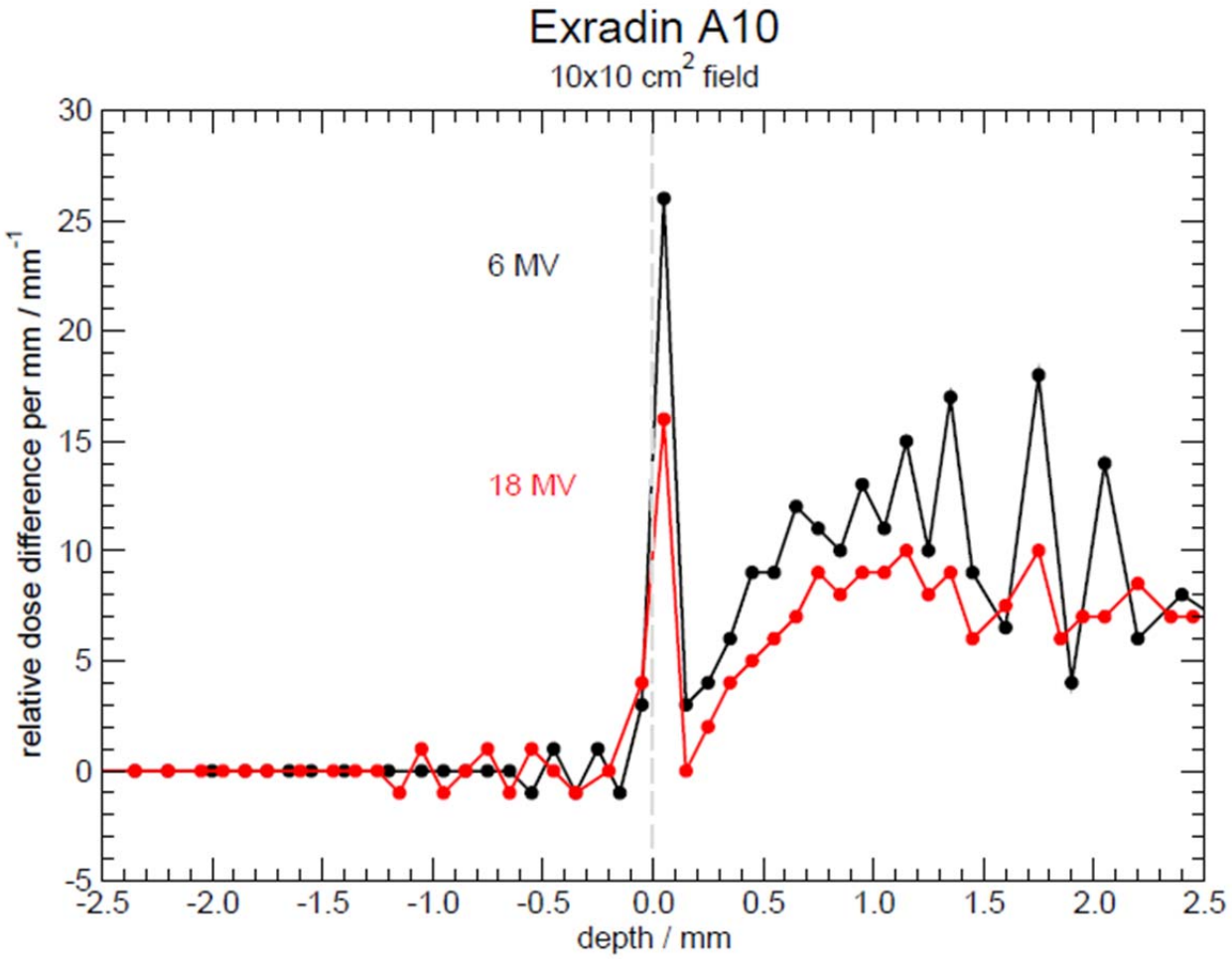

Figure 156: First derivatives of PDDs measured with the Exradin A10 parallel-plate IC for the Varian 2300 6 and 18 MV beams at a 10×10 cm^2 field. The grey dashed line marks the DeICERS.

Figure 157 shows a zoomed-in view of the water surface region from the Exradin A11 scans. As shown in Figure 69, scanning with 1 s/pt. sampling resolution can allow water to remain atop the IC face when the IC emerges from the water surface. To demonstrate the increase in relative dose caused by water buildup, the IC is dried after completing the scans at 1 s/pt. sampling resolution and scanned in the opposite direction to the water surface. The scan at 4 s/pt. has residual water on the IC surface at the end of the scan, giving a higher in-air dose. Scanning with 10 s/pt. sampling resolution results in a dry IC surface in air, indicating that the water drips off fully. Neither the air-to-water post-drying scan nor the water-to-air scan with 10 s/pt. measurement resolution met its intended terminal depth of 0.5 mm above the water

surface in air, due to the scanning system failing to record the final measurement of either scan. The Exradin A11 relative dose gradients are shown in Figure 158, along with a demonstration of the "stitching" process, by which data from different trials are combined into a single depth-ionization measurement. "Stitching" is done via an in-house computational routine to combine scans acquired at different sampling and/or spatial resolutions. The slowest scans provide the highest-quality data; therefore, the measurement over the longest period of time at each depth is selected. By stitching scans together, signal from a particularly noisy IC can be used to establish a gradient peak 0.15 mm deep in water for both energies.

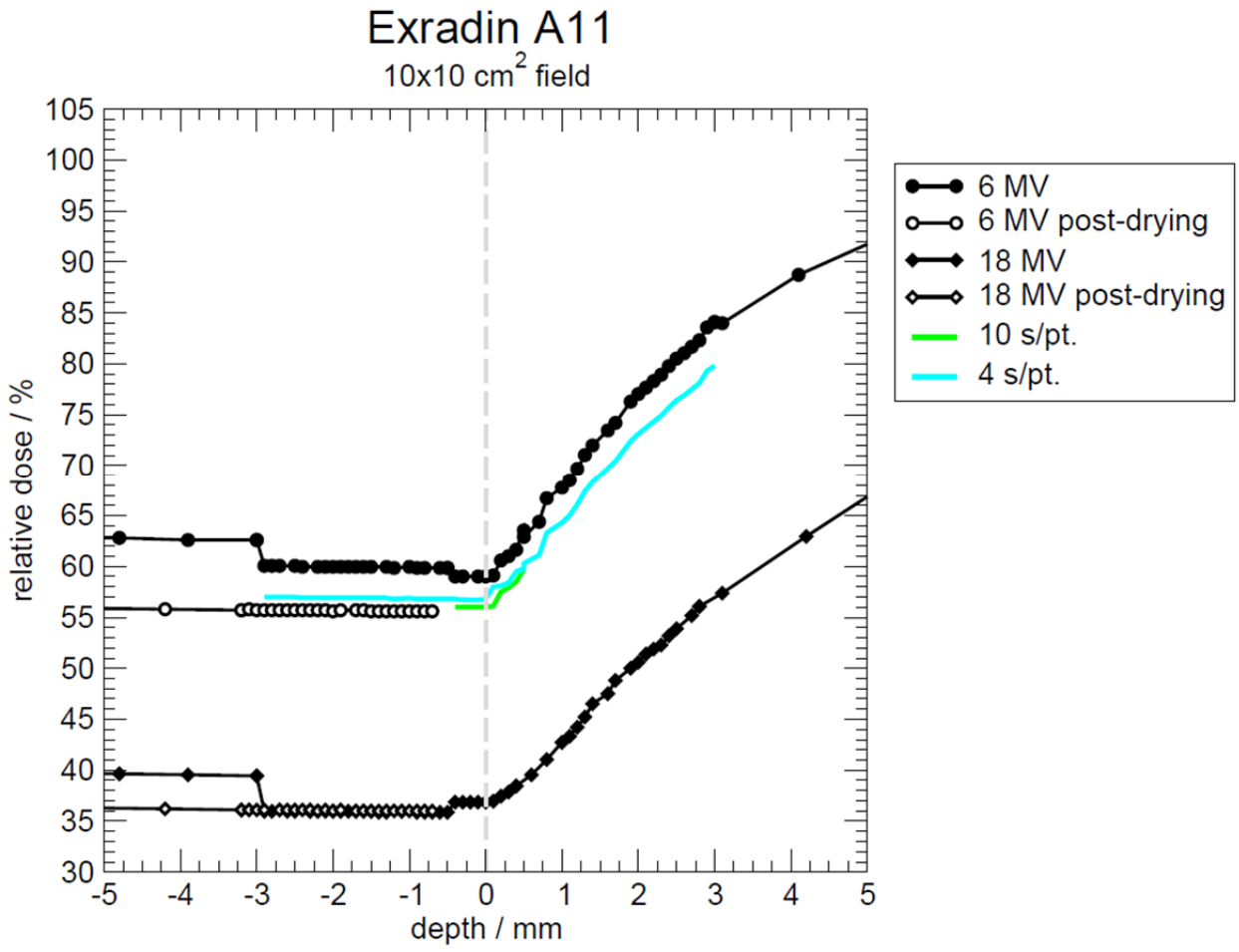

Figure 157: Zoomed-in view of the surface region for PDDs measured with the Exradin A11 parallel-plate IC for the Varian 2300 6 and 18 MV beams at a 10×10 cm^2 field. The strange jumps in the in-air signal at the non-standard water depths are artifacts caused by the way scans at different sampling times are stitched together. Figure 69 shows the physical explanation for the sampling time dependence and a solution. The grey dashed line marks the DeICERS.

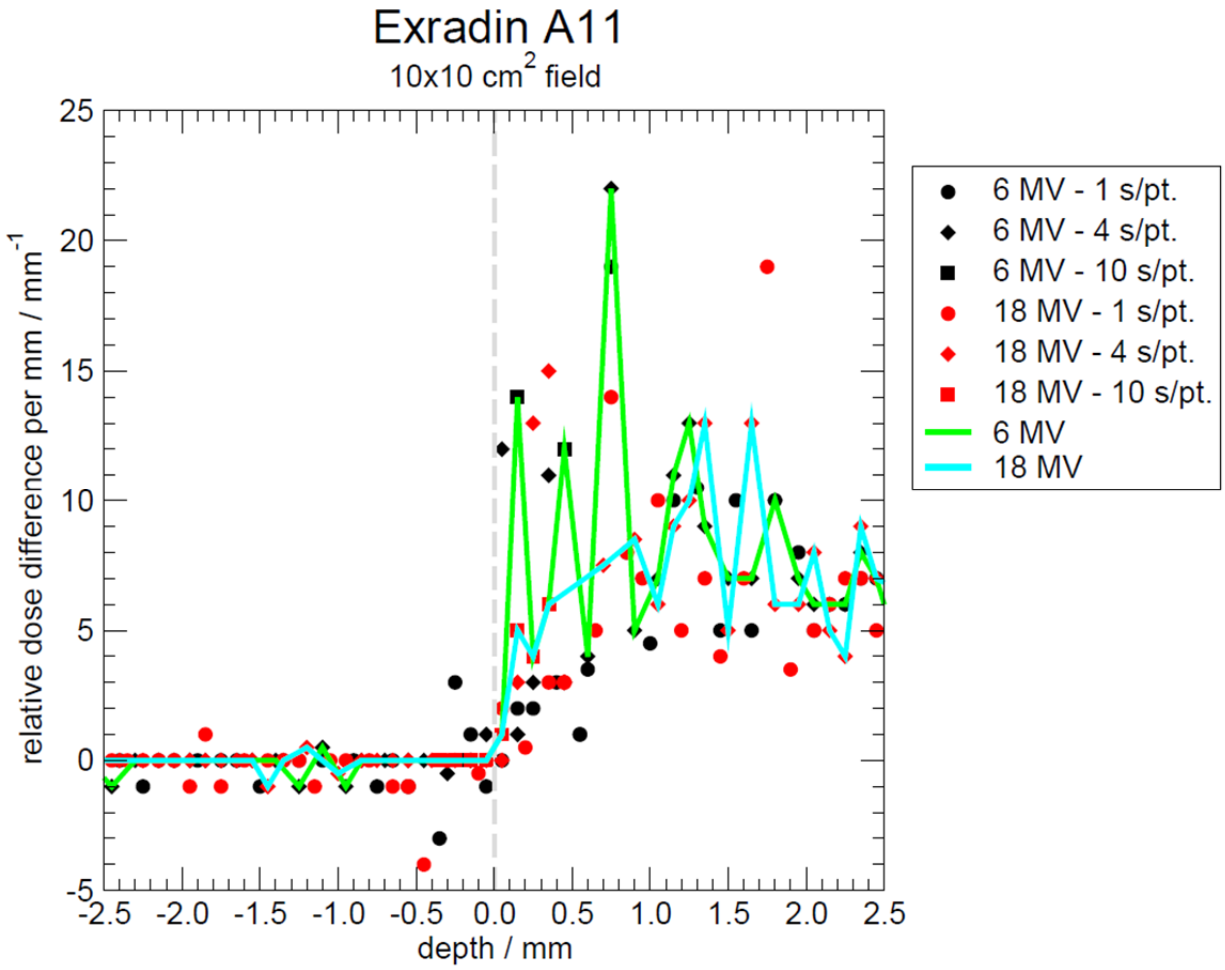

Figure 158: First derivatives of the scans shown in Figure 157. The colored lines are intended to demonstrate the stitching that is performed to join scans at different sampling times. The grey dashed line marks the DeICERS.

Figure 159 shows the relative dose gradients for the PTW 34001. For both incident beam energies, the gradient peaks occur at the same location. The gradient peaks occur at a depth of 0.05 mm in water. The PTW 34045 was created specifically to address the guard ring width deficiency in the classic Markus design, which is discussed in this thesis in Section 4.1.2. Despite the wider guard ring, a group at the United Kingdom National Physical Laboratory has found that the Advanced Markus type parallel-plate IC is not suitable for reference dosimetry, due mostly to a notable polarity effect (Pearce *et al.*, 2006). The relative dose gradients are shown in Figure 160. For both incident photon beam energies, gradient peaks occur at the same location. Gradient peaks occur at a depth of 0.05 mm above the water surface in air. All in-

house parallel-plate IC measurements show gradient peaks that occur within measurement uncertainty of the DeICERS for the respective ICs.

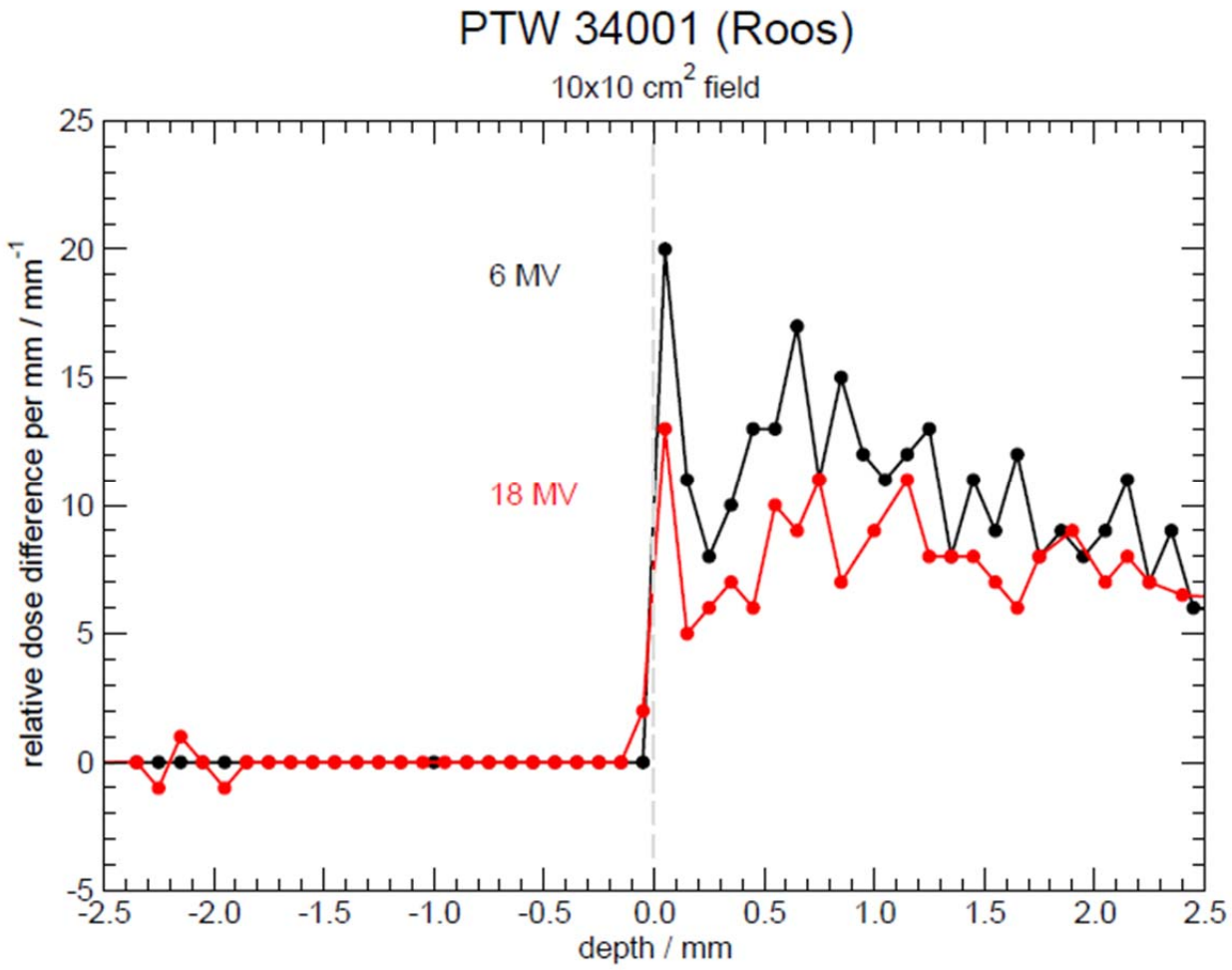

Figure 159: First derivatives of PDDs measured with the PTW 34001 parallel-plate IC for the Varian 2300 6 and 18 MV beams at a 10×10 cm^2 field. The grey dashed line marks the DeICERS.

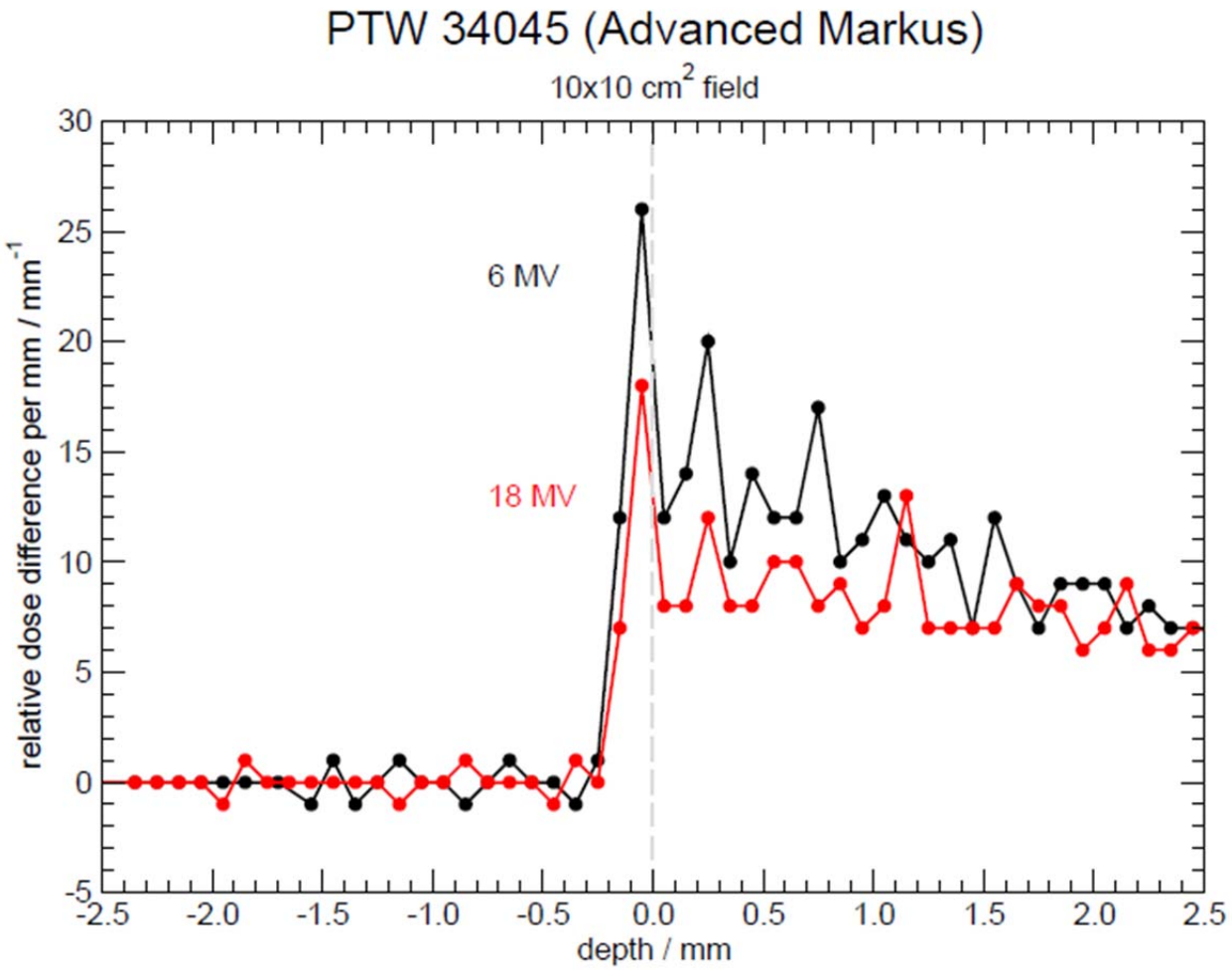

Figure 160: First derivatives of PDDs measured with the PTW 34045 parallel-plate IC for the Varian 2300 6 and 18 MV beams at a 10×10 cm^2 field. The grey dashed line marks the DeICERS.

4.5.2 National Research Council of Canada

All PDDs measured at the NRC are scanned using the custom-built high-precision scanning system described in Section 4.1.3. The IC alignment method used with this system is also described in Section 4.1.3. All measurements are taken from 50 mm in water to 20 mm above the water surface in air. Scans are acquired with variable resolution at different depths but near the depth at which the IC reaches the water surface, resolution is always 0.1 mm. Measurements are taken with 12 cylindrical ICs representing 11 different IC designs. All ICs are scanned for at least 6 and 25 MV photon beams produced by the Elekta Precise. These

measurements are shown in Figure 161. Three ICs are also used for scans in the Elekta Precise 10 MV photon beam. All measurements are taken in 10×10 cm^2 fields. The outer diameter of each IC is directly measured by Dr. Malcolm McEwen to within 0.020 mm using a pair of digital calipers. The results of the measurements with the digital calipers are shown in Table 9. The uncertainty in IC outer diameter is one component of the total uncertainty budget for IC positioning uncertainty relative to the water surface. One standard deviation for the NRC measurements has been estimated by Dr. McEwen to be 0.08 mm. The total uncertainty budget is shown in Table 10.

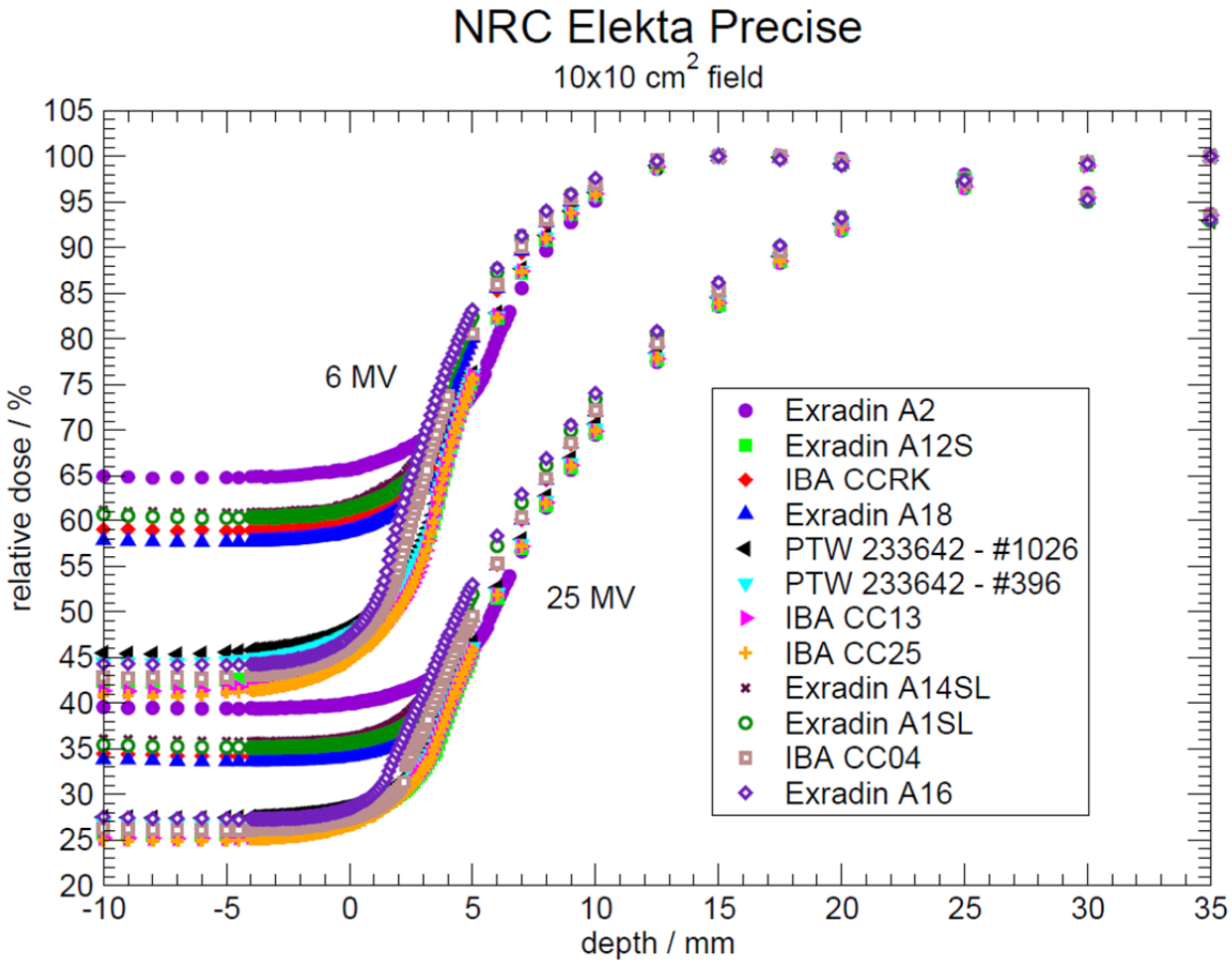

Figure 161: PDDs measured at the NRC on the Elekta Precise in 6 and 25 MV beams with 12 cylindrical ICs. The legend is sorted by IC outer radius.

Table 9: Cylindrical IC diameters measured by Dr. Malcolm McEwen using digital calipers providing accuracy within ±0.020 mm. The cylindrical ICs listed are those used in the work performed at the NRC.

IC Type	Diameter (mm)
Exradin A12S	6.95
Exradin A14SL	6.36
Exradin A16	3.40
Exradin A18	6.85
Exradin A1SL	6.34
Exradin A2	11.40
IBA CC04	4.77
IBA CC13	6.76
IBA CC25	6.74
IBA CCRK	6.95
PTW 233642	6.83

Table 10: Overall one-sigma uncertainty estimate calculated by Dr. Malcolm McEwen to find the total uncertainty in IC position relative to the water surface for measurements performed at the NRC. Generally, Type A uncertainties are statistical while Type B uncertainties are estimated by other means (International Organization for Standardization, 1993) .

Uncertainty source	Type A (mm)	Combined (mm)	Type B (mm)
Setting surface	0.020		0.028
Setting IC at surface	0.020		0.028
Stepper drive precision	0.005		0.028
IC holder displacement			0.050
Telescope drive calibration			0.014
Velmex drive calibration			0.014
IC radius	0.020		
Overall	0.04	0.08	0.07

The Exradin A12S relative dose gradients are shown in Figure 162. Generalized schematics of all of the Exradin ICs used in this thesis are shown in Figure 33. The gradient peak of the 6 MV scan is 0.1 mm shallower than the peaks from the 10 and 25 MV scans. The gradient peaks are within overall measurement uncertainty of one another; however, the peaks are not within measurement uncertainty of the DeICERS at 3.475 mm. It appears that the A12S may have been set up too shallowly, which should be difficult to accomplish using the optical telescope, or that measurement noise is contributing to an anomalous result.

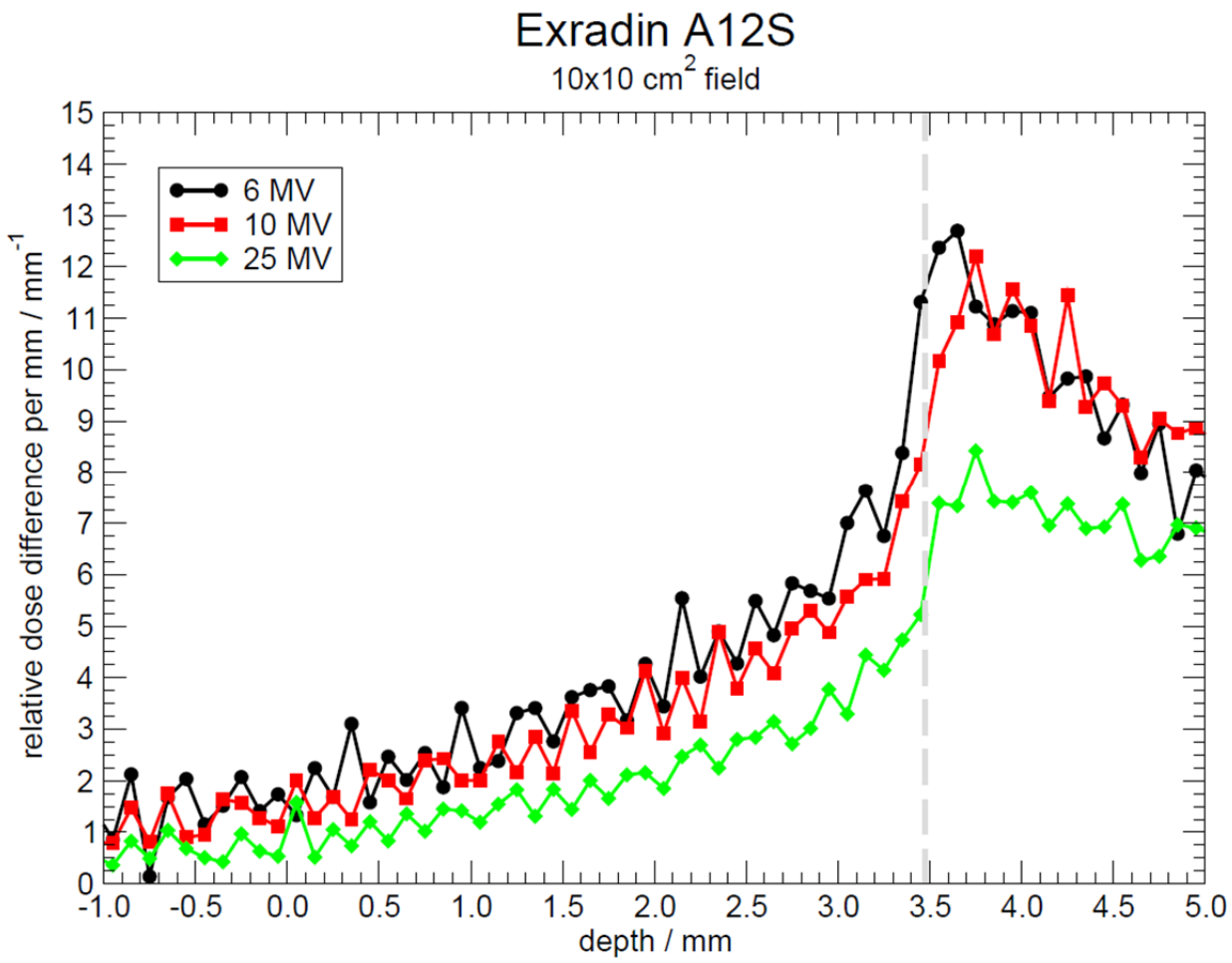

Figure 162: First derivatives of PDDs measured with the Exradin A12S cylindrical IC for the Elekta Precise 6, 10, and 25 MV beams at a 10×10 cm^2 field. The grey dashed line marks the DeICERS.

Though it will generally not be useful for scans conducted with typical clinical scanning systems, due to the noise level, the second derivative peak can be used for low noise data to bound the gradient peak. Recall from the results of the analytical model shown in Figure 15, that in an idealized noiseless system, the response gradient and curvature change discontinuously at the IC outer radius. The second derivative, in fact, changes asymptotically, where the second derivative maximum and minimum values occur at the same theoretical location. Mathematically, the gradient peak becomes a zero point, or inflection point, in the second derivative, as the gradient peak is the location where the function curvature changes sign. In real systems, the gradient peak and second derivative peak will not occur at the same location but

will occur increasingly closely for less noisy systems that more closely approximate the theoretical model. A plot of the Exradin A12S second derivatives is shown in Figure 163. Given that the 0.1 mm discrepancy between second derivative peaks of the scans at the three beam energies tested encompasses the DeICERS, it seems that measurement noise, not setup error, is to blame for the apparent discrepancy in scan gradients.

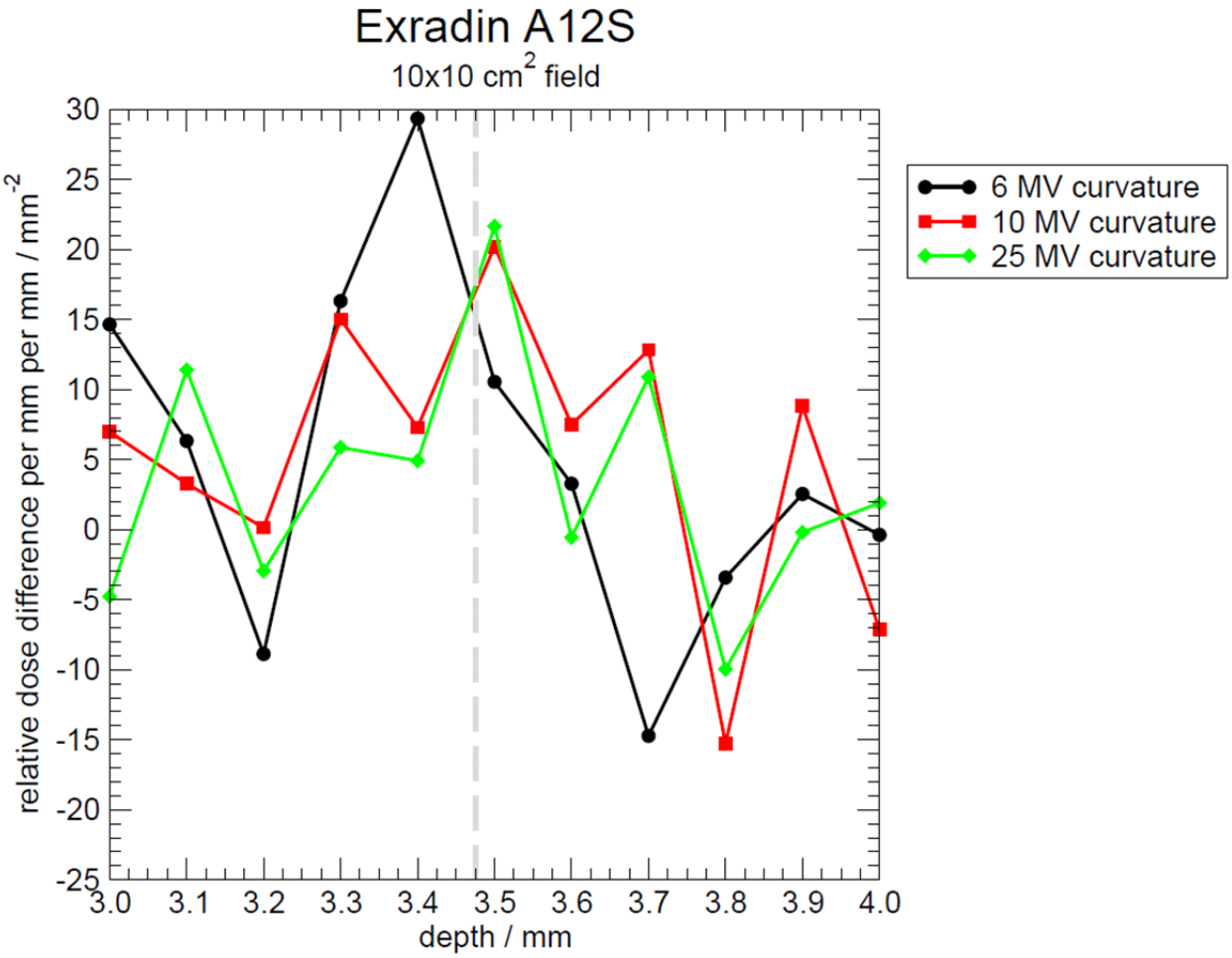

Figure 163: Second derivatives of the Exradin A12S PDDs. The 0.1 mm variation in second derivative peaks for the three beam energies encompasses the DeICERS.

The relative dose gradients for the Exradin A14SL are shown in Figure 164. The gradient peaks for both energies occur at 3.35 mm. The DeICERS for this IC is 3.18 mm. The measured gradient peaks are 0.01 mm away from being within two standard deviations of the DeICERS. The gradient of an additional measurement taken on a different day with the same IC

is added. This peak occurs 0.03 mm shallower than the DeICERS, which is within measurement uncertainty. The first measured gradient peak is considered anomalous, as the discrepancy between gradient peak and DeICERS location is more than twice the measurement uncertainty. The second measurement, however, demonstrates a gradient peak within measurement uncertainty of the DeICERS.

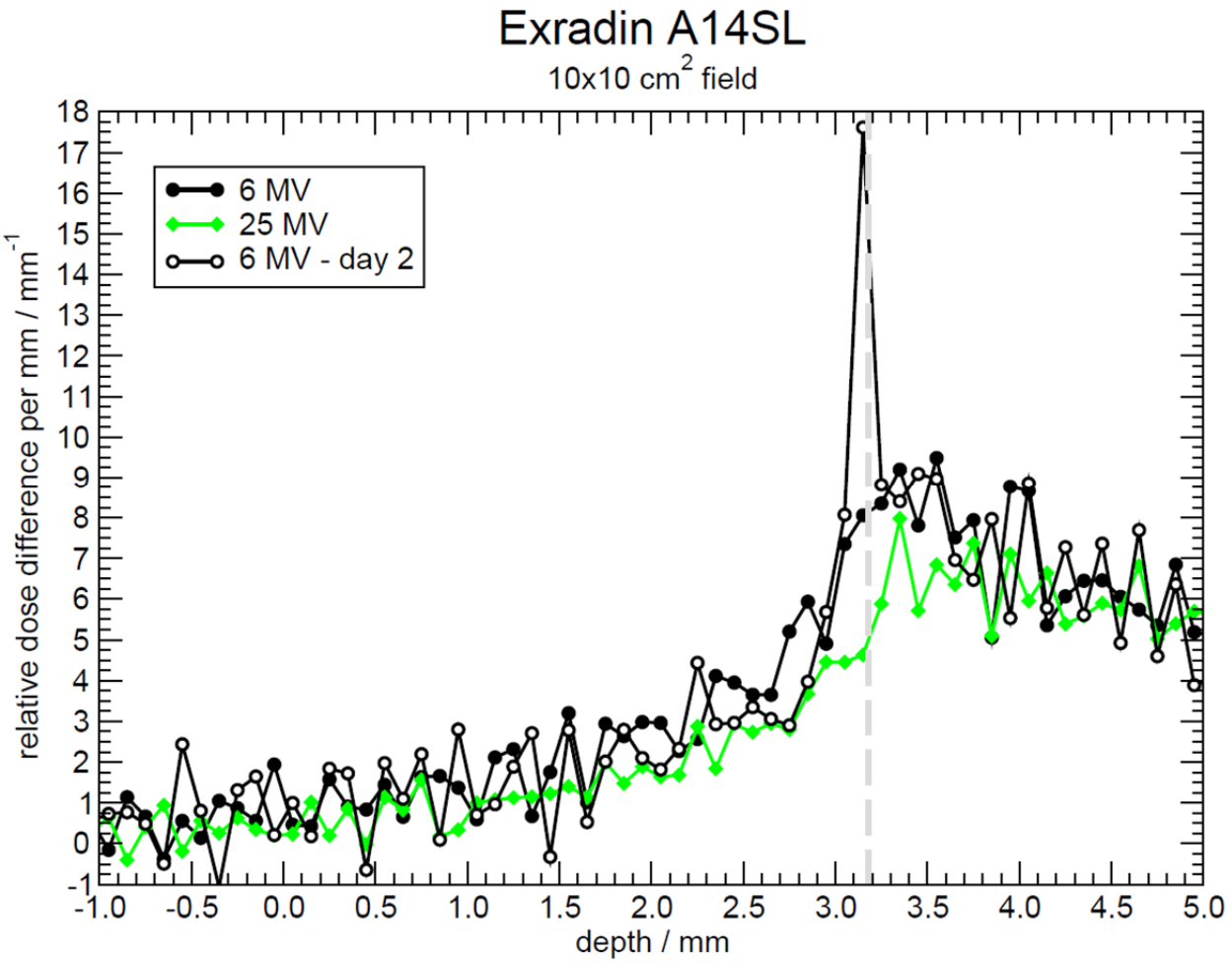

Figure 164: First derivatives of PDDs measured with the Exradin A14SL cylindrical IC for the Elekta Precise 6 and 25 MV beams at a 10×10 cm^2 field. The grey dashed line marks the DeICERS. The slope of an additional measurement is shown to demonstrate the influence of initial alignment variability on the observed gradient peaks.

Dose gradients for the Exradin A16 are shown in Figure 165. The gradient peaks of scans at both energies occur at the same location, 0.15 mm shallower than the DeICERS. This discrepancy is barely within two standard deviations but corresponds with less than twice the

scan resolution. The discrepancy between gradient peak and DeICERS location is also partially caused by the hemispherical portion of the IC cavity volume, where cavity outer radius is not constant with respect to the water surface. The Exradin A18 relative dose gradients are shown in Figure 166. The gradient peaks from scans at both energies occur within 0.1 mm of one another and are both within measurement uncertainty of the DeICERS of 3.425 mm.

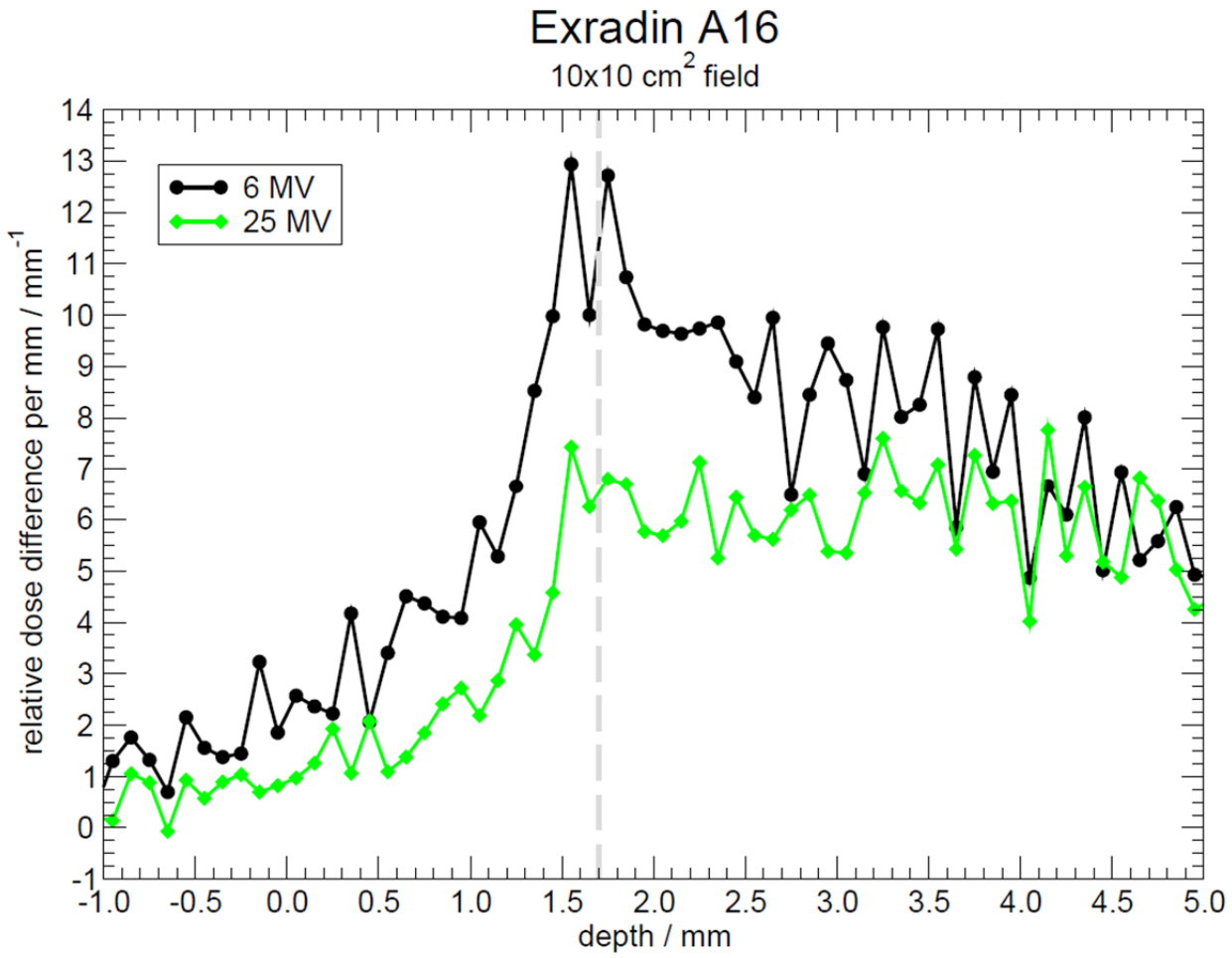

Figure 165: First derivatives of PDDs measured with the Exradin A16 cylindrical IC for the Elekta Precise 6 and 25 MV beams at a 10×10 cm^2 field. The grey dashed line marks the DeICERS.

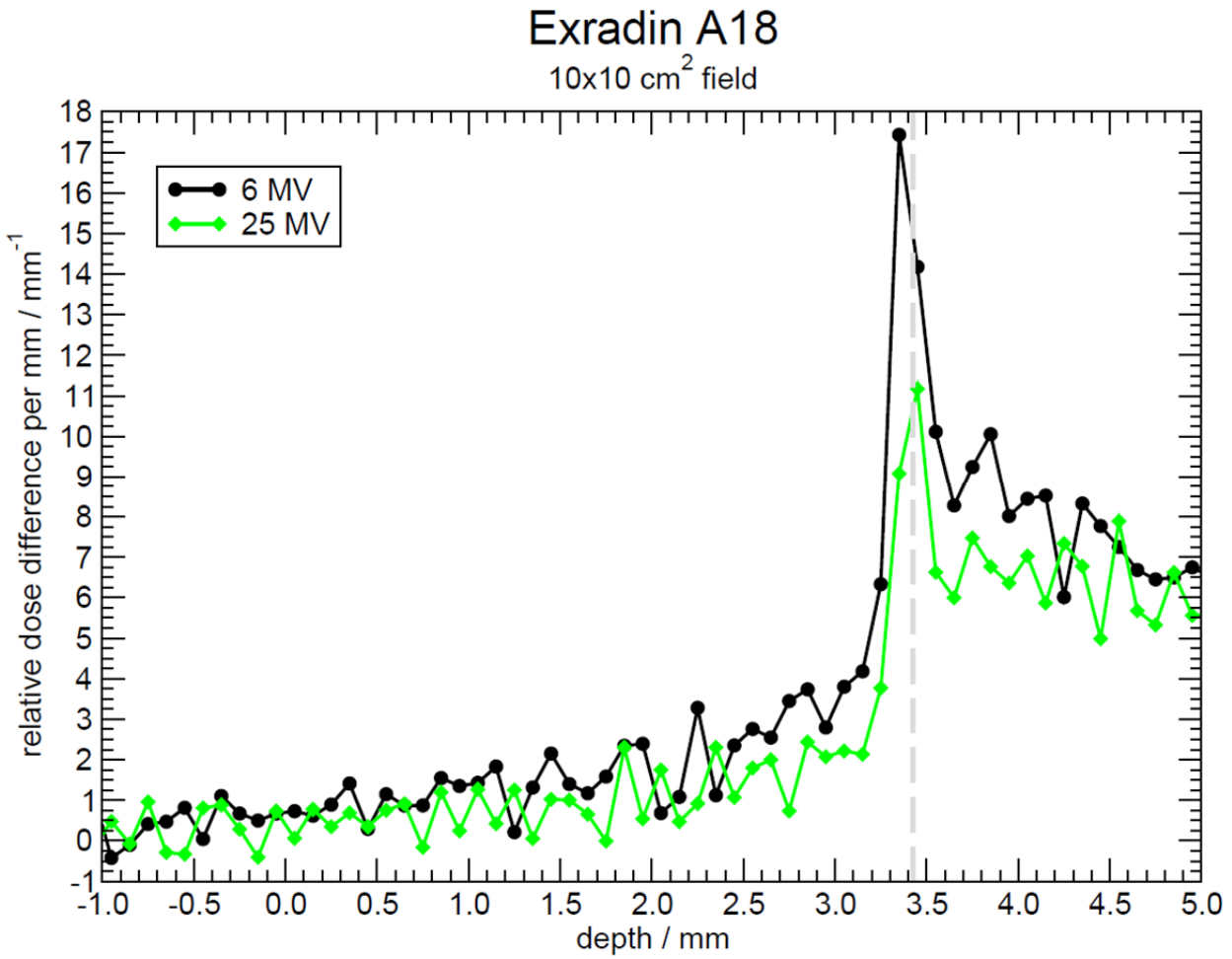

Figure 166: First derivatives of PDDs measured with the Exradin A18 cylindrical IC for the Elekta Precise 6 and 25 MV beams at a 10×10 cm^2 field. The grey dashed line marks the DeICERS.

Exradin A1SL relative dose gradients are shown in Figure 167. Scans at both energies exhibit gradient peaks within 0.02 mm of the DeICERS, while another 25 MV scan is within 0.12 mm of the DeICERS, which is within two standard deviations. The Exradin A2 relative dose gradients are shown in Figure 168. Gradient peaks from scans at both energies are within 0.1 mm of one another. The 6 MV gradient peak distance from the DeICERS is within twice the measurement alignment uncertainty. The distance of the 25 MV gradient peak from the DeICERS is within the estimated measurement alignment uncertainty.

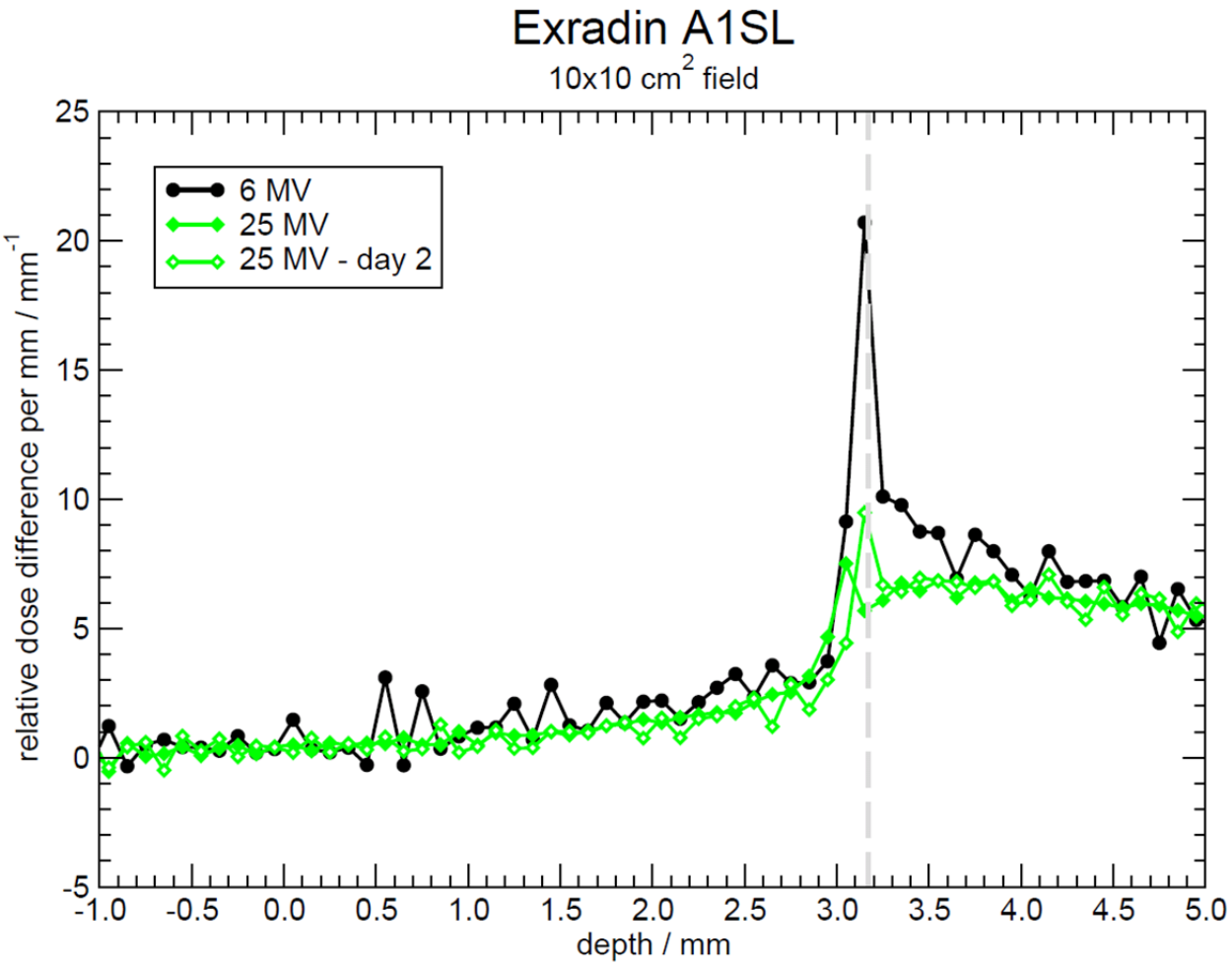

Figure 167: First derivatives of PDDs measured with the Exradin A1SL cylindrical IC for the Elekta Precise 6 and 25 MV beams at a 10×10 cm^2 field. The grey dashed line marks the DeICERS. The slope of an additional measurement is shown to demonstrate the influence of initial alignment variability on the observed gradient peaks.

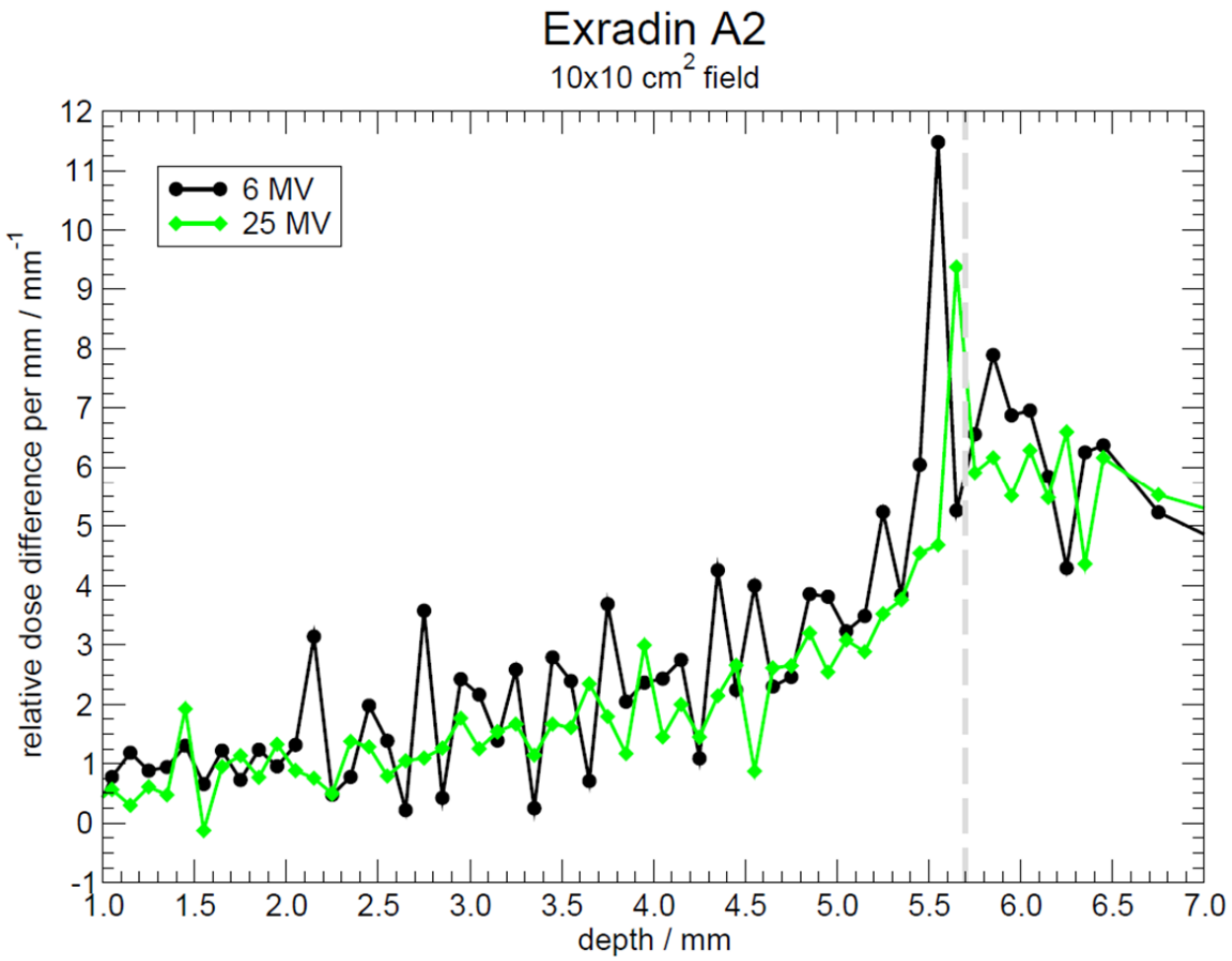

Figure 168: First derivatives of PDDs measured with the Exradin A2 cylindrical IC for the Elekta Precise 6 and 25 MV beams at a 10×10 cm^2 field. The grey dashed line marks the DeICERS.

Figure 169 shows the relative dose gradients for the IBA CC04. It appears that this IC yields a shallow gradient peak due to the large hemispherical portion of the overall IC cavity volume. Though the two gradient peak locations differ by only 0.1 mm, the average gradient peak location lies farther than two standard deviations from the DeICERS but within two measurement steps.

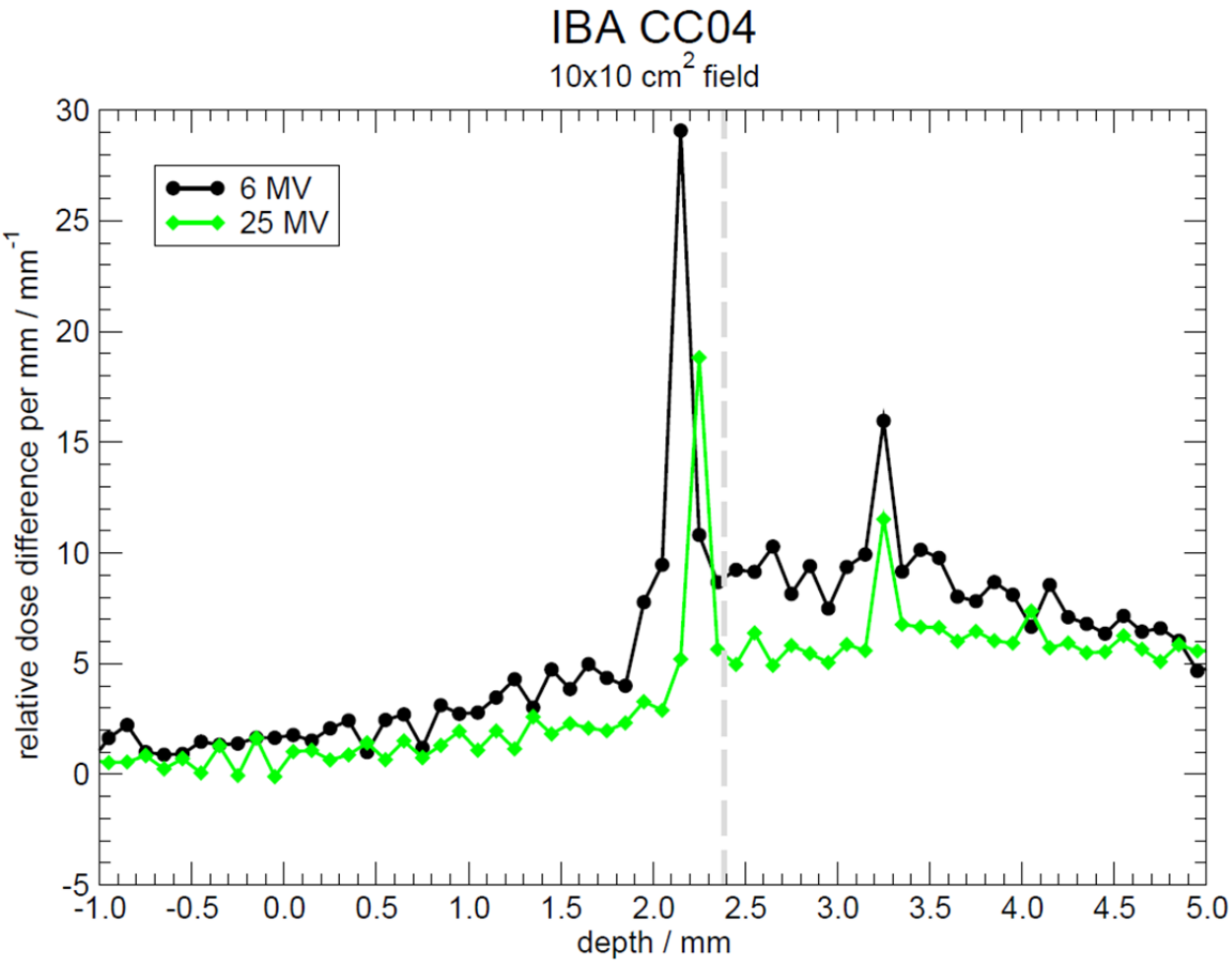

Figure 169: First derivatives of PDDs measured with the IBA CC04 cylindrical IC for the Elekta Precise 6 and 25 MV beams at a 10×10 cm^2 field. The grey dashed line marks the DeICERS.

The average relative dose gradients from three IBA CC13 measurement trials are shown in Figure 170. Repeated trials show the gradient peak at 3.45 mm, which is within 0.07 mm of the DeICERS, a difference that is within measurement uncertainty. Relative dose gradients for the IBA CC25 are shown in Figure 171. The gradient peak locations for scans at both energies differ by 0.1 mm, one scan step size, but both gradient peaks are within measurement alignment uncertainty of the DeICERS of 3.37 mm.

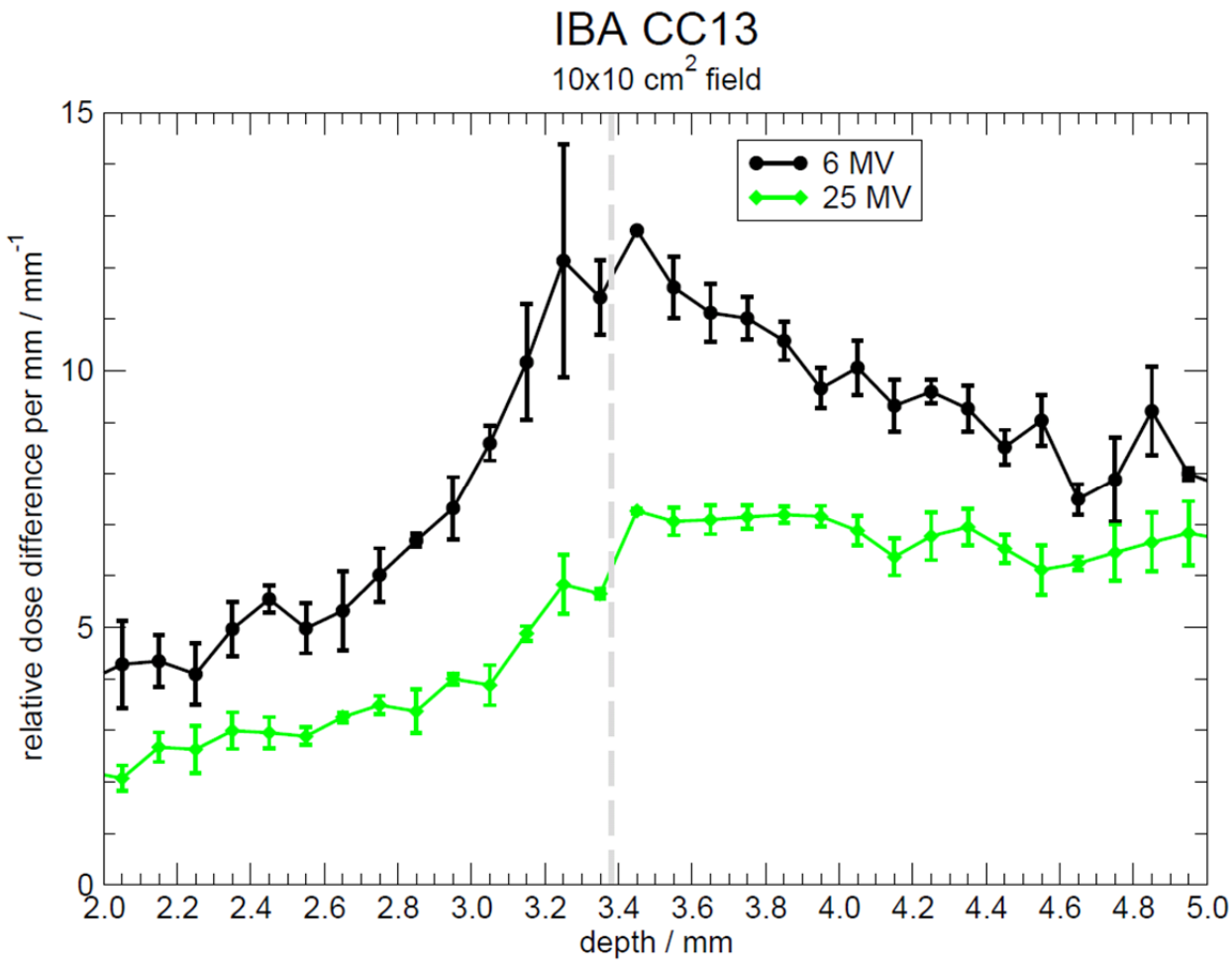

Figure 170: First derivatives of three trials of PDDs measured with the IBA CC13 cylindrical IC for the Elekta Precise 6 and 25 MV beams at a 10×10 cm^2 field. The grey dashed line marks the DeICERS.

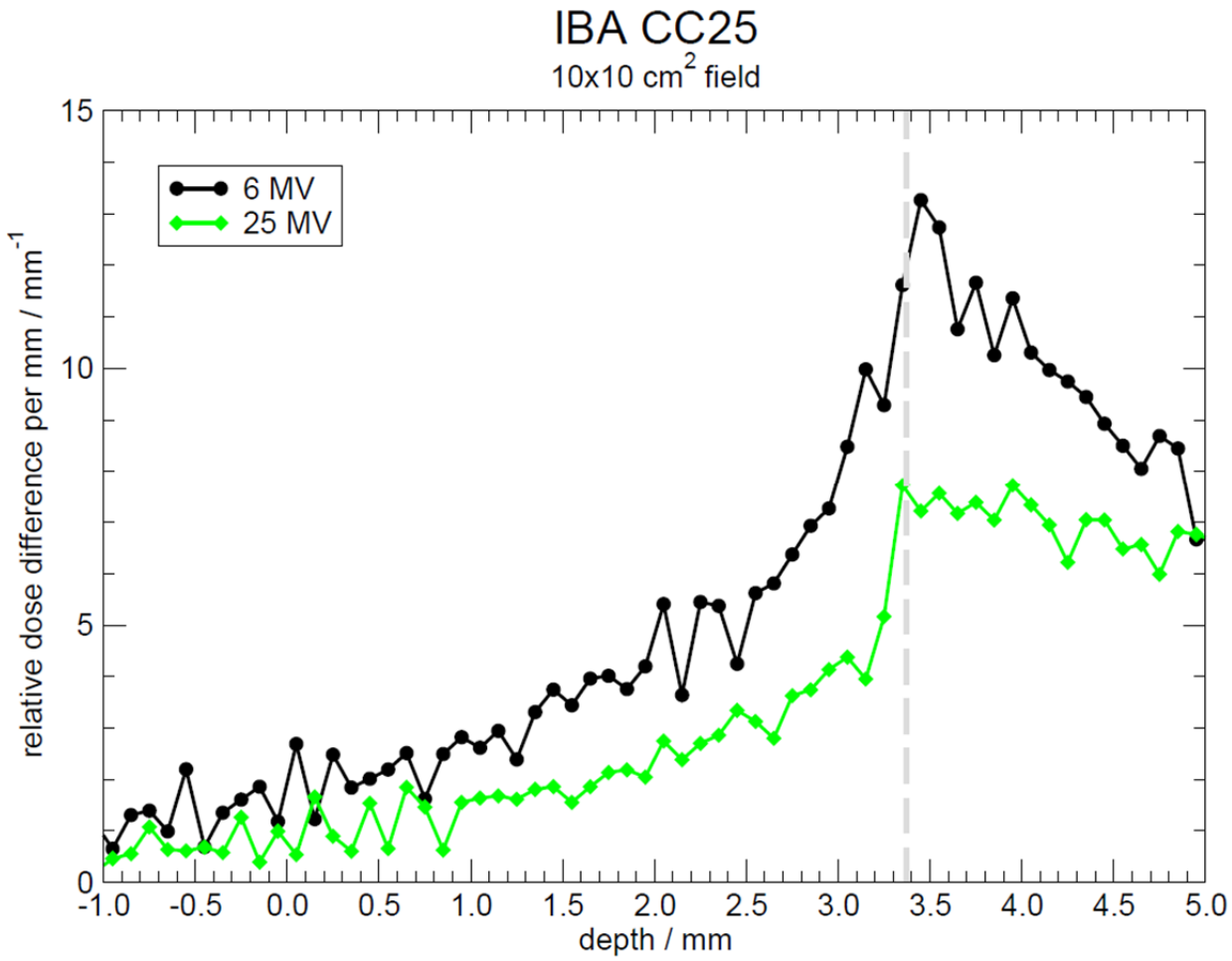

Figure 171: First derivatives of PDDs measured with the IBA CC25 cylindrical IC for the Elekta Precise 6 and 25 MV beams at a 10×10 cm^2 field. The grey dashed line marks the DeICERS.

Figure 172 shows the relative dose gradients for the IBA CCRK. The CCRK is a scanning IC that has an uncommonly thick wall, like the wall of the Exradin A1SL or A14SL, and no hemispherical cap. Scans for all three beam energies exhibit gradient peaks at 3.45 mm, which is 0.025 mm from the DeICERS. This difference is well within measurement uncertainty.

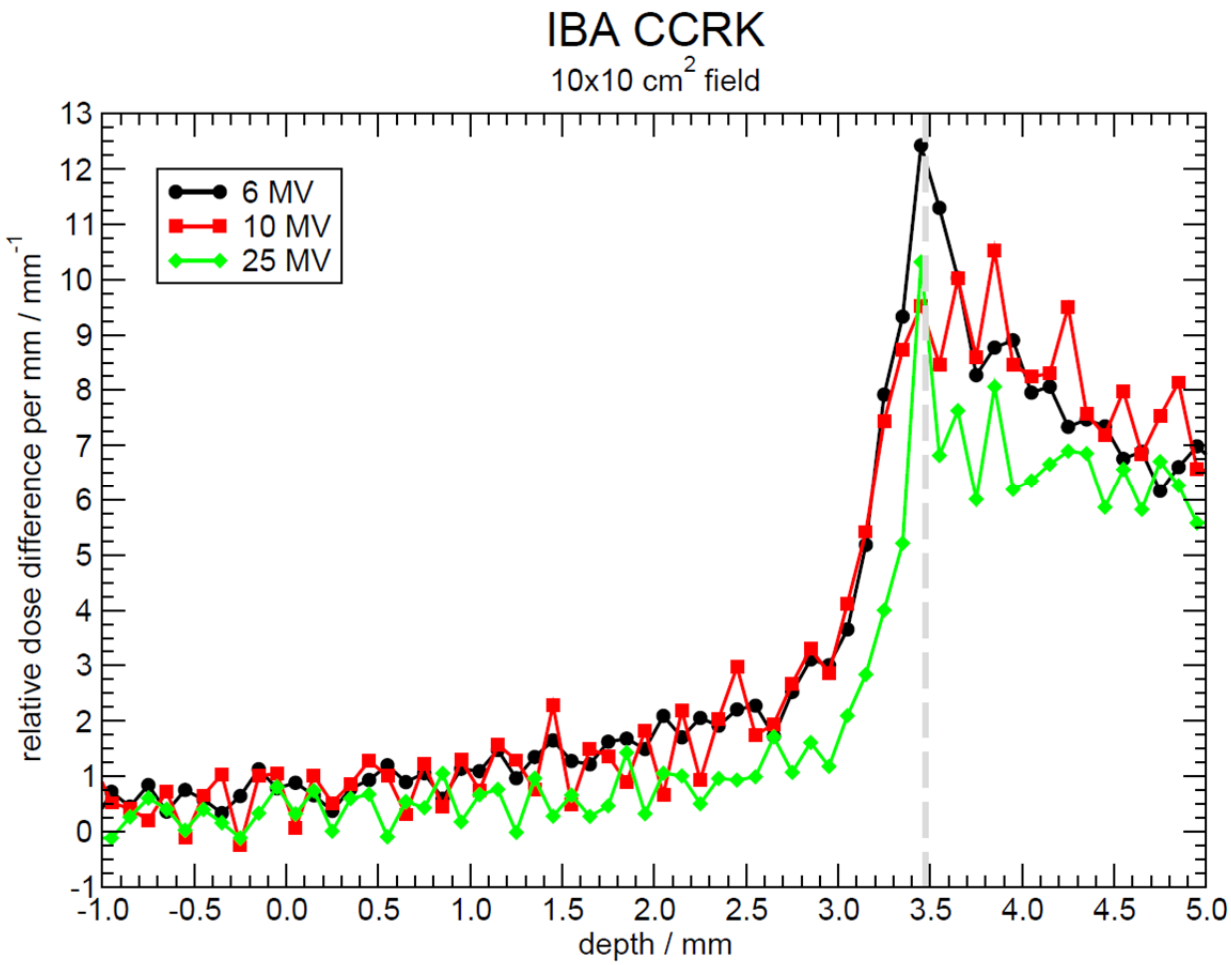

Figure 172: First derivatives of PDDs measured with the IBA CCRK cylindrical IC for the Elekta Precise 6, 10, and 25 MV beams at a 10×10 cm^2 field. The grey dashed line marks the DeICERS.

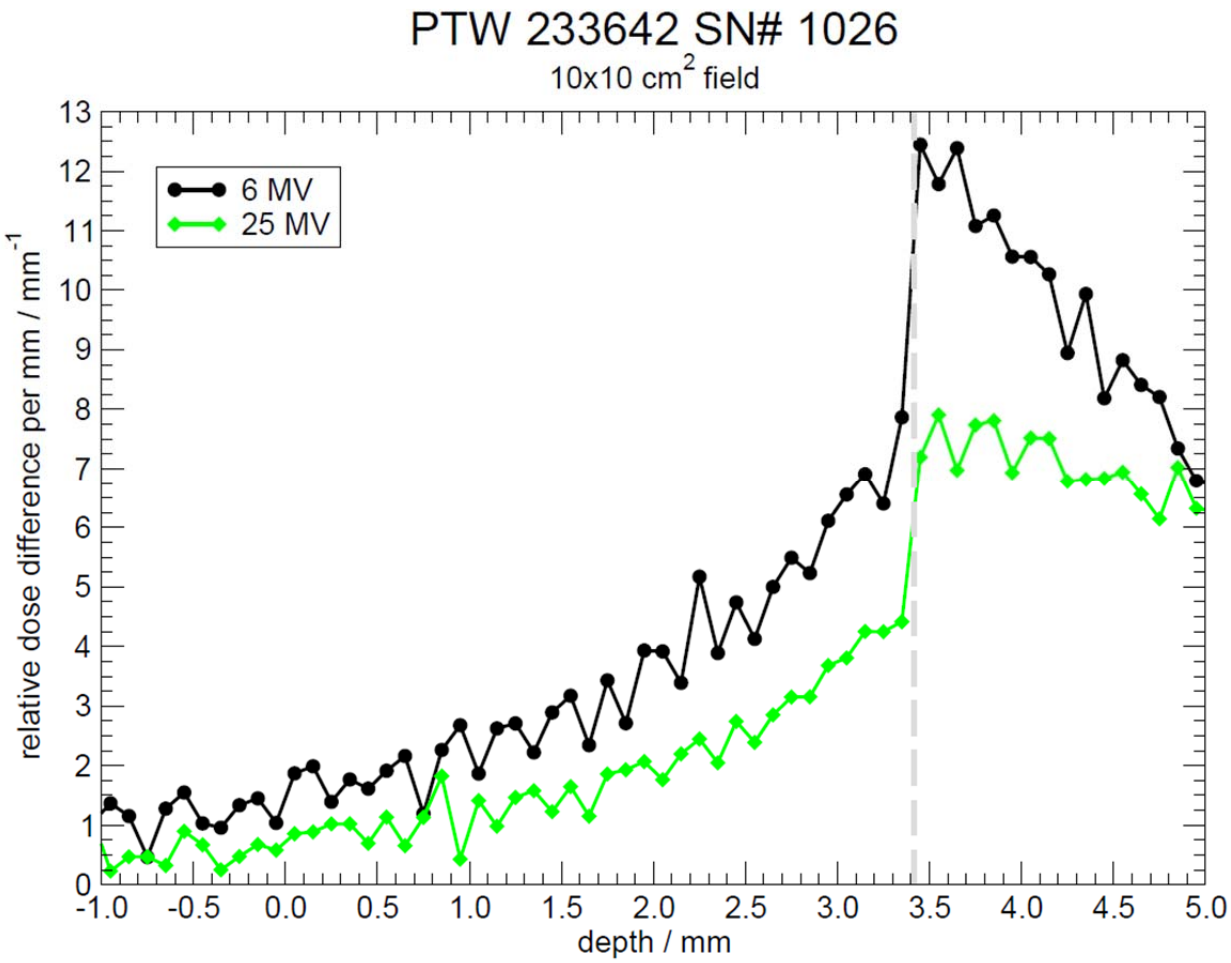

Figure 173: First derivatives of PDDs measured with the PTW 233642, serial number 1026, cylindrical IC for the Elekta Precise 6 and 25 MV beams at a 10×10 cm^2 field. The grey dashed line marks the DeICERS.

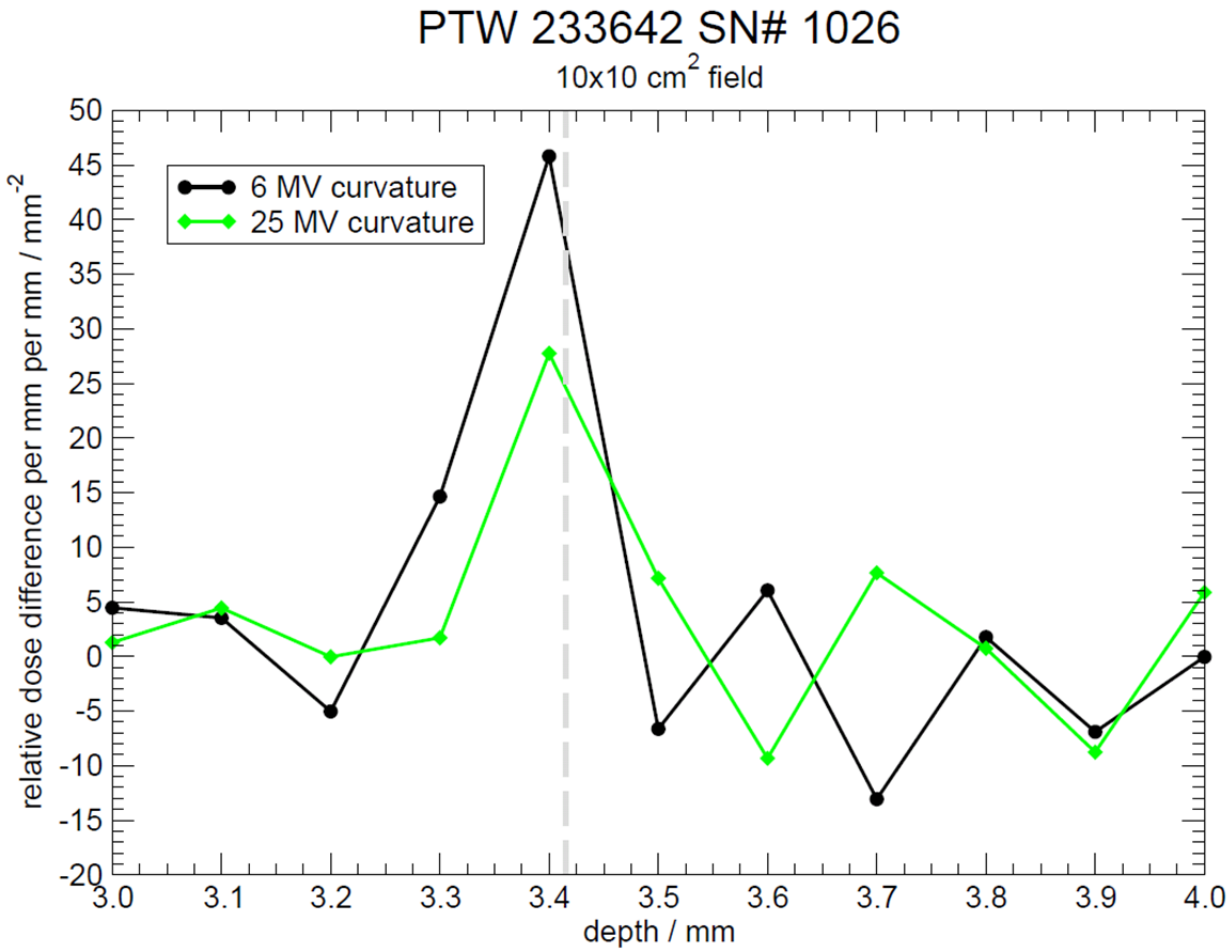

Figure 174: Second derivatives of the PDDs measured with the PTW 233642, serial number 1026. The second derivative peaks are consistent with beam energy and 0.02 mm from the DeICERS.

PDDs are measured for two PTW 233642 IC types, serial number 1026 and 396, respectively. The PTW 233642 has nominally been replaced by the PTW 31010. Scan gradients for the IC with serial number 1026 are shown in Figure 173. Gradient peaks differ by 0.1 mm but only the 6 MV peak occurs within measurement alignment uncertainty of the DeICERS. The 25 MV peak occurs within two measurement steps of the DeICERS. Second derivative plots for the IC serial number 1026 are shown in Figure 174. Both second derivative peaks occur at the same location, 0.02 mm from the DeICERS. This difference is within alignment uncertainty. The relative dose gradients of the scans with IC serial number 396 are shown in Figure 175. As observed with IC serial number 1026, the gradient peak from the 6 MV scan occurs near the

DeICERS within total measurement alignment uncertainty. The higher energy gradient peaks, however, are only located 0.1 mm, or 1 measurement step, deeper in the water than the gradient peak from the 6 MV scan.

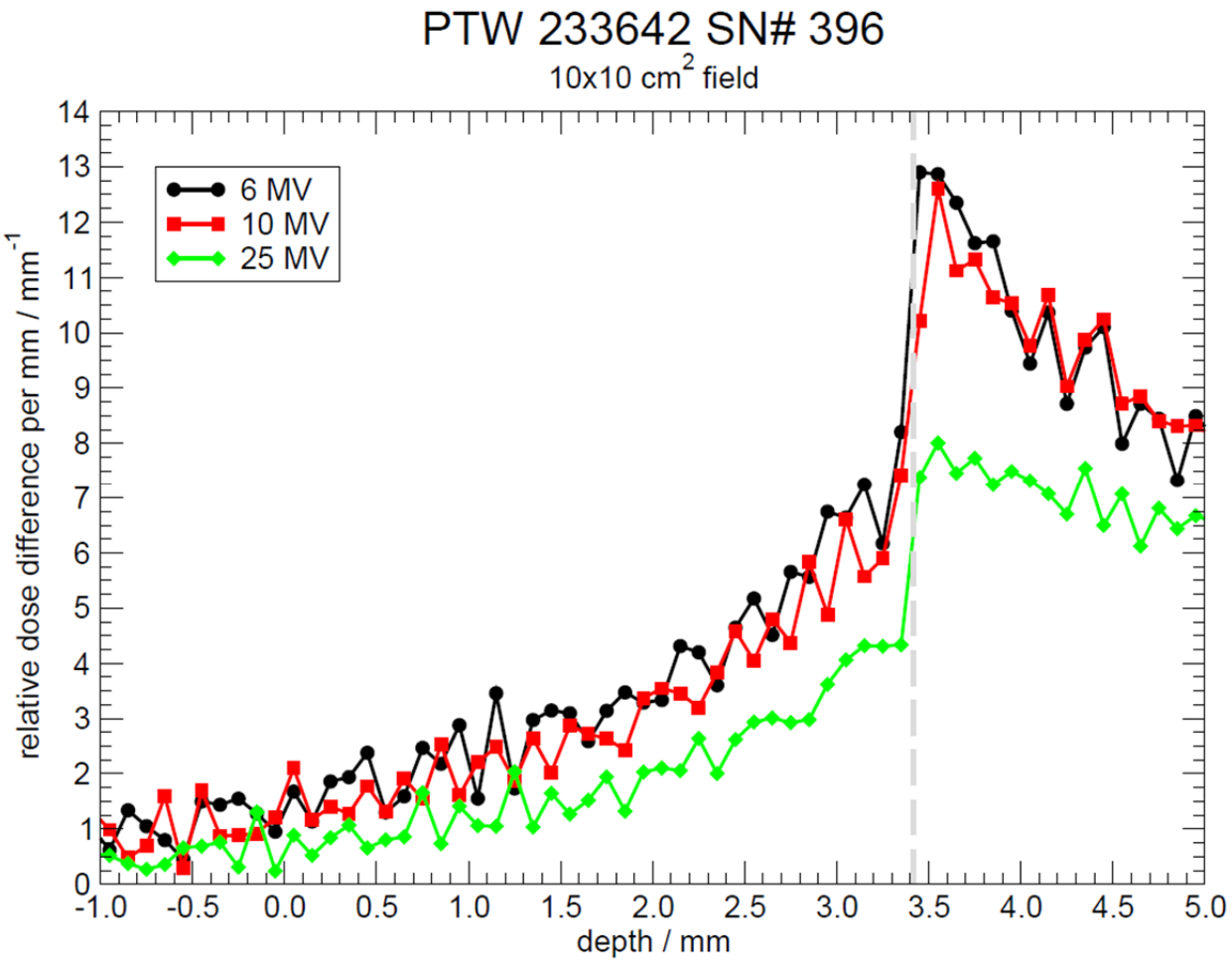

Figure 175: First derivatives of PDDs measured with the PTW 233642, serial number 396, cylindrical IC for the Elekta Precise 6, 10, and 25 MV beams at a 10×10 cm^2 field. The grey dashed line marks the DeICERS.

4.6 Conclusions

PDD measurements should be taken from depth in water toward the water surface. Scan speed and resolution can be chosen to optimize the tradeoff between required measurement time and required accuracy for a given user. For the highest possible accuracy from an available scanning system, scans should be performed at the finest spatial resolution possible using the system. The signal-to-noise ratio achieved by using a sampling rate of 4 s/pt. with the scanning

systems used in this work should be sufficient for most measurements with cylindrical ICs but parallel-plate IC measurements require 10 s/pt. sampling resolution near the water surface. Spatial and sampling resolution requirements can be relaxed away from the water surface. Cylindrical ICs are considerably more robust against angular offsets with respect to the water surface than are parallel-plate ICs. Water evaporation must be tracked at the level of accuracy required by a given user. The 0.075 mm/hr. water evaporation rate computed in this work causes the water surface to shift by a 0.1 mm measurement step every 75 minutes. If the evaporation rate in another clinic is slower, or the scanning resolution used is coarser, more time can elapse between water surface location checks. Care must be taken if scanning with a parallel-plate IC through the water surface to allow enough time for water to drip away from the IC front face in air. If water does not drip away from the IC front face, the IC surface must be dried and the measurement should be repeated from air to the water surface. Measured gradient peak location is robust against changes in radiation field parameters and bias voltage polarity. The gradient peak occurs at the DeICERS when scanning from water to air. The increased sensitivity of the NRC scanning system relative to the IBA Blue Phantom shows small discrepancies, within overall error, in measured gradient peak locations from each DeICERS that are not observed using standard clinical equipment. Using the NRC system, 16/30 (53.3%) measured gradient peaks are within one measurement step of the DeICERS, while 27/30 (90%) are within two measurement steps of the DeICERS. The errors observed using the NRC scanning system, however, are not large enough to affect typical clinical PDD scanning.

5 Prototype Depth-Ionization Scanning Protocol

It is the aim of this chapter to provide a generalized protocol for depth-ionization scanning that can be followed by a given user to ensure that his or her IC alignment to the water surface is of sufficient accuracy for his or her purposes. The general protocol will be discussed first. Following the general protocol, the scanning protocol followed to acquire PDD data at VCU as a part of this thesis will be discussed as an example.

5.1 General Scanning Protocol

A flow diagram of the proposed scanning protocol is shown in Figure 176. The first step to performing depth-ionization measurements is to align the IC to the water surface. It is assumed that the IC can be aligned by eye to the water surface within the dimension of the IC outer radius. Following the IC alignment method recommended by AAPM TG-106 (Das *et al.*, 2008), shown in Figure 5, should refine the visual alignment, minimizing the necessary amount of future correction. Provided that the IC is at least this well-aligned, the process starts by taking a 6 MV scan at the standard field size (10×10 cm^2 for conventional therapy-class accelerators) from at least 3.5 cm depth in water to 2 cm above the surface in air at the "regular" resolution the user would select for depth-ionization scanning. An inflection will be produced in the resulting PDD as the IC emerges from water into air. If the scan is taken with a parallel-plate IC, the IC must be inspected for water pooling on the IC face. If water is observed on the IC face, the IC

must be dried by gently dabbing the IC face with a paper towel without force such that the IC is not disturbed and the in-air portion of the scan should be repeated from air to the water surface.

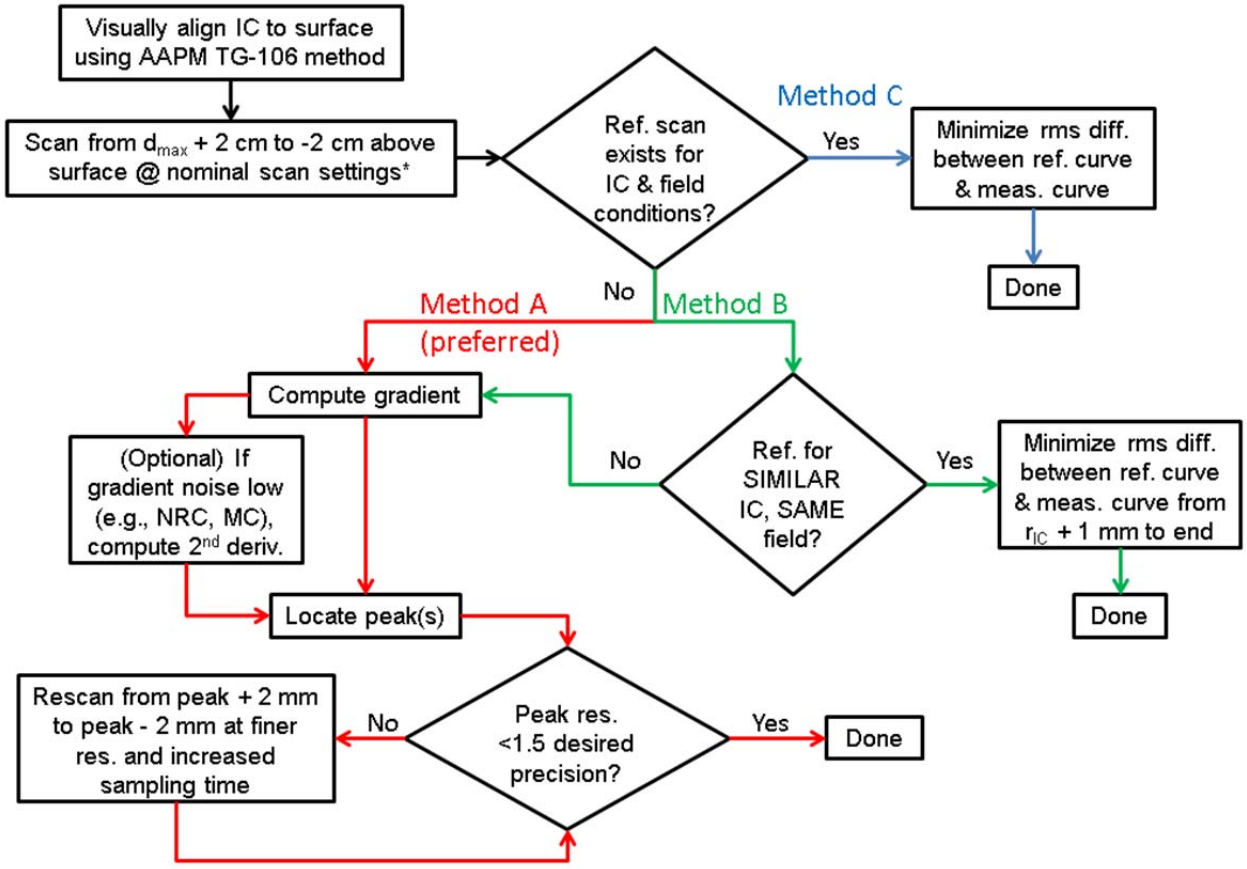

Figure 176: Proposed scanning protocol flow diagram.

If there is previously acquired reference data available for the radiation field conditions and IC used in the previous scan, this reference data may be used for comparison in what is described as "Method C" in Figure 176. For the purposes of this protocol, a reference scan must have been acquired since the date of the last annual QA accelerator test. The reference scan must have been acquired from at least 2 mm greater than the DeICERS in water to at least 1 mm above the water surface in air at 0.1 mm resolution. To be considered a reference scan, the data must also have been acquired at ≥4 s/pt. sampling resolution. It is not assumed that most users will have data previously acquired under these conditions. If, however, such data exists, the

newly measured curve may be shifted to the reference curve by minimizing the root-mean squared (rms) error between the two. Assuming similar normalization of the two curves, this should constitute shifting the measured curve along the depth axis to match the reference curve.

If reference data exists that was acquired under identical radiation field conditions with an IC similar to the one being used (e.g., IBA CC25/Exradin A12S), the user may choose to shift the measured curve to this reference curve, under "Method B" in Figure 176. In this situation, the rms error minimization should consider only the data acquired at depths greater than 1 mm beyond the IC outer radius. By considering only these points in the comparison, IC size-related effects on the depth-ionization data are minimized.

If no reference data exists, as will presumably most often be the case, the user should follow the preferred "Method A" of Figure 176. The user must compute the depth-ionization gradient and determine the gradient peak location. As has been shown in this thesis, the gradient peak will occur at the DeICERS. For cylindrical ICs, this depth is the IC outer radius. For parallel-plate ICs, this depth is the leading edge of the entrance window. If the gradient peak is not resolved to within 1.5 times the desired scan precision, a new scan should be conducted from 2 mm deeper than the apparent gradient peak location to 2 mm shallower than the apparent gradient peak location. This scan should be performed at finer spatial resolution and with increased sampling time. By decreasing the scan step size and increasing the signal sampling per point, the gradient peak should be successfully resolved. If the gradient peak location deviates from the DeICERS, IC alignment must be shifted to the proper location, which must be visually confirmed. Scans can then be performed at "regular" resolution again, knowing that the IC is well-aligned. Note that water evaporation will affect the surface location over time. If measurements are to be acquired over a long period, the alignment procedure should be followed

periodically to ensure proper alignment to the changing water surface location. "Method B" may be suitable for this purpose. For best results, the alignment procedure should also be followed after each time the IC and/or water tank setup is physically altered. For scans performed for an arbitrary field size or beam energy, scans should go to ≥10 mm beyond the water surface in air and the gradient peak location should be compared with the DeICERS. With correct alignment, the gradient peak should occur within the measurement step size of the DeICERS.

5.2 Virginia Commonwealth University Implementation

Initial scans at VCU as a part of this thesis are performed in three pieces. The in-water and in-air pieces are measured at 1 mm spatial resolution while the middle section in which the IC reaches the water surface is measured at 0.1 mm resolution. In this initial scan, 50 samples at each depth are taken from 50 mm below the water surface to 20 mm above the water surface in air in step-by-step mode at 1 mm resolution over a 1 s time interval. The IC is then fully submerged in water and a second scan is acquired over the same depth range around the DeICERS as the middle portion of the initial scan, e.g., 5 to -1 mm. In the second scan, more samples are acquired at each depth. For a cylindrical IC scan, 200 samples are typically taken at each depth over 4 s. A sampling resolution of 10 s/pt., yielding 500 samples at each depth, is generally used for parallel-plate IC scans. The middle section of the original scan is then cut out and the scan with higher sampling resolution is pasted into the original scan. This combined file is then saved separately from the original scan data. The combined file formed is shown in Figure 177.

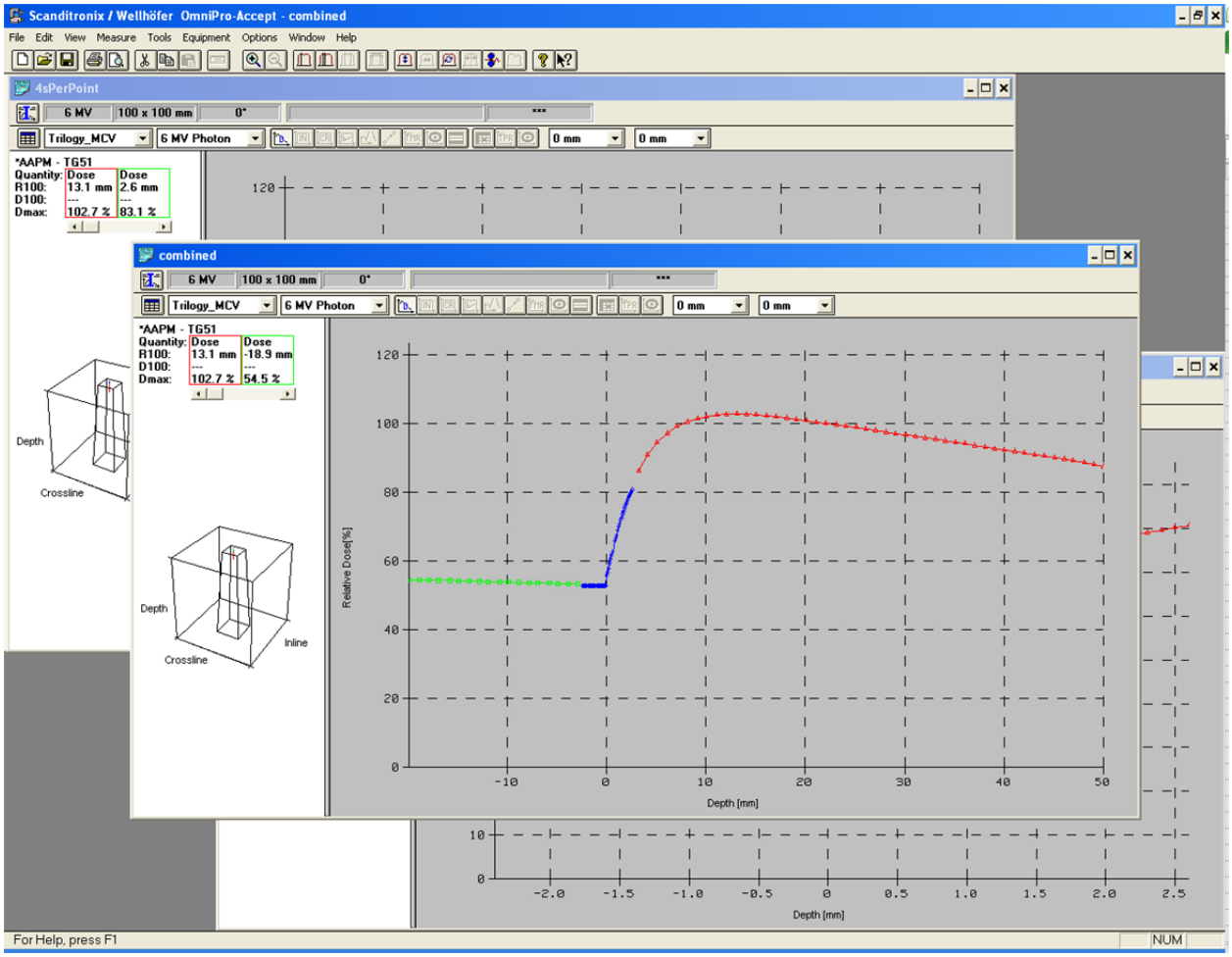

Figure 177: This scan combines the relatively quickly acquired data of the outer pieces with the data acquired as slowly as possible near the water surface. Scans are displayed in the OmniPro-Accept software, version 6.5.

An in-house software routine written by the author is then used to compute the derivatives of each part of the scan and store them in text files. A second routine is used to put the small pieces together into a combined file. Once the combined gradient file is created, inter-scan evaluation of gradient peak location is conducted by opening the combined gradient text file and plotting the file contents. For a cylindrical IC measurement, the feature of note is the gradient peak as shown in Figure 178. For a parallel-plate IC measurement, the feature of note is the local maximum beyond which the relative dose gradient falls to zero. Since parallel-plate IC gradients are often noisy, the relevant portion of the combined gradient text file is highlighted in

Figure 179. In the examples provided in Figure 178 and Figure 179, the ICs being used were well-aligned and no adjustment was necessary. If, however, a discrepancy is observed when results are plotted, measurement setup and the water surface location are re-evaluated before rescanning.

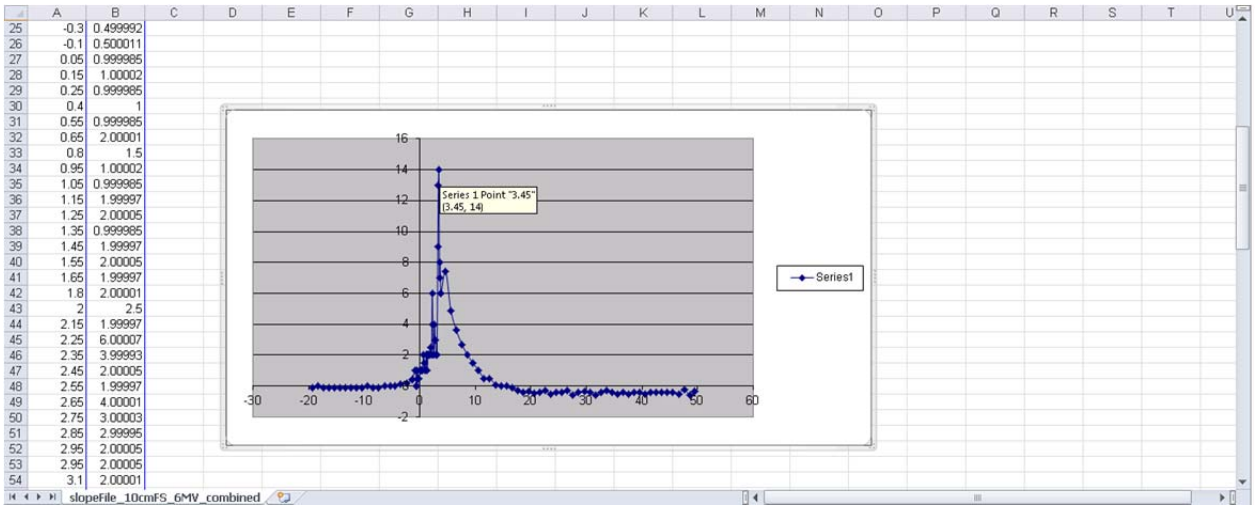

Figure 178: Depiction of the opening in Microsoft Excel® and plotting of a combined PDD gradient, or slope, file created by the stitchFiles.exe routine for a cylindrical IC. The screen grab shows the gradient peak is observed at 3.45 mm, the DeICERS.

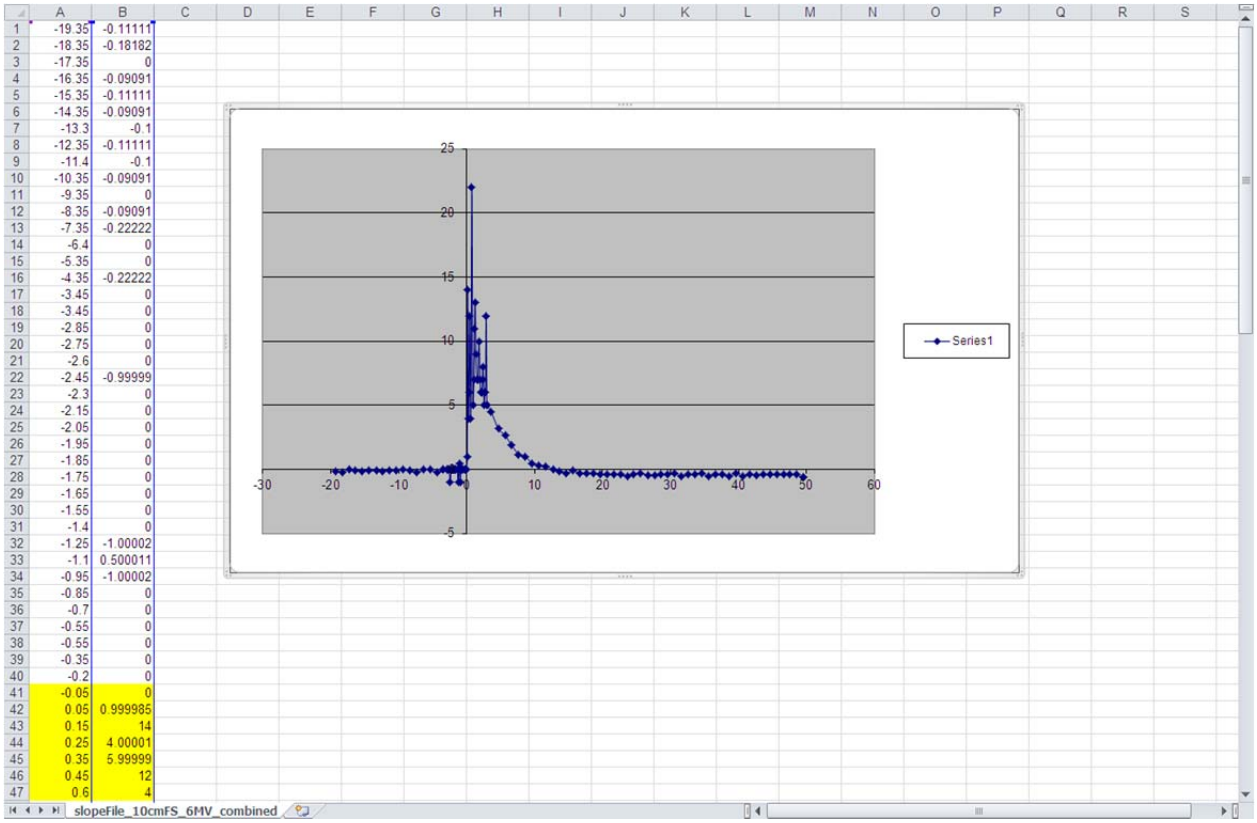

Figure 179: Depiction of the opening in Microsoft Excel® and plotting of a combined PDD gradient, or slope, file created by the stitchFiles.exe routine for a parallel-plate IC. The highlighted portion of the data file shows the peak beyond which the gradient goes to zero is observed at 0.15 mm, which is within tolerance of the DeICERS.

6 Conclusions

In this thesis, multiple methods for quantitatively evaluating IC alignment to a water surface were investigated. To precisely align an IC without a known reference of water surface location, scan gradients are chosen because they are relatively robust against input data noise and are based on physical reality, rather than the empiricism of the functional form-based curve fitting that was attempted. An analytical model was developed to test the theoretical basis of the change in a relative dose gradient at an air-water interface. The analytical model and MC simulation models were used to show that the relative dose gradient exhibits a peak at the point at which an IC reaches the water surface when moving from water to air. MC simulation models were modified to test dependencies of gradient peak location on cylindrical IC design parameters like wall and central electrode thickness. Gradient peak location was only found to depend on IC outer radius.

Measurements were performed in photon beams from Varian 2100 and 2300 accelerators, an Elekta Precise, and an Accuray CyberKnife and in electron beams from a Varian 2300. Commercially available and custom-built scanning systems were both used. Measurements were taken with twenty-four cylindrical IC types and five parallel-plate IC designs. It was found that scans from air through the surface into water do not exhibit gradient peaks at the DeICERS due to the surface tension of water. Water surface tension was investigated on a small scale with capillary tube measurements and on a large scale with IC measurements in a water tank containing ~1 L of liquid dishwashing detergent mixed into the water. It was found that water

surface tension can be reduced but not completely eliminated. Measurements from air to water are therefore explicitly not recommended.

It was found that scans at coarser resolution will degrade the gradient peak and shift it deeper into the water by roughly one-third of the scan resolution. Scans were taken at various speeds and sampling resolutions. It was found that slow speeds and long acquisition times provide the most accurate measured readings. A nominal VCU evaporation rate was found experimentally and used to retrospectively correct scans for water surface evaporation. A method of tracking the water surface at the 0.1-0.2 mm level with standard commercial scanning equipment was developed. Measurements were taken for changes in incident beam energy, particle type, field size, bias voltage polarity, SSD, and contaminant electrons. The relative dose gradient peak location was not found to depend on any of these factors. As shown for the 29 ICs studied, the relative dose gradient peak occurs where the IC reaches the water surface. For cylindrical ICs, the relative dose gradient peak location depends on IC outer radius. Parallel-plate IC entrance window thickness also affects gradient peak location.

The impact of this thesis will ultimately be decided by those who read it but will hopefully be determined by the success of the alignment method shown here and the ease with which the method can be implemented into clinical QA practice. The peak of the relative dose gradient can be used to quantitatively establish IC alignment to a water surface. In time, the author hopes to work with scanning equipment vendors to automate the water surface alignment process within commercial software. Currently, a scanning protocol that can be followed by a given user to determine his or her IC alignment without significantly affecting the timing of overall measurement workflow has been developed. This protocol should be followed by clinical users to improve inter-setup and intra-user scan reproducibility.

References

Abdel-Rahman W, Seuntjens J P, Verhaegen F, Deblois F and Podgorsak E B 2005 Validation of Monte Carlo calculated surface doses for megavoltage photon beams *Med Phys* **32** 286-98

Abdel-Rahman W, Seuntjens J P, Verhaegen F and Podgorsak E B 2006 Radiation induced currents in parallel plate ionization chambers: measurement and Monte Carlo simulation for megavoltage photon and electron beams *Med Phys* **33** 3094-104

Aget H and Rosenwald J C 1991 Polarity effect for various ionization chambers with multiple irradiation conditions in electron beams *Med Phys* **18** 67-72

Aird E G and Farmer F T 1972 The design of a thimble chamber for the Farmer dosemeter *Phys Med Biol* **17** 169-74

Almond P R, Andreo P, Mattsson O, Nahum A E and Roos M 1997 The use of plane-parallel ionization chambers in high-energy electron and photon beams. An international code of practice for dosimetry. (Vienna, Austria: IAEA)

Almond P R, Biggs P J, Coursey B M, Hanson W F, Huq M S, Nath R and Rogers D W O 1999 AAPM's TG-51 protocol for clinical reference dosimetry of high-energy photon and electron beams *Med Phys* **26** 1847-70

Andreo P, Burns D T, Hohlfeld K, Huq M S, Kanai T, Laitano F, Smyth V and Vynckier S 2001 Absorbed Dose Determination in External Beam Radiotherapy: An International Code of Practice for Dosimetry based on Standards of Absorbed Dose to Water. (Vienna: International Atomic Energy Agency)

Attix F H 1986 *Introduction to radiological physics and radiation dosimetry* (New York: Wiley)

Batchelor G K 1967 *An introduction to fluid dynamics* (Cambridge, U.K.: U.P.)

Bednarz B P 2008 Detailed Varian Clinac accelerator modeling for calculating intermediate-and low-level non-target organ doses from radiation treatment. (Troy, NY, USA: Rensselaer Polytechnic Institute)

Berger M J, Coursey J S, Zucker M A and Chang J 2006 Stopping-power and range tables for electrons, protons, and helium ions. (Gaithersburg, MD, USA: NIST Physics Laboratory)

Berger M J, Hubbell J H, Seltzer S M, Chang J, Coursey J S, Sukumar R, Zucker D S and Olsen K 1998 XCOM: Photon cross sections database. (Gaithersburg, MD, USA: NIST Physics Laboratory)

Bouchard H, Seuntjens J and Kawrakow I 2011 A Monte Carlo method to evaluate the impact of positioning errors on detector response and quality correction factors in nonstandard beams *Phys Med Biol* **56** 2617-34

Boutillon M and Perroche-Roux A M 1987 Re-evaluation of the W value for electrons in dry air *Physics in Medicine and Biology* **32** 213

Chamberlain E C and Baily N A 1964 Entrance and Exit Absorbed Dose Characteristics for a 6-MeV X-Ray Generator *Radiology* **82** 267-71

Chetty I J, Curran B, Cygler J E, DeMarco J J, Ezzell G, Faddegon B A, Kawrakow I, Keall P J, Liu H, Ma C M, Rogers D W O, Seuntjens J, Sheikh-Bagheri D and Siebers J V 2007 Report of the AAPM Task Group No. 105: Issues associated with clinical implementation of Monte Carlo-based photon and electron external beam treatment planning *Med Phys* **34** 4818-53

Chibani O and Ma C-M 2007 On the discrepancies between Monte Carlo dose calculations and measurements for the 18 MV Varian photon beam *Med Phys* **34** 1206-16

Chibani O, Moftah B and Ma C M 2011 On Monte Carlo modeling of megavoltage photon beams: a revisited study on the sensitivity of beam parameters *Med Phys* **38** 188-201

Das I J, Cheng C W, Watts R J, Ahnesjo A, Gibbons J, Li X A, Lowenstein J, Mitra R K, Simon W E and Zhu T C 2008 Accelerator beam data commissioning equipment and procedures: Report of the TG-106 of the Therapy Physics Committee of the AAPM *Med Phys* **35** 4186-215

Das I J, McNeeley S W and Cheng C W 1998 Ionization chamber shift correction and surface dose measurements in electron beams *Phys Med Biol* **43** 3419-24

DeWerd L A, Davis S D, Bartol L J and Grenzow F 2009 *Clinical dosimetry measurements in radiotherapy: proceedings of the American Association of Physicists in Medicine Summer School, Colorado College, Colorado Springs, Colorado, June 21-25, 2009),* ed D W O Rogers and J E Cygler (Madison, WI: Medical Physics Pub.) pp 181-204, 1128 p.

Ding G X 2002a Dose discrepancies between Monte Carlo calculations and measurements in the buildup region for a high-energy photon beam *Med Phys* **29** 2459-63

Ding G X 2002b Energy spectra, angular spread, fluence profiles and dose distributions of 6 and 18 MV photon beams: Results of Monte Carlo simulations for a Varian 2100EX accelerator *Phys Med Biol* **47** 1025-46

Ding G X, Duzenli C and Kalach N I 2002 Are neutrons responsible for the dose discrepancies between Monte Carlo calculations and measurements in the build-up region for a high-energy photon beam? *Phys Med Biol* **47** 3251-61

Fraass B, Doppke K, Hunt M, Kutcher G, Starkschall G, Stern R and Van Dyk J 1998 American Association of Physicists in Medicine Radiation Therapy Committee Task Group 53: quality assurance for clinical radiotherapy treatment planning *Med Phys* **25** 1773-829

Gerbi B J, Antolak J A, Deibel F C, Followill D S, Herman M G, Higgins P D, Huq M S, Mihailidis D N, Yorke E D, Hogstrom K R and Khan F M 2009 Recommendations for clinical electron beam dosimetry: supplement to the recommendations of Task Group 25 *Med Phys* **36** 3239-79

Gerbi B J and Khan F M 1987 The polarity effect for commercially available plane-parallel ionization chambers *Med Phys* **14** 210-5

Gerbi B J and Khan F M 1990 Measurement of dose in the buildup region using fixed-separation plane-parallel ionization chambers *Med Phys* **17** 17-26

Hartmann Siantar C L, Walling R S, Daly T P, Faddegon B, Albright N, Bergstrom P, Bielajew A F, Chuang C, Garrett D, House R K, Knapp D, Wieczorek D J and Verhey L J 2001 Description and dosimetric verification of the PEREGRINE Monte Carlo dose calculation system for photon beams incident on a water phantom *Med Phys* **28** 1322-37

Hills B A 1999 An alternative view of the role(s) of surfactant and the alveolar model *J Appl Physiol* **87** 1567-83

Hubbell J H and Seltzer S M 2004 Tables of x-ray mass attenuation coefficients and mass energy-absorption coefficients from 1 keV to 20 MeV for elements Z = 1 to 92 and 48 additional substances of dosimetric interest. (Gaithersburg, MD, USA: NIST Physics Laboratory)

IBA Dosimetry 2007 Ionization Chambers and Diode Detectors - Detectors for Relative and Absolute Dosimetry. (Bartlett, TN: IBA Dosimetry America)

International Commission on Radiation Units and Measurements 1963 *Clinical Dosimetry* (Washington, D.C.: United States Department of Commerce National Bureau of Standards)

International Commission on Radiation Units and Measurements 1973 *Measurement of absorbed dose in a phantom irradiated by a single beam of X or gamma rays* (Washington, D.C.: International Commission on Radiation Units and Measurements)

International Commission on Radiation Units and Measurements 1984 Stopping powers for electrons and positrons. (Bethesda, Md., U.S.A.: International Commission on Radiation Units and Measurements)

International Organization for Standardization 1993 *Guide to the expression of uncertainty in measurement* (Genève, Switzerland: International Organization for Standardization)

Johns H E, Aspin N and Baker R G 1958 Currents induced in the dielectrics of ionization chambers through the action of high-energy radiation *Radiat Res* **9** 573-88

Johns H E and Cunningham J R 1983 *The physics of radiology* (Springfield, Ill., U.S.A.: Charles C. Thomas)

Kase K R, Mao X S, Nelson W R, Liu J C, Kleck J H and Elsalim M 1996 Neutron fluence and energy spectra around the Varian Clinac 2100C/2300C medical accelerator. (Stanford, CA, USA: Stanford Linear Accelerator Center)

Kawrakow I 2000a Accurate condensed history Monte Carlo simulation of electron transport. I. EGSnrc, the new EGS4 version *Med Phys* **27** 485-98

Kawrakow I 2000b Accurate condensed history Monte Carlo simulation of electron transport. II. Application to ion chamber response simulations *Med Phys* **27** 499-513

Kawrakow I 2002 On the de-noising of Monte Carlo calculated dose distributions *Phys Med Biol* **47** 3087-103

Kawrakow I 2005 egspp: the EGSnrc C++ class library. (Ottawa: National Research Council of Canada)

Kawrakow I 2006 On the effective point of measurement in megavoltage photon beams *Med Phys* **33** 1829-39

Kawrakow I and Rogers D W O 2003 The EGSnrc Code System: Monte Carlo Simulation of Electron and Photon Transport. (Ottawa: National Research Council of Canada)

Keall P J, Siebers J V, Libby B and Mohan R 2003 Determining the incident electron fluence for Monte Carlo-based photon treatment planning using a standard measured data set *Med Phys* **30** 574-82

Khan F M, Doppke K P, Hogstrom K R, Kutcher G J, Nath R, Prasad S C, Purdy J A, Rozenfeld M and Werner B L 1991 Clinical electron-beam dosimetry: report of AAPM Radiation Therapy Committee Task Group No. 25 *Med Phys* **18** 73-109

Klein E E, Esthappan J and Li Z 2003 Surface and buildup dose characteristics for 6, 10, and 18 MV photons from an Elekta Precise linear accelerator *J Appl Clin Med Phys* **4** 1-7

Klein E E, Hanley J, Bayouth J, Yin F F, Simon W, Dresser S, Serago C, Aguirre F, Ma L, Arjomandy B, Liu C, Sandin C and Holmes T 2009 Task Group 142 report: quality assurance of medical accelerators *Med Phys* **36** 4197-212

Libby B, Siebers J and Mohan R 1999 Validation of Monte Carlo generated phase-space descriptions of medical linear accelerators *Med Phys* **26** 1476-83

McEwen M R 2010 Measurement of ionization chamber absorbed dose k(Q) factors in megavoltage photon beams *Med Phys* **37** 2179-93

McEwen M R 2011 personal communication.

McEwen M R, Kawrakow I and Ross C K 2008 The effective point of measurement of ionization chambers and the build-up anomaly in MV x-ray beams *Med Phys* **35** 950-8

McEwen M R, Williams A J and DuSautoy A R 2001 Determination of absorbed dose calibration factors for therapy level electron beam ionization chambers *Phys Med Biol* **46** 741-55

Nath R, Biggs P J, Bova F J, Ling C C, Purdy J A, van de Geijn J and Weinhous M S 1994 AAPM code of practice for radiotherapy accelerators: report of AAPM Radiation Therapy Task Group No. 45 *Med Phys* **21** 1093-121

Nilsson B and Montelius A 1986 Fluence perturbation in photon beams under nonequilibrium conditions *Med Phys* **13** 191-5

Nisbet A and Thwaites D I 1998 Polarity and ion recombination correction factors for ionization chambers employed in electron beam dosimetry *Phys Med Biol* **43** 435-43

Parsai E I, Shvydka D, Pearson D, Gopalakrishnan M and Feldmeier J J 2008 Surface and build-up region dose analysis for clinical radiotherapy photon beams *Applied Radiation and Isotopes* **66** 1438-42

Pearce J, Thomas R and DuSautoy A 2006 The characterization of the Advanced Markus ionization chamber for use in reference electron dosimetry in the UK *Phys Med Biol* **51** 473-83

PTW Dosimetry 2007 Ionizing Radiation Detectors. (Freiburg, Germany: PTW-Freiburg)

Rawlinson J A, Arlen D and Newcombe D 1992 Design of parallel plate ion chambers for buildup measurements in megavoltage photon beams *Med Phys* **19** 641-8

Richards T W and Carver E K 1921 A critical study of the capillary rise method of determining surface tension, with data for water, benzene, toluene, chloroform, carbon tetrachloride, ether and dimethyl aniline [second paper] *Journal of the American Chemical Society* **43** 827-47

Richards T W and Coombs L B 1915 The surface tensions of water, methyl, ethyl and isobutyl alcohols, ethyl butyrate, benzene and toluene *Journal of the American Chemical Society* **37** 1656-76

Rogers D W O, Kawrakow I, Seuntjens J P, Walters B R B and Mainegra-Hing E 2003 NRC user codes for EGSnrc. (Ottawa, Ontario, Canada: National Research Council of Canada)

Rogers D W O, Walters B R B and Kawrakow I 2006 BEAMnrc Users Manual. (Ottawa: National Research Council of Canada)

Schulz R J, Almond P R, Cunningham J R, Holt J G, Loevinger R, Suntharalingam N, Wright K A, Nath R and Lempert G D 1983 A protocol for the determination of absorbed dose from high-energy photon and electron beams *Med Phys* **10** 741-71

Schulz R J, Holt J G, Loevinger R, Shalek R J, Suntharalingam N, Almond P R, Karzmark C J, Lanzl L, Laughlin J S, Ovadia J, Wooton P, Worsnop R and Wright K 1971 Protocol for the dosimetry of x- and gamma-ray beams with maximum energies between 0-6 and 50 MeV. Scientific Committee on Radiation Dosimetry (SCRAD) of the American Association of Physicists in Medicine *Phys Med Biol* **16** 379-96

Siebers J V, Keall P J, Libby B and Mohan R 1999 Comparison of EGS4 and MCNP4b Monte Carlo codes for generation of photon phase space distributions for a Varian 2100C *Phys Med Biol* **44** 3009-26

Siebers J V, Ververs J D and McEwen M R 2009 Improving the accuracy of entrance dosimetry measurements for dose modeling. In: *World Congress 2009 on Medical Physics & Biomedical Engineering,* (Munich, Germany: Springer) pp 523-6

Standard Imaging 2008 Exradin Ion Chambers. (Middleton, WI: Standard Imaging, Inc.)

Tailor R C and Tello V M 1995 Depth of ionization chamber in water *Phys Med Biol* **40** 1389-92

Tessier F, Hooten B D and McEwen M R 2010 Zero-shift thimble ionization chamber *Med Phys* **37** 1161-3

Tessier F and Kawrakow I 2010 Effective point of measurement of thimble ion chambers in megavoltage photon beams *Med Phys* **37** 96-107

Tonkopi E, McEwen M R, Walters B R B and Kawrakow I 2005 Influence of ion chamber response on in-air profile measurements in megavoltage photon beams *Med Phys* **32** 2918-27

Treurniet J R, Walters B R, Kawrakow I and Rogers D W O 2010 BEAMnrc, DOSXYZnrc, and BEAMDP GUI User's Manual. (Ottawa: National Research Council of Canada)

Van Dyk J and Macdonald J C 1972 Penetration of high energy electrons in water *Phys Med Biol* **17** 52-5

Vargaftik N B, Volkov B N and Voljak L D 1983 International tables of the surface tension of water *J. Phys. Chem. Ref. Data* **12** 817

Velkley D E, Manson D J, Purdy J A and Oliver G D, Jr. 1975 Build-up region of megavoltage photon radiation sources *Med Phys* **2** 14-9

Verhaegen F and Seuntjens J 2003 Monte Carlo modelling of external radiotherapy photon beams *Phys Med Biol* **48** R107-64

Ververs J D, McEwen M R and Siebers J V 2009a SU-GG-BRC-08: Improving buildup region measurement accuracy using a surface location method *Medical Physics* **36** 2683

Ververs J D, Schaefer M J, Kawrakow I and Siebers J V 2009b A method to improve accuracy and precision of water surface identification for photon depth dose measurements *Med Phys* **36** 1410-20

Weon B M, Je J H, Hwu Y and Margaritondo G 2008 Decreased surface tension of water by hard-X-ray irradiation *Physical Review Letters* **100** 217403

Wulff J, Zink K and Kawrakow I 2008 Efficiency improvements for ion chamber calculations in high energy photon beams *Med Phys* **35** 1328-36

Appendix I: Single Cylindrical Ionization Chamber Study

A METHOD TO IMPROVE ACCURACY AND PRECISION OF WATER SURFACE IDENTIFICATION FOR PHOTON DEPTH DOSE MEASUREMENTS

James D. Ververs

Matthew J. Schaefer

Iwan Kawrakow

Jeffrey V. Siebers

Medical Physics 36(4), 2009

A method to improve accuracy and precision of water surface identification for photon depth dose measurements[a)]

J. D. Ververs[b)] and M. J. Schaefer
Department of Radiation Oncology, Virginia Commonwealth University, Richmond, Virginia 23298

I. Kawrakow
Ionizing Radiation Standards, National Research Council of Canada, Ottawa K1A OR6, Canada

J. V. Siebers
Department of Radiation Oncology, Virginia Commonwealth University, Richmond, Virginia 23298

(Received 25 November 2008; revised 30 January 2009; accepted for publication 21 February 2009; published 27 March 2009)

The objective of this study is to present a method to reduce the setup error inherent in clinical depth dose measurements and, in doing so, to improve entrance dosimetry measurement reliability. Ionization chamber (IC) depth dose measurements are acquired with the depth scan extended into the air above the water surface. An inflection region is obtained in each resulting percent depth ionization (PDI) curve that can be matched against other measurements or to an inflection region obtained from an analogous Monte Carlo (MC) simulation. Measurements are made with various field sizes for the 6 and 18 MV photon beams, with and without a Pb foil in the beam, to determine the sensitivity of the dose inflection region to the beam conditions. The offset between reference and test data set inflection regions is quantified using two separate methods. When comparing sets of measured data, maxima in the second derivative of ionization are compared. When comparing measured data to MC simulation, the offset that minimizes the sum of squared differences between the reference and test curves in the ionization inflection region is found. These methods can be used to quantify the offset between an initial setup (test) position and the true surface (reference) position. The ionization inflection location is found to be insensitive to changes in field size, electron contamination, and beam energy. Data from a single reference condition should be sufficient to identify the surface location. The method of determining IC offsets is general and should be applicable to any IC and other radiation sources. The measurement method could reduce the time and effort required in the initial IC setup at a water surface as setup errors can be corrected offline. Given a reliable set of reference data to compare with, this method could increase the ability of quality assurance (QA) measurements to detect discrepancies in beam output as opposed to discrepancies in IC localization. Application of the measurement method standardizes the procedure for localizing cylindrical ICs at a water surface and thereby improves the reliability of measurements taken with these devices at all depths. [DOI: 10.1118/1.3098125]

Key words: surface identification, quality assurance, ionization chamber, relative dosimetry

I. INTRODUCTION

Acquisition of depth ionization measurements at each beam energy for each radiotherapy treatment accelerator is a routine clinical task required during both initial commissioning and annual quality assurance (QA). The depth ionization data are input to the treatment planning system, which then either uses the data directly to compute treatment doses, or indirectly to fit algorithms which are then used for dose calculation. In setting up a water phantom, initial surface localization with respect to the ionization chamber (IC) is a primary concern since any errors in the surface identification result in a systematic error for all future uses of the measurement data. Surface identification is particularly challenging for cylindrical ICs. A recent AAPM taskgroup[1] recommends a method of looking at the IC reflection from beneath the surface and setting zero depth at the point where the reflected image and the cylindrical IC form a perfect circle. While this method will allow one to get close to properly matching the IC center with the water surface, this is still a qualitative determination. The fact is that although manufacturers, the AAPM,[1–6] and others[7–9] made several recommendations regarding procedures for depth ionization data acquisition, this process remains partly science, partly art. In addition, proper IC localization requires corrections such as those to account for the effective point of measurement (EPOM). Identification of the depth origin (typically, the surface of a water phantom) relies on operator's technique, skill, and patience. Due to this, ionization values in the entrance region are lightly regarded and infrequently clinically utilized.

However, the entrance ionization region contains valuable information for the commissioning of dose calculation algorithms. Differences between measurements and calculations in the entrance region, particularly for 18 MV 40×40 cm^2 fields, have served to identify Monte Carlo (MC) dose cal-

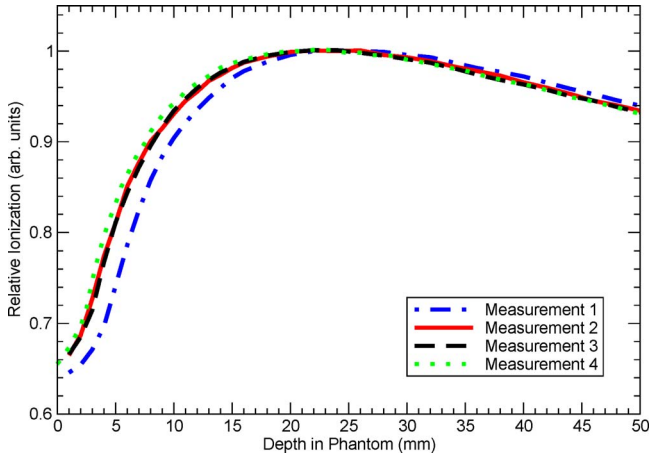

FIG. 1. Annual QA percent depth ionization (PDI) data from the same machine operating at 18 MV for a 40×40 cm^2 field measured with the RK IC showing the effect of IC misalignment on resulting PDI data.

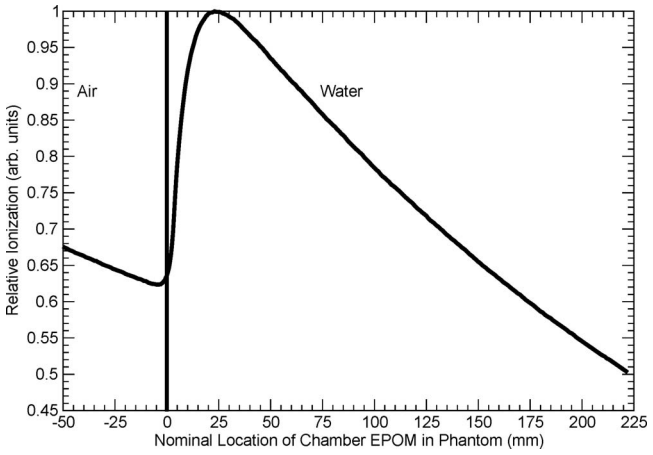

FIG. 2. Measured PDI curve, extending into air, showing an inflection region at the air/water interface. The data were acquired with the same IC under the same conditions used to acquire the data shown in Fig. 1. The IC EPOM is shifted by 1.2 mm upstream as recommended by TG-51 ($0.6\times r_{cav}$).

culation algorithm errors,[10,11] to resolve discrepancies in manufacturer-specified treatment head geometries,[12] and to verify physics models.[8] These differences have also motivated studies of contaminant particle sources[8,13–15] and the cylindrical IC EPOM.[9,16]

The primary purpose of this work is to describe an automated procedure for IC surface identification for photon beam depth ionization measurements that is not reliant on operator's technique, skill, and patience. The motivation for this work stemmed from a desire to create reference phase space data at 6 and 18 MV to submit to the IAEA phase space database. The IAEA phase space database project aims to create a database for linear accelerators and ^{60}Co units by compiling properly validated existing data.[17] Initially, the MC model was to be validated by comparing it with the measured depth ionization and profile data obtained during annual QA procedures. However, plotting the depth ionization results from three different acquisitions yielded the results shown in Fig. 1. In the entrance region, it is apparent that there is a discrepancy in IC positioning. Furthermore, although one measurement deviates from the others, there is no way to positively conclude that this is an erroneous data set. It is equally likely that a consistently incorrect IC positioning existed for the three measurements which coincide. In order to detect, and subsequently correct for, these sorts of systematic errors, the method presented here has been developed to determine IC location.

II. METHOD AND MATERIALS

II.A. Clinical measurements

A Scanditronix Type RK 83-05 cylindrical IC (Ref. 18) is used to acquire depth dose measurements from a Varian 21EX linac (Varian Medical Systems, Palo Alto, CA) with a $64\times40\times44$ cm^3 RFA-200 water tank (IBA Dosimetry, Bartlett, TN). Details of the IC geometry obtained from the manufacturer[18,19] indicate that the IC is 25 mm long with a 7 mm outer diameter. The steel stem is 55 mm long with an outer diameter of 4 mm. The internal air cavity has an active volume of 0.12 cm^3 with a length of 10 mm and a diameter of 4 mm. The central electrode, consisting of 50% epoxy resin and 50% graphite, is 9 mm long and 1 mm in diameter. The outer wall consists of 1 mm thick PMMA with an effective thickness of 0.12 g/cm^2. The inner wall (outer electrode) is a 0.5 mm thick mixture of 50% epoxy resin and 50% graphite with an effective thickness of 0.07 g/cm^2. The insulating material used in the IC is polystyrene.

For all measurements, the EPOM is taken to be shifted 1.2 mm ($0.6\times r_{cav}$) upstream from the center of the IC, following the recommendations of AAPM TG-51 (Ref. 5) and IAEA TRS-398,[20] and the water surface is located 1000 mm from the nominal source location. Using the Scanditronix/Wellhöfer OmniPro-Accept software (Version 6.5), the large step size is set to 1 mm, while the small step size is set to 0.5 mm so that ionization readings are taken every 1 mm of IC movement except in the buildup region and within ~2 mm of the surface in air where ionization readings are recorded in 0.5 mm intervals. The scans are performed at the medium speed setting, resulting in an IC velocity of ~30 mm/s. Each measurement scans from 222 mm deep in the water phantom to 50 mm upstream of the water surface to ensure observation of the ionization inflection region caused by the air-water interface. While finding the minimum scanning distance above the interface necessary to observe the inflection region was not a focus of this work, a second set of measurements not shown here indicates that scanning only 20 mm into air is sufficient to allow observation of the inflection region. Figure 2 demonstrates such an ionization inflection region, in this case acquired for an 18 MV 40×40 cm^2 field.

To determine the dependence of the ionization inflection region on irradiation conditions, depth ionization measurements are obtained in a single measurement session without disturbing the IC setup alignment. The IC is carefully set up per the previously referenced AAPM recommendations.

Measurements are made for the 6 and 18 MV beams at multiple field sizes, with and without a 1 mm thick Pb foil taped to the bottom of the treatment head. To ensure setup stability, the initial and final measurements are made with identical beam energy (6 MV), field size (10×10 cm^2), and Pb foil status (no Pb foil in the beam). Measurements taken at each beam energy with field sizes ranging from 5×5 to 40×40 cm^2 are compared to each other in the inflection region to determine if the inflection region location depends on variations in head-scatter conditions. Similarly, measurements with and without the Pb foil are compared to determine if changes in treatment head contaminant electron fluence alter the inflection region location. Also, the 6 and 18 MV data are compared to one another to inspect potential inflection region variations with gross changes in the incident beam energy.

II.B. MC simulations

To determine the absolute water surface location with respect to the IC-produced inflection region, a series of MC simulations is performed to reproduce several of the measurement scenarios. All MC calculations conducted as part of this work are done using the EGSnrc[21–23] codes. All calculations are performed using the same photon cutoff energy value (PCUT=0.01 MeV) and the EXACT boundary crossing algorithm, as recommended by Walters and Kawrakow.[11]

II.B.1. BEAMnrc treatment head simulations

A BEAMnrc (Ref. 24) model of the Varian 21EX is implemented as a shared library source, allowing the single module to be directly used as a source of particles for all dose calculation user codes used in this study. A detailed description of the use of BEAMnrc shared library sources in EGSnrc user codes has been previously provided by Tonkopi *et al.*[25] and the efficiency of their use has been examined by Kawrakow and Walters.[26] The accelerator model used here is developed based on proprietary information obtained from the accelerator manufacturer. The model differs from that used to generate previously published phase space data[27–29] in that (1) the position of the target relative to the primary collimator differs (motivated by the work of Chibani and Ma[12]), (2) a PYRAMIDS component module is added to approximate edge-of-field shielding that exists between the mirror and the jaws, and (3) an approximation has been made that the mirror lies flat perpendicular to the beam axis due to the fact that the mirror physically extends into the aforementioned shielding in the beam direction. The treatment head portion of each calculation is performed using an electron cutoff energy, ECUT, of 0.7 MeV. Directional bremsstrahlung splitting is used with a splitting number of 1000 for the 6 MV simulations and 750 for 18 MV. Range rejection is also employed with the cutoff energy set as ESAVE=2 MeV at 6 MV and ESAVE=5 MeV at 18 MV. These settings are chosen following the findings of Kawrakow *et al.*[30] and Kawrakow and Walters,[26] respectively.

To quantify the variations in contaminant electrons for the different measurement scenarios, a second set of BEAMnrc simulations of the Varian 21EX model is performed. In contrast to the simulations previously described, the treatment head model is used here to generate phase space files rather than as a shared library source. Files are generated for both 6 and 18 MV beams and both 10×10 and 40×40 cm^2 fields. For each of these cases, simulations are run with and without the Pb foil present in the beam path. These phase space files are then analyzed with BEAM data processor (BEAMDP).[31] BEAMDP allows users to derive spectral and planar fluence distributions from phase space data. Using this tool, each phase space file is read for electrons passing through a 3 cm radius around the central axis at 100 cm SSD. These particles are then separated into 20 equally spaced energy bins, and the energy fluence is plotted as a function of the incident electron kinetic energy. The results of these simulations are shown in Sec. III B 3.

II.B.2. Dose calculations with IC absent

To allow quantification of the effect of the IC on the percent depth dose (PDD) and the potential variations in the EPOM as a function of depth, DOSXYZnrc simulations of a pure water phantom are also performed. For these simulations, a $64\times40\times44$ cm^3 water phantom is utilized. Beginning from 5 cm above the water surface in air, voxel dimensions along the beam central axis are $2\times2\times0.5$ cm^3, except within a region from 1 cm above the surface to 4 cm depth in water in which the voxel dimensions used are $2\times2\times0.1$ cm^3. Voxel dimensions are then increased to $2\times2\times1$ cm^3 after a depth of 10 cm within the water tank. The results of three such simulations are compared with measurements and with the results of analogous simulations with the IC present, which are described in Sec. II B 3. This comparison for the 6 MV beam and a 10×10 cm^2 field is discussed in Sec. III B 1. The results of the same comparison conducted for both a 6 MV 40×40 cm^2 field and an 18 MV 40×40 cm^2 field are given in Sec. III B 2. Note that DOSXYZnrc simulations directly score the dose in water, while the simulations described in the next section effectively score the energy deposited in the air volume of the chamber. Thus, deviations between the with and without IC simulation results are not only due to electrons generated in the IC wall but also to variations in stopping powers and other IC corrections required to convert dose to air to dose in water and/or percent depth ionization (PDI) to PDD. Range rejection is also used in these calculations with the same settings as detailed in the previous section. In addition, photon splitting was employed with an n_split of 40. Here, ECUT is set to 0.521 MeV.

II.B.3. Dose calculations with IC present

Depth ionization calculations are done using the CAVITY and EGS_CHAMBER[32] user codes to allow direct inclusion of the IC in the simulation geometry. These user codes are built on egspp, the EGSnrc C++ class library,[33] which provides a flexible geometry allowing for detailed modeling of any IC geometry. Details of the RK IC geometry are modeled to match the design provided by the manufacturer. Figure 3

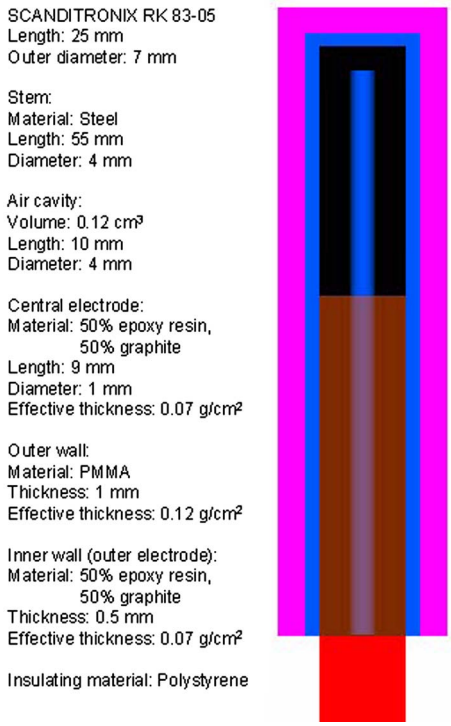

FIG. 3. A view of the internal components of the RK IC model. The internal and external electrodes consist of the same epoxy/graphite mixture. The bottom region is the beginning of the steel shaft. For more information about this IC, the reader is referred to Ref. 18.

shows the internal components of the RK chamber model, created using EGS_VIEW. The EGS_CHAMBER user code is a newly developed extension of CAVITY that uses several additional variance reduction techniques including photon cross-section enhancement,[34] intermediate phase space storage, and correlated sampling[35,36] to greatly enhance calculation efficiency over that which was previously achievable with CAVITY. For a more detailed discussion of the EGS_CHAMBER user code and/or the variance reduction techniques implemented within, the reader is referred to Ref. 32.

For these simulations, the "IC origin" is placed at the EPOM of the IC model, taken 1.2 mm ($0.6\times r_{cav}$) upstream from the geometrical center of the IC, also following the recommendations of AAPM TG-51 (Ref. 5) and IAEA TRS-398.[20] The CAVITY simulations use a $64\times40\times44$ cm^3 water phantom, while the EGS_CHAMBER simulations use a $60\times60\times2000$ cm^3 phantom. This difference in phantom size is not expected to affect the results. In the EGS_CHAMBER simulations the IC is simultaneously simulated at multiple depths in the phantom by utilizing intermediate phase space storage. ECUT is set to 0.521 MeV in these simulations.

All ionization calculations are run to $\leqslant1\%$ precision (one standard deviation) in water for all but a few voxels in air where "fat" electrons were scored. The most noticeable contributions from these electrons came in the EGS_CHAMBER simulations with the statistically worst voxels being in the 18 MV 40×40 cm^2 field simulation. The worst of these occurred 4.5 cm above the water surface where the statistical uncertainty was 8%. Five other voxels (out of 461 total) in this particular simulation are scored with uncertainties of $>1\%$.

II.C. Quantification of inflection region deviations and surface identification

Multiple methods could be used to determine variations in the location of the dose inflection point between various measurement field conditions or for deviations between measured and MC-simulated dose inflection locations. The aim of this portion of the study was to use a method that required as little data manipulation as possible. The method devised requires only calculation of each measurement curve's second derivative, d^2I/dx^2. This method works well when comparing measurements but the MC data proved too noisy for this technique to be useful. Therefore, the sum of the squared differences (SSQD) is used to quantify deviations in the dose inflection region between measurements and MC data for the various field conditions. In these comparisons, MC simulations are used as reference conditions in which the location of the water surface is known exactly with respect to the IC position. SSQD is computed using the formula,

$$\mathrm{SSQD}=\sum_x w_x[\mathrm{PDD}_{\mathrm{ref}}(x)-\mathrm{SF}\times\mathrm{PDD}_{\mathrm{test}}(x+\delta)]^2,$$

where ref and test refer to the reference and test conditions, SF represents a scaling factor used to account for the arbitrary normalization difference, δ represents the shift in the IC position between the ref and test depth dose conditions, and w_x represents a weighting factor taken as the inverse of the root mean squared combined variance of the ref and test data points at a given x. The variance of each measured data point is taken to be 1×10^{-10} (zero, for our purposes), while the variance of any MC-calculated data used is taken directly from the MC calculation. Results were found to be insensitive to the value of the constant variance assumed for the measurement data. Using this weighting allows the algorithm to give more importance to matching relatively well-determined data points while essentially ignoring points with larger variances. The summation is taken over depths x from 2.3 mm above the surface to 4.7 mm in water. This depth range is representative of the IC central electrode location, while the IC scans through the water surface from the point at which the IC reaches the water surface to the point at which the IC emerges fully into air. Doubling this range was shown to change any δ values by $\sim$0.1 mm. SF and δ are adjusted to minimize the SSQD to determine the deviation (δ) in the entrance dose inflection region for the IC. Alternatively, the MC data sets are smoothed using a Sovitzky–Golay filter as implemented by Kawrakow[37] and second derivatives are then computed and compared.

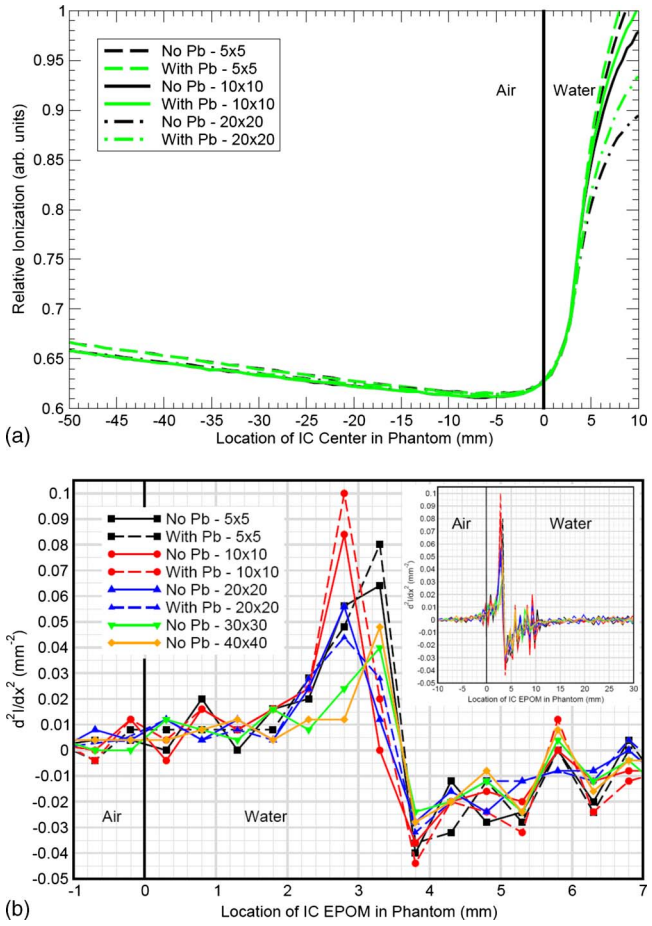

FIG. 4. (a) Measurements conducted with the RK IC for the 6 MV beam at various field sizes demonstrating that changes in field size and the with/without Pb foil differences in electron contamination do not affect the inflection location. (b) The second derivative of the measured relative ionization curve is plotted as a function of depth in the water tank. The insensitivity of the curves to these changes in beam conditions indicates that the major cause of the peak in the second derivative is the IC emerging from the water tank into air. The inset shows the same data plotted over a wider range of depths.

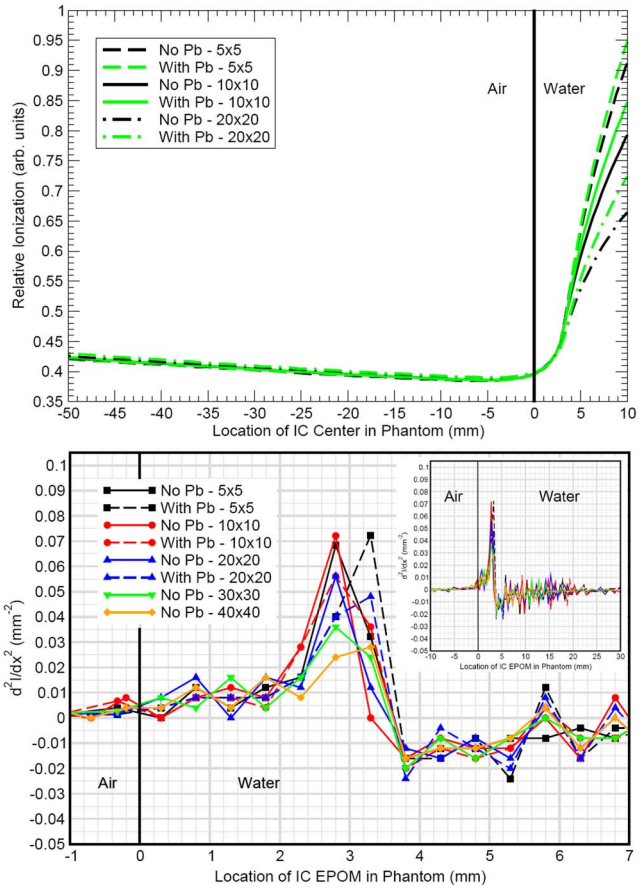

FIG. 5. (a) Measurements conducted with the RK IC for the 18 MV beam at various field sizes demonstrating that changes in field size and the with/without Pb foil differences in electron contamination do not affect the inflection location. (b) The second derivative of the measured relative ionization curve is plotted as a function of depth in the water tank. The insensitivity of the curves to these changes in beam conditions indicates that the major cause of the peak in the second derivative is the IC emerging from the water tank into air. The inset shows the same data plotted over a wider range of depths.

III. RESULTS

III.A. Clinical measurements

III.A.1. Field size and electron contamination effects on the inflection region

Figure 4 compares the 6 MV measurement results for three different field sizes, with and without a Pb foil located in the beam path. Figure 5 compares the 18 MV results. The location of the peak in the second derivative is independent of the field size and the with/without Pb foil differences in electron contamination. The 0.5 mm deviations observed correspond to the smallest resolution at which these measurements were taken; therefore, these deviations are not considered meaningful. The second derivative maximum occurs at a depth of ~3 mm. As is explained in Sec. III C, this corresponds to the point at which the IC leading edge physically emerges from water into air.

III.A.2. Beam energy effects on the inflection region

A comparison of measurements taken for a 10×10 cm^2 field with different beam energies is shown in Fig. 6. Although the 6 and 18 MV beams produce different depth ionization curves, the shape and location of the second derivative maximum do not vary by more than 0.5 mm. Logically, the size and shape of this region will be related to the IC dimensions. Again, the second derivative maximum occurs just as the IC emerges from the water into air, which occurs at the same depth for each measurement.

III.B. MC simulations

III.B.1. Dose calculations for 10×10 cm^2 *fields*

A comparison of simulation results with and without the IC present is shown in Fig. 7. Differences in the air region are immediately observable. Since the simulation without the IC present lacks contributions from secondary electrons produced within the chamber wall, these differences are to be

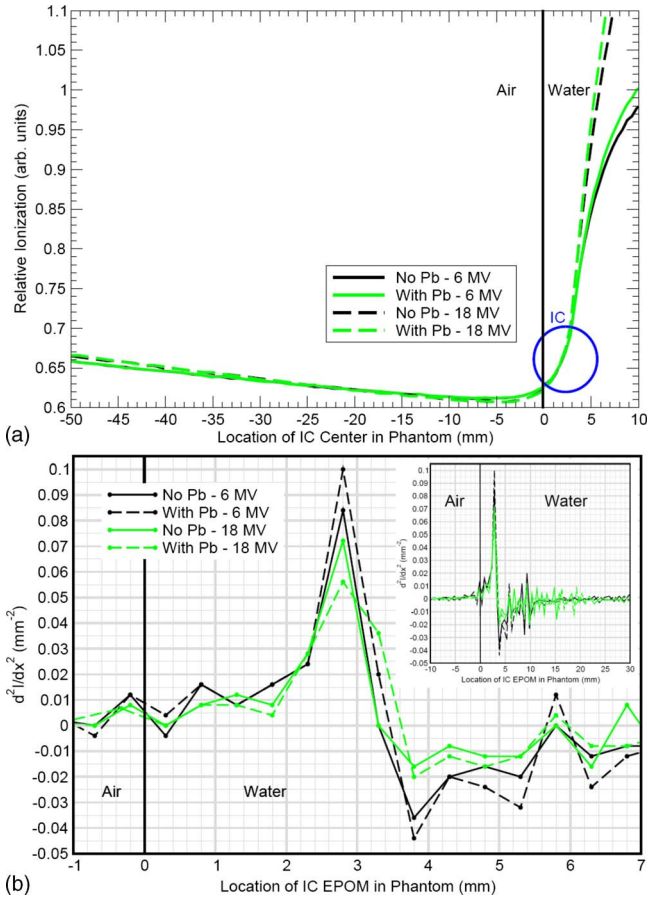

FIG. 6. (a) Comparison of the effect of contaminant electrons and different photon beam energies on the location of the inflection region for a 10 $\times$ 10 cm^2 field. The IC circle is intended to help guide the reader's eye to the inflection point. (b) The second derivative of the measured relative ionization curve is plotted as a function of depth in the water tank. The insensitivity of the curves to these changes in beam conditions indicates that the major cause of the peak in the second derivative is the IC emerging from the water tank into air. The inset shows the same data plotted over a wider range of depths.

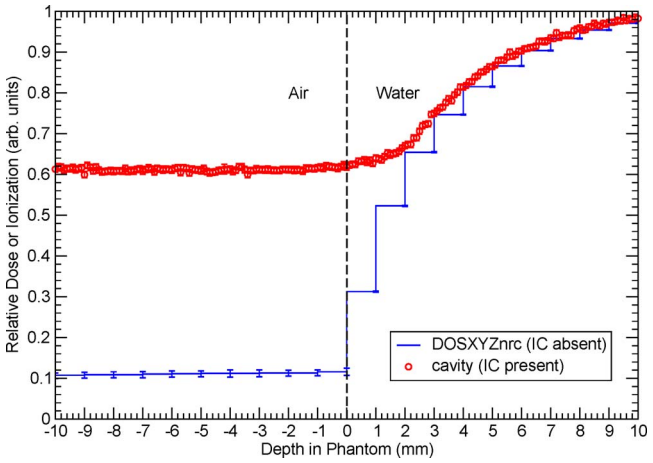

FIG. 7. Comparison of simulation results between CAVITY and DOSXYZnrc. Simulation with CAVITY allows for proper modeling of the cylindrical IC geometry, while DOSXYZnrc simulation only models dose to water. The dose differences observed over the first centimeter are attributable to the lack of contribution by secondary electrons produced within the IC wall to the dose deposited within the DOSXYZnrc simulation. The TG-51 recommended EPOM shift of 1.2 mm ($0.6 \times r_{cav}$) is applied to the CAVITY results.

expected. At the same time, excellent agreement is observed between the two simulations in water after d_{max}, confirming the $0.6 \times r_{cav}$ EPOM shift recommended by various dosimetry protocols. In the buildup region, the distance to agreement (DTA) varies, which can be attributed to a change in the EPOM shift as a function of depth, as has been shown elsewhere.[9,16] At the surface, DTA is over 2 mm, while by 1.0 cm depth, DTA is negligible. A comparison of CAVITY simulation results with measurement is shown in Fig. 8. The choice to shift measurement to MC in this figure, rather than vice versa, is made because the surface position is user defined in the MC simulation and therefore exactly known. The same cannot be said of the surface position in the measurements. Agreement within $(2.65 \pm 0.65)\%$ or better is observed at all depths.

III.B.2. Dose calculations for 40 $\times$ 40 cm^2 fields

The results of comparing measurement to MC simulation for the 40 $\times$ 40 cm^2 open field case, shown for 6 MV in Fig. 9 and for 18 MV in Fig. 10, exhibit poorer depth ionization agreement than the 6 MV 10 $\times$ 10 cm^2 field case. What appears to be an ionization overprediction after d_{max} is caused by the curve fitting algorithm being driven to minimize differences immediately surrounding the water surface. This will be described further in Sec. III C. However, the discrepancy is believed to be caused by an underestimate of the contribution from secondary electrons in the MC beam model. It may be the case that there is more of the observed edge-of-field shielding, previously mentioned in Sec. II B 1, present in the beam path than was previously believed. Further tuning of the beam model is an ongoing project.

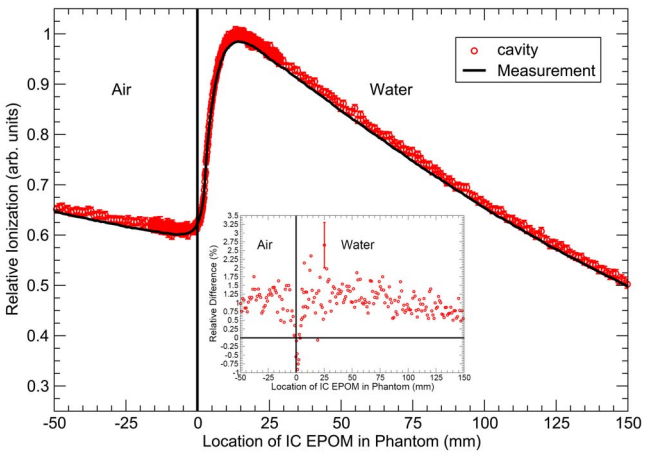

FIG. 8. Comparison of CAVITY simulation results with measurement for the 6 MV 10 $\times$ 10 cm^2 field case. The difference in the two curves along with the MC statistical uncertainty in the point of maximum discrepancy is shown in the inset. The TG-51 recommended EPOM shift of 1.2 mm ($0.6 \times r_{cav}$) is applied to the CAVITY results. The measurement curve displayed has been shifted and scaled to the CAVITY results by the δ and SF given by the algorithm.

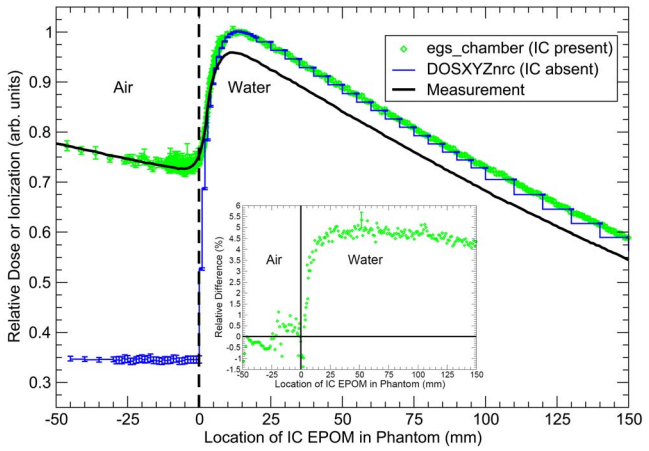

FIG. 9. Comparison of measurement and results of simulation with and without the IC present for the 6 MV 40×40 cm^2 field case. The difference between EGS_CHAMBER and measurement along with the MC statistical uncertainty in the point of maximum discrepancy is shown in the inset. The TG-51 recommended EPOM shift of 1.2 mm ($0.6\times r_{cav}$) is applied to the EGS_CHAMBER results. The measurement curve displayed has been shifted and scaled to the EGS_CHAMBER results by the δ and SF given by the algorithm.

III.B.3. BEAMnrc inspection of electron contamination with Pb foil

The variations in electron energy spectra at the phantom surface when increasing field size from 10×10 to 40×40 cm^2, as computed via MC simulation, are shown for the 6 MV beam in Fig. 11. The analogous results for the 18 MV beam are shown in Fig. 12. While electron energy increases with beam energy, the more important result is the change in the shape of the energy fluence distribution for the 40×40 cm^2 field at both beam energies when the Pb foil is placed in the beam. Doing so reduces the electron energy fluence distributions to appear very similar to those resulting from 10×10 cm^2 fields. These results increase the confidence that the deviations shown in the previous section result from an improperly modeled treatment head component, most likely the aforementioned edge-of-field shielding around the mirror. Small modifications to this modeling are likely to affect electron fluence but not the relative impact of the Pb foil demonstrated by a change in shape of the electron energy fluence distribution.

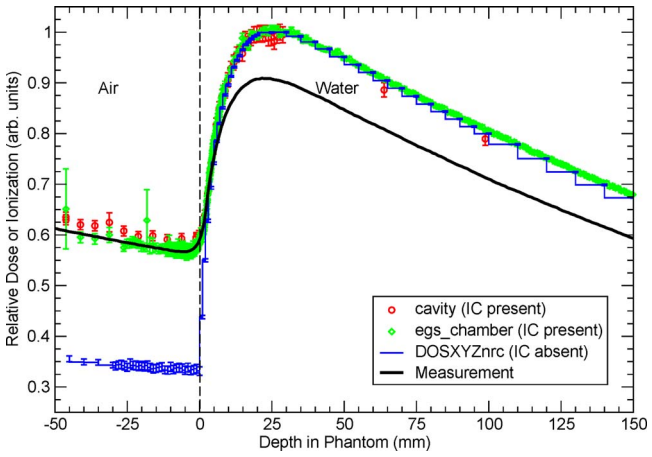

FIG. 10. Comparison of measurement and results of simulations with and without the IC present for the 18 MV 40×40 cm^2 field case. The discrepancy between measurement and both CAVITY and EGS_CHAMBER in the water region is caused by forcing the algorithm to focus on deviations near the surface with improperly modeled electron contamination from the previously mentioned edge-of-field shielding. The measured curve has been shifted to match the EGS_CHAMBER curve due to the much larger number of data points calculated with this code. The CAVITY curve is shown in the interest of comparison. The noticeably larger error bars around two of the in-air doses calculated with EGS_CHAMBER are attributable to contributions from "fat" electrons in these voxels. The TG-51 recommended EPOM shift of 1.2 mm ($0.6\times r_{cav}$) is applied to the CAVITY and EGS_CHAMBER results. The measurement curve displayed has been shifted and scaled to the EGS_CHAMBER results by the δ and SF given by the algorithm.

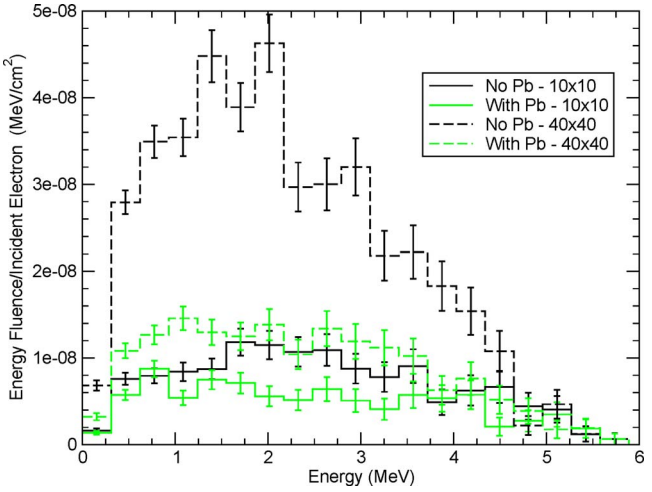

FIG. 11. Examination of the influence of the Pb foil on electron energy fluence from the 6 MV beam. Energy fluence is displayed as a histogram over 20 equally spaced energy bins from 0 MeV to the maximum energy of the particles.

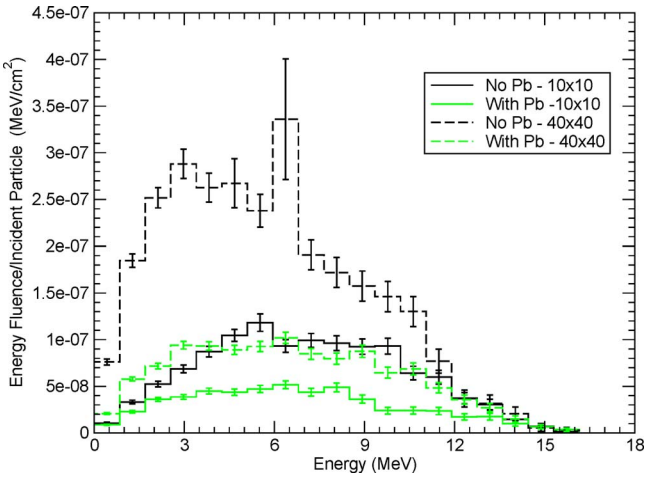

FIG. 12. Examination of the influence of the Pb foil on electron energy fluence from the 18 MV beam. Energy fluence is displayed as a histogram over 20 equally spaced energy bins from 0 MeV to the maximum energy of the particles.

TABLE I. IC inflection location offsets (δ) for comprisons of measurement and MC simulation. The data taken as the baseline (ref) for the comparison are shown in the left column, while the shifted data (set) are displayed across the top.

				Measurement			
				6 MV			18 MV
				10×10		40×40	40×40
			Test	Pb	No Pb	No Pb	No Pb
	Ref			δ (mm)	δ (mm)	δ (mm)	δ (mm)
CAVITY	6 MV	10×10	No Pb	···	−0.596	···	···
EGS_CHAMBER	6 MV	10×10	Pb	−0.700	···	···	···
			No Pb	···	−0.609	···	···
		40×40	No Pb	···	···	−1.064	···
	18 MV	40×40	No Pb	···	···	···	−1.200

III.C. Measurement surface identification

The minimization algorithm described in Sec. II C was applied to the data in Figs. 8–10. For the 6 MV 10×10 cm^2 field case, it was determined that the measurement data required a shift of δ=−0.596 mm and a scaling factor of SF=0.9837 to match the measurements to the MC results, where the negative shift denotes a shift upstream toward the treatment head. This shift between measurements and simulations performed for reference conditions indicates that the true water surface was actually ~0.6 mm downstream of where it was defined in the measurement acquisition software, i.e., zero depth. Note that the scaling factors are measured in arbitrary units and are not pertinent to the results stated here; therefore, they are not stated for any other cases. For the 6 MV 40×40 cm^2 field case, the shift determined was δ=−1.064 mm. For the 18 MV 40×40 cm^2 field case, the shift was δ=−1.200 mm. The full results of these comparisons are shown in Table I. The results of the Sovitzky–Golay smoothing are shown in Fig. 13. A peak occurs at ~2.2 mm depth for 6 MV 10×10 cm^2 field simulations. Comparison with the peak shown in Fig. 4(b) at 2.8 mm for 6 MV 10×10 cm^2 field measurements indicates a −0.6 mm IC offset, which agrees with the offset found by the SSQD minimization algorithm. A peak at ~2.2 mm is also visible for 40×40 cm^2 field simulations with a Pb foil in the beam path. The foil reduces electron contamination, allowing the peak to become visible, while simulations at the same field size without the Pb foil in place are dominated by noise so as to obscure the peak. This noise causes the discrepancies observed in Table I as the SSQD minimization algorithm "pulls" the measured data toward agreement with the MC data. The second derivative computation method of finding IC offsets is more robust to noise than the SSQD minimization method, which has a clear dependence on electron contamination. When the IC reaches the water surface, the central electrode is at a depth at 3.5 mm. Subtracting from this the 1.2 mm recommended EPOM shift gives an expected inflection peak location of 2.3 mm. The inflection peak in the smoothed MC data at ~2.2 mm agrees to ~0.1 mm. When one subtracts the ~0.6 mm setup offset found in the measurements, the inflection peak in the measured data at ~3 mm also agrees at the ~0.1 mm level.

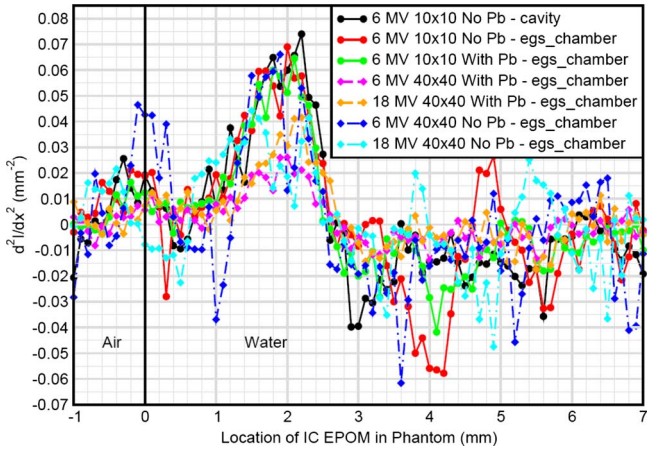

FIG. 13. The second derivatives of the MC-calculated relative ionization curves are plotted as a function of depth in the water tank. Peaks in the second derivative are visible at ~2.2 mm depth for 6 MV 10×10 cm^2 simulations (solid lines). Simulations performed for 40×40 cm^2 fields with a Pb foil in the beam path also exhibit peaks at this depth (dashed lines). Without the Pb foil in place, the peaks for these fields are obscured by noise caused by electron contamination (dot-dashed lines).

IV. DISCUSSION

In this work, the inflection region that exists in IC measurements at the air-water interface is used to determine the water surface location for depth ionization scanning. Measurements are performed with a variety of field conditions, demonstrating that the location of this inflection region is nearly invariant (within ~0.5 mm) to beam energy and reasonable variations in contaminant electrons. These measurements are fit to MC simulations to determine the absolute surface location offset δ. It is expected that this offset will be setup dependent. In this study, the δ values found are small since the IC is carefully aligned to the surface location. There is no requirement that δ be small—in fact, one could set up an IC at an arbitrary reference depth and use the through-interface scan to automatically identify the surface location. However, while it should be possible to find an offset of any amount using this procedure, the IC setup is not

unimportant. Careful IC alignment should result in a small offset, if any, found by application of the proposed method. However, if any such errors should exist, this method should make them easier to identify. Use of this method to identify the surface might heighten the focus on initial IC setup—following application of an automatic surface identification, a user should be able to visually inspect and validate the setup.

MC simulations are used as a reference for identifying the absolute surface location with respect to the IC in this work. Even without an absolute surface reference, the method of scanning through the air-water interface can improve dosimetric reproducibility. Measurements with a given IC at a given institution should agree in the ionization inflection region from one setup to the next, such as measurements made for initial accelerator commissioning and annual machine QA. Deviations in the surface ionization inflection regions should make the variability due to user setup readily observable. For measurements taken under the same field conditions, direct comparison of the depth ionization curves should reveal any shift. For measurements taken under different field conditions, the variability can be assessed by analyzing the peaks in the second derivative of ionization. Matching these data should result in a more consistent data acquisition from year to year and from physicist to physicist. In the context of this work, application of this scanning method could have avoided the deviations observed in Fig. 1. Without scanning through the air-water interface (as is the current clinical convention), there is no way to correct data offline if an error is discovered after the setup has been taken down. (In fact, such errors are likely to go undetected.) In the case that a setup error is detected, current scanning methods require a new setup and series of measurements to obtain depth ionization data. An offline correction, such as that possible using the ionization inflection region, renders this unnecessary.

The results presented in this paper only provide information sufficient to determine the surface location for a single IC, the Scanditronix RK IC. No general recommendations or prescriptions to determine the surface location from the location of the inflection region can be made having tested the method on data acquired with one type of IC. With that said, there is no reason that the method itself shouldn't be applicable to any arbitrary IC design, including parallel-plate ICs. The inflection region-matching method of surface identification should also apply for other sources of radiation although the size (and possibly the shape) of the perturbation may be radiation type dependent. In fact, Das *et al.* previously demonstrated the utility of scanning past the surface for electron beams.[38] The difference between their work and this work lies in the surface localization method. Due to the more linear buildup response in electron beams, Das *et al.* were able to use simple linear fitting to find the surface with one function representing the dose in air and the other representing dose in water. Given these two linear functions, valid to first approximation for electron dose near the water surface, both the surface position and dose at that depth can be found. However, this method is inadequate for photon beams due to the greater curvature of the depth dose curve in the buildup region. The application of our method to electron beam dosimetry will be a focus of future work.

Examining the relationship between the PDI inflection region and the water surface with other IC designs is a goal of future work. Broadening the study will be made simpler by the use of other methods of surface localization such as precise measurements for each IC design and the efficient MC user code, EGS_CHAMBER. The MC simulation portion of this work has been CPU intensive and time consuming. The CAVITY simulation results shown in this work required over 4400 (40 3 GHz CPUs $\times$ 110 h/simulation) and 6000 CPU hours (150 h/simulation) for the 6 and 18 MV cases, respectively. In contrast, the 6 MV open field results obtained with EGS_CHAMBER required just under 360 CPU hours (45 3 GHz CPUs $\times$ 8 h/simulation). The measurements taken in this study were all conducted at one scanning speed starting from depth in water and ending in air, with the water tank set at a single SSD. It is possible that reversing this scanning direction, varying the speed of measurement acquisition, and/or changing the SSD may have some impact on the shape and position of the inflection region. These effects are to be studied as part of future work. Inspection of the effect of factoring out the inverse square dependence of the in-air data showed no change in the results. The $\sim$0.1 mm agreement between the theoretical IC EPOM location at the water surface and that found in this study indicates the suitability of the $0.6 \times r_{cav}$ EPOM prescription in this work. Therefore, while an EPOM correction that varied as a function of depth could have been applied, this correction, if at all noticeable, would have been secondary to the issue of IC offset. The insensitivity of the measured IC-produced inflection region to field size, secondary electron contamination, and even beam energy implies that a single accurate determination of the phantom surface location with respect to the inflection region for a given IC design should be sufficient. Thus it is possible that one-time precise physical measurements for each IC model would be adequate to characterize the entrance region inflection region-surface correspondence. These measurements would most likely require some way of aligning the chamber with more precision than that of which the human eye is capable. Despite best efforts at initial alignment in this work, a -0.6 mm offset persists. Such measurements could be performed, for example, by a standard laboratory. Measurements with other IC designs will also prove useful to test the hypothesis, not tested here, that the location of the surface inflection region will be IC design dependent with the strongest dependencies being on the outer diameter of the IC wall and the wall thickness. A series of one-time MC simulations or precise measurements for each IC design could be used to quantify the inflection region location for each IC design, and from that, the surface location.

V. CONCLUSIONS

This work outlines a method for improving the accuracy and precision of initial IC setup at a water surface with the goal of improving the reproducibility and reliability of depth

ionization data. The method consists of scanning with the IC beyond the air-water interface to measure the ionization inflection region characteristic of the given IC. Scanning through the surface in this fashion allows standardization of surface definition, simplification of measurement setup procedures, reduction in user-to-user variability, and improvement of measurement reliability. This improved reliability is useful for a variety of tasks including MC model validation and treatment planning system commissioning. The measurement method provides a way to determine, and correct for, any offsets in IC setup that previously would have been impossible to quantify. Although this work used extensive MC simulations, clinical application of this surface matching procedure would require no user-specific MC calculations. The measured insensitivity of the inflection location to field size, beam energy, and electron contamination implies that reference data obtained for a given IC, either from MC simulations or precise measurements, should be sufficient to characterize the inflection region-surface location relationship.

ACKNOWLEDGMENTS

The authors thank Leif Gustafsson of Scanditronix-Wellhöfer for providing the RK IC report. They also thank Malcolm McEwen of NRC Canada for valuable discussion regarding the project.

[a]This work was presented in part at the annual AAPM meeting in Houston, 2008.
[b]Electronic mail: verversjd@vcu.edu

[1]I. J. Das, C. W. Cheng, R. J. Watts, A. Ahnesjo, J. Gibbons, X. A. Li, J. Lowenstein, R. K. Mitra, W. E. Simon, and T. C. Zhu, "Accelerator beam data commissioning equipment and procedures: Report of the TG-106 of the Therapy Physics Committee of the AAPM," Med. Phys. **35**(9), 4186–4215 (2008).
[2]G. J. Kutcher *et al.*, "Comprehensive QA for radiation oncology: Report of AAPM Radiation Therapy Committee Task Group 40," Med. Phys. **21**(4), 581–618 (1994).
[3]R. Nath, P. J. Biggs, F. J. Bova, C. C. Ling, J. A. Purdy, J. van de Geijn, and M. S. Weinhous, "AAPM code of practice for radiotherapy accelerators: Report of AAPM Radiation Therapy Task Group No. 45," Med. Phys. **21**(7), 1093–1121 (1994).
[4]B. Fraass, K. Doppke, M. Hunt, G. Kutcher, G. Starkschall, R. Stern, and J. Van Dyk, "American Association of Physicists in Medicine Radiation Therapy Committee Task Group 53: quality assurance for clinical radiotherapy treatment planning," Med. Phys. **25**(10), 1773–1829 (1998).
[5]P. R. Almond, P. J. Biggs, B. M. Coursey, W. F. Hanson, M. S. Huq, R. Nath, and D. W. O. Rogers, "AAPM's TG-51 protocol for clinical reference dosimetry of high-energy photon and electron beams," Med. Phys. **26**(9), 1847–1870 (1999).
[6]I. J. Chetty, B. Curran, J. E. Cygler, J. J. DeMarco, G. Ezzell, B. A. Faddegon, I. Kawrakow, P. J. Keall, H. Liu, C. M. Ma, D. W. O. Rogers, J. Seuntjens, D. Sheikh-Bagheri, and J. V. Siebers, "Report of the AAPM Task Group No. 105: Issues associated with clinical implementation of Monte Carlo-based photon and electron external beam treatment planning," Med. Phys. **34**(12), 4818–4853 (2007).
[7]B. J. Gerbi and F. M. Khan, "Measurement of dose in the buildup region using fixed-separation plane-parallel ionization chambers," Med. Phys. **17**(1), 17–26 (1990).
[8]W. Abdel-Rahman, J. P. Seuntjens, F. Verhaegen, F. Deblois, and E. B. Podgorsak, "Validation of Monte Carlo calculated surface doses for megavoltage photon beams," Med. Phys. **32**(1), 286–298 (2005).
[9]M. R. McEwen, I. Kawrakow, and C. K. Ross, "The effective point of measurement of ionization chambers and the build-up anomaly in MV x-ray beams," Med. Phys. **35**(3), 950–958 (2008).
[10]I. Kawrakow, "Efficient photon beam treatment head simulations," Radiother. Oncol. **81**(1), S82 (2006).
[11]B. R. B. Walters and I. Kawrakow, "Technical note: Overprediction of dose with default PRESTA-I boundary crossing in DOSXYZnrc and BEAMnrc," Med. Phys. **34**(2), 647–650 (2007).
[12]O. Chibani and C. M. Ma, "On the discrepancies between Monte Carlo dose calculations and measurements for the 18 MV Varian photon beam," Med. Phys. **34**(4), 1206–1216 (2007).
[13]C. L. Hartmann Siantar, R. S. Walling, T. P. Daly, B. Faddegon, N. Albright, P. Bergstrom, A. F. Bielajew, C. Chuang, D. Garrett, R. K. House, D. Knapp, D. J. Wieczorek, and L. J. Verhey, "Description and dosimetric verification of the PEREGRINE Monte Carlo dose calculation system for photon beams incident on a water phantom," Med. Phys. **28**(7), 1322–1337 (2001).
[14]G. X. Ding, "Dose discrepancies between Monte Carlo calculations and measurements in the buildup region for a high-energy photon beam," Med. Phys. **29**(11), 2459–2463 (2002).
[15]G. X. Ding, C. Duzenli, and N. I. Kalach, "Are neutrons responsible for the dose discrepancies between Monte Carlo calculations and measurements in the build-up region for a high-energy photon beam?," Phys. Med. Biol. **47**(17), 3251–3261 (2002).
[16]I. Kawrakow, "On the effective point of measurement in megavoltage photon beams," Med. Phys. **33**(6), 1829–1839 (2006).
[17]R. Capote, R. Jeraj, C. M. Ma, D. W. O. Rogers, F. Sanchez-Doblado, J. Sempau, J. Seuntjens, and J. Siebers, "Phase-space database for external beam radiotherapy: Summary report of a consultants' meeting," IAEA International Nuclear Data Committee Report No. INDC (NDS)-0484, 2006.
[18]K.-A. Johansson, R. Karlsson, and A. Thilander, "A small cylindric air ionization chamber with watertight protection, type RK 83-05: Tests according to international recommendations and evaluation of the applicability of these recommendations," University of Gothenburg Department of Radiation Physics Report No. GU-RADFYS 87:13, 1987.
[19]"Ionization chambers and diode detectors—Detectors for relative and absolute dosimetry," IBA Dosimetry America, Bartlett, TN, 2007.
[20]P. Andreo, D. T. Burns, K. Hohlfeld, M. S. Huq, T. Kanai, F. Laitano, V. Smyth, and S. Vynckier, "Absorbed dose determination in external beam radiotherapy: An international Code of Practice for Dosimetry based on Standards of Absorbed Dose to Water," International Atomic Energy Agency Report No. TRS-398, 2001.
[21]I. Kawrakow, "Accurate condensed history Monte Carlo simulation of electron transport. I. EGSnrc, the new EGS4 version," Med. Phys. **27**(3), 485–498 (2000).
[22]I. Kawrakow, "Accurate condensed history Monte Carlo simulation of electron transport. II. Application to ion chamber response simulations," Med. Phys. **27**(3), 499–513 (2000).
[23]I. Kawrakow and D. W. O. Rogers, "The EGSnrc code system: Monte Carlo simulation of electron and photon transport," National Research Council of Canada Report No. PIRS-701, 2003.
[24]D. W. O. Rogers, B. R. B. Walters, and I. Kawrakow, "BEAMnrc Users Manual," National Research Council of Canada Report No. PIRS-0509(A)revK, 2006.
[25]E. Tonkopi, M. R. McEwen, B. R. B. Walters, and I. Kawrakow, "Influence of ion chamber response on in-air profile measurements in megavoltage photon beams," Med. Phys. **32**(9), 2918–2927 (2005).
[26]I. Kawrakow and B. R. B. Walters, "Efficient photon beam dose calculations using DOSXYZnrc with BEAMnrc," Med. Phys. **33**(8), 3046–3056 (2006).
[27]B. Libby, J. Siebers, and R. Mohan, "Validation of Monte Carlo generated phase-space descriptions of medical linear accelerators," Med. Phys. **26**(8), 1476–1483 (1999).
[28]J. V. Siebers, P. J. Keall, B. Libby, and R. Mohan, "Comparison of EGS4 and MCNP4b Monte Carlo codes for generation of photon phase space distributions for a Varian 2100C," Phys. Med. Biol. **44**(12), 3009–3026 (1999).
[29]P. J. Keall, J. V. Siebers, B. Libby, and R. Mohan, "Determining the incident electron fluence for Monte Carlo-based photon treatment planning using a standard measured data set," Med. Phys. **30**(4), 574–582 (2003).
[30]I. Kawrakow, D. W. Rogers, and B. R. Walters, "Large efficiency improvements in BEAMnrc using directional bremsstrahlung splitting," Med. Phys. **31**(10), 2883–2898 (2004).
[31]C. M. Ma and D. W. O. Rogers, "BEAMDP as a general-purpose utility," National Research Council of Canada Report No. PIRS-0509(C)revA,

2006.
[32]J. Wulff, K. Zink, and I. Kawrakow, "Efficiency improvements for ion chamber calculations in high energy photon beams," Med. Phys. **35**(4), 1328–1336 (2008).
[33]I. Kawrakow, "egspp: the EGSnrc C++ class library," National Research Council of Canada Report No. PIRS-899, 2005.
[34]E. S. Ali and D. W. O. Rogers, "Efficiency improvements of x-ray simulations in EGSnrc user-codes using bremsstrahlung cross-section enhancement (BCSE)," Med. Phys. **34**(6), 2143–2154 (2007).
[35]C. M. Ma and A. E. Nahum, "Calculation of absorbed dose ratios using correlated Monte Carlo sampling," Med. Phys. **20**(4), 1189–1199 (1993).
[36]L. A. Buckley, I. Kawrakow, and D. W. O. Rogers, "CSnrc: Correlated sampling Monte Carlo calculations using EGSnrc," Med. Phys. **31**(12), 3425–3435 (2004).
[37]I. Kawrakow, "On the de-noising of Monte Carlo calculated dose distributions," Phys. Med. Biol. **47**(17), 3087–3103 (2002).
[38]I. J. Das, S. W. McNeeley, and C. W. Cheng, "Ionization chamber shift correction and surface dose measurements in electron beams," Phys. Med. Biol. **43**(11), 3419–3424 (1998).

Vita

James Douglas Ververs was born on February 23, 1985, in Oswego, New York, and is an American citizen. He graduated from Hannibal High School, Hannibal, New York in 2002. He received his Bachelor of Science in Physics and Bachelor of Arts in Mathematics from University of Rochester, Rochester, New York in May 2006 and joined the Virginia Commonwealth University Medical Physics Graduate Program in August 2006, working in the research group of Dr. Jeffrey Siebers. To date, he has contributed to six peer-reviewed national or international meeting abstracts and has published one peer-reviewed research article as primary author, entitled *A method to improve accuracy and precision of water surface identification for photon depth dose measurements*. He was named a Finalist in the American Association of Physicists in Medicine Young Investigators Competition in 2009.